

UCLA

UCLA Electronic Theses and Dissertations

Title

Kinematic Pile-Soil Interaction in Liquefied and Nonliquefied Ground

Permalink

<https://escholarship.org/uc/item/24v817mp>

Author

Turner, Benjamin

Publication Date

2016

Peer reviewed|Thesis/dissertation

UNIVERSITY OF CALIFORNIA

Los Angeles

Kinematic Pile-Soil Interaction in Liquefied and Nonliquefied Ground

A dissertation submitted in partial satisfaction of the

requirements for the degree Doctor of Philosophy

in Civil Engineering

by

Benjamin Turner

2016

© Copyright by
Benjamin Turner
2016

ABSTRACT OF THE DISSERTATION

Kinematic Pile-Soil Interaction for Liquefied and Nonliquefied Ground

by

Benjamin Turner

Doctor of Philosophy in Civil Engineering

University of California, Los Angeles, 2016

Professor Scott Joseph Brandenberg, Chair

In Part I of this dissertation, equivalent static analysis (ESA) procedures for computing foundation demands during lateral spreading are applied to two parallel bridges that were damaged during the 2010 **M** 7.2 El Mayor-Cucapah earthquake in Baja California, Mexico. A railroad bridge span collapsed, whereas the adjacent highway bridge survived with one support pier near the river having modest flexural cracking of cover concrete. Cone penetration and geophysical test results are presented along with geotechnical and structural conditions evaluated from design documents. ESA using a beam-on-Winkler foundation model is found to accurately predict observed responses when liquefaction-compatible inertia demands are represented as spectral displacements that account for resistance from other bridge components. Pier columns for the surviving bridge effectively resisted lateral spreading demands in part because of restraint provided by the superstructure. Collapse of the surviving bridge is incorrectly predicted when inertial demands are

computed for the individual bent in isolation from other components, and are represented by forces that do not consider global restraint.

In Part II, results of a parametric study of the influence of kinematic pile-soil interaction on foundation-input motions (FIM) are presented. One-dimensional nonlinear ground response analysis was used to define free-field motions, which were subsequently imposed on a beam-on-nonlinear-dynamic-Winkler-foundation pile model. The free-field ground surface motion (FFM) and top-of-pile “foundation-input motion” (FIM) computed from these results were then used to compute transfer functions and spectral ratios for use with the substructure method of seismic analysis. A total of 1,920 parametric combinations of different pile sizes, soil profiles, and ground motions were analyzed.

Results of the study show that significant reductions of the FFM occur for stiff piles in soft soil, which could result in a favorable reduction in design demands for short-period structures. Group effects considering spatially-variable (incoherent) ground motions are found to be modest over the footprint of a typical bridge bent, resulting in an additional reduction of FFM by 10 percent or less compared to an equivalent single pile. This study aims to overcome limitations of idealistic assumptions that have been employed in previous studies such as linear-elastic material behavior, drastically simplified stratigraphy, and harmonic oscillations in lieu of real ground motions. In order to capture the important influence of more realistic conditions such as material nonlinearity, subsurface heterogeneity, and variable frequency-content ground motions, a set of models for predicting transfer functions and spectral ratios has been developed through statistical regression of the results from this parametric study. These allow foundation engineers to predict kinematic pile-soil interaction effects without performing dynamic pile analyses.

The dissertation of Benjamin Turner is approved

Anne Lemnitzer

John Wright Wallace

Jonathan Paul Stewart

Scott Joseph Brandenburg, Committee Chair

University of California, Los Angeles

2016

This work is dedicated to those who have lost their lives during earthquakes. May our profession continue to advance so that structures in seismic areas around the world are safer.

CONTENTS

ABSTRACT OF THE DISSERTATION.....	II
CONTENTS.....	VI
LIST OF FIGURES	XII
LIST OF TABLES	XXVI
LIST OF SYMBOLS	XXVIII
ACKNOWLEDGMENTS	XXXII
VITA	XXXIV
1 INTRODUCTION.....	1
PART I: EVALUATION OF COLLAPSE AND NON-COLLAPSE OF PARALLEL BRIDGES AFFECTED BY LIQUEFACTION AND LATERAL SPREADING	3
2 INTRODUCTION TO PART I	4
3 SITE DESCRIPTION AND INVESTIGATION	7
3.1 Regional and Local Geology	7
3.2 Site topography and surface conditions	10
3.3 Subsurface Conditions	14
3.3.1 Previous Subsurface Investigations by Others.....	14
3.3.2 Subsurface Investigation for this Study	16
3.3.3 Interpretation of V_s Profile	20
3.4 Bridge Details	24
3.4.1 Highway Bridge (HWB).....	24
3.4.2 Railroad Bridge (RRB)	28
3.5 April 4, 2010 M 7.2 El Mayor-Cucapah Earthquake.....	29
3.6 Observed Damage.....	33
3.6.1 Ground Deformation.....	33

3.6.2	Structural Damage	35
4	ANALYSIS	39
4.1	Soil Properties	42
4.2	Lateral Spreading Displacement	50
4.3	Modeling of Structural Elements	54
4.3.1	Moment-Curvature Analysis	59
4.3.2	Elastomeric Bearings and Shear Tabs	61
4.4	Inertial Loads from Superstructure	65
4.4.1	Restraint-Compatible Spectral Displacement Method	69
4.4.2	Inertial Force Method	71
4.5	<i>Opensees</i> Finite-Element Analysis	72
4.6	Results	73
4.6.1	Response of Highway Bridge to Lateral Loading	73
4.6.2	Response of Railroad Bridge	75
4.6.3	Comparison of Combined Kinematic and Inertial Demand Methods	79
4.6.4	Settlement of Highway Bridge Bent 6	82
5	INTERACTION OF ADJACENT FOUNDATIONS DURING LATERAL SPREADING	86
5.1	Definitions of Pinning and Shielding	87
5.2	Approach	92
5.3	Results	98
5.4	Influence of Lateral Spread Length	100
5.5	Summary	102
6	CONCLUSIONS	105
	PART II: INFLUENCE OF KINEMATIC PILE-SOIL INTERACTION ON FOUNDATION INPUT MOTIONS FOR BRIDGES SUPPORTED ON DEEP FOUNDATIONS	110
7	INTRODUCTION TO PART II	111
7.1	Organization	114
7.2	Fundamentals	116

7.3	Previous Studies.....	127
7.3.1	Winkler Analysis and p - y Curves	127
7.3.2	Analytical and Numerical Solutions for Pile Dynamics	131
7.3.3	Normalization Schemes	136
7.3.4	Limitations of Elastic and Analytical Solutions	142
7.3.5	Experimental Investigations.....	145
7.3.6	Empirical Observations of Kinematic Pile-Soil Interaction	146
7.4	Kinematic SSI in Building Codes	159
7.5	Notes on Terminology and Notation.....	160
8	ELASTIC ANALYTICAL AND NUMERICAL SOLUTIONS	162
8.1	Elastic Analytical solution	162
8.2	Elastic Numerical Solution	170
8.3	Elastic Winkler Modulus	175
8.3.1	Terminology and Units	175
8.3.2	Previous Definitions of K_e	176
8.3.3	Diameter Effects	182
8.4	Questions of Pile Mass and inertia.....	185
8.5	Pile-Soil System Fundamental Frequency and Resonance.....	186
9	ANALYSIS	189
9.1	Approach.....	189
9.2	Parametric Study Bounds.....	190
9.3	<i>PySimple3</i> —Motivation and Model Updates.....	191
9.3.1	Motivation.....	192
9.3.2	Governing Equations and <i>OpenSees</i> Implementation.....	194
9.4	<i>PySimple3</i> —Parameter values	198
9.4.1	Initial Elastic Stiffness K_e	198
9.4.2	Ultimate Resistance	200
9.4.3	Curvature Parameter and Yield Force.....	200
9.4.4	Radiation Damping	206
9.5	Pile modeling	213
9.5.1	Pile Moment-Curvature Behavior.....	214

9.5.2	Pile Head Fixity Condition	217
9.5.3	Pile Shear Deformations	219
9.5.4	Pile Groups.....	221
9.6	SOIL PROFILES for Analyses.....	222
9.7	Ground Motions	224
9.7.1	Baker et al. (2011) Ground Motion Suite	224
9.7.2	Ground Response Analyses	228
9.7.3	Ground Motion Incoherence.....	230
9.8	OpenSEES Analysis.....	235
10	RESULTS	236
10.1	Single Piles.....	236
10.2	Normalized Results using Dimensionless Frequency.....	249
10.3	Controlling Parameters and Comparison to Elastic Solutions.....	253
10.4	Generalized Models for Predicting Transfer Functions.....	262
10.4.1	Functional Form.....	266
10.4.2	Approach.....	268
10.4.3	Models for Predicting Fixed-Head Transfer Function Coefficients	271
10.4.4	Models for Predicting Free-Head Displacement Transfer Function Coefficients	278
10.4.5	Models for Predicting Free-Head Rotation Transfer Function Coefficients	282
10.5	Generalized Models for Predicting Spectral Ratios.....	287
10.5.1	Functional Form.....	288
10.5.2	Models for Predicting Fixed-Head Spectral Ratio Coefficients	290
10.5.3	Models for Predicting Free-Head Spectral Ratio Coefficients	297
10.6	Pile Group Results	301
11	COMBINATION OF INERTIAL AND KINEMATIC PILE-SOIL INTERACTION.....	305
11.1	Combining Inertial and Kinematic SSI.....	305
11.1.1	Linear-Elastic SDOFO-Pile-Soil System.....	308
11.1.2	Effects of SDOFO Properties.....	319
11.1.3	Effect of Pile-Soil Kinematic Interaction Corner Frequency versus SDOFO Fundamental Frequency.....	322

11.1.4	Effect of Pile-Soil Interaction Nonlinearity	324
12	EXAMPLE APPLICATIONS OF TRANSFER FUNCTION AND SPECTRAL RATIO PREDICTION MODELS	332
12.1	Empirical Case Studies	332
12.1.1	Sendai, Japan Site after Givens et al. (2012)	332
12.1.2	Lancaster, California Site after Kim and Stewart (2003).	338
12.2	Example application of spectral Ratio Prediction Model for Pile-Supported Bridge.....	344
13	CONCLUSIONS AND RECOMMENDATIONS FOR ENGINEERING PRACTICE.....	351
13.1	Predictive models and limitations	356
13.2	Reinterpretation of Empirical Case Studies	357
13.3	Future Research Needs	359
APPENDIX A:	SUBSURFACE INVESTIGATIONS FOR MEXICO BRIDGES SITE	361
APPENDIX B:	LABORATORY TEST RESULTS FOR MEXICO BRIDGES PROJECT 366	
APPENDIX C:	SAMPLE CALCULATIONS FOR LATERAL SPREADING EQUIVALENT-STATIC ANALYSIS PROCEDURE.....	368
APPENDIX D:	SITE PROFILES FOR KINEMATIC PILE-SOIL INTERACTION ANALYSIS.....	384
D.1	Introduction.....	385
D.2	Site 1	386
D.3	Site 2	387
D.4	Site 3	389
D.5	Site 4	390
D.6	Site 5	392
D.7	Site 6	393
APPENDIX E:	A FRAMEWORK FOR FULL-SCALE EXPERIMENTAL MEASUREMENTS OF KINEMATIC PILE-SOIL INTERACTION.....	395
E.1	Pilot Study.....	397

E.2	Results	400
REFERENCES FOR PART I.....		402
REFERENCES FOR PART II		409

LIST OF FIGURES

Figure 3-1: Regional map and key geologic features. Fault rupture zones after GEER (2010); Cerro Prieto and Imperial Faults after Pacheco et al. (2006). Google Earth base image.	9
Figure 3-2: View of site looking west across the <i>Río Colorado</i> from atop the east river bank. People standing near the river are adjacent to the railroad bridge span that collapsed during the 2010 El Mayor-Cucapah earthquake as a result of lateral spreading; steel columns to support temporary replacement trestle are visible. Photo by B. Turner, January 2013.	12
Figure 3-3: Site plan showing locations of CPT, seismic survey lines, and sample collections from October 2013 site investigation and previous investigations. Mapped lateral spreading features and structural damage after GEER (2010).	13
Figure 3-4: Cross section along highway bridge centerline and penetration resistances from previous and current subsurface investigations. Explorations are offset from centerline as shown in Figure 3-3.	18
Figure 3-5: S- and P-wave velocity profiles and dispersion curves for Seismic Line 2 (location shown in Figure 3-3).	21
Figure 3-6: CPT-2 tip resistance, inferred shear-wave velocity profile, and dispersion curves used to fit parameters in Equation(3.1).	23
Figure 3-7: Profiles of shear wave velocity estimated at CPT test sites using Equation (3.1) with $\beta_0 = 0.5$, $\beta_1 = 0.58$, and $\beta_2 = 0.35$	24
Figure 3-8: Bent 1 of highway bridge showing shear tabs extending from transverse diaphragm into bent cap (top) and Bent 3 with no shear tabs (bottom). Photos B. Turner, 2013.	26

Figure 3-9: Construction of highway bridge foundations via casing and air lift method, circa 1999. Photo courtesy Ramón Pérez Alcalá, SCT.	28
Figure 3-10: USGS Shakemap for PGA. Contours show Shakemap estimated PGA in %g based on GMPE estimates (not constrained by recordings south of the U.S.–Mexico border). Measured PGA shown for SMA recording stations nearest the San Felipe Bridges. Adapted from USGS Shakemap (2010).....	32
Figure 3-11: Pseudospectral accelerations and spectral displacements estimated for SFB site during El Mayor-Cucapah earthquake.	33
Figure 3-12: Approximately 30–50 cm of apparent relative vertical displacement between the ground and river-side of columns at Bent 6 of the highway bridge. Apparent relative vertical displacement on the upslope side is about 10 to 15 cm. Photo by J. Gingery, Kleinfelder/UCSD, 2011.....	35
Figure 3-13: (a) Railroad bridge Bent 5 translated due to lateral spreading demand, causing an unseating collapse; arrow shows direction of movement. Photo during GEER reconnaissance by D. Murbach, City of San Diego, 2011; and (b): flexural cracking at base of highway bridge Bent 5 extended-shaft column. Photo B. Turner, 2013. Note that these two bents are adjacent to each other.	38
Figure 4-1: Numerical models of (a) highway bridge Bent 5 lateral analysis, (b) railroad bridge Bent 5 lateral analysis, and (c) highway bridge Bent 6 axial analysis.....	40
Figure 4-2: Cross section showing eastern spans of highway bridge and computed profiles of factor of safety against liquefaction and lateral spreading displacement.	45

Figure 4-3: Profiles of cone tip resistance and estimated factor of safety against liquefaction, shear strain, lateral spreading displacement index, and lateral spreading displacement for CPT-1 data during the El Mayor-Cucapah earthquake.....	53
Figure 4-4: Estimated surface free-field lateral spreading (LD) displacement versus distance from free face (river bank) based on CPT-1, CPT-2, and CPT-3 profiles using the Zhang et al. (2004) approach. Decreasing LD with increasing distance appear to fit a linear (shown) or hyperbolic decay trend.....	54
Figure 4-5: Highway bridge extended shaft column structural details. All dimensions in centimeters. Adapted from 1998 bridge construction plans (SCT, <i>personal communication</i> , 2013).	56
Figure 4-6: Railroad bridge member geometry and foundation group configurations considered for analysis. Clear edge spacing for all pile configurations is 0.4 m as shown for the 4×5 group. Refer to Table 4-8 for pile spacing and details used for analyses.	56
Figure 4-7: Moment-curvature behavior for highway bridge 1.2-m diameter reinforced-concrete extended-shaft columns with zero axial load and corresponding bilinear model implemented in <i>OpenSees</i>	61
Figure 3.4-8: Highway bridge shear tab detail (top) and spring definitions used to model connection between superstructure and bent cap (bottom).....	64
Figure 4-9: Formulation of rotational stiffness of railroad bridge deck spans transferring load to column through elastomeric bearings.	64

Figure 4-10: (a) Caltrans (2013a) force-based method for estimating top-of-foundation inertial shear and moment demands (V_{ToF} and M_{ToF}); (b) schematic of first-mode longitudinal oscillation; (c) single-bent model for modal and lateral spreading analyses	68
Figure 4-11: Highway bridge Bent 5 predicted response under imposed lateral spreading displacement demand of 4.6 m combined with superstructure inertia demand, represented as liquefaction-compatible spectral displacement demand, in opposite direction.	75
Figure 4-12: Railroad bridge Bent 5 analysis results showing collapse for a 4×5 group of 30-cm diameter reinforced concrete piles under imposed lateral spreading displacement demand of 1.0 m. Includes superstructure inertial demand, represented as liquefaction-compatible spectral displacement, in opposite direction from lateral spreading. Predicted column rotation $\approx 0.3^\circ$. Note the horizontal scale is exaggerated.	77
Figure 4-13: Numerical model and results of Bent 5 analyses of railroad bridge subjected to lateral spreading combined with inertial demands. Discontinuity in moment profile at pile-to-pile-cap connection occurs because the axial force in each pile row times its eccentricity from the pile cap centroid also contributes to moment resistance.	78
Figure 4-14: Comparison of moment and displacement profiles for highway bridge piles as computed from force- and restraint-compatible displacement-based methods for imposing superstructure inertial demands in the same and opposite directions as lateral spreading. Restraint-compatible displacement-based approach provides best match to observed behavior.....	80
Figure 4-15: Profiles of axial load (including downdrag) and axial resistance for highway bridge Bent 6 based on data from CPT-1 and CPT-2: (a): no liquefaction at tip—load carrying	

capacity is sufficient; and (b): loose layer at the depth of the foundation tip is liquefied, axial load exceeds the load carrying capacity of the foundation, resulting in bearing capacity failure and vertical settlement.	85
Figure 5-1: Three lateral spreading scenarios—(a) single pile subjected to broad field of lateral spreading, (b) pile group subjected to “short” lateral spread, and (c) laterally-spreading approach embankment resisted by abutment piles.....	90
Figure 5-2: Equivalent-static analysis results.	94
Figure 5-3: Finite element domain.....	95
Figure 5-4: Highway bridge mobilized force-displacement results for soil property calibration step.	96
Figure 5-5: Results of Phase2 simulations with 4.6 m of imposed free-field lateral spreading displacement, showing normal stress acting in direction of lateral spreading. Stress contours in kPa.	97
Figure 5-6: Displacement results (in meters) for finite element model including Bents 5, 6, and 7 of the highway bridge showing reduction in displacement at location of railroad bridge Bent 5 compared to free-field lateral spreading displacement of 4.6 m.....	99
Figure 5-7: Influence of lateral spread length; only the length of the lateral spread is varied between the two cases.	101
Figure 7-1: Substructure method of analysis for bridge bent supported on a pile group. Note that vertical impedance is not shown, but could also be considered.	118
Figure 7-2: Profiles of soil and free-head pile displacement for three frequencies of harmonic free-field excitation.....	120

Figure 7-3: Profiles of soil and fixed-head pile displacement for three frequencies of harmonic free-field excitation.....	120
Figure 7-4: Kinematic pile-soil interaction transfer functions computed for idealized linear-elastic conditions.....	121
Figure 7-5: Time- and frequency-domain representations of pile seismic response for computation of kinematic transfer function.	124
Figure 7-6: Time-domain and response spectrum representations of pile seismic response for computation of kinematic spectral ratios.	126
Figure 7-7: Kinematic pile-soil transfer functions from Fan et al. (1991) study for single pile with length-to-diameter ratio of 20.	134
Figure 7-8: Static kinematic pile-soil interaction transfer functions using improved dimensionless frequency definition from Anoyatis et al. (2013). Applies for a free-tip pile with $\lambda L \geq 5$ and homogeneous soil of any stiffness.	140
Figure 7-9: Comparison of observed versus model prediction transfer functions for a 5-story hospital building in Lancaster, California during the 1994 Northridge earthquake. After Kim and Stewart (2003).	148
Figure 7-10: Comparison of observed versus model prediction transfer functions for a 4-story building at Tohoku Institute of Technology in Sendai, Japan during the 2011 Tohoku earthquake. After Givens et al. (2012).	149
Figure 7-11: Influence of small changes between input and output signals on system transfer functions. Relative to input signal, the output signal (a) is identical, (b) is perfectly out-of-phase, (c) is out of phase by 0.1, and (d) exhibits slight baseline drift.....	156

Figure 8-1: Soil and pile response under imposed 10 Hz harmonic ground motion using elastic analytical solutions.....	167
Figure 8-2: Transfer function for kinematic soil-structure interaction effects for three diameters of 25-m long, fixed-head reinforced concrete piles in soft and stiff soil profiles.....	169
Figure 8-3: Transfer functions from Figure 8-2 plotted versus dimensionless frequency and compared to Anoyatis et al. (2013). All solutions lie within the same narrow band.....	170
Figure 8-4: Analytical and numerical solution transfer functions for sine-sweep input motion.	172
Figure 8-5: Fourier amplitude spectra for free-field and foundation-input motions (top) and corresponding transfer functions (bottom).....	173
Figure 8-6: (a) Normal and (b) shear stress contours around a laterally-loaded pile. Color key indicates change in stress from initial condition.....	178
Figure 8-7: Values of Winkler coefficient δ proposed in previous pile SSI research.	182
Figure 8-8: Normalized elastic transfer functions computed with and without pile mass.....	186
Figure 8-9: Effect of resonance at pile-soil system fundamental frequency on kinematic transfer functions.....	187
Figure 9-1: Numerical modeling approach.	190
Figure 9-2: Basic features of <i>PySimple3</i> material under monotonic loading. After Choi et al. 2015.....	192
Figure 9-3: Comparison of Boulanger et al. (1999) dynamic <i>p-y</i> material and later implementation in <i>OpenSees</i>	193
Figure 9-4: <i>PySimple3</i> viscoelastic-plastic material model formulation.	194

Figure 9-5: Comparison of <i>PySimple1</i> and <i>PySimple3</i> material models.	194
Figure 9-6: Effect of initial elastic stiffness K_e on <i>PySimple3</i> behavior for typical soft clay properties.....	198
Figure 9-7: Transfer functions (left) and p - y curve initial stiffness parameter versus depth plots (right) for free-head pile with uniform and variable values of Winkler coefficient δ over the depth of the pile.	200
Figure 9-8: Effect of <i>PySimple3</i> curvature parameter C	201
Figure 9-9: <i>Phase2</i> finite element domain for plane-strain analyses of laterally-loaded pile. Pile is displaced from left to right during the analyses.	203
Figure 9-10: Comparison of normalized y_{50} values using (a) existing p - y relationships and (b) from results of plane-strain finite element simulations of laterally-loaded piles in <i>Phase2</i> using Duncan-Chang nonlinear-elastic (D-C) and Mohr-Coulomb (M-C) soil constitutive models.	205
Figure 9-11: Effect of radiation damping in <i>PySimple3</i> material.	207
Figure 9-12: Normalized dashpot coefficient for $\nu = 0.25$, $\rho_s = 1.7 \text{ Mg/m}^3$ and $E_p/E_s \approx 690$..	211
Figure 9-13: Moment curvature analyses conducted at axial load $P = 0.05 * A_g * f'_c$ for (a) 2-m and (b) 0.5-m diameter pile sections.....	215
Figure 9-14: Pile group layout considered for analyses.....	222
Figure 9-15: Shear wave velocity and reference strain (γ_r) profiles for Sites 1 through 6.	224
Figure 9-16: Acceleration (top) and displacement (bottom) time series for seed motion (1971 San Fernando earthquake, Lake Hughes #4 recording station) and simulated spatially-variable	

ground motions at locations corresponding to other piles in group layout shown in Figure 9-14.	234
Figure 10-1: Transfer functions for Site 1 fixed-head piles.	238
Figure 10-2: Transfer functions for Site 2 fixed-head piles.	239
Figure 10-3: Transfer functions for Site 3 fixed-head piles.	240
Figure 10-4: Transfer functions for Site 4 fixed-head piles.	241
Figure 10-5: Transfer functions for Site 5 fixed-head piles.	242
Figure 10-6: Transfer functions for Site 6 fixed-head piles.	243
Figure 10-7: Transfer functions for Site 1 free-head piles.	244
Figure 10-8: Transfer functions for Site 2 free-head piles.	245
Figure 10-9: Transfer functions for Site 3 free-head piles.	246
Figure 10-10: Transfer functions for Site 4 free-head piles.	247
Figure 10-11: Transfer functions for Site 5 free-head piles.	248
Figure 10-12: Transfer functions for Site 6 free-head piles.	249
Figure 10-13: Normalized horizontal displacement transfer function results for fixed-head piles.	251
Figure 10-14: Normalized horizontal displacement transfer function results for free-head piles.	252
Figure 10-15: Normalized rotation transfer function results for free-head piles.	253
Figure 10-16: Mean fixed-head transfer function results for each pile/site combination.	255

Figure 10-17: Influence of changes in stiffness over pile length for $B = 2.0$ m, $L = 30$ m pile subjected to (a) 1971 San Fernando earthquake (NGA record sequence number 72), (b) 1994 Northridge earthquake (NGA record 1011), and (c) 1999 Chi-Chi, Taiwan earthquake (NGA record 2661).	256
Figure 10-18: Competing effects of radiation damping and stiffness degradation due to pile-soil interaction.	257
Figure 10-19: Mean fixed-head transfer function results for each pile/site combination plotted versus dimensionless frequency. (a) Shows variability in results due to pile stiffness, and (b) shows lack of variability in results due to pile slenderness ratio L/B .	259
Figure 10-20: Example of nonlinear least-squares regression to determine coefficients for free-head pile functional form [Equation (10.7)] using computed data for $B = 2$ m, $L = 60$ m pile embedded in Site 4 and subjected to 1999 Hector Mine earthquake (NGA record sequence number 1786).	271
Figure 10-21: Residuals versus predicted values plots (left) and normal Q-Q plots (right) for fixed-head transfer function coefficient prediction models. Lines on residuals plots show trend and \pm one standard deviation.	275
Figure 10-22: Variability in fixed-head transfer function results for the two pile diameters considered in this study.	276
Figure 10-23: Mean fixed-head transfer function model prediction for $B = 0.5$ m compared to computed results.	277
Figure 10-24: Mean fixed-head transfer function model prediction for $B = 2.0$ m compared to computed results.	278

Figure 10-25: Residuals versus predicted values plots (left) and normal Q-Q plots (right) for free-head displacement transfer function coefficient prediction models. Lines on residuals plots show trend and \pm one standard deviation.....	280
Figure 10-26: Mean free-head displacement transfer function model prediction for $B = 0.5$ m compared to computed results.	281
Figure 10-27: Mean free-head displacement transfer function model prediction for $B = 2.0$ m compared to computed results.	282
Figure 10-28: Residuals versus predicted values plots (left) and normal Q-Q plots (right) for free-head rotation transfer function coefficient prediction models. Lines on residuals plots show trend and \pm one standard deviation.	284
Figure 10-29: Variability in free-head rotation transfer function results for the two pile diameters considered in this study.....	285
Figure 10-30: Mean free-head rotation transfer function model prediction for $B = 0.5$ m results.	286
Figure 10-31: Mean free-head rotation transfer function model prediction for $B = 2.0$ m results.	287
Figure 10-32: Fixed-head pile spectral ratio functional form after Di Laora and Sanctis (2013).	288
Figure 10-33: Free-head pile spectral ratio functional form.....	290
Figure 10-34: Residuals versus predicted values plots (left) and normal Q-Q plots (right) for fixed-head spectral ratio coefficient prediction models. Lines on residuals plots show trend and \pm one standard deviation.	294

Figure 10-35: Fixed-head spectral ratio results.	295
Figure 10-36: Fixed-head pile spectral ratio predictive model residuals.....	296
Figure 10-37: Residuals versus predicted values plots (left) and normal Q-Q plots (right) for free-head spectral ratio coefficient prediction models.	299
Figure 10-38: Free-head pile spectral ratio results.	300
Figure 10-39: Free-head pile spectral ratio predictive model residuals.....	301
Figure 10-40: Group versus single-pile results for $B = 2.0$ m. $L = 30$ m pile, Site 1, subjected to 1994 Northridge earthquake (NGA record sequence number 957).	303
Figure 10-41: Group versus single-pile results for $B = 2.0$ m. $L = 30$ m pile, Site 1, subjected to 1971 San Fernando earthquake (NGA record sequence number 72).	303
Figure 10-42: Group versus single-pile results for $B = 2.0$ m. $L = 30$ m pile, Site 4, subjected to 1971 San Fernando earthquake (NGA record sequence number 72).	304
Figure 11-1: (a) Schematic of pile-soil kinematic interaction, which produces foundation-input motion (FIM) to free-field motion (FFM) transfer function (b), and (c) application of kinematic transfer function using substructure approach to represent a structure supported by a fixed-head pile. (d) The foundation motion (FM) transfer function differs from the FIM transfer function because of additional foundation displacements resulting from superstructure inertial forces.....	307
Figure 11-2: Idealized system used for direct analysis method.....	308

Figure 11-3: Comparison of transfer functions computed for pile-soil system and combined single-degree-of-freedom-oscillator and pile-soil systems using direct and substructure analysis methods.	310
Figure 11-4: Comparison of transfer functions computed with and without consideration of kinematic pile-soil interaction.....	313
Figure 11-5: (a) Phase angle frequency-response curves for SDOFO-pile-soil system (inset) and (b)-(e) response history of system components at different frequencies of harmonic free-field excitation.	317
Figure 11-6: Response of SDOFO-pile-soil system to harmonic free-field excitation.	318
Figure 11-7: Transfer functions computed for variable single-degree-of-freedom oscillator properties. Note fixed-base fundamental frequency $f_{1,SDOFO} = 7$ Hz for all cases.	321
Figure 11-8: Effect of varying fixed-base fundamental frequency of SDOFO-pile-soil system relative to kinematic pile-soil interaction transfer function corner frequency.....	323
Figure 11-9: Effect of nonlinear pile-soil interaction on SDOFO-pile-soil system transfer functions for homogeneous soil subjected to sine-sweep free-field excitation.	325
Figure 11-10: Formulation of nonlinear and equivalent-linear impedance spring macro-elements to replace pile in substructure method of analysis.	326
Figure 11-11: Effect of nonlinear pile-soil interaction on SDOFO-pile-soil system transfer functions for Site 1 subjected to 1971 San Fernando earthquake Lake Hughes #4 recording.	330
Figure 12-1: Tohoku Institute of Technology building layout after Givens et al. (2012) and idealized single-degree-of-freedom oscillator representation.....	334

Figure 12-2: Subsurface information for Sendai site after Givens et al. (2012). Subsurface data originally reported by OYO Corporation (2007).	334
Figure 12-3: Model predictions versus empirical data for Tohoku Institute of Technology building during 2011 Tohoku earthquake after Givens et al. (2012).	337
Figure 12-4: Lancaster, California hospital building layout and idealized single-degree-of-freedom oscillator representation after Stewart and Stewart (1997).	339
Figure 12-5: Subsurface conditions at Lancaster site after Stewart and Stewart (1997).	340
Figure 12-6: Predicted kinematic pile-soil interaction transfer function for Lancaster site plotted versus (a) plain frequency and (b) dimensionless frequency.	342
Figure 12-7: Model predictions versus empirical data for Lancaster building during 1994 Northridge earthquake after Kim and Stewart (2003).	343
Figure 12-8: Longitudinal elevation view of proposed Linden Street overcrossing replacement (after Caltrans 2016).	345
Figure 12-9: Transverse elevation view of interior bent for proposed Linden Street overcrossing replacement (after Caltrans 2016).	345
Figure 12-10: Acceleration response spectrum used for proposed Linden Street overcrossing replacement (after Caltrans 2016).	346
Figure 12-11: Shear-wave velocity profile measured using P-S suspension logging (after Caltrans 2016).	346
Figure 12-12: Predicted spectral ratios for Linden Street Overcrossing.	349
Figure 12-13: Kinematic pile-soil interaction effect on acceleration response spectrum.	349

LIST OF TABLES

Table 4-1: Estimated soil properties for Bent 5 lateral spreading analyses.....	44
Table 4-2: Non-liquefied crust load-transfer parameters.....	50
Table 4-3: Concrete (unconfined) properties.....	57
Table 4-4: Steel properties.....	57
Table 4-5: Elastomeric bearing properties.....	57
Table 4-6: Timber (piles) properties.....	57
Table 4-7: Structural Properties for Lateral Spreading Analysis, Highway Bridge.....	58
Table 4-8: Structural Properties for Lateral Spreading Analysis, Railroad Bridge.....	58
Table 8-1: Ground motions for elastic numerical analyses; numbering follows Baker et al. (2011)	173
Table 8-2: δ expressions from previous researchers derived by matching results of BDWF analyses to continuum analyses.....	181
Table 9-1: Parametric Study Bounds for Single Piles	190
Table 9-2: Site time-averaged shear wave velocity characteristics for Sites 1-6.	224
Table 9-3: Ground motion records used for analyses (after Baker et al. 2011).....	226
Table 9-4: Intensity measures for ground motion set.	227
Table 9-5: Summary of ground motion intensity measures.....	228
Table 9-6: Site fundamental frequencies.	230

Table 9-7: Segment duration (L) and frequency bands (b) used in the FDW routine.	233
Table 10-1: Fixed-head transfer function coefficient prediction model metrics.	274
Table 10-2: Metrics for free-head displacement transfer function coefficient prediction models.	279
Table 10-3: Metrics for free-head rotation transfer function coefficient prediction models.	283
Table 10-4: Fixed-head spectral ratio coefficient prediction model metrics.	293
Table 10-5: Metrics for free-head spectral ratio coefficient prediction models.	298

LIST OF SYMBOLS

LATIN SYMBOLS (default units listed in parenthesis unless otherwise noted in text)

a_0^p	Dimensionless frequency for pile dynamics
A_g	Pile gross cross-sectional area (m ²)
B	Pile diameter, or beam transverse width for beam-on-springs methods (m)
c	Dashpot coefficient (kN·s/m)
c_0	Phase speed of flexural waves in cylindrical rod (m/s)
E	Young's modulus (kPa)
E_s	Soil elastic Young's modulus (kPa)
E_p	Pile elastic Young's modulus (kPa)
EI_{SDOFO}	Flexural rigidity of single-degree-of-freedom oscillator column (kN·m ²)
f	Frequency (Hz)
$f_{1,SDOFO}$	First-mode fundamental frequency of fixed-base single-degree-of-freedom oscillator (Hz)
$\tilde{f}_{1,SDOFO}$	First-mode fundamental frequency of flexible-base single-degree-of-freedom oscillator, <i>i.e.</i> considering foundation flexibility (Hz)
f_c	Corner frequency of kinematic pile-soil interaction transfer function, defined as frequency beyond which significant deamplification of the free-field motion occurs due to kinematic pile-soil interaction (Hz)
f'_c	Concrete 28-day nominal compressive strength (kPa)
f_m	Ground motion mean frequency; inverse of T_m (Hz)
G	Shear modulus (kPa)
H	Thickness of soil profile from ground surface to bedrock (m)
H_{SDOFO}	Height of single-degree-of-freedom oscillator from ground surface to lumped mass centroid (m)

H_u	Transfer function ordinate
I_p	Pile gross moment of inertia (m^4)
k	Linear-elastic soil p - y curve stiffness $[(\text{kN/m})/\text{m} = \text{kPa}]$
k_{msr}	Modulus of subgrade reaction $[\text{kN/m}^2/\text{m} = \text{kPa}/\text{m} = \text{kN/m}^3]$
k_{SDOFO}	Horizontal swaying stiffness of single-degree-of-freedom oscillator (kN/m)
K_e	Soil p - y curve elastic stiffness $[(\text{kN/m})/\text{m} = \text{kPa}]$
$K_{e,10B}$	Average value K_e computed over upper ten pile diameters $[(\text{kN/m})/\text{m} = \text{kPa}]$
K_{xx}	Foundation impedance for horizontal translation degree of freedom (kN/m)
K_0	At-rest coefficient of lateral earth pressure
L	Pile length (m)
l_c	Pile active length (m)
m_{SDOFO}	Mass of single-degree-of-freedom oscillator (kg)
M	Moment ($\text{kN}\cdot\text{m}$)
M	Earthquake moment magnitude
M_{cr}	Moment corresponding to cracking of concrete in tension for reinforced-concrete section ($\text{kN}\cdot\text{m}$)
M_y	Moment corresponding to yielding of longitudinal reinforcing steel in tension for reinforced-concrete section ($\text{kN}\cdot\text{m}$)
M_y	Yield moment for reinforced-concrete section ($\text{kN}\cdot\text{m}$)
p	Soil p - y curve force, per unit length of pile (kN/m)
P	Pile axial load (kN)
s_u	Soil undrained shear strength (kPa)
S_{DS}	Short-period spectral acceleration as defined in ASCE 7 (ASCE 2010); (g)
S_{ij}	Cross power spectral density between signals i and j
S_{ii}	Auto power spectral density for signal i

T_m	Ground motion mean period computed using Rathje et al. (2004); (s)
u_g	Ground surface displacement (m)
u_p	Pile head displacement (m)
$u(t)$	Displacement signal in time domain (m)
$U(\omega)$	Frequency-domain representation of the time domain signal $u(t)$
V_S	Soil shear wave velocity (m/s)
$V_{S,10B}$	Time-averaged shear wave velocity computed over upper ten pile diameters (m/s)
$V_{S,30}$	Time-averaged shear wave velocity computed over upper 30 m of site profile (m/s)
$V_{S,H}$	Time-averaged shear wave velocity computed over full thickness of soil profiles used for ground response analyses, H (m/s)
$V_{S,L}$	Time-averaged shear wave velocity computed over length of pile, L (m/s)
y	Soil p - y curve relative horizontal displacement between pile and soil (m)
z	Depth below ground surface measured as a positive number (m)

GREEK SYMBOLS AND OPERATORS

α	Static stiffness modifier for pile lateral translation
β	Damping, expressed as percentage of critical damping.
δ	Ratio of Winkler modulus K_e to soil elastic modulus E_s
Δt	Time increment for discrete time signal (s)
ε_{50}	Strain mobilized at one-half of maximum stress during laboratory strength tests on soil
\mathcal{F}	Fourier transform operator
γ_{avg}	Average soil shear strain in pile-soil interaction zone of influence for laterally-loaded pile
γ_r	Reference strain corresponding to 50-percent modulus reduction

γ^2	Coherence
κ	Wavenumber
λ	Characteristic term or “Winkler parameter” for laterally loaded pile (m^{-1})
λ_{ff}	Wavelength of free-field soil column under harmonic excitation (m)
ν	Poisson’s ratio
ω	Angular frequency (rad./s)
ϕ	Within-event aleatory uncertainty in Part I; Curvature (m^{-1}) in Part II.
ϕ_{pk}	Soil peak friction angle (deg.)
θ	Pile head rotation (radians)
ρ_p	Mass density of pile (Mg/m^3)
ρ_s	Mass density of soil (Mg/m^3)

ACKNOWLEDGMENTS

The projects described in Parts I and II of this dissertation were sponsored by the Pacific Earthquake Engineering Research Center's (PEER's) Program of Applied Earthquake Engineering Research of Lifelines Systems supported by the California Department of Transportation (Caltrans) and the Pacific Gas and Electric Company. Any opinions, findings, and conclusions or recommendations expressed in this material are those of the author and do not necessarily reflect those of the sponsors. I greatly appreciate the financial and technical support of the PEER Center, especially the feedback from Tom Shantz of Caltrans acting as research coordinator of the Lifelines Program.

I am deeply indebted to Professor Scott Brandenburg for his guidance, mentorship, and friendship throughout my studies. Thanks, Scott. Thanks also to Professors Stewart, Wallace, and Lemnitzer for serving on my committee, challenging me in the classroom, providing thoughtful insights, and for your friendship. Thanks to the many friends and colleagues I have made during my time at UCLA—too many to name.

I am especially grateful for the many people and agencies that assisted in the case study of the San Felipe Bridges that is described in Part I, in particular Enrique Hernandez Quinto, Ramón Pérez Alcalá, Raúl Flores Berrones (who happens to also have conducted pioneering work in the field of pile kinematics discussed in Part II), Alberto Salamanca, Bob Nigbor, and Chris Krage. Special thanks as well to Bill and Kathy Brandenburg for allowing us to stay in their home in Calexico during the field testing and meetings with SCT. Professor Atsushi Mikami provided helpful guidance on re-evaluating the case studies in Part II, and Dr. Timothy Ancheta assisted the project by computing incoherent ground motions for use in my numerical models. I would also

like to acknowledge the support of TRC Software in providing a license of *XTRACT* for moment-curvature analysis, and Rocscience for providing an educational license of their software suite which I used extensively throughout my research.

Finally, thanks to my family for supporting me throughout this journey, especially to my father, who I can always count on for an engineering reality check, and to my loving wife, for keeping me sane. Thanks also to my brother, Ryan, for the Caltrans insights.

Portions of the work presented in this dissertation have been previously published or are available online ahead of print publication. Committee chair Scott J. Brandenburg and committee member Jonathan P. Stewart were principal investigator and co-principal investigator, respectively, of the San Felipe Bridges case study project described in Part I, and coauthored the following with me:

Turner, B, Brandenburg, SJ, and Stewart, JP, 2014. Evaluation of collapse and non-collapse of parallel bridges affected by liquefaction and lateral spreading. *PEER report 2014/10*, Pacific Earthquake Engineering Research Center, University of California, Berkeley. 94 pp.

Turner, B., Brandenburg, S., and Stewart, J. (2016). Case study of parallel bridges affected by liquefaction and lateral spreading. *J. Geotech. Geoenviron. Eng.*, DOI: [http://dx.doi.org/10.1061/\(ASCE\)GT.1943-5606.0001480](http://dx.doi.org/10.1061/(ASCE)GT.1943-5606.0001480).

In addition, Scott J. Brandenburg and I coauthored the following paper which describes the work presented in Chapter 5:

Turner, BJ, and Brandenburg, SJ (2015). Pile pinning and interaction of adjacent foundations during lateral spreading. *DFI Journal – The Journal of the Deep Foundation Institute*, 9(2), 92-102. DOI:10.1179/1937525515Y.0000000009

VITA

Education

M.S., Civil Engineering, California Polytechnic State Univ., San Luis Obispo, California, 2010

B.S., Civil Engineering, California Polytechnic State Univ., San Luis Obispo, California, 2009

Professional Experience

Staff Engineer, Shannon & Wilson, Inc., Los Angeles, California (2010-2014)

Asst. Project Manager, AIS Construction Company, Carpinteria, California (2007-2009)

Engineer's Asst., GeoSolutions, Inc., San Luis Obispo, California (2005-2008)

Selected Publications

Turner, B., Brandenburg, SJ and Stewart, JP (2016). "Case study of parallel bridges affected by liquefaction and lateral spreading." *J. Geotech. Geoenviron. Eng.*, published electronically ahead of print: DOI 10.1061/(ASCE)GT.1943-5606.0001480.

Turner, BJ, Brandenburg, SJ, and Stewart, JP (2015). "Influence of kinematic SSI on foundation input motions for pile-supported bridges." *Proc. 6th International Conf. on Geotechnical Earthquake Eng.*, 1-4 Nov. 2015, Christchurch, New Zealand.

Turner, BJ, and Brandenburg, SJ (2015). "Pile pinning and interaction of adjacent foundations during lateral spreading." *DFI Journal – The Journal of the Deep Foundations Institute*, 9(2), 92-102.

Turner, B., Brandenburg, SJ, and Stewart, JP (2015). "Analysis of drilled shaft settlement caused by liquefaction." *Proc. International Foundations Congress and Equipment Expo (IFCEE)* 2015, published as ASCE GSP 256, 17-21 March 2015, San Antonio, TX, p. 1176-1188.

Turner, B., Brandenburg, SJ, and Stewart, JP (2014). "Evaluation of Collapse and Non-Collapse of Parallel Bridges Affected by Liquefaction and Lateral Spreading" *Report No. PEER 2014/10*, Pacific Earthquake Engineering Research (PEER) Center, University of California, Berkeley, 111 p.

1 Introduction

During a major earthquake, attention is drawn to the response of bridges, buildings, and other infrastructure. To a large extent, the response of these structures is controlled by what happens underground, at the interface between the structure's foundations and moving soil or rock. Dynamic behavior of the foundation and ground materials along with the subsequent impact on the structure's response due to relative movements at this interface are described by the field of *kinematic soil-structure interaction*.

The purpose of the studies described in this dissertation is to validate existing design guidelines and provide new, simplified design tools for capturing this complex mechanism in the routine design of structures supported on deep foundations. While two- or three-dimensional dynamic numerical modeling techniques that attempt to recreate these complexities are available, they are beyond the scope of most projects. Instead, foundation engineers desire robust and well-validated equivalent-static analysis (ESA) methods for seismic design than can be integrated with the level of design methodologies already in day-to-day use. Two cases are examined:

Part I of the dissertation investigates the demands placed on foundations by permanent ground displacements resulting from liquefaction-induced lateral spreading. Existing ESA

methods are shown to be capable of adequately predicting both the collapse and non-collapse of a pair of bridges in Mexico during the 2010 **M** 7.2 El Mayor-Cucapah earthquake, with the important caveat that inertial demands from the superstructure should be represented in a manner that considers resistance provided by all above-ground bridge components, not just the foundations.

In Part II of the dissertation, simplified models are developed for predicting transfer functions and spectral ratios to capture kinematic pile-soil interaction in non-liquefied ground. These models can be used to modify free-field ground motions resulting from a seismic hazard analysis or building code without the need for conducting dynamic analysis of the foundations. Use of the modified motions rather than free-field motions is more realistic, and is shown to provide a beneficial reduction in design forces for large-diameter piles in soft soil conditions. To develop these models, a parametric study is performed considering typical ranges of pile, soil, and ground motion conditions encountered in practice, with explicit consideration of nonlinear material behavior and the complexity of real ground motions. While previously-available elastic analytical models are shown to be capable of predicting the average results of this study, they do not adequately reflect the amount of variability in the results that arises from consideration of more realistic conditions. The new model is also used to re-examine available case history data that could not be explained by existing models.

Part I: Evaluation of Collapse and Non-Collapse of Parallel Bridges Affected by Liquefaction and Lateral Spreading

Are simplified, equivalent-static analysis methods adequate to capture the complex mechanism of lateral spreading for design of bridge deep foundations?

2 Introduction to Part I

The 2010 **M** 7.2 El Mayor-Cucapah (EMC) earthquake triggered liquefaction-induced lateral spreading in the vicinity of two bridges (highway and railroad) that cross the Colorado River in Baja California, Mexico. The bridges exhibited significantly different performance levels, despite being separated by only a few meters and both bridges being supported on deep foundations. The railroad bridge (RRB) suffered unseating collapse of one span and near collapse of another span, while the highway bridge (HWB) suffered moderate repairable damage without collapsing.

Since the soil conditions and imposed lateral spreading demands were essentially equivalent for the two bridges, this case study provides an excellent opportunity to validate recently-proposed equivalent-static analysis (ESA) procedures (Ashford et al. 2011; Caltrans 2013a) for analyzing bridge foundations subjected to lateral spreading. The objectives of this study were to apply the recommended ESA procedures to the two bridges and compare the predicted behavior to the performance that was observed following the EMC earthquake. Design procedures are often validated against failure case studies, but validation against cases of moderate to good performance is less common. The ability of a single method to predict the full range of possible performance levels indicates that it is a particularly robust tool that will be useful in practice.

An alternative to the ESA procedure for lateral spreading is to perform nonlinear dynamic numerical analyses where the soil and structure are modeled using two- or three-dimensional continuum elements, and input ground motions are provided that exhibit appropriate levels of spatial variability. Although this method can capture features of behavior neglected by ESA, dynamic methods can be costly and time-consuming to implement, require advanced user-expertise, and are limited in accuracy by the user's ability to adequately estimate the parameters needed to define the material constitutive models. For routine design, this approach is not practical. Hence, the ESA procedure is a useful design tool as long as its predictive capabilities are properly validated. The ESA procedure can also be used to check the results of more advanced analyses when such analyses are justified by the nature of the project.

The remainder of Part I of the dissertation is organized as follows:

- Chapter 3 presents an overview of the San Felipe Bridges site and observed damage following the EMC earthquake.
- Chapter 4 describes the geotechnical and structural modeling parameters used for the analyses, and how they were selected based on the known project conditions and existing guidance documents. Results are presented which demonstrate that ESA procedures are capable of predicting the full range of performance exhibited by the San Felipe Bridges, but only when inertial demands from the superstructure were represented in a manner that captured the resistance provided by all bridge components, not just foundations. A simplified procedure is developed for capturing this effect using a model of a single bridge bent.

- Chapter 5 investigates the concepts of “pinning” and “shielding” in the context of interaction between adjacent structures during lateral spreading. A novel analysis method combining the results of ESA with two-dimensional finite-element analysis is presented to quantify these effects.
- Chapter 6 presents conclusions and recommendations for implementing the findings of this case study in practice.

3 Site Description and Investigation

The San Felipe Bridges (SFB) cross the Colorado River near the geographic center of the Mexicali Valley in the Mexican state of Baja California, about 60 km southeast of the city of Mexicali and 6 km southeast of the nearest town, Guadalupe Victoria. The Mexicali Valley and its counterpart to the north of the Mexico/United States border, the Imperial Valley, represent the terminus of the Colorado River as it flows into the Gulf of California.

The following sections describe the SFB site, from a regional scale down to the site-specific results of geotechnical investigations, and will present a summary of the EMC earthquake.

3.1 REGIONAL AND LOCAL GEOLOGY

The Mexicali and Imperial Valleys are located in the Salton Trough, a transtensional basin formed during the last five million years by tectonic activity along the transform boundary between the Pacific and North American Plates. To the northwest, the San Andreas Fault system accommodates primarily right-lateral strike-slip movement at the continental-transform boundary between the two plates. To the southeast, the Gulf of California is a result of extension due to divergent fault step-over at the ridge-transform plate margin, driven by oceanic ridge spreading at the Eastern Pacific Rise (Merriam and Bandy 1965; Brothers et al. 2009; McCrirk et al. 2011). The Mexicali area is

located at the junction of these two tectonic regions, leading to complex faulting patterns and seismicity (Hauksson et al. 2011; Wei et al. 2011).

The Colorado River (known as the *Río Colorado* in Mexico) enters the east side of the basin at Yuma, Arizona, on the Mexico-U.S. border, depositing fine-grained fluvio-deltaic sediments over existing marine, deltaic, lacustrine, and locally derived coarse-grained alluvial fan and fluvial deposits for a total thickness of up to 10-12 km (Merriam and Bandy 1965; Dorsey 2010). Petrographic studies by Merriam and Bandy confirmed that the majority of the fine sand and smaller-sized sediment in the basin originates from the Colorado Plateau and was not derived locally from the crystalline Peninsular Range mountains that bound the valleys to the east, north, and west.

Continual extension and depression has thus resulted in a series of basins filled with deposits from the Colorado River extending far below present-day sea level. The depositional environment within the basins has alternated between marine and non-marine depending on the contemporary topography during deposition. Periodically, the Colorado River has terminated as a series of distributaries and shallow freshwater lakes that do not reach the Gulf of California, similar to the present configuration, although currently this phenomenon is exacerbated by human withdrawal of the majority of the river's flow for agriculture and domestic consumption. Resulting lacustrine deposits of silt and clay can thus be found throughout the region. Flood overbank deposits are also responsible for fine-grained sediment in the area, particularly in the Imperial Valley as a result of floods of the river extending north of its usual course (Merriam and Bandy 1965; Dibblee 1984; Pacheco et al. 2006; Dorsey 2010).

Several faults cross the region as shown in Figure 3-1, primarily accommodating strike-slip movement in the northwest-southeast direction in combination with smaller oblique normal

faults accommodating extension at the divergent step-over zones. The major plate boundary faults in the region are, from north to south, the San Andreas fault, the Imperial fault, and the Cerro Prieto fault. The EMC earthquake occurred as a sequence of ruptures along a series of faults considered to be west of the active plate boundary, including the Pescadores, Borrego, and previously unknown Indiviso faults (GEER 2010; Hauksson 2011).



Figure 3-1: Regional map and key geologic features. Fault rupture zones after GEER (2010); Cerro Prieto and Imperial Faults after Pacheco et al. (2006). Google Earth base image.

Pacheco et al. (2006) estimated the average depth to crystalline bedrock in the central and eastern Mexicali Valley to be about 4 km using exploratory well data and geophysical methods. Basin depth further west of the Cerro Prieto fault has not been directly measured but is estimated to be significantly deeper than 4 km (Dorsey 2010). Sediment depth has not been measured directly at the SFB site, but the studies by Pacheco et al. as well as others by the Mexican Federal Electricity

Commission in support of the Cerro Prieto Geothermal Field (Davenport et al. 1981) indicate that unconsolidated (in the geologic sense) Quaternary sediments in the region vary in thickness between approximately 500 and 2500 m. Late Miocene and Pliocene sediments below this depth are mostly consolidated and in places have been subjected to low-grade metamorphism.

3.2 SITE TOPOGRAPHY AND SURFACE CONDITIONS

Nearly-level agricultural fields surround the area adjacent to the river, as can be seen in the background of Figure 3-2. Approach embankments that maintain the grade of the road at the elevation of the surrounding land are sufficient to provide about ten meters of clearance between the base of the bridges and the river surface during average flow.

The bridges cross the river at a gentle meander that has caused the active channel to migrate to the west side of its flood plain, which is about 175 m wide as seen in Figure 3-3. In the vicinity of the SFB crossing, the active river channel is approximately 50 m wide during the low and average flows that appear to be predominant for most of the year based on vegetation patterns observed at the site. The active channel is incised about 2–4 m below the flood plain terraces by a steep bank on the west side, and a more gradual slope on the east side (approximately 1.5 horizontal to 1 vertical (1.5H:1V) and 3~5H:1V, respectively). The flood plain terraces extend for about 25 m west of the active channel and about 90 m east of the active channel until meeting slopes that lead up to the adjacent fields. These slopes are about 2-3H:1V on the west bank and more gradual on the east bank. Constructed fills surrounding the bridge abutments slope down to the flood plain terraces at approximately 1.5H:1V.

The average natural ground slope is steeper on the west side of the river than on the east side because the bend in the river results in higher flow velocity and thus more erosive energy on

the west side, with corresponding low velocity and sediment deposition on the inside of the bend. This pattern of topography is typical at bends in rivers flowing through alluvial valleys, and the resulting differences in relative density on each side of the river can significantly affect the behavior during earthquakes as was observed at the SFB site.

The ground surface is barren under and immediately north and south of the bridges, but in general the area is characterized by thick growth of tamarisk and other semi-aquatic and terrestrial bushes, extending from the water's edge to between about 20 and 150 m away from the active channel banks. Rip-rap armoring has been placed around the abutment fills to provide erosion protection, visible in Figure 3-2.



Figure 3-2: View of site looking west across the *Río Colorado* from atop the east river bank. People standing near the river are adjacent to the railroad bridge span that collapsed during the 2010 El Mayor-Cucapah earthquake as a result of lateral spreading; steel columns to support temporary replacement trestle are visible. Photo by B. Turner, January 2013.

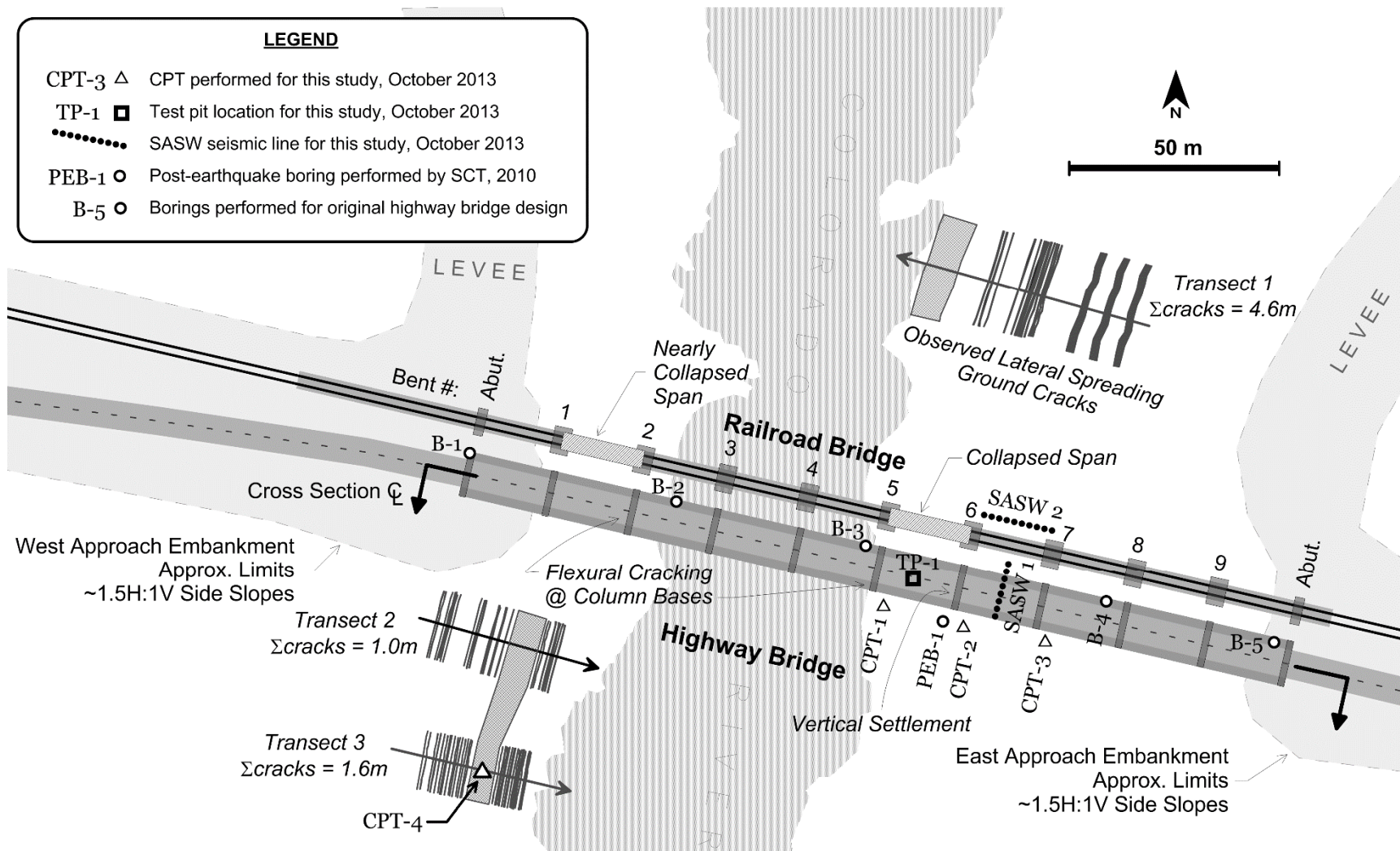


Figure 3-3: Site plan showing locations of CPT, seismic survey lines, and sample collections from October 2013 site investigation and previous investigations. Mapped lateral spreading features and structural damage after GEER (2010).

3.3 SUBSURFACE CONDITIONS

Characterization of the subsurface conditions is based on review of previous reports and other documents associated with the original design and construction of the highway bridge (HWB), borings performed after the El Mayor-Cucapah (EMC) earthquake in support of repair efforts, and additional subsurface tests performed for this study. The results of each will be discussed in the following sections.

3.3.1 Previous Subsurface Investigations by Others

The Mexican highway authority, Secretaría de Comunicaciones y Transportes (SCT), provided us with a cross section of the HWB showing profiles of blowcounts for five borings performed during the original subsurface investigation for the bridge design in 1998 as well as blowcounts from a post-earthquake boring (SCT, *personal communication*, 2013). The approximate locations of these borings are shown on Figure 3-3. The documents provided by SCT indicate that the original exploratory borings were advanced using hydro-jetting and sampled using a standard penetration test (SPT) split spoon sampler. The post-earthquake boring was observed by members of the GEER reconnaissance team to be advanced in a similar manner, notably without the use of casing or slurry (GEER 2010). Other design documents that SCT provided us indicate that index tests were performed on the samples retrieved during the original investigation, but the results of these tests were not available.

In general, the stratigraphy indicated by the SCT cross section consists of about 6 to 10 m of loose silty sand that gradually increases in relative density with depth, overlying a very dense layer of silty sand that resulted in refusal blow counts. The soil profile is uniformly described on the SCT cross section as poorly graded, light brown, very loose to very dense silty sand. Of the six borings, three show penetration resistance gradually increasing with depth. The other three

borings, including the post-earthquake boring, show erratic increases and decreases in penetration resistance in the upper 10 m, with SPT N-values above 25 immediately below the surface and refusal at depths as shallow as 5 m, interbedded with low N-value layers. Some of the high penetration resistances may have been caused by friction along the sampling rods due to caving of the borehole prior to, or during, driving of the sampler.

The SCT also provided us with a cross section of the railroad bridge (RRB) that shows three post-earthquake borings performed in June 2012 by Ferrocarril Mexicano (Ferromex), the owner of the railroad, along with a complete log for one of the borings, which is included in Appendix A (SCT, *Personal communication*, 2013). The boring log does not indicate whether hydro-jetting or a different form of drilling was used. The SPT samples were taken, and results of index tests performed on the retrieved samples are included on the boring log.

The Ferromex boring log shows SPT N-values between about 12 and 20 in the upper 7 m, followed by a gradual increase in relative density to refusal over the next 5 m. The general trend of these blow counts with depth is reasonable, but the average values are unexpectedly high in the shallow soil given that liquefaction and resulting lateral spreading were severe enough to cause collapse of the adjacent RRB span. The unexpectedly high penetration resistance measured in these borings may be due to the “nonstandard” nature of the SPT tests that were performed, i.e., that the use of hydro-jetting the unsupported borehole, using a rope and cathead hammer system, unknown hammer efficiency, etc., may have resulted in field blow counts that do not correspond to typical U.S. energy standards of 60–90% efficiency.

Groundwater encountered in each of the borings suggests that the surface of the groundwater table is relatively constant across the site at approximately the same elevation as the

river surface. Given the primarily course-grained soil at the site and the lack of geologic structural features that could cause artesian pressures, this interpretation is reasonable.

3.3.2 Subsurface Investigation for this Study

As a result of the uncertain nature of the SPT N-values from the previous investigations, as well as a lack of available index test results and the need to characterize the subsurface as accurately as possible in order to complete the analyses for this study, the research team opted to supplement the available information by performing additional subsurface explorations at the site consisting of *in situ* testing and laboratory testing of retrieved samples.

The investigation, completed in October of 2013, consisted of cone penetration testing (CPT) with shear wave velocity and porewater pressure measurements, hand sampling of near-surface soil, and spectral analysis of surface waves (SASW) geophysical testing. The locations of each exploration are shown on Figure 3-3.

The CPT soundings were performed using the NEES@UCLA 20-ton truck-mounted Hogentogler rig, which is capable of pushing to a maximum cone tip resistance (q_t) of approximately 30 MPa. Four CPT's were successfully advanced to depths between 4.5 and 16.5 m, and several more attempted tests were stopped by obstructions at shallow depths. The obstructions were likely rubble from the original bridge construction or post-earthquake repair efforts. Shear wave velocity (V_s) measurements were taken at the CPT-3 location.

Profiles of cone tip resistance are shown in the Figure 3-4 cross section, and detailed profiles of tip resistance and friction ratio are presented in Appendix A.

Minimum and maximum void ratio and grain size analysis tests were performed on a bulk sample collected at the surface from location TP-1 (shown in Figure 3-3) in general accordance

with ASTM standards. Laboratory test results are presented in Appendix B. The sample was found to be a uniformly graded silty fine sand, and the fines fraction was non-plastic. The fines content of 45% is higher than expected for the deeper layers, and most likely because a large amount of silt is deposited on the ground surface by wind and the river on a regular basis. This is supported by the grain size analysis results on the railroad boring; see Appendix A.

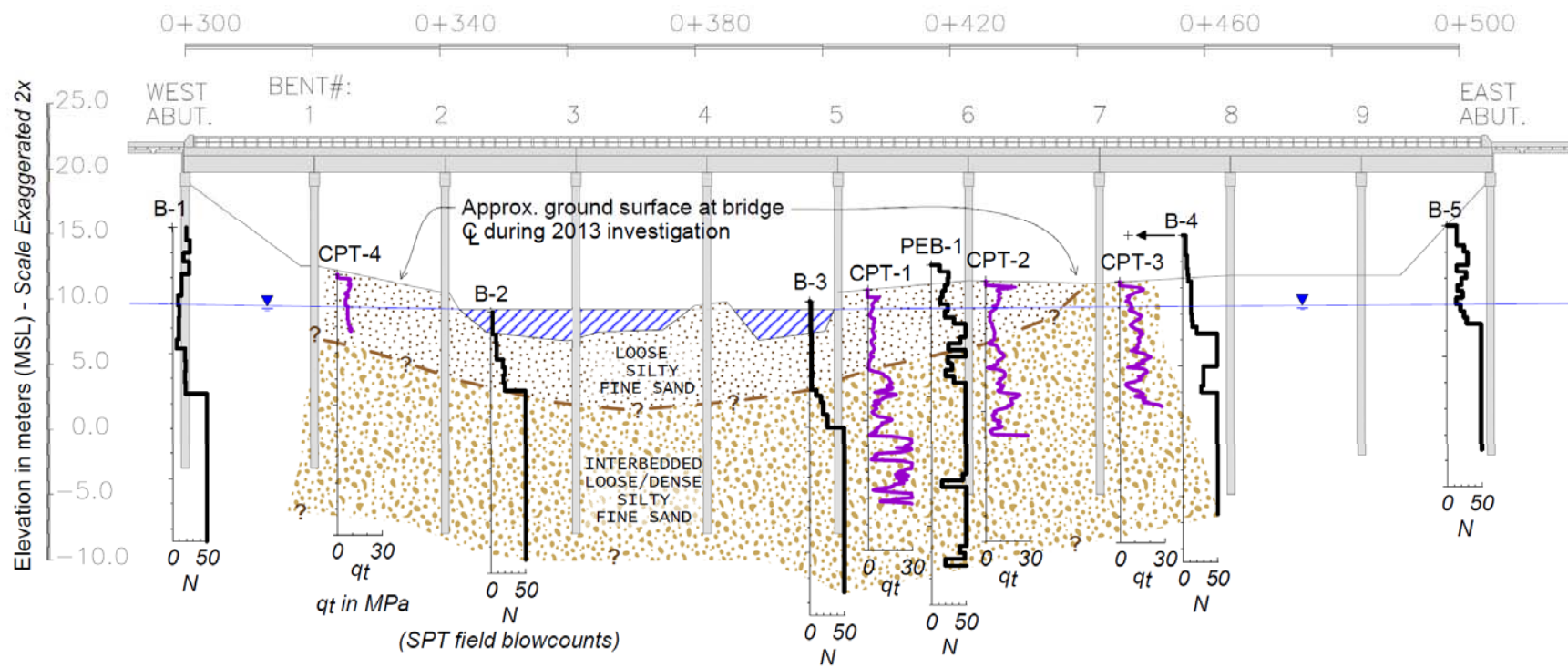


Figure 3-4: Cross section along highway bridge centerline and penetration resistances from previous and current subsurface investigations. Explorations are offset from centerline as shown in Figure 3-3.

Two SASW geophysical surveys were conducted at the locations shown in Figure 3-3. Four sensors were placed at 2-m and 4-m horizontal spacings to record signals generated by a vertical constant-force shaker performing a sine wave sweep over a frequency range of 5 to 35 Hz. Recordings were also taken with a sledgehammer impacting a steel plate as a high-frequency source. Results of the SASW interpretation are presented in Section 3.3.3.

The stratigraphy inferred from the CPT generally agrees with the inferred stratigraphy from the SCT/Ferromex borings over the upper 6–10 m, although the higher resolution of the CPT data reveals that the interbedded loose and dense layers are thinner than captured by the SPT in some cases. Below depths of about 10 m, the SCT/Ferromex borings suggest a continuous very dense layer extending well below the tips of the foundations (with one notable exception in PEB-1 that will be discussed later). Of the CPT's performed, only CPT-1 was able to extend a significant depth into this supposedly very dense layer; in fact, the results show that the pattern of interbedded loose and dense layers continues over this depth. This further supports the notion that the method of drilling and sampling used for these borings may have resulted in erroneous N-values, or that the SPT sampling intervals were inadequate to identify the loose layers.

Considering all the available information, the stratigraphy in the vicinity of the eastern spans of the bridges is summarized as follows: surficial soil consists of a loose, uniformly graded, silty, fine sand crust above the groundwater table, which is about 1.5 to 2 m below the ground surface. In the vicinity of the bridges, this layer is highly disturbed from construction and post-earthquake repair efforts, so it is considered fill, though it consists of the naturally deposited sediments. The fines portion of the soil consists of nonplastic silt expected to behave as a granular material. This loose layer extends below the groundwater table to a depth of about 6 m near the river. Moving from west to east, (i.e., away from the river), the thickness of the loose surface layer

decreases and its relative density increases. Below the loose layer, interbedded dense and loose layers continue to the maximum depth of CPT exploration (16.6 m) and a similar interbedded pattern is expected below this depth. Within the interbedded strata, the dense layers range in thickness from about 1 to 3 m, while the loose layers are generally thinner, ranging from about 0.25 to 1 m thick. The CPT results and index testing from the Ferromex boring suggest that the soil at depth has the same general consistency as the near-surface soil, i.e., fine to medium sand with varying amounts of nonplastic to low plasticity fines. Some thin layers of predominantly fine-grained soil are present within the interbedded granular layers.

Stratigraphy on the western side of the bridges is less certain because only one CPT was performed on the west bank, and only to a depth of about 4.5 m due to equipment problems. The subsurface conditions are expected to fit the same pattern as described for the east bank zone, except that the transition from low to high relative density is expected to occur over a shorter distance because this area is on the outside of the river bend. The CPT tip resistance measured on the west bank was slightly higher than the tip resistance measured near the river on the east bank, confirming this trend.

Based on a review of photographs from the post-earthquake reconnaissance team (GEER 2010), the river level at the site around the time of the earthquake was approximately the same as the level during the October 2013 site investigation. This conveniently eliminates the need to re-interpret the CPT data for a different groundwater level.

3.3.3 Interpretation of V_s Profile

The shear-wave velocity profile was interpreted by combining the results of the SASW data with the CPT and SCPT measurements. This is a non-standard procedure that makes appropriate use of

all of the available measurements. Typically, SASW inversion is performed based only on the measured Rayleigh wave dispersion curve. A problem with this procedure is that the inversion from the Rayleigh wave dispersion curve to a V_s profile is non-unique. For example, the velocity profiles in Figure 3-5 are associated with essentially identical first-mode Rayleigh wave dispersion curves, yet the velocity profiles clearly differ from each other. The dispersion curves in this case were computed using the finite element formulation developed by Lysmer (1970). The vertical variations in the V_s profile could be important depending on the manner in which the velocity profile is utilized. For example, a one-dimensional site response analysis using the Profile 1 would likely differ significantly from the same analysis performed on Profile 3. Furthermore, V_s -based liquefaction triggering procedures could provide significantly different outcomes for the three profiles in Figure 2.5. However, a blind inversion of the first-mode Rayleigh wave dispersion curve (common practice in SASW) cannot possibly resolve the vertical variation of the velocity profile. For this reason, the CPT tip resistance data was utilized to constrain the inversion of the dispersion curve.

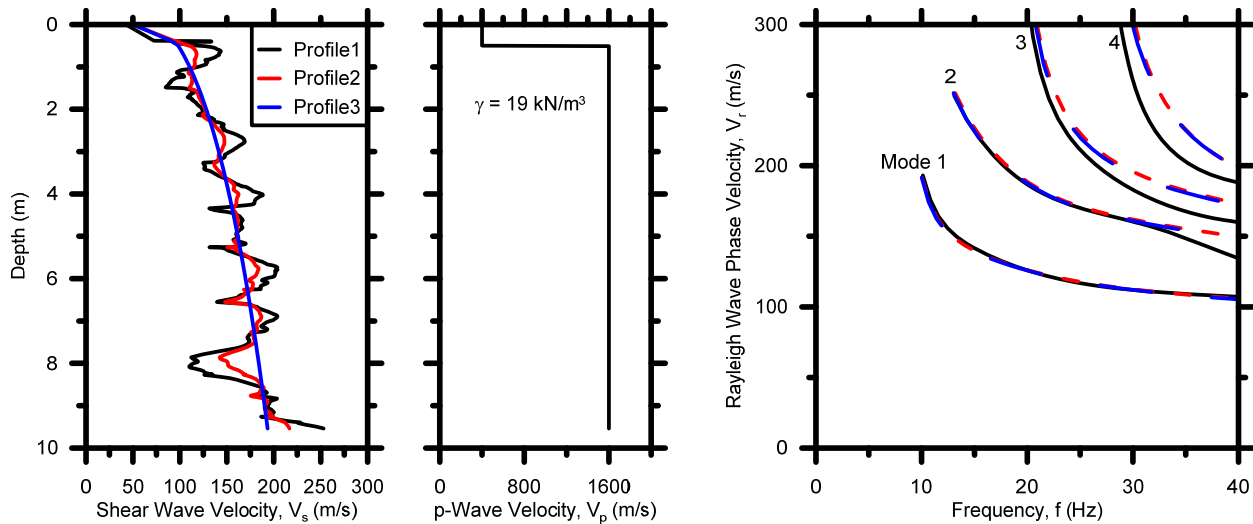


Figure 3-5: S- and P-wave velocity profiles and dispersion curves for Seismic Line 2 (location shown in Figure 3-3).

Correlations between V_s and penetration resistance have been formulated previously [e.g., Brandenberg et al. (2010) and DeJong et al. (2006)]. The correlation tends to be rather poor, but provides an improvement in velocity estimates based on surface geology or topography alone. Much of the dispersion in the relation between V_s and penetration resistance arises from site-to-site variability rather than random variability within a specific site. For this reason, a site-specific calibration in which V_s and penetration resistance are independently measured can improve accuracy.

The approach adopted in this study is to utilize the functional relation between V_s , q_t , and vertical effective stress (σ'_v) shown in Equation (3.1), and adjust the fitting parameters, β_0 , β_1 , and β_2 , such that the resulting V_s profile produces a dispersion curve that matches the measured curve. Note that the definition of the overburden scaling factor, n , is based on Robertson (2012); see Appendix C. An overburden scaling term is required in the relation between V_s and q_t because these parameters are known to scale differently with overburden stress.

$$\begin{aligned} V_s &= \beta_0 \cdot q_t^{\beta_1} \cdot \sigma_v'^{\beta_2 \cdot n} \\ n &= 0.381(I_c) + 0.05(\sigma'_v/p_a) - 0.15 \leq 1.0 \end{aligned} \quad (3.1)$$

where V_s is in m/sec, q_t is in kPa, σ'_v is vertical effective stress in kPa, p_a is atmospheric pressure (101.325 kPa), and I_c is the soil behavior type index.

The CPT-2 sounding and dispersion curve measured for Seismic Line 2 were used in this study, and the following constants were found to provide a good fit as shown in Figure 3-6: $\beta_0 = 0.5$, $\beta_1 = 0.58$, and $\beta_2 = 0.35$. This particular combination of CPT-2 and Seismic Line 2 were selected because: (1) they are at similar distances from the river, and site conditions are known to

depend on this distance; and (2) the soil directly below the HWB at the location of Seismic Line 1 is known to have been significantly reworked during post-earthquake construction to retrofit the bridge foundations. Therefore this soil does not represent site conditions outside of the bridge footprint.

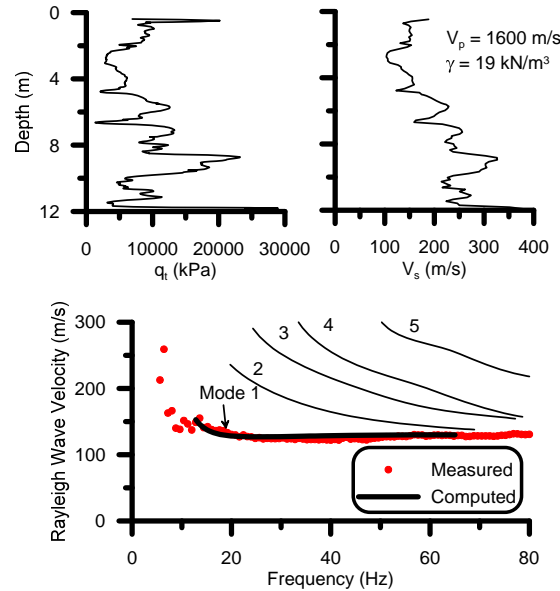


Figure 3-6: CPT-2 tip resistance, inferred shear-wave velocity profile, and dispersion curves used to fit parameters in Equation(3.1).

Utilizing the β values determined for CPT-2 and Seismic Line 2, V_s profiles can be computed at the location of other CPT test sites, as shown in Figure 3-7. Comparing CPT-1, 2, and 3, the velocity profile tends to stiffen with increasing distance from the river, which is consistent with the interpreted geology at the site and the trends in the penetration resistance tests. Comparing CPT-1 and CPT-4, which are similar distances from the river but on opposite banks, the west bank of the river tends to be stiffer than the east bank. This is also consistent with geological conditions since younger deposits exist on the east side of the river. Time-averaged shear wave velocity over the upper 30 m (V_{s30}) was estimated to range between approximately 180 and 230 m/sec for subsequent calculations.

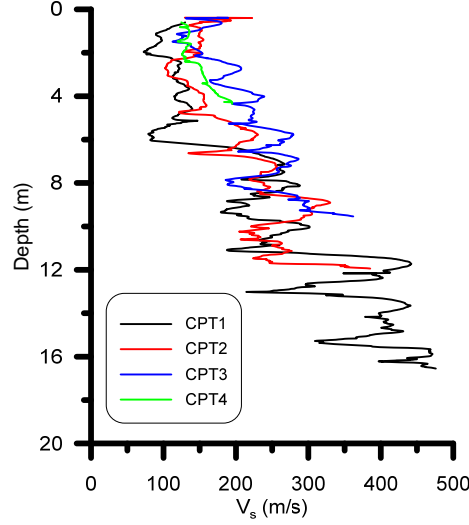


Figure 3-7: Profiles of shear wave velocity estimated at CPT test sites using Equation (3.1) with $\beta_0 = 0.5$, $\beta_1 = 0.58$, and $\beta_2 = 0.35$.

3.4 BRIDGE DETAILS

The HWB and RRB both consist of precast-prestressed simply supported concrete spans on elastomeric bearings resting atop reinforced concrete bents supported on deep foundations. The bents of the HWB were designed to match the 20-m spacing of the RRB, with ten spans total for an overall length of 200 m. The primary difference between the two bridges is the size and number of foundations that support each bent, which will be described further in the following sections.

3.4.1 Highway Bridge (HWB)

The following structural details are primarily based on the bridge construction plans (1998) provided to the research team by SCT. The HWB was designed by a private engineering firm from Mexico City, *Sigma Ingenieria Civil, S.A. de C.V.*

Each of the bridge's ten 20-m-long spans consists of seven precast-prestressed 1.15 m-deep I-shaped girders. Vertical post-tensioned diaphragms connect the ends of the girders in the transverse direction. Precast slab panels rest on the top flanges of adjacent girders, covered by a

cast-in-place deck slab. The total deck width is about 11 m. Plain laminated elastomeric bearings transfer loads from the girders to 60-cm-wide concrete masonry plates atop the 1.6-m-wide bent caps, which are in turn supported on four extended-shaft columns.

At the bents between spans 3–4 and 7–8, as well as at the end supports at the abutments, the only connection between the girders/diaphragm and the bent cap is the elastomeric bearings. The bearings transfer load and allow for relative displacement and rotation between the superstructure and the substructures by compressing and deforming in shear. The deck slabs are separated by a polymer-filled joint at these locations to allow for thermal expansion and contraction.

At the remaining bents, including Bent 2 and Bent 5 that suffered flexural damage during the EMC earthquake, translation of the girders is restrained by anchorage via two rectangular shear tabs that extend from the base of the diaphragm into the bent cap, as shown in Figure 3-8. The anchorage tabs fit into a rectangular slot cast into the bent cap such that translation is restrained in both the longitudinal and transverse directions. A felt pad lines the joint between the anchorage tabs and the bent cap; no reinforcing bars form a positive connection between the two elements. A small amount of rotation is allowed at these connections, hence they are considered to be “pinned” as opposed to moment-resisting connections. It is assumed that the elastomeric bearings are intended to accommodate lateral deformation under service loads, while the anchorage tabs are meant to prevent unseating during extreme events. The end conditions of all ten spans are considered simply supported.

At each bent, four 1.2-m-diameter extended-shaft columns are continuous with four drilled shaft foundations of the same size and reinforcement detail. A transverse beam near the ground level joins the shafts at each bent with the exception of Bent 2, which has a larger pile cap. The

foundations in the river extend to the deepest elevation, approximately 17 m below the river surface elevation, as shown in Figure 3-4, while the foundations nearest the abutments and beneath the eastern spans where the river flows less frequently are shorter by 3 to 6 m. A cross section of the bridge adapted from the construction plans is shown in Figure 3-4.

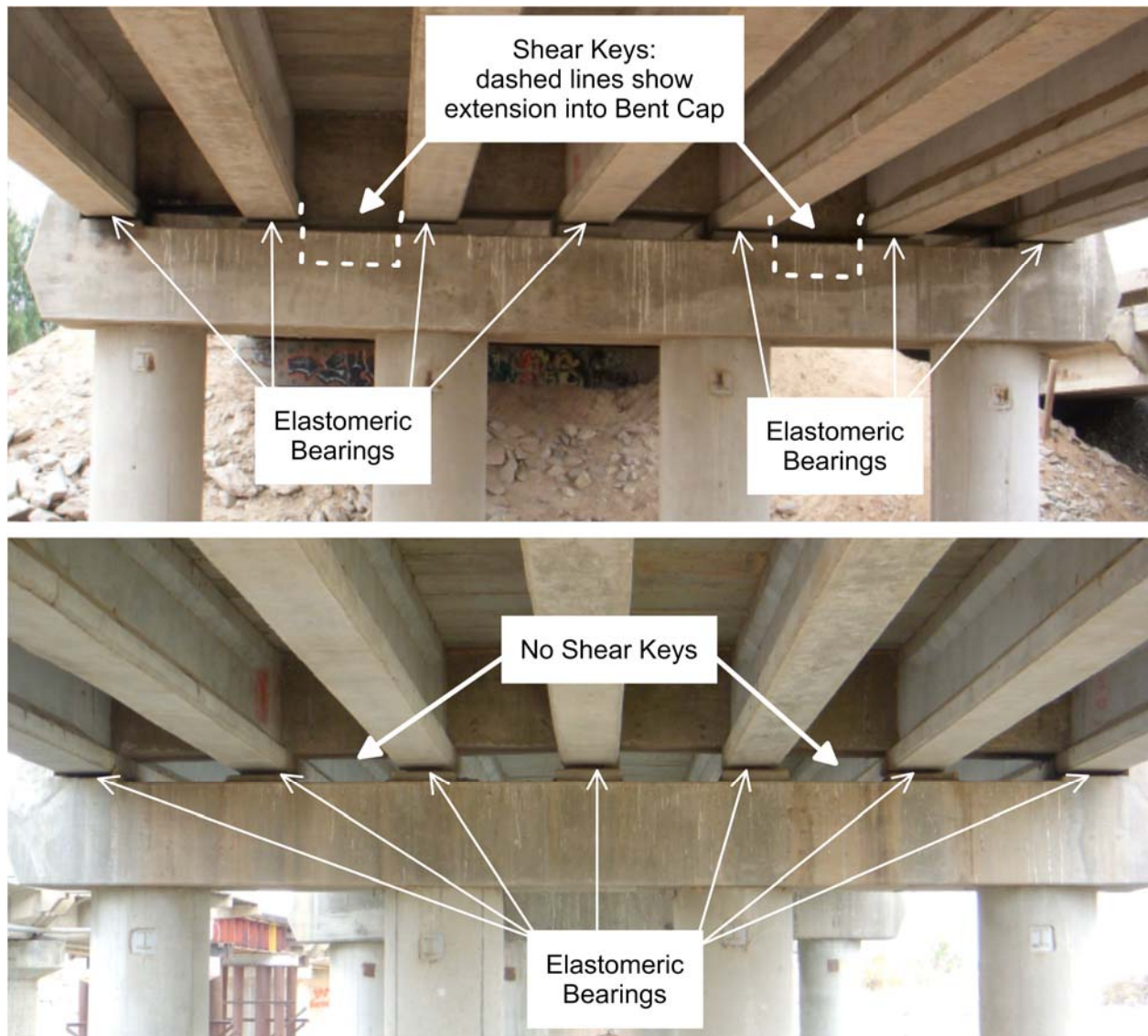


Figure 3-8: Bent 1 of highway bridge showing shear tabs extending from transverse diaphragm into bent cap (top) and Bent 3 with no shear tabs (bottom). Photos B. Turner, 2013.

Design documents provided by SCT indicate that each shaft was designed to carry an allowable axial load of about 2100 kN. Axial dead load estimated from the superstructure (girders, deck, and nonstructural components) was approximately 1,050 kN, which is consistent with a static factor of safety against axial failure of 2.0, although this does not consider the self-weight of the column. It is not known if the bridge was explicitly designed to resist loads resulting from liquefaction such as downdrag or lateral spreading, but the absence of any discussion of these subjects in the design documents suggests they were not considered.

During the October 2013 site investigation, Mr. Ramón Pérez Alcalá, an engineer for SCT who was responsible for overseeing construction of the bridge in 1998–1999, provided information on the methods used to construct the foundations. Temporary steel casing was advanced under its own weight, or using hydraulic jacks in stiff layers, while the spoils were removed by air lifting. Water was pumped from the river and maintained at or above ground level to keep a positive head within the hole. Concrete was placed using the tremie method after the reinforcing cages were in place. All the foundations were installed to the depths shown on the construction plans. A cold joint exists at the approximate ground surface elevation during construction since the columns were not ready to be constructed when the foundations were poured. Based on photographs provided by Mr. Alcalá, such e.g., Figure 3-9, the foundation reinforcing cages are lap spliced with the column reinforcement by approximately 3 to 4 m.



Figure 3-9: Construction of highway bridge foundations via casing and air lift method, circa 1999.
Photo courtesy Ramón Pérez Alcalá, SCT.

Mr. Alcalá also explained why Bent 2 has a pile cap not present at the other bents. A void related to a previous structure was encountered during construction of the foundations. Since a foundation passing through the void could not be relied upon, a fifth shaft was constructed south of the bridge and connected to the other foundations and columns via the pile cap.

Further information regarding the dimensions and mechanical properties of the bridge elements is provided in Section 4.3

3.4.2 Railroad Bridge (RRB)

The RRB, constructed in 1962 (EERI 2010), consists of a single track supported on three 1.2 m-deep I-shaped girders. The simply supported spans rest on plain elastomeric bearings atop oblong-shaped reinforced concrete pier walls that are most likely supported on driven pile foundations. No shear keys or other form of anchorage were observed to prevent an unseating failure if the

elastomeric bearing capacity is exceeded. Simply supported concrete slab walkways parallel the track on each side. The research team was unable to obtain construction plans or design documents for the RRB.

Foundation details are unknown, but given the timeframe of construction, the fluvial environment, and the propensity of North American railroad companies to use driven pile foundations to this day (e.g., the post-earthquake repair of the RRB utilized driven steel piles), it is most likely that the pile caps are supported on driven pile foundations as opposed to drilled shafts. Because it is not known whether timber, concrete, or steel piles were used, analyses were performed considering all three materials over a range of sizes and group layouts; see Chapter 4.

In order to quantify the structural properties of the RRB for modeling purposes, direct measurements of the above-ground member geometry were taken during the October 2013 site investigation. The size of the pile cap was inferred from photographs taken by members of the GEER team (2010) during the repair efforts by Ferromex in which the soil above and around the pile cap had been excavated to facilitate installing new driven piles.

Given the date of construction, it is almost certain that the RRB foundations were not designed to resist the effects of liquefaction and lateral spreading.

3.5 APRIL 4, 2010 M 7.2 EL MAYOR-CUCAPAH EARTHQUAKE

The Mexicali and Imperial Valley region is known to be seismically active, with several major earthquakes occurring in recent history, including an estimated **M** 7.2 event in 1892 (Hough and Elliot 2004). The EMC earthquake caused widespread damage to buildings, utilities, and transportation and agricultural infrastructure throughout the Mexicali and Imperial Valleys (GEER 2010; EERI 2010).

Rupture occurred mainly along the Pescadores and Borrego faults through the Sierra El Mayor mountain range northwest of the epicenter and the previously unknown Indiviso fault to the southeast, which was buried beneath sediments of the Colorado River delta prior to the earthquake (GEER 2010; USGS 2010; McCrink et al. 2011). This series of faults represents the southern continuation of the Elsinore fault zone in Southern California. Fault offset was oblique with the primary component being strike-slip. Further details of the complex rupture propagation, which appears to have started along a short unnamed normal fault and then propagated north and south along the strike-slip faults, are provided in GEER (2010), Hauksson et al. (2011), and Wei et al. (2011).

The SFB site is approximately 14.5 km east of the fault rupture zone (R_{jb} ; note $R_{jb} = R_{rup}$ for vertical strike-slip faults). The three nearest strong-motion recording stations are *Riito*, *Saltillo*, and *Geotérmica*, located approximately 12, 21, and 24 km from the SFB, respectively (see Figure 3-10). Peak ground accelerations (PGA) recorded at the three stations were 0.40, 0.15, and 0.29g, respectively. A weighted average based on distance of these three values yields a PGA of 0.29g for the SFB site, but this estimate fails to consider site effects and is clearly inaccurate due to the variability of the three recorded motions.

The USGS PGA Shakemap (USGS 2010) for the EMC earthquake estimates a PGA of about 0.32g for the SFB site, as shown in Figure 3-10. However, the Shakemap PGA values south of the U.S.–Mexico border are based entirely on estimated ground motions using “standard seismological inferences and interpolation” and are not constrained by recorded motions (USGS 2014). The nearest recording station to the SFB site used to generate the USGS Shakemap is approximately 50 km to the northwest; hence the estimated value is only approximate and does not consider local site effects.

In order to estimate PGA at the SFB site including site effects, the procedures described by Kwak et al. (2016) were used. In this method, a Kriging (spatial interpolation) procedure is used to estimate the residual of the selected ground motion prediction equation (GMPE) at the location of interest considering the residuals at nearby recording stations and the event term. (The residual is the misfit between a recorded motion and the GMPE prediction for that location, and the event term is the average of the residuals for all recordings from the earthquake, essentially representing the average misfit of the GMPE to the recordings.) This procedure captures the event term directly and approximately accounts for region-specific path terms. Site effects are captured at the level of resolution of the site term in the GMPE [i.e., they are not site-specific, hence this does not correspond to a single-station sigma condition; e.g., Rodriguez-Marek et al., (2011)]. This technique was used to estimate the residual at the SFB site (about -0.04 for PGA, in natural log units), which was subsequently added to the median predicted PGA from the BSSA 2014 GMPE (Boore et al. 2014) with appropriate site and distance parameters. The resulting estimated PGA range is 0.26 to 0.27g for estimated V_{s30} values of 180 to 230 m/sec, respectively. The same procedure was repeated for spectral acceleration at periods corresponding to the estimated first mode periods of the SFB (determination of these values is discussed in Section 4.4). The estimated values of spectral acceleration are shown in Figure 3-11, including error bars that represent within-event aleatory uncertainty ($\pm\phi$). Estimated spectral displacements at the bridge first-mode periods are also shown; spectral displacements will be used with the proposed analysis method discussed in Chapter 4.

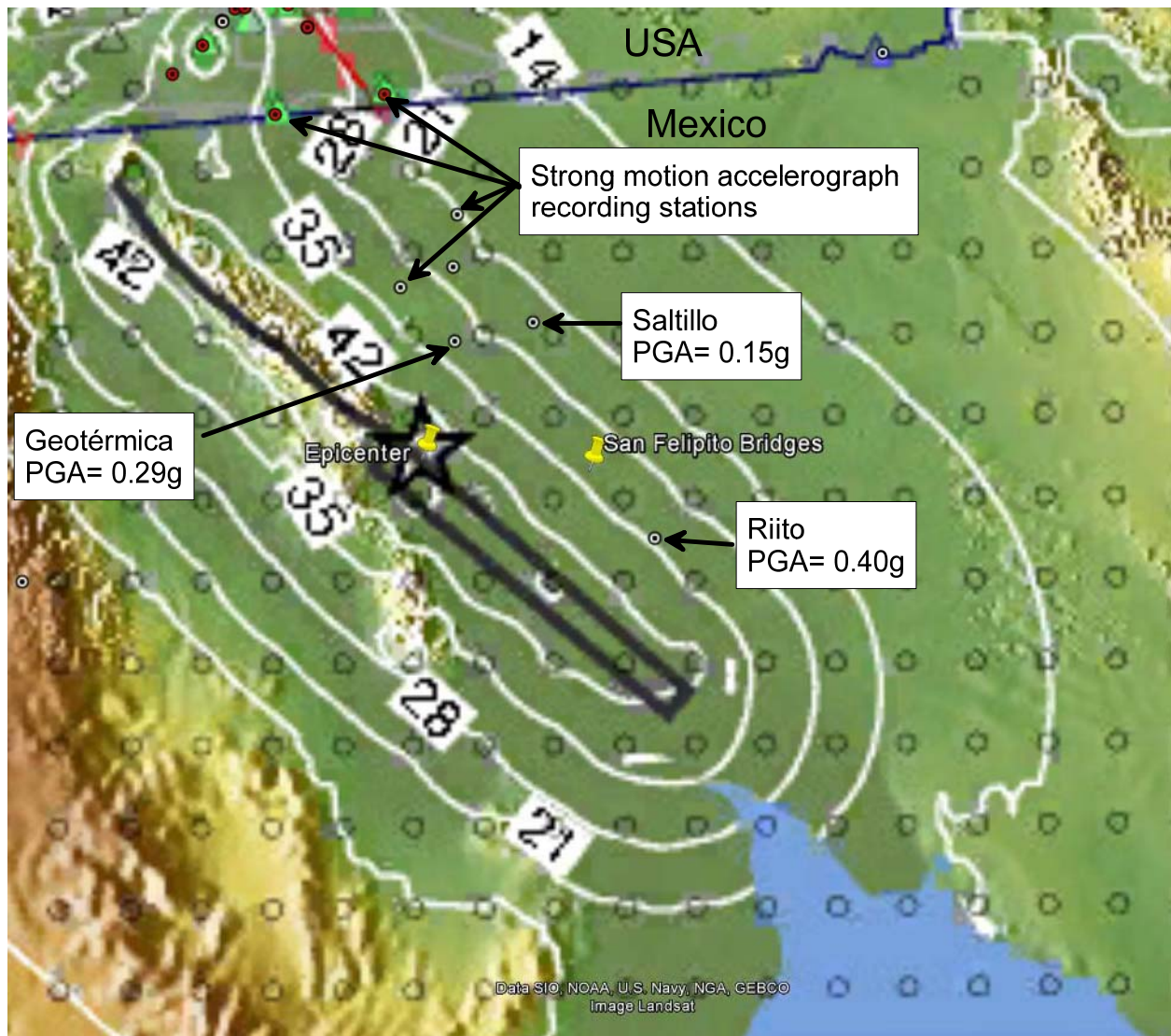


Figure 3-10: USGS Shakemap for PGA. Contours show Shakemap estimated PGA in %g based on GMPE estimates (not constrained by recordings south of the U.S.–Mexico border). Measured PGA shown for SMA recording stations nearest the San Felipe Bridges. Adapted from USGS Shakemap (2010).

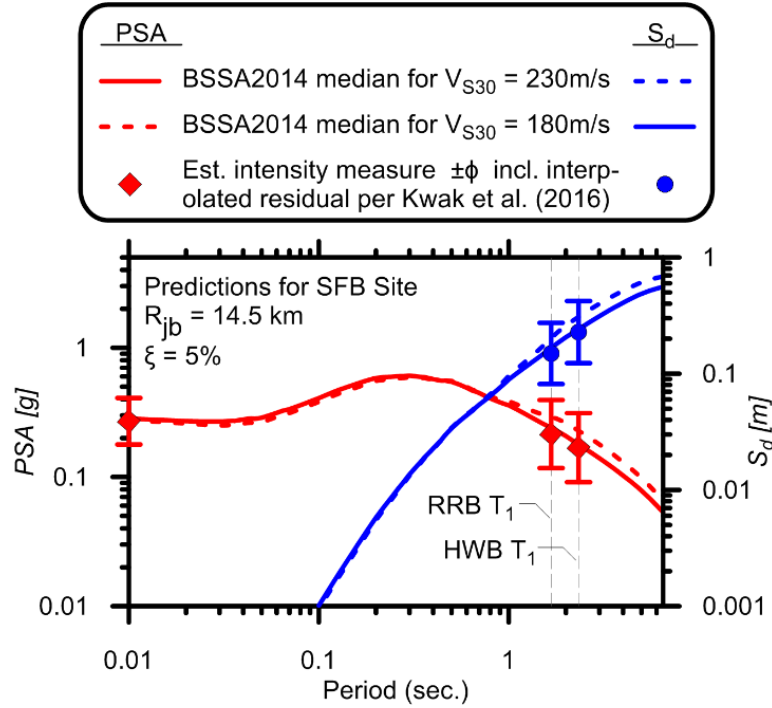


Figure 3-11: Pseudospectral accelerations and spectral displacements estimated for SFB site during El Mayor-Cucapah earthquake.

3.6 OBSERVED DAMAGE

This section summarizes the observed ground failure and structural damage attributed to the EMC earthquake at the SFB site as documented by the GEER (2010) and EERI (2010) teams. Further details of the damage are available in the respective reconnaissance reports. The observed behavior was used as the basis for evaluating the predictive capability of the analyses described in Chapter 3.

3.6.1 Ground Deformation

Lateral spreading cracks were documented by the GEER team; see Figure 3-3. The maximum documented lateral spreading surface displacement, based on summing the width of cracks at the ground surface along a transect, was 4.6 m towards the east river bank about 60 m north of the bridges. Lateral spreading along the bridge alignment was reduced due to the restraining influence

of the bridge foundations. However, this is not a traditional "pinning" effect (e.g., Martin et al. 2002) because the out-of-plane width of the spreading deposit is very large relative to the bridge foundations; therefore, the resistance provided by the foundations is negligible compared to the inertial force of the displacing crust. (In contrast, the foundation resistance is significant for the case of a finite-width earth structure such as an embankment). Thus a free-field ground displacement profile is needed for structural analysis, and the measurements 60 m north of the bridge are considered reasonable estimates of the free-field conditions.

Lateral spreading deformation was observed to be greater on the east bank of the river than the west bank, which is likely because the river currently flows along the western margin of its floodplain so the alluvial sediments on the east bank are looser and more susceptible to liquefaction. Similar deformation patterns at a river bend are documented by Robinson et al. (2012). In general, lateral displacements were observed to decrease with increasing distance from the river, as well as in close proximity to the bridges.

At the HWB Bent 6, apparent vertical ground settlement of about 30 to 50 cm relative to the bridge columns was observed on the river-side of the columns; see Figure 3-12. The apparent relative vertical displacement on the upslope side of the columns was smaller, about 10 to 15 cm. These estimates of settlement are based on the assumption that the height of soil stuck on the sides of the columns (as shown in Figure 3-12) is representative of the ground level immediately preceding the earthquake; however, other explanations for the soil marks cannot be ruled out. The settlement was likely due to a combination of post-liquefaction reconsolidation of the liquefied soil layers and extension/shear strains associated with lateral spreading of the crust. As a result, there is no means for independently measuring the amount of vertical settlement that occurred due to reconsolidation alone.



Figure 3-12: Approximately 30–50 cm of apparent relative vertical displacement between the ground and river-side of columns at Bent 6 of the highway bridge. Apparent relative vertical displacement on the upslope side is about 10 to 15 cm. Photo by J. Gingery, Kleinfelder/UCSD, 2011.

The Bent 6 columns themselves also settled about 50 cm as evidenced by vertical displacement in the bridge deck. Combined with the 30–50 cm of apparent relative displacement between the ground and the river-side of the column, this indicates that the total ground settlement may have been as much as 0.8–1.0 m downslope of the columns, and about 0.6 m upslope of the columns.

3.6.2 Structural Damage

The bents of the RRB closest to the east and west river banks translated toward the river due to lateral spreading, which exceeded the lateral displacement capacity of the elastomeric bearings and led to unseating of the girders for a span on the eastern bank and near-collapse of a span on the west bank (Figure 3-13). The translation was observed to occur with relatively little corresponding pier rotation. The bridge deck also displaced in the transverse direction relative to

the bents; although displacements in the longitudinal direction were greater. Ferromex erected steel trestles to replace the collapsed span and support the nearly collapsed span on the west bank.

Damage to the HWB was concentrated in discrete zones and was moderate overall. In contrast to the RRB, the HWB exhibited much better performance; it remained in operation immediately following the earthquake and required repair efforts that were completed with minimal disruption to traffic. The damage documented by the reconnaissance teams is summarized as follows:

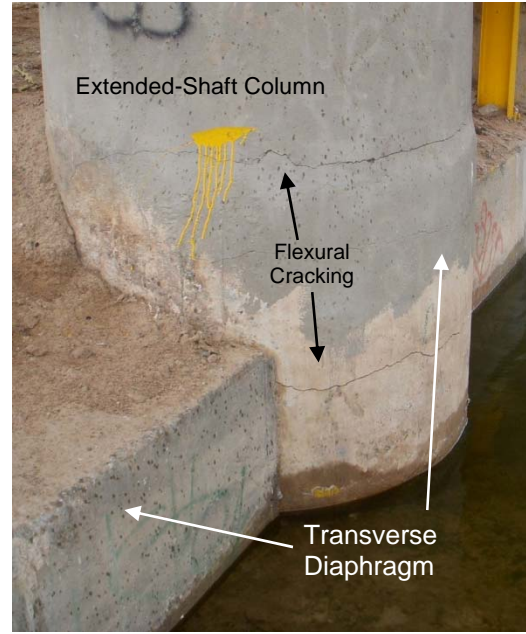
- Shear keys extending up from the ends of the bent caps intended to prevent unseating of the girders in the transverse direction were damaged, indicating that inertial demands in this direction were significant. Shear keys on the west abutment bent cap were damaged in a similar manner.
- Flexural cracking was observed on the inward (river side) of the base of the columns of the bents on both sides of the river (Bent 2 and Bent 5), indicating horizontal movement of the foundations and pile cap towards the center of the river due to lateral spreading. Cracks on Bent 5 are shown in Figure 3-13. The bridge deck showed minor cracking above these damaged bents.
- Bent 6 settled vertically about 50 cm, which cracked the pavement immediately above the bent. SCT subsequently installed six additional 1.2-m diameter drilled shafts to a depth of 27.8 m around the perimeter of the existing Bent 6 foundations and connected the new and old foundations via a post-tensioned pile cap (SCT, personal communication, January 2013). Post-earthquake boring 1 (PEB-1, shown in Figure 3-3) was performed

adjacent to Bent 6 in support of the design effort for the additional foundations. The deck was subsequently re-leveled and the concrete masonry pads that support the elastomeric bearings were extended vertically to accommodate the height change.

Column rotations were measured for the bridge bents on the east side of the river during the October 2013 site investigation. HWB Bent 5 columns were rotated between approximately 0.9° and 1.7° away from the river, i.e., the bottom of the column was displaced towards the river relative to the top of the column. The measured rotation was smallest for the column closest to the RRB and increased approximately linearly to the south, indicating that more lateral spreading demand was imposed on the south columns than the north. HWB Bent 6 columns were uniformly rotated about 1.1° away from the river. Rotations for Bents 7, 8, and 9 ranged between about 0.4° and 0.1° , with a clear trend of decreasing rotation with increasing distance from the river. The RRB Bent 5 column, which translated enough to cause unseating of one of the spans it supported, rotated about 0.4° away from the river and about 0.6° to the north; it was difficult to measure the rotation because the surface of the column was rough. The remaining RRB bents on the east side of the river had essentially zero measureable rotation.



(a)



(b)

Figure 3-13: (a) Railroad bridge Bent 5 translated due to lateral spreading demand, causing an unseating collapse; arrow shows direction of movement. Photo during GEER reconnaissance by D. Murbach, City of San Diego, 2011; and (b): flexural cracking at base of highway bridge Bent 5 extended-shaft column. Photo B. Turner, 2013. Note that these two bents are adjacent to each other.

4 Analysis

In order to validate the equivalent static analysis (ESA) procedures recommended by Ashford et al. (2011) and Caltrans (2013a), the San Felipito Bridges (SFB) were analyzed as described in this chapter and the results compared to the observed behavior described in the previous chapter. Three separate analyses were performed as depicted in Figure 4-1:

- Highway bridge (HWB) Bent 5 with imposed lateral spreading and inertial demands,
- Railroad bridge (RRB) Bent 5 with imposed lateral spreading and inertial demands, and
- The axial response of HWB Bent 6.

The locations of Bents 5 and 6 are shown on the Figure 3-3 site plan and the cross sections in the previous chapter.

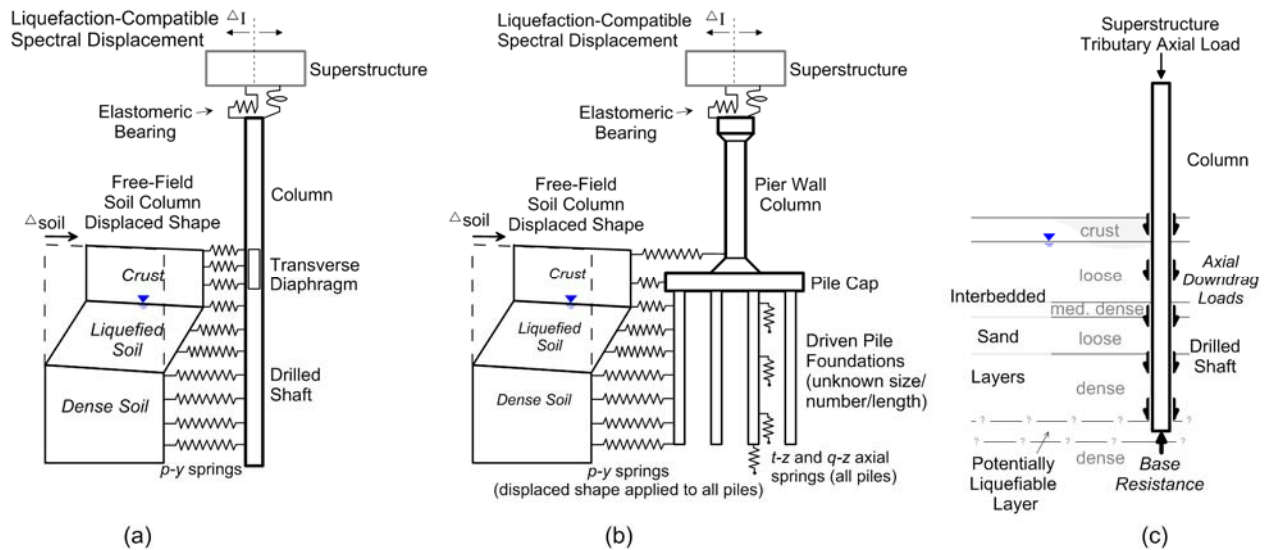


Figure 4-1: Numerical models of (a) highway bridge Bent 5 lateral analysis, (b) railroad bridge Bent 5 lateral analysis, and (c) highway bridge Bent 6 axial analysis.

The project scope initially included analyzing HWB Bent 2 under lateral spreading demand. However, the research team was unable to perform site investigation at this location due to a malfunction of the CPT rig. Furthermore, the revelation that an additional foundation was installed here because of an underground void discovered during construction complicated the structural modeling.

A detailed treatment of the steps required to perform the ESA procedure is given by Ashford et al. (2011) and Caltrans (2013a) and will not be repeated here, however some of the calculations performed to quantify input parameters for the analyses are included in Appendix C. In summary, the methods provide a set of relatively simple tools that foundation engineers can use to estimate the engineering demand parameters (EDP) necessary to design bridge foundations in laterally spreading ground. The foundation design is intended to be performed in concert with the design of the superstructure in order to provide compatible behavior at the desired performance level.

The ESA procedure is performed using a two-dimensional static beam on nonlinear Winkler foundation (BNWF) approach. The analyses for this project were performed with the finite-element modeling platform *OpenSees* (McKenna 1997; McKenna et al. 2010). In theory, the analysis could be performed with any numerical analysis software that incorporates the BNWF approach and allows the user to impose a displacement profile to the free ends of the soil springs to simulate lateral spreading, and permits adequate consideration of important structural details. For example, the Caltrans (2013a) lateral spreading design guidelines describe how to perform the analysis using the finite-difference method program *LPILE* made by ENSOFT (Reese et al. 2005). *OpenSees* was used instead of *LPILE* because (1) it permits more detailed structural modeling (e.g., bearings between piers and girders, rotational stiffness at the top of the pier column, etc.), (2) it permits modeling of groups of piles (ENSOFT also makes *GROUP*, which permits analysis of pile groups), and (3) *OpenSees* is freely available.

Since the HWB bents consist of four identical extended-shaft columns with approximately equal tributary loads, the analysis was performed for a single shaft, and the results are assumed to represent the behavior of all four shafts at the bent. The shafts form a single row in the bridge transverse direction, so group-interaction effects do not apply for lateral spreading loading in the bridge longitudinal direction. In contrast, the RRB bents consist of a single column supported on a pile cap that connects multiple rows of piles (it is assumed that multiple rows of piles exist based on traditional construction methods). To accurately capture the foundation group-interaction effect (i.e., the overturning resistance provided by the axial load in each row of piles times its eccentricity from the pile cap centroid), the system was explicitly modeled with multiple rows of piles. Each row of piles for the RRB is represented by a single pile with a flexural rigidity (EI) equal to the EI of a single pile times the number of piles in the transverse row. The actual number of rows of piles

and number of piles per row for the RRB is unknown; Section 4.6.2 includes discussion on how this uncertainty was addressed in the analysis.

Above-ground portions of the bridge bents were modelled explicitly up to the elastomeric bearings. An alternative that is often used when modeling using *LPILE* or *GROUP* is to decouple the column demands from the foundation demands and impose the estimated column demands on the foundation for the BNWF analysis. However, explicitly modeling the columns is a superior approach because in many cases the lateral spreading demands are resisted by a combination of the foundation(s) and superstructure (i.e., the columns, girders, and deck segments), and knowing the demands at the base of columns *a priori* is often not possible. Furthermore, knowledge of the damage to the bridges in this study is based primarily on post-earthquake observations of above-ground structural elements, namely cracking, rotation, and translation of columns. Since this damage was used as the basis for evaluating the accuracy of the predicted EDP, it was necessary to include the above-ground elements in the model.

The following sections document the input parameters used in the *OpenSees* models of the bridges followed by results of the analyses.

4.1 SOIL PROPERTIES

CPT data were correlated to soil properties using the procedures described by Robertson (2012) and Idriss and Boulanger (2008). Peak friction angle was estimated in a manner consistent with critical state soil mechanics with an assumed critical state friction angle of 32° for quartz sand (Bolton 1986). Further details of the correlations are provided in Appendix C. Soil properties for each layer of the idealized soil profile used for the lateral spreading analyses are presented in Table 4-1.

Using the overburden-normalized penetration resistance profiles presented in Appendix A and the soil properties presented below, liquefaction susceptibility and triggering analyses were performed per the recommendations of Idriss and Boulanger (2006; 2008). Soil layers with I_c less than 2.6 were assumed susceptible to liquefaction, which is supported by the laboratory tests performed on samples collected during the field investigation that showed that the fines fraction of the silty sand consisted of nonplastic silt. Groundwater depth was taken as 1.5 m below the ground surface.

Because lateral spreading demand acting on the bridges represents a liquefied soil condition, discretization of the soil profile into the idealized layers presented in Table 4-1 was based primarily on the results of the liquefaction triggering analysis. Correlated soil properties such as relative density and peak friction angle were then computed based on the average values estimated over the depth interval of each layer.

Analyses were performed for the estimated PGA range of 0.17 to 0.41g to capture the uncertainty in V_{s30} and the within-event aleatory uncertainty (ϕ) in the estimated shaking intensity. Triggering of lateral spreading is dependent on the upper loose layer (layer 1 in Table 4-1) liquefying, which it is predicted to do for PGA values greater than about 0.15g. Hence, liquefaction and lateral spreading are predicted for the entire range of PGA values considered for this analysis (0.17 to 0.41g). The estimated lateral spreading displacement at the ground surface using the data from CPT-1 was 3.77 m for the median predicted PGA of 0.27g, with a range of 2.78 to 3.82 m for the median minus/plus one standard deviation PGA values of 0.17 and 0.41g, respectively. The predicted lateral spreading displacement saturates at values of PGA exceeding about 0.23g because maximum shear strains trend towards a limiting value for low factors of safety against liquefaction (FS_{liq}). From these results it is concluded that lateral spreading demand is relatively insensitive to

the range of PGA considered, and thus the median estimated PGA of 0.27g is used from this point forward.

Profiles of FS_{liq} and estimated lateral spreading displacement using data from CPT-1 are shown in Figure 4-2 and are included alongside the CPT data profiles in Appendix A. Estimation of lateral spreading displacement is discussed in Section 4.2.

Table 4-1: Estimated soil properties for Bent 5 lateral spreading analyses.

Layer	Description	Depth range (m)	Unit wt. ^a (kN/m ³)	D_r ^b (%)	Peak friction angle ^c	N_{60} ^d	Excess PWP ratio ^e r_u (%)	Fully-liquefied P -multiplier ^f $m_{p,liq}$	P -multiplier m_p
1	unsaturated silty sand crust	0–1.5	17	55	35°	10	N/A	N/A	N/A
2	loose sand	1.5–6.5	18	42	35°	8	100	0.14	0.14
3	dense sand	6.5–8.4	18	77	40°	27	40	0.47	0.93
4	medium-dense sand	8.4–11.2	18	54	37°	20	100	0.28	0.28
5	very dense sand	>11.2	19	82	41°	44	5	0.70	0.98

^aBased on judgment.

^bBased on a weighted average of Idriss and Boulanger (2008)—40%, Zhang et al. (2004)—30%, and Kulhawy and Mayne (1990)—30%; see Appendix C.

^cRobertson (2012) and Bolton (1986)

^dBased on correlation to q_t and I_c per Robertson (2012); see Appendix C.

^ePWP = porewater pressure; median prediction of correlation by Cetin and Bilge (2012) between shear strain and r_u is shown.

^fBrandenberg (2005)

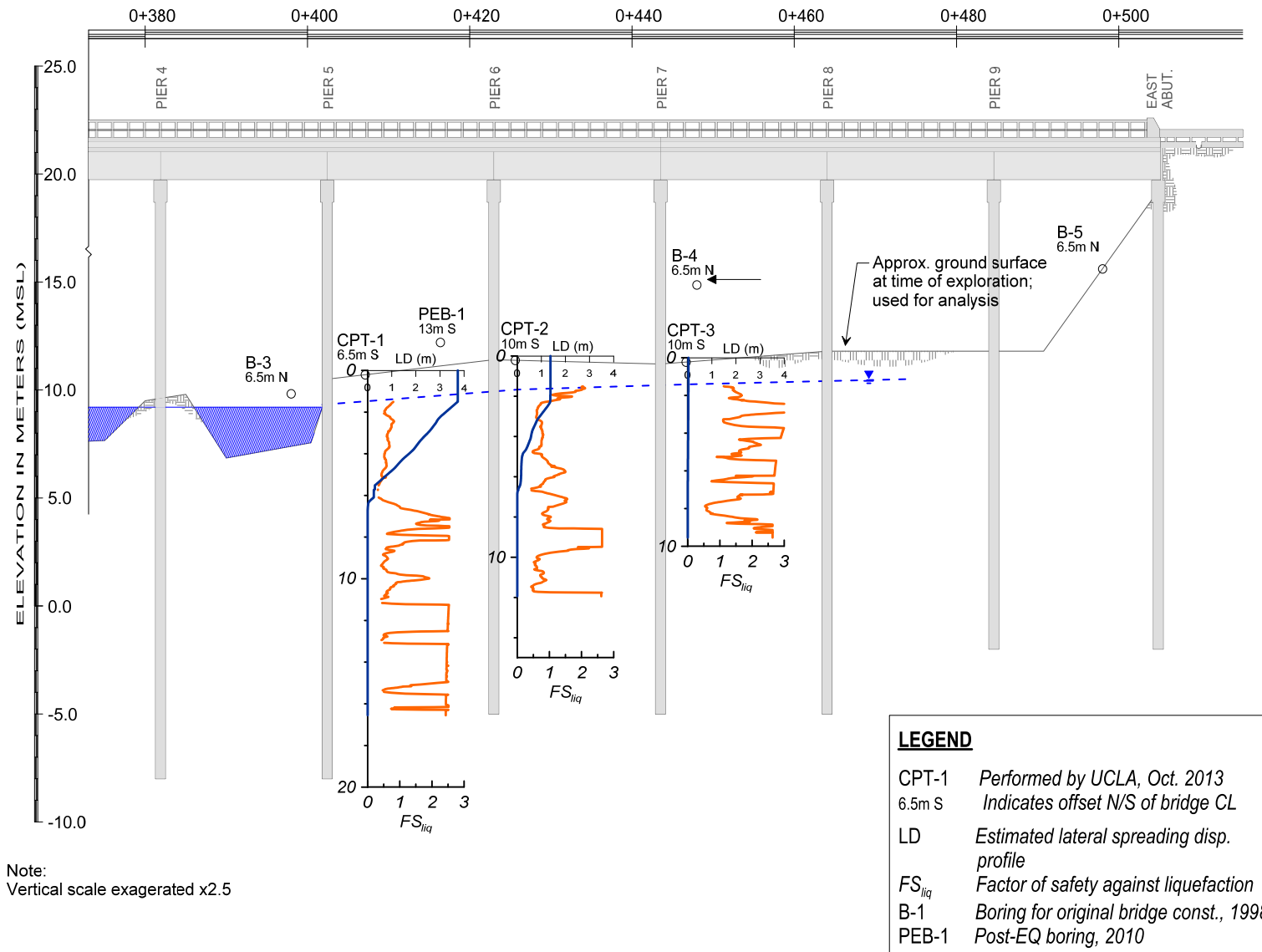


Figure 4-2: Cross section showing eastern spans of highway bridge and computed profiles of factor of safety against liquefaction and lateral spreading displacement.

Interaction between the soil and foundations was modeled using nonlinear p - y springs for lateral loading and t - z and q - z springs for axial side and base resistance, respectively, using the *PySimple1*, *TzSimple1*, and *QzSimple1* uniaxial material models in *OpenSees*. The p - y springs are based on the API (1993) sand formulation considering modulus of subgrade reaction based on relative density values and peak friction angles presented in Table 4-1. The t - z springs utilize the backbone curve of Mosher (1984) with an ultimate resistance based on the effective stress at the spring depth and assumptions of interface friction angle equal to the peak friction angle following the recommendations of Brown et al. (2010) and at-rest (K_0) lateral earth pressure conditions. K_0 was computed as (Jaky 1944):

$$K_0 = 1 = \sin \phi \quad (4.1)$$

Where ϕ is the peak friction angle given in Table 4-1. Q - z springs following the functional form of Vijayvergiya (1977) were created from an estimated unit base resistance of 1500 kPa for the dense bearing layer. Unit base resistance (q_b) was estimated from the CPT data using the following equation (Salgado 2006):

$$q_b = c_b q_{cb} \quad (4.2)$$

where q_{cb} is the cone tip resistance at the pile base level, and c_b is a constant that quantifies the ratio of base resistance to cone tip resistance based on soil type and pile material. A range of c_b values between 0.25 and 0.5 was considered based on the recommended values in Salgado (2006) and a range of q_{cb} values between 1500 and 15,000 kPa. These ranges reflect the uncertainty in pile length, material, and end condition (i.e., full displacement versus open pipe piles). The analysis results are relatively insensitive to the chosen value of base resistance since the majority

of the axial resistance of the piles comes from side resistance. For the HWB, axial resistance does not affect the response to lateral spreading since axial-interaction group effects are not a factor for the single row of extended-shaft columns. However, the end bearing resistance plays a crucial role in the observed settlement at Bent 6, as discussed later.

The t - z and q - z springs are based on the assumption that 50% of the spring's ultimate resistance is mobilized at relative displacements (z_{50}) of 1.5 mm and 1.25% of the foundation diameter, respectively. These z_{50} values imply that the full resistance of the t - z and q - z springs will be mobilized at relative displacements of about 1.5 cm and 10% of the foundation diameter, respectively. For the RRB, the ultimate resistance of the soil springs was multiplied by the number of piles per row in the transverse direction.

The influence of liquefaction on p - y behavior was accounted for by multiplying the computed ultimate resistance of the p - y spring (p_{ult}) by the p -multiplier values (m_p) presented in Table 4-1, which range between 0.14 and 0.28 for the liquefied layers. The p -multipliers were also applied to the t - z springs per the recommendations of Ashford et al. (2011). For the non-liquefied layers, p_{ult} values were reduced to account for the buildup of excess porewater pressure during shaking. Following the recommendation of Dobry et al. (1995), p -multipliers were then linearly interpolated between values corresponding to $r_u = 100\%$ (i.e., $m_{p,liq}$) and the estimated r_u using the following equation:

$$m_p = 1 - r_u (1 - m_{p,liq}) \quad (4.3)$$

Excess porewater pressure ratio (r_u) was estimated using the correlation to maximum shear strain (γ_{max}) by Cetin and Bilge (2012). Maximum shear strains were estimated using the procedure described in Idriss and Boulanger (2008) based on the results of laboratory tests relating

FS_{liq} to γ_{max} by Ishihara and Yoshimine (1992). The Cetin and Bilge strain-based approach tends to predict similar r_u values in comparison to the Marcuson et al. (1990) method that relates FS_{liq} directly to r_u for FS_{liq} values less than or equal to 1.0 (i.e., full liquefaction), and above about $FS_{liq} \approx 1.5$ to 1.9 (depending on D_R). For intermediate values of FS_{liq} in the range of 1.0 to 1.5, the Marcuson et al. method tends to predict lower r_u values than the strain-based method. FS_{liq} values for the idealized stratigraphy presented in Table 4-1 tended to fall outside this intermediate range; hence the analysis results were found to be relatively insensitive to the method used.

P - y springs for the non-liquefied crust layer are based on the lesser of the resultants of Rankine passive earth pressure acting over the height of the non-liquefied crust (i.e., the equivalent block mechanism in which soil becomes trapped between the piles) and log-spiral passive pressure acting over the thickness of the pile cap plus loads on the pile segments beneath the cap (i.e., the individual pile mechanism in which soil flows between the piles). In the out-of-plane direction, these forces are considered over the full transverse width of the pile cap or foundation group. For the RRB, the bottom of the non-liquefied crust does not extend below the level of the base of the pile cap, so the resistance of the piles within the crust was not a factor and the Rankine mechanism controlled. The transverse width of the RRB oblong columns is close to the transverse width of the pile cap, so the pile cap height was taken as the full vertical thickness of the crust (1.5 m). For the HWB, the pressure of a Rankine wedge acting over the full 1.5-m crust thickness was considered. The calculations are shown in Appendix C.

Computed p - y spring parameters for the non-liquefied crust following the Caltrans (2013a) guidelines are presented in Table 4-2. The Rankine passive force resultant includes a three-dimensional modification term to account for the wedge-shaped failure surface (k_w) based on the formulation by Ovesen (1964). The y_{50} term for the p - y springs was estimated using the best-fit

curves given by Caltrans (2013a) based on the recommendations of Brandenberg et al. (2007) considering the softened load-transfer behavior of a crust layer overlying liquefied soil.

Profiles of p_{ult} were “smeared” over a depth equivalent to two foundation diameters per the recommendations of Ashford et al. (2011) to account for the reduction in resistance of stiff soil layers at the interface with liquefied soil. This “smearing” reduces the unreasonably large flexural demands that can occur when abrupt changes in stiffness are encountered at a particular depth, and is supported by three-dimensional finite element modeling by Yang and Jeremić (2002). “Smearing” was not performed within the crust layer, which is relatively thin compared to two foundation diameters, because Rankine earth pressure theory accounts for the loss of friction at the base of the crust layer, and because reducing the crust strength would be unconservative.

Profiles of p_{ult} were “smeared” over a depth equivalent to two foundation diameters per the recommendations of Ashford et al. (2011) to account for the reduction in resistance of stiff soil layers at the interface with liquefied soil. This “smearing” reduces the unreasonably large flexural demands that can occur when abrupt changes in stiffness are encountered at a particular depth, and is supported by three-dimensional finite element modeling by Yang and Jeremić (2002). “Smearing” was not performed within the crust layer, which is relatively thin compared to two foundation diameters, because Rankine earth pressure theory accounts for the loss of friction at the base of the crust layer, and because reducing the crust strength would be unconservative.

P -multipliers were also applied to the rows of piles supporting the RRB to represent shadowing effects during group lateral loading, the phenomenon for which p -multipliers were originally formulated. For the pile configurations that had four rows, p -multipliers of 0.6, 0.6, 0.75, and 0.93 were applied to the furthest trailing row of piles, 3rd row, 2nd row, and leading row, respectively. For the two-row configuration, the p -multipliers were 0.7 and 0.5 for the trailing and

leading rows, respectively. The various group configurations that were analyzed are discussed in Section 4.6.2. P -multipliers were applied in the non-liquefied layers only since shadowing effects are negligible in relatively weak liquefied soil. Note that the leading row of piles is on the side of the pile cap opposite the side exposed to the lateral spreading demand for this condition.

For the axial analysis of HWB Bent 6 under downdrag loads, unit side and base resistances were estimated from the CPT-1 and CPT-2 data as described in 4.6.4. The predicted post-liquefaction vertical reconsolidation settlement of the ground adjacent to Bent 6 was 0.16 m based on the CPT-2 data using the Idriss and Boulanger (2008) approach. The observed vertical settlement at this location was approximately 0.6 m on the upslope side of the columns, about four times the predicted value.

Table 4-2: Non-liquefied crust load-transfer parameters.

Bridge	Passive Force Resultant (kN)	y_{50} for Crust p - y Spring (m)
Highway Bridge	201*	0.12
Railroad Bridge	569	0.07

*Per extended-shaft column, i.e., one-fourth of the demand on the group of four shafts

4.2 LATERAL SPREADING DISPLACEMENT

Lateral spreading surface displacement was computed using methods that integrate mobilized shear strains with depth (Zhang et al. 2004; Faris et al. 2004, 2006) and also using the empirical procedure by Youd et al. (2002). The strain-based methods have a benefit of providing a profile of lateral spreading displacement, which is required as an input to the analysis, whereas the Youd et al. procedure provides only the surface displacement. Both the Zhang et al. and Faris et al. methods involve the following steps: (1) estimate mobilized shear strains in each liquefiable layer based on

correlations with FS_{liq} and shear strains observed in lab tests, (2) integrate strains from the bottom up, beginning in a layer below which no lateral spreading occurs, and (3) adjust the computed ground surface displacement by an empirical factor that depends on static driving shear stress (either from a free-face or sloping ground) to provide a least-squares fit with case histories of measured lateral spreading surface displacements. This procedure is demonstrated in Figure 4-3 using the Zhang et al. (2004) method with the CPT-1 data.

The Zhang et al. (2004) method was implemented as presented in Idriss and Boulanger (2008), and the Faris et al. (2004; 2006) procedure was implemented as presented in the Caltrans lateral spreading guidelines (2013a) using the Idriss and Boulanger (2008) procedure to estimate maximum shear strain. Free-face height was estimated to be about $H = 3.5$ m, the difference in elevation between the river bank and the bottom of the river channel. Lateral spreading demand was truncated at a depth of $2H = 7$ m based on the procedures described by Chu et al. (2006) because static driving shear stresses are not anticipated to be significant below this depth. The Zhang et al. empirical factors based on static driving shear stress were approximately 2.0, 1.3, and 1.0 at locations of CPT 1, 2, and 3, respectively. The decrease of this factor with increasing distance from the river bank free face represents the decrease in static driving shear stress.

Profiles of estimated lateral spreading displacement (LD) using the Zhang et al. method are shown in the Figure 4-2 cross section. The maximum estimated surface LD of about 4 m based on the CPT-1 data is consistent with the maximum observed free-field LD of 4.6 m. The estimated LD using the Faris et al. method of about 1.0 m adjacent to Bent 5 was significantly less than the observed displacement. The large difference between the predictions of the two methods is caused by the difference in estimated shear strain, which reflects the inherent uncertainty in relating penetration resistance to shear strain potential. Utilizing multiple methods to predict lateral

spreading displacement is important for understanding this sort of inherent uncertainty, as suggested by Ashford et al. (2011). More discussion is given in Appendix C.

Estimated LD at the surface using Zhang et al. (2004) versus distance from the free face is shown in Figure 4-4. A clear trend of decreasing LD with increasing distance from the free face can be observed. This is attributed to the increasing relative density with increasing distance from the free face, and decrease in static driving shear stress (captured by the empirical factor relating shear strain potential to LD based on the slope conditions).

For comparison, lateral displacement was also estimated using the empirical Youd et al. (2002) procedure for the free-face condition. The Youd et al. method considers the cumulative thickness of layers within the zone being considered for lateral spreading with overburden and energy-corrected SPT blow counts $[(N_1)_{60}]$ less than 15. It is assumed that a CPT tip resistance (q_c) (of about 8 MPa corresponded to $(N_1)_{60} = 15$ following the procedures used by Chu et al. (2006)). The estimated LD adjacent to Bent 5 based on the CPT-1 data is about 6 m, but the ratio of the free-face height to the distance from the free face at this location falls outside the bounds of the empirical database upon which the method is based. For locations adjacent to Bents 6 and 7, the estimated LD are about 2 m and 1 m, respectively, which is significantly greater than predicted using the semi-empirical strain potential methods. The Bent 6 and Bent 7 locations do fall within the bounds of the empirical database for the method.

For the structural analyses of HWB and RRB Bent 5, the free-field LD profile estimated based on the CPT-1 data (3.75 m at the ground surface) was applied to the free ends of the soil springs as recommended by Ashford et al. (2011). The estimated profile predicts relatively uniform displacement (i.e., minimal shear strain) within the crust layer as seen in Figure 4-3, so it was

represented by a tri-linear approximation, which is consistent with the recommendations of Ashford et al. (2011).

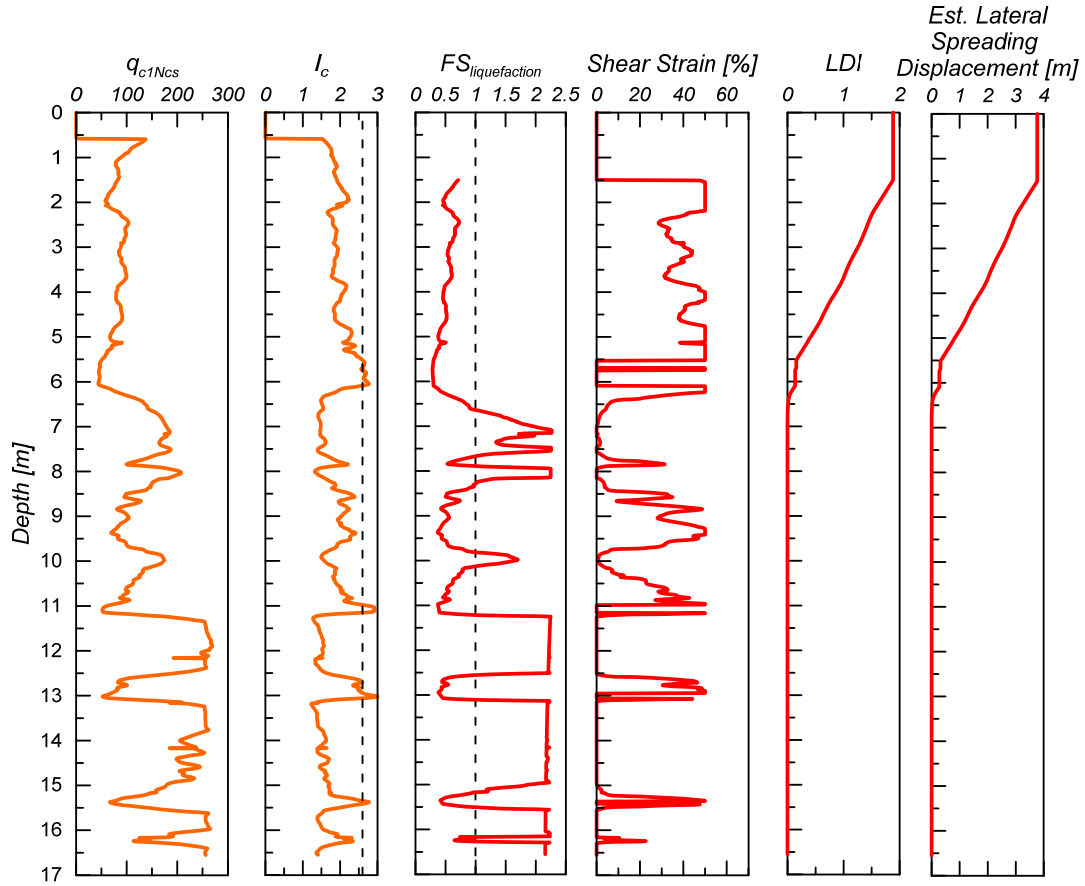


Figure 4-3: Profiles of cone tip resistance and estimated factor of safety against liquefaction, shear strain, lateral spreading displacement index, and lateral spreading displacement for CPT-1 data during the El Mayor-Cucapah earthquake.

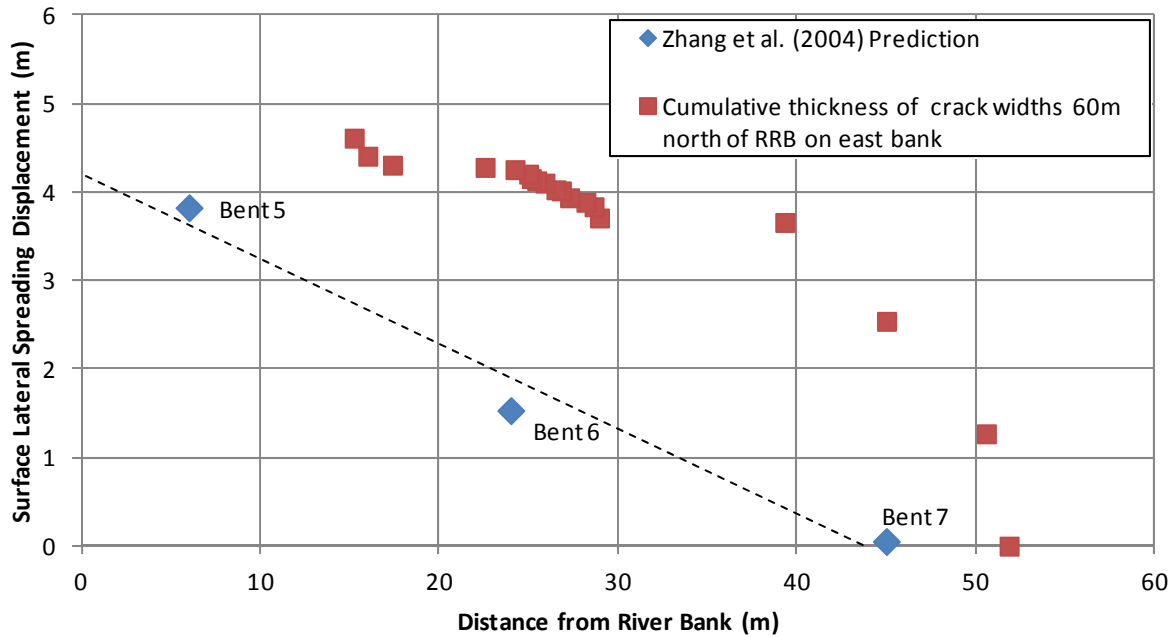


Figure 4-4: Estimated surface free-field lateral spreading (LD) displacement versus distance from free face (river bank) based on CPT-1, CPT-2, and CPT-3 profiles using the Zhang et al. (2004) approach. Decreasing LD with increasing distance appear to fit a linear (shown) or hyperbolic decay trend.

4.3 MODELING OF STRUCTURAL ELEMENTS

Structural properties of the HWB elements are based on the dimensions and material properties shown on the construction plans provided by *SCT*, listed in the tables below. Construction plans for the RRB were not available, so measurements were taken of the above-ground components during the 2013 investigation. The RRB foundations could not be visually inspected, and foundation type is unknown. However, considering that the bridge was constructed in 1962 by a railroad authority, it is most likely supported on groups of driven piles. Since the foundation type is unknown, a list of pile group configurations and material properties spanning the likely range of foundations installed for the RRB was compiled (Table 4-8), and all of these cases were analyzed.

The extended-shaft columns of the HWB and the piles and columns of the RRB were modeled as nonlinear beam-column elements idealized as bilinear with pre- and post-yield stiffness and yield moment based on moment-curvature analyses that modeled concrete cracking and steel rebar yielding and strain-hardening. For the timber and steel piles considered for the RRB, a yield stress of 11 MPa and 414 MPa (i.e., Grade 60 steel), respectively, were used in the moment-curvature analysis. Pile caps and bent caps were modeled as elastic beam-column elements. Each structural element was discretized into 0.1-m-long segments, and five integration points were used for interpolating the element response. The finite element analyses in *OpenSees* were performed using penalty constraints to enforce boundary conditions, using the norm of the displacement increment (*NormDispIncr* command) to test for convergence with a tolerance of 10^{-8} m, and using a Newton-Raphson solution algorithm. A “*P*-delta” transformation was utilized to capture moments induced by offset axial loads.

A cross section of the HWB extended-shaft columns is shown in Figure 4-5, and the railroad bridge elements are shown in Figure 4-6. Structural material properties, member geometry, and nominal strengths used for the *OpenSees* analyses are presented in Tables 3.4–3.8.

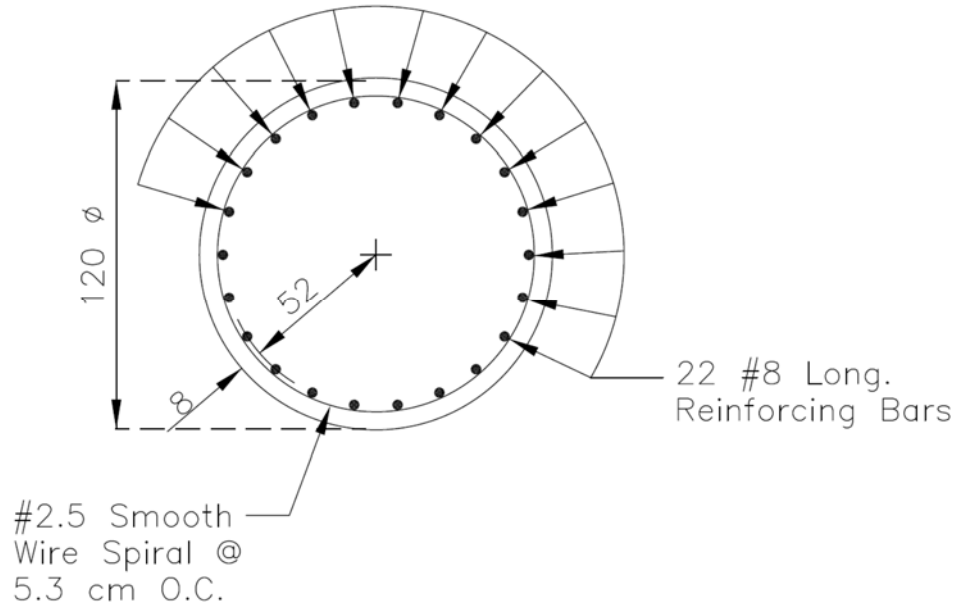


Figure 4-5: Highway bridge extended shaft column structural details. All dimensions in centimeters. Adapted from 1998 bridge construction plans (SCT, *personal communication*, 2013).

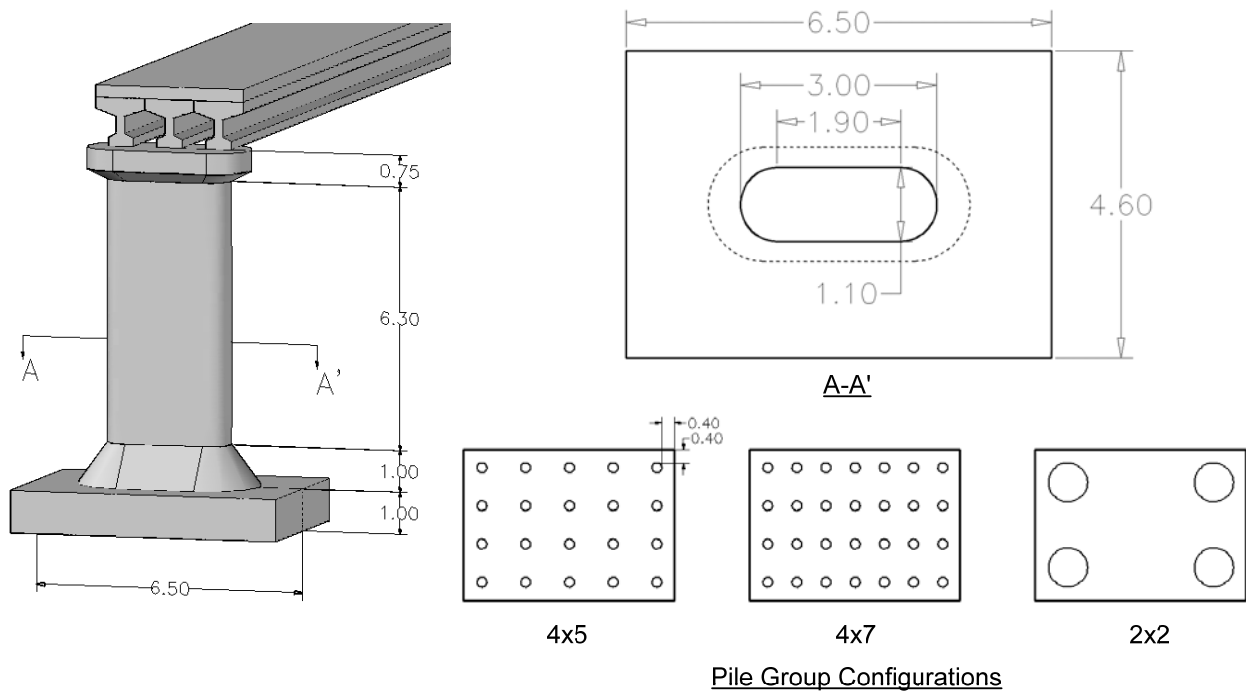


Figure 4-6: Railroad bridge member geometry and foundation group configurations considered for analysis. Clear edge spacing for all pile configurations is 0.4 m as shown for the 4×5 group. Refer to Table 4-8 for pile spacing and details used for analyses.

Table 4-3: Concrete (unconfined) properties.

Compressive strength (f'_c)	Young's modulus (E_c)	Unit weight (γ_c)	Poisson's ratio (ν)
34.3 MPa (5 ksi)	27 GPa	24 kN/m ³	0.2

Table 4-4: Steel properties.

Yield stress (f_y)	Young's modulus (E_s)	Ultimate stress (f_u)	Poisson's ratio (ν)
414 MPa (60 ksi)	200 GPa	552 MPa (80 ksi)	0.3

Table 4-5: Elastomeric bearing properties.

Compression and rotation modulus^a	Young's modulus (E_b)	Shear modulus (G_b)	Shore Hardness
12.2 MPa	3.6 MPa	0.9 MPa	60

^aPer recommendations in AASHTO LRFD Bridge Design Specifications (2012)

Table 4-6: Timber (piles) properties.

Yield stress^a (f_{yt})	Young's modulus^a (E_t)	Poisson's ratio (ν)
11 MPa	7 GPa	0.4

^aReference: Colin (2002)

Table 4-7: Structural Properties for Lateral Spreading Analysis, Highway Bridge.

Member	Dimensions	Cracking moment M_{crack} (kN•m)	Yield moment M_{yield} (kN•m)	Misc. Notes
Elastomeric Bearing	0.3-m width in BTD ^a ; 0.2-m width in BLD ^a 4.1-cm height	N/A	N/A	Post-yield stiffness ratio = 10%; 3.5 bearings per column
Bent Cap	1.0-m height 1.6-m width in BLD	N/A (elastic)	N/A (elastic)	Modeled as 10x stiffer than columns
Extended-shaft Column ^b	1.2-m diameter 9.2-m column height 17.5-m foundation length (Bent 5) 16.4-m foundation length (Bent 6)	620	2,000	See moment-curvature relationship description in Section 4.3.1
Transverse Diaphragm	1.2-m height	N/A ^c	N/Ac	Visible in Figure 3-8

^a BLD = bridge longitudinal direction; BTD = bridge transverse direction.

^b Column and drilled shaft foundation have same dimensions and properties.

^c Not included in model because the contribution to bending resistance is considered negligible.

Table 4-8: Structural Properties for Lateral Spreading Analysis, Railroad Bridge.

Element	Dimensions		Flexural Rigidity ^a (EI) (MN•m ²)	Yield moment M_{yield} (kN•m)
RR-Bridge Pile Foundations ^{b,c} (Case #)	(1)	4x5 group of timber piles, $D = 30\text{cm}$, $L = 10\text{m}$, $CCS = 4/4.5$	2.8	30
	(2)	4x5 group of RC piles, $D = 30\text{cm}$, $L = 10\text{m}$, $CCS = 4/4.5$	11	58
	(3)	4x5 group of RC piles, $D = 30\text{cm}$, $L = 15\text{m}$, $CCS = 4/4.5$	11	58
	(4)	2x5 group of RC piles, $D = 30\text{cm}$, $L = 10\text{m}$, $CCS = 12/4.5$	11	58
	(5)	4x5 group of steel piles, $D = 30\text{cm}$, $L = 10\text{m}$, $WT = 1\text{ cm}$, $CCS = 4/4.5$	19	265
	(6)	4x5 group of steel piles, $D = 30\text{cm}$, $L = 10\text{m}$, $WT = 2\text{cm}$, $CCS = 4/3$	35	480

^a Represents cracked sections properties for reinforced concrete sections.

^b Range of properties considered in analyses due to uncertainty with regards to actual foundation properties

^c Abbreviations used in table: D = diameter, L = length, RC = reinforced concrete, WT = steel pile wall thickness, $CCS = (l/t)$ center-to-center spacing of piles in bridge longitudinal/transverse directions, respectively, in terms of number of pile diameters.

4.3.1 Moment-Curvature Analysis

Behavior of foundation elements is highly nonlinear when demands exceed the foundation yield capacity. Hence, numerical models intended to accurately capture post-yield behavior must include nonlinear material load-deformation relationships. For this project, it was assumed that the foundation performance at large displacements was dominated by flexural behavior, and the moment-curvature ($M-\phi$) relationships were modelled using bilinear approximations of the nonlinear curves. Shear and axial load-deformation relationships were modeled as elastic.

The first step in this process was estimating the actual nonlinear $M-\phi$ relationships for the bridge structural elements under a prescribed axial load so that bilinear approximations could be developed. The commercially available software *XTRACT* (TRC Software 2011) was used to perform this task. An example of the resulting $M-\phi$ curve for the HWB extended-shaft columns is shown in Figure 4-7, along with a comparison using the section properties module in *LPILE*.

The bilinear “Hardening uniaxialMaterial” model was implemented in *OpenSees* to approximate the nonlinear $M-\phi$ curves as shown in Figure 4-7. For the HWB extended-shaft columns, a yield moment of 2000 kN•m and post-yield stiffness of 1% of the initial stiffness were found to provide a reasonable match to the nonlinear curve. For the RRB, a post-yield stiffness of 1% was used with the yield moments shown in Table 4-8 to define the bilinear approximations for $M-\phi$ behavior. Note that the $M-\phi$ model implemented in *OpenSees* continues at the post-yield slope indefinitely, i.e., there is no option to implement an ultimate moment capacity. As a result, the model is capable of predicting that a plastic hinge has the ability to sustain extremely large values

of rotation when in fact complete failure and loss of flexural resistance would have occurred in the real system.

The initial slope of the bilinear $M-\phi$ curve corresponds to the cracked section stiffness, not the gross section stiffness. A factor of approximately 0.2 was multiplied by the gross stiffness to capture this reduction based on trial-and-error fit to the post-cracking, pre-yield slope of the curves shown in Figure 4-7. This does not affect the accuracy of the solution for problems in which the cracking moment is exceeded as is the case for the SFB.

The $M-\phi$ behavior depends on axial load. For tension-controlled sections, compressive axial load acts to stiffen the element by retarding the onset of cracking due to flexure. Accordingly, it is necessary to specify an accurate axial load when computing $M-\phi$ behavior. For this project, it was assumed that axial foundation loads would vary between compressive and tensile as the bridge bents rocked back and forth, and that assuming an axial load equivalent to the tributary dead load of the superstructure (i.e., the girders, deck segments, and nonstructural components supported by each bent) represented an average condition that was appropriate for the ESA.

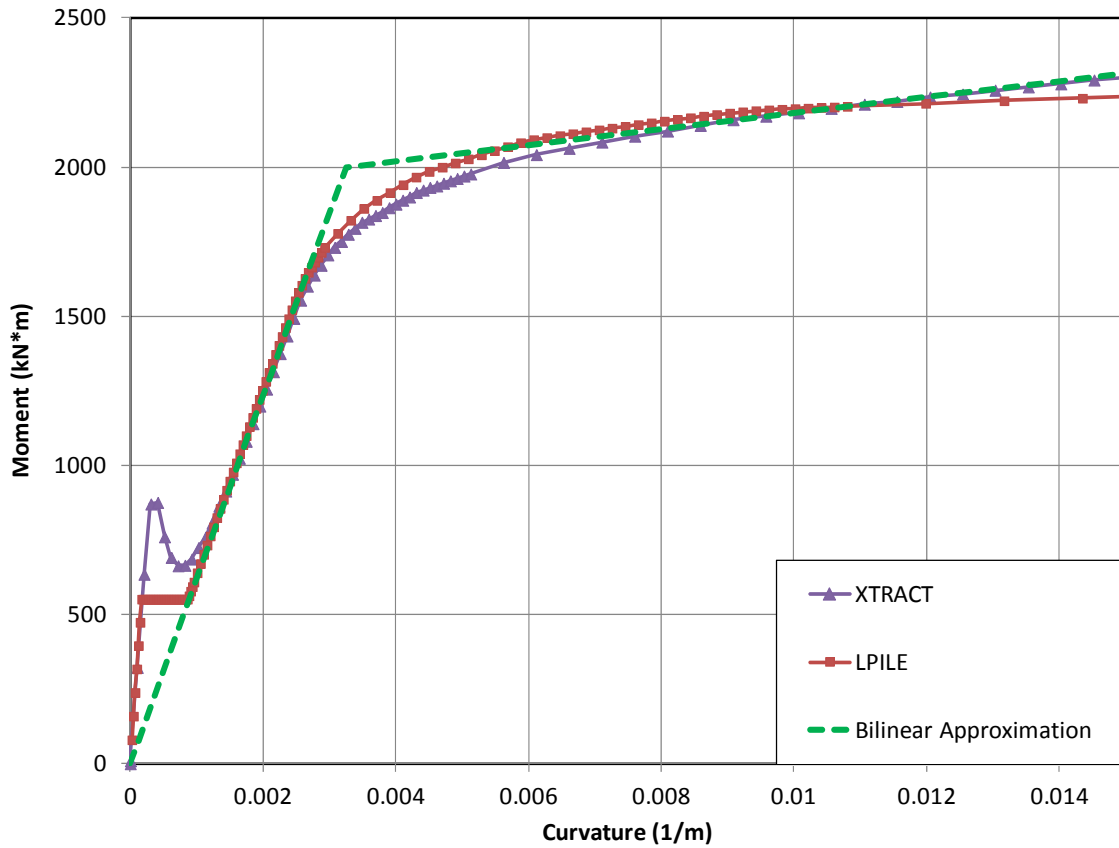


Figure 4-7: Moment-curvature behavior for highway bridge 1.2-m diameter reinforced-concrete extended-shaft columns with zero axial load and corresponding bilinear model implemented in *OpenSees*.

4.3.2 Elastomeric Bearings and Shear Tabs

Both bridges utilize plain (i.e., no steel or lead core) laminated elastomeric bearings to transfer loads from the girders to the columns. In the *OpenSees* models of the bridges, these bearings provide translational and rotational stiffness at the top of the columns.

For the HWB, the rotational and translational (shear) stiffness of the elastomeric bearings were estimated to be 60 kN•m/radian and 1320 kN/m, respectively, following the guidelines presented in Chapter 14 of the AASHTO LRFD Bridge Design Specifications (2012). Details of the computation of the HWB bearing stiffness are included in Appendix C.

As described in Section 3.4.1, the HWB Bent 5 transverse diaphragms feature a positive structural connection to the bent caps via shear anchorage tabs. The shear tabs rest in a slightly oversized block-out cast into the bent cap (depicted in Figure 3.4-8) and are meant to engage under extreme-event loading to prevent an unseating failure such as the one that occurred at the adjacent RRB span. Shear tabs were modelled using an elastic-perfectly-plastic gap spring with an ultimate capacity equal to the estimated shear capacity of the tabs, about 500 kN. The gap accommodates 1 cm of relative displacement between the girders and the bent cap before engaging the shear tab resistance. The elastomeric bearings were modeled with an elastic-perfectly-plastic spring with an ultimate resistance corresponding to sliding between the bearing and the girders, about 230 kN. The spring implemented in the *OpenSees* model is a combination of the elastomeric bearing spring and the shear tab spring in parallel as illustrated in Figure 3.4-8(3). The springs in Figure 3.4-8 represent the tributary stiffness for one extended-shaft column (i.e., 14 bearings per bent/4 columns = 3.5 bearings per column; 4 shear tabs per bent / 4 columns = 1 shear tab per column).

For the RRB, the post-earthquake observations clearly showed that the shear capacity of the bearings was exceeded and sliding occurred between the top of the bearings and the base of the girders. Accordingly, the bearings were modeled with an essentially-rigid perfectly-plastic spring with a capacity equal to the coefficient of friction for bearing-concrete contact (taken as 0.2) multiplied by the estimated vertical load from the deck and girders (1325 kN).

The weight of the RRB deck bearing on the top of the column also provides rotational restraint, since a rotation of the top of the column would necessarily have to lift up the bridge deck as depicted in Figure 4-9. A rotational spring was formulated to represent this restraint, which is in addition to the overturning restraint provided by the group-action of the piles. The stiffness of

this rotational spring was estimated to about 400 kN•m/radian (computations are shown in Appendix C).

Because the boundary conditions at the tops of the bridge columns are modeled using springs, the shear, moment, and displacement reactions change during the analysis based on the amount of deformation of the springs. In contrast, a decoupled analysis in which the column response is replaced by a mobilized shear, moment, displacement, or slope at the top of the foundation (as is commonly performed in *LPILE*) removes the ability of the boundary condition (i.e., reactions) to vary during the analysis based on the response of the foundation and above-ground components. As previously noted, the latter approach may not be able to accurately simulate the realistic behavior when above-ground components play a significant role in resisting lateral spreading forces.

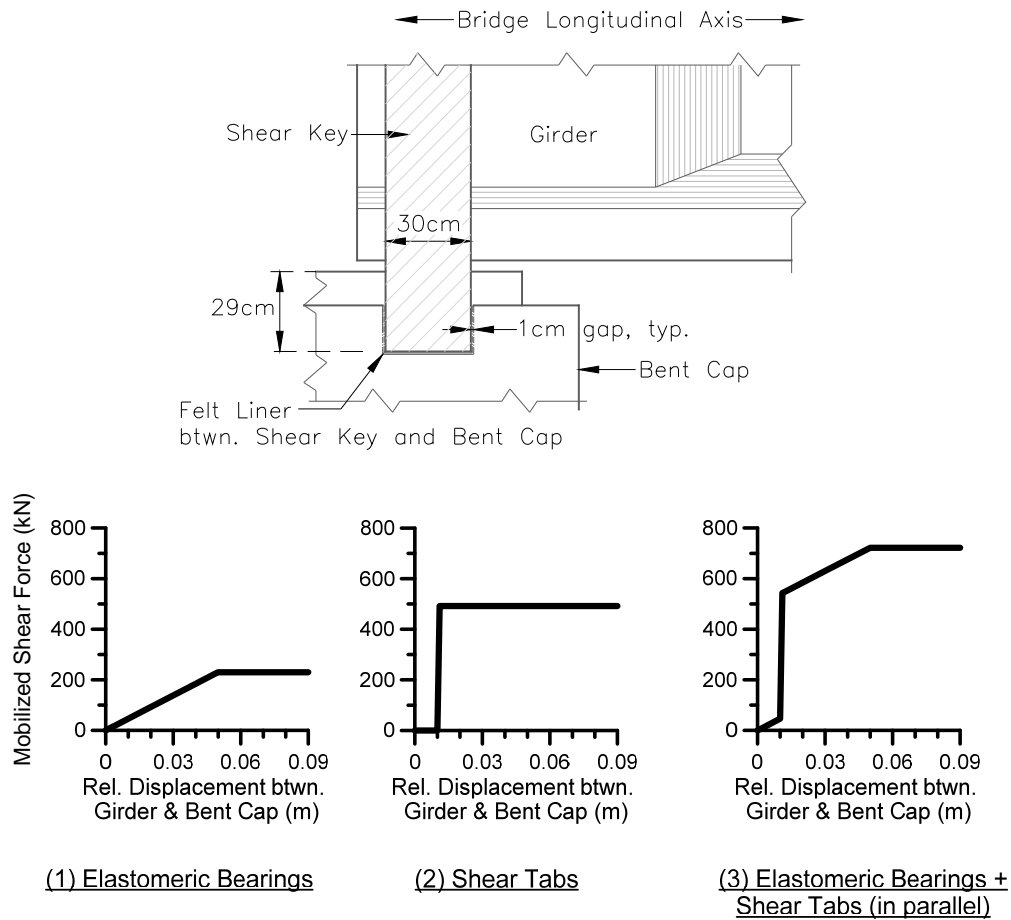


Figure 3.4-8: Highway bridge shear tab detail (top) and spring definitions used to model connection between superstructure and bent cap (bottom).

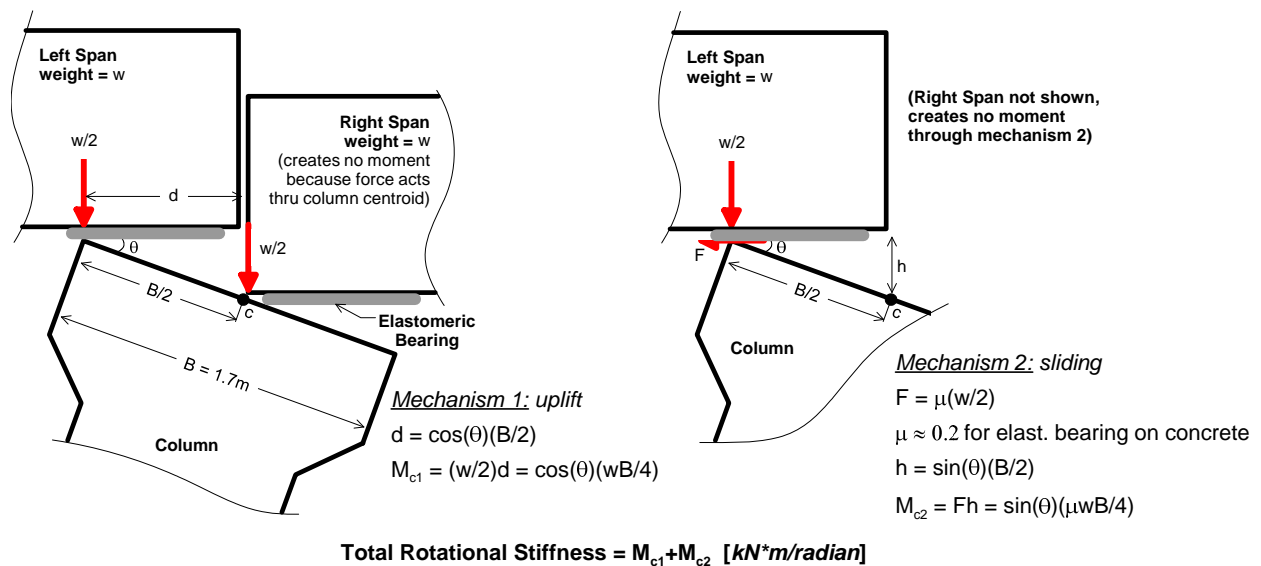


Figure 4-9: Formulation of rotational stiffness of railroad bridge deck spans transferring load to column through elastomeric bearings.

4.4 INERTIAL LOADS FROM SUPERSTRUCTURE

Some fraction of the peak inertial demands was expected to occur simultaneously with kinematic demands imposed by lateral spreading (e.g., Brandenberg et al. 2005). The approach suggested by Ashford et al. (2011) differs from the Caltrans (2013) guidelines regarding modeling of liquefaction-compatible inertial demands. Whereas the Caltrans guidelines specify a simple force-based approach for all scenarios, Ashford et al. distinguish pier columns not restrained by the superstructure from those that are restrained. An example of an unrestrained pier column is a simply-supported bent oscillating in the bridge transverse direction, where the response of other bents and the abutments has negligible influence on the response of the bent in question. Inertial demands for unrestrained pier columns can be represented either as spectral displacements or as inertial forces. Oscillation of the bent in the bridge longitudinal direction is an example of restrained oscillation, since resistance provided by other bents and/or the abutments (which tend to oscillate out-of-phase with the deck during first-mode excitation) can have a significant influence on the response of the bent in question. Inertial demands for restrained pier columns should be represented in a manner that considers the restraint provided by all relevant bridge components. An estimate of the inertial demands considering the restraint provided by all relevant bridge components, such as the abutments, will be referred to as a “restraint-compatible” demand in this text. This is in contrast to an estimate of the demand that ignores the resistance provided by bridge components other than the bent and foundations being analyzed. Further details of each approach are given in the following sections.

The force-based approach as recommended by the Caltrans guidelines is problematic for cases where pier columns are restrained by the superstructure because the pier columns may help resist lateral-spreading demands, thereby reducing demands on the foundations while

simultaneously increasing demands on the pier columns. Restrained bridge piers have been damaged in earthquakes when the foundation displacement has exceeded the superstructure displacement because of lateral spreading demands (e.g., the Landing Road Bridge; Berrill et al. 2001). The restraint-compatible displacement-based approach is more realistic in this regard because (1) the loads mobilized in above-ground components are an outcome of the analysis rather than a prescribed boundary condition, and (2) the spectral displacement accounts for the influence of other bridge components on global dynamic response. For these reasons, the displacement-based procedure is used in this study, and it is subsequently demonstrated that the force-based procedure results in an overestimate of foundation demands.

In either method, it is first necessary to perform a modal analysis of the structure to estimate the relevant modal frequencies so that spectral demand can be determined from an appropriate response spectrum. (For this study, it was assumed that the response of the bridge in the longitudinal direction is governed by the first mode.) An exception to this is when columns are expected to yield at their base, in which case the inertial demands transferred to the foundations are limited by the plastic moment capacity of the columns. For the SFB, the columns did not yield at their base, so it was necessary to estimate the bridge first-mode periods to quantify inertial demands.

Determining the first-mode period of a bridge in the longitudinal direction using a model of a single bent is difficult, because the bent interacts with other bridge components during lateral loading. Furthermore, the connection between the top of the bent and the superstructure is typically not rigid, but consist of elastomeric bearings (and possibly shear tabs) which dissipate energy at the connection. For most projects, the structural designer would perform a modal analysis on a global model of the bridge, so the interaction of the superstructure, bents, and abutments would be

explicitly captured, and the resulting first-mode period would be passed on to the foundation engineer to estimate inertial forces. For foundation design, especially at the preliminary stages of a project, it is desirable to avoid creating a model of an entire bridge. An alternative, simplified procedure for modal analysis is used here in which a spring is used to represent the restraint provided at the top of the individual bents in the longitudinal direction, and additional translational and rotational springs are used to capture the flexibility of the bent-to-deck connection. This is illustrated in Figure 4-10(c).

For modal analysis, it was assumed that all bents would oscillate in-phase during first-mode longitudinal excitation, and that the only out-of-phase component providing restraint in the longitudinal direction would be the abutments. Accordingly, springs were formulated to represent the translational stiffness of the abutment-seat bearings for each bridge. For the HWB, the estimated stiffness of this spring is about 4.6 MN/m for each of the four columns. An elastic translational spring with this stiffness was attached to the superstructure mass to restrain oscillation in the longitudinal direction during modal analysis. No evidence of pounding was observed at the abutment-deck connections—for example, complete closure of the gap between the abutment and deck, which would have partially mobilized passive soil resistance against the abutment wall in addition to elastomeric bearing stiffness.

The *eigen* command in *OpenSees* was used to perform modal analyses of the bridge bents including the appropriate superstructure tributary mass, which was estimated as 1335 kN per RRB bent and 1150 kN per each extended-shaft column of the HWB. Mass of the substructure elements (columns, pile cap, and foundations), computed based on the member dimensions and material properties presented in Section 4.3, was distributed over the nodes in the numerical model. The rotational and translational stiffness of the foundations were explicitly captured for the modal

analyses by inclusion of the soil springs discussed in Section 4.1. The resulting first-mode period for the HWB Bent 5 is approximately 1.7 sec. For comparison, the estimated first-mode period of the HWB column modeled as fixed against rotation at its top and bottom is about 0.27 sec. The additional flexibility in the real system is contributed by the foundation flexibility and the elastomeric bearing flexibility in roughly equal amounts.

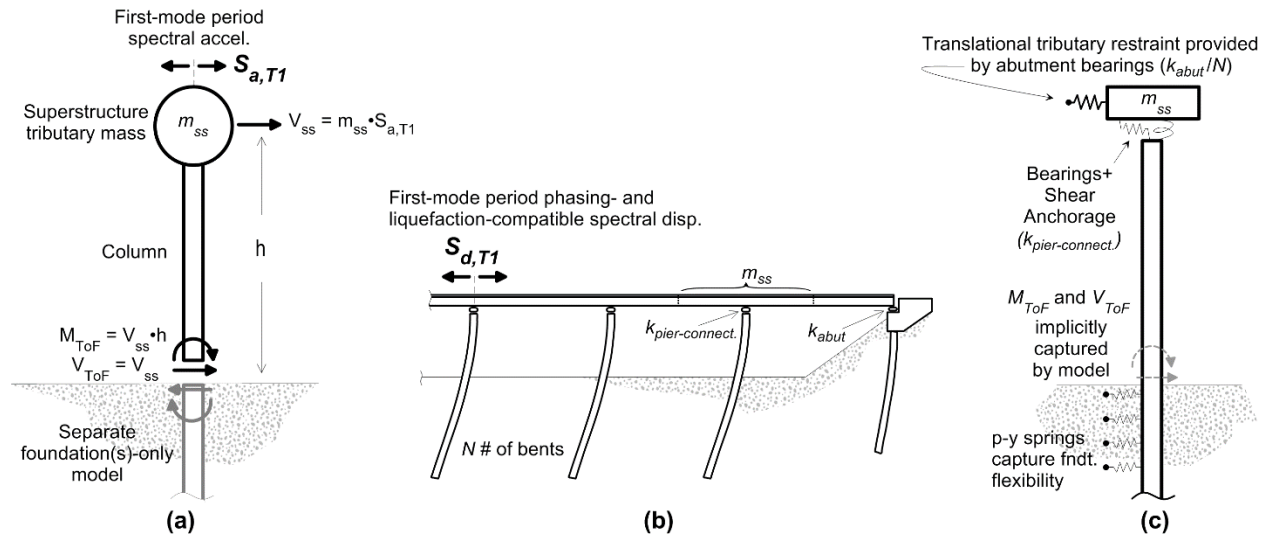


Figure 4-10: (a) Caltrans (2013a) force-based method for estimating top-of-foundation inertial shear and moment demands (V_{ToF} and M_{ToF}); (b) schematic of first-mode longitudinal oscillation; (c) single-bent model for modal and lateral spreading analyses

The same procedure was repeated for the RRB, but less is known about the elastomeric bearings for this bridge. It was estimated that the total longitudinal translational restraint was between 3 and 5 MN/m, which resulted in a first mode period of about 2.3 sec. For comparison, the estimated first-mode period of the RRB column modeled as fixed against rotation at its top and bottom is about 0.12 sec.

There is considerable uncertainty in the estimates of the bridge first-mode periods. There is additional error in the predicted response because higher-mode effects and period lengthening associated with inelastic response are not captured. As will be discussed in Section 4.6.3, the response of the bridges was considered over the range of pseudo-spectral accelerations (PSA)

represented by the aleatory uncertainty of the ground motion estimation, which showed that the predicted response is relatively insensitive to variability in the inertial demand. Although the variation of the estimated first-mode period was not considered directly, the effect of varying the period estimates has been considered indirectly by considering this range of ground motion intensity.

4.4.1 Restraint-Compatible Spectral Displacement Method

Ashford et al. (2011) recommend modeling inertial demands for the restrained case using spectral displacements estimated at the first-mode period of the bent, which is the approach used herein. It should be noted that restraint-compatible demands could be modelled either as inertial forces or displacements, as long as they are computed at a first-mode period that realistically captures the resistance provided by all relevant bridge components. However, seismic design of bridges often utilizes a displacement-based approach [e.g., following the AASHTO Guide Specifications for LRFD Seismic Bridge Design (2009) or the Caltrans Seismic Design Criteria (2013b)], so this approach is used for this study and is generally recommended. Furthermore, quantifying inertial demands as displacements is conceptually attractive, because the amount of displacement demand that is dissipated by the flexibility of the bent-to-deck connection (e.g., by bearings, shear tabs, etc.) can be directly investigated as an outcome of the analysis.

Inertial demands from the superstructure represented as spectral displacements were combined with lateral spreading demands according to the recommendations of Boulanger et al. (2007) as presented in Ashford et al. (2011). Boulanger et al. discuss nonlinear dynamic finite element simulations that were performed for pile group foundations supporting single-degree-of-freedom (SDOF) structures with various natural frequencies. The influence of liquefaction on the inertial demands of the structure was quantified by two constants: C_{liq} which quantifies the peak

inertial demand with liquefaction to that without liquefaction, and C_{cc} which quantifies phasing of the inertial and kinematic demands. The factors were quantified as constants that depend on the shape of the acceleration response spectrum for the surface motion without liquefaction, and were found to be $C_{liq} = 0.55$ and $C_{cc} = 0.65$ for motions with typical spectral shape.

It should be noted that the C_{liq} and C_{cc} factors recommended by Boulanger et al. (2007) are based on simulations of bridge bents modeled as SDOF oscillators that are unrestrained against translation at the superstructure mass level. While this may be a reasonable assumption for multiple-span bridges loaded in the transverse direction, it does not apply to bridges that exhibit restraint in the longitudinal direction from abutments and adjacent piers founded in non-liquefied ground. Lateral spreading demands are most common in the longitudinal direction since bridges often cross water bodies and lateral spreading occurs toward the water. Further research is needed to understand the influence of longitudinal restraint on these factors.

Spectral displacement demand is related to pseudo-spectral acceleration as follows:

$$S_d = \frac{PSA}{\omega^2} \quad (4.4)$$

$$\omega = 2\pi f \quad (4.5)$$

where S_d is spectral displacement in meters, PSA is pseudo-spectral acceleration in m/sec^2 , ω is the angular frequency of interest in radians per second, and f is the frequency in Hz, defined as the inverse of the period in seconds. The estimated spectral displacement demand was imposed on the free ends of the elastomeric bearing spring in the model as shown in Figure 4-10(c).

4.4.2 Inertial Force Method

The Caltrans (2013a) lateral spreading guidelines provide recommendations for estimating inertial force demands for two cases. The first case is when the columns are expected to yield at their base during the design seismic event, which is often how bridge columns are designed in order to prevent below-ground damage that is difficult to inspect and repair (e.g., Caltrans “Type II” columns). In this case, the inertial demand that can be transferred to the foundation(s) is limited by the plastic moment capacity of the column. The maximum shear that can be transmitted to the foundations under this condition is also limited to the shear corresponding to the plastic moment capacity. For the second case in which columns are not expected to yield, the amount of shear and moment imposed on the foundation(s) depends on the inertial force generated by excitation of the superstructure. The SFB columns were observed to have not yielded at their base during the EMC earthquake, so the latter case applies, but this would not be known *a priori* for a forward design. In the author’s experience, the first case—imposing the full plastic moment capacity and corresponding shear, including material overstrength—is sometimes a project design requirement regardless of whether the actual estimated inertial demands would generate this level of top-of-foundation force effects.

The Caltrans (2013a) approach for estimating inertial demands when the column does not yield is to multiply the appropriate superstructure tributary mass by the pseudo-spectral acceleration at the bridge first-mode period as shown in Figure 4-10(a). This force is multiplied by the column height to compute the moment demand at the column base, essentially a “base shear” design approach. The full kinematic demand from lateral spreading is then combined with half of the inertial demand; the reduction approximately accounts for the influence of liquefaction and phasing on the inertial demand. For the HWB, this moment demand was computed as

$0.5 \cdot (0.43g) \cdot (117Mg) \cdot (10.2m) = 2,500 \text{ kN}\cdot\text{m}$. This demand exceeds the yield capacity of the column, which suggests that the plastic moment and associated shear should be imposed in design calculations.

However, the prediction of plastic hinges in the HWB foundations is inconsistent with post-earthquake observations that the columns slightly cracked but did not yield. The Caltrans procedure assumes that the column is the only lateral-force-resisting component, whereas in reality, the columns are restrained against rotation and translation by other bridge components due to loads transferred through the superstructure. This restraint affects both the modal properties of the system and the response to lateral spreading loads. For this study, the restraint was captured in the modal analyses that were performed to estimate the first-mode periods of the bridges and corresponding inertial demand at the deck level. However, no restraint at the superstructure-level was included during the lateral spreading ESA to be consistent with the Caltrans guidelines [i.e., the numerical model depicted in Figure 4-10(a) was used]. The results presented below demonstrate that this misrepresentation of the structural resistance leads to an over prediction of foundation-level demands.

4.5 *OPENSEES* FINITE-ELEMENT ANALYSIS

The following settings were used in the *OpenSees* finite-element analysis:

- Penalty constraints to enforce boundary conditions,
- Norm of the displacement increment (NormDispIncr command) to test for convergence with a tolerance of 10^{-8} m ,
- Newton-Raphson solution algorithm used to solve nonlinear system of equations,

- Displacement-controlled integrator, and
- A p - Δ transformation was utilized to capture secondary moments induced by offset axial loads.

4.6 RESULTS

4.6.1 Response of Highway Bridge to Lateral Loading

Results of the analysis of the highway bridge under lateral spreading conditions are presented in Figure 4-11. Superstructure inertial demand, represented as liquefaction-compatible spectral displacement, was imposed in the opposite direction of lateral spreading displacement because this configuration resulted in the highest flexural demand. The peak mobilized bending moment near the ground surface was 1,130 kN•m, which lies between the cracking moment of 620 kN•m and the yield moment of 2000 kN•m. A slightly smaller negative moment was mobilized at the interface between the upper liquefied sand layer and the underlying dense sand, -910 kN•m. This is consistent with field observations that cracks formed on the river-side of the pier column, but that a plastic hinge did not form. The ESA predicted that the extended-shaft columns would crack near the ground surface under an imposed lateral spreading demand of about 0.2 m or more. Furthermore, a column rotation of about 0.3° was predicted, which is on par with the measured rotations of about 1°. The predicted displacement at the base of the columns ranges between about 3.1 and 5.4 cm depending on whether the inertial demands are applied in the same direction or opposite direction as the lateral spreading force. This amount of displacement satisfies the allowable foundation demand performance criteria for poorly-confined columns given in Table 3.1 of the Caltrans lateral spreading guidelines (2013a).

Because the HWB foundations have sufficient embedment into the dense bearing layer and sufficient stiffness and strength to prevent large deformation under the imposed loads, the relative displacement between the foundations and the laterally spreading crust is nearly equal to the imposed lateral spreading displacement demand. That is to say that the foundations are sufficiently stiff and strong that the laterally spreading crust mobilizes full passive pressure (i.e., it “fails”) and flows around the foundations. The mobilization of full passive pressure occurs at imposed lateral spreading displacement demands greater than about 0.6 m. Lateral spreading displacement in excess of this amount does not contribute to structural demands. The EDPs plotted in Figure 4-11 are nearly identical to the predicted EDPs for any imposed lateral spreading demand greater than about 0.6 m. In this case, the method used to predict the amount of free-field lateral spreading displacement is unimportant as long as the predicted LD exceeds about 0.6 m.

Although it is difficult to accurately assess the actual lateral spreading demand imposed on each bridge during the EMC earthquake as a result of the restraint provided by the foundations, the predicted behavior is shown to be relatively insensitive to the demand. As long as the imposed lateral spreading displacement demand exceeds 0.2 m, the HWB columns are expected to crack, and if the demand exceeds about 1.0 m, the RRB is expected to collapse.

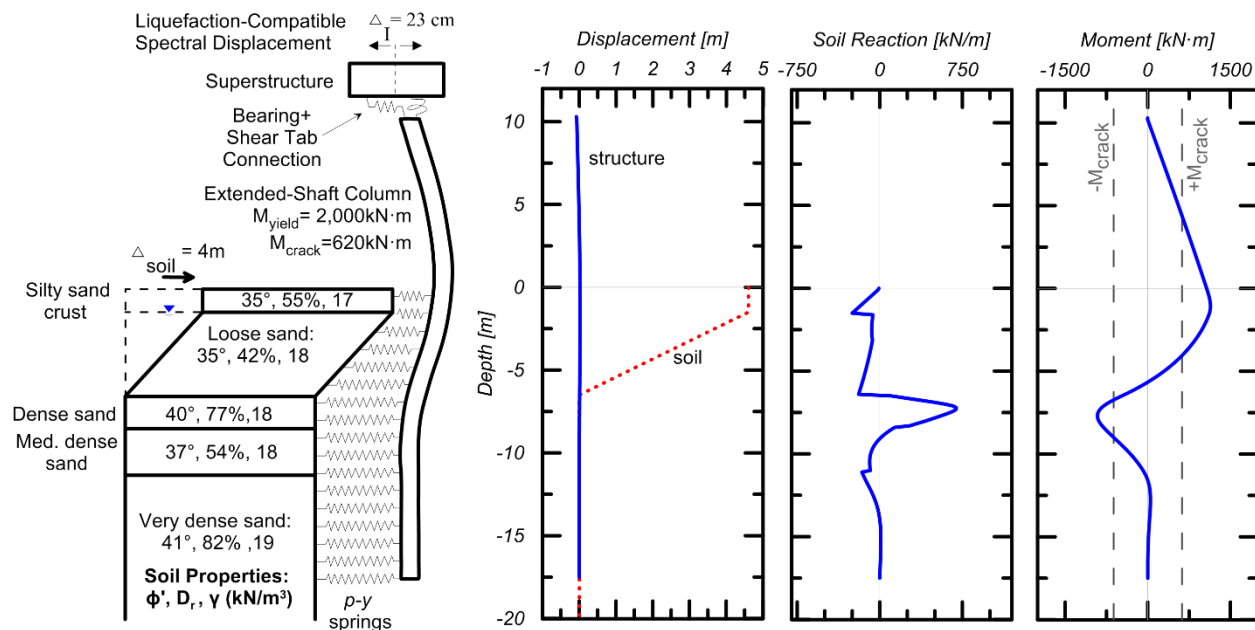


Figure 4-11: Highway bridge Bent 5 predicted response under imposed lateral spreading displacement demand of 4.6 m combined with superstructure inertia demand, represented as liquefaction-compatible spectral displacement demand, in opposite direction.

4.6.2 Response of Railroad Bridge

Response of the RRB to combined inertial and lateral spreading demands are summarized in Figure 4-12 and Figure 4-13. Baseline analyses apply for the assumed condition of multiple rows of piles. These analyses show that in contrast to the HWB, the RRB foundations were not capable of resisting the passive pressure of the crust acting against the pile cap. The resulting foundation displacements are large, hence relative displacement between the structure and the laterally spreading crust is low (as seen in Figure 4-13), and the full passive pressure mechanism was not mobilized. Moreover, this analysis correctly predicts that Bent 5 of the RRB would translate enough to cause unseating collapse of the span between Bents 5 and 6 under imposed lateral spreading demands greater than or equal to about 1 m for all of the pile material and group configurations considered (recall that actual lateral spread displacements in the free-field at the location of Bent 5 were approximately 4.6 m). Translations at the top of the bent greater than 0.85

m relative to the superstructure are required to cause unseating. After the collapse mechanism has formed, results from the equivalent static analysis for further increases in lateral spreading displacement demand are no longer meaningful. Accordingly, the analyses are terminated at a lateral spreading displacement demand of 1 m rather than extending to the full free-field lateral spreading of 4.6 m.

The large horizontal displacement demand imposed on the RRB foundations by laterally spreading soil is predicted to cause formation of plastic hinges in the piles at the pile cap connections and at the interface between the dense sand layer and the overlying liquefied layer in the simulations. The analysis predicts relatively small column rotations (about 1° or less) even at large horizontal displacements, which is consistent with the observed performance. The lack of rotation is attributed to the rotational restraint provided by the overturning resistance of the pile group and the weight of the superstructure. The lack of rotation associated with such significant translation was a feature of the observed response that was initially perplexing but is explained by the simulations.

Additional simulations were performed using only one row of piles or two closely-spaced rows of piles. Under these assumptions, the pile groups lack significant overturning resistance through group interaction in the bridge longitudinal direction. The result is predictions of large column rotations, even with the restraint provided to the top of the column from the superstructure, which is contrary to observations.

The collective results for the RRB demonstrate that (1) the structure is predicted to collapse over a wide range of foundation types and (2) the observed behavior is best explained by a group of piles with multiple rows that have a large overturning resistance through group interaction but

relatively low individual stiffness and strength such that the piles are displaced horizontally and plastic hinges form.

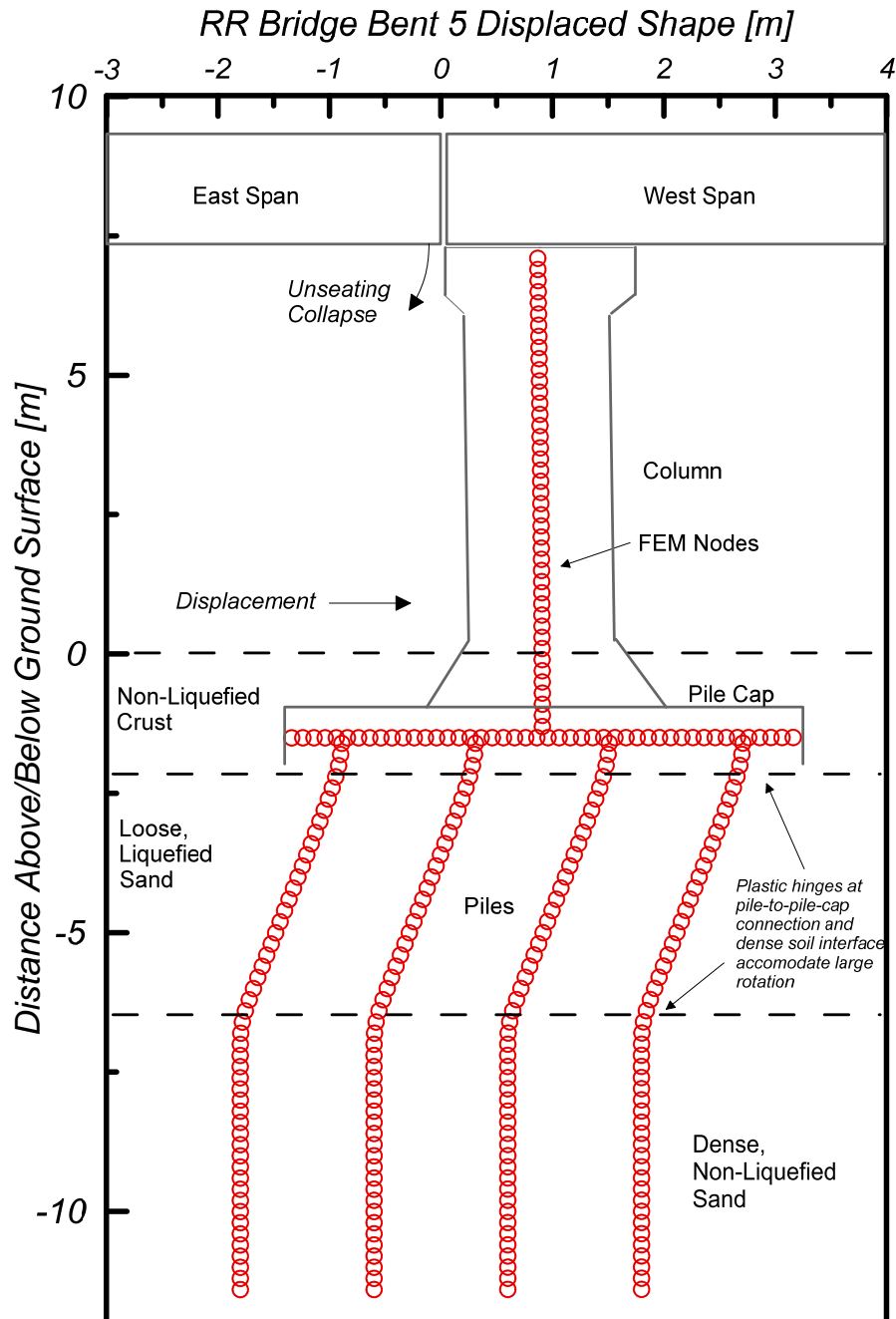


Figure 4-12: Railroad bridge Bent 5 analysis results showing collapse for a 4×5 group of 30-cm diameter reinforced concrete piles under imposed lateral spreading displacement demand of 1.0 m. Includes superstructure inertial demand, represented as liquefaction-compatible spectral displacement, in opposite direction from lateral spreading. Predicted column rotation $\approx 0.3^\circ$. Note the horizontal scale is exaggerated.

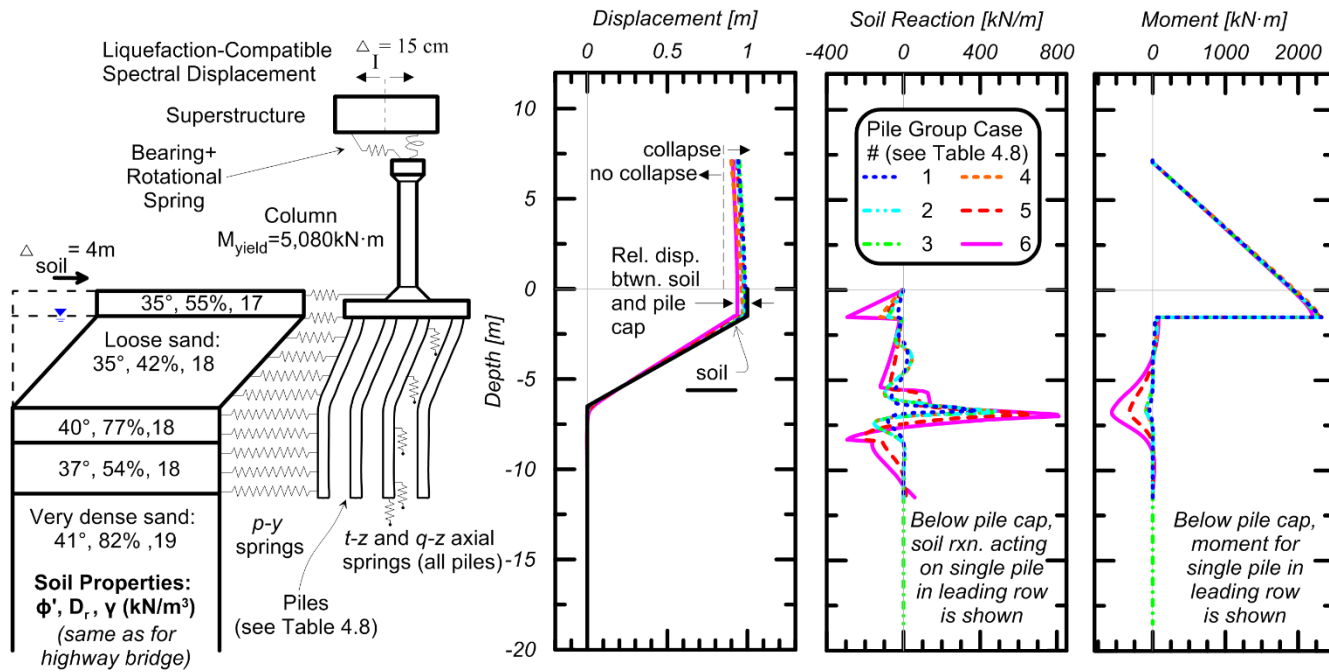


Figure 4-13: Numerical model and results of Bent 5 analyses of railroad bridge subjected to lateral spreading combined with inertial demands. Discontinuity in moment profile at pile-to-pile-cap connection occurs because the axial force in each pile row times its eccentricity from the pile cap centroid also contributes to moment resistance.

4.6.3 Comparison of Combined Kinematic and Inertial Demand Methods

The results presented in Sections 4.6.1 and 4.6.2 include superstructure inertial demands imposed as displacements at the superstructure level as described in Section 4.4.1, i.e., the restraint-compatible spectral displacement method. Much of the imposed superstructure displacement demand manifests as bearing shear deformation with relatively little deformation of the column top, hence the influence of superstructure inertia was found to be negligible in terms of the resulting effects on foundation demand. This is expected for bridges in which longitudinal movement of the superstructure is restrained, as discussed above, and corresponding displacement demands in the longitudinal direction are low. The restraint-compatible displacement-based approach captured the observed behavior of the SFB well.

As discussed in Section 4.4.2, the Caltrans (2013a) guidelines do not recommend a displacement-based approach, but rather advocate a force-based approach in which spectral acceleration is multiplied by tributary mass and the resulting inertial force is imposed at the top of the column without consideration of global restraint. Flexural and shear demands at the foundation level are then computed from these forces, limited by the flexural capacity of the columns. The highway bridge was re-analyzed using the force-based approach for comparison with the spectral displacement approach.

Using the Caltrans (2013a) force-based procedure for quantifying inertial demands, the HWB columns were predicted to yield at their base as shown in Figure 4-14. When combined with lateral spreading demands, collapse of the HWB was predicted, which is inconsistent with observations. This erroneous prediction is an outcome of failing to model translational and rotational restraint at the top of the columns, which allows loads to be distributed to other components through the deck. Note that column demands presented in Figure 4-11 arise from the

combination of inertial loading and lateral spreading; such insight is not provided with a foundation(s)-only model in which column demands are prescribed as boundary conditions in the force-based approach. Figure 4-14 demonstrates that collapse is predicted using the force-based method whether the inertial demands are imposed in the same direction as the lateral spreading or in opposite directions, whereas the results utilizing the displacement-based approach are relatively insensitive to the direction of inertial demands and match the observed behavior well in both cases.

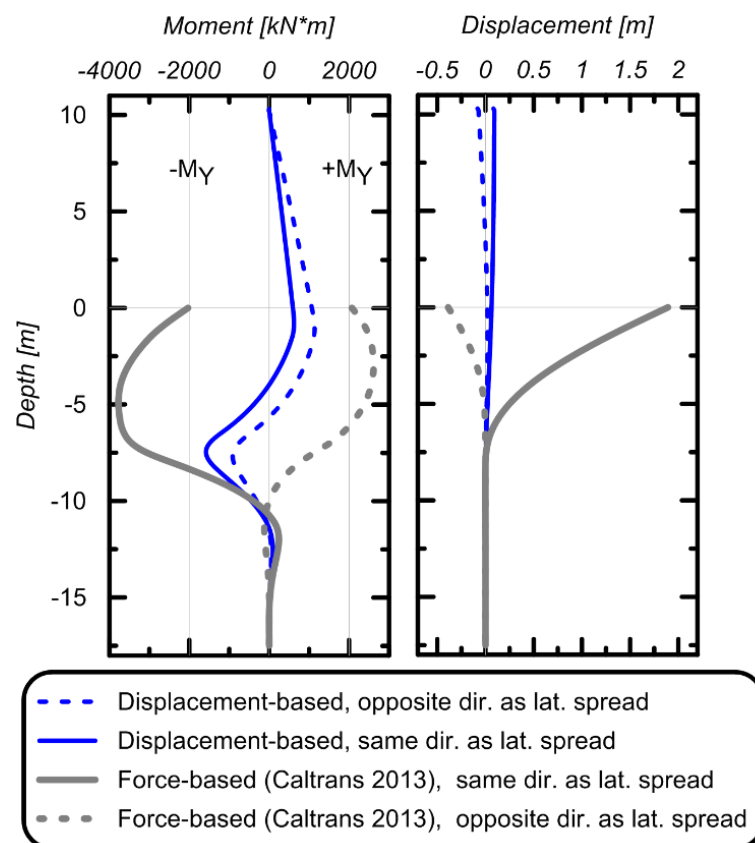


Figure 4-14: Comparison of moment and displacement profiles for highway bridge piles as computed from force- and restraint-compatible displacement-based methods for imposing superstructure inertial demands in the same and opposite directions as lateral spreading. Restraint-compatible displacement-based approach provides best match to observed behavior.

Based on these results, the force-based procedures as described in the Caltrans (2013a) guidelines is found to produce an unrealistic overestimate of foundation demands for structural systems in which the column is restrained at the connection with the superstructure. In such systems, the translational and rotational restraint at the top of the column (i.e., partial fixity) may help resist lateral spreading demands by transferring loads through the superstructure to other components such as piers founded in non-liquefied soil or abutments. This resistance may be mobilized even in cases where the inertial demand and lateral spreading are applied in the same direction, as demonstrated for the analysis of the HWB in Figure 4-14. The only way to properly model this load transfer behavior is to explicitly model the columns and connection with the superstructure, along with appropriate inertial demands at the superstructure level. Furthermore, the liquefaction-compatible inertial demands are less than those for non-liquefied soil conditions. As a result, the force-based method will always result in smaller flexural demands in the pier columns than the non-liquefied inertial analysis. This means that lateral spreading will never contribute to the design of pier columns using the force-based approach. However, lateral spreading can clearly cause pier column demands that are more significant than those from non-liquefied inertial loading. These demands can only properly be captured using a global analysis of the entire bridge, or using a global restraint-compatible approach for analysis of a local component.

For the RRB, the force-based approaches provided results that are reasonably similar to the displacement-based approach in terms of foundation shear and moment demand and the displaced shape of the pile cap and foundation group. However, the performance of this structure was poor as the foundation essentially moved with the spreading soil. The pier column therefore did not contribute significantly to resisting lateral spreading demands, and the force-based and displacement-based approaches provide similar predictions as a result. However, the

displacement-based approach as implemented herein still provides more insight because it informs the structural designer of the column demands mobilized during the lateral spreading load case.

The displacement-based approach can be implemented in *LPILE* for extended column shafts or single piles, similar to the HWB, because an above-ground column can be included and displacement conditions (translation and rotation) can be prescribed at the top of the column. However, this approach cannot be utilized for pile groups because a rotational stiffness at the foundation level representing the rotational stiffness provided by axial interaction of a pile group cannot be prescribed in combination with displacement demands at the top of an above-ground segment of column. Furthermore, the force-based procedure also cannot be utilized properly for pile groups in *LPILE* since only two boundary conditions can be prescribed at the head. For example, if an inertial shear force is applied at the foundation head, the user must decide to either prescribe (1) a corresponding inertial moment or (2) a rotational stiffness that represents group overturning action or the restraint provided by the column. The inability to prescribe both simultaneously limits the accuracy of the model. In cases when longitudinal restraint of the bridge bents provides only minor resistance to the lateral spreading demands, it may still be possible to obtain a reasonably accurate estimate of foundation shear and moment demand for design. A more desirable solution would be to use *GROUP*, *OpenSees*, or other software that explicitly captures group action and allows the user to specify shear and moment demand at the foundation level in addition to translational and rotational restraint provided by the column and other above-ground components.

4.6.4 Settlement of Highway Bridge Bent 6

Settlement of Bent 6 of the HWB is attributed to a bearing capacity failure associated with decreased side and base resistance in layers that experienced excess porewater pressure generation

during the earthquake. Documents provided by SCT indicate that each shaft was designed to carry an allowable axial load of about 2,100 kN. Based on the construction plans, the axial dead load supported by each shaft is about 1,050 kN, consistent with a static factor of safety against axial geotechnical failure of 2.0. However, this does not consider the self-weight of the column, and is significantly less than the estimated axial resistance in the absence of liquefaction.

Two cases are considered to evaluate whether a geotechnical failure could have resulted in the observed settlement, as shown in Figure 4-15. The first case essentially represents the original foundation design assumption that the sand is continuously dense below a depth of about 10 m. For this case, the dense soil at the depth of the foundation tips did not liquefy during the earthquake, and all of the layers above the foundation tip contributed drag loads in the same direction as the applied axial load (downward) based on static strengths corresponding to the end of reconsolidation. Although it is unlikely that all the overlying layers would contribute drag loads, this scenario represents the maximum possible axial load at the foundation tip depth. This scenario is presented simply to demonstrate that if the shaft bases were indeed founded in dense soil that did not undergo strength loss, the available base resistance alone (about 13,000 kN) is sufficient to carry the maximum applied axial load (about 3,500 kN) by a factor of almost three, even with the conservative assumption that all layers apply dragload. Hence, plunging failure would not have occurred.

In the second considered case, a loose layer is present at the foundation tips, as indicated by the post-earthquake boring performed by SCT and the CPT sounding performed for this study at the adjacent Bent 5. It was assumed that this loose layer would liquefy based on the results of liquefaction triggering analyses performed using data from CPT-1 for a similar depth range. Axial side and base resistance were computed for the appropriate liquefied/non-liquefied conditions by

explicitly considering r_u in the computation of effective stresses. Since the layer at the shaft base was assumed to liquefy, it was assumed that all overlying layers contributed drag loads.

When liquefied soil is present at the tip, the reduced base resistance (35 to 185 kN for the range of residual undrained strengths considered) in combination with the shaft friction resistance (950 to 1,300 kN range considered) is smaller than the applied load at the ground surface (1,900 kN, including the column self-weight); drag loads from post-liquefaction reconsolidation would further lower the safety margin. Accordingly, a bearing capacity failure is predicted. Under such conditions, the foundation would “plunge” through the weak material underlying the base until it reaches a denser layer that provides sufficient base resistance to carry the axial load. The magnitude of settlement (about 0.5 m) and the thickness of the potentially liquefiable layers in the vicinity of the shaft tip (about 0.25 to 0.5 m) are roughly equivalent, so this failure mechanism can explain the observed settlement.

Given that the presence of loose layer(s) in the vicinity of the foundation tip depth can explain the observed behavior well, it appears that significant strength loss of these layers occurred during the earthquake, causing a plunging failure. Even if the soil at the shaft tip did not completely liquefy (i.e., r_u did not reach 100%), generation of significant excess porewater pressure could still reduce the bearing capacity of the soil, which would cause settlement if the total resistance drops below the applied load. Had the Bent 6 foundations been a different length such that their tips were not coincident with a loose layer, the failure likely would not have occurred. Ironically, a shorter foundation length may have satisfied this criterion, provided that the shaft tip was founded in a nonliquefied layer thick enough to prevent punching failure.

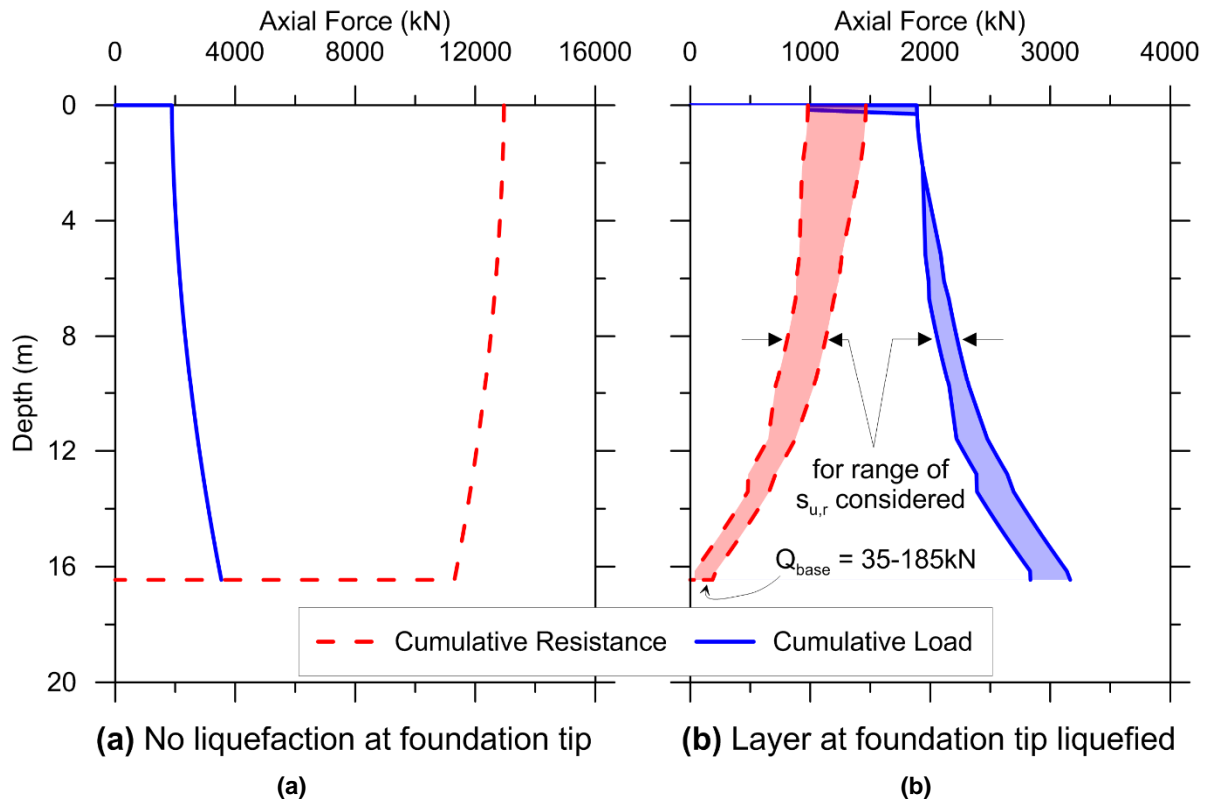


Figure 4-15: Profiles of axial load (including downdrag) and axial resistance for highway bridge Bent 6 based on data from CPT-1 and CPT-2: (a): no liquefaction at tip—load carrying capacity is sufficient; and (b): loose layer at the depth of the foundation tip is liquefied, axial load exceeds the load carrying capacity of the foundation, resulting in bearing capacity failure and vertical settlement.

5 Interaction of Adjacent Foundations during Lateral Spreading

Analyses presented in the previous chapter were based on the simplifying assumption that the foundations supporting the railroad bridge (RRB) or highway bridge (HWB) interacted with the laterally spreading ground without being influenced by the presence of the other bridge, or by other bents of the same bridge. Furthermore, because the extent of the lateral spread was large relative to the zone of influence of each individual bent being analyzed, the full free-field lateral spreading displacement was used for the analyses. In some cases, a refined consideration of these two simplifying assumptions can provide a beneficial reduction in lateral spreading demand used for deep foundation design. This chapter focuses on (1) pinning effects that occur when the areal extent of the lateral spread feature is inadequate to fully encompass the passive loading zone of influence, and (2) shielding effects that occur when one foundation interacts with a lateral spread feature to reduce demands on an adjacent foundation. First, clear definitions of pinning and shielding are established. The influence of these mechanisms on the behavior of the Mexico bridges is then examined using a novel procedure that combines two-dimensional finite element simulations with the equivalent-static analysis (ESA) results from the previous chapter.

5.1 DEFINITIONS OF PINNING AND SHIELDING

The so-called “pinning” phenomenon is sometimes misunderstood and must be clearly defined to avoid confusion and misuse. In this text, pinning is defined as a reduction in demand on a foundation embedded in a lateral spread feature with finite areal extent compared to the demand that would be mobilized in an infinite-extent lateral spread. In the context of a beam on nonlinear Winkler foundation (BNWF) analysis, lateral spreading demands are represented as displacements imposed on the free-ends of p - y elements attached to the piles. If the areal extent of the spread feature is large enough to fully encompass the zone of influence of soil-pile interaction, the free-field soil displacement is the appropriate input for the free-ends of the p - y elements. However, if the areal extent of the spread feature is smaller than the zone of influence, the displacement demand must be reduced to account for pinning effects. The zone of influence of the foundations is defined as the region over which ground displacements are less than the free-field displacement.

Lateral spreading soil displacements in the vicinity of stiff foundations are often observed to be smaller than those in the "free-field" at some distance away from the foundation during post-earthquake reconnaissance efforts. This is true for both finite-extent and essentially infinite-extent lateral spread features. It is tempting to conclude that pile pinning must be responsible for this reduction in soil displacement. However, a reduction in soil displacement in the vicinity of the foundation is not a sufficient condition to conclude that pinning has occurred. Whether pinning occurred can only be determined by assessing whether a reduction in demands resulted from the finite areal extent of the spread feature.

To further clarify the definition of pinning in the context of lateral spreading problems, consider the single pile in the lateral spread feature with large horizontal spatial extent in Figure 5-1(a). This will be referred to as an “infinite-extent” lateral spread condition because, although

the spread is of course not actually infinite in any of its dimensions, further increases in size would not increase the demand placed on foundations within the spread. Assume for illustrative purposes that the pile foundation is embedded in underlying stiff soil, and the strength and flexural stiffness of the foundation is sufficiently high to limit the foundation displacements to negligible amounts as the spreading soil flows around the foundation. At large distances beyond the zone of influence of the foundation, the soil will exhibit a free-field displacement profile. However, within the zone of influence of the foundation the soil displacement will be reduced, and immediately behind the center line of the pile the soil displacement will equal the foundation displacement. The free-field soil displacement is clearly the correct input to a BNWF model in this case because the zone of influence of soil-pile interaction is completely contained within the spread feature. Therefore, consideration of pinning effects is not warranted. However, the stiffness of the load-transfer relationship between the pile and spreading crust may be significantly softer for liquefied soil profiles than for non-liquefied profiles due to a loss of shear stress on the bottom of the nonliquefiable crust layer (Brandenberg et al. 2007).

Now consider the finite-length lateral spread in Figure 5-1(b). [*Note: the following terminology is adopted for the remainder of this chapter—the length of the lateral spread is measured in the direction of free-field soil displacement, and its width is measured along the transverse direction, as shown in Figure 5-1(b)*]. The zone of influence of soil-foundation interaction in this case extends to the upslope margin of the spread feature. Therefore, the areal extent of the spread feature influences the formation of the soil passive failure mechanism, thereby reducing demands imposed on the foundation elements. Pinning effects therefore should be considered for this problem.

Finally, consider the finite-length, finite-width approach embankment spreading against a pile-supported abutment in Figure 5-1(c). For this case, the zone of influence for soil-foundation interaction is geometrically limited by both the length and width of the spread feature. Demand could therefore be appreciably lower compared with the demand that would be mobilized by an embankment extending significantly further in one direction, such as a levee parallel to a river. Pinning is therefore an important consideration. For example, McGann and Arduino (2014) used 3-D finite element modeling to demonstrate through back-analysis of damage to the Mataquito River Bridge in Chile that the width of an approach embankment undergoing lateral spreading has a significant influence on abutment pile demands.

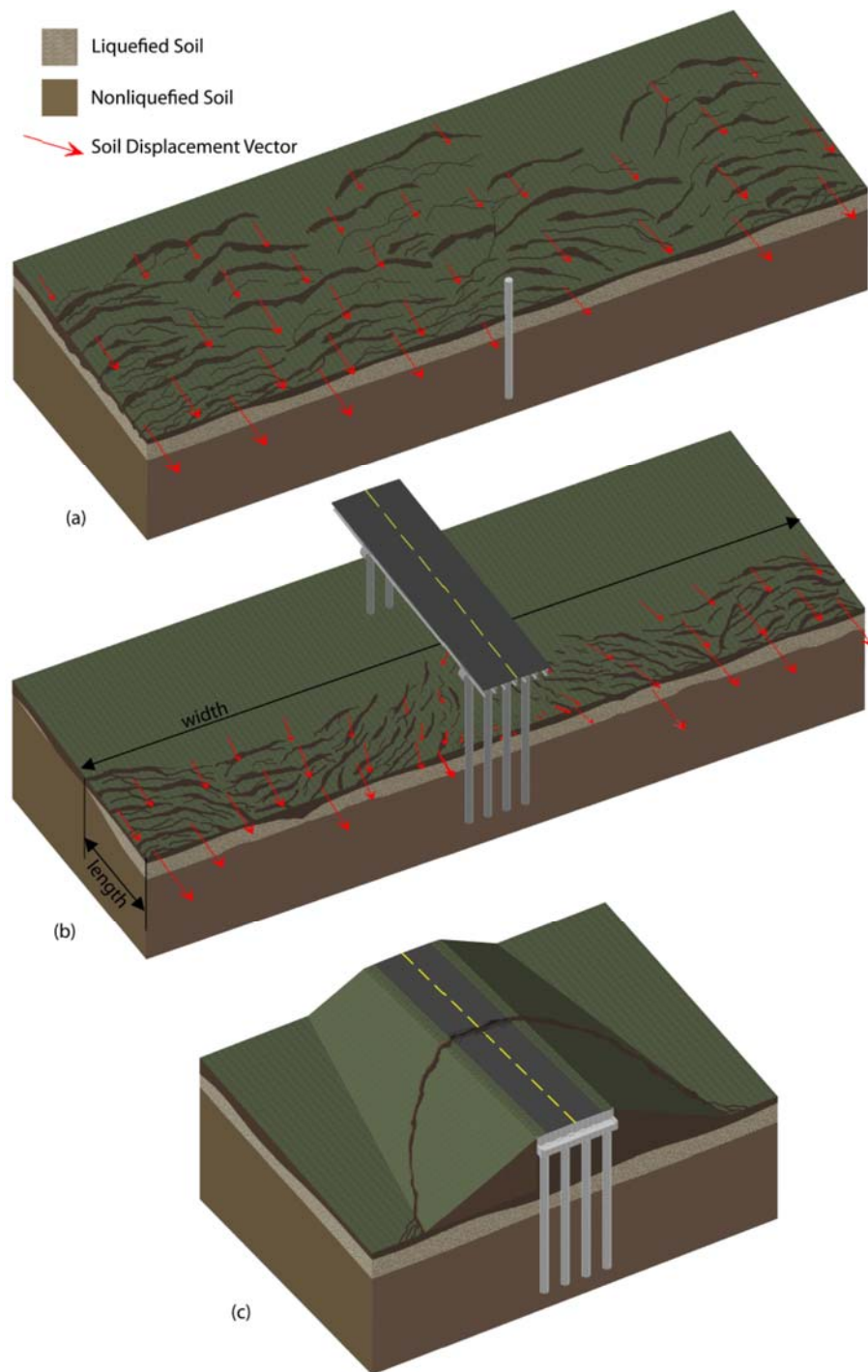


Figure 5-1: Three lateral spreading scenarios—(a) single pile subjected to broad field of lateral spreading, (b) pile group subjected to “short” lateral spread, and (c) laterally-spreading approach embankment resisted by abutment piles.

Methods have been proposed for analyzing the infinite-extent lateral spread cases in Figure 5-1(a) and the finite-width spread feature in Figure 5-1(c). For infinite-extent lateral spreads the free-field displacement should be imposed, and can be crudely estimated using various procedures described in Chapter 4 (e.g., Youd et al. 2002, Faris et al. 2006, Olson and Johnson 2008). Finite-width lateral spreads [Figure 5-1(c)] can be analyzed using an iterative procedure combining a pushover ESA analysis with limit equilibrium slope stability analyses with Newmark-type displacement estimates (e.g., Bray and Travasarou 2007). This procedure results in a compatible slope displacement and foundation resistance for design [e.g., MCEER 2003, Boulanger et al. 2005; an example of this approach is given in the Caltrans (2013) lateral spreading design guidelines]. By contrast, pinning for “short” lateral spreads [Figure 5-1(b)] has not received adequate attention.

Shielding is defined as the reduction in demand imposed on one foundation component arising from soil-foundation interaction effects for an adjacent component. Imagine that the bridge in Figure 5-1(b) is adjacent to a second parallel bridge, such as the condition at the San Felipe Bridges site under consideration. If one of the bridges has foundations that are adequately stiff and strong to resist lateral spreading demands while the other bridge has weaker foundation elements that yield before mobilizing the passive resistance from the crust, the stronger foundation elements may exert a "shielding" effect that reduces lateral spreading demands on the weaker foundation elements. The shielding effect for bridges in lateral spreads has not received adequate attention.

As described in the previous chapter, Bent 5 of the RRB was observed to have translated about 1 m based on measurements taken following the earthquake. From the ESA analyses, Bent 5 was predicted to undergo sufficient translation to cause an unseating collapse (about 0.85 m of movement was required) for imposed free-field lateral spreading displacements exceeding about

1 m. However, if the full free-field lateral spreading displacement of approximately 4.6 m was imposed, Bent 5 was predicted to displace about 4.1 m, which greatly exceeds the observed movement. A working hypothesis is that shielding provided by the HWB is responsible for the translation of RRB Bent 5 being less than predicted under free-field lateral spread demands. In addition, RRB bents further away from the river bank (6, 7 etc.) would be predicted to undergo significant translation when subjected to the level of lateral spreading observed in the free-field at the respective distance from the bank, but they underwent no measureable displacement. It is hypothesized that this better-than-predicted behavior arises from a combination of shielding provided by the HWB, and pinning resulting from the upslope extent of the lateral spread behind the bents being small relative to the HWB foundations' zone of influence.

This San Felipe Bridges case study provides a unique opportunity to explore methods for quantifying the shielding effect, since the site is well characterized, free field lateral spreading displacements were measured, the performance of the bridges during the earthquake was well documented, and the ESA of the foundations under lateral spreading demand has already been performed.

5.2 APPROACH

The approach adopted to quantify shielding and pinning effects consists of two-dimensional finite element analyses (FEA) of a domain that represents a plan-view section of the site combined with parameters obtained from the previously-performed ESA simulations. Although lateral spreading acting on foundations is a 3-D problem, a 2-D simulation was adopted for simplicity. The FEA domain represented a 1-m thick horizontal slice of the crust in the out-of-plane direction (i.e., vertical in the physical system) and were conducted using the program *Phase2* by Rocscience

(2013). The initial model included Bents 5, 6, and 7 of the highway bridge in the center of a 150-m wide by 60-m long domain. The domain is sufficiently large so that a free-field response occurs outside the zone of influence of the foundations. Bents further to the east (Bents 8, 9 etc.) were not included since they are beyond the zone of observed lateral spreading in the free field, which extended about 50 m upslope from the east river bank. Bent 4 is not included in the model because it is located in the middle of the river channel; the lateral spread is assumed to have stopped shortly after entering the river from the east bank and likely did not interact with Bent 4. Bents of the railroad bridge were not included in the initial model so that the shielding effect provided by the highway bridge on the railroad bridge could be studied independently. In reality, the two bridge systems constitute an interacting system in which the railroad bridge may have also provided a shielding effect for the highway bridge. This effect is considered small in this case because the railroad bridge foundations were weaker and more flexible than those for the highway bridge. The interaction would be important for adjacent foundations with similar strength and stiffness.

The relationship between mobilized passive pressure and free-field displacement was obtained from the *OpenSees* ESA (Figure 4-11). The average horizontal stress was found to be 78 kPa with 4.6 m of free-field soil displacement, inducing a corresponding foundation displacement of 4.0 cm at the ground surface. This horizontal pressure represents a Rankine passive limit state corresponding to a friction angle of 35° . These results were used to define an elastic perfectly-plastic model for the crust soil in *Phase2* with uniform shear strength of 54 kPa such that the same passive limit state would be mobilized in the plain strain simulations. The perfectly-plastic behavior ensures that the soil cannot transfer additional load to the foundations once the passive limit state has been reached. Although the individual soil elements are modeled with a bilinear stress-strain relationship, the pile lateral response obtained from the simulations is nonlinear due

to incremental shear failure of the soil elements. Since the two-dimensional, plain-strain analysis used here does not fully capture the three-dimensional boundary conditions of the lateral spreading problem, the material properties for the two-dimensional analysis must be carefully selected so that the desired passive pressure is achieved.

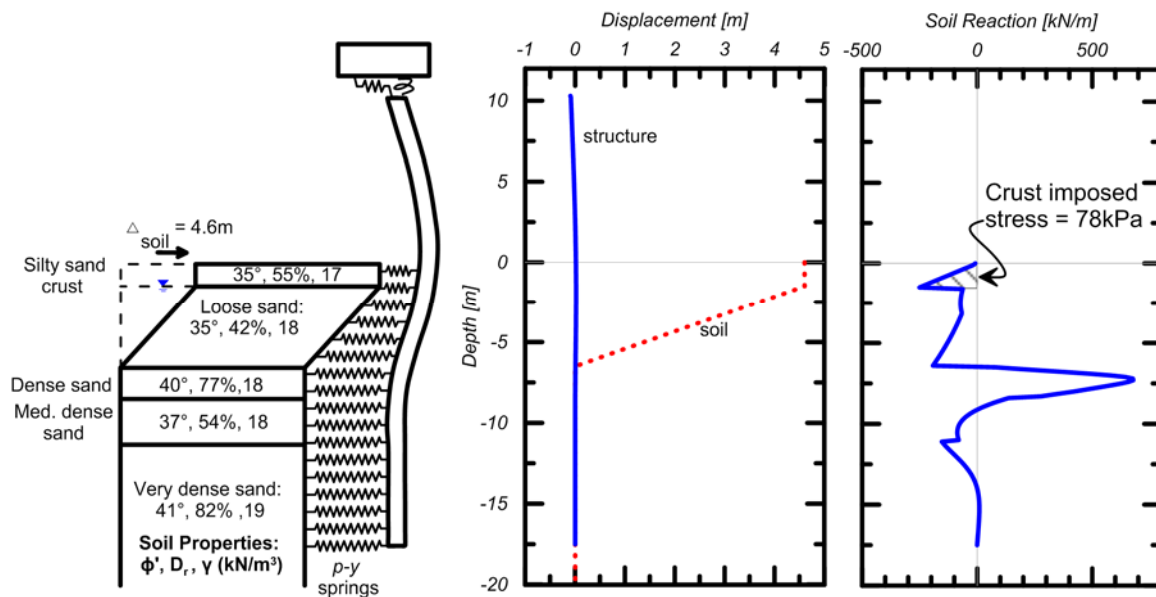


Figure 5-2: Equivalent-static analysis results.

The lateral boundaries of the finite element domain were restrained against displacement in the x -direction (i.e., the domain could not change width) and a uniform displacement of 4.6 m was imposed on the lateral boundaries in the y -direction (i.e., towards the river) as shown in Figure 5-3. In reality there was a non-uniform gradient of displacement along the length of the lateral spread, though most of the soil displacement was accommodated by several large cracks approximately 40 meters upslope from the river. In other words, a block about 40 meters long displaced relatively uniformly towards the river. A uniform displacement imposed on the boundaries is therefore considered reasonable for this exercise.

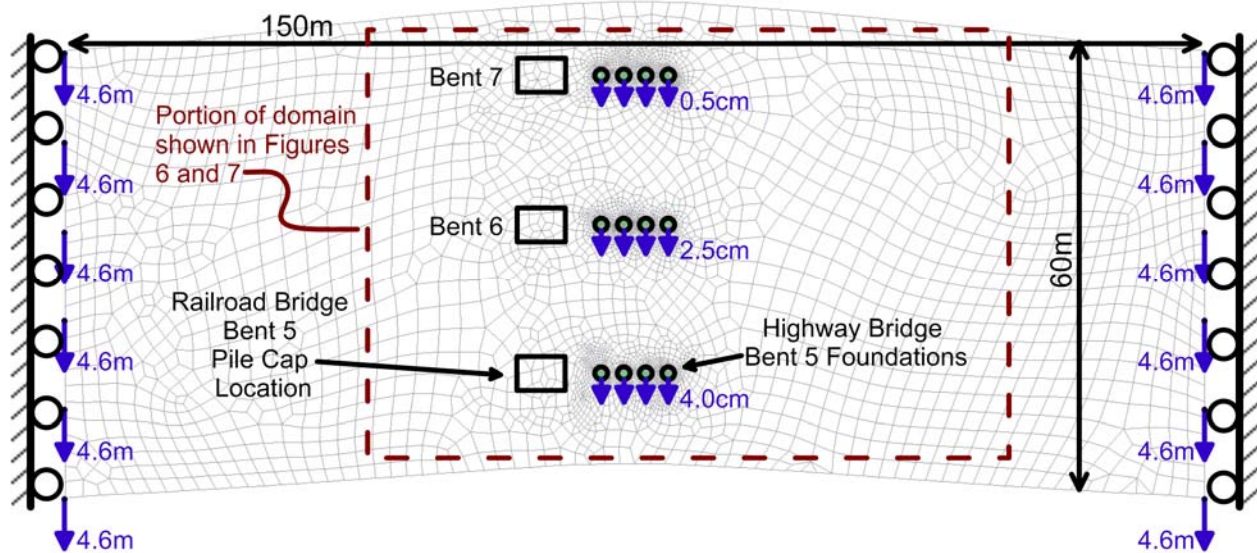


Figure 5-3: Finite element domain.

To define an appropriate Young's modulus for the crust soil, the lateral boundaries of the domain were displaced 4.6 m and the Bent 5 foundations were displaced by the amount predicted from the ESA, 4.0 cm, as shown in Figure 5-3. Bents 6 and 7 of the highway bridge were initially held fixed against translation; the Young's modulus of the crust soil and displacement of Bents 6 and 7 were then adjusted until the average reaction force of the crust acting against the foundations of each bent and the corresponding displacement were in agreement with the ESA results as shown in Figure 5-4. A modulus of 875 kPa was found to provide a good match. This value is significantly less than the small-strain modulus for cohesionless soils under typical loading conditions, which can be attributed to the low confining pressure near the surface and large modulus reduction at high strain as well as the loss of shear resistance at the bottom of the spreading layer (Brandenberg et al. 2007). The results were found to be relatively insensitive to a range of soil Poisson's ratio between 0.2 and 0.35, typical for loose cohesionless soil (Bowles 1996). A small amount of tensile strength (5 kPa) was assigned to the soil to prevent excessive deformation for soil elements that yield in tension. Foundation resistance provided by the railroad bridge was not included in the

domain for the soil modulus calibration step. If the foundations of the secondary structure have comparable resistance to the primary structure, they should be included in the calibration step. Concrete drilled shafts were modeled in *Phase2* with an elastic material having a Young's modulus of 27 GPa and a Poisson's ratio of 0.2.

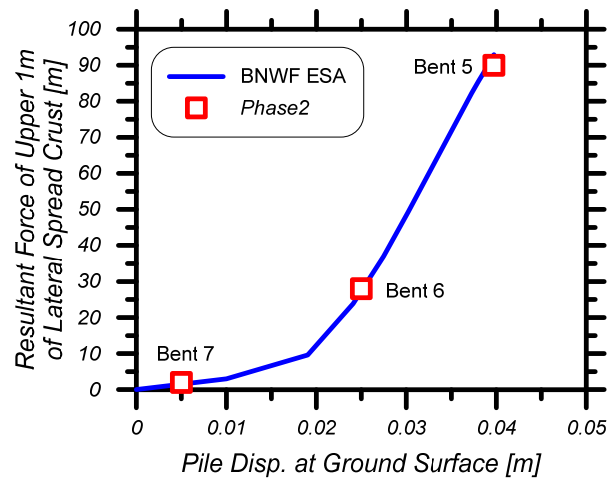


Figure 5-4: Highway bridge mobilized force-displacement results for soil property calibration step.

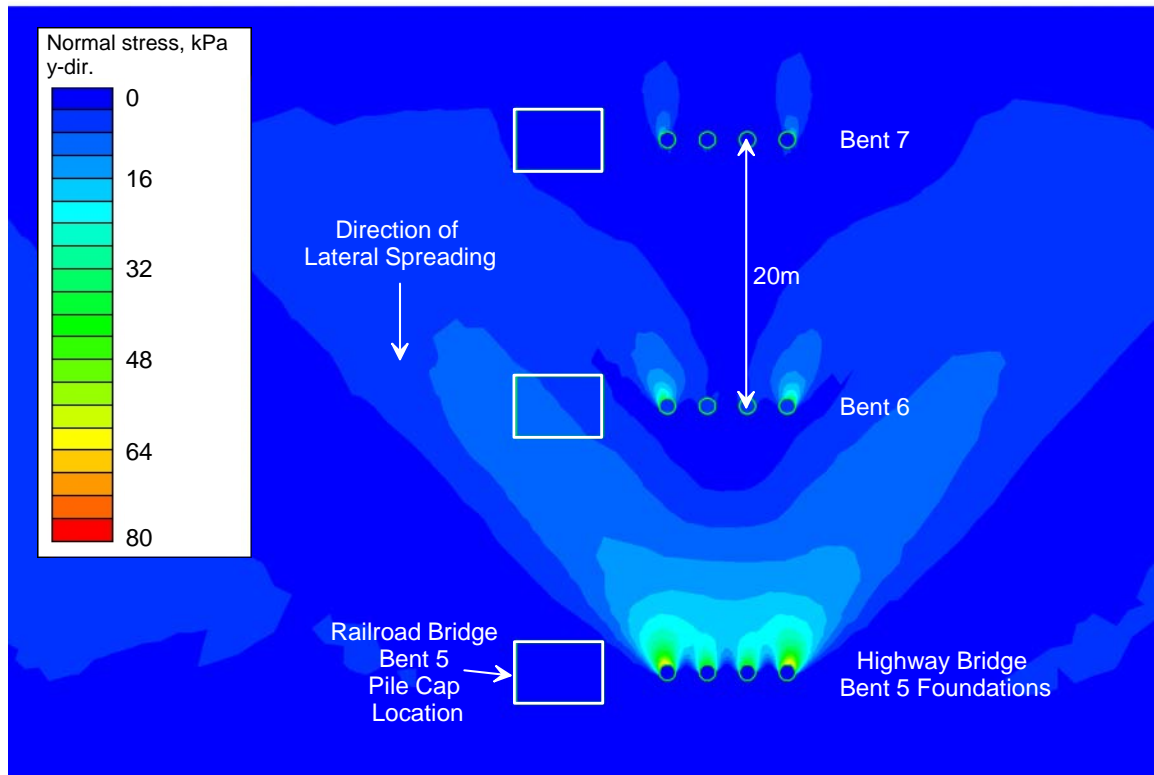


Figure 5-5: Results of Phase2 simulations with 4.6 m of imposed free-field lateral spreading displacement, showing normal stress acting in direction of lateral spreading. Stress contours in kPa.

The steps followed to estimate the reduced demand at the location of a secondary structure due to shielding by the foundations of a primary structure were:

1. Performed ESA for the primary structure foundations using the free-field lateral spreading displacement to determine the average stress intensity acting on the foundations (Figure 4-11) and the corresponding foundation displacement versus soil reaction force relationship (Figure 5-4);
2. Developed finite element model of the crust layer, including foundations of the primary structure, and adjusted soil modulus and foundation displacement until soil reaction force and foundation displacement were in agreement with the ESA results determined in step 1 (i.e., the “calibration step” depicted by Figure 5-3 through Figure 5-5);

3. Determined reduction of free-field lateral spreading displacement at the location of the secondary structure foundations;
4. Performed ESA for secondary structure foundations using reduced lateral spreading displacement demand.

5.3 RESULTS

Average predicted displacement towards the river at the location of Bent 5 of the railroad bridge was 1.36 m for an imposed free-field lateral spreading displacement of 4.6 m as shown in Figure 5-6. This represents a 70-percent reduction from the free-field lateral spreading demand. When the reduced demand is imposed on an ESA model of the bent, the bent is predicted to displace about 1.2 m, which induces unseating collapse of the span and agrees reasonably with the measured pier displacement of about 1 m.

Further studies were conducted to isolate the shielding effect in the transverse and longitudinal directions. A model that only included Bent 5 of the highway bridge (Bents 6 and 7 removed) provided a 68-percent reduction of the free-field displacement at the location of Bent 5 of the railroad bridge, which represents shielding only in the transverse direction. If the railroad bridge had been located an additional 15 m away from highway bridge, the predicted shielding effect would decrease to 45 percent. A model that only included Bents 6 and 7 of the highway bridge provided a 42-percent reduction for the railroad bridge Bent 5, which is primarily longitudinal shielding in the “downstream” lateral spreading direction. In the “upstream” shielding case, a model that only included Bent 5 of the highway bridge provided an 87-percent reduction at the location of Bent 6 of the railroad bridge. It is also apparent that the highway bridge shielded itself, with the presence of Bents 6 and 7 reducing demand on Bent 5 by about 45 percent. These

results demonstrate that longitudinal and transverse shielding effects are both significant, and can be investigated separately with the proposed approach.

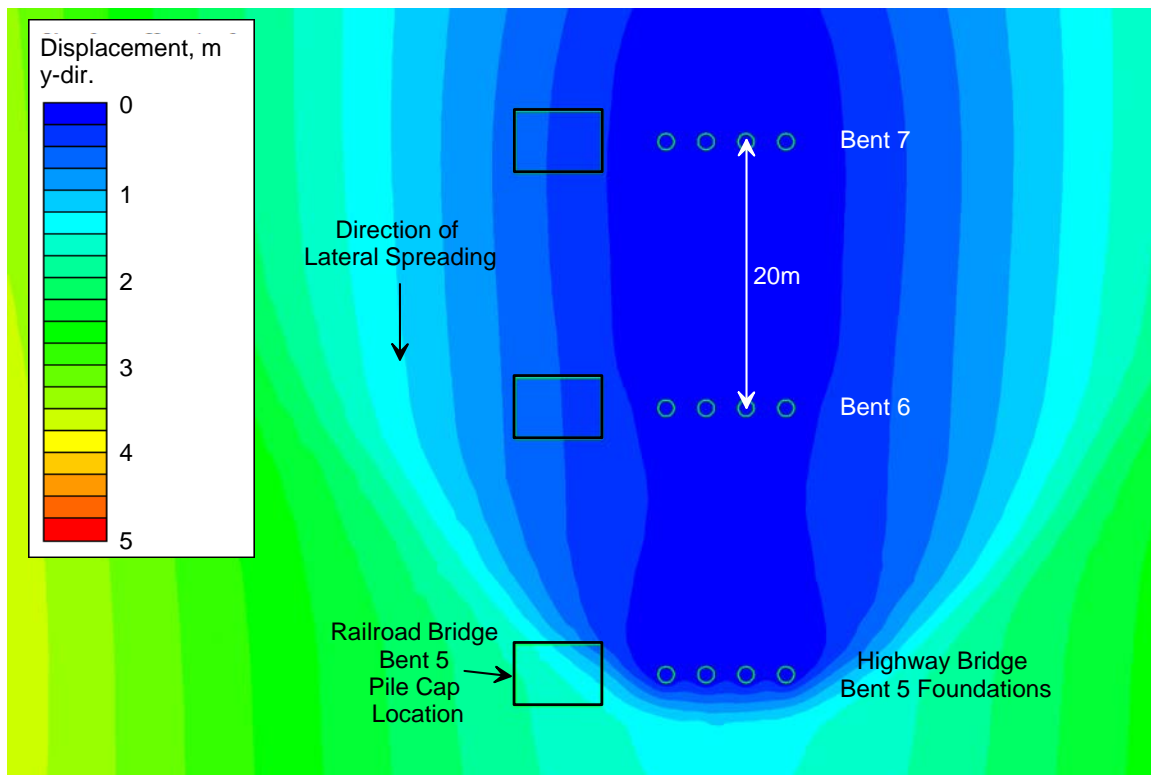


Figure 5-6: Displacement results (in meters) for finite element model including Bents 5, 6, and 7 of the highway bridge showing reduction in displacement at location of railroad bridge Bent 5 compared to free-field lateral spreading displacement of 4.6 m.

For bents of the railroad bridge further from the river bank (No.'s 6 and 7), the predicted reduced displacement demand still results in prediction of significant displacement during the ESA, about 0.4 m, which is contrary to the observed behavior. This can partially be explained by the uniform displacement gradient that was imposed on the model and the fact that the soil properties are different at these locations compared to the Bent 5 location, notably that the thickness of the liquefiable layer decreases further from the river. For forward design cases, knowingly underestimating the shielding effect is a reasonable approach given the uncertain nature of estimating the magnitude and margins of lateral spreading.

In contrast to the shielding provided by the highway bridge, Bent 5 of the railroad bridge only provides an 8 to 10 percent reduction in the lateral spreading displacement demand at the location of Bent 5 of the highway bridge. Since the highway bridge foundations have sufficient strength and stiffness to resist the fully-mobilized passive pressure of the laterally spreading crust, the low shielding effect provided by the railroad bridge is of little consequence. Nonetheless, the analysis did correctly predict that the highway bridge shaft closest to the railroad bridge experienced slightly less demand than the furthest shaft, which agrees with the observed gradient of residual rotations measured in the four columns of HWB Bent 5 following the earthquake.

5.4 INFLUENCE OF LATERAL SPREAD LENGTH

A separate issue, also missing from the literature, is the influence of the length of the lateral spread (recall that length is measured parallel to the direction of lateral spreading displacement). Spread features that are “short” in length along the longitudinal axis of the bridge can be restrained more effectively by the bridge foundations than an equivalent-width lateral spread that extends upslope for a larger distance but undergoes the same free-field displacement. The zone of stress influence for loading conditions below that which is required to fully mobilize passive failure can be relatively large in lateral spread features because the low friction along the base of the spreading crust (i.e., at the interface with the liquefiable sand) results in horizontal pressures transferring further upslope than they otherwise would in a non-liquefied soil profile (e.g., Brandenburg et al. 2007). As a result, lateral spreading occurring a significant distance upslope from a foundation can be “felt” by the foundation even when soil displacement at this location under non-liquefied conditions would have a negligible influence on the foundation. The areal extent of the spread no

longer has an influence when full passive pressures are mobilized in the soil, since the passive pressure limit state does not depend on the length of the spread feature, although the size of the passive wedge will still be larger than in a non-liquefaction case. An exception is when the passive wedge extends beyond the upslope extent of the spread feature, in which case a reduction in passive force would be anticipated relative to the case in which the entire passive wedge is contained within the spread feature.

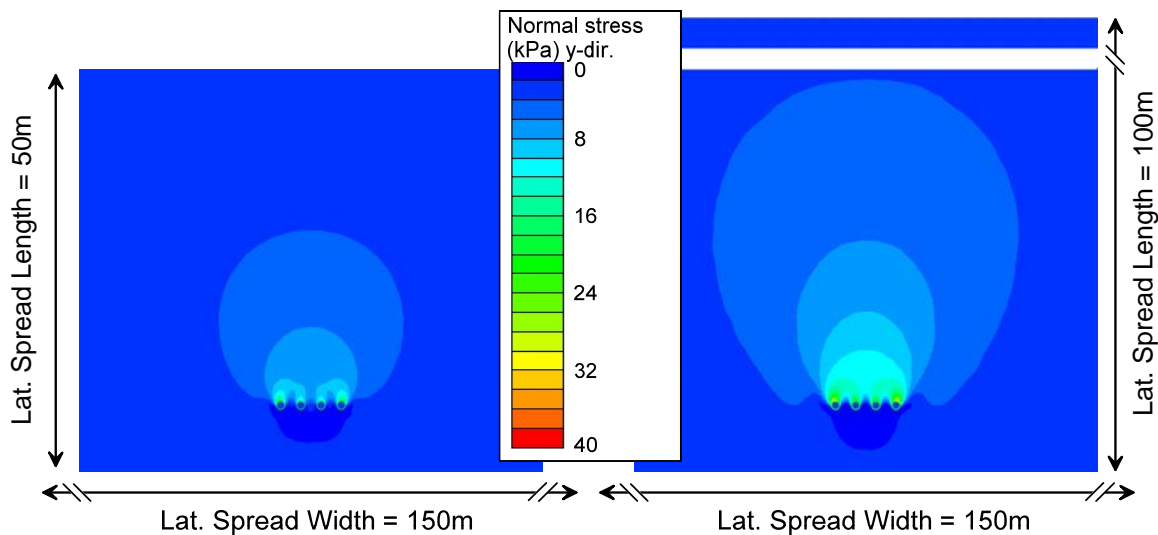


Figure 5-7: Influence of lateral spread length; only the length of the lateral spread is varied between the two cases.

For example, if the entire flood plain on the east bank of the San Felipe Bridges site had liquefied and undergone lateral spreading (lateral spread length of approximately 100 m instead of 50 m), predicted pressures acting against the Bent 5 HWB foundations are about 40 percent higher when the free-field lateral spreading displacement is 0.5 m (less than the amount required to mobilize full passive pressure) as shown in Figure 5-7. This trend confirms that as the length of a lateral spread increases and the foundation zone of influence becomes smaller relative to the areal extent of the lateral spread, the appropriate demand for an ESA approaches the free-field displacement.

5.5 SUMMARY

In this chapter, a novel procedure combining the results of the ESA from the previous chapter with two-dimensional finite element analyses of the laterally spreading crust layer was utilized to study pinning and shielding effects for pile foundations. The results confirm that for foundation groups subjected to very broad lateral spreads in which the zone of influence is entirely contained within the spread feature, the appropriate input displacement for ESA is the free-field displacement. For pile groups subjected to “short” lateral spreads in which the zone of influence of the foundations extends beyond the areal extent of the lateral spread, demands on the foundation are reduced relative to inputting a free-field displacement profile on the free-ends of the p - y elements in an ESA.

Lateral spreading demand at the location of the railroad bridge foundations that were damaged during the earthquake was predicted to be reduced by about 70 percent compared to the free-field displacement measured at the same distance upslope from the river bank. The results of ESA performed using this reduced displacement closely match the observed bridge performance, whereas ESA performed using the free-field displacement over-predicts foundation displacement.

Since the resistance provided by the foundation being investigated is not included in the proposed modeling approach, the displacement reduction may be underestimated for cases when the resistance of the individual foundation represents a significant portion of the total foundation group resistance. This would be most significant for cases where few large-diameter shafts are used and the resistance against lateral spreading provided by a single shaft is significant. In this case, all the foundations providing significant resistance should be included in the soil modulus calibration step. For the San Felipe Bridges case study considered here, the resistance provided

by the railroad bridge foundations was small relative to the resistance provided by the highway bridge foundations.

A limitation of the proposed method as described herein is that only a single layer is considered to dominate the load-transfer behavior between the lateral spread and the foundations, in this case the nonliquefied crust. If multiple nonliquefied layers exist between liquefied layers and undergo significant displacement relative to the foundations, it may not be possible to adequately simplify the behavior to two dimensions. Nonetheless, in many lateral spreading scenarios a single layer of nonliquefied crust overlying liquefied soil does impose the majority of the demand on the foundations, and the two-dimensional approach may be adequate.

The findings of this study show that the length and width of the lateral spread feature relative to the size of the foundation zone of influence affects the load imposed on the foundations by the moving soil. The traditional pinning approach does not account for these effects well when applied to mid-span bents. For example, Kato et al. (2014) applied the pinning approach to back-analysis of three bridges and found that the observed performance was not matched in all cases, concluding that the three-dimensional geometry of the problem has a clear influence on the pile response.

The analysis method proposed herein can also be used to assess the appropriate demand for foundation groups. The free-field displacement should be applied for mono-foundations or in very broad lateral spreads, including softened p - y behavior to account for loss of shear resistance at the bottom of the spreading layer following recommendations by Brandenberg et al. (2007). Additionally, the sensitivity of the two-dimensional analysis results to changes in areal extent and magnitude of free-field displacement can provide insight to the potential consequences of actual lateral spreading displacements exceeding the estimated amount. Because there is large uncertainty

inherent in current methods available for estimating lateral spreading displacements, the ability to investigate the sensitivity of bridge performance to this uncertainty with the simple tool presented here could present significant cost and time savings for many projects.

Foundation engineers are cautioned to carefully consider the boundary conditions of each individual project and whether or not two-dimensional analyses can adequately capture the real system behavior. It is important to recognize that the results of the procedure presented here are approximate and should not be treated as a guaranteed representation of actual system performance. For high-value or critical projects, the results of two-dimensional analyses could be used to decide whether or not more sophisticated analyses are warranted, or whether the cost associated with mitigating lateral spreading rather than designing for its consequences are justified.

6 Conclusions

Equivalent static analysis (ESA) procedures for evaluating the effects on bridges of lateral spreading displacements (Ashford et al., 2011; Caltrans, 2013a) have been applied to two adjacent bridges that exhibited different performance levels in similar soil conditions and under approximately the same lateral spreading demands. These procedures correctly predicted the observed behavior of both bridges, indicating that they are appropriate for routine practice. The difference in behavior of the two bridges can ultimately be attributed to the cumulative lateral resistance of the railroad bridge pile group being less than the fully-mobilized passive pressure demand from the laterally spreading crust, whereas the highway bridge foundations had sufficient strength and flexural stiffness to resist the passive pressure without undergoing significant displacement. The ESA procedures correctly predicted the response of both bridges using a common framework for assigning input parameters. In addition, a novel procedure combining the results of the ESA with two-dimensional finite element analyses of the laterally spreading crust layer was utilized to study pinning and shielding effects for pile foundations.

The effects of restraint-compatible displacement-based inertial demands were found to be negligible in comparison to kinematic loads from lateral spreading, which dominated the response of both bridges. This is expected for bridges that are restrained against translation in the direction

of lateral spreading. Force-based methods for combining inertial demands with lateral spreading for models that only included below-ground foundation elements of the bridges did not capture the observed behavior of the bridges and in some cases predicted collapse where none occurred. Using a restraint-compatible spectral-displacement-based approach—as opposed to the current force-based approach— is recommended to impose inertial demands that explicitly consider the translational and rotational restraint provided by other bridge components.

To adequately assess the predictive capability of the ESA procedures in the context of this case study, it was necessary to model the above-ground components of the bridge bents in addition to the foundation elements. *OpenSees* provides far more flexibility in structural modeling compared with tools commonly used by geotechnical engineers such as *LPILE*. It is difficult to accurately predict foundation and superstructure performance when analyses of the two systems are performed independently because the complex interaction that occurs between them cannot easily be replaced by simple shear, moment, or displacement boundary conditions. It is therefore recommended to perform such simulations using a structural design software package that can capture these more complex features of the structural behavior. It should be stressed that this does not necessitate a dynamic or even pseudo-static analysis of the entire superstructure combined with the foundations; a novel approach has been presented here for capturing the restraint of above ground components for modal analysis and subsequent combined inertial and kinematic analysis with a single-bent model [see Figure 4-10(c)]. This approach will have the added benefit of facilitating better communication between structural and geotechnical designers.

This case study demonstrates several lessons with broad applicability:

- The equivalent-static BNWF approach is a valuable tool for estimating foundation shear and moment demands for structural design, as well as for

predicting displacements and rotations for performance evaluation. However, proper implementation of the method requires correctly modeling both the soil and the structural elements that resist lateral spreading demands, which likely includes above-ground bridge components. This requires geotechnical and structural expertise and can best be achieved using software that allows explicit modeling of structural components and connections, such as *OpenSees*.

- The foundation response predicted by the ESA procedures can be sensitive or insensitive to virtually any of the input parameters, and in most cases it is difficult to assess this sensitivity *a priori* without actually performing parametric studies over a range of the input values. The ESA should be utilized as a tool to understand the performance of a proposed design and guide further geotechnical investigation as well as to facilitate interaction with the bridge superstructure designers.
- Large ground displacements occurred at the San Felipe Bridges case study site, and the railroad bridge was not stable against the passive pressure of the laterally spreading non-liquefied crust layer. Since there is considerable uncertainty in estimating lateral spreading displacements, if significant lateral spreading is expected at a site (i.e., several meters or more), it is reasonable to assume that enough displacement will occur to fully mobilize passive pressure of a crust layer. Proposed foundation designs should therefore exhibit tolerable rotation and displacement (i.e., be stable) in response to the fully-mobilized demand. In most cases, a stable design will

prevent yielding of the foundations and columns; where column or foundation yielding is permitted, significant ductility capacity is required.

- Modeling superstructure inertial demands as the base shear and overturning moment of a laterally-unrestrained SDOF bent model can result in erroneous overestimates of foundation demands. Inertial demands are better represented as spectral displacements at the superstructure level. These spectral displacement demands should be generated from a modal analysis which explicitly considers bridge restraint from all bridge components.
- Axial failure of Bent 6 of the highway bridge could potentially have been prevented by using a measure of penetration resistance with greater resolution than typical SPT sampling intervals, which would have identified the loose layer near the foundation tip. More suitable exploratory techniques in heterogeneous alluvial environments include CPT or continuous SPT sampling.
- Analysis of axial behavior of deep foundations during seismic loading should explicitly consider generation of excess porewater pressure for computation of effective stress even if full liquefaction is not predicted.
- For single piles and foundation groups subjected to very broad lateral spreads in which the zone of influence is entirely contained within the spread feature, the appropriate input displacement for ESA is the free-field displacement. For pile groups subjected to “short” lateral spreads in which the zone of influence of the foundations extends beyond the areal extent of

the lateral spread, demands on the foundation are reduced relative to inputting a free-field displacement profile on the free-ends of the p - y elements in an ESA.

Part II: Influence of Kinematic Pile-Soil Interaction on Foundation Input Motions for Bridges Supported on Deep Foundations

How can earthquake ground motions estimated from a seismic hazard analysis be reliably modified to account for differences between movement in the free-field and movement of the foundations due to kinematic pile-soil interaction?

7 Introduction to Part II

Seismic design of bridges and other structures supported on bored or driven piles often utilizes a substructure method of dynamic analysis in which the foundation elements are not explicitly modeled, but are replaced by springs and dashpots representing the foundation impedance. The ground motion appropriate for input to the free end of the springs, known as the *foundation input motion* (FIM) differs from the free-field motion (FFM) due to the difference in stiffness and deformation characteristics between the pile(s) and soil, which is the concept of kinematic soil-structure interaction (SSI). As with many other aspects of SSI, the difference between the FIM and FFM often results in a favorable reduction in demand placed on the structure, yet it is typically ignored in practice. In some cases, however, the FIM could actually be greater than the FFM, which is also typically overlooked.

Within the substructure method, the problem of relating the FFM to the FIM is solved separately from the dynamic analysis of the superstructure. Ground motions from a seismic hazard analysis represent shaking in the free field, and must be modified to account for kinematic SSI. For example, the PEER ground motions database (Ancheta et al., 2014), a commonly used source for accelerograms used for dynamic analyses, excludes records influenced by SSI. Similarly, response spectra representative of the FFM rather than the FIM are typically used for pseudo-static

response spectrum analysis. Pseudo-spectral accelerations (PSA) on seismic hazard maps and site amplification factors used in building codes and seismic design guidelines (e.g., ASCE-7, 2010) do not include the influence of SSI.

Whereas kinematic SSI for shallow foundations is relatively well understood and tools are available for implementation in routine practice (e.g., NIST 2012), similar tools are not yet available for piles. Since the 1960's, several researchers have studied the response of piles and pile groups using simplifying assumptions such as linear elasticity, homogeneous soil properties, and harmonic ground motions, including Tajimi (1969), Flores-Berones and Whitman (1982), Gazetas and Dobry (1984a), Fan et al. (1991), Kaynia and Novak (1992), and many others. More recent developments such as Anoyatis et al. (2013), Sica et al. (2013), and Di Laora and Rovithis (2014) have incorporated the effects of inhomogeneous and layered soil profiles and different pile boundary conditions. However, the previous studies to-date have yet to produce tools such as formulas for transfer functions and response spectrum scaling factors that reliably account for the complexity of realistic pile, soil, and ground motion conditions—in particular, nonlinear material behavior—yet are simple enough for implementation in routine practice. The purpose of this study is to develop such tools with consideration of realistic dynamic material behavior and subsurface conditions using the type of information known for a typical project. Emphasis is placed on evaluating the influence of the following factors:

- Nonlinearity due to (i) free-field site response, (ii) interaction at the pile-soil interface, and (iii) nonlinear pile structural behavior,
- Inhomogeneous soil profiles, which for this study are developed from the results of real subsurface investigations,

- The complexity of real ground motions, including variable frequency content, intensity, and incoherence (i.e., spatial variability), and
- Pile group behavior, in particular the influence of ground motion incoherence over the spatial extent of the pile group in light of the preceding factors.

Previous computational studies using elastic material properties and other highly idealized conditions have generally concluded that reductions between the FIM and FFM are insignificant and can be ignored in practice. This study demonstrates that large-diameter piles used in soft soil conditions can result in reductions to design ground motions that are significant and could result in appreciable cost savings.

The few documented case studies of measured kinematic pile-soil interaction effects provide conflicting evidence as to whether or not it is a significant phenomenon that should be of interest to foundation engineers. This research seeks to explain these case studies and clearly demonstrate the conditions under which pile kinematic SSI should be considered, and likewise can safely be ignored.

The outcome of this work is a set of “generalized models” for predicting transfer functions and spectral ratios for use in routine practice. The terminology “generalized model” is used here to refer to a mathematical model (i.e., equation with a specified functional form) intended to cover a wide range of conditions encountered in routine practice. The generalized model is implemented for specific project conditions by computing coefficients based on known project parameters such as pile size and soil shear wave velocity. The coefficients have been determined by statistical regression of the results of a parametric analysis covering typical foundation, subsurface, and ground motions conditions.

7.1 ORGANIZATION

Part II of this dissertation is organized as follows:

- The remainder of Chapter 7 introduces the fundamentals of kinematic pile-soil interaction, followed by a literature review of previous work on the subjects of pile dynamics and lateral load analyses using the p - y method. Since most of the available pile kinematic solutions rely on simplifying assumptions of linear elasticity and highly idealized subsurface conditions, a critique is given in the context of the limitations of these assumptions and the motivation to overcome them with the present study. The limited amount of empirical and experimental evidence of pile kinematic SSI is also presented.
- Chapter 8 presents a derivation of an elastic analytical solution for kinematic pile-soil interaction. The closed-form solution that results is used for validating the numerical modeling approach that will subsequently be used for nonlinear analyses.
- Chapter 9 defines the bounds of the parametric study performed to investigate the kinematic pile problem, and lays out the means by which the input parameters for the nonlinear analyses were formulated.
- Chapter 10 presents the results of the parametric study, followed by development of generalized models for predicting those results in a forward-design scenario. The forward prediction models consists of a specified functional form with coefficients that are predicted via equations developed through statistical regression. Comparisons are made between

the nonlinear analysis results and idealized elastic solutions, which show that the elastic solutions generally are capable of predicting the average response of the nonlinear system. However, the elastic solutions fail to capture the large variability exhibited by the nonlinear analysis results, which is caused by the complexity of realistic subsurface conditions and ground motions, and soil nonlinearity.

- Chapter 11 investigates issues related to the combination of inertial and kinematic SSI effects. An understanding of the combined effects is necessary for the re-examination of case history data presented in the following chapter.
- Chapter 12 provides example applications of the generalized models through (i) re-examination of existing case history data, and (ii) a hypothetical bridge design scenario.
- Chapter 13 provides conclusions and recommendations for implementation of the generalized results in engineering practice.
- Appendix D contains profiles of soil properties that define the sites used for nonlinear analyses.
- Appendix E discusses a pilot field study done as part of this project to measure kinematic pile-soil interaction transfer functions for full-scale conditions. The framework used for this pile study is documented with the intent that it will be repeated in the future for further validation of computational approaches.

7.2 FUNDAMENTALS

Soil-structure interaction can be broadly classified into two effects¹:

- *Inertial interaction*, which describes how inertial forces generated in the structure induce foundation displacements and rotations that would not occur if the structure had a fixed base, resulting in additional displacements in the structure and a change of fundamental frequency or “period lengthening”, and
- *Kinematic interaction*, which describes how waves propagating in the free-field differ from the motion of the foundation(s) due to differential foundation-soil stiffness, ground motion incoherence, and wave scattering effects.

In the context of the substructure method, foundation “impedance” (defined below) depends primarily on inertial SSI, and kinematic SSI determines the appropriate FIM to be used for the analysis. For pile-supported structures, kinematic SSI will be referred to as “kinematic pile-soil interaction” in this text.

Two effects resulting from kinematic pile-soil interaction are of interest to foundation engineers. The first, which is the primary subject of this study, is the difference between the FIM and the FFM. The second topic of interest is quantifying demands placed on the pile directly as a result of excitation of the surrounding soil. Pile foundations are typically designed only to resist force effects from the superstructure, including inertial demands during earthquake loading in

¹ Professor Robert V. Whitman is credited with coining the terms inertial and kinematic during the 1970’s (Roesset 1994; Kausel 2010).

seismic regions. Kinematic loads coming from the ground are often ignored, except for cases of large permanent ground displacement such as lateral spreading as discussed in Part I of this dissertation. However, kinematic pile-soil interaction can impose large demands on piles even in the absence of permanent ground deformation, particularly where a significant soil stiffness contrast exists over the length of the pile. While kinematic demands are not the focus of this study, the analysis method described herein sheds lights on the problem and could be used for future studies.

The substructure method of SSI analysis (e.g., Roesset et al. 1973) for a pile-supported structure can be summarized in three steps:

1. Determine the kinematic response of the pile foundation with the mass of the supported structure set equal to zero; this provides an estimate of the demand on the pile resulting from the ground vibration as well as the motion at the top of the pile (the FIM);
2. Determine the dynamic impedance at the pile head, consisting of frequency-dependent springs and dashpots that relate an applied force or moment at the pile head to a unit displacement or rotation, respectively; and
3. Evaluate the response of the structure supported on the springs and dashpots from step 2 and excited by the FIM from step 1.

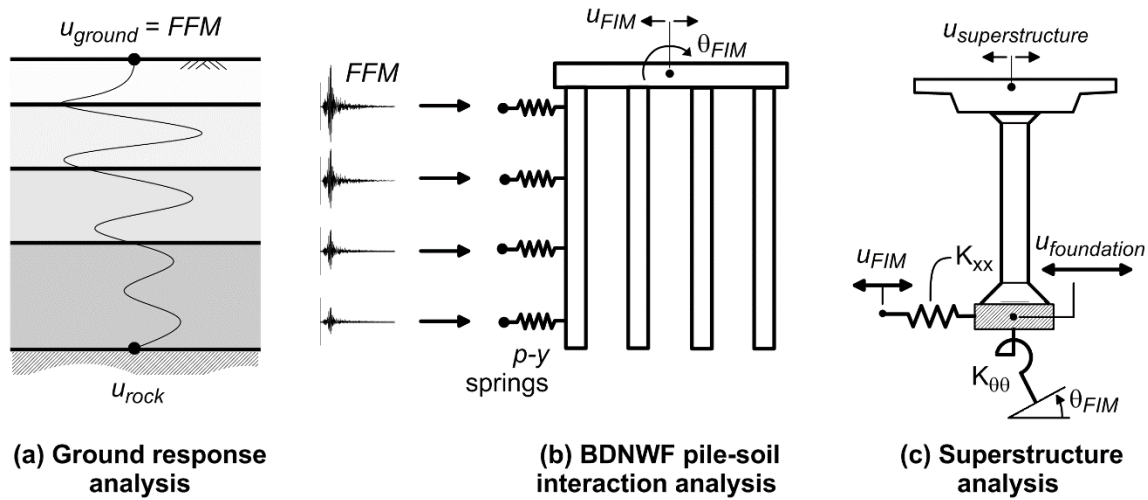


Figure 7-1: Substructure method of analysis for bridge bent supported on a pile group. Note that vertical impedance is not shown, but could also be considered.

The substructure method for a pile-supported bridge bent is depicted in Figure 7-1. The alternative to the substructure method is to analyze the complete structure-pile-soil system simultaneously, known as the “direct” method of analysis. While this approach overcomes certain issues associated with combining the different steps of the substructure method, it is computationally expensive, difficult to perform using existing commercial software, and requires advanced expertise in both geotechnical and structural engineering. Hence for routine practice, tools and associated guidance for facilitating use of the substructure method are preferred.

The stiffness contrast between a pile and surrounding soil is the primary mechanism driving kinematic pile-soil interaction. A stiff pile in a relatively soft soil profile will generally undergo less deformation than the free-field soil, whereas the deformed shape of a flexible pile in stiff soil will be closer to the deformation of the surrounding ground.

Frequency of the free-field excitation has a strong influence on kinematic pile-soil interaction, because the wavelength of the free-field motion ($\lambda_{ff} = V_s / f$, where V_s is soil shear

wave velocity and f is the excitation frequency) determines the extent to which the ground movement varies over the length of the pile. This is illustrated in Figure 7-2 for a “floating” pile with free-head and free-tip boundary conditions of length $L = 20$ m, subjected to harmonic free-field excitation representing idealized vertically-propagating shear waves. The pile flexural rigidity $E_p I_p = 1,325 \text{ MN}\cdot\text{m}^2$ (E_p and I_p are the pile Young’s modulus and moment of inertia, respectively) corresponds to a $B = 1$ -m diameter circular reinforced concrete section. Figure 7-3 depicts the response of the same system, but for a fixed-head pile boundary condition in which the pile head is restrained against rotation to simulate connection to a pile cap or other stiff structural element.

For low-frequency excitation, the pile moves in concert with the ground since the ground displacement is relatively uniform over L . For high-frequency, short-wavelength excitation, the ground displacement reverses directions many times over L . The pile flexural stiffness prevents it from conforming exactly to the ground displacement, instead averaging the variable ground displacements imposed over its length. This average displacement approaches zero at high frequencies corresponding to low ratios of λ_{gf}/L . This is similar to the concept of base-slab averaging for shallow foundations [e.g., see Veletsos and Prasad (1988)], in which the stiffness and strength of the foundation average the spatially variable ground motions imposed across its footprint. As for shallow foundations, spatial variability (incoherence) of real ground motions has the potential to further increase the averaging effect for pile groups that cover a large area, such as the footprint of a building.

Between these extremes, intermediate-frequency excitation places the largest flexural demands on the pile for the example parameters considered here. Notice that the free-field excitation has the same displacement amplitude for each of the frequencies shown.

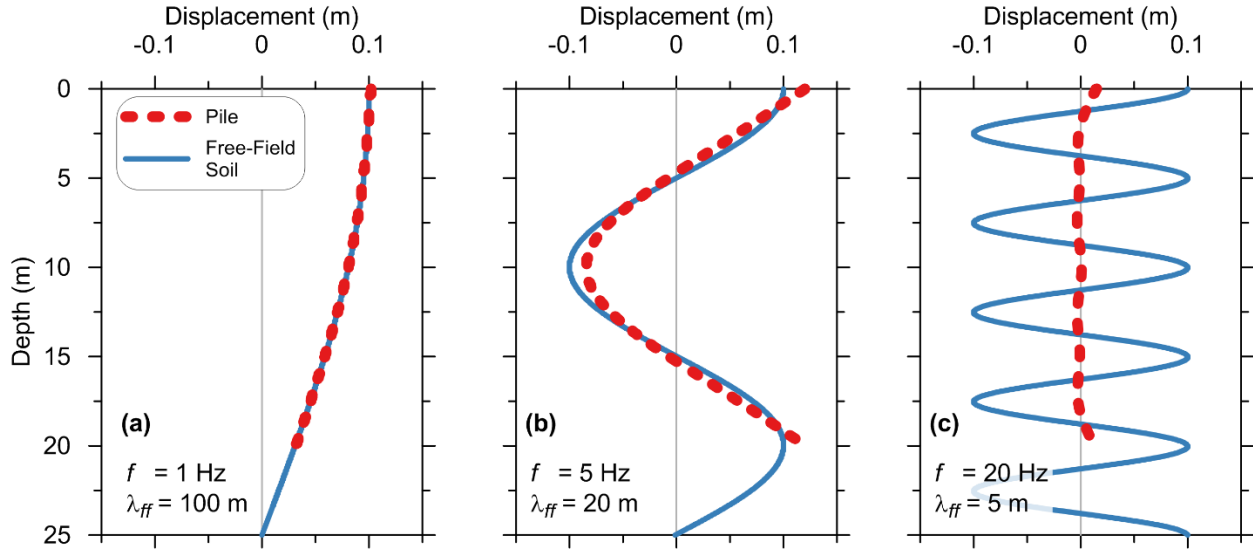


Figure 7-2: Profiles of soil and free-head pile displacement for three frequencies of harmonic free-field excitation.

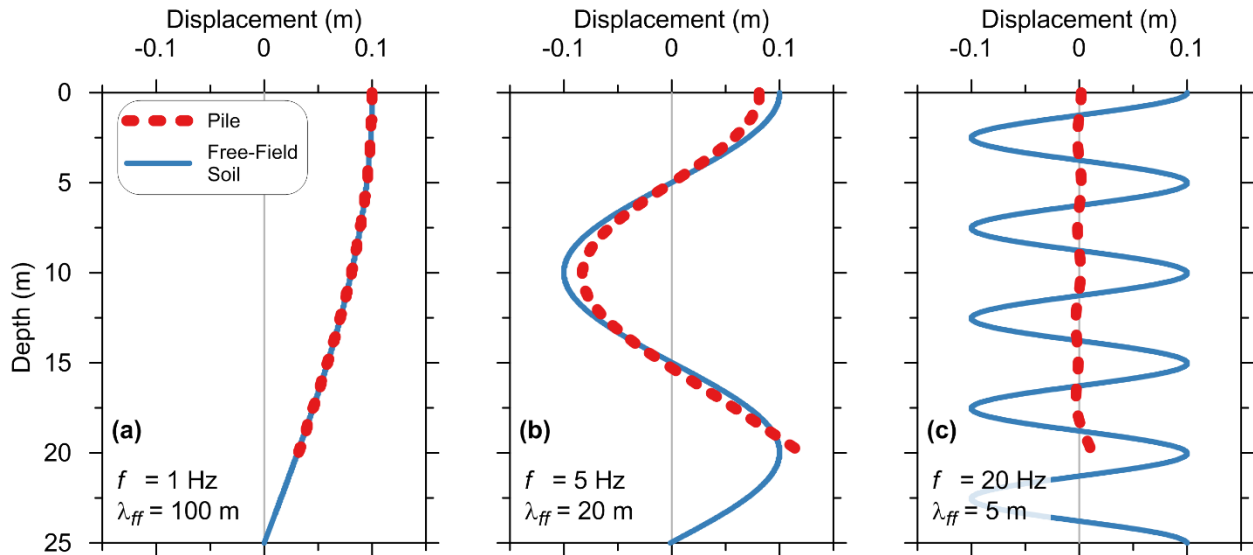


Figure 7-3: Profiles of soil and fixed-head pile displacement for three frequencies of harmonic free-field excitation.

Taking the pile head motion u_p as the FIM and the ground surface displacement u_g as the FFM, the ratio FIM/FFM can be expressed as a frequency-dependent transfer function by computing FIM/FFM at several frequencies over a range of interest. The transfer function can be thought of as a filter which describes how the pile-soil system modifies an input signal (the FFM) to produce an output signal (FIM). A transfer function ordinate H_u of unity indicates that the soil

and pile move in unison, such as depicted in Figure 7-2(a), while $H_u \approx 1.2$ and 0.15 for the conditions depicted in Figure 7-2(b) and (c), respectively. Transfer functions for the free- and fixed-head piles are depicted in Figure 7-4. Notice that for the free-head pile, H_u exceeds 1.0 for frequencies up to about 7 Hz, indicating that the pile amplifies the ground motion ($u_p > u_g$), while the fixed-head pile displaces less than the free-field at all frequencies. The phenomenon of $H_u > 1.0$ for free-head piles, which occurs when $\lambda_g \approx L$ as depicted in Figure 7-2(b), will be referred to as “kinematic amplification” in this study.

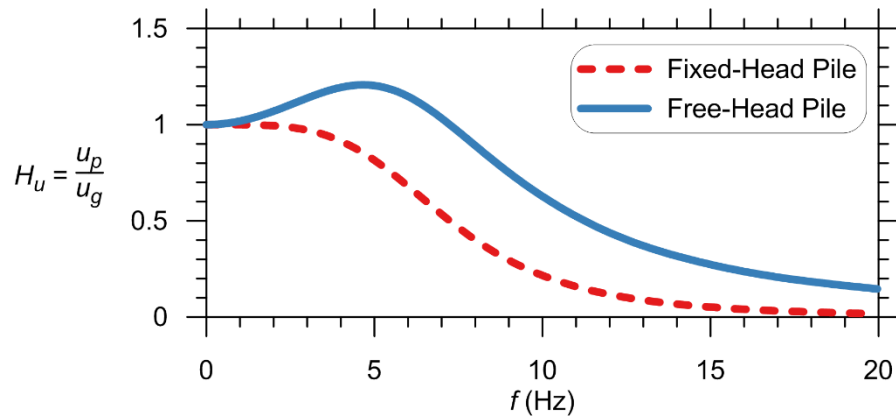


Figure 7-4: Kinematic pile-soil interaction transfer functions computed for idealized linear-elastic conditions.

For both fixed- and free-head piles, the FIM is reduced from the FFM at high frequencies, implying that a structure supported by the piles will experience a beneficial reduction in demand at these frequencies if the FIM is used for design. The frequency beyond which H_u descends below unity will be referred to as the “corner frequency” (f_c) of the transfer function in this text. Since H_u is technically less than unity for any $f > 0$ for elastic fixed-head transfer functions, an arbitrary definition of f_c will be adopted as the frequency at which $H_u \approx 0.95$, for example about 3.5 Hz for the fixed-head case in Figure 7-4. Whether or not the corner frequency falls within the frequency range of engineering interest (approximately 0.2 to 20 Hz for typical structures) depends on factors

such as the relative stiffness contrast between the pile and soil, changes in soil stiffness over the length of the pile, and whether or not restraint against rotation is provided at the pile head.

In addition to the differences in displacement between the pile and soil, Figure 7-2 shows that a free-head pile also undergoes rotation at the pile head due to the kinematic response. To compute the response of a structure supported by free-head piles using the substructure method, the pile head rotation θ_{FIM} must be input to the base of the structural model in addition to u_{FIM} . Since rotation of the free-field soil column is zero at the ground surface for vertically propagating shear waves (since shear strain has to be zero for a zero stress condition), the transfer function for free-head pile rotation is instead normalized by the free-field displacement, and is usually multiplied by pile diameter such that is dimensionless (i.e. $H_\theta = \theta_{FIM} \cdot B / u_{FFM}$)

The transfer functions depicted in Figure 7-4 were computed using an analytically-derived linear-elastic solution that is presented in detail in Chapter 8. For more realistic pile, soil, and ground motion conditions typical of a real project, numerical techniques such as the finite-element method can be used to compute the dynamic response of the system, which is the approach used in this study. Because real earthquakes cause the free-field and structure to respond at multiple frequencies simultaneously, and because of nonlinearity in the system response, the results of dynamic analyses cannot be used directly to compute u_p/u_g at a single isolated frequency. Instead, the response history of the pile-head and ground-surface motions must be transformed to the frequency domain, for example using a Fourier transform. This allows H_u to be computed as the ratio of Fourier amplitude spectra (FAS) at each frequency over the range of interest as depicted in Figure 7-5. The following notation is used to denote these operations:

$$\mathcal{F}(u(t)) = U(\omega) \quad (7.1)$$

$$H_u(\omega) = |U_{FIM}(\omega)| / |U_{FFM}(\omega)| \quad (7.2)$$

In Equations (7.1) and (7.2), $u(t)$ is the time-domain signal of either the FIM (u_p) or FFM (u_g), and \mathcal{F} denotes a Fourier transform operation which produces a complex-valued frequency-domain signal denoted by capital letter $U(\omega)$. The amplitude and phase of the signal are computed from its real and imaginary parts $[Re(U(\omega))$ and $Im(U(\omega))]$ as:

$$|U(\omega)| = \sqrt{Re(U(\omega))^2 + Im(U(\omega))^2} \quad (7.3)$$

$$\phi_U(\omega) = \arctan\left(\frac{Im(U(\omega))}{Re(U(\omega))}\right) \quad (7.4)$$

For simplicity, the abbreviation FAS is sometimes used as a shorthand for the magnitude of the Fourier amplitude spectra, that is $FAS = |U(\omega)|$. The frequency domain signal can be represented equivalently in terms of either frequency f or angular frequency ω .

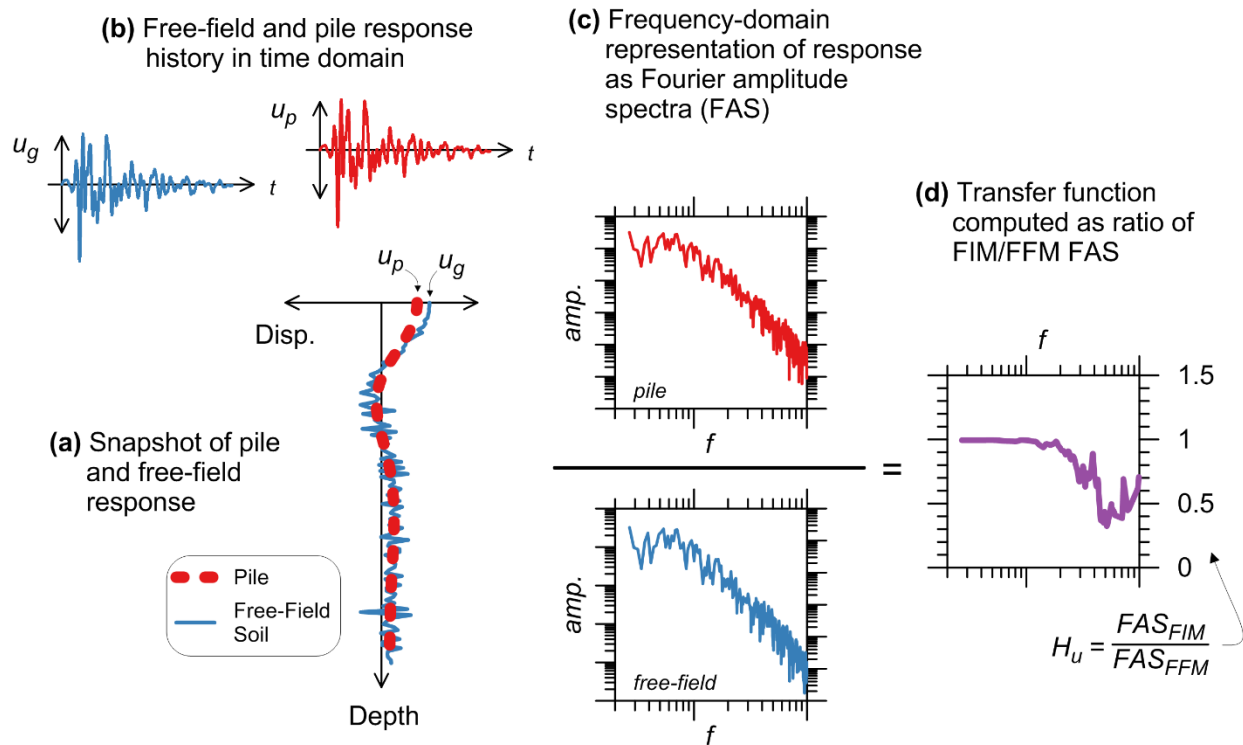


Figure 7-5: Time- and frequency-domain representations of pile seismic response for computation of kinematic transfer function.

Although transfer functions may be unfamiliar to foundation engineers outside the realm of pile dynamics, they are a very useful tool for seismic design. Once a kinematic pile-soil interaction transfer function has been defined, it can be used to compute a FIM given a FFM without repeating the actual dynamic analysis of the pile subjected to the FFM. This is accomplished by convolving the transfer function with the FFM in the frequency domain (i.e., multiplying the Fourier amplitude spectral ordinates of the FFM and transfer function at each frequency), then performing an inverse-Fourier transform to recover the FIM signal in the time-domain—essentially performing the process depicted in Figure 7-5(b) through (d) in reverse. These operations can easily be performed with commonly used mathematical software. Hence, if a reliable predictive model is made available to define a transfer function using parameters known for a typical project—pile and soil properties and estimates of ground motion intensity measures

from a seismic hazard analysis—then foundation engineers can skip the dynamic pile analysis, yet still provide the structural designer an estimated FIM instead of FFM for more realistic dynamic analysis of the superstructure.

While response history analysis may be used for major bridges or other critical infrastructure, for routine projects, seismic design is usually performed via pseudo-static response spectrum analysis. By computing response spectra from a FIM and FFM, the ratio of spectral ordinates at each period can be computed as depicted in Figure 7-6. These “spectral ratios” (also referred to as ratio-of-response-spectra or RRS) can then be used in a forward-design scenario to modify FFM response spectra generated from the building code or site-specific seismic hazard analysis to represent a FIM. Hence, just as in the case of the transfer functions for dynamic analysis, if foundation engineers can reliably estimate spectral ratios using known project parameters, FIM response spectra can be generated for design purposes without performing dynamic pile analyses.

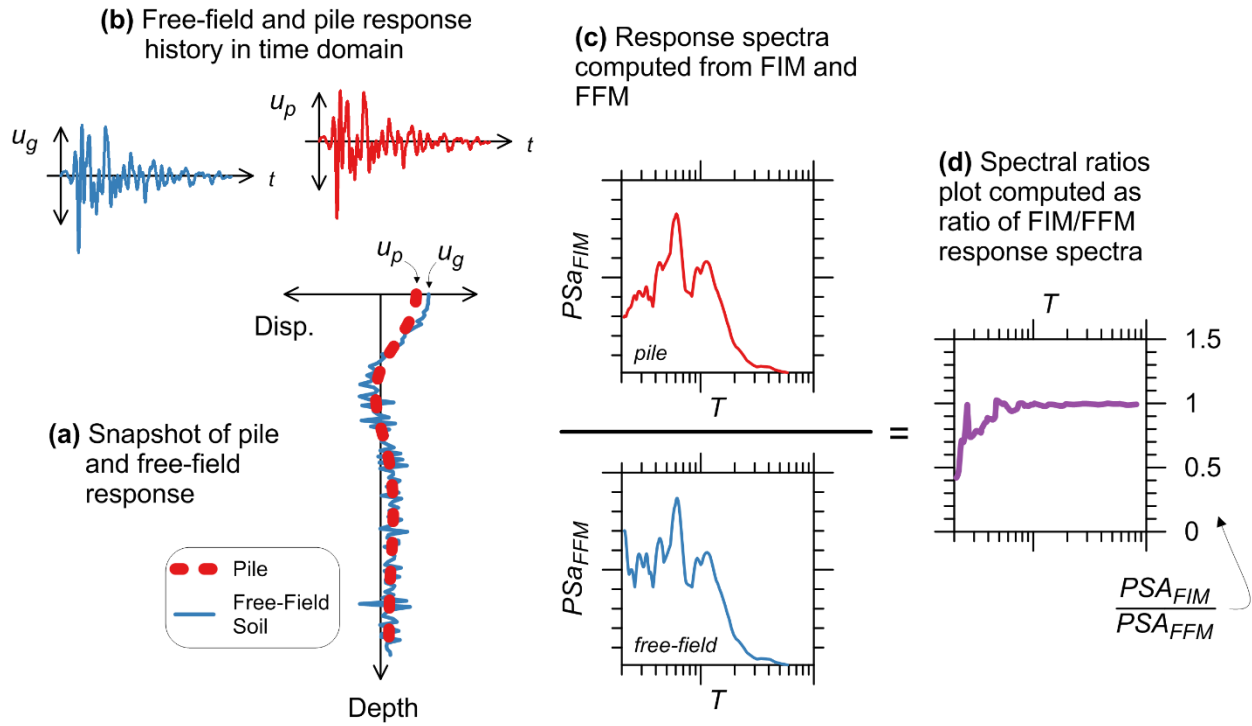


Figure 7-6: Time-domain and response spectrum representations of pile seismic response for computation of kinematic spectral ratios.

Although the spectral ratio plot in Figure 7-6(d) appears to be equal to the transfer function plot in Figure 7-5(d) with the horizontal axes flipped, spectral ratios should not be interpreted simply as the inverse of the kinematic transfer function. A response spectrum represents the response of a single-degree-of-freedom oscillator to an input ground motion, and therefore depends on the properties of both the ground motion and the oscillator. Whereas the response spectrum ordinate at longer natural periods (low natural frequency) is heavily dependent on the flexibility of the oscillator, at short natural periods (high natural frequency) the spectral ordinate is controlled by the largest amplitude peak in the ground motion, which is usually dominated by intermediate frequency energy.

7.3 PREVIOUS STUDIES

7.3.1 Winkler Analysis and p - y Curves

The approach used in this study is the beam-on-dynamic-nonlinear-Winkler-foundation (BDNWF) model solved numerically with the finite-element method. The Winkler method refers to the response of a beam supported on a bed of springs characterized by a constant elastic stiffness or “modulus of subgrade reaction,” the term favored by Terzaghi and Peck (1948). Winkler’s (1867) hypothesis is that the pressure exerted by the subgrade on a loaded beam at a given point is proportional to the deflection of the beam at that point, and independent of the response at other locations. Hetenyi (1946) and Vesic (1961) demonstrated that the error between Winkler models and elastic continuum models is small for many realistic scenarios involving flexible beams, and that when used within the appropriate bounds the Winkler method can generate reliable results for foundation design. For analysis of piles, the Winkler family of methods considers a discretized foundation element attached to the ground through springs representative of horizontal and/or vertical pile-soil interaction, and has been extended to include nonlinear pile-soil interaction through p - y , t - z , and q - z curves.

While the majority of previous studies of pile-soil interaction using the Winkler method have utilized linear-elastic Winkler foundation springs, this study utilizes nonlinear soil springs. Accounting for soil nonlinearity directly is a more robust approach than equivalent-linear methods which approximate nonlinearity through a strain-compatible degraded stiffness. This is particularly true when soil strains vary over the duration of a dynamic problem and over the length of a pile. Several variations of the Winkler method are possible ranging from static analysis with linear-elastic springs (BWF), to static analysis with nonlinear springs (BNWF), to the dynamic

analyses performed for this project. These methods will be collectively referred to as Winkler-type to distinguish them from continuum models.

Early nonlinear p - y curves (e.g., McClelland and Focht 1958) were developed by matching the results of full-scale load tests to simple functional forms that were based on the theoretical state of stress around a laterally-loaded pile. The offshore oil drilling industry funded seminal work by Matlock (1970) for soft clays, Reese and Welch (1975) for stiff clay above groundwater, Reese et al. (1975) for submerged stiff clays, and Reese et al. (1974) for sand. Reese et al. (2006) provides an overview of the theoretical and experimental development of these p - y curves. Much of this original work has been improved upon and adapted for specific conditions, for example Reese et al. (1974) was updated by O'Neill and Murchison (1983) and is often known as the “API sand” curve (API 1993). Boulanger et al. (2003) recommended further modifying the API (1993) curve to reflect the fact that the modulus of sand tends to increase approximately in proportion to the square root of confining pressure rather than increasingly linearly with depth.

The first-widely available computer-based implementation of the p - y method was a finite-difference solution called *COM624* (Reese and Sullivan 1980). This code later became the basis for the commercial program *LPILE* (Reese et al. 2005) and other similar software that is widely used in practice. For many projects, the extent of “seismic” foundation design is that the project structural engineer provides the foundation engineer with top-of-pile force effects (shear, axial, and moment), and the foundation designer sizes the pile in terms of diameter and length to adequately resist these loads. Even in cases when the design loads are pseudo-static representations of seismic inertial forces, *LPILE* or an equivalent program is often used to design for seismic lateral loads as if though they were static, without consideration of the fact that the default p - y curves available in the software are not intended for dynamic problems. While top-of-pile spring

stiffness matrices (impedance functions) are sometimes provided back to the structural designer for further analyses, kinematic pile-soil interaction is rarely considered.

While the p - y curves described above have seen widespread use in practice, they were initially developed for static or slow-monotonic loading conditions. In some instances, effects of cyclic degradation over time were taken into account, but these were meant to represent repeated cyclic loading from wave action for offshore applications—not rapid, high intensity cyclic loading from earthquakes. Existing p - y curve definitions have several shortcomings, including (after Khalili-Tehrani et al. 2014):

- Inaccurate small-strain stiffness,
- A functional dependence on diameter that is not thoroughly validated, since the curves are based on a limited number of tests, and
- A lack of functional dependence on the pile head boundary condition.

For dynamic analyses, the initial stiffness problem is of greatest concern. There are two issues to consider. First, some of the functional forms (e.g., Matlock 1970 and Reese and Welch 1975) have an initial tangent stiffness of infinity. While this may be trivial for conventional problems in which loads applied at the pile head induce significant head displacement and thus reach the nonlinear range of the p - y curve, infinite stiffness is problematic for dynamic problems where small relative displacements may occur between the pile and soil, especially at depth. Small trial displacements during numerical solution routines will result in erroneously large forces, causing convergence problems. Furthermore, infinite initial stiffness is problematic when performing modal analyses to compute natural frequencies of the pile-soil or structure-pile-soil system.

Second, because of the rudimentary equipment used in the early tests, accurate measurements of pile strains could not be achieved in the range of truly elastic soil behavior (Choi et al. 2015). This error is further propagated when the strains are numerically double integrated to compute displacement and double differentiated to compute soil reaction, which are necessary steps to generate p - y curves from load test results. Hence, even if the functional form of the p - y curve allows specification of the initial stiffness, the available load test results are not adequate for accurately defining it. A more attractive approach would relate the initial stiffness of the soil-pile interaction to the elastic soil stiffness measured *in-situ* using geophysical methods (e.g., maximum shear modulus G_{max}), which is described further in §9.4.1.

Lam (2009) questions the applicability of initial stiffness corresponding to G_{max} for practical applications of p - y curves, noting that several lateral load tests of full- and model-scale piles have shown that the measured initial p - y stiffness is significantly softer than the elastic stiffness computed from the results of small-strain geophysical site investigation methods, by a factor of as much as ten. In reality, however, the instrumentation used during the load test is not capable of measuring the true initial stiffness. Hence, the experimental measurements to which Lam (2009) refers are actually in the nonlinear, albeit small-strain, range.

Numerical implementation of p - y curves to accommodate cyclic loading via unload/reload rules is described by Wang et al. (1998) and Boulanger et al. (1999). With some exceptions that will be discussed further in §9.3, the p - y macro-element described by Boulanger et al. is implemented in *OpenSees* as the material *PySimple1*. The backbone curve defined by the *PySimple1* material is formulated to match the shapes of the Matlock (1970) and API (1993) curves for clay and sand, respectively. The infinite initial stiffness problem of Matlock (1970) is overcome

in *PySimple1* by using a finite elastic stiffness computed using the method of Vesic (1961) up to a value of 35% of the ultimate resistance of the spring (p_{ult}).

7.3.2 Analytical and Numerical Solutions for Pile Dynamics

Computational studies of pile dynamics can generally be divided into two groups: (i) loading is applied at the pile head by machine vibrations or seismically-induced inertial forces in the structure, thereby inducing inertial SSI, and (ii) loading is applied by excitation of the free-field, typically from seismic sources, inducing kinematic SSI. Studies falling into the latter category may or may not include inertial effects in addition to kinematic effects depending on whether or not a superstructure mass is included. Studies can be further classified based on (i) the computational method used to arrive at the solution—analytical versus numerical; (ii) whether the domain is represented as a continuum or is discretized into thin layers using, for example, Winkler's assumption; and (iii) whether linear or nonlinear material properties are used. While even further subcategories could be defined (two- versus three-dimensional domains, homogeneous versus layered soil, mixed linear/nonlinear materials, etc.), the preceding classification broadly outlines the existing body of work on pile dynamics and will guide the following literature review.

Two of the earliest studies of pile dynamics, Penzien et al. (1964) and Tajimi (1969), considered a complete soil-pile-superstructure system excited by seismic waves. Penzien et al. performed one-dimensional ground response analysis of a clay layer using a lumped mass model and applied these free-field excitations to the pile foundations via viscoelastic Winkler springs, which in turn excited the superstructure. Soil nonlinearity was approximated using bilinear rather than linear springs, and connection details within the bridge superstructure were modeled explicitly. The entire system was solved simultaneously using a numerical time-stepping approach, a considerable achievement given computational power in the 1960's. Penzien (1970) describes

application of this method for design of the Elkhorn Slough Bridge in California, with a detailed account of how the soil properties were selected based on results of a rigorous field investigation and laboratory testing program. Tajimi (1969) derived an elasticity-based analytical solution for a rigid structure supported by a flexible pile in a three-dimensional elastic continuum. While an exact solution is not reached, approximate solutions are given for the amplification of the structure displacement relative to the free-field ground displacement and for the pile head impedance.

In much of the pile dynamics work that followed, and especially over the following decade, emphasis was placed on inertial SSI with less attention given to kinematic effects. In inertial SSI studies, loading is applied at the pile head, and the goal is to generate impedance functions to represent foundation stiffness and damping for use in the substructure method. This includes studies utilizing Winkler models by Novak (1974), Matlock et al. (1978), Kagawa and Kraft (1981), Dobry et al. (1982), Gazetas and Dobry (1984a), Nogami and Konagi (1988), Nogami et al. (1992), and Chau and Yang (2005) as well as continuum model approaches by Novak et al. (1978), Kuhlemeyer (1979), Kaynia and Kausel (1982; 1991), Sen et al. (1985), Wolf (1985), Pak and Jennings (1987), Tronchanis et al. (1991), and Mamoon and Banerjee (1992). While the inertial SSI results are not directly applicable to this study, the analytical framework developed by these researchers was often used subsequently to investigate kinematic effects. Additionally, studies that focused on inertial SSI provide the only available references for quantifying certain parameters, such as the dashpot coefficient used to model radiation damping for Winkler-type analyses.

Blaney et al. (1976) generated perhaps the first kinematic transfer functions for free-head piles from results of a finite-element continuum model considering a limited parametric range of pile and soil profile properties. At roughly the same time, R. Flores-Berrones was completing a

Ph.D. (1974) focused on the pile kinematic problem but utilizing a Winkler model. In their seminal 1982 paper, Flores-Berrones and Whitman provide a chart-based solution for predicting the amplification or deamplification of the pile head relative to the free-field soil displacement as a function of excitation frequency and the soil profile fundamental frequency. The kinematic response is isolated by using a massless superstructure; the work also considers combination of inertial and kinematic effects. Other studies including kinematic response include Gazetas (1984), Gazetas and Dobry (1984a), Banerjee et al. (1987), Fan et al. (1991), Makris and Gazetas (1992), Makris et al. (1996), Giannakou et al. (2010) for battered piles, Di Laora et al. (2012), Di Laora and Sanctis (2013), Anoyatis et al. (2013), and Di Laora and Rovithis (2014). The most recent references provide analytical solutions for increasingly complex soil profiles (e.g., stiffness increasing as a nonlinear function of depth) and new insight into normalization of the results.

While most of these studies model seismic excitation by vertically-propagating shear waves, similar solutions for inclined waves have been presented by Barghouthi (1984), Mamoon and Banerjee (1990), and Kaynia and Novak (1992). Kaynia and Novak (1992) and Makris (1994) also provided solutions for Rayleigh waves, and solutions are available for axial kinematic response due to vertical P-wave excitation (e.g., Mylonakis and Gazetas 2002).

Kaynia and Kausel (1982) formulated a boundary-integral solution to the Green's functions for a loaded circular disc in an elastic halfspace, meant to represent a pile. Their rigorous approach produced impedance functions and kinematic transfer functions for single piles and pile groups, and became the standard by which many other studies were judged throughout the 1980's and 1990's. Fan et al. (1991) implemented a computer-based solution of the Kaynia and Kausel (1982) formulation, which allowed computation of transfer functions for single piles and pile groups for a variety of pile/soil stiffness ratios, pile length/diameter ratios, and pile head-fixity conditions.

Up until this point most studies had failed to present generalized recommendations that could easily be applied in a forward design sense. Fan et al. (1991) thus became the standard against which future pile KSSI studies were judged. Transfer functions from the Fan et al. (1991) study are shown in Figure 7-7.

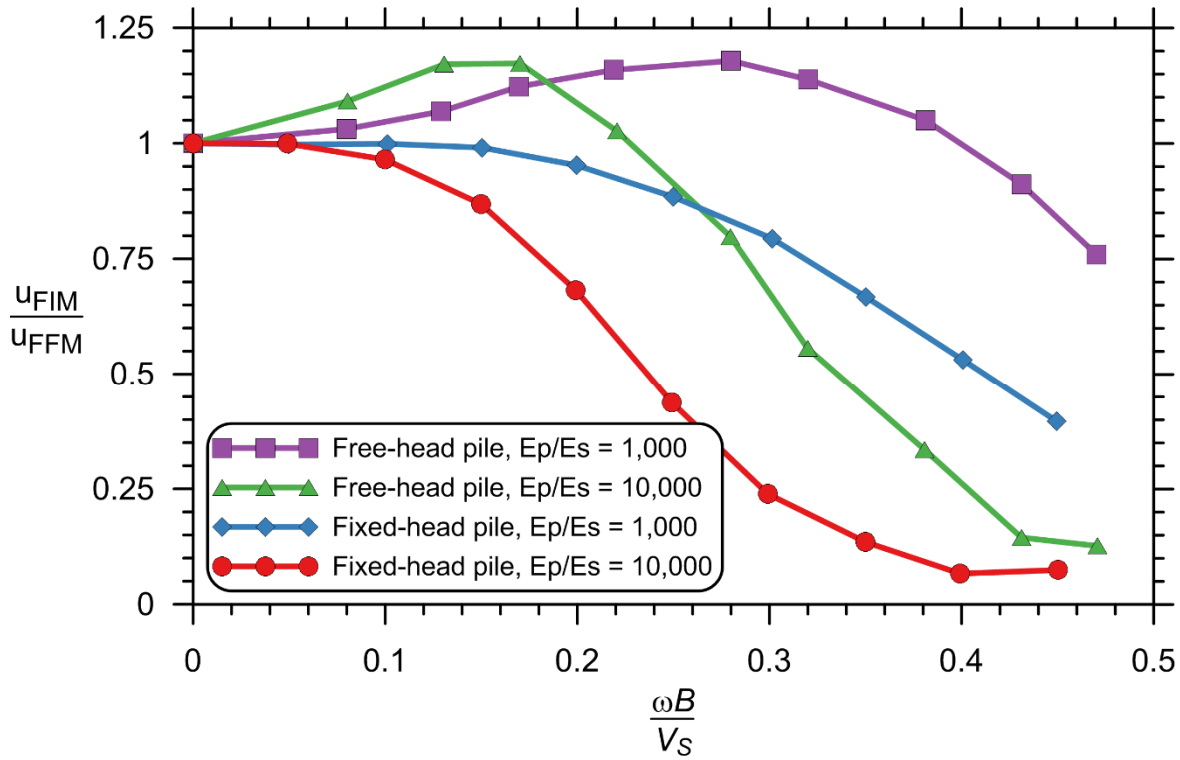


Figure 7-7: Kinematic pile-soil transfer functions from Fan et al. (1991) study for single pile with length-to-diameter ratio of 20.

The results of these studies showed that pile kinematic SSI effects depend primarily on (i) the stiffness contrast between the pile and soil, often expressed as a ratio of pile to soil modulus (E_p/E_s), (ii) the variation of soil stiffness over the length of the pile, e.g. homogeneous soil versus layered or increasing stiffness with depth, (iii) the pile head-fixity condition, and (iv) the pile length to diameter or “slenderness” ratio (L/d). With regards to L/d , recent work by Anoyatis et al. (2013) as well as the results of this study show that for piles longer than the active length (i.e., flexible piles), which deep foundations typically are, kinematic effects are not strongly dependent

on the slenderness ratio as a standalone parameter. Fan et al. also considered pile groups, and concluded that the group response was similar to that for a single pile for typical pile spacing when coherent ground motions are considered.

For the studies that do center on kinematic effects, the focus is often placed on the flexural and/or shear demands imposed on the pile by the deforming soil (e.g., Banerjee et al. 1987; Kavvadas and Gazetas 1993; Kaynia and Mahzooni 1996; Mylonakis 2001; Nikolaou et al. 2001; Saitoh 2005; Maiorano et al. 2009; Di Laora et al. 2012, Sica et al. 2013) rather than on modification of the FIM relative to the FFM. This is likely in part due to the prevailing opinion that piles in general do not have sufficient stiffness to significantly reduce the FIM over the frequency range of engineering interest. However, this may not be true considering that (1) large diameter drilled shafts and cast-in-steel-shell piles on the order of 2-m to 3-m diameter or more are now commonplace for supporting large bridges, (2) soil nonlinearity effectively increases the stiffness contrast between pile and soil, and explicit consideration of nonlinearity has been missing from most previous studies, and (3) the ability to reduce high frequency motions may be of significant interest for certain structures, higher modes of conventional structures, and vibration-sensitive nonstructural components, even if there is no significant reduction near the first-mode period of the structure.

Beginning in the early 1990's and continuing to the present, the advent of personal computers and commercial and open-source finite-element/difference software has produced a number of studies that expand upon previous work by incorporating more realistic assumptions such as soil and pile nonlinearity, three-dimensional domains, and dynamic analysis with realistic earthquake motions. This includes Nogami et al. (1992), Badoni and Makris (1996), Wu and Finn (1997a; 1997b), Boulanger et al. (1999), Bentley and El Naggar (2000), Klar and Frydman (2002),

Maheshwari et al. (2004), Chau and Yang (2005), Kampitsis et al. (2013), Hussein et al. (2014), Pecker (2014), and others. In most cases these studies attempted to recreate the results of model-scale dynamic tests, and/or to compare to previous simplified approaches. While the findings provide valuable insight, especially on the importance of considering nonlinearity explicitly, in most cases results were not generalized for use with simplified design methods in forward analysis. One of the primary goals of this study is to fill that gap.

7.3.3 Normalization Schemes

In order for the results of numerical pile kinematic SSI studies to be made useful for practical design applications, and indeed for SSI in general, it is desirable to find normalization schemes that capture kinematic pile response using variables that capture the physics of the problem, and are themselves tractable to predict. For solutions based on linear-elasticity, closed form solutions may be tractable because the solution does not depend on shaking intensity or other ground motion parameters, and involves a small number of input parameters. The task is more complicated for nonlinear problems and inhomogeneous soil domains, because the solution becomes sensitive to shaking intensity and involves significantly more input parameters.

For pile dynamics problems, transfer functions are often presented versus dimensionless frequency a_0^p , typically defined as (e.g., Kaynia and Kausel 1982, Fan et al. 1991):

$$a_0^p = \frac{\omega B}{V_s} \quad (7.5)$$

where $\omega = 2\pi f$ is the angular frequency of excitation, B is pile diameter (or radius for some studies, e.g., Novak et al. 1978, Gazetas and Dobry 1984a) and V_s is the soil shear wave velocity. This dimensionless frequency was borrowed from the equivalent term for shallow foundations,

where the B term represents the shallow foundation radius (e.g., Gazetas 1983). While this form of a_0 is essentially the only available choice for shallow foundations, pile behavior can be better characterized by terms other than diameter, which is a poor standalone representation of stiffness and characteristic patterns of deformation.

To incorporate the effect of pile-to-soil stiffness ratio, results of early studies are often presented as families of transfer function curves for various ratios of pile-to-soil modulus E_p/E_s . For example, the Fan et al. (1991) results in Figure 7-7 indicate that the same result is achieved for any size pile and soil stiffness as long as the slenderness ratio L/B and E_p/E_s are held constant. While the ratio of pile-to-soil stiffness is a very significant parameter in terms of its influence on the kinematic pile-soil interaction, the simple quantity E_p/E_s is a poor representation of this mechanism for practical applications because it does not contain any information on the geometric properties of the pile cross section. An “effective” pile modulus can be computed that equates a hollow section such as a steel pipe to an equivalent solid section, but this calculation is cumbersome and unfamiliar in routine foundation engineering. A more informative and familiar quantity to describe the pile stiffness is its flexural rigidity, which is the product of the pile material elastic modulus E_p and its moment of inertia I_p . By using flexural rigidity, explicit consideration can be made of (1) any pile geometry (e.g., rectangular, circular, hollow, octagonal, etc.), (2) composite sections such as cast-in-steel-shell concrete piles, and (3) material nonlinearity such as cracking of concrete in tension or yielding of reinforcing steel. Likewise, the use of B in Equation (7.5) serves only as a proxy for pile stiffness because it does not contain information about the material modulus. Accordingly, a more desirable dimensionless frequency parameter would be one that contains the pile flexural rigidity directly along with a measure of the soil stiffness. A useful parameter that combines these quantities is (Hetenyi 1946):

$$\lambda = \sqrt[4]{\frac{k}{4E_p I_p}} \quad (7.6)$$

Hetenyi referred to λ as the “characteristic” term, because it appears in the roots of the characteristic equation of the homogeneous form of the governing differential equation for a laterally-loaded pile (presented in §8.1). Hetenyi also noted that since λ has the units $[\text{length}^{-1}]$, the quantity $1/\lambda$ has units of length and hence he dubbed it “characteristic length”. More recent researchers sometimes refer to λ as the “Winkler parameter”, not to be confused with the Winkler coefficient δ as defined for this study in §8.3.

Randolph (1981) used the term “critical length” (and, interchangeably, “active length”) to refer to the portion of a laterally-loaded pile which effectively resists a lateral load, approximated as:

$$L_a \approx 4 \left(\sqrt[4]{\frac{E_p I_p}{k}} \right) \quad (7.7)$$

For piles that are longer than the active length, further increases in length will not affect the response to lateral loads at the pile head and thus the piles are classified as “long” or “flexible” in comparison to “short” piles that are shorter than the active length. Close inspection of Equation (7.7) reveals that it is not equal to the inverse of Equation (7.6). The ratio of $1/\lambda$ to Equation (7.7) is $4^{-3/4} \approx 0.35$, and therefore the definitions of “characteristic” and “critical” length used by Hetenyi and Randolph, respectively, are different. To avoid confusion, “active length” will be used in this text to refer to the portion of the pile that effectively resists the lateral load such as defined by Equation (7.7).

Di Laora and Sanctis (2013), expanding on the work of Rovithis et al. (2009) and recognizing the aforementioned shortcomings of the typical definition of a_0^p given by Equation (7.5), proposed a revised dimensionless frequency that incorporated the characteristic length directly. Similarly, Anoyatis et al. (2013) proposed the following dimensionless frequency:

$$a_0^p = \frac{\omega}{\lambda V_s} \quad (7.8)$$

where λ is consistent with the definition given by Equation (7.6). This term improves upon the previous form given by Equation (7.5) because it contains (i) the ratio of pile stiffness expressed as flexural rigidity to soil stiffness contained in the λ term, and (ii) the ratio of pile characteristic $(1/\lambda)$ length to the wavelength of soil free-field excitation ($\lambda_{ff} = V_s/\omega$). The latter quantity captures a fundamental aspect of the problem at hand, which is that a stiff pile will not conform to the deformed shape of the free-field under high-frequency excitation as shown in Figure 7-2. Because the new normalization scheme better captures the underlying physics of the problem, the static results (radiation damping and pile inertia not considered) for a flexible pile ($L > L_a$) with any combination of soil and pile stiffness conveniently collapse into a narrow band as shown in Figure 7-8, which can be represented by a simple best-fit equation. Similarly, transfer functions for free-head pile rotation collapse into a narrow band when the transfer function ordinate is defined as $H_\theta = \theta_{FIM} / \lambda \cdot u_{FFM}$, where $1/\lambda$ is used to normalize the result in lieu of B . This finding is perhaps the most significant advancement in elastic analytical solutions for pile kinematic SSI in recent years.

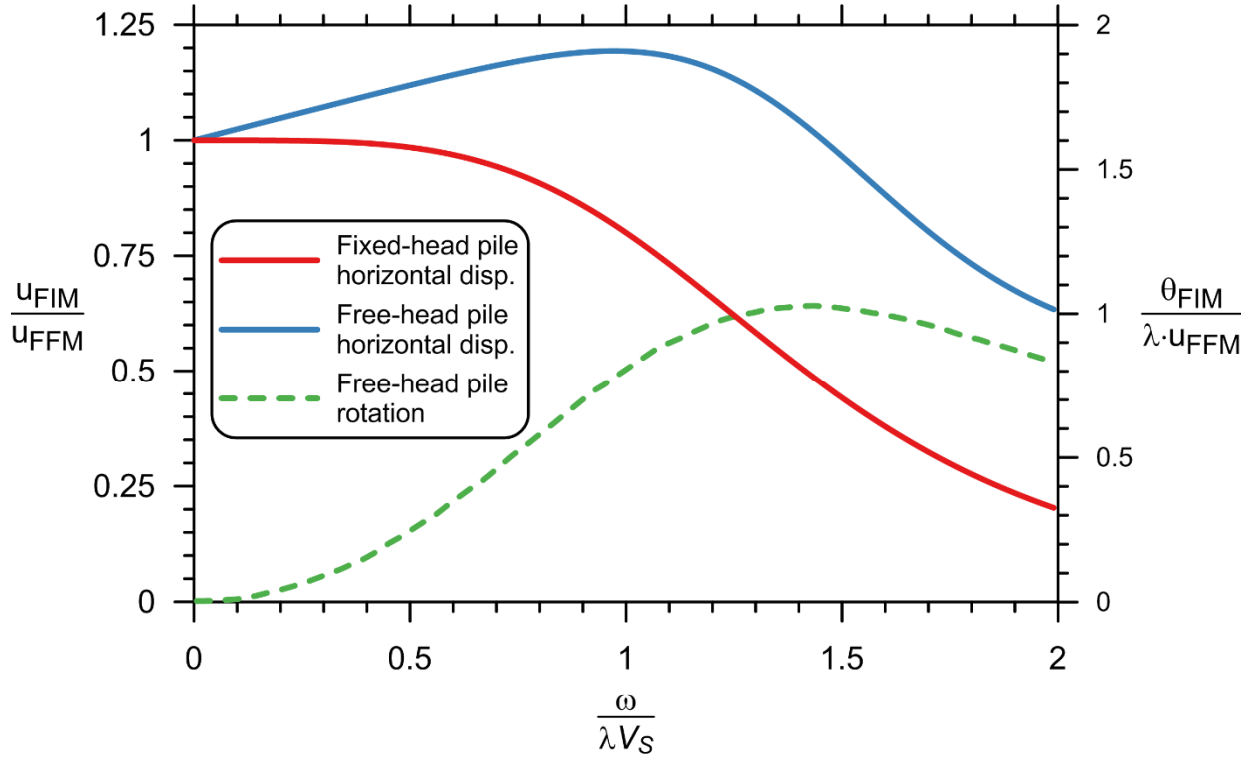


Figure 7-8: Static kinematic pile-soil interaction transfer functions using improved dimensionless frequency definition from Anoyatis et al. (2013). Applies for a free-tip pile with $\lambda L \geq 5$ and homogeneous soil of any stiffness.

The Anoyatis et al. (2013) study considered a uniform, homogeneous viscoelastic soil profile such that the λ and V_s terms in Equation (7.8) are constant over the length of the pile. To extend these results to more realistic soil profiles in which the soil stiffness varies as a function of depth, Di Laora and Rovithis (2014) proposed a dimensionless frequency with the same form as Equation (7.8) except with λ and V_s computed as average values over a depth interval equal to the uppermost active pile length. They described increases in soil stiffness versus depth using a generalized power law function such that analytical solutions could still be derived in closed-form for the pile kinematic response. This approach provides a convenient framework to account for the fact that the soil profiles considered for this study, and real soil profiles in general, do not have uniform shear wave velocity or modulus. To compute λ for use in Equation (7.8) for this study, the following will be used:

$$\lambda_{L_a} = \sqrt[4]{\frac{K_{e,L_a}}{4E_p I_p}} \quad (7.9)$$

where K_{e,L_a} is the average value of p - y curve initial elastic stiffness (K_e) computed over the upper active length of the pile. Likewise, V_s for use in Equation (7.8) will be computed as the time-averaged shear wave velocity computed over the upper pile active length, V_{s,L_a} . From this point forward, any plots or discussion of normalizing by dimensionless frequency use the definition of Equation (7.8) unless noted otherwise.

The pile active length L_a is usually on the order of $10B$ to $15B$ (Randolph 1981; Gazetas and Dobry 1984a), depending on the pile-to-soil stiffness ratio. In general, increasing soil stiffness results in a decreasing L_a if the pile properties are held constant. While this is a useful first-order approximation, a more precise value will be computed for this study as the length for which $\lambda \cdot L = 4$ (Timoshenko 1948; Reese et al. 2006), where λ is computed using the average values [as in Equation (7.9)] over the trial pile length L . Because the soil properties vary with depth, a simple iterative calculation is required to determine L_a in this manner.

Because the concept of active length refers specifically to the upper portion of a pile which responds to a lateral load imposed at the pile head, it is not directly applicable to the pile kinematic SSI case in which kinematic demands are imposed over the full length of pile. Nonetheless, the results of this study have shown that the pile-soil interaction near the surface has the greatest influence on the foundation input motion, and therefore considering some portion of the pile length near the surface is useful descriptor of the system response.

7.3.4 Limitations of Elastic and Analytical Solutions

The previous studies described above generally considered highly idealized soil-pile domains, such as uniform or simple layered combinations of uniform elastic soil layers, rigid bedrock, rigid and/or infinitely long piles, and simple harmonic excitation in lieu of realistic earthquake ground motions. Linear-elastic solutions are useful for elucidating the driving mechanisms behind complex SSI problems, and have some advantages over nonlinear approaches. The primary attraction is that they require low computational effort, and in many cases chart-based or closed-form solutions are available. This makes them amenable to preliminary analysis when full details of a project or soil conditions are not yet known, and the solutions can quickly be updated as more information becomes available. Also, the principle of superposition is exactly valid for use with the substructure method when linear-elasticity is used to model all system components, and because the elastic solutions are exact, they should be reproducible for verification. However, to quote the late professor A.S. Vesic (1977), “...analyses of this kind assume that the surrounding soil acts as an elastic-isotropic solid defined by a constant modulus of deformation and a Poisson’s ratio. This assumption represents a serious departure from reality...” Put simply, this is because lateral pile-soil interaction is nonlinear, and real subsurface conditions are inhomogeneous.

Highly idealized assumptions can have unintended and unrealistic consequences on the dynamic behavior of the system. For example:

- Pile radiation damping cannot occur for a pile embedded in an elastic soil layer underlain by rigid bedrock at frequencies below the fundamental frequency of the soil profile [e.g., see Gazetas (1991), Syngros (2004), Anoyatis et al. (2013)], which is unrealistic for real systems.

- Theoretical transfer functions for fixed-head piles suggest that the pile head motion is always less than the free-field motion for any pile and soil properties and at all frequencies. Not only is this shown to be false when realistic stratigraphy is considered, but it is erroneous in the unsafe direction, potentially resulting in an underestimate of actual demands imposed on the structure.

A primary issue with elastic SSI solutions is that a single value of strain-compatible soil stiffness must be specified to approximate nonlinearity. Simplified methods are available for estimating the average shear modulus reduction induced in the free-field by a ground motion of a given amplitude [e.g., Table 2-1 in NIST (2012)]. However, no similar method is available for estimating a reduced modulus to represent pile-soil interaction which considers the non-uniform relative pile-soil displacement occurring over the length of the pile. An accurate equivalent-linear modulus must combine the effects of modulus degradation due to pile-soil interaction and shearing by the ground motion during free-field site response².

Furthermore, even in the simplest case of an approximately uniform soil layer such as stiff overconsolidated clay, because the amount of relative pile-soil displacement will vary over the depth of the layer [e.g., see Figure 7-2(b)], the equivalent-linear soil stiffness needed to accurately capture the response changes with depth. This has been recognized since the early work on pile dynamics began, for example by Kagawa and Kraft (1980). Although the stiffness specified in an equivalent-linear analysis could be varied with depth, this further complicates the selection of appropriate equivalent-linear properties.

² Stewart et al. (2000) referred to these as “secondary” and “primary” nonlinearities, respectively. These terms could be misleading for pile-soil interaction because the nonlinearity induced by pile-soil interaction can exceed that due to site response for large earthquakes.

Relative to the total number of publications concerning pile dynamics for elastic material properties, the amount of guidance on selection of equivalent-linear properties for actual implementation is comparatively sparse. While back-analyses of single case studies or model studies may be able to determine a single value of reduced modulus which can be used in equivalent-linear analysis to match the desired response, doing so in a generalized manner for forward design cases presents significant challenges and uncertainty.

A shortcoming of continuum solutions, whether solved analytically or numerically, is that the interaction between the pile and soil is often distilled to a simple condition of displacement compatibility (e.g., Tajimi 1969, Novak et al. 1978, Kaynia and Kausel 1982). Even if the independent behavior of soil and pile materials could be captured by constitutive models, a pile-soil system cannot be accurately modeled without capturing interaction at the interface. While the assumption of displacement compatibility (i.e., no slip) may be appropriate for relatively small amplitude loading, such as produced by vibrating machinery, design-level earthquakes will induce significant nonlinearity at the pile-soil interface.

While the simplifications adopted for theoretical, elasticity-based solutions may have been state-of-the-art and the “best available” tools for practicing engineers in the decades before modern personal computing power became widely available, this is simply no longer the case. Tools such as dynamic p - y analysis using nonlinear finite elements that enable significantly more accurate modeling of realistic pile, soil, and ground motion characteristics are now at the disposal of our profession. Nonetheless, use of these tools is beyond the scope of most projects and the expertise of most practitioners. The present work is meant to address these disparities by providing simplified tools that capture realistic complexities of soil and pile dynamics in a more rigorous manner than previous efforts.

7.3.5 Experimental Investigations

Experimental studies of pile dynamics are limited relative to the number of computational studies described in the previous section. Of the experiments that have been conducted, most use dynamic loading applied at the pile head to generate inertial SSI as opposed to loading the pile via free-field excitation. From a practical standpoint, it is much easier to apply load directly to a test structure via actuators or shakers than to load the structure indirectly by loading the adjacent ground. To measure a purely kinematic response, (i) no superstructure mass can be supported by the pile, and (ii) it must be excited by the free-field. Hence, experimental results for purely kinematic pile SSI are very limited.

1-g model-scale tests of piles undergoing dynamic loading at the pile head by Gaul (1958), Novak and Grigg (1976), Novak and El Sharnouby (1984), Blaney and O'Neill (1986), Han and Novak (1988), and El-Marsafawi et al. (1992) along with centrifuge tests by Prevost et al. (1981) were useful for validating early analytical procedures. More recent full-scale tests by Vaziri and Han (1992), centrifuge tests by Ashlock and Pak (2009), and model-scale tests by Burr et al. (1997), Tokimatsu et al. (2005), and Manna and Baidya (2010) have been compared favorably to nonlinear analyses. Durante et al. (2015) describe a series of 1-g tests that provide an opportunity to validate combined kinematic and inertial analysis techniques.

Only a handful of full-scale dynamic tests are reported, and only for inertia loading. Vaziri and Han (1992) conducted ground-level forced vibration tests on a group of six 7.5-m long, 0.32-m diameter drilled shafts connected by a concrete pile cap. McManus and Alabaster (2004) performed cyclic loading on a group of four 5.5-m long, 0.75-m diameter piles. Appendix E documents an attempt made as part of this study to measure transfer functions for full-scale piles by exciting the free-field, and establishes a repeatable method for this type of testing in the future.

Apart from this effort, the author is not aware of any full-scale experiments of purely kinematic SSI for piles. Further experimental testing to validate the results of this study is an important future research need.

A common finding of the experimental tests listed here, especially for the full-scale tests, is that the stiffness and damping of the piles are highly strain-dependent. This makes it difficult to choose a single value of stiffness or damping that is appropriate for design, supporting the notion that nonlinear analyses are superior to analytical or theoretical methods utilizing a single value of equivalent-linear stiffness or damping.

7.3.6 Empirical Observations of Kinematic Pile-Soil Interaction

Due to the same challenges that make experimental measurements of purely kinematic pile-soil interaction difficult—namely, the necessary absence of a superstructure mass atop the pile—empirical observations of pile kinematic SSI during past earthquakes are also limited. A few well-documented cases of pile-supported buildings instrumented with accelerographs at the foundation-level and in the adjacent free-field undergoing strong earthquakes are available. However, interpretation of these cases is complicated by the fact that the foundation-level response includes not only the influence of pile kinematic SSI, but also inertial SSI due to the superstructure response. The issue of combined kinematic and inertial SSI effects is examined in more detail in Chapter 11.

7.3.6.1 Empirical Transfer Functions

Stewart et al. (1999a, 1999b) considered pairs of instrumented structure and adjacent free-field recordings to compare foundation-level and free-field intensity measures from earthquake recordings at 57 building sites in California and Taiwan, including 23 buildings supported on deep foundations. The intensity measures considered were PGA and pseudo-spectral acceleration (PSA)

at the flexible-base, first-mode building period. The results indicated that kinematic reduction of the foundation-level PGA was appreciable, whereas the reductions of first-mode PSA was relatively modest. However, this study did not present foundation/free-field transfer functions, and hence provides limited insight into kinematic interaction effects.

Kim and Stewart (2003) focused specifically on kinematic interaction and considered recordings from 16 of the pile-supported buildings, all of which utilized grade beams or mat slabs to connect the piles. Figure 7-9 shows a comparison from the Kim and Stewart study between the Fan et al. (1991) kinematic pile model and the observed “transmissibility” function at one of the sites. (A transmissibility function represents the same concept as a transfer function, but is computed from ratios of power spectral density functions rather than spectral amplitude; the motivation for this alternative approach is discussed below.) The Fan et al. model generally underpredicts the reduction seen in the observed transfer function, while a base-slab averaging model representing shallow foundation kinematic SSI by Veletsos et al. (1997), using a site-specific value of a parameter controlling ground motion incoherence (κ_a), provided a closer match. Kim and Stewart concluded that kinematic interaction between the ground and surface foundation elements likely dominated the response of the pile-supported buildings in their study. However, Kim and Stewart recognized that the Fan et al. model and other existing kinematic pile models fail to include the effects of ground motion incoherence (spatial variability), and pose a lingering question as to whether or not consideration of incoherence in a pile kinematic model would provide a closer match to observed behavior.

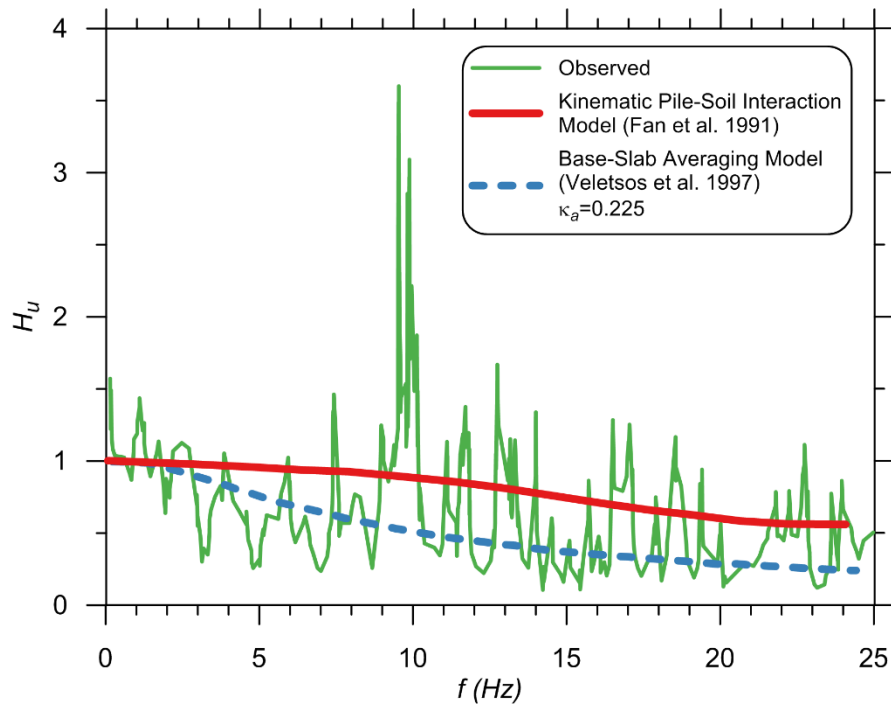


Figure 7-9: Comparison of observed versus model prediction transfer functions for a 5-story hospital building in Lancaster, California during the 1994 Northridge earthquake. After Kim and Stewart (2003).

Mikami et al. (2006, 2008) and Givens et al. (2012) describe recordings from a pile-supported building in Sendai, Japan during the 2003 Off-Miyagi and 2011 Tohoku earthquakes that show a stronger reduction of foundation-level motion to FFM than the California and Taiwan recordings reported above. Three modeling approaches were applied in an attempt to match the observed transfer function: (i) a shallow foundation base-slab averaging model (Veletsos et al., 1997; Kim and Stewart, 2003) similar to that ultimately published in NIST (2012), (ii) a linear-elastic model including piles in the program SASSI [a System for Analysis of Soil-Structure Interaction; Ostadan (2005)] subjected to coherent ground motions, and (iii) a second SASSI model without piles but with incoherent ground motions. The results are shown in Figure 7-10.

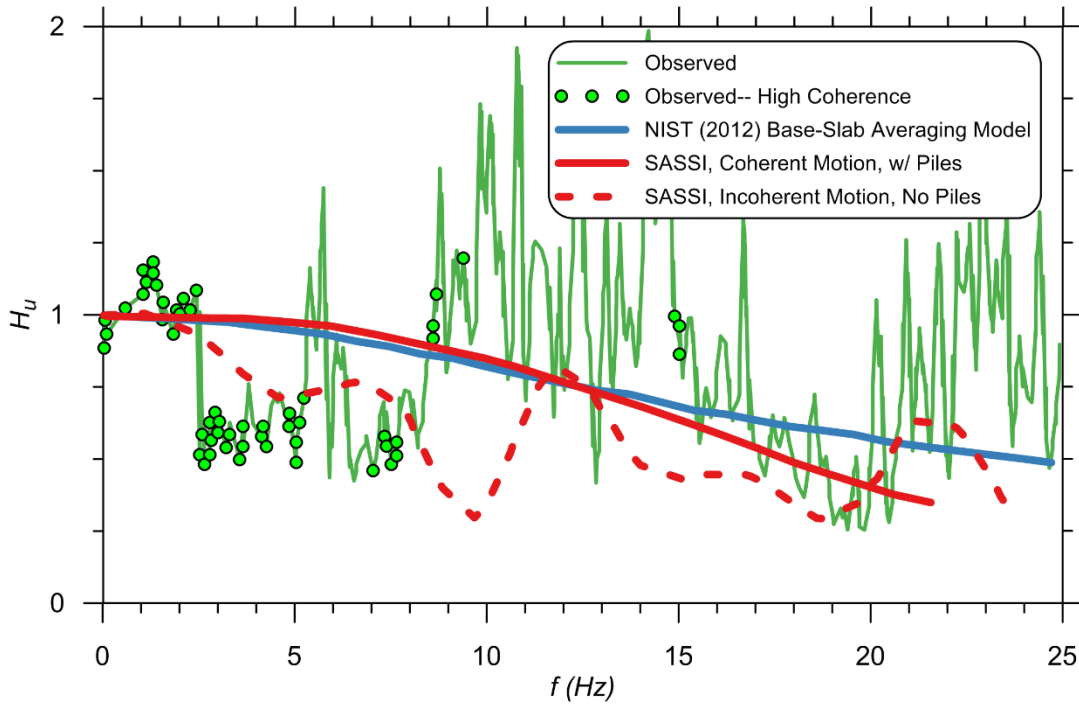


Figure 7-10: Comparison of observed versus model prediction transfer functions for a 4-story building at Tohoku Institute of Technology in Sendai, Japan during the 2011 Tohoku earthquake. After Givens et al. (2012).

The NIST model and SASSI model with coherent ground motions and piles both fail to capture the significant reduction in the observed transfer function between about 2 and 7 Hz. The SASSI model with incoherent ground motions but no piles comes closer to capturing the reduction, but misses the sharp drop-off occurring around 2 Hz. Mikami et al. and Givens et al. speculate that the misfit of these models may be due to inadequate consideration of incoherence in combination with the pile kinematic interaction, or failure to capture the end-bearing resistance of the piles. Recent discussion with Professor Atsushi Mikami (personal communication, 2015) and a re-examination of this case in Chapter 12 make it clear that the influence of inertial SSI is the dominant factor causing the significant reduction in the observed transfer function.

7.3.6.2 Signal Processing Techniques

Empirical transfer functions computed from recorded earthquake motions exhibit sudden changes in amplitude over short frequency ranges as seen in Figure 7-9 and Figure 7-10. Especially at high frequencies where the motion amplitude is typically low, this is due in part to the fact that the ratio of two very small numbers is being computed, such that small oscillations in either the free-field or foundation-level motion can result in spurious peaks in the transfer functions. The level of displacement required to produce such a spike may be close to the recording accuracy of the accelerographs, and therefore representative of “noise” in the signal rather than a meaningful representation of the system response. Noise could also result from energy sources other than seismic waves that affect either the free-field or foundation-level accelerographs, but not both, such as vibrating machinery near one of the recording stations.

Kim and Stewart (2003), and Mikami et al. (2008) describe signal processing techniques to separate the meaningful transfer function ordinates from noise by utilizing an alternative transfer function definition:

$$H_u(\omega) = \sqrt{S_{pp}(\omega) / S_{gg}(\omega)} \quad (7.10)$$

where S_{pp} and S_{gg} are the smoothed auto power spectral density functions of the foundation-level and FFM, respectively³. Auto (S_{pp} and S_{gg}) and cross (S_{gp}) power spectral density functions are defined as:

$$S_{pp}(\omega) = U_{pp}(\omega)U_{pp}^*(\omega) \quad (7.11)$$

³ Kim and Stewart (2003) and Mikami et al. (2006, 2008) use the notation x and y to refer to the free-field and foundation-level, respectively; p and g will be used here to be consistent with the previous notation and to retain the physical interpretation as the pile and ground-surface motions.

$$S_{gg}(\omega) = U_{gg}(\omega)U_{gg}^*(\omega) \quad (7.12)$$

$$S_{gp}(\omega) = U_{gg}(\omega)U_{pp}^*(\omega) \quad (7.13)$$

where $U^*(\omega)$ is the complex conjugate of $U(\omega)$:

$$U^*(\omega) = \text{Re}(U(\omega)) - \text{Im}(U(\omega)) \cdot i \quad (7.14)$$

and i is the imaginary number defined by $i^2 = -1$. In signal processing terms, H_u computed using Equation (7.10) is called a transmissibility function, while Equation (7.2) produces a transfer function. The concept is the same—describing the manner in which a system modifies an input signal to produce an output signal—so the term transfer function will be used from this point forward.

There are two benefits to using Equation (7.10) rather than defining the transfer function directly as the ratio of Fourier amplitude spectra:

- Coherence can be computed, which allows quantitative identification of the transfer function ordinates with the highest signal-to-noise ratio, and
- Smoothing of the power spectral density functions, a necessary step for computing coherence, further reduces the spurious nature of the transfer functions computed from raw signals.

Coherence (γ^2) between the foundation-level and FFM signals is defined as (Pandit 1991):

$$\gamma^2 = \frac{|S_{gp}(\omega)|^2}{S_{gg}(\omega)S_{pp}(\omega)} \quad (7.15)$$

Coherence indicates the strength of the relationship between an input and output signal; values near 1.0 indicate a strong dependence of the output on the input, while smaller values indicate a weak relationship. Hence, coherence can be used as a quantitative measure of whether certain frequency components of the foundation-level motion are likely a result of the system responding to excitation by the FFM, or represent noise. By using a threshold value of coherence below which data are discarded, empirical transfer functions can effectively be filtered to discern the most meaningful data points. Points with coherence greater than 0.8 are shown in Figure 7-10, which is the cutoff used by Mikami et al. and Givens et al.

Prior to computing coherence with Equation (7.15), the power spectral density functions must be smoothed. Coherence computed between unsmoothed input and output signals over the full frequency bandwidth of the signals will be unity at every frequency and thus is not a useful metric. The smoothing operation is accomplished by replacing each ordinate of the unsmoothed power spectrum with a weighted average value of the unsmoothed ordinates over a frequency band (i.e., window) centered on the point of interest. Mikami et al. (2008) examined the influence of the parameters used to define the smoothing window, which ultimately affect the computed value of coherence, and found that an 11-point Hamming window provided qualitatively good results. Mikami et al. also recommend not only emphasizing empirical transfer function points with high coherence, but bandwidths that have high coherence at multiple successive frequencies. This is an important secondary criterion, because even pairs of white noise signals will occasionally have coherence greater than 0.8 despite having a mean value of approximately 0.15 to 0.25 (the exact value depends on the shape and bandwidth of the windowing function used for smoothing).

As the terminology implies, *incoherent* or spatially-variable ground motions resulting from stochastic effects such as wave scattering and subsurface variability will result in differences in

the foundation-level and FFM that are not due to foundation kinematic interaction; this ground motion incoherence will manifest as low coherence in the computed empirical transfer function. Since the incoherence of real ground motions tends to increase with increasing frequency, this mechanism is especially significant at higher frequencies. Mikami et al. (2008) conclude that empirical transfer function ordinates at high frequencies are usually dominated by incoherence, and thus should be deemphasized relative to low frequency ordinates when quantifying kinematic SSI. For the examples described in their paper, the usable frequency range is typically below about 10 Hz.

Although interpretation of empirical transfer functions is not the main focus of this study, the signal processing techniques described above turn out to be very useful, if not necessary, for interpreting the results of the numerical simulations. Ground motions used as input to the pile-soil interaction analyses are sourced from earthquake recordings at a single location, and the foundation is modeled as occupying the same physical location. Therefore, the incoherence of real ground motions between the physical locations of the free-field and foundation-level recording stations that can cause low coherence for high-frequency empirical transfer function ordinates does not apply, at least for single pile models. Nonetheless, variability between the computed FIM and FFM when represented in the frequency domain can mimic the variability between empirical foundation-level and FFM signals because:

- Numerical oscillations in the finite-element solution on the order of the tolerance that satisfies the convergence criterion are significant relative to the Fourier amplitude of the computed FIM, particularly at higher frequencies, and

- Transfer functions are an imperfect representation of seismic response due to the finite-duration and non-stationary nature of the signals used to compute them (discussed further below).

As a result, transfer functions computed from the numerical simulations look similar to the empirical transfer functions described above, in particular exhibiting large variability at higher frequencies. This is true even when the numerical solution approach is used to compute transfer functions for elastic pile and soil conditions subjected to harmonic free-field ground motions, and thus is not solely an artifact of nonlinearity in the system response. To facilitate extraction of meaningful trends from the simulations performed in this study, the same signal processing techniques described by Mikami et al. (2008) are applied, specifically:

- Transfer functions are computed using Equation (7.10),
- Power spectral density functions are smoothed with an 11-point Hamming window,
- A minimum coherence threshold of 0.8 is applied to the computed transfer functions, while in some instances a more stringent value of 0.9 is used to clarify the trend exhibited by the results, particularly for stiffer soil sites for which the transfer function corner frequency is relatively high, and
- Transfer functions are only defined up to the frequency at which a smoothed version of the coherence-versus-frequency curve is above the minimum threshold (0.8 or 0.9).

Although other approaches could be taken for smoothing the results, for example simply smoothing the computed transfer functions directly, the approach used for interpretation of

empirical data is adopted here because of its demonstrated applicability to the mechanisms governing kinematic SSI.

The last criterion in the above list is intended to satisfy the recommendation by Mikami et al. (2008) that not only should high coherence points be emphasized, but a further restriction should be implemented of focusing on bandwidths over which high coherence occurs for a series of successive frequencies. The coherence versus frequency curve is smoothed using a 25-point median smoothing window, which replaces each value with the median of the 25 points centered on that frequency. This allows automated processing of the thousands of results from the parametric study.

In addition to the insights provided in the context of interpreting empirical transfer function data, the concept of using transfer functions as a means of quantifying SSI has additional limitations, and some discussion is warranted here.

Strictly speaking, the concept of a transfer function applies only to an infinitely-repeating stationary process, which is defined as an entirely stochastic (random) process that displays no trends in mean or variance with time. While certain aspects of SSI are approximately stochastic, time signals of earthquake ground motions and the response of structures to these ground motions exhibit strong trends with time, and are of a finite duration. While advanced signal processing techniques are available to transform the time response of some physical systems from non-stationary to approximately stationary (e.g., White and Boahash 1990), they are generally not applicable to ground motions.

In particular, the ordinates of Fourier amplitude spectra can be unintentionally altered by the non-repeating nature of ground motions, and by the simple fact that the Fast-Fourier transform (FFT) algorithm used to perform the Fourier transform generates very small numbers at

frequencies away from the predominant energy of the signal. Consider the following simple examples to illustrate these points.

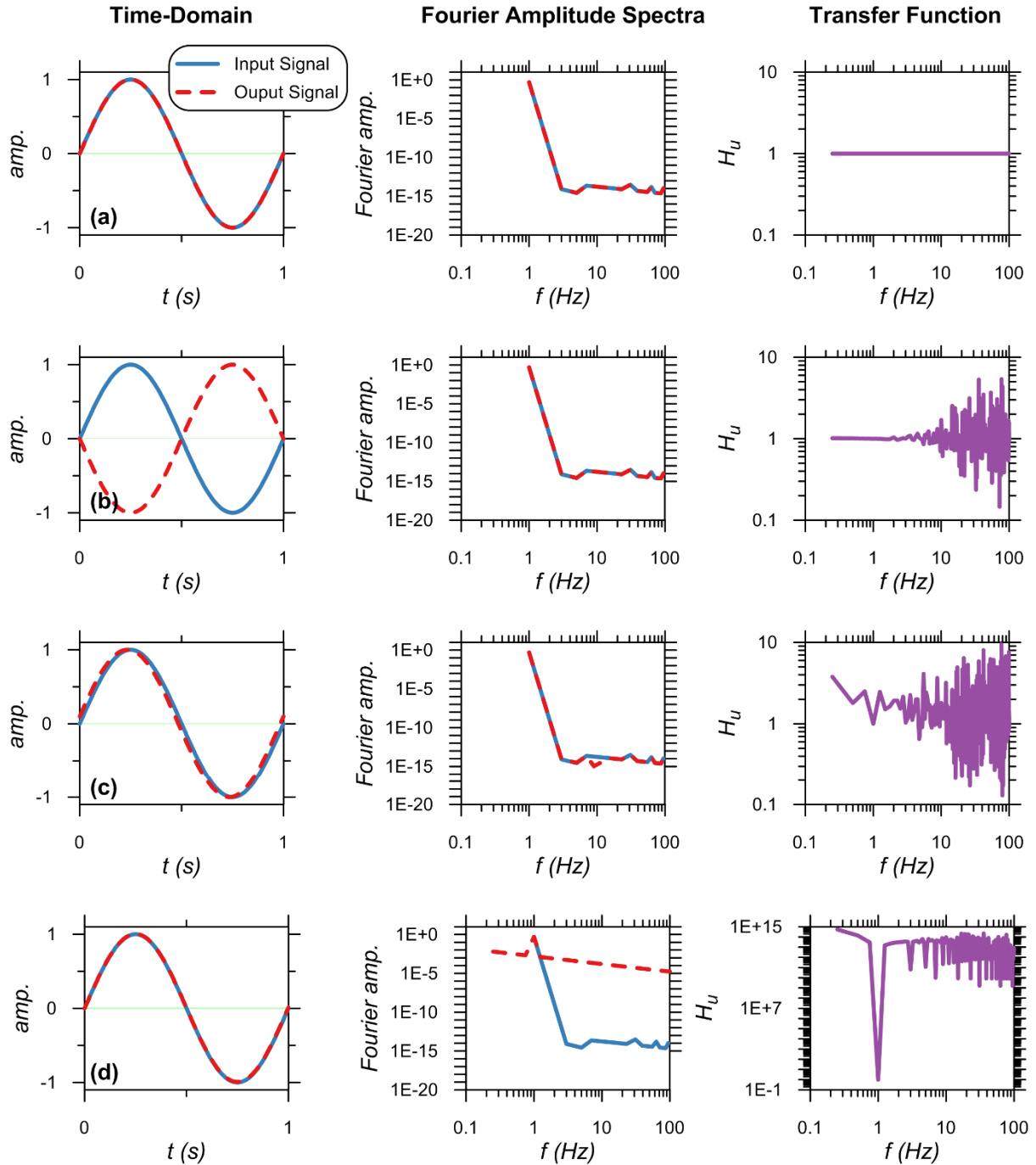


Figure 7-11: Influence of small changes between input and output signals on system transfer functions. Relative to input signal, the output signal (a) is identical, (b) is perfectly out-of-phase, (c) is out of phase by 0.1, and (d) exhibits slight baseline drift.

A signal defined as a sine wave with amplitude of unity and frequency 1 Hz is passed through a system which has the ability to modify the input signal and produce an output signal. Since the FFT algorithm applied to a discrete time signal requires that the signal have 2^n points, where n is an integer, the input signal for this example is chosen to have $2^{11} = 2,048$ points. The time step Δt is taken as 4 times the inverse of n ($4/2,048$ s) so that the vector of frequencies at which the FFT is defined includes $f = 1$ Hz without the need for interpolation. The amplitude is zero at time $t = 0$, and the amplitude of the 2,048th point is $\sin[2\pi f \Delta t (n-1)] \approx -0.012$ such that the 2,049th point would have an amplitude of zero and the signal could repeat indefinitely.

The time- and frequency-domain representations of the input and output signals are presented in Figure 7-11, along with the transfer functions computed between them using Equation (7.2). First consider that the system makes no modification to the input signal, such that the input and output are identical [Figure 7-11(a)]. The FFT captures the amplitude of the signal at 1 Hz exactly. Theoretically, the amplitude at all other frequencies is zero since the signals are perfect 1 Hz sine waves, but the FFT returns a non-zero, albeit very small, amplitude ranging between $1.0\text{E-}13$ and $1.0\text{E-}15$. Nonetheless, the values are exactly the same for the input and output, thus the transfer function ordinate is exactly unity at all frequencies. Figure 7-11(b) shows the results when the output signal is perfectly out of phase by $\pm\pi$ radians. Even though the transfer function amplitude is defined only as the ratio of Fourier amplitude spectra and should not be affected by phase, the small, yet non-zero oscillations in computed Fourier amplitude now vary between the input and output signals, such that the transfer function is erratic away from $f = 1$ Hz. This highlights an important point—the transfer function amplitude does not reflect the amplitude of the input and output signals over different frequencies, only the ratio of their amplitudes. Hence by simply examining a transfer function without viewing the corresponding Fourier amplitude

spectra, it cannot be known which transfer function ordinates correspond to the predominant energy in the system and are therefore most meaningful.

Figure 7-11(c) shows the effect of a small phase offset, which produces similar high frequency noise in the transfer function. Again, the amplitude of the output signal is identical to the input signal for (b) and (c). Figure 7-11(d) shows the effect of a small baseline drift in the output signal (linear change of 0.01 over 1 s), which also has a drastic effect on the transfer function away from $f = 1$ Hz.

These example of changes between input and output signals were chosen because, to some extent, they all appear in signals representing the free-field and a structure during seismic excitation. The intent in pointing out their influence on the computed transfer functions is not to suggest that the transfer function approach should not be used; on the contrary, it is an excellent tool for earthquake engineering. These issues simply need to be kept in mind when trying to discern the meaningful trends from noise.

7.3.6.3 Pile Damage due to Kinematic Demands

Many of the same earthquakes that inspired the seminal work in geotechnical earthquake engineering on topics such as soil liquefaction and ground motion estimation also provided evidence that kinematic demands caused damage to pile foundations. The documented cases include damage to concrete piles supporting bridges during the 1964 Alaska Earthquake (Kachadoorian 1968) and a building during the 1964 Niigata Earthquake (Nishizawa et al. 1984). Mizuno (1987) documented pile performance during several Japanese earthquakes that occurred between 1923 and 1983, including several cases of piles damaged by kinematic demands, although most appear to be cases with large permanent ground displacement. Tazoh et al. (1987) instrumented the Ohba-Ohashi bridge in Japan and recorded the structural response during several

earthquakes, including a **M** 6.0. They found that the peak strains recorded by longitudinal strain gauges in the piles supporting one of the main piers occurred deep in the soil profile at the interface between the bearing stratum and softer overlying soil.

Studies by Nikolaou et al. (2001) and others cite this evidence as motivation for considering kinematic demands in design, which eventually became a building code requirement as discussed in the following section. It is worth noting that the number of documented cases in which ground failure (e.g. liquefaction), permanent ground displacement, and inertial loads could be ruled out as the cause of damage is relatively low. This does not necessarily imply that this damage mechanism is not common, but is likely more attributable to the difficulty and cost associated with post-earthquake inspections of piles at significant depths.

7.4 KINEMATIC SSI IN BUILDING CODES

The influence of kinematic pile-soil interaction on foundation input motions (FIM) receives little or no attention in US building codes. On the other hand, demands resulting from pile-soil interaction must be considered according to most building codes. For example, ASCE 7-10 (ASCE 2013) §12.13.6.7 “Pile Soil Interaction” requires that piles be designed for the moment, shear, and deflections “considering the interaction of the shaft and soil.” Unlike the specifications in Chapter 19 of ASCE 7-10 “Soil-Structure Interaction for Seismic Design”, which are optional and can be ignored at the designer’s discretion, the requirement that piles be designed to resist kinematic demands in addition to superstructure demands is required in all cases. Nonetheless, in the author’s experience it is often neglected in practice.

7.5 NOTES ON TERMINOLOGY AND NOTATION

Because the terms used to describe various types of deep foundations tend to evolve over time, a few clarifications are noteworthy in the context of this study.

During the timeframe of the early work on this subject (1960's-1980's), the term “pile” was most commonly used to refer specifically to driven piles. Drilled shafts were often referred to as “caissons” or “piers”. This distinction is important, because driven piles were categorically assumed to be more flexible than their drilled counterparts. Early work on this subject often applied specifically to relatively flexible driven piles for which kinematic SSI effects are less significant in comparison to larger-diameter, stiffer drilled shafts. For example, in the seminal 1982 paper by Flores-Berrones and Whitman, “Seismic Response of End-Bearing Piles,” the authors conclude that:

... Piles located in seismic zones are subjected to two very important effects; one is the action of the soil along the pile length [kinematic SSI] and the other one is related to the supported mass at the pile's head [inertial SSI]. Regarding the first of these effects, very often neglected in dynamic analysis for piles subjected to seismic forces, there are two extremes... (1) Piles behave as flexible elements and follow the ground displacements; and (2) piles behave as rigid elements, and their tendency is to remain still while the soil moves around them... Most “piles” fall into the first of these categories while piers and caissons might fall in the second one... Generally speaking, piles do not reduce significantly the horizontal movements of a structure...

Consistent with this conclusion, much of the work on the topic of kinematic pile-soil interaction has focused on the shear and moment demands imposed on relatively flexible piles, while less

attention has been paid to the beneficial reduction in FIM that large, stiff piles can provide. Because large-diameter piles in soft soil conditions are now commonplace, especially for the support of bridges, this topic is worth revisiting.

For simplicity, the term “pile” foundation will be used herein to refer to both driven piles and drilled, cast-in-place deep foundations, also known as drilled shafts or piers, bored piles (the predominant term outside the U.S.), cast-in-drilled-hole piles (Caltrans), etc. The distinction between driven and drilled shaft-type piles will be noted when relevant; otherwise the content of this study is intended to apply to both.

Early work (1960’s – 1990’s) on pile KSSI and much of the contemporary work using analytical solutions use the term I_u , short for interaction factor, to represent the transfer function ordinate. This study adopts the term H_u based on the work of Kim and Stewart (2003), who applied signal processing techniques borrowed from the field of electrical engineering, where H is typically used to represent the transfer function between input and output signals.

8 Elastic Analytical and Numerical Solutions

Elastic solutions for kinematic pile-soil interaction are useful for elucidating the fundamental mechanisms that control the physics of the problem, and for formulating the bounds of the nonlinear numerical analyses performed subsequently. In this chapter, a closed-form elastic analytical solution is derived, then compared to previous solutions by other researchers and used to validate the proposed numerical modeling approach.

In addition, for the nonlinear numerical analyses that follow, pile-soil interaction is characterized by elastic behavior at very small strains. Hence, issues related to the small-strain elastic behavior of the nonlinear system are explored in the second half of this chapter.

8.1 ELASTIC ANALYTICAL SOLUTION

Derivation of the closed-form static solution for a vertical elastic pile in elastic soil begins with the following fourth-order differential equation for a laterally-loaded pile (after Hetenyi 1946):

$$\frac{d^4 u_p}{dz^4} E_p I_p + \frac{d^2 u_p}{dz^2} P - k \cdot u_p = 0 \quad (8.1)$$

in which u_p is horizontal pile displacement, z is depth measured downwards from the pile head, $E_p I_p$ is the pile flexural rigidity, P is axial load, and k is the soil-pile interaction stiffness intensity,

all defined in a consistent set of units. Equation (8.1) states that the force applied externally by the soil reaction ($k \cdot u_p$ term) is in equilibrium with the internal forces in the pile described by the 4th derivative of the transverse displacement multiplied by the pile flexural rigidity, plus second-order (“ $P-\Delta$ ”) effects. The pile is treated as an Euler-Bernoulli beam in this formulation. For the purpose of this derivation going forward, axial load is taken as zero such that second-order effects are dropped⁴.

For a kinematic pile-soil interaction dynamic solution, the pile-soil interaction modulus k is replaced with the complex-valued $k^* = k + i\omega c$, where c is the dashpot coefficient for equivalent viscous damping, the displacement term is replaced with the relative displacement between the pile and free-field soil, and an additional term is added to capture the inertial force generated by acceleration of the pile mass per unit length \tilde{m}_p :

$$\frac{d^4 u_p}{dz^4} E_p I_p + k^* [u_p - u_{g0}] + \tilde{m}_p \frac{d^2 u_p}{dt^2} = 0 \quad (8.2)$$

If the free-field ground motion is represented as harmonic excitation by vertically propagating shear waves (after Kramer 1996):

$$u_g(z) = u_{g0} \cdot \cos(\kappa \cdot z) \quad (8.3)$$

where u_{g0} is the ground displacement at the surface due to the harmonic seismic excitation and κ^* is the complex-valued wave number defined as the ratio of excitation angular frequency (ω) to soil complex-valued shear wave velocity ($V_s^* = V_s \sqrt{1 + 2i\beta_s}$, where β_s is the soil hysteretic damping ratio), then Equation (8.3) can be substituted into (8.2) to give:

⁴ Second-order moments are included in the nonlinear numerical analyses performed for this study.

$$\frac{d^4 u_p}{dz^4} E_p I_p + k^* [u_p - u_{g0} \cos(\kappa z)] + \tilde{m}_p \frac{d^2 u_p}{dt^2} = 0 \quad (8.4)$$

Although a solution is available to the dynamic equation (8.4) (e.g., Anoyatis et al. 2013), the static solution without consideration of damping or pile inertia is still a reasonable means of investigating the controlling mechanisms of kinematic pile-soil interaction. The static version of (8.4) is:

$$\frac{d^4 u_p}{dz^4} E_p I_p + k[u_p - u_{g0} \cos(\kappa z)] = 0 \quad (8.5)$$

The solution to (8.5) is the sum of complementary and particular solutions. Finding the complementary solution begins by solving the homogeneous form of (8.5), which does not include the ground displacement term since it is not a function of pile displacement u_p :

$$\frac{d^4 u_p}{dz^4} E_p I_p + k(u_p) = 0 \quad (8.6)$$

The characteristic equation for the homogeneous form is:

$$r^4 + \frac{k}{E_p I_p} = 0 \quad (8.7)$$

The roots of (8.7) are equal to the 4th roots of the $k/E_p I_p$ term:

$$r = \sqrt[4]{\frac{-k}{E_p I_p}} = \sqrt[4]{\frac{k}{E_p I_p}} \exp \left[\left(\frac{\pi}{4} + \frac{\pi \cdot j}{2} \right) i \right]_{j=1,2,3,4} = \sqrt[4]{\frac{k}{4E_p I_p}} \pm i \left(\sqrt[4]{\frac{k}{4E_p I_p}} \right) \quad (8.8)$$

Recalling that a complex root of the characteristic equation results in two terms in the complementary solution, the complementary solution to (8.4) can be written as:

$$u = e^{\beta z} \cos(\beta z) \chi_1 + e^{\beta z} \sin(\beta z) \chi_2 + e^{-\beta z} \cos(-\beta z) \chi_3 + e^{-\beta z} \sin(-\beta z) \chi_4 \quad (8.9)$$

where χ_1 through χ_4 are constants and the characteristic term β is a substitution variable defined as:

$$\beta = \sqrt[4]{\frac{k}{4E_p I_p}} \quad (8.10)$$

This is the origin of the familiar “Winkler’s parameter”, and the inverse of (8.10) is often called the characteristic length.

The particular solution is found using the method of undetermined coefficients as:

$$u = \frac{k \cdot u_{g0}}{E_p I_p \cdot \kappa^4 + k} \cos(\kappa \cdot z) \quad (8.11)$$

and the sum of (8.9) and (8.11) is the complete solution to (8.4) for the pile horizontal displacement at any depth z :

$$u_p(z) = e^{\beta z} \cos(\beta z) \chi_1 + e^{\beta z} \sin(\beta z) \chi_2 + e^{-\beta z} \cos(-\beta z) \chi_3 + e^{-\beta z} \sin(-\beta z) \chi_4 + \frac{k \cdot u_{g0}}{EI \cdot \kappa^4 + k} \cos(\kappa \cdot z) \quad (8.12)$$

A similar derivation can be found in Flores-Berrones and Whitman (1981) for pile-soil kinematic interaction, and in Hetenyi (1946) for conventional lateral loading at the pile head in the absence of free-field excitation.

Successive derivatives of Equation (8.12) provide expressions for slope (S), curvature (ϕ), moment (M), shear (V), and soil reaction (p):

$$S(z) = \frac{du_p}{dz} = \beta \left[e^{\beta z} (A\chi_1 + B\chi_2) - e^{-\beta z} (B\chi_3 + A\chi_4) \right] - \kappa \cdot C \sin(\kappa z) \quad (8.13)$$

$$\begin{aligned}
M(z) &= \frac{d^2 u_p}{dz^2} E_p I_p \\
&= E_p I_p \left(2\beta^2 \left\{ e^{\beta z} \left[-\sin(\beta z) \chi_1 + \cos(\beta z) \chi_2 \right] + e^{-\beta z} \left[\sin(\beta z) \chi_3 + \cos(\beta z) \chi_4 \right] \right\} - \kappa^2 C \cos(\kappa z) \right)
\end{aligned} \tag{8.14}$$

$$\begin{aligned}
V(z) &= \frac{d^3 u_p}{dz^3} E_p I_p = E_p I_p \left(2\beta^3 \left[e^{\beta z} (-B\chi_1 + A\chi_2) + e^{-\beta z} (A\chi_3 - B\chi_4) \right] + \kappa^3 C \sin(\kappa z) \right)
\end{aligned} \tag{8.15}$$

$$\begin{aligned}
p(z) &= \frac{d^4 u_p}{dz^4} E_p I_p \\
&= E_p I_p \left(4\beta^4 \left\{ e^{\beta z} \left[-\cos(\beta z) \chi_1 - \sin(\beta z) \chi_2 \right] + e^{-\beta z} \left[-\cos(\beta z) \chi_3 + \sin(\beta z) \chi_4 \right] \right\} - \kappa^4 C \cos(\kappa z) \right)
\end{aligned} \tag{8.16}$$

The following substitutions were used to abbreviate Equations (8.13) through (8.16):

$$A = \cos(\beta z) - \sin(\beta z) ; \quad B = \cos(\beta z) + \sin(\beta z) ; \quad C = \frac{k \cdot u_{g0}}{E_p I_p \cdot \kappa^4 + k} \tag{8.17}$$

To solve for the constants χ_1 through χ_4 , a set of four permissible boundary conditions must be imposed. Typically the boundary conditions are prescribed at the pile head and tip since these can be determined on the basis of details such as embedment into a pile cap or a stiff bearing stratum. For example, in the absence of superstructure force or moment demands (required for a kinematic pile-soil interaction analysis) the boundary conditions for a fixed-head, free-tip pile of length L are:

$$V_{z=0} = 0 ; \quad S_{z=0} = 0 ; \quad V_{z=L} = 0 ; \quad M_{z=L} = 0 \tag{8.18}$$

An example of the solution in terms of pile-versus-soil displacement, moment, and shear is shown in Figure 8-1 for the following input parameters:

- $E = 27 \text{ GPa}$, $I = 0.0031 \text{ m}^4$ (corresponding to a 0.5-m diameter reinforced concrete pile), length (L) = 10 m,
- $V_s = 100 \text{ m/s}$ (soft soil), $k = 47 \text{ MPa}$,
- $u_{g0} = 0.1 \text{ m}$, $f = 10 \text{ Hz}$,
- Boundary condition at pile head = zero slope and zero shear; i.e., a fixed-head pile with no superstructure demands so that the kinematic pile-soil interaction can be evaluated independently, and
- Boundary condition at pile tip = zero shear and zero moment; i.e., the pile tip is unrestrained

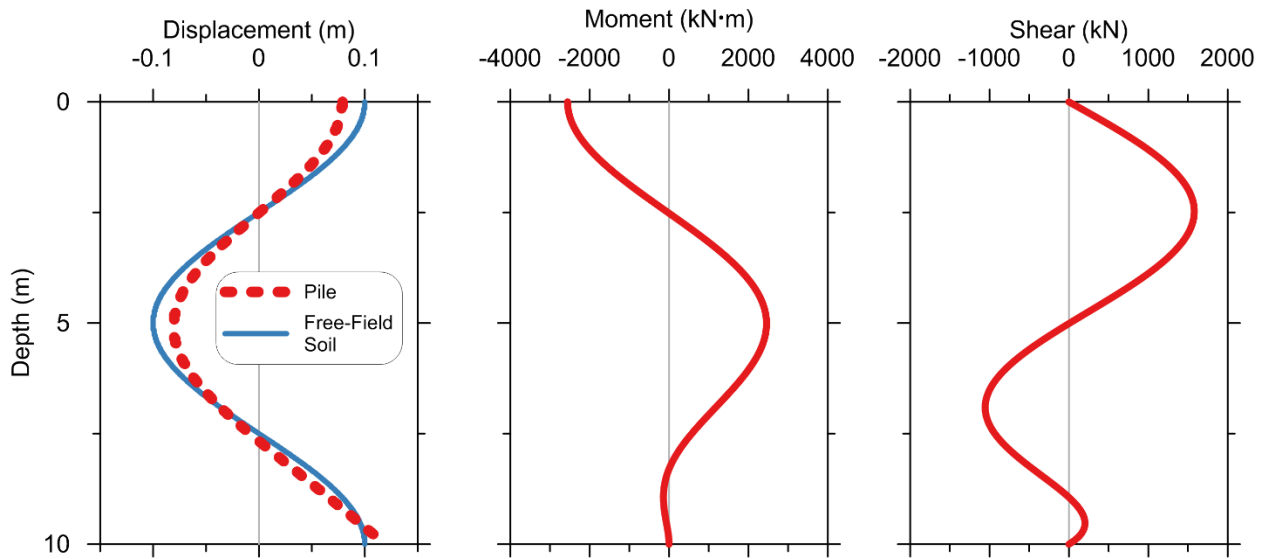


Figure 8-1: Soil and pile response under imposed 10 Hz harmonic ground motion using elastic analytical solutions.

To produce an analytical transfer function, the pile head displacement determined from Equation (8.12) at depth $z = 0$ is normalized by the amplitude of the harmonic ground motion, u_{g0} , and computed over the frequency range of interest (recall that the solution is frequency-dependent

even for the simplified static version because it contains the wavenumber term κ). Parametric studies using elastic solutions can provide valuable insight into the range of pile and soil stiffness for which kinematic pile-soil interaction is significant over the frequency range of engineering interest. Figure 8-2 shows kinematic pile-soil interaction transfer functions computed using the elastic analytical solution for three diameters of a 25-m long pile in two homogeneous soil profiles representative of relatively soft and relatively stiff soil. The boundary conditions for the pile are the same as shown in Figure 8-1—the pile tip is free (zero shear, zero moment), and the pile head is restrained against rotation to model a fixed-head condition with zero applied shear. The ranges of pile and soil properties considered are as follows:

- Pile flexural rigidity ($E_p I_p$) between $82 \text{ MN}\cdot\text{m}^2$ and $21,200 \text{ MN}\cdot\text{m}^2$. These values approximately correspond to a 50-cm diameter reinforced concrete pile, such as might be used in a pile group, and a 2.0-m diameter pile that would likely be used as a mono-shaft to support a single column or in a pile group for a very large suspension or cable-stayed bridge.
- Pile-soil interaction stiffness k of 60 MPa, corresponding to the initial elastic stiffness for a $V_s = 100 \text{ m/s}$ soft soil site, and 1,050 MPa, corresponding to a $V_s = 400 \text{ m/s}$ stiff soil site.

The transfer functions shown in Figure 8-2 represent the bounds of these ranges of soil and pile properties over a frequency range of 0.1 to 100 Hz. The first-mode period for most bridges and building structures typically falls in the range of about 0.1 to 2 seconds, so the value of the transfer function ordinate H_u over this range is of most significance. This corresponds to a frequency range of 0.5 to 10 Hz.

Figure 8-2 shows that the pile/soil combination with the greatest reduction in H_u within the frequency range of interest is the larger diameter 1.0-m and 2.0-m piles embedded in the soft soil profile. In contrast to the stiff pile/soft soil cases, there is little reduction in H_u for the piles embedded in the stiff soil profile over the frequency range of interest, even for the 2.0-m diameter shaft. Significant reduction is predicted only for frequencies greater than about 20 Hz (corresponding to a period less than 0.05 seconds). Such high-frequency energy usually does not have a large influence on the behavior of a structure relative to the energy content at the structure fundamental frequency. Structures supported on stiff soil with significant participation from higher modes may still be affected in some cases. These findings are consistent with the previous elastic studies by Flores-Berrones and Whitman (1982) and Fan et al. (1991).

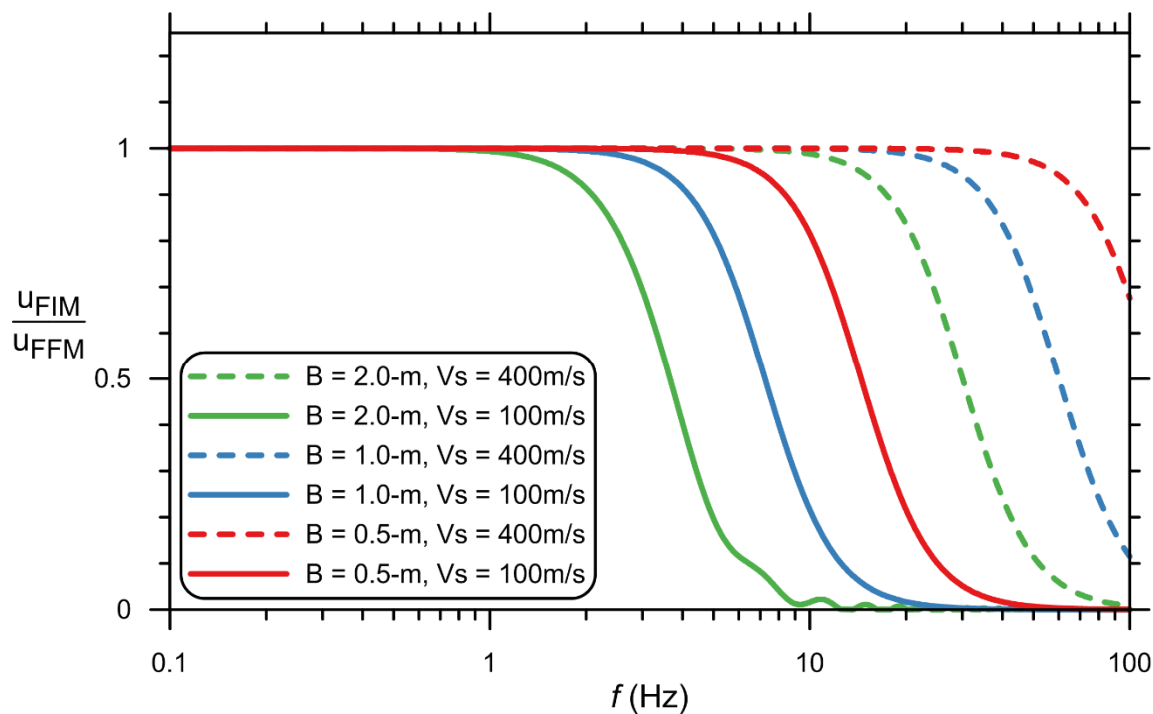


Figure 8-2: Transfer function for kinematic soil-structure interaction effects for three diameters of 25-m long, fixed-head reinforced concrete piles in soft and stiff soil profiles.

As discussed in the previous chapter, transfer functions are usually presented in a normalized manner by plotting versus dimensionless frequency. The version of dimensionless frequency given in Equation (7.8), proposed by Di Laora and Sanctis (2013) and Anoyatis et al. (2013), is demonstrated in Figure 8-3 to provide “perfect normalization” (i.e., the results all collapse onto a single line) for the parametric bounds considered here.

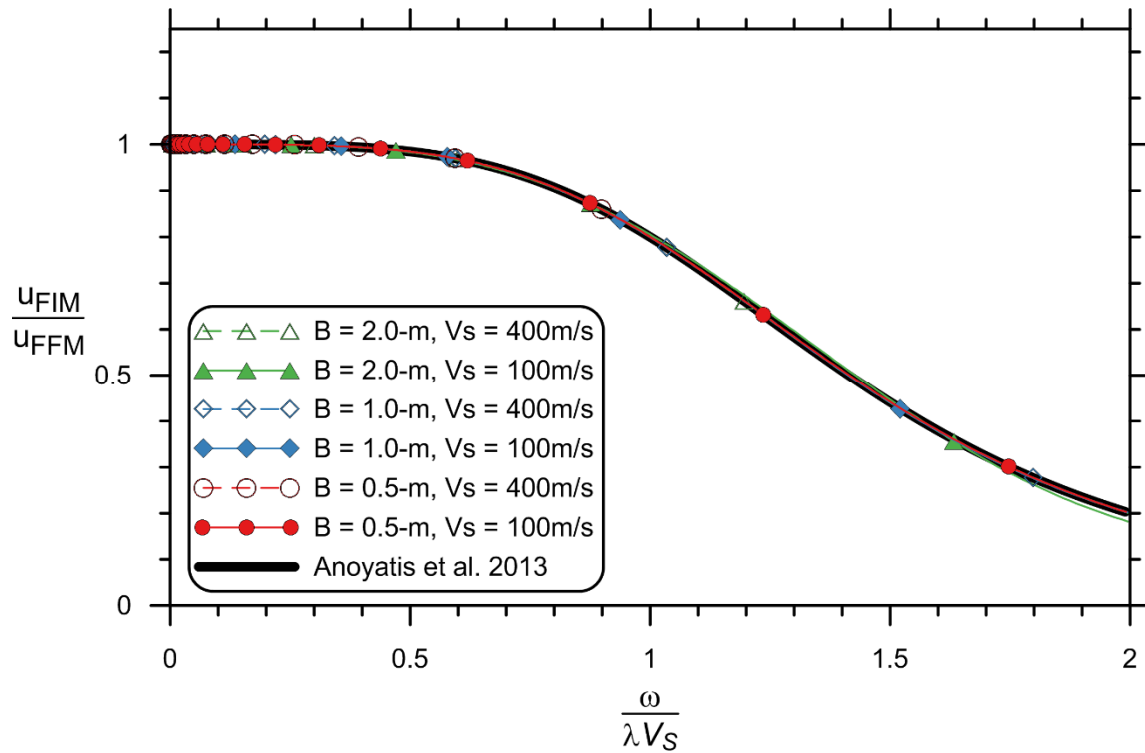


Figure 8-3: Transfer functions from Figure 8-2 plotted versus dimensionless frequency and compared to Anoyatis et al. (2013). All solutions lie within the same narrow band.

8.2 ELASTIC NUMERICAL SOLUTION

The numerical modeling approach used for this study consists of discretized pile segments attached to soil springs at each node as depicted in Figure 7-1(b). The elastic analytical solution from the preceding section provides an opportunity to verify that the proposed numerical modeling approach provides an accurate solution, since the elastic analytical solution is explicit and the numerical solution should converge to a high degree of accuracy for elastic conditions. While each

component of the numerical modeling approach is discussed in detail in Chapter 9, this section will focus only on the results of elastic simulations. The pile and soil are modeled using elastic beam-column and elastic zero-length uniaxial materials, respectively, in *OpenSees*.

Two categories of input excitation are considered, sine-sweep motions consisting of uniform-displacement amplitude broadband frequency content from 0.1 to 50 Hz, and recorded ground motions with variable bandwidth. The free-field input motions were specified at the ground surface and motions at the depth of each soil spring were computed using Equation (8.3). By specifying the input motion at the ground surface rather than the base of the soil profile, the problem of infinite amplification at resonant site frequencies is avoided. The amplitude of the input excitation does not affect the computed transfer functions since the model is linear-elastic.

Soil and pile properties for the numerical analyses match the properties used in the analytical solution so that a direct comparison of the computed transfer functions can be made. The soil-pile interaction stiffness (k) at depth z is defined as (Gazetas and Dobry 1984):

$$k = 1.69 E_s \left(\frac{E_p}{E_s(z)} \right)^{-0.137} ; \quad E_s(z) = 2 \rho V_s^2 (1 + \nu) \quad (8.19)$$

where E_p is the pile elastic modulus, taken as 2.7E7 kPa for reinforced concrete, and E_s is depth-dependent elastic soil modulus computed from V_s based on classical elasticity theory with assumed soil density $\rho = 1.6 \text{ Mg/m}^3$ and Poisson's ratio $\nu = 0.3$. The uniaxial spring stiffness is defined as k divided by the tributary length of the pile element to which it is attached. The soil springs connected to the pile head and tip are assigned a tributary length equal to half of the pile segment discretization length.

Transfer functions for the analytical solution are compared to the numerical solution results for a sine-sweep input motion in Figure 8-4 and for recorded earthquake ground motions in Figure

8-5. Two sizes of circular concrete piles are considered, 0.5-m and 2.0-m diameter, for a site with $V_S=150\text{m/s}$. Both fixed-head and free-head restraint conditions are considered. The sine-sweep input motion transfer functions show near-perfect agreement with the analytical solution for both pile sizes over the entire frequency range considered.

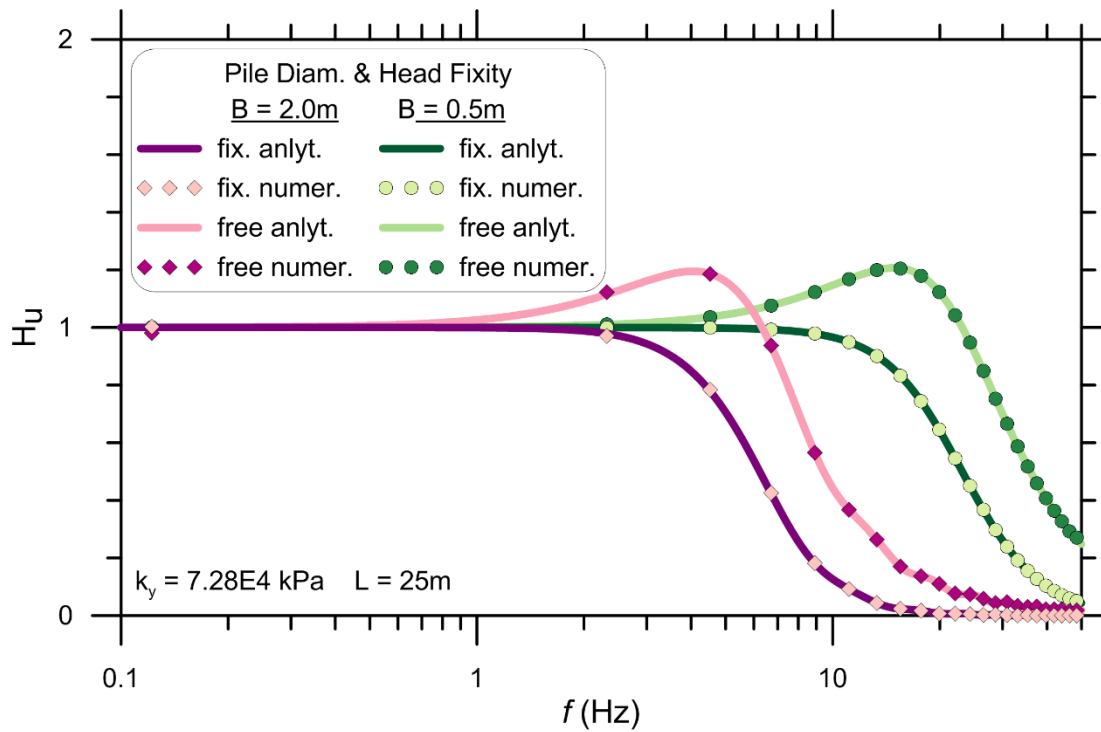


Figure 8-4: Analytical and numerical solution transfer functions for sine-sweep input motion.

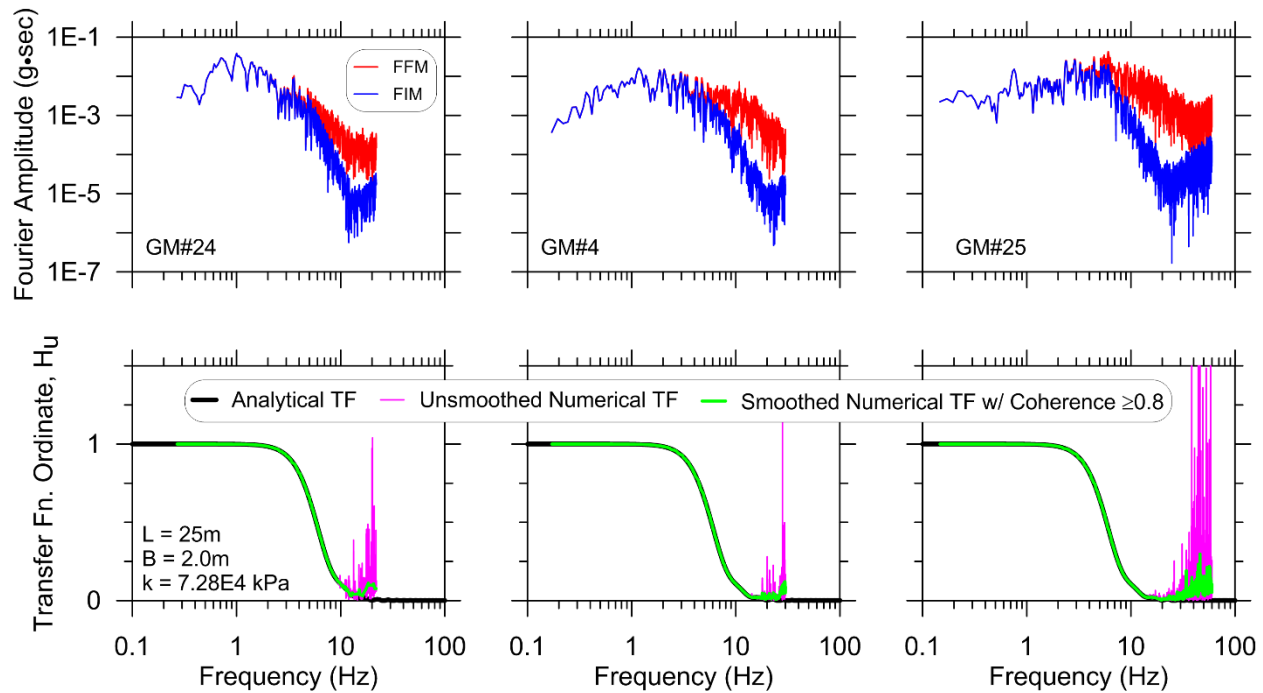


Figure 8-5: Fourier amplitude spectra for free-field and foundation-input motions (top) and corresponding transfer functions (bottom).

For the nonlinear parametric study described in the following chapter, ground motions are sourced from a set of 40 records with broad frequency content and statistical variability compiled by Baker et al. (2011). These motions and their characteristics are described in detail in §9.7.1. For the current comparison, three of the 40 the motions were selected that have variable frequency content as seen in the Fourier amplitude spectra in Figure 8-5. The three motions are described in Table 8-1.

Table 8-1: Ground motions for elastic numerical analyses; numbering follows Baker et al. (2011)

Motion #	Earthquake	Recording Station	M	PGA (s)
25	1989 Loma Prieta	UCSC	6.9	0.34
4	1994 Northridge	LA – Wonderland Ave.	6.7	0.13
24	1989 Loma Prieta	Golden Gate Bridge	6.9	0.16

Figure 8-5 shows acceleration Fourier amplitude spectra (FAS) for the pile head motion (FIM) and ground surface motion (FFM) for each of the three input ground motions. Note that each ground motion FAS is only plotted over the useable frequency range of the ground motion, which depends on the processing applied to the original recording (Ancheta et al. 2014). The ratio of the displacement FAS is the unsmoothed transfer function shown along with the high-coherence transfer function computed using Equation (7.10) in the lower portion of the figure. At frequencies up to about 20 Hz, the analytical solution matches the numerically-computed transfer functions exactly. At higher frequencies, the numerical transfer functions are dominated by noise, although the smoothed, high coherence transfer function reduces the noise significantly.

The finding that the transfer functions computed for the three ground motions with variable frequency content all agree perfectly with the analytical solution (and therefore with each other) highlights the underlying assumption of elastic material behavior and superposition of the response at each frequency. For realistic nonlinear conditions, the response of the system will change for input motions with different frequency content.

In light of the findings that the numerical results provide a near-perfect match to the analytical solution (Figure 8-4 and Figure 8-5), and that the analytical solution matches previous solutions by others (e.g., Figure 8-3), it has been verified that the proposed numerical modeling approach is valid, at least for elastic material properties.

The remaining sections in this chapter discuss elastic behavior that applies to the small-strain, initial stiffness range of pile-soil interaction for the nonlinear analyses that follow.

8.3 ELASTIC WINKLER MODULUS

8.3.1 Terminology and Units

In the past, terms such as modulus of subgrade reaction, coefficient of subgrade reaction, Winkler stiffness, Winkler modulus, normalized Winkler modulus, and other similar combinations of these phrases have been used somewhat interchangeably to refer to two concepts that are distinct and must be clearly differentiated. Some clarification is warranted here to avoid confusion.

The concept of “modulus of subgrade reaction” refers to the soil settlement that occurs beneath a uniformly loaded area, and hence has units of $[(\text{force}/\text{length}^2)/\text{length} = \text{force}/\text{length}^3]$. Herein the symbol k_{msr} refers to this definition. It is formulated in this way because of its usefulness in structural models for estimating settlement resulting from the bearing pressure exerted by a structure, and has limited usefulness as a standalone descriptor of soil behavior (true soil modulus E_s is more meaningful). Values of modulus of subgrade reaction can be crudely measured in the field using the “plate load test” (ASTM D 1194) by applying a measured force to a steel plate of known area (stress = force/area) and measuring the downward deflection. Terzaghi (1955) provided tabulated values of k_{msr} for different relative densities of sand that were widely used for lateral pile analyses until full-scale pile testing began in the 1970’s.

When used with a beam-on-springs Winkler approach, the soil stiffness term must be modified to account for the out-of-plane (transverse) width of the beam over which the soil pressure acts, since Winkler models consider only two dimensions—the longitudinal axis of the beam and the orthogonal direction in which load is applied, parallel to the beam height. For example, if a measured value of k_{msr} was to be used for a Winkler analysis, it would be multiplied by beam width to obtain $K_e = k_{msr}B$, where K_e is the Winkler modulus with units of distributed load per unit deflection $[\text{force}/\text{length}/\text{length}]$, which is equivalent to the units of stress $[\text{force}/\text{length}^2]$.

The symbol K_e will be used in this text in reference to both (1) Winkler stiffness for elastic analyses and (2) the initial elastic stiffness of p - y springs for nonlinear analyses.

Confusion may arise because K_e and soil Young's modulus E_s share the same units and are sometimes presented as being related by a dimensionless coefficient for pile analysis. A discussion of the basis for this assumption is provided in the following sections, but it should be noted that E_s cannot be exactly defined from a measured value of k_{msr} . To define E_s , a measurement of strain parallel to the direction of loading is needed. In a laboratory test this is trivial because the specimen height and boundary conditions are known. To measure strain during a plate load test would require knowing the height of the soil column (h) that is influenced by the load applied at the surface, which for an elastic halfspace is theoretically infinite. While finite values of h are more reasonable and could be estimated by taking into account the three-dimensional attenuation of stress below the plate, the computed value of E_s scales linearly with h and is therefore highly sensitive to the estimate. Hence any tabulated values relating k_{msr} to E_s [e.g., Bowles (1997) Table 9-1] contain an inherent assumption about the plate load test depth of influence and how this will scale with size between the test and real foundations. Likewise any relation between measured or tabulated k_{msr} and Winkler modulus for lateral pile analysis contain a similar embedded assumption, or represent the results of specific load test(s).

8.3.2 Previous Definitions of K_e

Existing p - y relationships such as the widely-used API (1993) curve for sand and Matlock's (1970) curves for clay were derived by fitting equations that have a theoretically-derived functional form to the results of full-scale load tests. While load tests may provide a reasonable estimate of the near-surface ultimate lateral soil resistance p_{ult} , the instrumentation used to measure pile strain in the original tests was not capable of accurately measuring small enough deformations to capture

the truly elastic soil behavior (Choi et al. 2015). Since E_s can be related to the small-strain shear modulus measured using geophysical methods, and since geophysical tests are an increasingly common part of site investigations for projects in seismic regions, a more attractive approach would relate the soil elastic Young's modulus E_s directly to the initial stiffness of the p - y curve, K_e . Soil shear modulus G , shear wave velocity V_s , and Young's modulus are related through the following well known equations from elasticity theory:

$$G = \rho_s V_s^2 \quad (8.20)$$

$$E_s = 2G(1 + \nu) \quad (8.21)$$

Where ν and ρ_s are the soil Poisson's ratio and mass density, respectively.

Vesic (1961) provided the following expression for K_e :

$$k_{msr} B = K_e = 0.65 \left(\frac{E_s}{1 - \nu^2} \right)^{1/2} \sqrt{\frac{E_s B^4}{E_p I_p}} \quad (8.22)$$

which explicitly recognizes that beam width B must be taken into account when formulating a Winkler modulus from k_{msr} . This is straightforward for the case that Winkler (1867), Hetenyi (1946), and Vesic (1961) were considering—an infinitely-long rectangular or wide-flange beam which only exerts normal stress at the contact between the flat base of the beam and the ground surface. For the case of a laterally-loaded circular pile, the stress field at the pile-soil interface is a combination of shear and normal stresses, and the relative contribution and direction of each component changes around the circumference of the pile as shown in Figure 8-6. Equation (8.22) has been used in the past to define p - y curve elastic stiffness (e.g., Boulanger et al. 1999) despite not being derived for these conditions.

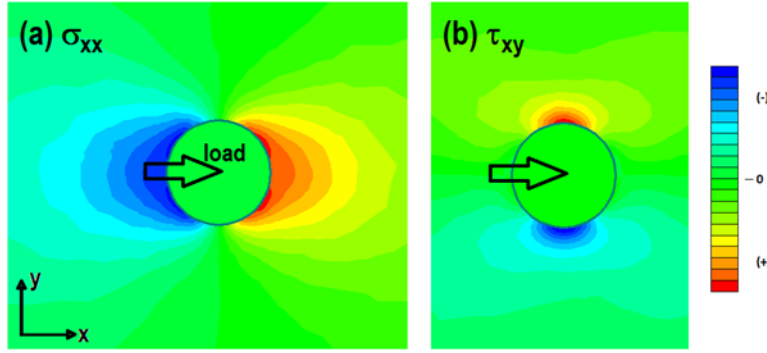


Figure 8-6: (a) Normal and (b) shear stress contours around a laterally-loaded pile. Color key indicates change in stress from initial condition.

Several researchers performing elastic pile KSSI analyses have quantified a Winkler spring coefficient δ , where the linear-elastic Winkler spring stiffness is defined as the product of the dimensionless parameter δ and the soil modulus E_s :

$$K_e = \delta E_s \quad (8.23)$$

In other words, δ is the ratio of the p - y elastic stiffness to the soil elastic stiffness:

$$\delta = \frac{K_e}{E_s} \quad (8.24)$$

Values and equations for δ for fixed- and free-head piles and for various soil properties (homogeneous, layered, stiffness increasing linearly with depth, etc.) have been proposed by many researchers including Kagawa and Kraft (1980), Roesset (1980a), Dobry et al. (1982), Gazetas and Dobry (1984b), Kavvadas and Gazetas (1993), and Syngros (2004). In these studies, a single value of δ was applied over the length of the pile in an elastic BDWF model; the value of δ was then adjusted until the pile head displacement matched the displacement computed with finite-element or boundary-element continuum solutions under the same applied lateral force at the pile head. In other words, the pile-head lateral impedances were matched between the two numerical modeling

approaches. Regression models to determine best-fits to parametric results were then used to determine coefficients for the expressions. A selection of these expressions and notes on their derivation are given in Table 8-2 and plotted in Figure 8-7.

Even in the case of a homogeneous soil profile, relative pile-soil displacement varies with depth for both inertial and kinematic loading due to the deformation pattern of the pile. Since a single value of δ was applied over the entire pile length in these comparative studies, the mechanics controlling the interaction at a single depth are not directly reflected in the result, which represents an average response. This is counterproductive for practical applications, because real soil profiles are inhomogeneous, and foundation designers need reliable methods for specifying accurate p - y curve parameters at a single depth within a given soil layer. Furthermore since this approach simply equates one numerical study with another, the outcome is perhaps less a reflection of reality than it is of the difference between the modeling approaches. A more rigorous derivation of δ based on theory and rigorous numerical modeling complemented by validation from accurate small strain measurements during physical modeling studies is a future research need.

Since loading was applied at the pile head in these studies, the resulting values of δ were not derived for the fundamental mechanics governing kinematic interaction from free-field excitation. Anoyatis et al. (2013) showed that the commonly used value of $\delta = 1.2$, initially proposed by Roesset (1980a), does not provide a good match to finite-element solutions for kinematic loading for certain pile and soil stiffness combinations. Furthermore, the parametric results of Anoyatis et al. showed that even for the same pile and soil conditions, different values of δ are required to match the BDWF results to the continuum finite-element results depending on which result is being matched (e.g., curvature ratios between the pile and soil at the pile head versus pile tip, maximum pile bending moment, etc.), which has also been reported by Kavvadas

and Gazetas (1993). This is again a reflection of the fact that the approach of obtaining δ by matching impedances from BDWF and continuum analyses does not faithfully capture the underlying pile-soil interaction mechanics; if it did then a single expression would work for a variety of boundary conditions. A useful finding of Anoyatis et al. is that the δ parameter is not strongly frequency-dependent, which is convenient because of the difficulties involved in performing frequency-domain analyses.

Despite the shortcomings of the impedance-matching approach, the difference between δ values for fixed- and free-head piles in Figure 8-7 clearly shows that pile rotation or the lack thereof has a significant influence on the magnitude of the mobilized soil resistance. Near the head of a free-head pile where rotation is significant, the pile encounters greater soil resistance than a fixed-head pile because pile rotation mobilizes soil shear resistance in addition to the predominantly compressive stress induced by translation. Ideally, p - y curves should be formulated as p - y - θ curves, where θ is pile rotation. This is another future research need and will not be addressed in the current study.

Table 8-2: δ expressions from previous researchers derived by matching results of BDWF analyses to continuum analyses.

Applicable soil condition	Pile head-fixity condition	Source:	Roesset (1980a)	Dobry et al. (1982)	Kavvasdas and Gazetas (1993) ^b	Syngros (2004) ^c
<i>Any, or not specified</i>	Any, or not specified	$\delta =$	1.2	-	-	-
<i>Constant stiffness w/ depth</i>	Fixed		-	$1.67 \left(\frac{E_p}{E_s} \right)^{-0.053}$	-	$2.0 \left(\frac{E_p}{E_s} \right)^{-0.075}$
	Free		-	$1.67 \left(\frac{E_p}{E_s} \right)^{-0.053}$	$\frac{3}{1-\nu^2} \left(\frac{E_s}{E_p} \right)^{1/8} \left(\frac{L}{B} \right)^{1/8}$	$3.5 \left(\frac{E_p}{E_s} \right)^{-0.11}$
<i>Linearly increasing stiffness w/ depth^a</i>	Fixed		-	-	-	$3.0 \left(\frac{E_p}{E_s} \right)^{-0.08}$
	Free		-	-	-	$5.8 \left(\frac{E_p}{E_s} \right)^{-0.13}$

^aSoil stiffness E_s defined as the stiffness at the pile tip, decreases linearly to zero at the ground surface.

^bMain emphasis of study was matching peak bending moments between BDWF and finite-element (FEM) continuum analyses

^cFEM studies performed using *K-PAX* software, described in Syngros (2004) dissertation. The axisymmetric domain is two-dimensional and formulated in radial coordinates. Soil-pile interaction represented by a strain compatibility condition at interface.

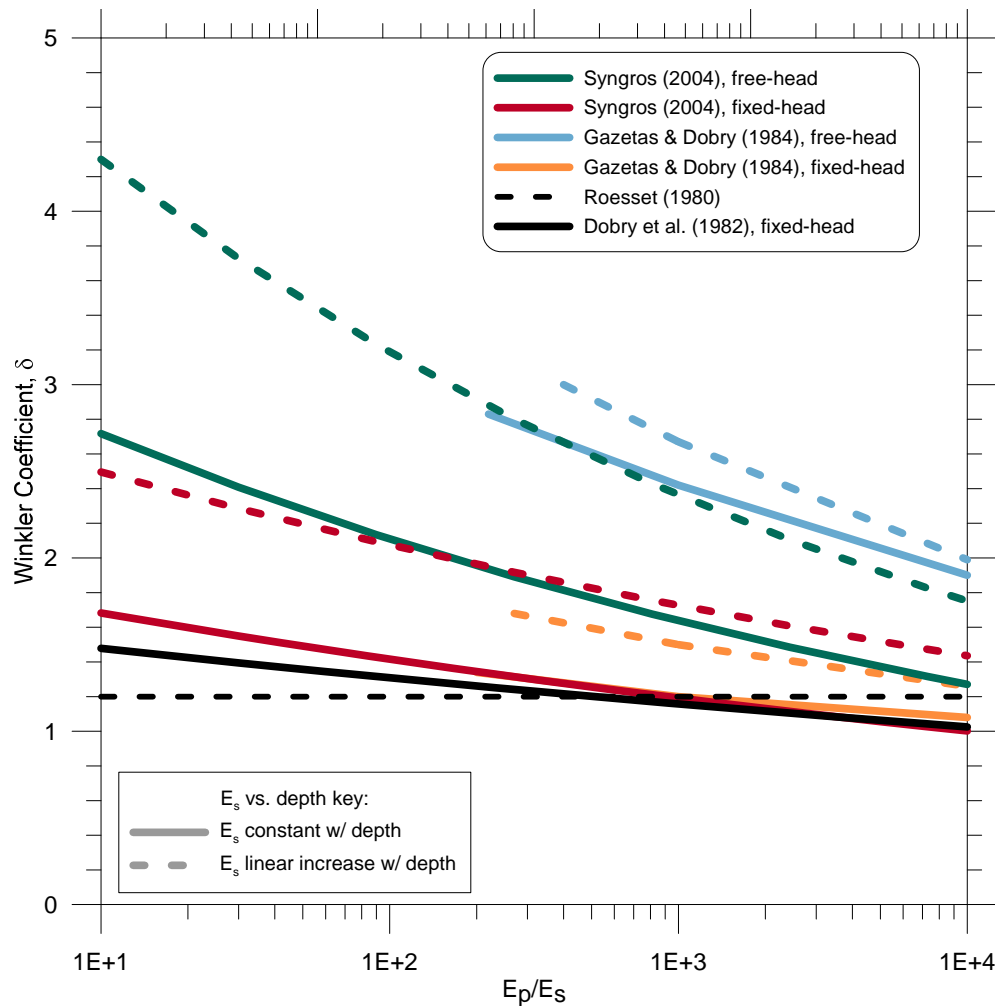


Figure 8-7: Values of Winkler coefficient δ proposed in previous pile SSI research.

8.3.3 Diameter Effects

The relationships for δ in Table 8-2 generally lack a functional dependence on pile diameter, suggesting that pile-soil interaction initial stiffness is independent of diameter. While this holds true for plane-strain elastic solutions considering a homogeneous full-space domain, solutions using more realistic boundary conditions along with experimental results (e.g., see Carter 1984 and Pender 2004) indicate that initial stiffness does depend on pile diameter. Conversely, experimental work by Ashford and Juirnarongrit (2003) showed that a diameter-independent estimate of K_e provided the best match to full-scale experimental results, but only for piles with active length contained within a uniform-stiffness stiff clay layer.

A dependence on diameter is intuitive—it would seem that a pile undergoing lateral displacement will encounter greater soil resistance than a smaller diameter pile undergoing the same displacement, due simply to the fact that it is wider than the small-diameter pile. Pile rotation and changes in soil stiffness with depth also affect the resistance encountered by the pile as a function of its diameter (Pender 2004). These effects are due to the dependence of the pile’s flexural response on EI (and hence B), and because a larger diameter pile mobilizes soil resistance over an increasingly larger depth increment and hence “feels” an increase in stiffness with depth. Pender (2004) and others have suggested that previous experimental campaigns failed to identify these trends because only a small number of pile diameters were tested—in some cases, one.

Nonetheless, the majority of elastic pile dynamics work and many nonlinear p - y studies (e.g., Kagawa and Kraft 1981, Boulanger et al. 1999) have proceeded with the assumption of K_e being independent of pile diameter. The underlying assumption for this approach is that a small-diameter pile will induce greater average soil strain than a large-diameter pile for the same lateral displacement by a factor proportional to the difference of the two piles diameters. This is consistent with Terzaghi’s (1955) assumption that the zone in which significant strain is mobilized beneath a loaded footing scales in proportion to the size of the footing.

Kagawa and Kraft (1980) adapted a formulation by Matlock (1970) as the basis for applying this assumption to pile dynamics⁵, suggesting that the average shear strain γ_{ave} which

⁵ It is worth noting that further examination of the underlying theory behind Equation (8.25) reveals that it has little relation to lateral pile-soil interaction. The basis for Equation (8.25) is Skempton’s (1951) method for estimating the immediate settlement of an embedded strip footing on clay based on a combination of elasticity theory, limit-state concepts, and laboratory tests results. Skempton estimated that the ratio of E_s to undrained strength (s_u) for typical clays is about 50 to 200, and assumed that the inverse of this range (0.005 to 0.02) could be used to approximate the strain occurring at one-half the measured strength (ε_{50}). Using these values and an assumption of the size of the stress zone of influence below the footing, a simple approximation for settlement was provided. Matlock adopted this for piles by taking the average of the ε_{50} range (≈ 0.01) and substituting pile diameter for footing width, resulting in the expression that average normal strain around the pile could be approximates as $y/2.5B$ —hardly a

develops around a laterally loaded pile is a linear function of the ratio of displacement to pile diameter (y/B), such that as B increases, the relationship between stress and strain, and hence p/y , scales at the same rate:

$$\gamma_{ave} = \frac{(1 + \nu) y}{2.5 B} \quad (8.25)$$

To test this hypothesis, a series of simple plane-strain elastic analyses were run for this study in the finite-element program *Phase2* (Rocscience 2013). The results showed that δ is independent of diameter, but only if the domain size is scaled to match changes in pile size—a significant caveat. This is in agreement with previous two- and three-dimensional elastic analyses (e.g., see Pender 2004), so further details will not be provided here.

The potential error introduced by using a diameter-independent K_e is likely minor for many applications in which large relative pile-soil displacements are expected, since the tangent modulus of a nonlinear p - y curve depends on both the initial stiffness and the ultimate resistance. The results of Ashford and Juirnarongrit (2003) also suggest that the error is minor for small-strain dynamic loading if the soil stiffness is approximately constant with depth.

Despite its shortcomings, the framework of Equation (8.25) is convenient because it allows the relative pile-soil displacement defining the onset of nonlinearity y_{yield} to be defined as a function of shear strain at the onset of soil nonlinearity, the latter of which has been studied extensively through laboratory testing (e.g., Vucetic and Dobry 1991). Hence, a diameter-independent

rigorous consideration of pile-soil interaction mechanics. Kagawa and Kraft (1980) later adopted this approach for their theoretical pile dynamics study. Noting that the strain orthogonal to ε is $-\nu\varepsilon$ and therefore the maximum shear strain is $(1+\nu)\varepsilon$, they came up with Equation (8.25).

definition for K_e based on Equation (8.25) will be adopted for this study, with the opportunity to revise the findings in the future if more rigorous relationships between δ and B (or γ_{ave} and B) become available.

8.4 QUESTIONS OF PILE MASS AND INERTIA

For static loading, since acceleration is zero (or is ignored for pseudo-static analysis) no inertial force is associated with movements of the pile mass. During the rapid and potentially large-amplitude loading from an earthquake, however, pile inertia contributes to the overall response of the pile-soil system and should be included in dynamic analyses, as recognized early on by Novak (1974). To produce more tractable and simplified solutions, previous researchers using Winkler models have often neglected the pile mass such that a static solution is being used to approximate the dynamic response (e.g., Dobry et al. 1982, Anoyatis et al. 2013). Others assigned a mass density greater than the true pile mass (e.g., Berger et al. 1977; Marshall et al. 1977) to account for the fact that some portion of the soil surrounding the pile moves in phase with the pile, amplifying its inertia. The volume of soil which moves with the pile likely varies depending on the frequency and amplitude of the excitation along with the pile and soil properties, and is therefore difficult to quantify.

The influence of pile mass is demonstrated in Figure 8-8, which compares normalized elastic transfer functions computed for two pile sizes with and without mass. In general these elastic analyses indicate that the effect of pile mass is minor, which agrees with previous findings by Kagawa and Kraft (1980), and only deviates from the no-mass condition over a limited frequency range. The effect does not appear to scale with pile diameter, since the difference between the with-mass and without-mass curves is approximately equal for the two sizes

considered when plotted versus dimensionless frequency. The effect of pile inertia may not be as consistent when system nonlinearity is considered. As discussed in the following section, including pile mass in numerical simulations can complicate interpretation of the kinematic transfer function because of inertial resonance near the fundamental frequency of the pile-soil system. Because of this, and in light of the finding that the influence of pile inertia is minor, piles will be modelled as massless for the numerical simulations that follow.

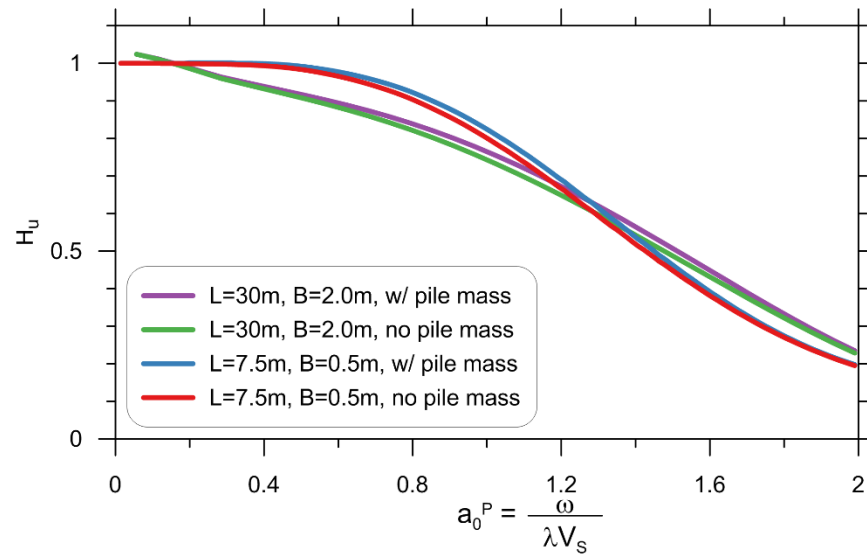


Figure 8-8: Normalized elastic transfer functions computed with and without pile mass.

8.5 PILE-SOIL SYSTEM FUNDAMENTAL FREQUENCY AND RESONANCE

When pile mass is included in a Winkler model, the pile-soil system will have a defined fundamental frequency. It is important to recognize that this represents a somewhat fictitious mode of vibration in the context of a real structure, since in general the dynamic response of a system depends on the coupled response of the superstructure and foundation-soil components. Nonetheless, transfer functions computed for this study have the potential to be influenced by inertial resonance when pile mass is included. To investigate the potential influence of resonance,

transfer functions were computed for pile-soil systems with and without pile mass, similar to the analyses presented in the previous section.

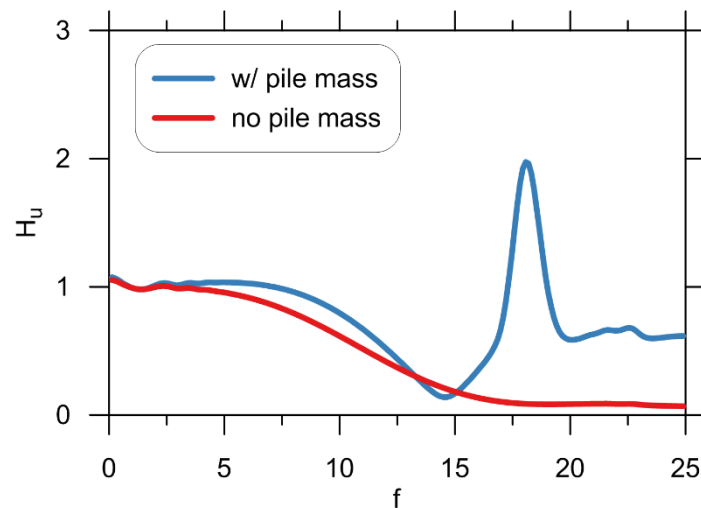


Figure 8-9: Effect of resonance at pile-soil system fundamental frequency on kinematic transfer functions.

An example of the results is shown in Figure 8-9. It is clear that the kinematic transfer function is strongly influenced by resonance near the first mode period of the pile-soil system (at about 17 Hz), amplifying the free-field motion by a factor of nearly five. Also of note is that the bandwidth of the zone influenced by first-mode resonance is on the order of 5 Hz. In general this bandwidth will increase with increasing fundamental frequency of the system (Rathje et al. 2004; Chopra 2007). Hence, it is possible for resonance to influence the kinematic transfer function over the frequency range of interest even if the fundamental frequency of the pile-soil system lies beyond this this range.

Inflation of transfer function ordinates due to inertial resonance further compounds the difficulties associated with accurately defining kinematic transfer functions at high frequencies discussed in §7.3.6.2. In light of this, pile mass will be set to zero for the analyses that follow unless otherwise noted. This approach is especially helpful for nonlinear analyses in which the

fundamental frequency of the system changes over the duration of the problem, which makes it difficult to discern which portions of the resulting transfer function are strongly affected by resonance.

9 Analysis

9.1 APPROACH

The approach for investigating kinematic pile-soil interaction for this study is through numerical analyses using the finite element modeling platform *OpenSees*. A model of a single pile or pile group connected to nonlinear p - y springs is formulated as shown in Figure 9-1(b). Dynamic time-domain analyses are then conducted in which the free ends of the p - y springs are displaced to simulate free-field ground response due to earthquake excitation; the free-field ground motions are computed separately using one-dimensional nonlinear ground response analysis in *DEEPSOIL* (Hashash et al. 2015) as depicted in Figure 9-1(a). Transfer functions and spectral ratios are then computed using the pile head and free-field ground surface response histories.

In the following sections, the various components used in the beam-on-dynamic-nonlinear-Winkler-foundation (BDNWF) and ground response models for this study are discussed. Background on the parameters is first given in the context of previous efforts by other researchers studying pile dynamics, followed by an explanation of how the parameters were quantified for this study.

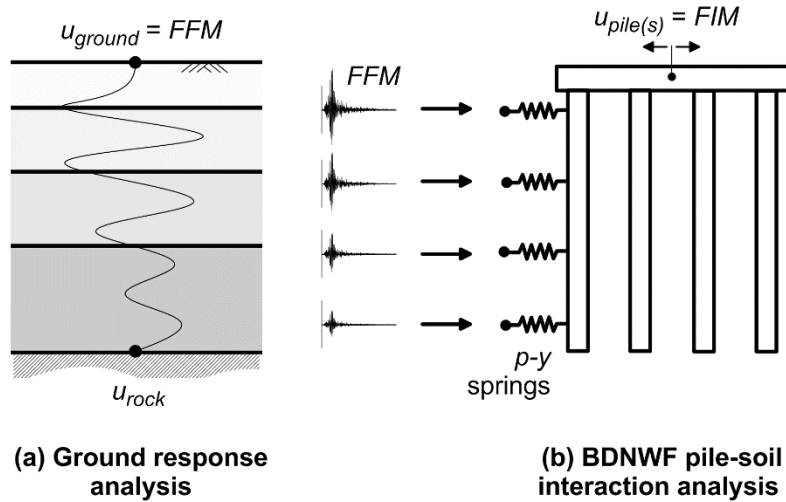


Figure 9-1: Numerical modeling approach.

9.2 PARAMETRIC STUDY BOUNDS

The range of pile and soil properties considered for this study are intended to span the conditions encountered in typical bridge design practice. The study bounds were further refined based on the combinations of pile and soil stiffness found to result in significant kinematic interaction based on elastic solutions in the previous chapter.

Table 9-1: Parametric Study Bounds for Single Piles

Length (L)	Diameter (B)	Slenderness Ratio (L/B)	Cracked Section Stiffness (MN·m)
7.5 m	0.5 m	15	28
15 m	0.5 m	30	28
30 m	2.0 m	15	7,220
60 m	2.0 m	30	7,220

Table 9-1 presents the range of single pile properties considered. Models of each of the four piles in Table 9-1 have been analyzed for six different soil profiles each subjected to 40 ground

motions for free- and fixed- head pile boundary conditions. This represents 960 analyses for each head-fixity, for a total of 1,920 single pile analyses. Properties of sites 1 through 6 are discussed in §9.6, and the 40 ground motions are discussed in §9.7. In addition, a limited number of pile group analyses were performed to investigate group effects and the influence of ground motion incoherence, as discussed in §9.5.4 and §9.7.3, respectively.

9.3 *PySimple3*—MOTIVATION AND MODEL UPDATES

It is well known in the geotechnical community that the generic p - y springs typically used in practice do not sufficiently capture realistic soil behavior, especially for dynamic analysis. For this study, a modified version of the p - y model developed by Choi et al. (2015) is used, known as *PySimple3* in *OpenSees*. The *PySimple3* model was developed specifically for dynamic analysis of laterally-loaded piles and includes several features not found in previously available models such as the ability to independently specify small strain stiffness, the force at which yielding/nonlinearity occurs, and hysteretic and radiation damping. The model consist of an initial linear portion followed by nonlinear behavior according to a bounding-surface plasticity formulation (e.g., Dafalias 1986) as illustrated in Figure 9-2. The user specifies the initial elastic slope of the curve K_e , the ultimate resistance p_{ult} , the resistance at yielding p_y , and a shape parameter C that describes curvature and hence affects the amount of soil hysteric damping. Radiation damping can also be modeled by specifying an optional viscous damping coefficient.

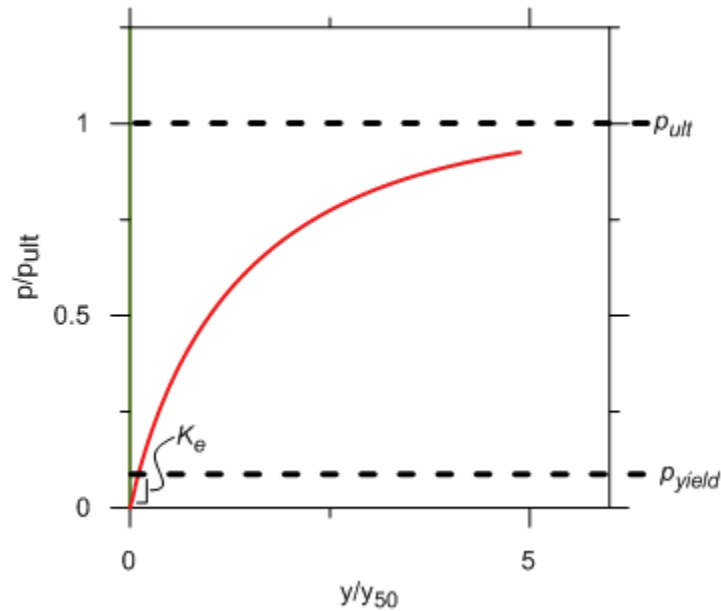


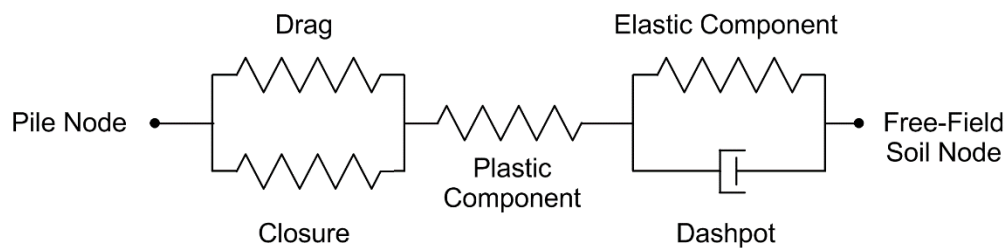
Figure 9-2: Basic features of *PySimple3* material under monotonic loading. After Choi et al. 2015.

9.3.1 Motivation

Prior to development of *PySimple3*, the primary tool available for pile SSI modeling with a BNWF approach was the *PySimple1* material model in *OpenSees*, which is based on a framework presented by Boulanger et al. (1999). The implementation of *PySimple1* in *OpenSees* is formulated to approximate the shape of the API (1993) or Matlock (1970) p - y curves for sand and clay, respectively. Because the material model is coded to match the shapes of these previous p - y definitions, the user has limited control over specific aspects of the curve. For example, the initial stiffness cannot be specified directly, only adjusted indirectly by changing the other parameters. In addition, as shown in Figure 9-3 the viscous dashpot used to represent radiation damping is placed in parallel with the entire material instead of just the far-field elastic component as presented in Boulanger et al. (1999). For the *OpenSees* implementation, the dashpot force is computed after force and displacement compatibility has been achieved between the gap, plastic, and elastic components based on the proportion of the total displacement that occurs in the elastic

component relative to the total element. In other words, the dashpot force is not considered while solving for compatible forces and displacements in the other components, only after the fact. While this approach is computationally stable, it is more desirable to have a true viscoelastic-plastic implementation as shown in Figure 9-4(b). Note that placing the dashpot in parallel with the elastic component, also known as the Kelvin-Voigt viscoelasticity model, is distinct from placing the two components in series, known as the Maxwell model (Simo and Hughes 1998). The *PySimple1* and *PySimple3* materials are compared for sand and clay in Figure 9-5.

(a) after Boulanger et al. (1999)



(b) *PySimple1* OpenSees implementation

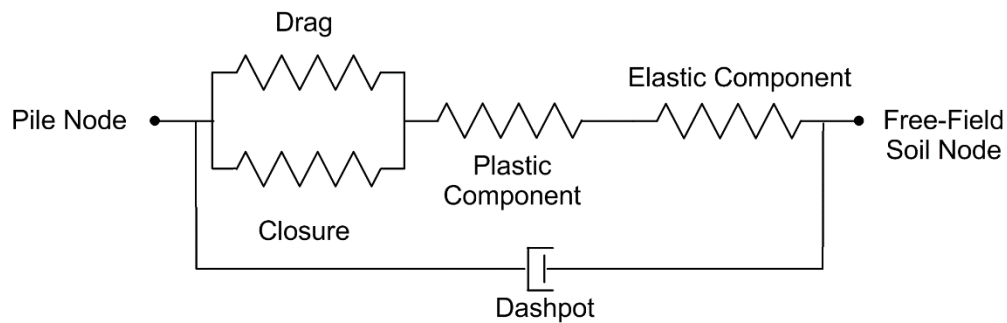
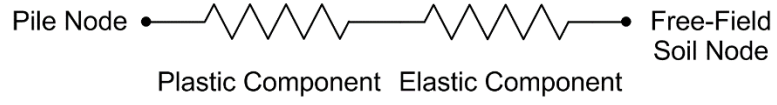


Figure 9-3: Comparison of Boulanger et al. (1999) dynamic p - y material and later implementation in *OpenSees*.

(a) *PySimple3* (Choi et al. 2015, JGGE)



(b) Updated *PySimple3* (current study)

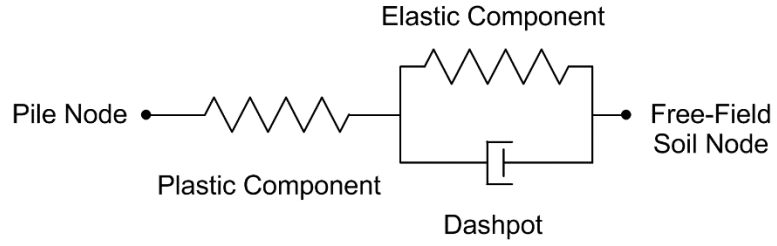


Figure 9-4: *PySimple3* viscoelastic-plastic material model formulation.

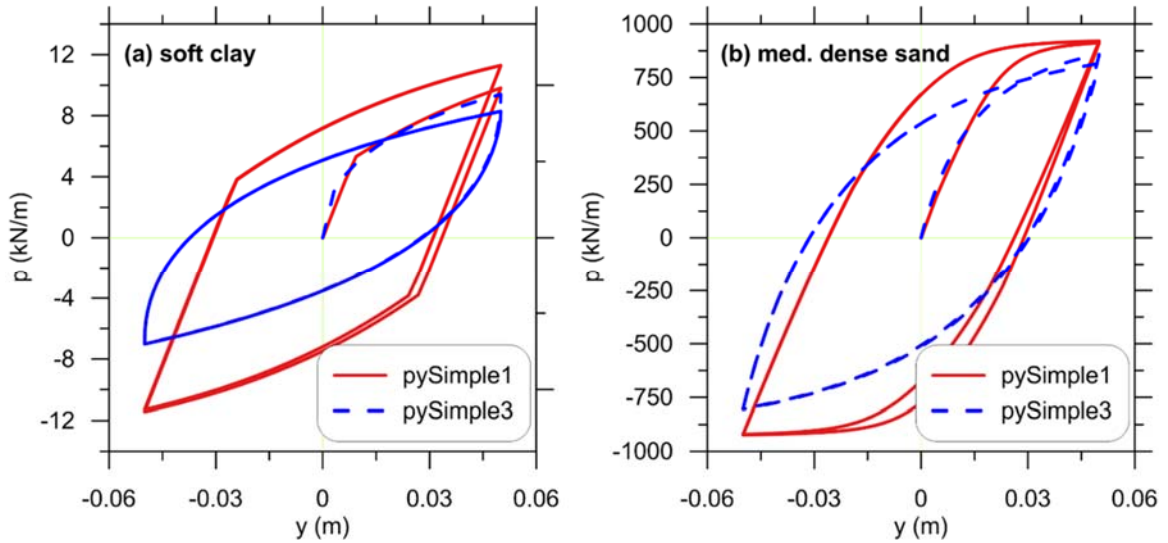


Figure 9-5: Comparison of *PySimple1* and *PySimple3* material models.

9.3.2 Governing Equations and *OpenSees* Implementation

The *PySimple3* constitutive model by Choi et al. (2015) is based on a bounding-surface plasticity formulation according to the following governing equations:

$$\dot{p} = K_e \dot{\gamma}_e = K_e (\dot{\gamma} - \dot{\gamma}_p) \quad (9.1)$$

$$f = |p - p_\alpha| - p_y \quad (9.2)$$

$$K_p = C \cdot K_e \frac{\left| \left[p_u \cdot \text{sign}(\dot{y}) \right] - p \right|}{|p - p_{in}|} \quad (9.3)$$

$$\dot{p}_\alpha = K_p \dot{y}_p \quad (9.4)$$

$$K = \frac{\dot{p}}{\dot{y}} = \frac{K_p K_e}{K_p + K_e} \quad (9.5)$$

Equation (9.1) is the elastic constitutive law relating the rate of change versus time (signified by the overdot) of force in the element \dot{p} to the elastic displacement rate \dot{y}_e based on the elastic stiffness K_e . The right-hand side of (9.1) shows that the elastic displacement rate is equivalent to the total displacement rate minus the plastic displacement rate. Equation (9.2) is the yield function used to determine if yielding has occurred ($f = 0$) or if the current state remains in the elastic region ($f < 0$). When yielding has occurred, Equations (9.3) - (9.5) define the plastic modulus, kinematic hardening law, and elastoplastic (tangent) modulus. The force p_α tracks the center of the elastic region, which evolves with the yield surface during continued post-yield loading. This is equivalent to the concept of backstress in classical plasticity formulations, but in this case is a “backforce”. The plastic modulus is determined by how close the current state p lies to the ultimate resistance (bounding surface) represented by p_{ult} and the force at the onset of yielding p_{in} . The formulation allows for a smooth transition between elastic and post-yield behavior since the plastic modulus is infinite at the onset of yielding, such that the elastoplastic modulus is initially equal to the elastic modulus, then undergoes degradation with continued displacement. Further details are available in Choi et al. (2015).

Three updates were made to *PySimple3* to meet the needs of this study and to improve the performance of the material for general use in other pile dynamics problems: (i) optional viscoelastic behavior was added to model radiation damping, (ii) a backforce-updating routine was added to prevent overestimates of force following an unload-reload cycle, and (iii) the implicit integration scheme used for solving the governing equations was updated to use the unconditionally-stable and efficient Ridders' method (Ridders 1979).

An elastic spring in parallel with a viscous dashpot as shown in Figure 9-4(b) is known as the Kelvin-Voigt viscoelasticity model. The instantaneous force in a Kelvin-Voigt material is the sum of the force in the elastic component due to the material's elastic stiffness plus the force in the dashpot:

$$\dot{p} = K_e \dot{y}_e + c \ddot{y}_e \rightarrow \frac{dp}{dt} = K_e \left(\frac{dy_e}{dt} \right) + c \left(\frac{d^2 y_e}{dt^2} \right) \quad (9.6)$$

where c is the dashpot coefficient. This formulation defines the elastic (now viscoelastic) constitutive law for the updated *PySimple3* material. The viscoelastic-plastic tangent becomes:

$$K = \frac{dp}{dy} = \frac{\left(\frac{dp}{dy_e} \right) K_p}{\left(\frac{dp}{dy_e} \right) + K_p} \quad (9.7)$$

The term relating change in force to change in elastic displacement (dp/dy_e) can be isolated from Equation (9.6) in incremental form as follows:

$$dp = K_e dy_e + c \left(\frac{dy_e}{dt} - \frac{dy_{e,last}}{dt} \right) \rightarrow \frac{dp}{dy_e} = K_e + c \left(\frac{dy_e}{dy_e dt} - \frac{dy_{e,last}}{dy_e dt} \right) = K_e + \frac{c}{dt} \left(1 - \frac{dy_{e,last}}{dy_e} \right) \quad (9.8)$$

where $dy_{e,last}/dt$ is the elastic displacement rate during the last converged step. Note that the following possible alternative formulation for dp/dy_e :

$$\frac{dp}{dt} = K_e \frac{dy_e}{dt} + c \left(\frac{d^2 y_e}{dt^2} \right) \rightarrow dp = K_e dy_e + c \left(\frac{dy_e}{dt} \right) \rightarrow \frac{dp}{dy_e} = K_e + \frac{c}{dt} \quad (9.9)$$

implies that the dashpot force would continue to be added to the total force in the viscoelastic component even if the elastic displacement rate stays constant. This is an incorrect formulation; if the elastic displacement rate (i.e., velocity) is constant, then the dashpot force should remain constant between successive increments. Only the force in the elastic spring component changes if the elastic displacement rate is constant, and Equation (9.8) is formulated to capture this.

The approach for solving the governing equations in the *OpenSees* implementation of the *PySimple3* material is as follows:

- A trial displacement step is passed to the material by the program; if yielding does not occur, the resulting force is determined from Equation (9.6) directly;
- If yielding occurs, an initial guess is made which divides the trial displacement increment into elastic and plastic sub-increments;
- The force in the plastic and viscoelastic components is computed based on the imposed trial displacements;
- Since the plastic and viscoelastic components are in series, the force in the two components must be equal. Hence the unbalanced force between the two components is cast as a residual equation, and the trial amount of elastic versus plastic displacement is adjusted until the residual unbalanced force falls below a specified tolerance. Ridder's method is used to solve this iteration scheme.

9.4 *PySimple3*—PARAMETER VALUES

The following sections describe how each of the parameters that define the *PySimple3* model are defined for this study.

9.4.1 Initial Elastic Stiffness K_e

The initial horizontal interaction between a laterally-loaded pile and soil does not induce nonlinearity in the pile or soil. Although the nonlinear *PySimple3* model used for this study is linear only for very small displacements [on the order of y/B of 2×10^{-5} (after Choi et al. 2015)], the elastic slope has a significant impact on the shape of the p - y curve and the resulting tangent stiffness and hysteresis at displacements large enough to induce nonlinearity. Figure 9-6 demonstrates that for all other parameters being equal, the amount of hysteretic damping during harmonic loading is significantly different when K_e is varied by a factor of two—even at displacements less than 1 cm. Hence, it is important to make an accurate estimate of K_e in order to capture nonlinear behavior at larger strains.

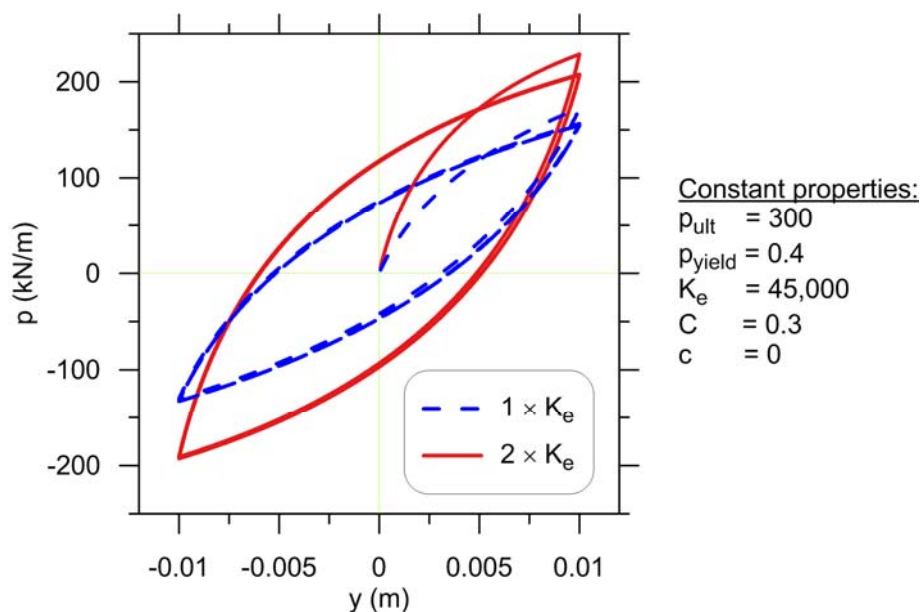


Figure 9-6: Effect of initial elastic stiffness K_e on *PySimple3* behavior for typical soft clay properties.

Values of the parameter δ that relates K_e to the soil elastic modulus were discussed in §8.3.2. In general these values apply to inertial interaction cases and have not been validated against real pile behavior. In the absence of more rigorous studies specifically targeting δ for kinematic pile SSI applications, lower- and upper-bound values of 1.0 and 3.0 are used for this study. The lower-bound value 1.0 is used for fixed-head piles, including pile groups connected by a stiff pile cap, which undergo translation with little corresponding rotation. The finite-element simulations discussed in the following section indicate that this value is reasonable. A value of $\delta = 3.0$ is used in this study for free-head piles such as extended-shaft bridge columns. These values fall within the range implied by the elastic solutions presented in Figure 8-7 and Table 8-2.

The effect of head-fixity condition on the pile response is most significant near the pile head, within the uppermost pile active length L_a . Hence, it is possible that using a δ value of 3.0 over the full length of a free-head pile results in an overestimate of the pile-soil interaction stiffness. To investigate whether or not this has a significant effect on the transfer functions computed for this study, a comparison was made between transfer functions computed using a uniform value of $\delta = 3.0$ over the full length of a free-head pile versus using $\delta = 3.0$ over a depth increment from the surface to eight pile diameters, and $\delta = 1.0$ below this depth. An example of the results is shown in Figure 9-7, which indicates that there is a negligible influence of the value of δ used over the lower portion of the pile on the computed transfer function. Hence, a uniform value of $\delta = 3.0$ will be used for free-head piles for simplicity.

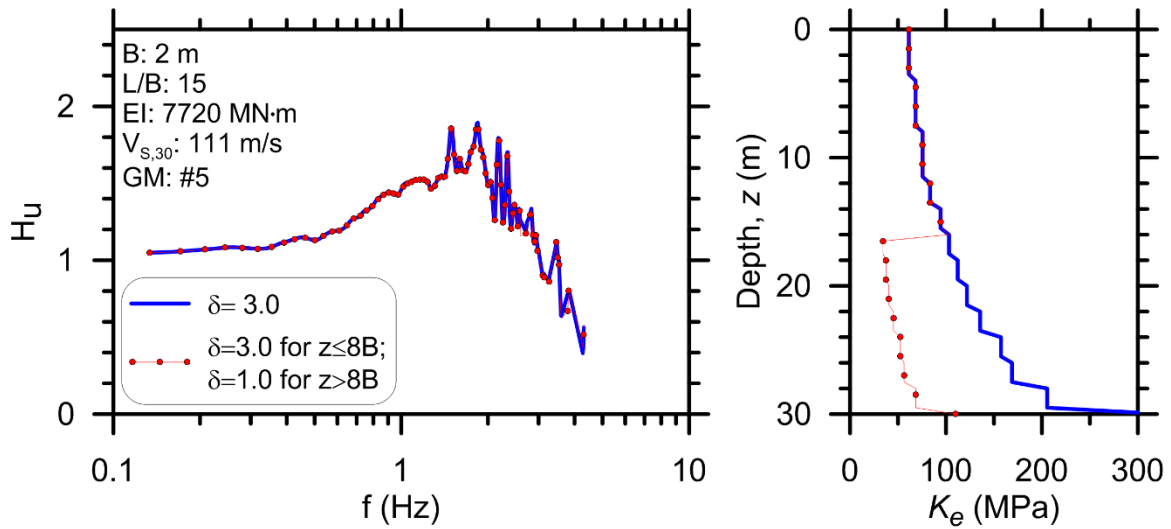


Figure 9-7: Transfer functions (left) and p - y curve initial stiffness parameter versus depth plots (right) for free-head pile with uniform and variable values of Winkler coefficient δ over the depth of the pile.

9.4.2 Ultimate Resistance

The API (1993) and Matlock (1970) values for p - y spring ultimate resistance are adopted for this study for sand and clay, respectively. Although these relationships are semi-empirical and do not account for seismic loading conditions, they provide a convenient method for estimating ultimate resistance. Furthermore, since the relative displacement between the pile and the soil due to kinematic interaction is small over the majority of the length of the pile, the ultimate resistance of the p - y springs will rarely be mobilized and the initial stiffness K_e and yield force p_{yield} are more important terms. Further research is needed to better characterize the ultimate resistance for both static and dynamic loading conditions.

9.4.3 Curvature Parameter and Yield Force

The parameter C controls the shape of the $PySimple3$ curve between the elastic region and the ultimate resistance, with smaller values of C resulting in more curvature if K_e and p_{ult} are held

constant (Figure 9-8). C can be calibrated to fit the results of model- or full-scale load tests, or can be set such that the curve passes through a target point.

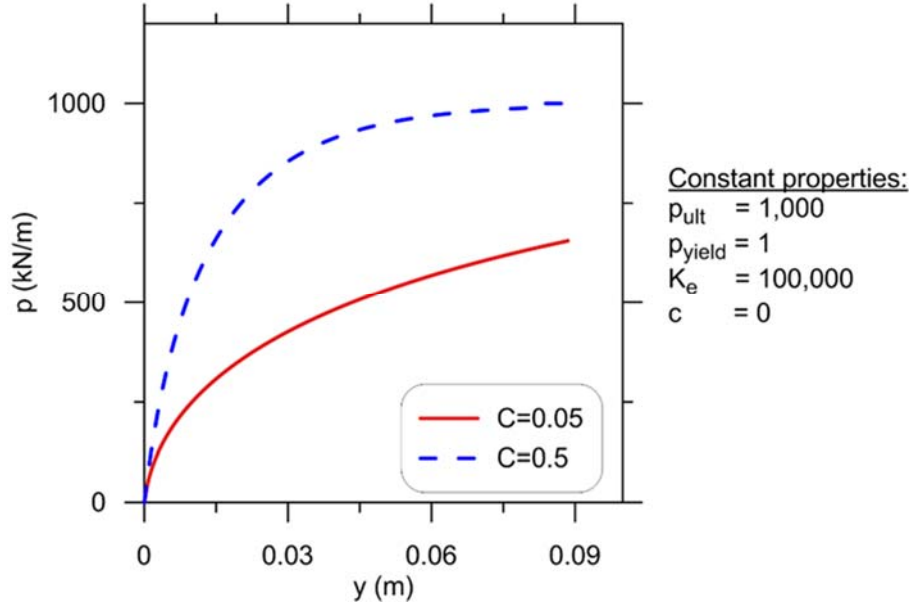


Figure 9-8: Effect of *PySimple3* curvature parameter C .

In this study, C is computed such that the curve passes through a target y_{50} point, where y_{50} is the deformation at which 50% of p_{ult} has been mobilized and, conveniently, is a parameter usually defined for existing p - y curve models. Choi et al. (2015) derive the following expression for C as a function of y_{50} and the remaining *PySimple3* parameters from the governing equations (9.1) through (9.5) presented above:

$$C = \frac{(p_{ult} - p_y) [\ln(p_{ult} - p_y) - \ln(p_{ult})] + p_{ult} [\ln(2) - 0.5] + p_y [1 - \ln(2)]}{K_e y_{50} - 0.5 p_{ult}} \quad (9.10)$$

where $p_y = K_e y_{yield}$ is the value of p at which yielding occurs. The relative pile-soil displacement y_{yield} is the value of y at the onset of soil nonlinearity. For this study, y_{yield} is estimated using Equation (8.25), the same approach taken in the Choi et al. (2015) study. Shear strain

corresponding to the onset of soil nonlinearity is approximated as 0.001% based on laboratory direct simple shear test results performed by Darendeli (2001).

As the target y_{50} value becomes smaller and the denominator of Equation (9.10) approaches zero, C approaches infinity. Very large values of C result in approximately elastic perfectly-plastic p - y behavior, which can lead to numerical instability in the finite element solution. (The trend towards this behavior is shown in Figure 9-8.) Permissible values of y_{50} must satisfy the expression:

$$y_{50} > \frac{0.5 p_{ult}}{K_e} \quad (9.11)$$

One approach for establishing the target y_{50} is to use expressions from an existing p - y relationship such as API (1993) or Matlock (1970). For sand, the API relationship tends to predict y_{50} values that are close to the lower bound defined by Equation (9.11), especially for loose to medium-dense sands at confining pressures greater than about 400 kPa. This is partially due to the implicit assumption in the API formulation that the stiffness of sand increases linearly with depth; the stiffness of sand can more accurately be described as scaling in proportion to the square root of confining stress (Hardin and Drnevich 1972). Hence, the API formulation tends to overpredict sand stiffness, with the magnitude of the overprediction increasing with depth. This results in a corresponding underestimate of y_{50} . The modified version of the API sand formulation described by Boulanger et al. (2003), in which soil stiffness is assumed to increase in proportion to the square root of confining pressure, also resulted in y_{50} values near the lower bound defined by Equation (9.11).

To address the shortcoming described above for estimating y_{50} for sand, a series of plane-strain finite element analyses of laterally-loaded piles were conducted using the program *Phase2*

(Rocscience 2013). The domain consists of a horizontal slice through the pile and the surrounding soil as shown in Figure 9-9. The plane-strain behavior is meant to capture the lateral pile-soil interaction below the depth at which a passive pressure wedge would form and displace upward near the ground surface. The sand was characterized as having minimum and maximum void ratios of 0.4 and 0.9, respectively, and a critical state friction angle of 32° (Bolton 1986). For three relative densities corresponding to loose, medium-dense and dense sand (20%, 50%, and 80%) and assumptions of 100% saturation and a specific gravity of solids of 2.65, unit weights and corresponding vertical stresses were calculated at depths of 5, 10, 20, and 40 m. Shear strength and stiffness properties of the sand were then estimated using a consistent framework to ensure that the properties scaled uniformly with changes in stress.

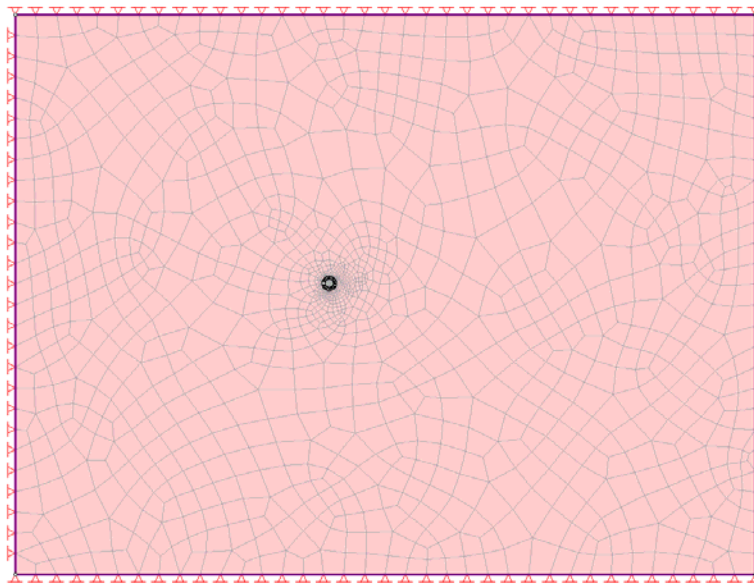


Figure 9-9: *Phase2* finite element domain for plane-strain analyses of laterally-loaded pile. Pile is displaced from left to right during the analyses.

Peak friction angles were calculated based on relative density, confining pressure, and mean effective stress at failure assuming a triaxial stress path after Bolton (1986). The resulting

values of ϕ' ranged from 32 to 45°; these values were used to compute the coefficient of lateral earth pressure at-rest K_0 using the expression for normally consolidated sand by Jaky (1948):

$$K_0 = 1 - \sin \phi' \quad (9.12)$$

Values of Young's modulus for the sand were estimated using an expression proposed by Lewis (1990) with the coefficients representing the average results of laboratory testing on sands at different relative densities and confining stresses. The expression captures the increase in stiffness of sand as a function of square root of confining pressure:

$$E_s = 1700 (p')^{0.5} \frac{p_a^{(0.5)}}{(0.3 + 0.7e^2)} \quad (9.13)$$

where p' is mean effective stress, p_a is atmospheric pressure in the same units as p' , and e is void ratio. The parameters ϕ' and E_s were used to define the Duncan-Chang (1970) nonlinear-elastic hyperbolic material model is *Phase2*. Soil Poisson's ratio $\nu = 0.3$ and a failure ratio $R_f = 0.9$ were used for the model. Although the Duncan-Chang model does not include plasticity, it provides a reasonable representation of the stress-strain behavior of soil up to the point of shear failure and is simple to define based on readily-quantifiable soil parameters.

Analyses were performed for the four depths listed previously for pile diameters of 0.5 and 2.0 m. The loose soil ($D_r = 20\%$) was not considered at the 40-m depth. The plane-strain behavior results in p - y curves that do not reach an asymptotic value of p_{ult} since increasing pile displacement mobilizes resistance in an increasingly larger zone of soil (which is likely a realistic behavior, although current p - y curves are not formulated this way). As such, p_{ult} was defined somewhat arbitrarily as the value of p for which the secant slope of the p - y curve decreased to 5% of the initial slope.

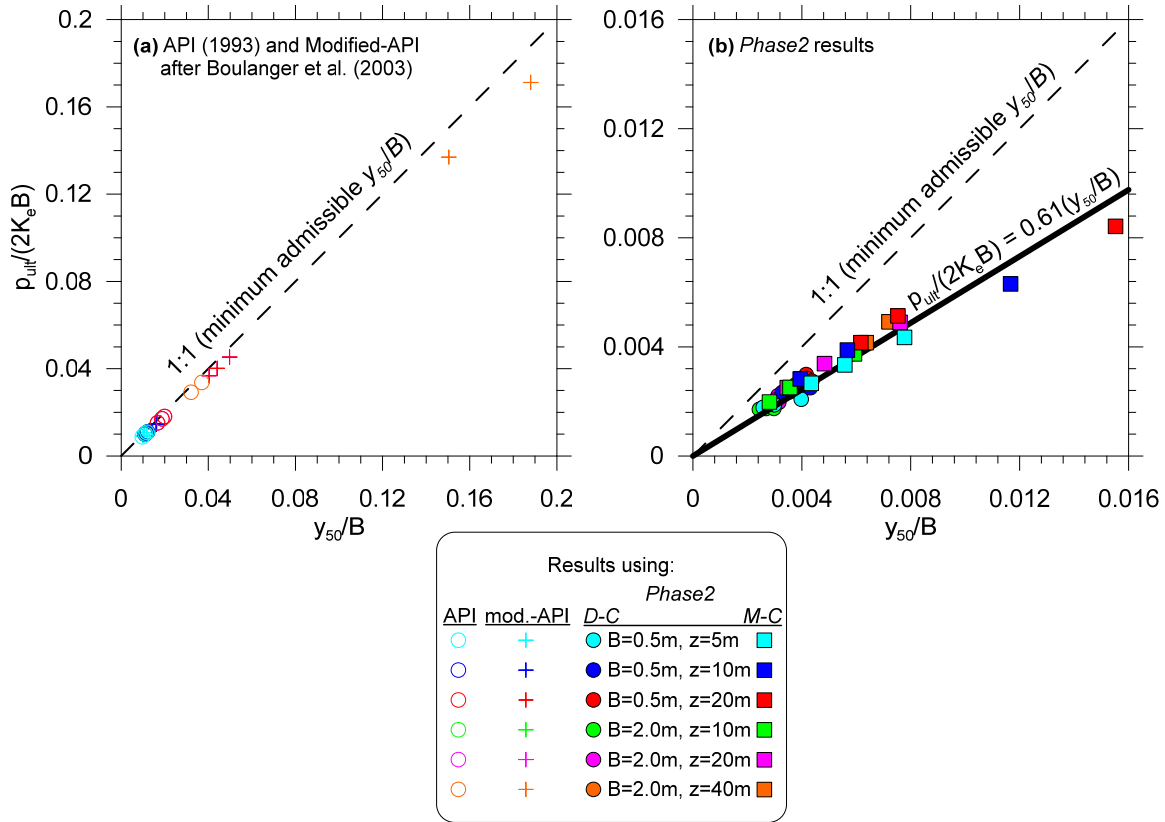


Figure 9-10: Comparison of normalized y_{50} values using (a) existing p - y relationships and (b) from results of plane-strain finite element simulations of laterally-loaded piles in *Phase2* using Duncan-Chang nonlinear-elastic (D-C) and Mohr-Coulomb (M-C) soil constitutive models.

The results of the simulations are presented in normalized form in Figure 9-10(b) along with the normalized values predicted by API (1993) and the modified API relationship presented by Boulanger et al. (2003) in Figure 9-10(a). The 1:1 slope line in Figure 9-10 represents the minimum value of y_{50}/B that satisfies Equation (9.11) for a given pile diameter; values of y_{50}/B plotting to the left of this line are inadmissible and values plotting near the line indicate approximately elastic perfectly-plastic behavior that can result in numerical instability. The best-fit linear trendline passing through the *Phase2* results can be simplified to the following expression:

$$y_{50} = \frac{0.82 p_{ult}}{K_e} \quad (9.14)$$

Equation (9.14) is used to define y_{50} for sand layers in this study.

9.4.4 Radiation Damping

As a pile vibrates, stress waves propagate or “radiate” away into the surrounding soil. This form of energy dissipation is known as radiation damping, or alternatively as geometric damping because the radiated energy tends to attenuate with increasing propagation distance. For dynamic pile analyses using continuum elements, radiation damping is usually accounted for by using an energy-absorbing boundary that prevents incident stress waves from reflecting back into the domain (e.g., Lysmer and Kuhlemeyer 1969). For Winkler-type analyses, if radiation damping is to be considered it must be incorporated into the pile-soil interaction elements. Equivalent viscous damping, modeled through a rate-dependent viscous dashpot, is typically utilized for this purpose. The viscous dashpot component is characterized by a dashpot coefficient, c , which is defined as the ratio of the force in the dashpot $p_{dashpot}$ to velocity dy/dt , i.e.:

$$p_{dashpot} = c \frac{dy}{dt} = c\dot{y} \quad (9.15)$$

The dashpot coefficient has units of $[F][T][L]^{-1}$ or equivalent, such that when multiplied by a velocity a force results.

For Winkler-type analyses, the energy dissipation due to radiation damping can be thought of as additional soil resistance for a given amount of relative pile-soil displacement (y) compared to the equivalent static or slow-monotonic loading case. Hence, a dynamic p - y curve including radiation damping would be stiffer than the p - y curve for the same pile and soil conditions undergoing static loading. This is depicted in Figure 9-11.

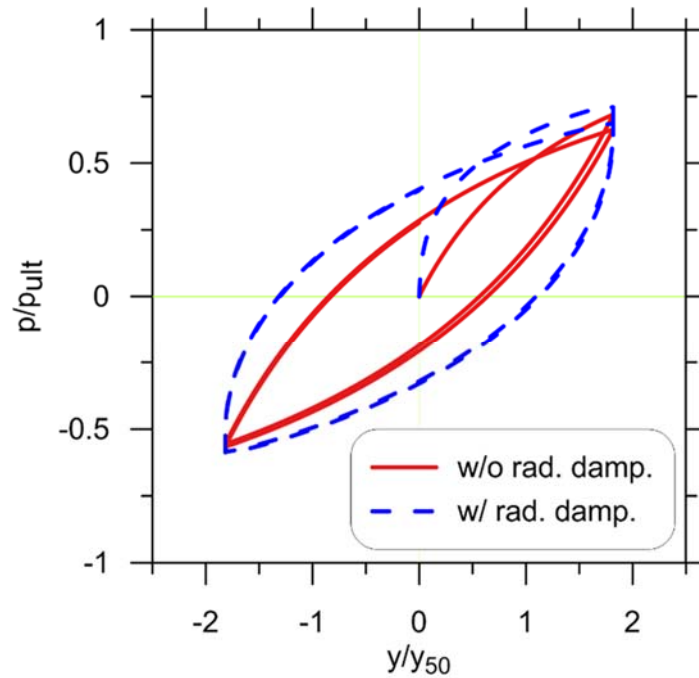


Figure 9-11: Effect of radiation damping in *PySimple3* material.

Cyclic lateral load tests of a full-scale four-pile group in granular soil by McManus and Alabaster (2004) found an increase in dynamic stiffness of about 50 percent over the static stiffness, which they concluded was at least partially due to radiation damping effects, supporting this concept. Ignoring radiation damping for dynamic loading conditions would therefore result in an underestimate of foundation stiffness and a corresponding overestimate of superstructure displacement and rotation. This may be a conservative design assumption for certain scenarios, but for the purpose of quantifying foundation input motions it could result in an unconservative overestimate of the kinematic pile-soil interaction effect, since the stiffness contrast between the pile and soil is a dominant factor controlling the interaction. Indeed, even the pioneering work on pile dynamics (e.g., Novak 1974) recognized the importance of radiation damping in forming an accurate solution.

Much of the previous research utilizing Winkler-type and continuum models for dynamic analysis of piles used equivalent-linear viscoelastic elements without a plastic component [e.g., Novak (1974), Kaynia and Kausel (1982), Gazetas and Dobry (1984a), Banerjee et al. 1987, Fan et al. (1991)]. Recognizing the importance of soil nonlinearity, especially for dynamic time domain analyses, other researchers have attempted to modify nonlinear p - y relationships to include dynamic effects, including radiation damping. Matlock et al. (1978) proposed adding a viscous dashpot in parallel with existing static p - y curves (Matlock 1970), perhaps the first attempt to explicitly capture dynamic effects with the nonlinear p - y method. Nogami and Konogai (1988) formulated a dynamic p - y element with separate near-field and far-field elements, where the nonlinear near-field element captured material hysteretic damping and the linear far-field element included a dashpot in parallel with a linear spring; a similar formulation has been adopted for the *PySimple3* material as described above. Badoni and Makris (1996) and Bentley and El Naggar (2000) also performed analyses with viscous damping in parallel to the hysteretic p - y response. However, Wang et al. (1998) demonstrated that this arrangement, which they term “parallel radiation damping”, can produce erroneous results because forces in the pile can effectively bypass the near-field hysteretic pile-soil interaction during high-velocity loading pulses by transmitting through the dashpot component directly to the far field. Wang et al. propose that a more appropriate arrangement is “series radiation damping” in which a nonlinear near-field element accounts for elastic or elastoplastic interaction at the soil-pile interface and a separate far-field element, connected in series to the near-field element, captures radiation damping. This formulation satisfies the intuitive notion that lateral loads must mobilize a response in the zone immediately surrounding the pile before energy can be radiated away to the far field. The modified *PySimple3* element uses series radiation damping.

While the conceptual motivation for including radiation damping is clear, successful implementation is dependent on accurately quantifying the dashpot coefficients, which is nontrivial and unfamiliar in the realm of traditional foundation design. Engineers face two significant challenges when quantifying dashpots: (i) choosing an appropriate relationship from the many available in the literature, and (ii) addressing frequency-dependence.

Quantifying pile radiation damping based on experimental results is a difficult proposition, to say the least. While it is feasible to estimate the total damping of a pile-soil system during forced-vibration testing (e.g., Ashford and Juirnarongrit 2003), this will include the combined effects of hysteretic damping in the pile and soil materials as well as radiation damping. While the former can be approximately inferred from material stress-strain curves if extensive instrumentation is used, there is no simple means for measuring radiation damping directly. Furthermore, even if the contribution of radiation damping to the total damping could be determined, there is an additional challenge in formulating the corresponding dashpot coefficients to be used with distributed springs and dashpots for Winkler-type analysis. Even if these results could be generated from a single test, there remains the issue of formulating generalized expressions for practical use. In light of these challenges, the available models for c are derived from a theoretical approach. Future experimental campaigns which are able to measure pile radiation damping more directly would be a valuable contribution to the field of pile dynamics.

Many researchers have used the theory of wave propagation in a linear viscoelastic medium to derive expressions for c . Berger et al. (1977) derived theoretical frequency-independent dashpot coefficients for a wave propagating in a one-dimensional elastic rod. Novak et al. (1978), expanding on the work of Novak (1974), developed a plane-strain solution based on a cylindrical elastic rod embedded in a viscoelastic halfspace (Baranov's solution). Gazetas and Dobry (1984a,

1984b) took a similar approach but assumed the rod was rigid and infinitely long, hence their expression does not include a pile modulus or length term. Makris and Gazetas (1992) proposed a simplified expression for c based on the results of the aforementioned studies and their own further analyses, and Kavvadas and Gazetas (1993) provided yet another expression with the same form as Gazetas and Dobry (1984a) but with slightly simplified coefficients. Nogami & Konagai (1988) approximated frequency-independent dashpot coefficients by calibrating the results of equivalent-linear viscoelastic time-domain BDWF analyses of a pile undergoing inertial head loading to frequency domain solutions. The relationship between normalized c and dimensionless frequency a_0 [defined in this case using the Equation (7.5) definition] from these references are shown in Figure 9-12. Note that the Nogami and Konagai (1988) far-field element formulation is actually a series of three elements; the value plotted in Figure 9-12 is the third and softest of the three dashpots. Note also that NIST (2012) Table 2-4b provides an impedance function for the equivalent pile head radiation damping to be used with the substructure method, but not dashpot coefficients for distributed Winkler-type springs for BDWF analyses.

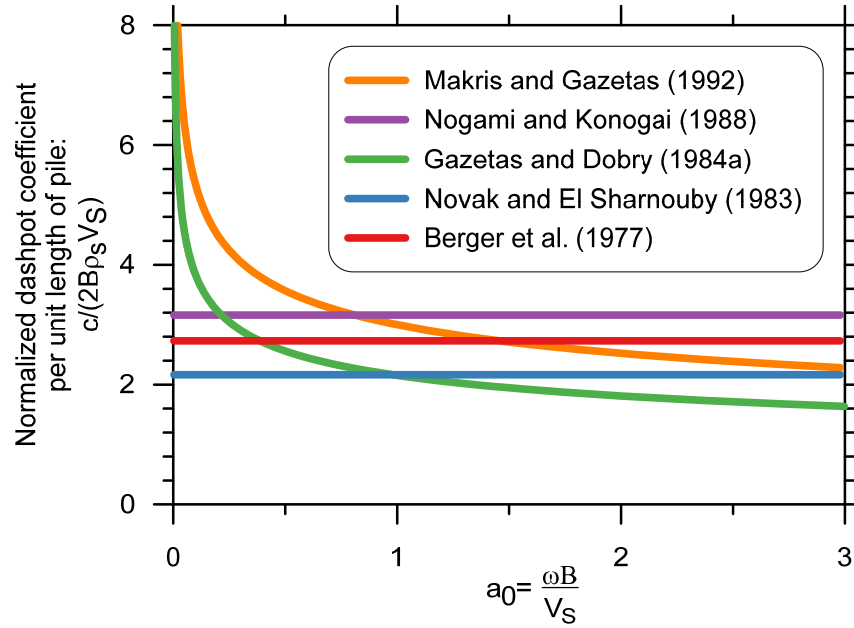


Figure 9-12: Normalized dashpot coefficient for $\nu = 0.25\text{m}$, $\rho_s = 1.7 \text{ Mg/m}^3$ and $E_p/E_s \approx 690$.

The frequency-dependent models indicate a sharp increase in c at low frequencies, but an approximately constant value for a_0 greater than about 0.5. While c may indeed be frequency-dependent, only frequency-domain solution approaches [e.g., Banerjee et al. (1987); Wu and Finn (1997a)] can explicitly implement such behavior. For time-domain solutions, which are used for this study and are the predominant method used for structural and geotechnical nonlinear analyses, it is necessary to specify a single value of c for the entire duration of the analysis. To do so, the foundation designer can either (1) choose a representative frequency, such as the fundamental frequency of the pile-soil system, to be used with a frequency-dependent expression for c , or (2) use a frequency-independent expression for c . Researchers that have made an effort to develop and evaluate nonlinear time-domain solution approaches for laterally-loaded piles tend to favor the latter, while those that have focused on developing analytical solutions can accommodate frequency dependence.

Using a computer implementation of the plane-strain solutions of Novak et al. (1978), Novak and El Sharnouby (1983) found an approximately linear relationship between pile damping and increasing frequency above the fundamental frequency of the soil profile. They concluded that a constant value of c can be used to represent equivalent viscous radiation damping at frequencies above the profile fundamental frequency, and that below this frequency only the soil hysteretic damping (also referred to as “material” damping) was significant. Gazetas (1991) and Syngros (2004) also proposed that radiation damping only be considered above a dimensionless “cutoff frequency” defined as:

$$a_{0,CUTOFF} = \frac{\omega_s B}{V_s} = \frac{2\pi \left(\frac{V_s}{4H} \right) B}{V_s} = \frac{\pi B}{2H} \quad (9.16)$$

where B is pile diameter and ω_s is the natural angular frequency of the site, based on the natural site period T computed from the well-known formula relating one-quarter wavelength of a harmonic oscillation to the thickness of the soil profile H :

$$T = \frac{4H}{V_s} \quad (9.17)$$

where V_s is the soil shear wave velocity. The fundamental frequency of the site is the inverse of Equation (9.17).

The concept that pile radiation damping cannot occur at frequencies below the site fundamental frequency only applies for an elastic pile embedded in an elastic soil layer underlain by rigid bedrock, hardly representative of realistic soil conditions. In this author’s opinion, this limitation can safely be ignored for realistic conditions.

The approach taken for this study is to define the dashpot coefficient using the Gazetas and Dobry (1984a) relationship at the frequency corresponding to the dimensionless frequency $\omega/\lambda V_s = 1.25$. This value approximately corresponds to $H_u = 0.5$ for the elastic analytical solutions (e.g., see Figure 8-3), and as will be shown in the next chapter, for the nonlinear analyses as well. The frequency corresponding to a 50-percent reduction in free-field motions was chosen because the purpose of this study is to define the conditions for which kinematic pile-soil interaction is significant, and especially to identify the frequency range over which significant deamplification of free-field motions could occur.

In addition to radiation and hysteretic damping, Rayleigh damping is used in the *OpenSees* analyses to achieve damping at low-strain. Unlike hysteretic damping or the type of radiation damping discussed above that are incorporated into the material model, Rayleigh damping operates directly on the mass and stiffness matrices in the formulation of the equation of motion that is solved in the finite-element method. Since soil is known to exhibit damping even at the smallest levels of measurable strain (e.g., Vucetic and Dobry 1991), incorporating small-strain damping is realistic, and is also computationally beneficial for achieving convergence.

9.5 PILE MODELING

For the present study, piles are modeled using 0.5-m long displacement-based beam-column elements. Pile nonlinearity is considered by using an equivalent EI representative of a reduced moment of inertia due to concrete cracking. The following subsections describe specific aspects of the structural modeling approach.

9.5.1 Pile Moment-Curvature Behavior

Reinforced-concrete (RC) elements exhibit nonlinear moment-curvature ($M-\phi$) behavior when flexural demands exceed the yield strength of either the concrete or reinforcing steel in tension or compression. Of greatest interest in the context of a laterally-loaded pile is the reduction in stiffness that occurs when concrete cracks in tension, since flexural demands during extreme event loading would typically be expected to exceed the cracking moment. As illustrated in Figure 9-13, the initial portion of the $M-\phi$ curve corresponds to linear-elastic material behavior across the entire section. The slope of a $M-\phi$ curve is the flexural rigidity of the section, so the slope of the elastic region corresponds to the elastic $E_p I_p$ computed using the gross moment of inertia of the section. The upper-bound of the elastic region is defined by cracking of the concrete in tension, which is typically the first nonlinear material behavior. In accordance with §5.6.1.1 of the Caltrans (2013) Seismic Design Criteria, for this study the cracked section stiffness is defined by the secant slope of the $M-\phi$ plot between the origin and the moment corresponding to the first yielding of the longitudinal reinforcing steel in tension, M_y .

For the generalized transfer function and spectral ratio prediction models generated from the results of this study, flexural rigidity of the pile is an input variable. Whether or not the value used should correspond to the elastic or cracked section stiffness depends on the anticipated behavior under design loading, and the foundation engineer is responsible for making this decision.

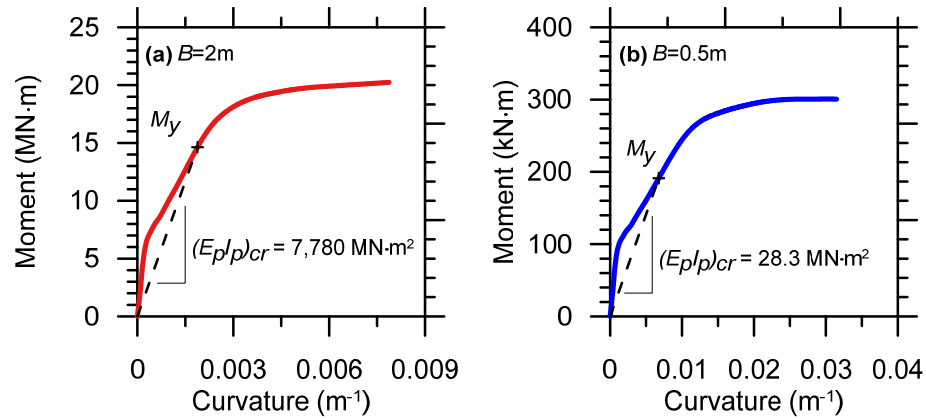


Figure 9-13: Moment curvature analyses conducted at axial load $P = 0.05 \cdot A_g \cdot f'_c$ for (a) 2-m and (b) 0.5-m diameter pile sections.

The $M-\phi$ plots shown in Figure 9-13 were computed using fiber models of the 2-m and 0.5-m diameter pile sections in *OpenSees*. In the fiber-modeling approach, the section is discretized into separate zones (fibers) characterized by unique uniaxial stress-strain behavior representative of, for example, reinforcing steel, confined concrete, and unconfined concrete. Radial discretization is used to define the circular cross sections. The following assumptions and analysis parameters were used for the $M-\phi$ analyses:

- The longitudinal reinforcing steel layout was based on a target steel ratio (ρ_{steel}) of 1.5-percent, with the following layouts used for the analyses:
 - For the 2-m diameter shaft, 32 No. 14 bars bundled in groups of two (to achieve adequate spacing between adjacent bars) with 6 inches (15.2 cm) of clear cover— $\rho_{steel} = 1.48\%$;
 - For the 0.5-m diameter shaft, 8 No. 7 bars with 3 inches (7.6 cm) of clear cover— $\rho_{steel} = 1.58\%$;

- Clear-cover from the edge of the pile to the edge of the longitudinal bars is based on the recommendations in the FHWA drilled shaft design manual (Brown et al. 2010) based on the diameter of the pile;
- Assumed concrete compressive strength of 5 ksi (34.5 MPa) modelled with the *ConcreteCM* uniaxial material model in *OpenSees*;
- Grade 60 steel for the longitudinal bars modelled using the *ReinforcingSteel* uniaxial material model with expected material properties (i.e., accounting or overstrength in accordance with the Caltrans (2013) Seismic Design Criteria)
- Confinement of the core concrete was not considered, where the core is the portion of the section inside the perimeter formed by the longitudinal bars. Because confined and unconfined concrete exhibit similar stress-strain behavior up to point of crushing of the unconfined concrete in compression, the effect on the $M-\phi$ behavior is only significant in the post-yield range;
- The number of discrete fibers was increased until the results were stable, which was achieved with 24 radial and 24 angular divisions within the core of the section and four radial and 24 angular divisions outside the core for the cover concrete; and
- Analysis were performed for an axial load P equal to 5-percent of the gross compressive capacity of the concrete section, i.e. $P = 0.05 * A_g * f'_c$.

The axial load imposed on a pile is a function of the tributary load supported by each bridge bent, the number and layout of piles relative to the number of columns or pier walls per bent,

geotechnical conditions over the length of the pile, whether axial or lateral loads govern the pile diameter, and many other factors. In addition, the pile axial load is likely to fluctuate during an earthquake as bents undergo frame action, and the axial load changes over the depth of the pile as load is shed into or added from the ground. Clearly there is no unique definition for a “typical” axial load for a pile foundation based solely on the section diameter. As discussed above, the axial load used to define the effective flexural rigidity for design cases should be based on the actual anticipated axial load during extreme event loading. In the absence of such information for the parametric analyses performed for this study, the arbitrary definition of $P = 0.05 * A_g * f'_c$ was adopted for simplicity, which is consistent with the typical axial load for reinforced concrete columns and is therefore a good approximation for extended-shaft column type foundations.

9.5.2 Pile Head Fixity Condition

The pile head-fixity conditions used in this study are either “fixed-head”—perfectly fixed against rotation, or “free-head”—completely free to rotate without encountering any rotational resistance. While these idealized assumptions are conceptually attractive and convenient for analytical purposes, the pile head boundary condition in a real structure falls somewhere between the two extremes.

Piles embedded in a reinforced pile cap or interconnected with stiff grade beams are often characterized as fixed-head, which implies that an imposed moment will result in zero rotation at the connection. However, the true rotational stiffness of these connections is less than rigid. Rotation at the connection could be accommodated either on a global or local scale, for example by rocking of the entire pile cap or by strain concentrated in the zone around the connection, respectively. Short of experimental measurements or continuum numerical modeling, the author is not aware of any geotechnical or structural references that provide general guidance on

quantifying this rotational stiffness. However, previous experience by the author has shown that while allowing a small amount of rotation at the pile head in BNWF analyses can significantly decrease moment demands, it does not have a significant influence on the pile head horizontal translation. Hence, use of a less-than-rigid boundary condition would not be expected to significantly change transfer functions computed for free-field versus pile-head horizontal displacement.

For conventional foundation design applications in which superstructure loads are carried through the foundation into the ground, a free-head assumption is reasonable for extended-shaft columns (i.e., the “flagpole” condition), or for piles that lack significant embedment or structural anchorage into a pile cap. However, for the kinematic pile-soil interaction case, it is important to remember that the load path acts in the opposite direction—ground movement results in foundation displacements and force effects which are subsequently imposed on the base of the superstructure. Hence, the pile-head fixity condition should be assessed in terms of the question *what resisting force/moment would be mobilized in above-ground structural elements due to a unit displacement/rotation at the pile head?* For extended-shaft columns, pile head rotation due to kinematic interaction would encounter resistance as the resulting rotation and corresponding moment and translations are carried up the column, through the column-to-superstructure connection (e.g., bearings and/or other anchorage between the bent cap and girders), and into the superstructure. Clearly these elements would provide some resistance to rotation such that the pile head is not truly “free” to rotate.

Despite these inconsistencies between real behavior and the idealized extremes, fixed- and free-head boundary conditions will be used for this study for several reasons. First, these extremes provide bounds on the problem. The true behavior is somewhere in between, and the foundation

designer can use judgment to interpret where in between these bounds their problem lies, or simply use whichever assumption results in greater demands. The latter approach is advocated in the realm of conventional deep foundation design for lateral loading by Reese et al. (2005). Second, the rotational resistance provided by pile-to-pile-cap connections and other above-ground structural elements depends on the specific geometry and material properties of each project, and thus is hard to generalize in a simplified design tool such as the transfer function models being developed for the present study. Finally, because free-head or fixed-head boundary conditions are the standard of practice for routine design, and because there are no established guidelines for quantifying rotational resistance, including rotational stiffness as a parameter in the transfer function model would make the model more difficult to implement in practice. The intent of this study is to provide a transfer function model that is compatible with the current state of practice for seismic design, so such a limitation would be counterproductive. Future studies could investigate the influence of head-fixity through parametric analysis of varying rotational spring stiffness applied at the pile head.

9.5.3 Pile Shear Deformations

Conventional beam-on-Winkler-foundation analyses treat the pile as an Euler-Bernoulli beam, for which flexural demands are resisted structurally by the flexural rigidity (EI) of the pile (see derivation in §8.1). Shear deformations are neglected in this approach, which is a reasonable assumption when it is kinematically possible for the pile to respond to imposed demands primarily in flexure, such as for the “flagpole” configuration. However, significant rotational resistance provided by embedment into a pile cap or toe embedment into rock may result in shear deformations that are significant within a few pile diameters of the point of rotational restraint. For example, Massone and Lemnitzer (2012) found that shear deformations accounted for up to 40

percent of total horizontal displacement near the pile head connection during full-scale lateral load tests of 24-inch (0.61-m) diameter piles. Moreover, when flexural demands approach the pile plastic moment capacity, these shear deformations can be nonlinear in terms of the shear-stress versus shear-strain behavior even when shear stresses are well below the shear strength of the concrete (e.g., Massone and Wallace 2004), which further complicates interpretation of load test results. The Massone and Lemnitzer study along with follow-up work by Khalili-Tehrani et al. (2014) suggests that commonly used semi-empirical p - y curve models derived from free-head lateral load test results (e.g., API 1993) are inaccurate for fixed-head conditions because shear deformations were not considered explicitly in their derivation.

For the case of kinematic pile-soil interaction for fixed-head piles, using a numerical model that allows shear deformations would be expected to result in slightly larger total displacement near the pile head, and thus increase transfer function ordinates (H_u) relative to the same case analyzed without consideration of shear deformations, such as done herein. However, simply using a structural model that accounts for shear deformations, such as the Timoshenko beam column element in *OpenSees*, or the recently added cyclic shear-flexure interaction model by Kolozvari et al. (2015a,b), could provide misleading results. This is because, as determined from the experimental work described above, alternative p - y curves should be used in combination with structural consideration of shear deformations, and a generalized p - y model for this purpose is not currently available. A future study that integrates the Kolozvari et al. cyclic shear-flexure interaction elements and p - y curves that explicitly consider shear deformations into the numerical modeling framework used for the present study could shed light on the influence of shear-flexure interaction for kinematic transfer functions.

9.5.4 Pile Groups

Pile groups are modeled as multiple individual piles connected at their heads through massless rigid links using the *equalDOF* command in *OpenSees*. Pile caps are not modelled explicitly because their mass and stiffness would result in inertial and kinematic interaction in addition to the pile-soil interaction. The rigid link between piles combined with a fixed-head pile boundary condition essentially captures the restraint offered by the pile cap without introducing additional SSI, such that pile-soil interaction can be studied independently. In real systems utilizing pile groups, the pile cap motion which excites the superstructure depends on kinematic pile-soil interaction as well as kinematic interaction between the pile cap and the ground. For example, an embedded pile cap is subjected to ground motions imposed through lateral earth pressure on its sides, horizontal motions imposed on its base, and the motions of the piles which it connects. Depending on the surficial soil stiffness and the pile cap dimensions, particularly the depth of embedment, the pile cap motion could be dominated by cap-soil interaction more than pile-soil interaction. Future studies could investigate this effect by explicitly modeling pile caps in addition to piles.

The pile group layout considered for the present study is for a 2x3 group of 2-m diameter piles on a 7.5-m center-to-center spacing (i.e., $3.75 \cdot B$) as shown in Figure 9-14. This configuration is typical for support of large bridge bents, and use of $B = 2$ -m piles allows for direct comparison to the 2-m single pile results. The incoherent ground motions discussed below in §9.7.3 were imposed on the piles such that each pile in the group experienced a different input motion. The motion at each pile head is identical because of the rigid links, and effectively is an average of the motions imposed on the individual piles, similar to the concept of base slab averaging.

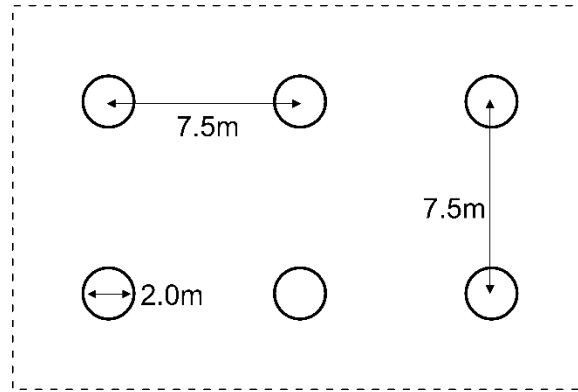


Figure 9-14: Pile group layout considered for analyses.

Additional group configurations were not considered because of the considerable effort required to generate incoherent ground motions at each pile location as well as the significant computational demand for running dynamic group analyses.

9.6 SOIL PROFILES FOR ANALYSES

Six soil profiles were developed based on cone penetration test (CPT) soundings. The purpose of developing soil profiles from real sites rather than using simple fictitious homogeneous or layered models such as those used in past studies is to examine the effect that realistic subsurface variability has on the results. Soil stiffness, quantified by the time-averaged shear wave velocity in the upper 30 m of the profile ($V_{s,30}$) ranges between about 100 and 400 m/s for the six soil profiles. These bounds are intended to capture the range of soil stiffness over which kinematic pile-soil interaction is likely to be significant as suggested by the elastic solutions presented in the previous chapter. Likewise, for a given pile stiffness, the range is intended to extend to high enough soil stiffness such that the conditions for which kinematic interaction is no longer significant can be defined.

CPT data used to develop the six soil profiles was obtained from the United States Geological Survey (USGS) research division's repository of CPT data, available online (<http://earthquake.usgs.gov/research/cpt/>). As indicated by the shear wave velocity profiles in Figure 9-15, sites were chosen that showed relatively uniform gradients of shear wave velocity versus depth in order to avoid the large shear demands that are imposed on piles at such an impedance contrast. Sites 1, 2, and 4 contain a combination of granular and cohesive layers, while Sites 3 and 6 are all granular, and Site 5 is all stiff clay. Layer thicknesses and relevant soil properties for each of the six sites are presented in Appendix D. A general description is also provided of the real sites which are represented, including their inferred geologic history and depositional environment. In general the profiles were discretized into 0.5-m thick layers to match the discretization of pile elements so that input displacement time series could be computed from ground response analysis without interpolation.

The arbitrary metric $V_{S,30}$ was used as a convenient measure of the site stiffness and because of its familiarity in practice (e.g., for building code site classifications); as will be shown in the results chapter, shear wave velocity computed over the length of the pile is more relevant for describing pile-soil interaction. Table 9-2 gives values of time-averaged V_S computed over depth intervals corresponding to the four pile lengths from Table 9-1, denoted as $V_{S,z}$, where z is the depth increment over which the computation is made. When not referring to a specific pile length, this term will subsequently be denoted by the variable $V_{S,L}$.

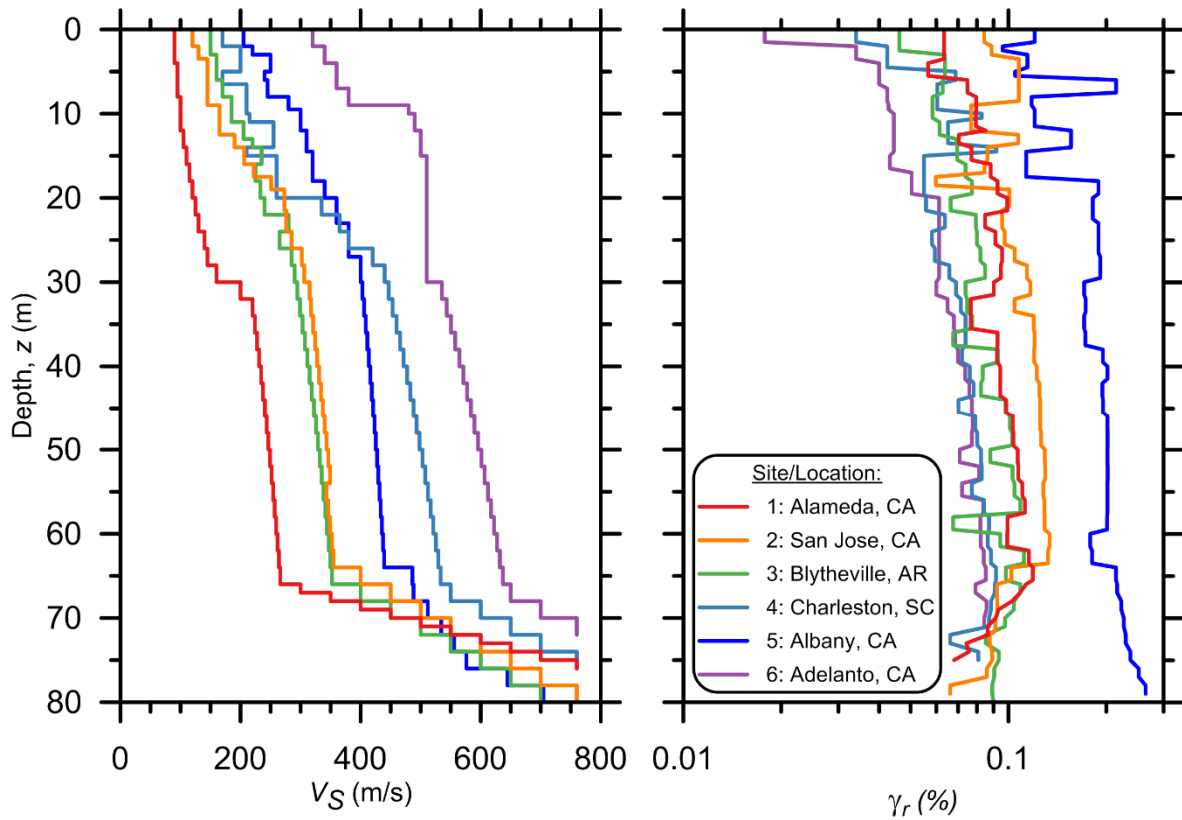


Figure 9-15: Shear wave velocity and reference strain (γ_r) profiles for Sites 1 through 6.

Table 9-2: Site time-averaged shear wave velocity characteristics for Sites 1-6.

Site:	1	2	3	4	5	6
$V_{S,7.5}$ (m/s)	92	134	158	186	230	344
$V_{S,15}$ (m/s)	97	150	176	204	259	396
$V_{S,30}$ (m/s)	111	192	217	264	305	446
$V_{S,60}$ (m/s)	151	244	253	332	351	504
$V_{S,H}$ (m/s)	173	280	289	367	383	525
Thickness (H , m)	76.0	80.0	82.0	76.0	80.0	72.00

9.7 GROUND MOTIONS

9.7.1 Baker et al. (2011) Ground Motion Suite

Input motions for the ground response analyses were sourced from the collection of motions developed by Baker et al. (2011) for PEER Transportation Research Program projects. Multiple

sets of motions are included in the Baker et al. set; for this study the “*Set #2, broad-band ground motions corresponding to $M 7.0$, R [source-to-site distance] = 10 km, and rock conditions*” are used. These motions are specifically intended to represent rock conditions with an average V_s of 760 m/s for use in ground response analysis, and were selected by Baker et al. such that the median and \pm standard deviation response spectra computed from the 40 unscaled motions match the Boore and Atkinson (2008) ground motion prediction equations. A basic description of the motions is provided in Table 9-3, and Table 9-4 lists their peak ground acceleration, velocity, and displacement (PGA, PGV, and PGD) values. Table 9-5 lists minimum, maximum, and mean PGA/PGV/PGD for the 40 motions, showing that the set covers a wide range in terms of these intensity measures. For each motion, a fault-normal (FN), fault-parallel (FP), and vertical record are available. The fault normal (FN) component of each ground motion is used for this study, which on average is slightly stronger than the FP component. Further details of the motions are available in the Baker et al. report.

Table 9-3: Ground motion records used for analyses (after Baker et al. 2011).

Record number	NGA Record Sequence Number	Earthquake Name	Year	Station	Magnitude	Closest Distance
1	72	San Fernando	1971	Lake Hughes #4	6.6	25.1
2	769	Loma Prieta	1989	Gilroy Array #6	6.9	18.3
3	1165	Kocaeli, Turkey	1999	Izmit	7.5	7.2
4	1011	Northridge-01	1994	LA - Wonderland Ave	6.7	20.3
5	164	Imperial Valley-06	1979	Cerro Prieto	6.5	15.2
6	1787	Hector Mine	1999	Hector	7.1	11.7
7	80	San Fernando	1971	Pasadena - Old Seismo Lab	6.6	21.5
8	1618	Duzce, Turkey	1999	Lamont 531	7.1	8.0
9	1786	Hector Mine	1999	Heart Bar State Park	7.1	61.2
10	1551	Chi-Chi, Taiwan	1999	TCU138	7.6	9.8
11	3507	Chi-Chi, Taiwan-06	1999	TCU129	6.3	24.8
12	150	Coyote Lake	1979	Gilroy Array #6	5.7	3.1
13	572	Taiwan SMART1(45)	1986	SMART1 E02	7.3	-
14	285	Irpinia, Italy-01	1980	Bagnoli Irpinio	6.9	8.2
15	801	Loma Prieta	1989	San Jose - Santa Teresa Hills	6.9	14.7
16	286	Irpinia, Italy-01	1980	Bisaccia	6.9	21.3
17	1485	Chi-Chi, Taiwan	1999	TCU045	7.6	26.0
18	1161	Kocaeli, Turkey	1999	Gebze	7.5	10.9
19	1050	Northridge-01	1994	Pacoima Dam (downstr)	6.7	7.0
20	2107	Denali, Alaska	2002	Carlo (temp)	7.9	50.9
21	1	Helena, Montana-01	1935	Carroll College	6.0	-
22	1091	Northridge-01	1994	Vasquez Rocks Park	6.7	23.6
23	1596	Chi-Chi, Taiwan	1999	WNT	7.6	1.8
24	771	Loma Prieta	1989	Golden Gate Bridge	6.9	79.8
25	809	Loma Prieta	1989	UCSC	6.9	18.5
26	265	Victoria, Mexico	1980	Cerro Prieto	6.3	14.4
27	1078	Northridge-01	1994	Santa Susana Ground	6.7	16.7
28	763	Loma Prieta	1989	Gilroy - Gavilan Coll.	6.9	10.0
29	1619	Duzce, Turkey	1999	Mudurnu	7.1	34.3
30	957	Northridge-01	1994	Burbank - Howard Rd.	6.7	16.9
31	2661	Chi-Chi, Taiwan-03	1999	TCU138	6.2	22.2
32	3509	Chi-Chi, Taiwan-06	1999	TCU138	6.3	33.6
33	810	Loma Prieta	1989	UCSC Lick Observatory	6.9	18.4
34	765	Loma Prieta	1989	Gilroy Array #1	6.9	9.6
35	1013	Northridge-01	1994	LA Dam	6.7	5.9
36	1012	Northridge-01	1994	LA 00	6.7	19.1
37	1626	Sitka, Alaska	1972	Sitka Observatory	7.7	34.6
38	989	Northridge-01	1994	LA - Chalon Rd	6.7	20.5
39	748	Loma Prieta	1989	Belmont – Envirotech	6.9	44.1
40	1549	Chi-Chi, Taiwan	1999	TCU129	7.6	1.8

Table 9-4: Intensity measures for ground motion set.

Record number	Earthquake Name	Year	Magnitude	PGA (g)	PGV (m/s)	PGD (m)
1	San Fernando	1971	6.6	0.15	0.08	0.02
2	Loma Prieta	1989	6.9	0.16	0.17	0.06
3	Kocaeli, Turkey	1999	7.5	0.15	0.23	0.10
4	Northridge-01	1994	6.7	0.16	0.11	0.03
5	Imperial Valley-06	1979	6.5	0.15	0.18	0.08
6	Hector Mine	1999	7.1	0.34	0.37	0.14
7	San Fernando	1971	6.6	0.09	0.07	0.01
8	Duzce, Turkey	1999	7.1	0.16	0.13	0.08
9	Hector Mine	1999	7.1	0.07	0.07	0.03
10	Chi-Chi, Taiwan	1999	7.6	0.20	0.41	0.36
11	Chi-Chi, Taiwan-06	1999	6.3	0.34	0.17	0.06
12	Coyote Lake	1979	5.7	0.45	0.52	0.07
13	Taiwan SMART1(45)	1986	7.3	0.13	0.13	0.05
14	Irpinia, Italy-01	1980	6.9	0.19	0.29	0.10
15	Loma Prieta	1989	6.9	0.27	0.26	0.13
16	Irpinia, Italy-01	1980	6.9	0.12	0.18	0.11
17	Chi-Chi, Taiwan	1999	7.6	0.60	0.44	0.38
18	Kocaeli, Turkey	1999	7.5	0.24	0.52	0.44
19	Northridge-01	1994	6.7	0.50	0.49	0.06
20	Denali, Alaska	2002	7.9	0.09	0.10	0.05
21	Helena, Montana-01	1935	6.0	0.15	0.06	0.01
22	Northridge-01	1994	6.7	0.16	0.18	0.02
23	Chi-Chi, Taiwan	1999	7.6	0.96	0.69	0.31
24	Loma Prieta	1989	6.9	0.14	0.29	0.07
25	Loma Prieta	1989	6.9	0.37	0.12	0.06
26	Victoria, Mexico	1980	6.3	0.63	0.31	0.13
27	Northridge-01	1994	6.7	0.23	0.14	0.03
28	Loma Prieta	1989	6.9	0.29	0.31	0.07
29	Duzce, Turkey	1999	7.1	0.11	0.10	0.09
30	Northridge-01	1994	6.7	0.11	0.08	0.02
31	Chi-Chi, Taiwan-03	1999	6.2	0.13	0.20	0.04
32	Chi-Chi, Taiwan-06	1999	6.3	0.06	0.09	0.04
33	Loma Prieta	1989	6.9	0.41	0.18	0.05
34	Loma Prieta	1989	6.9	0.43	0.39	0.07
35	Northridge-01	1994	6.7	0.58	0.77	0.20
36	Northridge-01	1994	6.7	0.38	0.22	0.05
37	Sitka, Alaska	1972	7.7	0.10	0.07	0.05
38	Northridge-01	1994	6.7	0.19	0.19	0.02
39	Loma Prieta	1989	6.9	0.14	0.20	0.06
40	Chi-Chi, Taiwan	1999	7.6	1.01	0.60	0.51

Table 9-5: Summary of ground motion intensity measures

Value	PGA (g)	PGV (m/s)	PGD (m)
Minimum	0.06	0.06	0.01
Maximum	1.01	0.77	0.51
Mean	0.28	0.25	0.11

9.7.2 Ground Response Analyses

To define the free-field ground motion at the p - y spring depths for the BDNWF models, each of the 40 motions was propagated through a one-dimensional ground response analysis model in the program *DEEPSOIL* (Hashash et al. 2015). *DEEPSOIL* analyses were conducted using the nonlinear time-domain total stress method. Using the idealized profiles for each of the six sites presented in Appendix D, modulus reduction and damping curves were developed using the procedures of Menq (2003) and Darendeli (2001) for granular and cohesive materials, respectively. The “hybrid” procedure recommended by Yee et al. (2013) was used to ensure that the modulus reduction curves matched the inferred shear strength of the material at large strain, although strains approaching these levels were generally not mobilized during the analyses. Profiles of reference strain γ_r for the modulus reduction curves are shown alongside the V_s profiles in Figure 9-15. The reference strain corresponds to 50-percent modulus reduction (i.e., $G/G_{max} = 0.5$) and thus is a good proxy for the amount of nonlinearity exhibited by the material, with smaller values indicating the soil will exhibit greater nonlinearity at small strains.

As described above, the idealized site stratigraphy is based on real CPT data to the approximate maximum depth of the CPT sounding, typically between 30 and 40 m. Below this depth, additional layers were added to the profile to create a gradual transition to the elastic bedrock. This was done so that the input motions, which are representative of outcrop motions on

rock with an average $V_S=760$ m/s, would not encounter a strong impedance contrast at the base of the profiles.

The following options were used for the *DEEPSOIL* analyses:

- Pressure-dependent modified Kodner-Zelesko nonlinear backbone formulation (Matasovic 1993) with non-Masing unloading/reloading formulation;
- Input motions specified as outcrop motions;
- Elastic half-space (bedrock) with $V_S=760$ m/s and unit weight 22 kN/m^3 underlying the soil profiles;
- Frequency-independent damping formulation; and
- When needed to achieve convergence, sub-stepping of time increments using linear interpolation of input motion with maximum strain increment of 0.005.

Acceleration time series computed from *DEEPSOIL* for each layer were manually post-processed to generate displacement records, which are needed as the input to the soil nodes of the p - y springs for the *OpenSees* analyses. Performing the integration necessary to compute displacement from acceleration time series, whether executed in the time or frequency domain, is a nontrivial exercise that can result in spurious amplification of low frequency noise if proper filtering procedures are not implemented. Recent versions of *DEEPSOIL* offer the option to export displacement records computed during direct integration of the equation of motion, but no filtering is applied to these records.

For this study, high-pass filtering was applied to remove low-frequency noise using a third-order Butterworth filter at frequencies above about 0.1 to 0.2 Hz. To remove spurious high frequency noise, the motions were also filtered using a low-pass Butterworth filter at the higher of (i) the low-pass frequency used for the original PEER ground motion processing or (ii) the maximum frequency which could be propagated through the *DEEPSOIL* model, which depends on thickness and shear wave velocity of the layers. Generally the former controlled. In addition, the acceleration time series were baseline corrected and zero-padded at the beginning and end of each record. The transition between a displacement of zero and the computed displacement was achieved with a cosine filter over 20 time increments; failure to do so can result in significant low frequency noise even if the beginning and end displacements have relatively small amplitudes.

The fundamental frequency of each site as computed by *DEEPSOIL* is given in Table 9-6.

Table 9-6: Site fundamental frequencies.

Site:	1	2	3	4	5	6
Site Fundamental Frequency f_s (Hz)	0.57	0.87	0.88	1.21	1.20	1.82

9.7.3 Ground Motion Incoherence

Real ground motions exhibit incoherence, or variation between two physical locations, because of two effects. The first is the wave-passage effect, which for inclined waves simply characterizes the delay in arrival time of a uniform planar wavefront between two locations. The second effect, termed “stochastic” incoherence, is due to the inherent spatial variability of the ground motion itself, since earthquake ground motions are generated not at a single point but along a heterogeneous fault, and from the scattering of waves due to material heterogeneity at the site. Abrahamson (1992a) and others have demonstrated that this can have important consequences for SSI.

Because *DEEPSOIL* performs one-dimensional ground response analysis assuming vertically-propagating shear waves, the only component of incoherence that is captured is the influence of changing soil properties with depth; the wave passage effect and stochastic incoherence are not captured. For single pile foundation, this is acceptable. For pile groups, however, ground motion incoherence results in different motion being imposed on each pile within the group. Much like the concept of base-slab averaging for shallow and mat foundations, the response of a stiff pile cap represents an average of the motions imposed on each pile within the group.

To capture ground motion incoherence in the horizontal direction for the pile group simulations in this study, spatially-variable ground motions (SVGM) have been generated using the program *FDW2D.r*, based on a simulation routine described by Ancheta and Stewart (2015). Starting with one of the 40 input motions as a “seed” motion corresponding to a corner pile location within the pile group shown in Figure 9-14, a motion was generated at each of the five remaining pile locations that matches a set of target spatially variable ground motion (SVGM) functions. Dr. Timothy Ancheta was hired as a sub-consultant for this project to generate the incoherent motions, and the following is a summary of his work.

The basic process of simulating an incoherent motion is to modify a seed ground motion by adding a random phase and amplitude at each frequency to match target coherency and amplitude models that are consistent with empirical observations. Additionally, for the method used here, the coherency between the seed-to-simulation and simulation-to-simulation matches the target coherency function for all locations simultaneously. The *FDW2D.r* simulation method uses an energy randomization process called Frequency Dependent Windowing (FDW). The FDW method is used to conserve the low frequency (coherent) energy and resample the high frequency

(random) energy to be consistent with a set of SVGGM functions without introducing unwanted spectral leakage.

The FDW method is a non-stationary simulation routine that utilizes a modified short-time Fourier transform (MSTF) routine. The MSTF routine allows preservation of the non-stationary properties of the motion and incorporation of time-varying nonlinear spectral modifications. The routine is summarized in the following steps:

- The seed time series is split into short time segments;
- A discrete Fourier transform (DFT) is performed on the segment;
- Phase angles at each frequency within a desired frequency range (dependent on segment length) are modified consistent to a coherency function for each segment [this procedure is fully described in Ancheta (2010)];
- The new set of Fourier phase angles is combined with the seed Fourier amplitudes and transformed into the time domain with an inverse Fourier transform (IFT);
- The modified short time segments are recombined to form a modified time series;
- The preceding steps are performed multiple times for multiple segment lengths, with each segment length having a specified frequency range over which phase angles are modified. Hence, multiple modified time series are created. Segment lengths and corresponding frequency limits used are shown in Table 9-7;

- The multiple modified time series are band-pass filtered within the limits of the pass-band matching the band of the modification to combine the modified frequency bands in the frequency domain;
- The non-overlapping frequency bands are transformed back to the time domain to create the final broadband modified time series.

Table 9-7: Segment duration (L) and frequency bands (b) used in the FDW routine.

Segment Duration (sec)	Frequency limits (Hz)
1.28	2-Nyquist
2.56	1-2
5.12	0.5-1
10.24	0.25-0.5
20.48	0.12-0.25
Full duration of time series	0-0.12

The SVGGM generated using this procedure all occur within a single horizontal plane. In other words, the seed and simulated motions exist at different x and y horizontal locations, but at the same depth z . For the purpose of this study, this depth corresponds to the base of the soil profiles. To generate motions at each depth increment for input to the BDNWF group analyses, transfer functions were computed from the *DEEPSOIL* results relating the seed input motions to the motion computed at the depth of each layer. These transfer functions were then used to compute a ground motion at the depth of each layer from the SVGGM, effectively propagating the same amount of spatial variability generated at the base of each profile from *FDW2D.r* uniformly over the full depth of the profile. In other words, horizontal and vertical incoherence are uncoupled in the approach used here, but both are ultimately reflected in the ground motions imposed on the pile group.

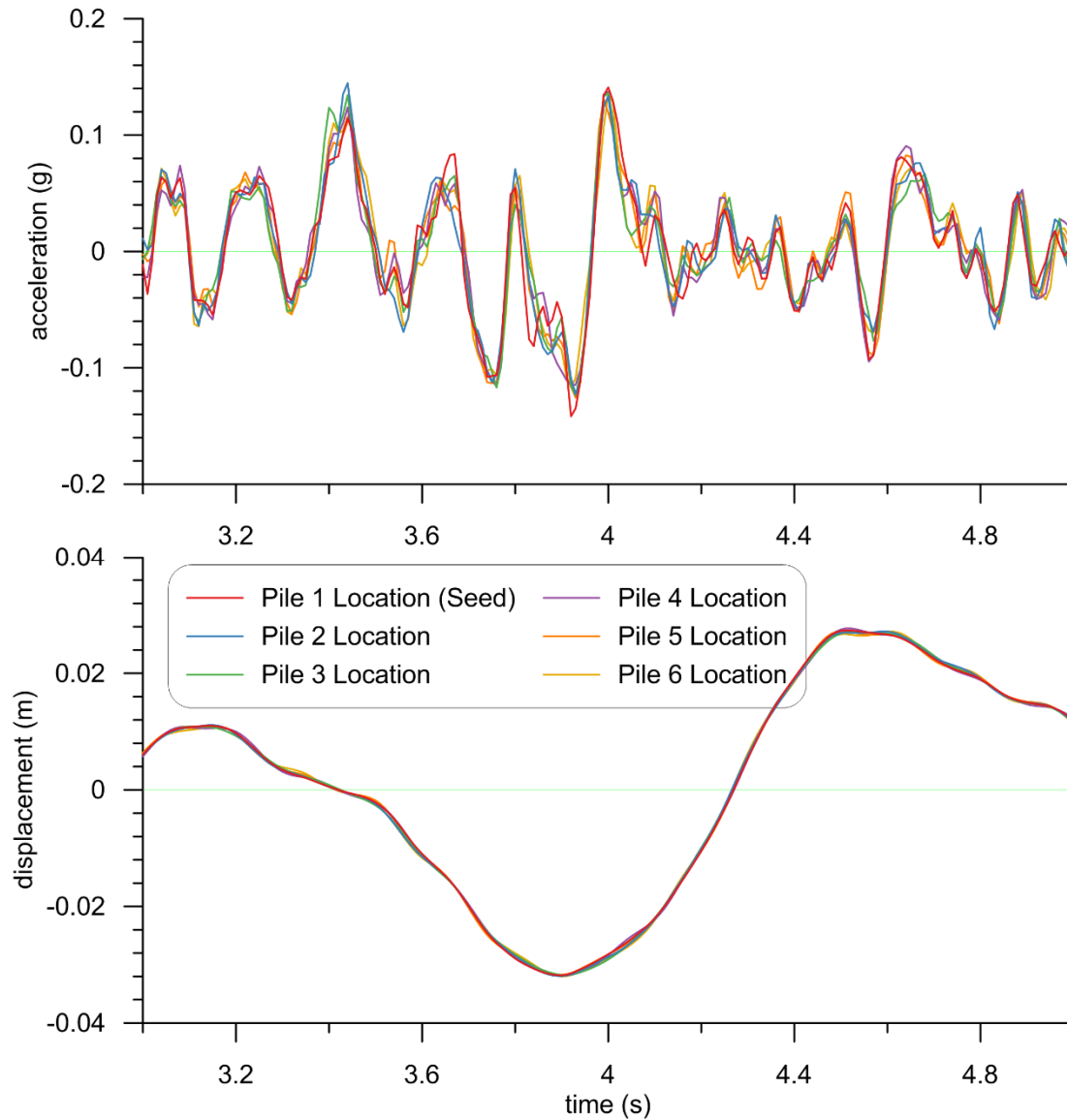


Figure 9-16: Acceleration (top) and displacement (bottom) time series for seed motion (1971 San Fernando earthquake, Lake Hughes #4 recording station) and simulated spatially-variable ground motions at locations corresponding to other piles in group layout shown in Figure 9-14.

An example of the seed and SVGM is shown in Figure 9-16 in terms of acceleration and displacement. Note that only a short time window of two seconds is shown. It is apparent from this figure that while a modest amount of variability exists between pile locations in terms of acceleration, the displacement time series are nearly identical. This is because incoherence

increases with increasing frequency, and displacement tends to amplify low frequency energy and de-amplify high frequency energy relative to acceleration.

9.8 OPENSEES ANALYSIS

The following parameters were used to define the *OpenSees* finite-element analyses:

- Penalty constraints to enforce boundary conditions,
- Norm of the displacement increment (NormDispIncr command) to test for convergence with a starting tolerance of 10^{-6} m;
- Krylov-Newton solution algorithm (Scott and Fenves 2010) used to solve nonlinear system of equations,
- If convergence was not achieved at a particular step, the modified-Newton algorithm with initial stiffness was used; if this failed to converge, the tolerance was decreased by an order of magnitude and the Krylov-Newton algorithm was used again,
- Newmark integrator with $\gamma = 0.5$ and $\beta = 0.25$, and
- A $P-\Delta$ transformation was utilized to capture secondary moments induced by offset axial loads.

10 Results

10.1 SINGLE PILES

Horizontal displacement transfer function results for each pile/site/motion combination are presented in Figures 10-1 through 10-12. Each figure is for one site and contains four plots, one for each of the four piles, where each plot contains the computed transfer functions ordinates with high coherence for the 40 ground motions along with the mean and \pm one standard deviation of the results shown in that plot. Separate figures are presented for the fixed- and free-head conditions. Collectively, the plots represent the results of 1,920 single pile simulations.

Because the time step, duration, and high- and low-pass filtering for the input ground motions vary, the frequency vector computed during the Fast Fourier Transform (FFT) operation varies between ground motions. To accommodate computing the mean and standard deviation at each frequency, the data are binned into 200 log-evenly spaced frequency bins spanning between the minimum high-pass and maximum low-pass frequencies used during processing of the 40 motions (0.0375 and 62.5 Hz, respectively). Furthermore, within each frequency bin it is typically the case that not all 40 transfer functions exceeded the minimum coherence threshold of 0.8. In general, the number of transfer functions meeting the minimum coherence threshold decreases with increasing frequency above the corner frequency. To avoid spurious fluctuations at these

higher frequencies, the mean and \pm one standard deviation are only computed if at least 25 percent (10) of the 40 transfer functions exist in a given frequency bin. For this reason, the plots show individual transfer functions at higher frequencies than the mean and \pm one standard deviation are generally plotted.

Following presentation of the single pile results versus plain frequency, normalized plots versus dimensionless frequency are presented in §10.2. This is followed by identification of the controlling parameters for kinematic pile-soil interaction and a comparison to previous elastic solutions in §10.3. Models for predicting transfer functions and spectral ratios for design applications are developed in §10.4 and §10.5. The chapter concludes with a summary of pile group simulation results.

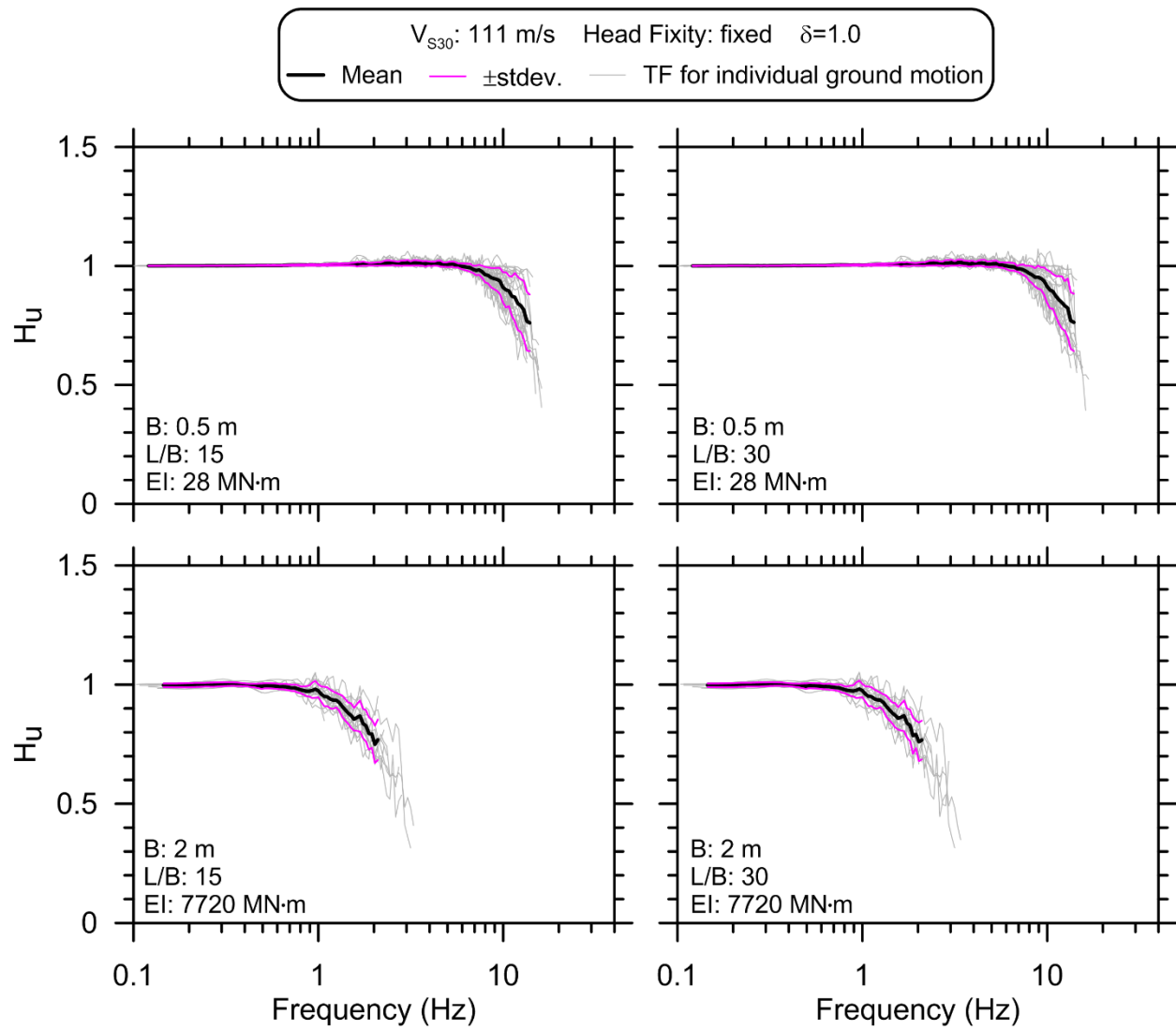


Figure 10-1: Transfer functions for Site 1 fixed-head piles.

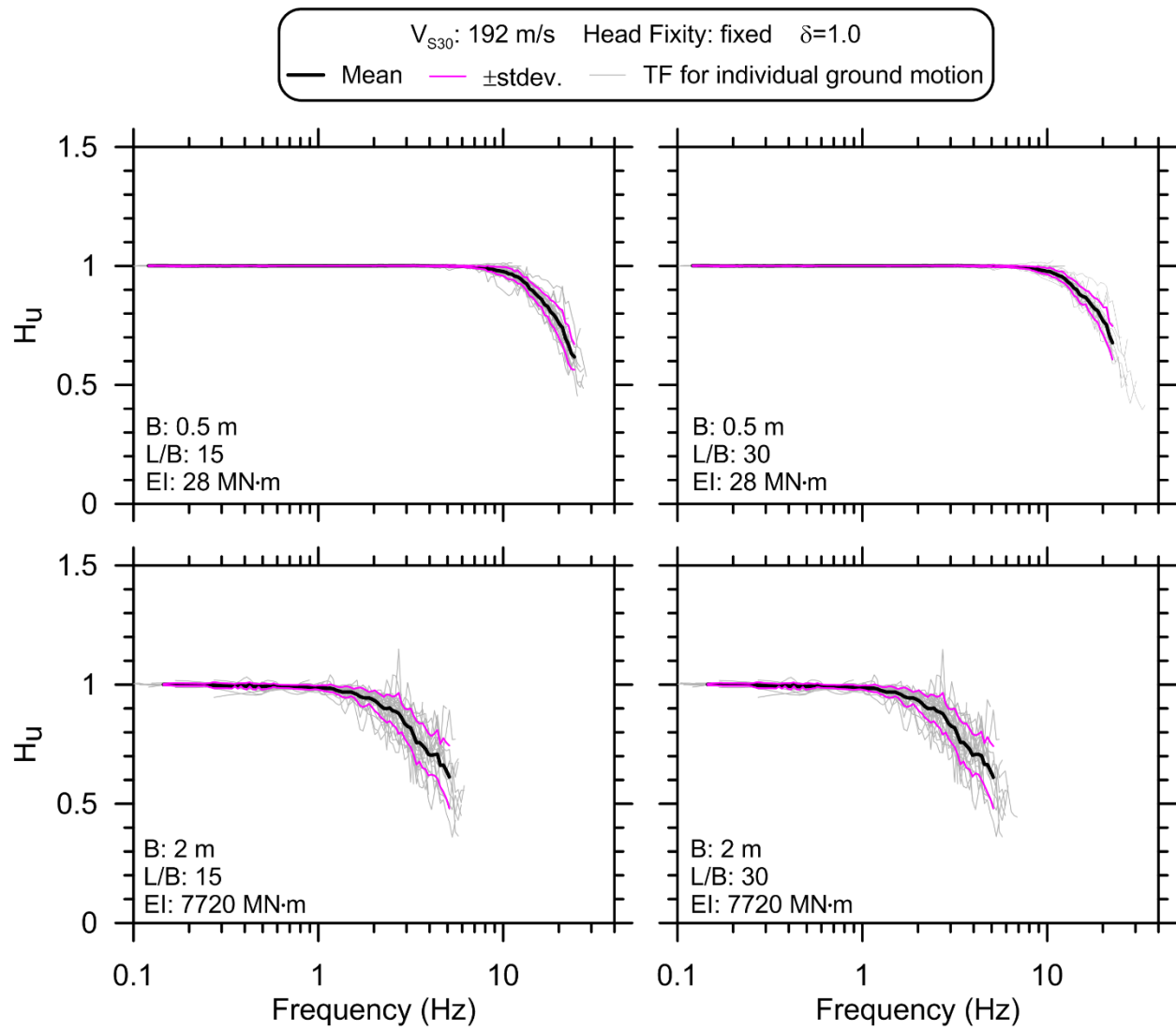


Figure 10-2: Transfer functions for Site 2 fixed-head piles.

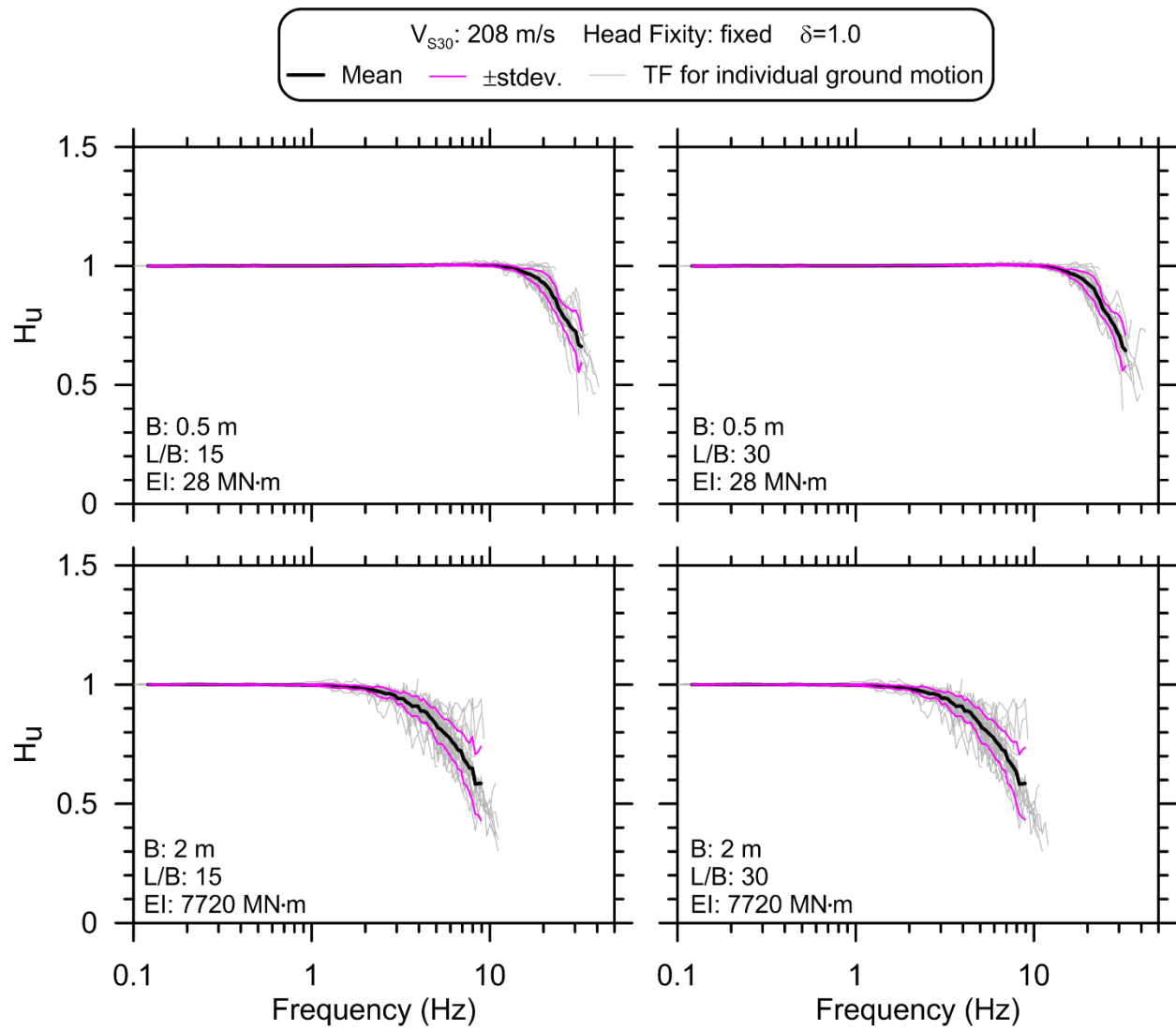


Figure 10-3: Transfer functions for Site 3 fixed-head piles.

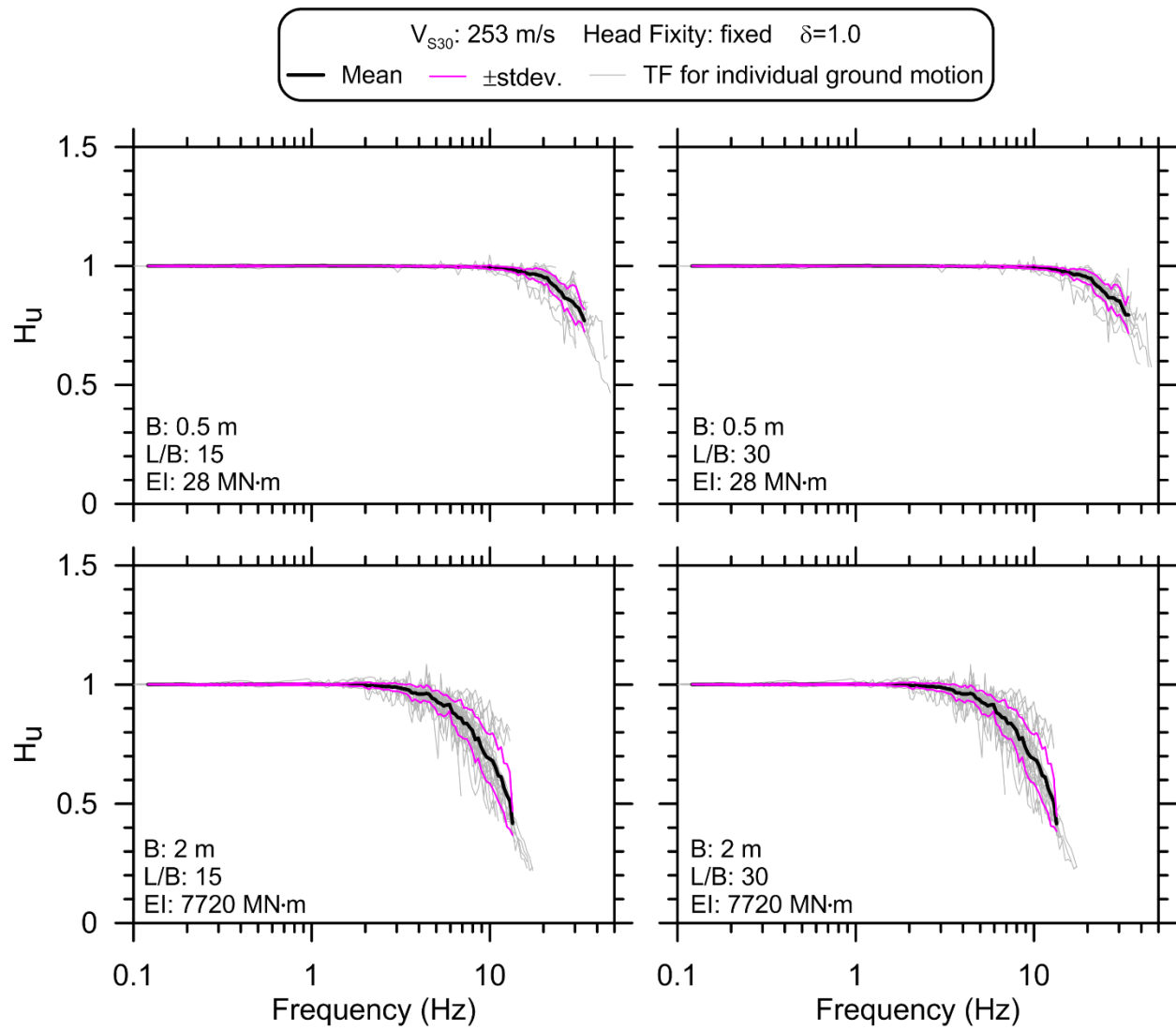


Figure 10-4: Transfer functions for Site 4 fixed-head piles.

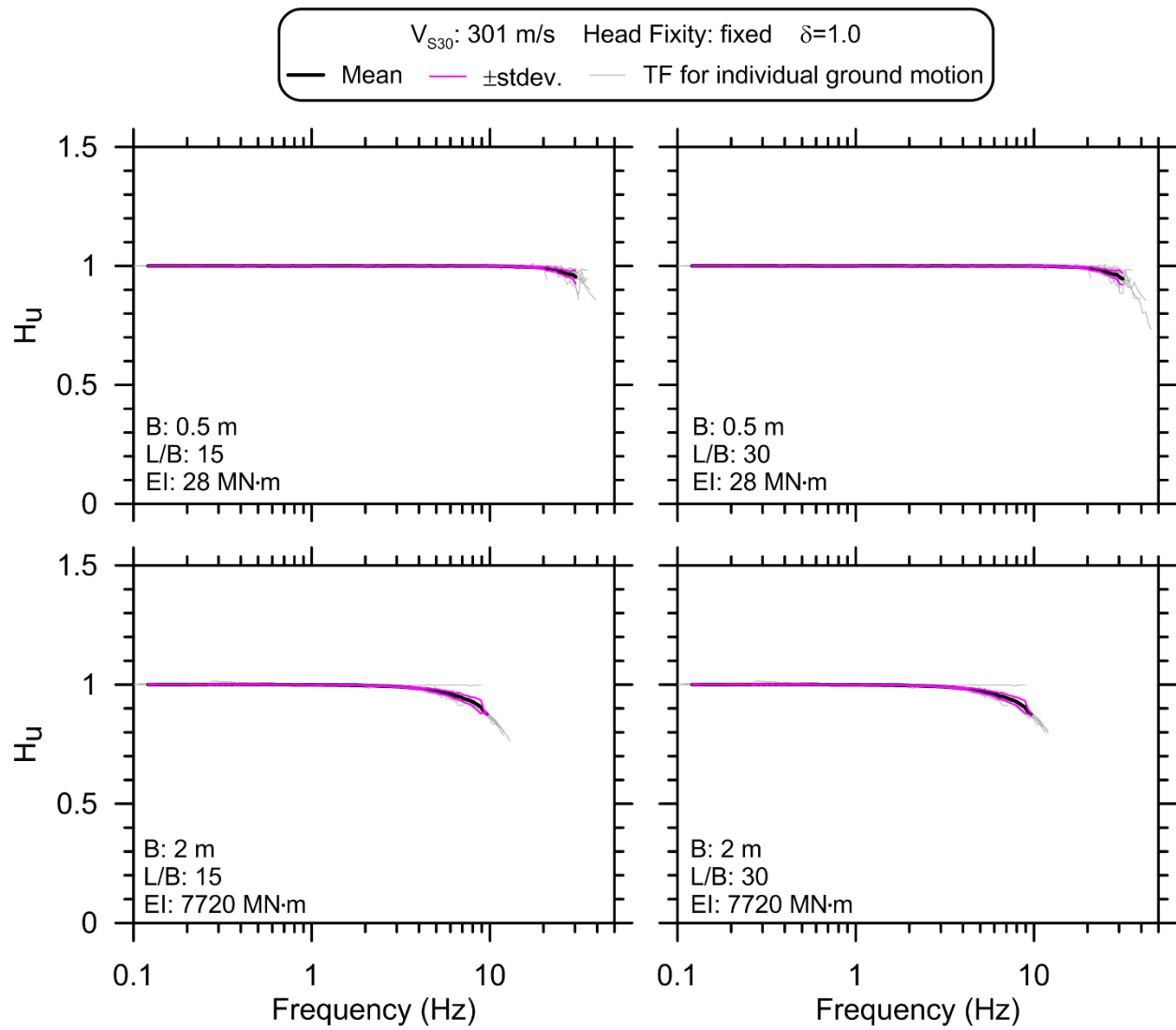


Figure 10-5: Transfer functions for Site 5 fixed-head piles.

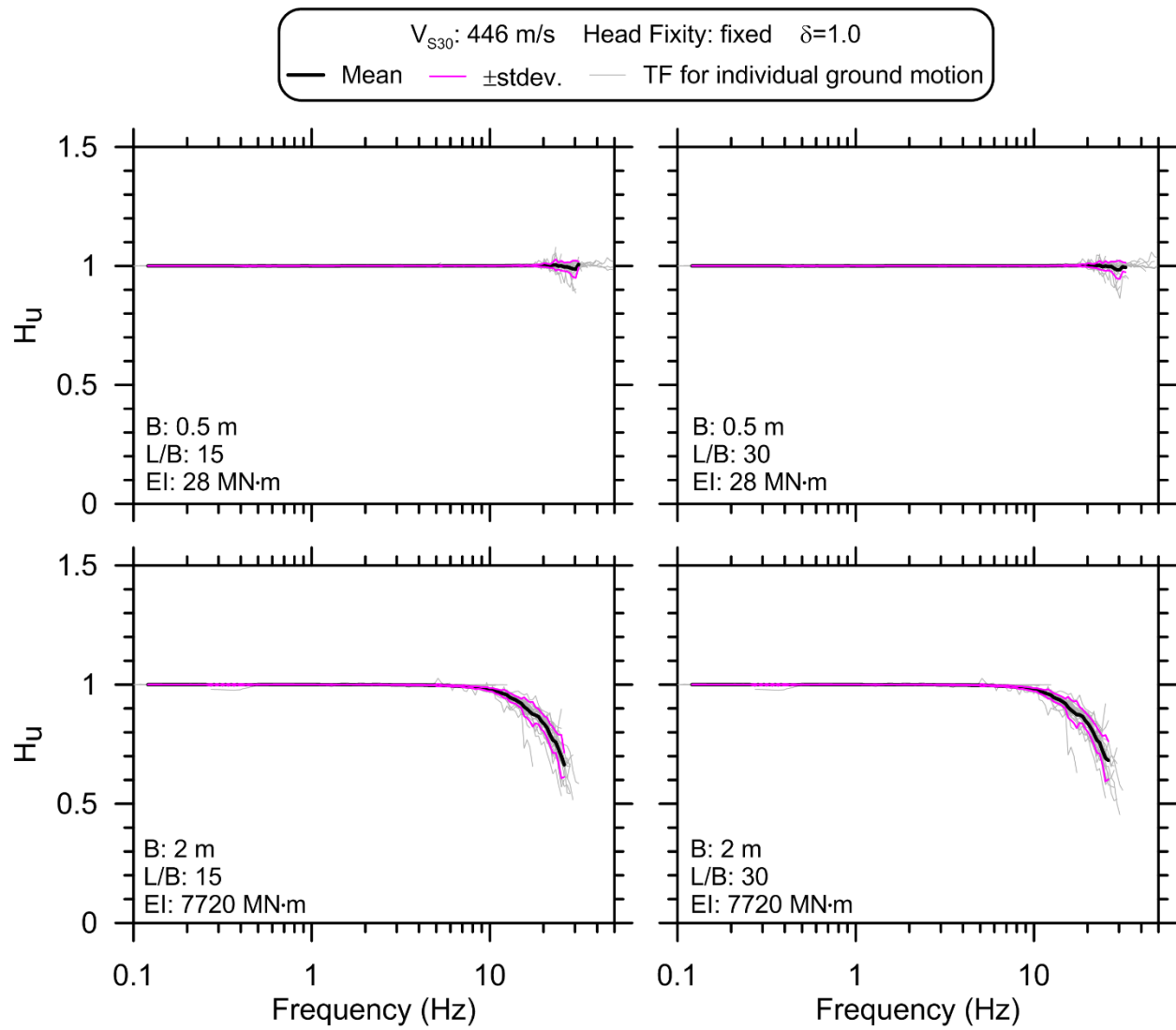


Figure 10-6: Transfer functions for Site 6 fixed-head piles.

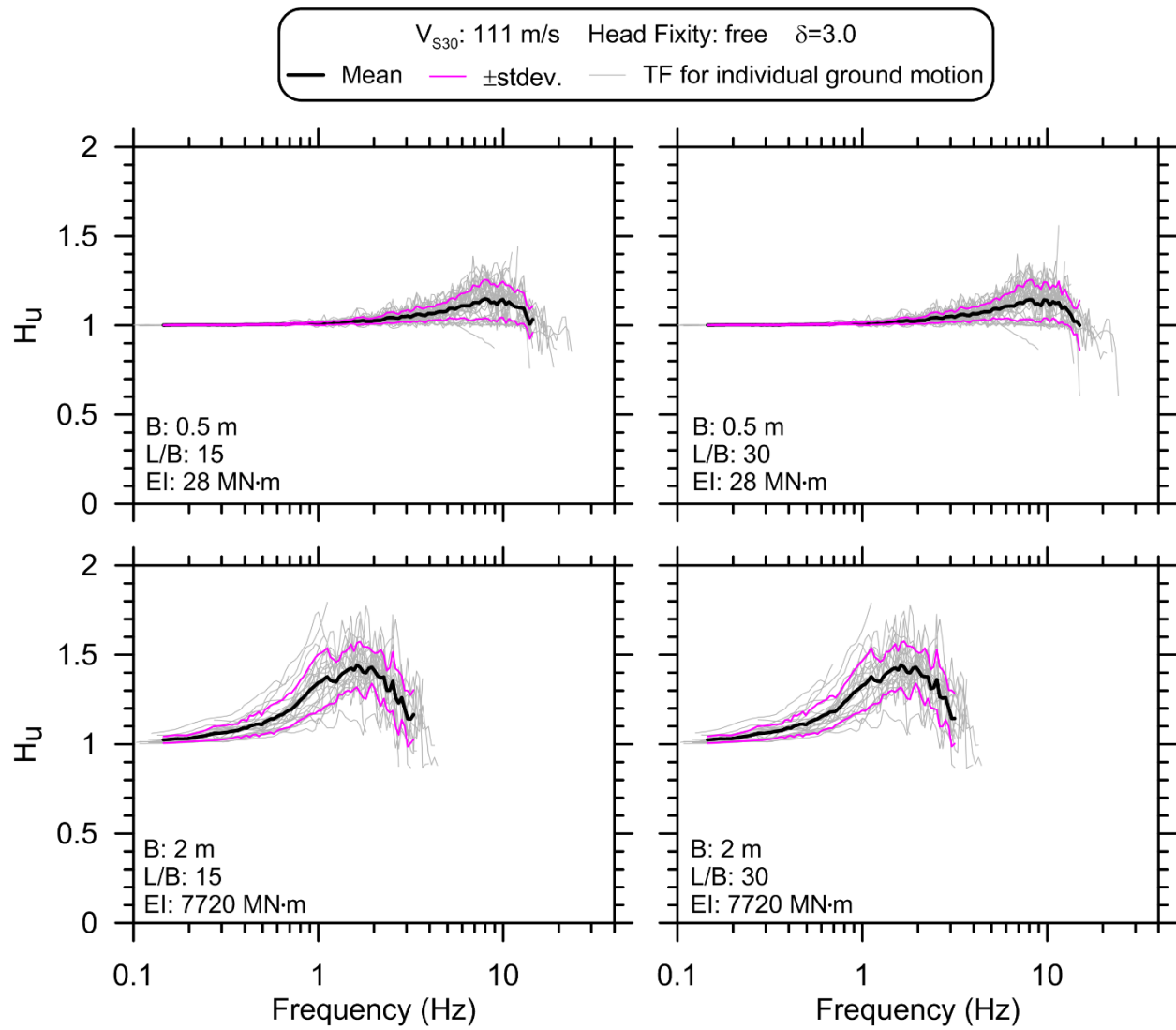


Figure 10-7: Transfer functions for Site 1 free-head piles.

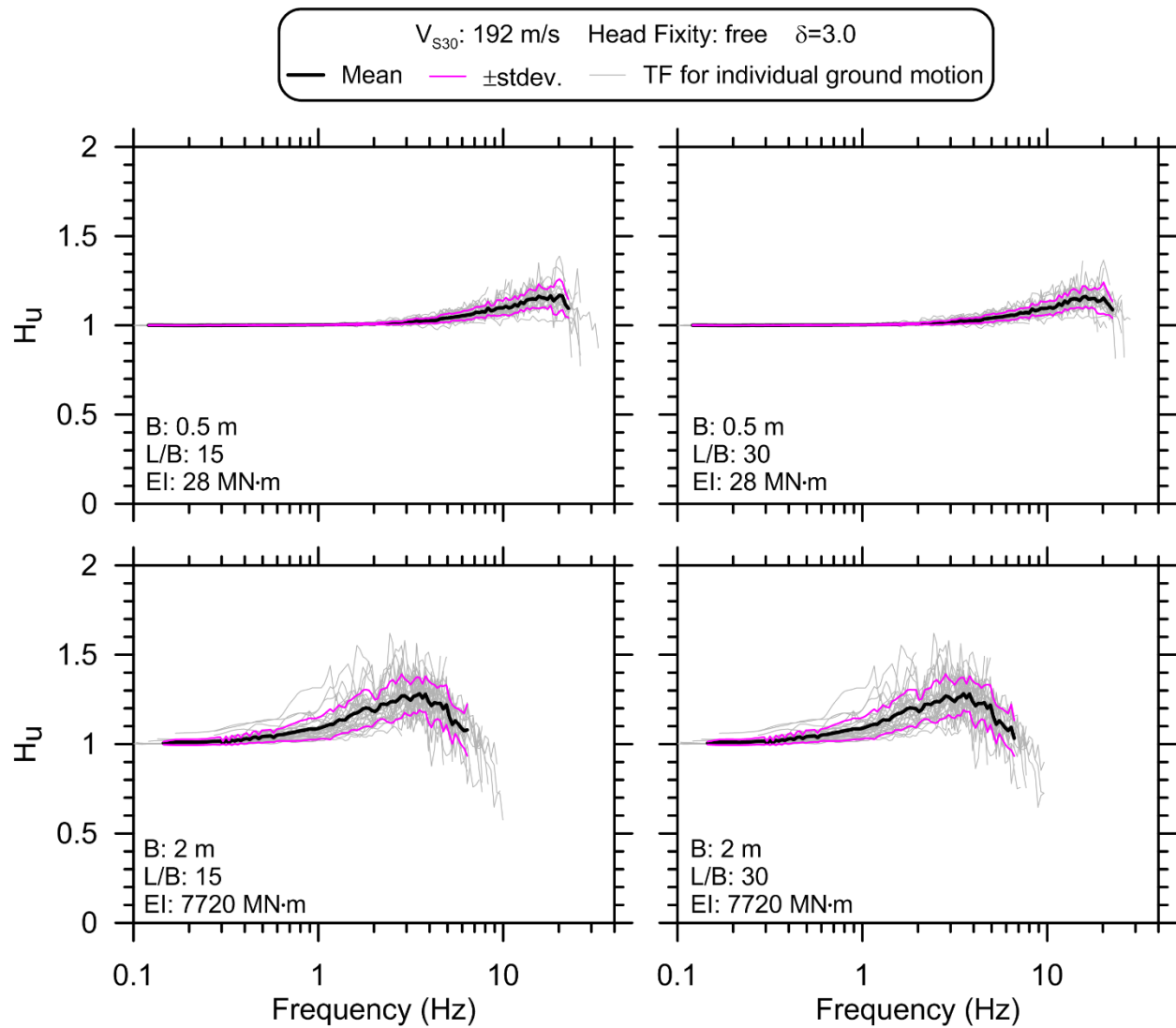


Figure 10-8: Transfer functions for Site 2 free-head piles.

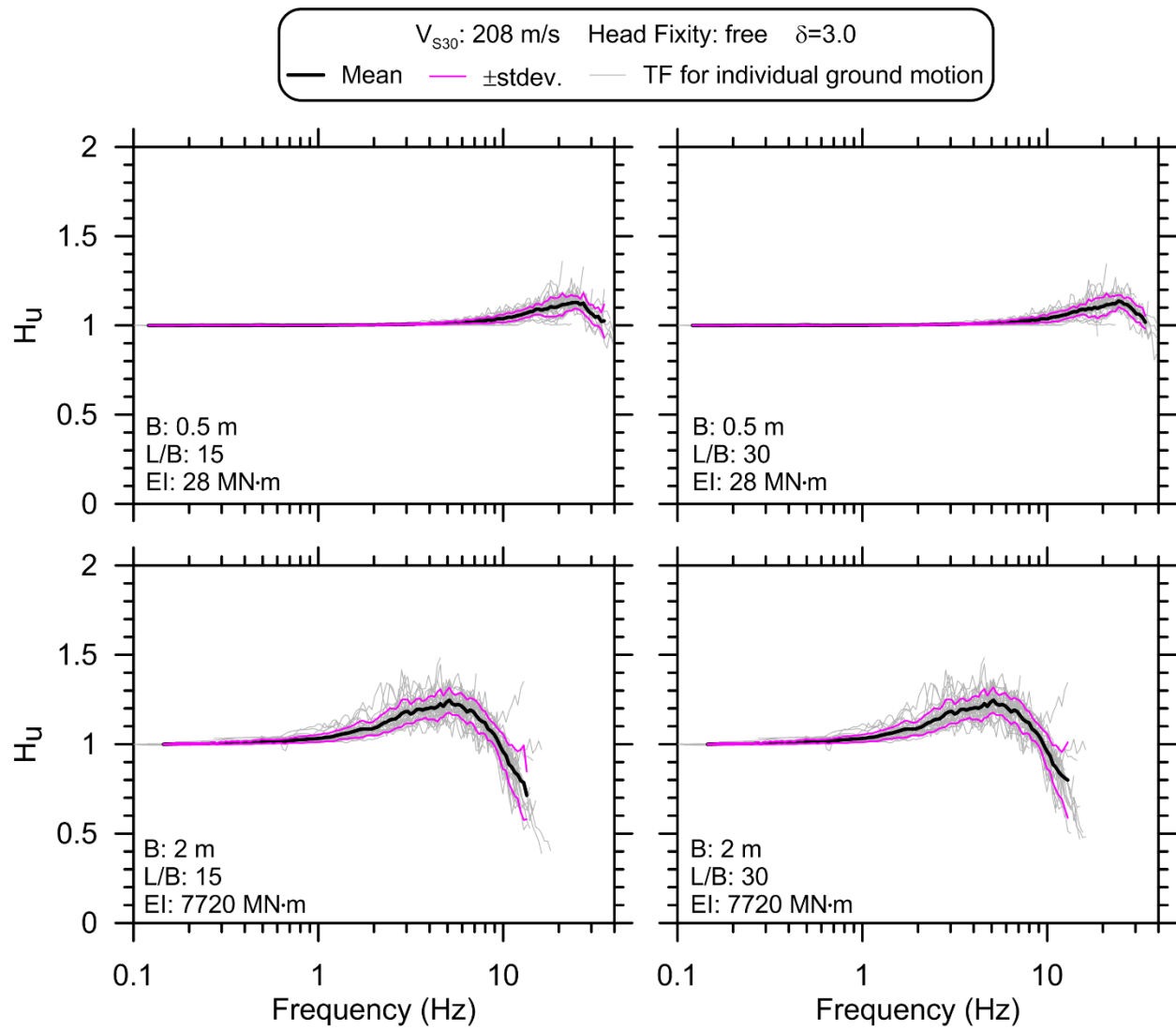


Figure 10-9: Transfer functions for Site 3 free-head piles.

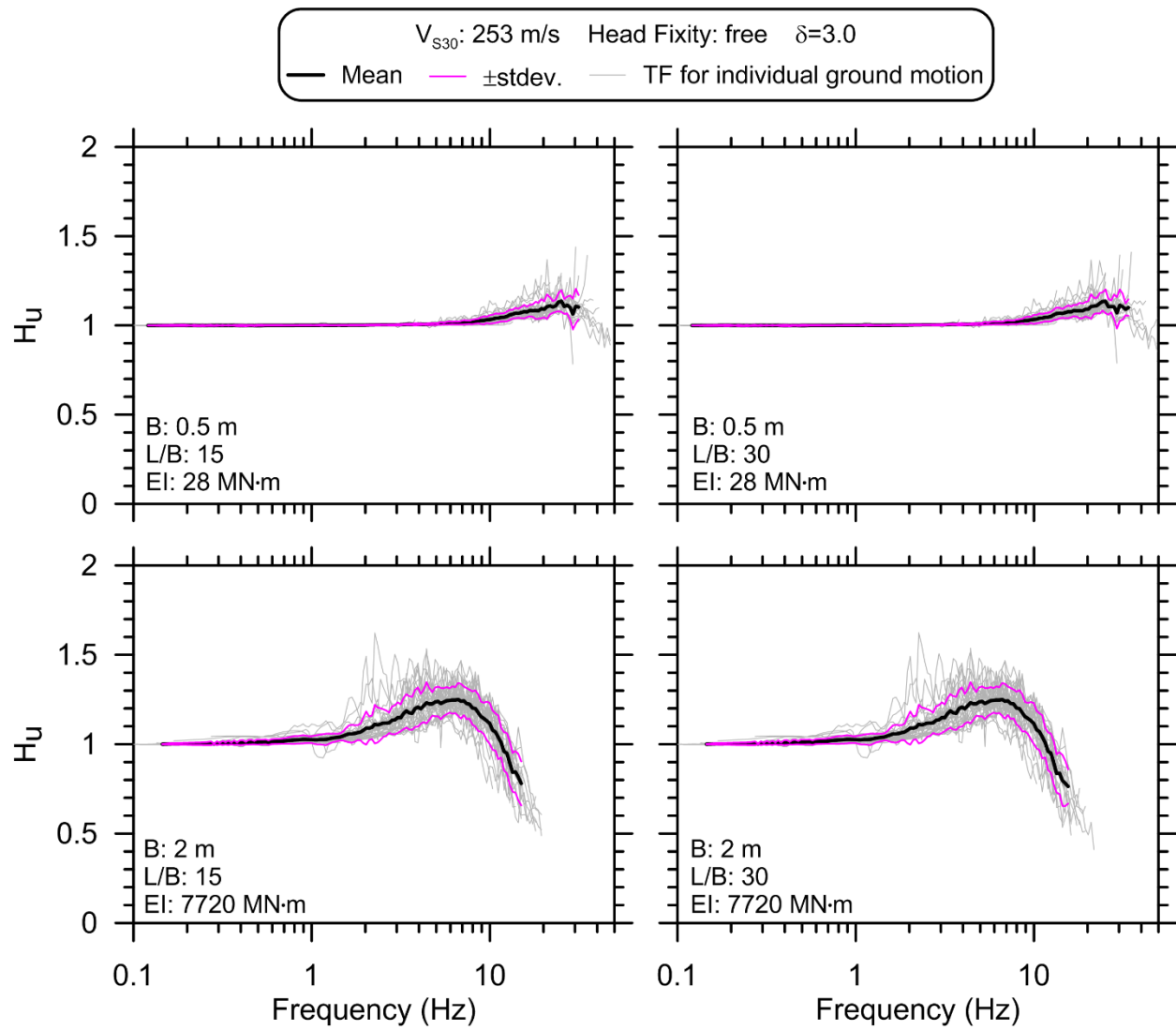


Figure 10-10: Transfer functions for Site 4 free-head piles.

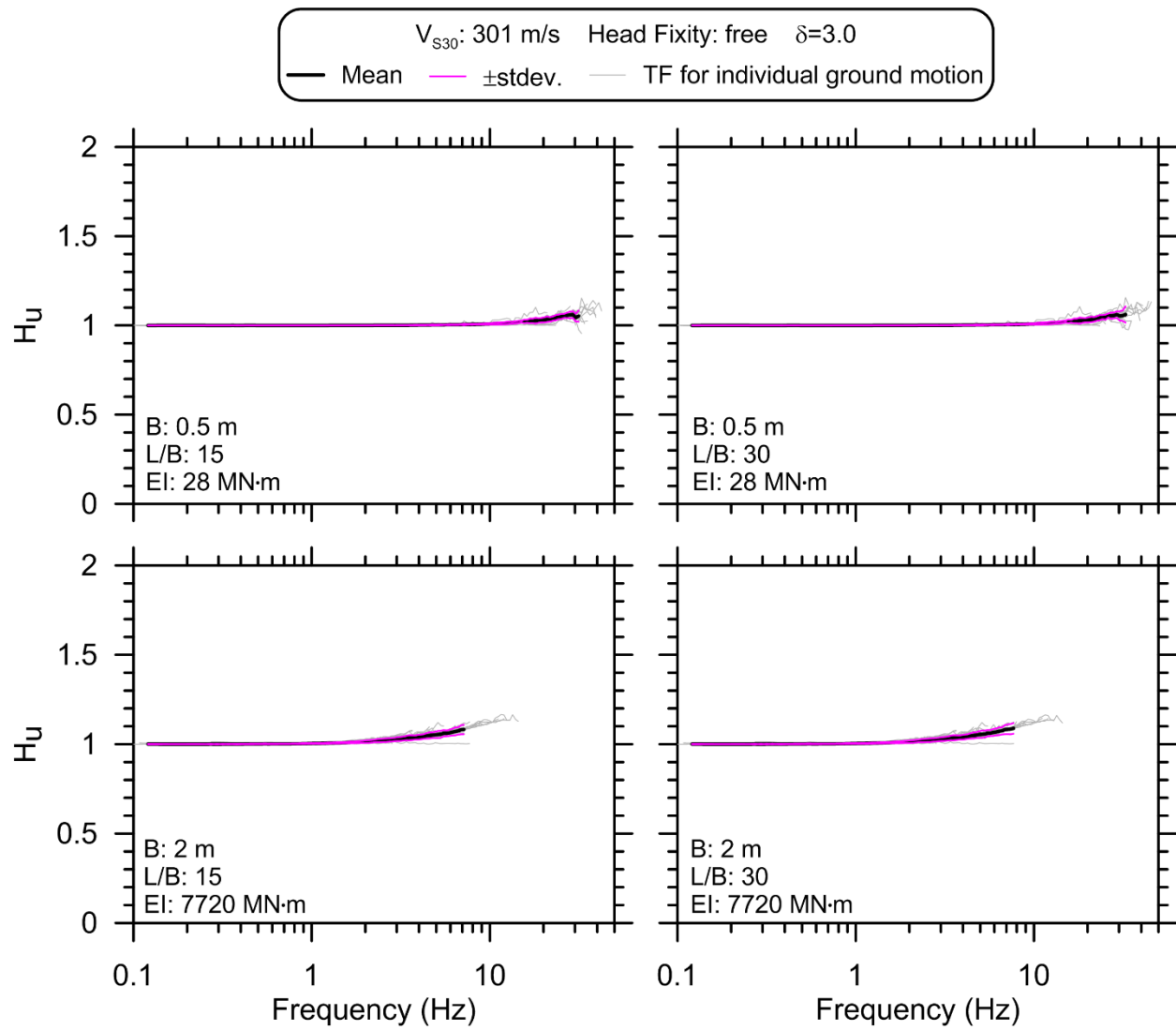


Figure 10-11: Transfer functions for Site 5 free-head piles.

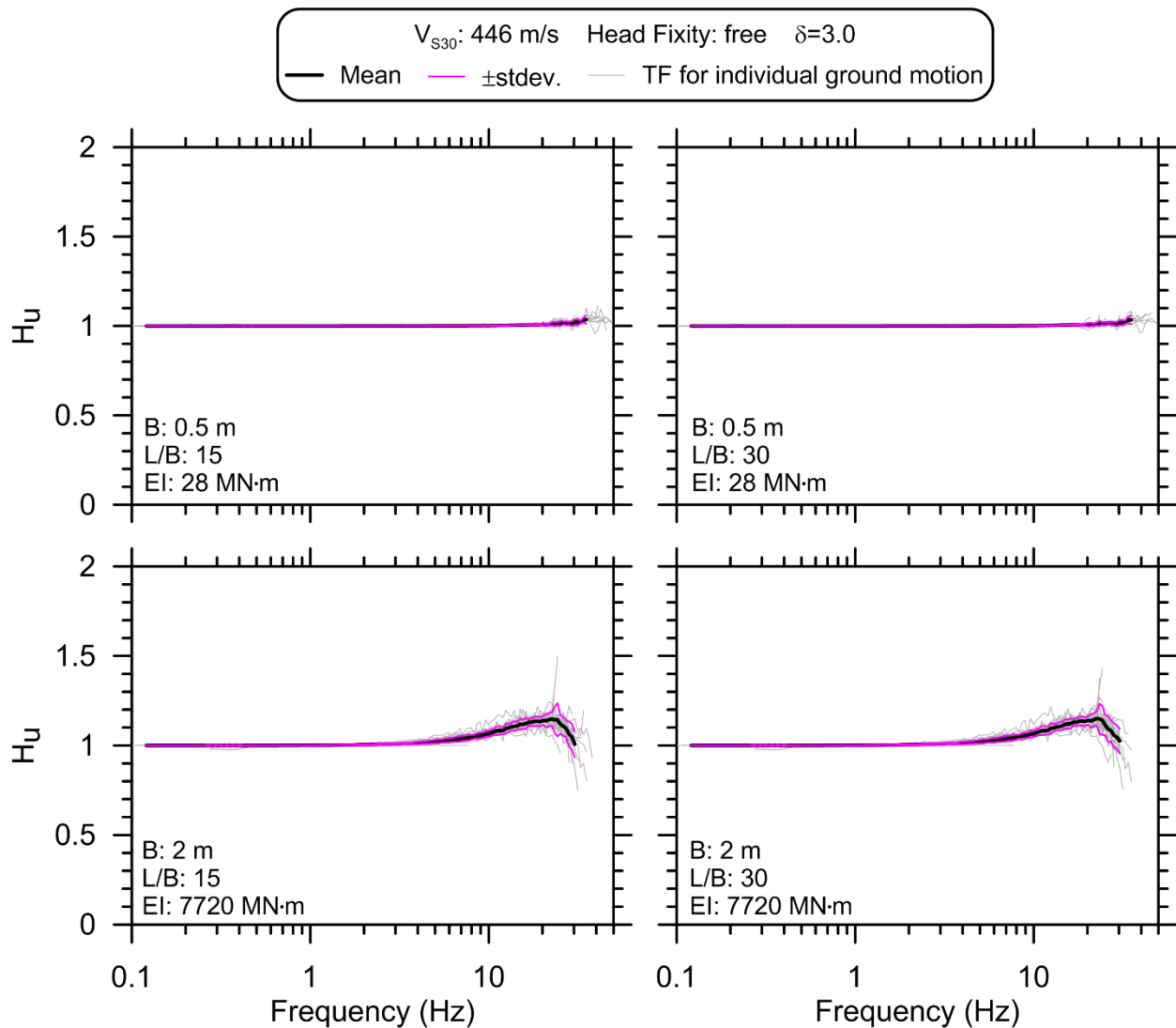


Figure 10-12: Transfer functions for Site 6 free-head piles.

10.2 NORMALIZED RESULTS USING DIMENSIONLESS FREQUENCY

To be of practical use in foundation design, the results of soil-structure interaction studies are usually presented in a normalized fashion in which the independent variable is a dimensionless function of frequency rather than plain frequency. The intention of normalization is to collapse the range of results into a narrow band which can then be represented by a single mathematical model (equation) for use in a forward-design scenario.

The normalization scheme developed by Di Laora and Sanctis (2013) and Anoyatis et al. (2013) is adopted here because of its strong fundamental basis and demonstrated ability to achieve near-perfect normalization for flexible piles considering elastic behavior. Furthermore, this allows for comparison between the elastic analytical solutions and the nonlinear results computed for this study. The dimensionless frequency for this approach is computed as $\omega/(\lambda V_s)$. Recall that the improvements realized with this normalization scheme over the previous $(\omega B)/V_s$ scheme are due to (i) the use of flexural rigidity $E_p I_p$ in the λ term instead of diameter and (ii) inclusion of the characteristic length relative to the free-field wavelength, which drives the frequency-dependence of the problem.

Following the approach of Di Laora and Rovithis (2014), λ and V_s are computed over the depth increment corresponding to the uppermost pile active length, denoted by λ_{La} and $V_{s,La}$. Consistent with Equation (7.9), λ_{La} is computed using the initial stiffness of pile-soil interaction K_e . Nonlinearity due to degradation of the p - y springs is reflected in the results and will be considered in development of the prediction models.

Figure 10-13 presents the normalized transfer functions for fixed-head piles. Free-head pile transfer functions for horizontal displacement and head rotation are presented in Figures 10-14 and 10-15. Unlike the plots in the previous section, computed transfer functions for the normalized versions are plotted as points rather than lines. This is simply because plotting 960 lines within a narrow band would make it nearly impossible to discern one from another. In contrast, plotting only points that represent transfer function ordinates with high coherence makes the overall trend clear, but also provides a visual guide to where the greatest concentration of points lie. Prior to plotting, the results were binned into 200 equally-spaced dimensionless frequency bins. The results were further grouped into nine equally-spaced dimensionless frequency bins for computing mean

and standard deviation trends as shown in the figures. Note that the “Best-fit to functional form” curves in these figures are for the functional forms discussed subsequently in §10.4.

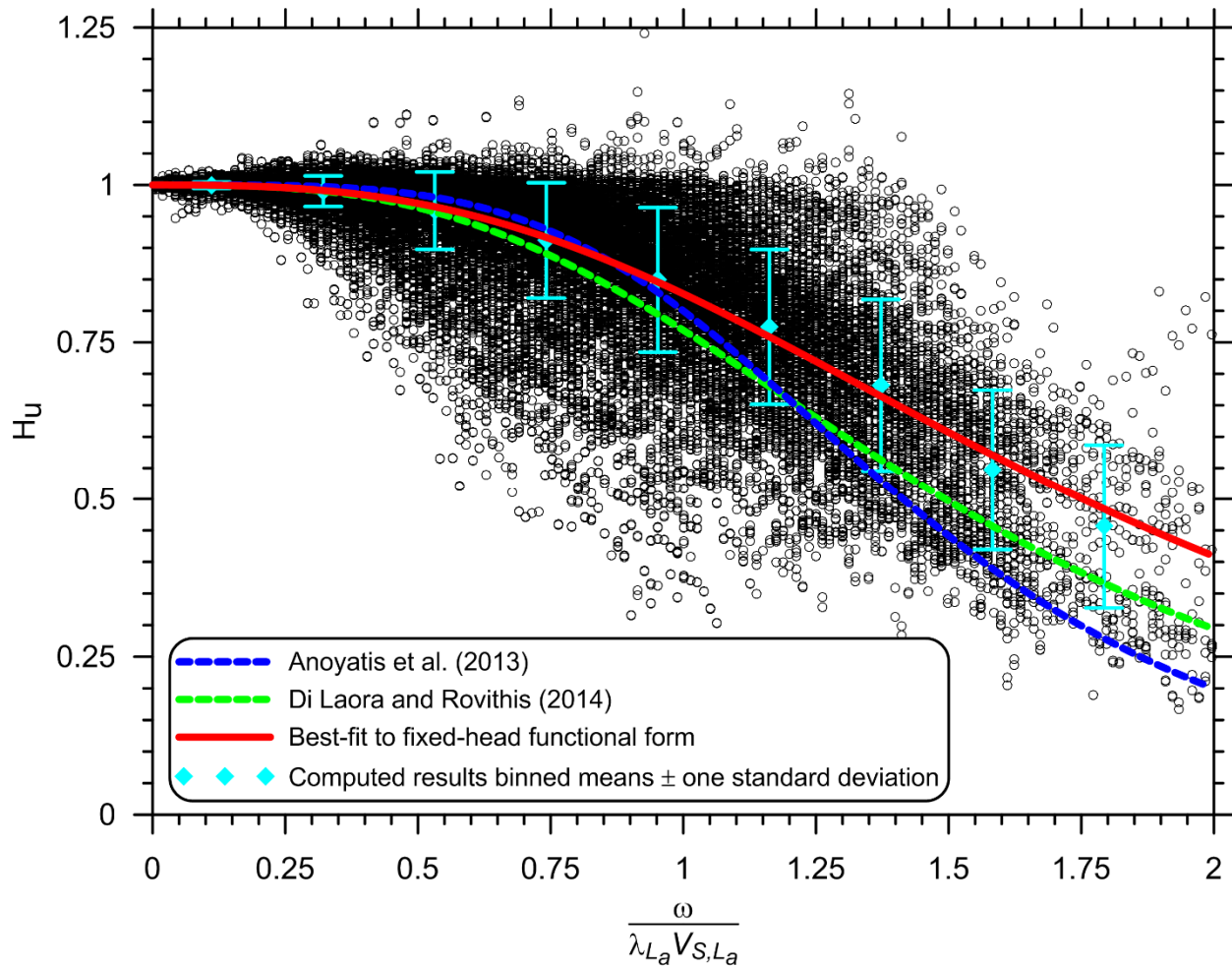


Figure 10-13: Normalized horizontal displacement transfer function results for fixed-head piles.

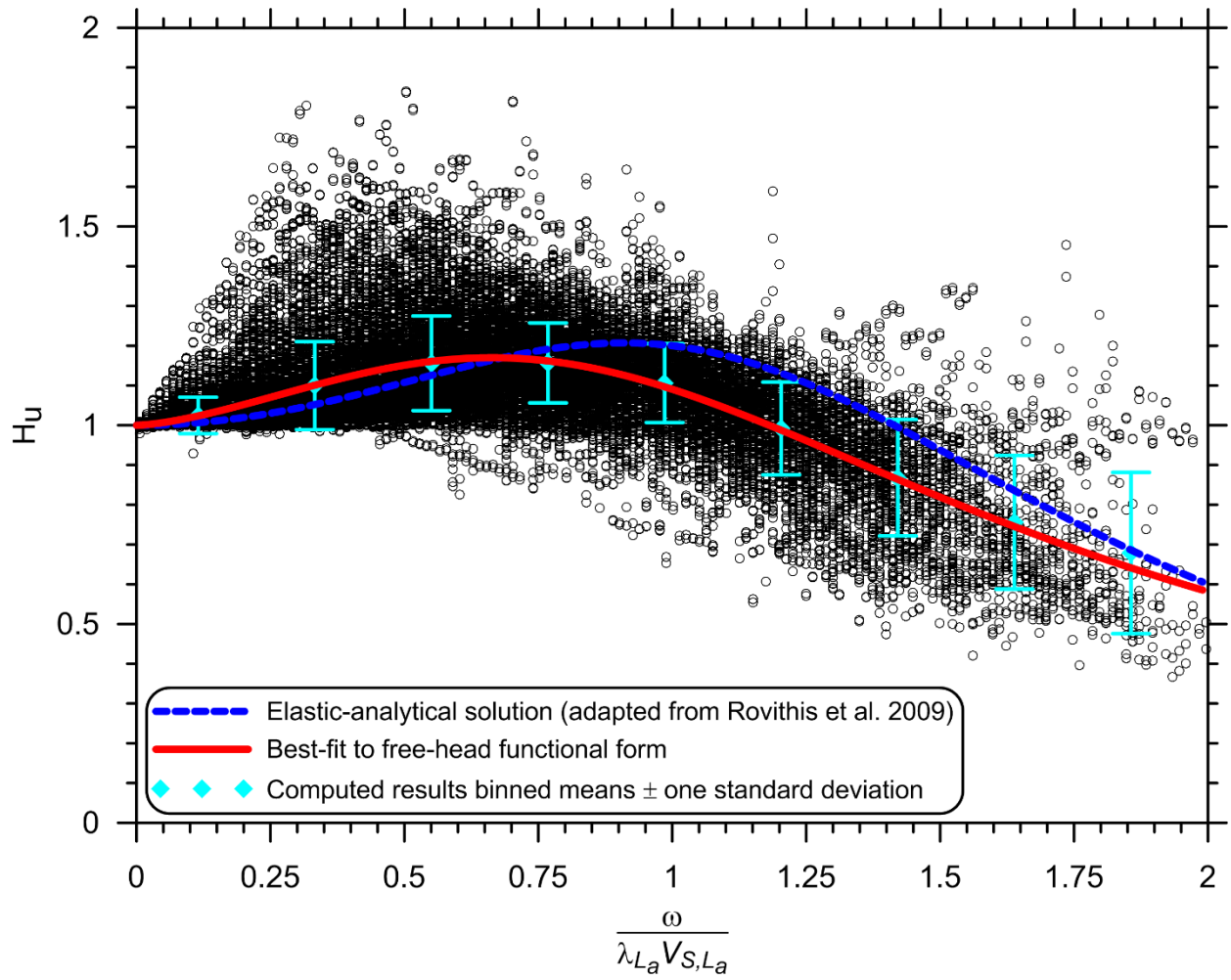


Figure 10-14: Normalized horizontal displacement transfer function results for free-head piles.

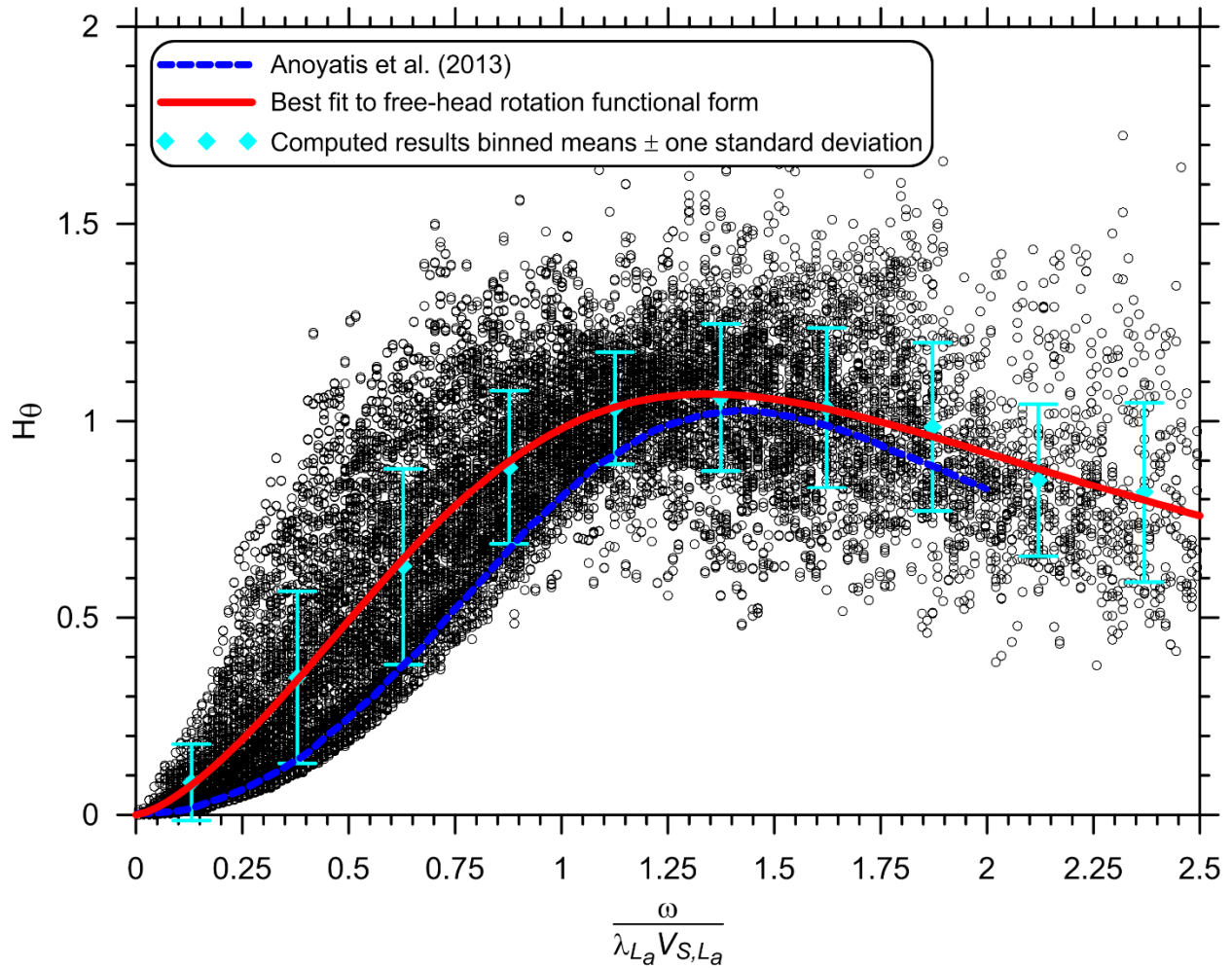


Figure 10-15: Normalized rotation transfer function results for free-head piles.

10.3 CONTROLLING PARAMETERS AND COMPARISON TO ELASTIC SOLUTIONS

The normalized and plain-frequency transfer function results presented above allow the key parameters that control kinematic pile-soil interaction to be identified. These findings will be used subsequently to guide development of models for predicting transfer functions and spectral ratios for design applications. While identifying the key parameters, a comparison is also made to elastic analytical solutions to highlight the important effects of realistic modeling assumptions and material nonlinearity.

Previous work using simplified elastic models (e.g., Fan et al. 1991) identified the key parameters for kinematic pile-soil interaction as (i) pile-to-soil stiffness contrast, (ii) variations (or lack thereof) in soil stiffness over the length of the pile, and (iii) pile head-fixity condition. The effect of head-fixity is so significant that the results of fixed- and free-head piles must be considered separately. This is because free-head piles show “kinematic amplification” over a frequency range where the free-field wavelength is similar to the pile length. Because of this fundamental difference, head-fixity is considered less of a controlling parameter than simply a different category of results from this point forward, and separate predictive models will be developed for each case.

Consistent with elastic solutions, pile-to-soil stiffness ratio remains the dominant factor that determines over what frequency range kinematic pile-soil interaction will be significant. Comparison of the mean results for each pile/site combination (Figure 10-16) reveals that the corner frequency⁶ shifts higher with decreasing pile-to-soil stiffness contrast (i.e., as the sites get stiffer), while the shape of the transfer function remains relatively consistent.

⁶ Recall from Chapter 7 that “corner frequency” is the term used herein to refer to the frequency beyond which significant pile-soil interaction occurs such that the transfer function ordinates fall below about 0.95.

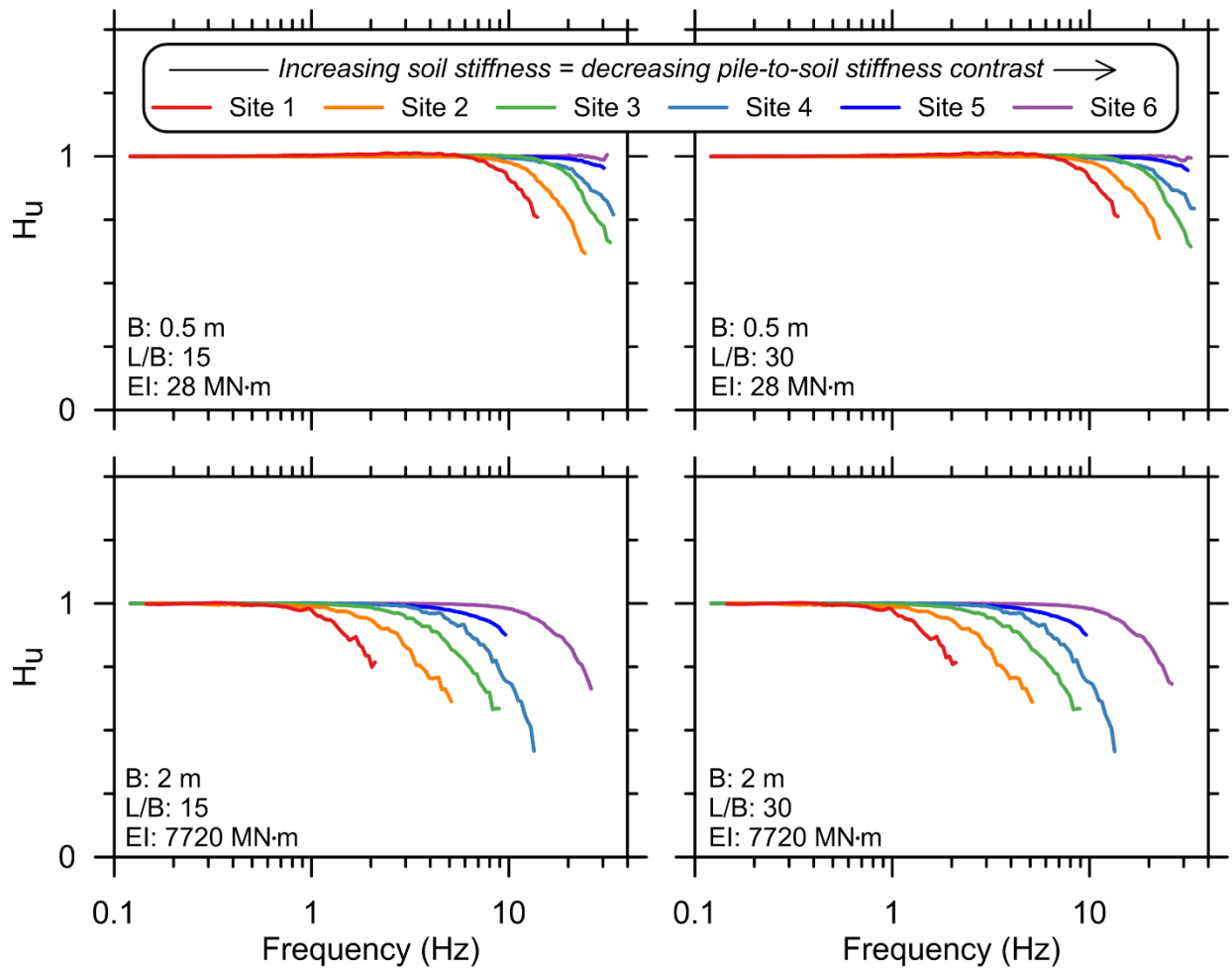


Figure 10-16: Mean fixed-head transfer function results for each pile/site combination.

Variations in soil stiffness over the length of pile also play an important role as suggested by Fan et al. (1991) and others. For example, the difference between the Anoyatis et al. (2013) and Di Laora and Rovithis (2014) curves in Figure 10-13 is due to the fact that Di Laora and Rovithis used a soil profile with increasing stiffness versus depth, while Anoyatis et al. considered a homogeneous profile. Figure 10-17 compares transfer functions computed for the $B = 2.0$ m, $L = 30$ m pile for three ground motions at Sites 3 and 4. Recall that Sites 3 and 4 have similar shear-wave velocity profiles over the upper 20 m (see Figure 9-15), and both consists of predominantly granular soil; the only significant difference between the two sites is that the stiffness of Site 4

shows a marked increase below 20 m. The portion of the pile embedded in this stiffer layer influences the response of the upper portion of the pile at Site 4, whereas Site 3 lacks this behavior.

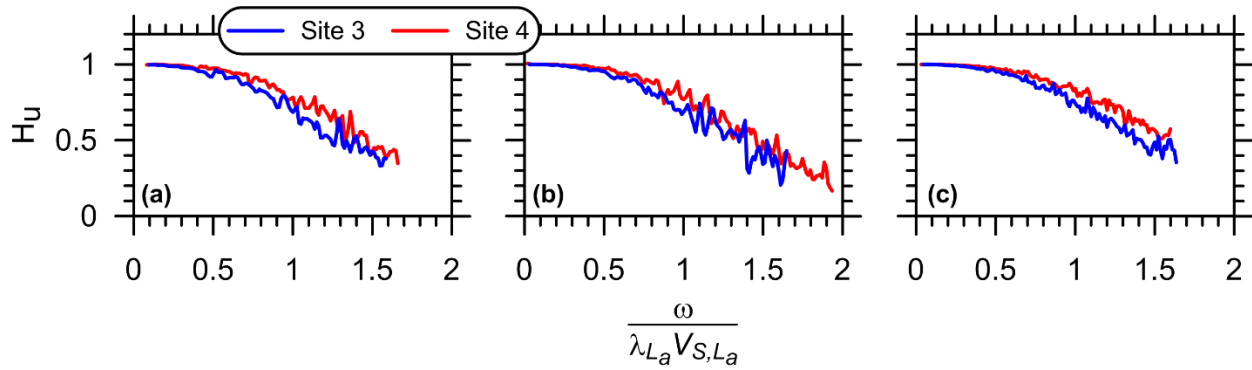


Figure 10-17: Influence of changes in stiffness over pile length for $B = 2.0$ m, $L = 30$ m pile subjected to (a) 1971 San Fernando earthquake (NGA record sequence number 72), (b) 1994 Northridge earthquake (NGA record 1011), and (c) 1999 Chi-Chi, Taiwan earthquake (NGA record 2661).

The two most significant effects that are not reflected in the elastic analytical solutions are (i) nonlinearity due to pile-soil interaction and (ii) radiation damping. An increase in ground motion intensity generally results in greater pile-soil relative displacement and corresponding p - y softening, effectively increasing the pile-to-soil stiffness contrast and shifting transfer function ordinates to lower values. On the other hand, because radiation damping manifests as an increase in stiffness for dynamic p - y curves, its effect is to decrease the pile-to-soil stiffness contrast and shift transfer function ordinates higher. Hence, nonlinearity due to pile-soil interaction and radiation damping are competing effects in terms of their influence on the transfer functions.

This is illustrated in Figure 10-18, which shows transfer functions computed for the $B = 0.5$ m, $L = 7.5$ m pile in the Site 1 profile subjected to the 1971 San Fernando earthquake (NGA record sequence number 72). A comparison of the transfer functions computed with (i) a constant value of elastic p - y stiffness set equal to the initial stiffness K_e , versus (ii) an equivalent-linear degraded stiffness, verifies that a decrease in soil stiffness shifts the transfer function ordinates

down. However, when a dashpot representing radiation damping is added to the degraded stiffness model, the transfer function ordinates are shifted back up, in this case above the transfer function representing initial stiffness but without the dashpot. Finally, the transfer function for the fully-nonlinear model is shown, which on average plots above the elastic transfer functions computed without radiation damping. Thus, the effect of nonlinearity due to pile-soil interaction is effectively outweighed by the increase in stiffness due to radiation damping for this case. (Note that all four models were subjected to the same input ground motions, so the effect of nonlinearity due to site response is equal for all cases).

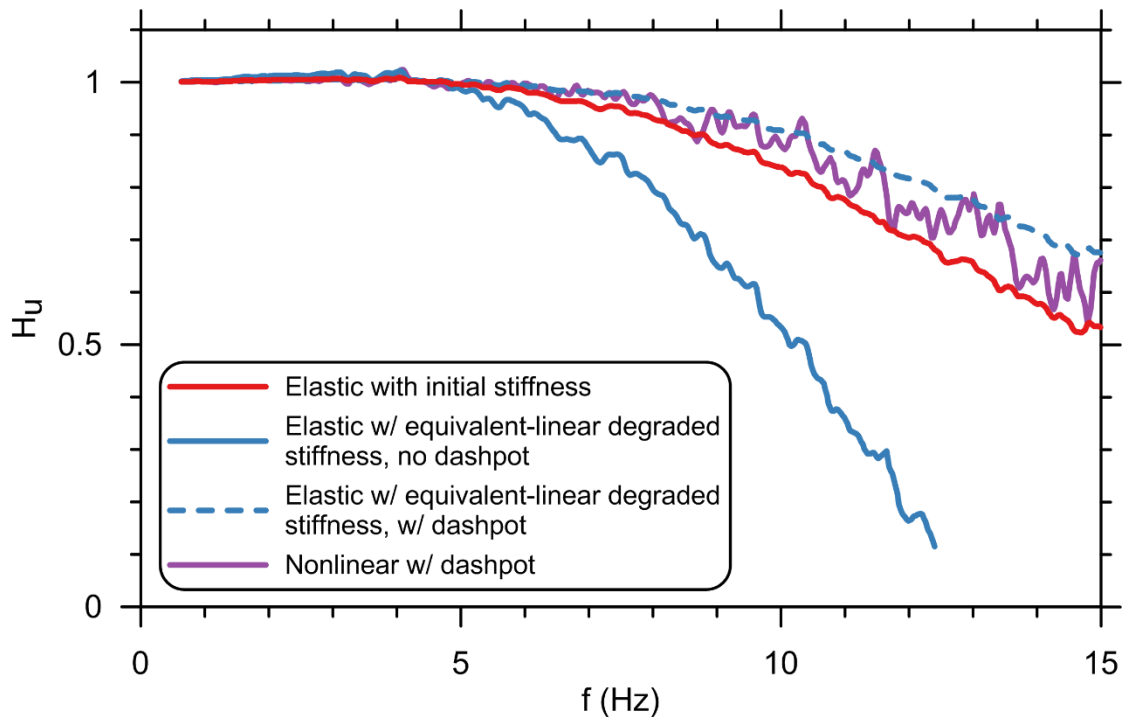


Figure 10-18: Competing effects of radiation damping and stiffness degradation due to pile-soil interaction.

Comparison of the trends indicated by the binned means in Figures 10-13 through 10-15 shows that the nonlinear results computed for this study plot near or slightly above the elastic analytical solution. This is somewhat counterintuitive, as it would seem that including pile-soil

interaction nonlinearity would shift the results below the elastic analytical solution due to soil softening. However, because the elastic solutions in these plots do not include radiation damping, this is a somewhat misleading comparison. Although radiation damping is included in the full derivation by Anoyatis et al. (2013), the best-fit curves from their study that are shown on the normalized transfer function plots in the previous section are for a static simplification in which pile inertia and radiation damping are ignored (the influence of hysteretic damping on the free-field ground response can be included by using a complex shear wave velocity V_s^*). Furthermore, ground motion intensity does not influence elastic solutions except to the extent that the soil modulus values specified by the designer should be consistent with the anticipated level of strain. Unfortunately, little guidance is available on predicting this strain due to pile-soil interaction, and methods for predicting free-field nonlinearity due to site response [e.g., NIST (2012)] are only approximate. Additionally, the elastic solutions will produce essentially the same transfer function regardless of the pile-to-soil stiffness contrast for any flexible pile as demonstrated in Chapter 8.

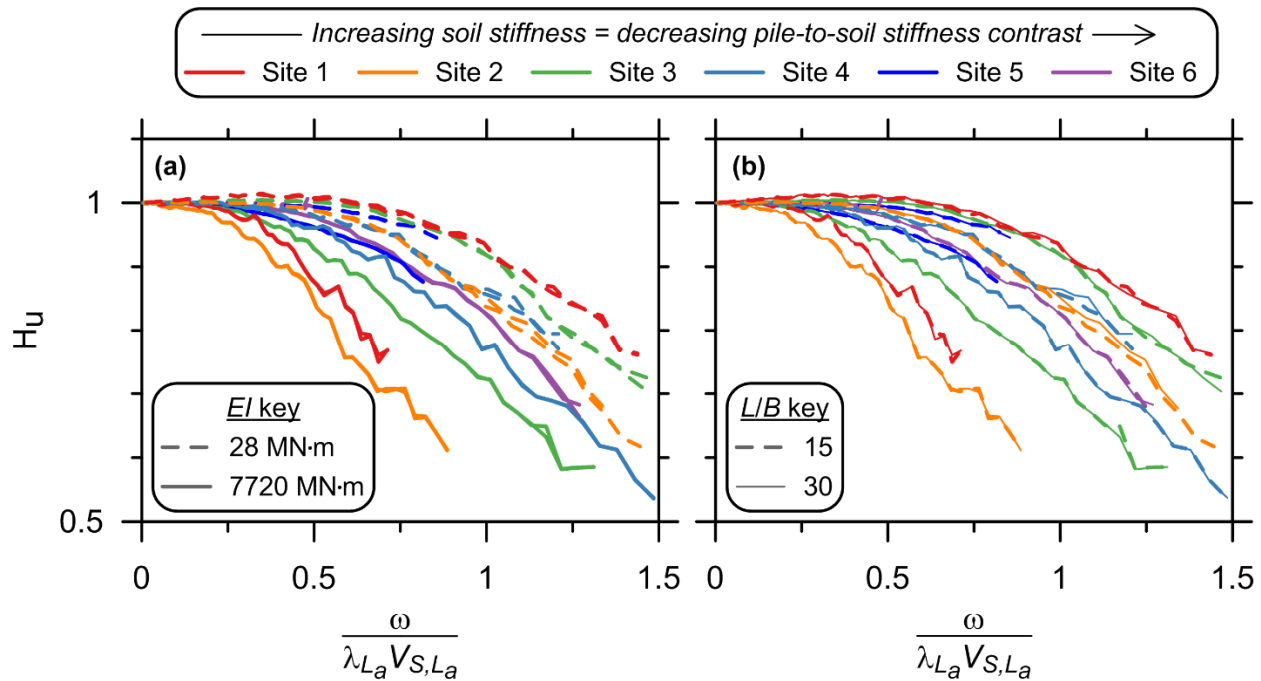


Figure 10-19: Mean fixed-head transfer function results for each pile/site combination plotted versus dimensionless frequency. (a) Shows variability in results due to pile stiffness, and (b) shows lack of variability in results due to pile slenderness ratio L/B .

It is immediately clear when examining the normalized transfer function plots that significant dispersion exists in the computed results relative to the perfect normalization suggested by elastic solutions. Figure 10-19 provides insight into this variability by showing only the mean transfer functions for each pile/site combination (rather than all 40), with all 24 pile/site combinations plotted versus dimensionless frequency on a single graph. Three key trends are apparent from this figure:

- Increasing soil stiffness (and thus decreasing pile-to-soil stiffness contrast) still shifts the corner frequency higher, as was seen in Figure 10-17 when the results were plotted versus plain frequency.
- Likewise, increasing pile stiffness (which is best characterized by flexural rigidity $E_p I_p$) shifts the corner frequency down—it is apparent in Figure 10-19(a) that the

larger-diameter piles result in more significant pile-soil interaction and thus produce lower transfer function ordinates.

- Figure 10-19(b) confirms a lack of dependence on pile slenderness ratio L/B , consistent with Anoyatis et al. (2013).

Again, it should be reiterated that the first two trends in the above list are not captured by elastic analytical solutions. The primary driver of these trends is that decreasing soil stiffness and increasing pile stiffness result in greater pile-soil interaction nonlinearity.

In addition to the variability exhibited by the means of each pile/site combination relative to one another, it is apparent that individual transfer functions show significant fluctuations relative to the smooth curves produced by elastic solutions (e.g., examine the individual transfer functions plotted in Figures 10-1 through 10-12). One of the causes of this variability is that pile/site combinations which are initially the same but then subjected to different ground motions exhibit different levels of nonlinearity due to free-field site response and pile-soil interaction. While the former effect is only approximately reflected in the results by means of the variable displacement time series imposed on each p - y spring, nonlinearity due to pile-soil interaction directly alters the pile-to-soil stiffness contrast. The effect of this interaction nonlinearity is difficult to isolate in the resulting transfer function, because the level of nonlinearity varies over the duration of the earthquake.

A related effect is due to the variable frequency content between the different input motions. By using a nonlinear time-domain solution, the pile-soil system is subjected and responds to energy at multiple frequencies and amplitudes simultaneously, just like in a real earthquake. The resulting interaction of nonlinear responses to different frequencies can have a significant influence on the results that is not captured by elastic solutions, which assume the system response

to all frequencies can be superimposed. As a simple example, consider excitation of a pile-soil system by a signal containing a low frequency, large amplitude pulse, and a second high frequency component with a smaller amplitude. For an elastic system, the transfer function will be the same regardless of when the low frequency energy arrives relative to the high frequency waves. For a nonlinear system, if the high frequency energy arrives during the low-frequency pulse such that the pulse has resulted in significant p - y softening, the high-frequency excitation effectively occurs during a period of softened pile-to-soil stiffness contrast. Hence, the transfer function ordinate at the high frequency will be lower compared to a case where the high frequency energy excitation occurs prior to the low-frequency pulse arrival.

Again, the effect of variable frequency content demonstrated by the preceding example is hard to pinpoint in the computed transfer functions, because many more than two frequencies of excitation are present in the input motions, and the effect of variable frequency content is conflated with the other effects discussed in this section. Rather, it can generally be stated that the effect of variable frequency content along with time-variable pile-soil interaction nonlinearity is to increase fluctuations in the computed transfer functions relative to the idealized elastic case. Moreover, the interplay of these effects with highly variable stratigraphy, as opposed to uniform or smoothly varying soil stiffness, further increases the irregularity of the transfer functions computed herein relative to elastic solutions.

In summary, the key parameters controlling kinematic pile-soil interaction are:

- Pile head-fixity condition,
- Pile-to-soil stiffness contrast,
- Variations in soil stiffness over the pile length,

- Nonlinear soil behavior due to pile-soil-interaction, which depends on relative pile-to-soil stiffness contrast, and due to free-field ground response,
- Radiation damping, and
- Variable frequency content of the free-field excitation.

The key differences between simplified elastic solutions and the nonlinear results computed for the more realistic conditions considered in this study are caused by the latter three factors in the above list.

The results presented above make it clear that although using an elastic solution may provide a reasonable approximation of average behavior, it would fail to capture the variability that is possible when more realistic subsurface conditions and ground motions are used along with explicit consideration of nonlinearity. It is noteworthy, and rather convenient, that the elastic solutions are approximately coincident with the average results of this study. While this suggests that elastic solutions provide a reasonable first-order approximation of behavior, it also means that they would over-predict reductions in free-field motions roughly half the time. A need to capture the impact of realistic conditions, which is reflected by the variability in the results computed for this study, is the motivation for development of predictive models in the following sections.

10.4 GENERALIZED MODELS FOR PREDICTING TRANSFER FUNCTIONS

The results presented above demonstrate that when the nonlinear transfer functions computed for this study are normalized using dimensionless frequency $\omega/(\lambda V_s)$, consistent trends are exhibited between the individual results, but significant dispersion still exists about the mean trend. In this section, predictive models (i.e., equations with a specified functional form) are developed to predict this variability so that it can be represented in transfer functions used for design

applications. Coefficients used in these models depend on the controlling parameters identified in the previous section. Similar models are developed for predicting spectral ratios in the following section.

Two potential approaches for developing the models were considered. Each begins with specifying a functional form, which is described in more detail in the following subsection. For now, consider the functional form suggested by Anoyatis et al. (2013) for fixed-head piles:

$$H_u = \frac{u_{FIM}}{u_{FFM}} = \frac{1}{1 + C_0 \left(\frac{\omega}{\lambda V_s} \right)^{C_1}} \quad (10.1)$$

in which Anoyatis et al. recommended values of $C_0 = 0.25$ and $C_1 = 4$ for the coefficients. Equation (10.1) with these values for the coefficients is plotted in Figures 10-13 through 10-15. The first option for a fixed-head pile transfer function predictive model would be to add terms to Equation (10.1) that are functions of dimensionless frequency and other parameters in an attempt to achieve better normalization, for example:

$$H_u = \frac{1}{1 + C_0 \left(\frac{\omega}{\lambda V_s} \right)^{C_1}} + f_0 \left(\frac{\omega}{\lambda V_s}, parameter_0 \right) + f_1 \left(\frac{\omega}{\lambda V_s}, parameter_1 \right) + \dots etc. \quad (10.2)$$

Mathematically speaking, many potential variations of this approach are possible, for example including terms in the denominator of the fraction rather than as additive terms. The alternative approach is to leave the functional form of the model unchanged—for example, use Equation (10.1)—and develop regression models to predict the coefficients:

$$C_j = \beta_0 f(predictor_0) + \beta_1 f(predictor_1) + \dots \beta_n f(predictor_n) + intercept \quad (10.3)$$

Equation (10.3) is an example of a multiple linear regression model for predicting a coefficient C_j as a linear combination of functions of predictor variables, each with an independent coefficient (slope) β . In a multiple linear model, functions of predictor variables do not necessarily have to be linear, but they must be combined in a linear fashion. For example, the following is a permissible multilinear model:

$$C_j = \beta_0(\text{predictor}_0) + \beta_1(\text{predictor}_0^2) + \text{intercept} \quad (10.4)$$

while this is not:

$$C_j = \beta_0(\text{predictor}_0) + [\beta_1(\text{predictor}_0)]^2 + \text{intercept} \quad (10.5)$$

The approach of using multiple linear regression to predict individual coefficients rather than attempting to modify the functional form has several benefits. First, performing multiple linear regression for one coefficient model at a time is much simpler and faster than performing a nonlinear mixed-effects regression on the entire 60,000+ data points reflected in each of the Figures 10-13 through 10-15. Second, it maintains the ability to compare to elastic solutions. If the functional form were modified to improve normalization of the nonlinear results, the x -axis value of the normalized plots would no longer have a clear physical meaning like $\omega/(\lambda V_s)$ does. A modified x -axis variable would also complicate the process of converting the normalized transfer function back to H_u as a function of plain frequency, a necessary step to actually implement the transfer function for practical applications. Furthermore, there would be no clear way to express the elastic solutions in the new normalized space if the x -axis values were functions of parameters describing nonlinearity. It is useful to retain the ability to make the elastic versus nonlinear comparison, because it highlights the shortcoming of elastic solutions in terms of their inability to

predict the variability that occurs when realistic conditions are modelled. Hence, the multiple linear regression approach is used here.

Predictor variables used in the multiple linear regression models must capture the physical mechanisms that control kinematic pile-soil interaction in order for the models to be meaningful and reliable. The recent work by Anoyatis et al. (2013) and Di Laora and Rovithis (2014) shows that the $\omega/(\lambda V_s)$ normalization scheme captures two of the controlling parameters well for elastic conditions: (i) pile-to-soil stiffness contrast and (ii) the ratio of pile characteristic length to the wavelength of free-field excitation, which controls the frequency-dependence of the problem. Hence, the primary goal of the of the coefficient prediction models is to capture the effects that are not present in the elastic solutions, namely:

- Nonlinearity due to pile-soil interaction,
- The influence of ground response on the free-field motions that excite the pile, and nonlinearity associated with the free-field response, and
- Ground motion intensity and frequency content characteristics.

Furthermore, parameters used in the models should be:

- Dimensionless, if possible;
- Easy to define with routine project information, i.e. without the need for *in-situ* or laboratory testing that is outside the bounds of conventional practice, and using readily-quantifiable structural properties;
- Based on parameters consistent with the level of seismic hazard analysis appropriate for the project. For example, if spectral ratios are desired for a response-spectrum based design, the parameters in the spectral ratio

prediction model should be based on the free-field response spectrum rather than requiring parameters that describe an appropriate acceleration time series.

10.4.1 Functional Form

The functional forms used here for fixed- and free-head horizontal displacement transfer functions are adopted from the Anoyatis et al. (2013) and Rovithis et al. (2009) studies, respectively. Note that Anoyatis et al. provide results for free-head piles in terms of plots of normalized transfer functions, but they only present a best-fit function for the fixed-head case. Although Rovithis et al. do not present the free-head function in the same form that it is presented below, the form below can be derived from other equations presented in their paper.

Prior to adopting these previously-established functional forms, an independent study was conducted to derive expressions for the fixed- and free-head cases in order to evaluate if alternative forms existed that could capture the underlying trends with fewer coefficients, or simply provide a better fit. To do this, the derivation presented in Chapter 8 was distilled down to the simplest possible mathematical form and then terms were dropped one at a time to evaluate whether or not each term was necessary to capture the underlying trends. This exercise produced results that are essentially the same as Anoyatis et al. (2013) and Rovithis et al. (2009), presumably because they used a similar process, so their functional forms will be used herein.

The functional form for normalized (i.e., versus dimensionless frequency) fixed-head transfer functions is:

$$H_u = \frac{u_{FIM}}{u_{FFM}} = \frac{1}{1 + C_0 \left(\frac{\omega}{\lambda_{L_a} V_{S,L_a}} \right)^{C_1}} \quad (10.6)$$

The only difference between this functional form and Equation (10.1) used by Anoyatis et al. (2013) is that (10.6) uses λ_{L_a} and V_{S,L_a} , that is, values of λ and V_S computed over the depth increment corresponding to the uppermost active length of the pile. This makes (10.6) consistent with the form recommended by Di Laora and Rovithis (2014), who proposed $C_0 = 0.3$ and $C_1 = 3$ as an approximate best-fit to their elastic results.

The functional form for normalized free-head horizontal displacement transfer functions is:

$$H_u = \frac{u_{FIM}}{u_{FFM}} = \frac{1}{1 + C_2 \left(\frac{\omega}{\lambda_{L_a} V_{S,L_a}} \right)^{C_3}} \left(1 + C_4 \left(\frac{\omega}{\lambda_{L_a} V_{S,L_a}} \right)^{C_5} \right) \quad (10.7)$$

The second term in (10.7) containing coefficients C_4 and C_5 captures the kinematic amplification exhibited by free-head piles. Note that although (10.6) appears as the first term in (10.7), coefficients C_0 and C_1 generally do not take on the same values as C_2 and C_3 for a given pile/site/ground motion combination in which all factors are equal other than the head-fixity condition. Although Rovithis et al. (2009) take the approach of using the same coefficients for this portion of their free- and fixed-head equations, the models developed here were found to have more predictive power if the coefficients were defined independently for each head-fixity case.

To the best of the author's knowledge, no functional form for the underlying trend of free-head pile rotation transfer functions has previously been established. The curve shown in Figure

10-15 for Anoyatis et al. is simply a replication of results they presented graphically. Based on the similarity between these transfer functions (see Figure 10-15) and the kinematic amplification region of free-head horizontal displacement transfer functions (see Figure 10-14), the following functional form for normalized free-head rotation transfer functions has been established for this study:

$$H_{\theta} = \frac{\theta_{FIM}}{u_{FFM} \cdot \lambda_{L_a}} = \frac{C_6 \left(\frac{\omega}{\lambda_{L_a} V_{S, L_a}} \right)^{C_7}}{1 + C_8 \left(\frac{\omega}{\lambda_{L_a} V_{S, L_a}} \right)^{C_9}} \quad (10.8)$$

10.4.2 Approach

The statistical software package *R* (*R* Core Team 2015) was used to aid in development of the multiple linear regression for each coefficient prediction model. The steps taken to develop the models can be summarized as follows:

- Use *R* software to perform nonlinear least-squares regression (NLSR) to determine best-fit coefficients for each transfer function result for fixed- and free-head piles. For example, see Figure 10-20. These values of coefficients become the “targets” which the coefficient models will be used to predict. Computed transfer functions that lacked a significant number of high coherence points or did not extend to a high enough dimensionless frequency such that the underlying trend was well-constrained by the data were excluded from the regression model at this step.

- Evaluate a number of statistically independent predictive parameters for possible inclusion in the models by looking for strong correlation, low standard error, and an approximately linear trend between a given parameter and coefficient. In most cases, a log transformation of both the predictive parameters and pool of target coefficients [i.e., $\log(\text{parameter}_0)$ and $\log(C_0)$] was found to improve linearity, correlation, and normality/variance structure of residuals, while in other cases either no transformation or a power transformation was found to be optimum. The Box-Cox test (Box and Cox 1964) was used to determine the optimum transform power.
- Once best candidates for predictive parameters have been identified, use R to assess the performance of the models. Begin with a null model (predicted coefficient = mean of best-fit results from NLSR), then add the single-best standalone predictor and test for statistical significance; look for next-best predictor that can be added that will have most predictive power and statistical significance, etc., until adding additional predictors does not significantly increase the predictive power of the model. This saturation usually occurred once three strong predictors were identified.
- After a model has been developed for each coefficient needed for a given functional form, identify the predictors which (i) have the clearest physical meaning, (ii) have the most predictive power, and (iii) appear in multiple coefficient prediction models. Reformulate all coefficient prediction models to use the same set of predictors. While this may decrease the predictive

capability of an individual coefficient prediction model, using the same predictors in each model makes them easier to implement.

- Throughout the process outlined by the above steps, but especially when a potential set of final models has been produced, check that the underlying assumptions of multiple linear regression are satisfied (after Kutner et al. 2004):
 - Linear relationship between predictor and target parameter,
 - Normally-distributed predictor variables, e.g. as tested by a Q-Q plot,
 - Little or no multicollinearity between predictor variables, and
 - Homoscedasticity and lack of autocorrelation of residuals.

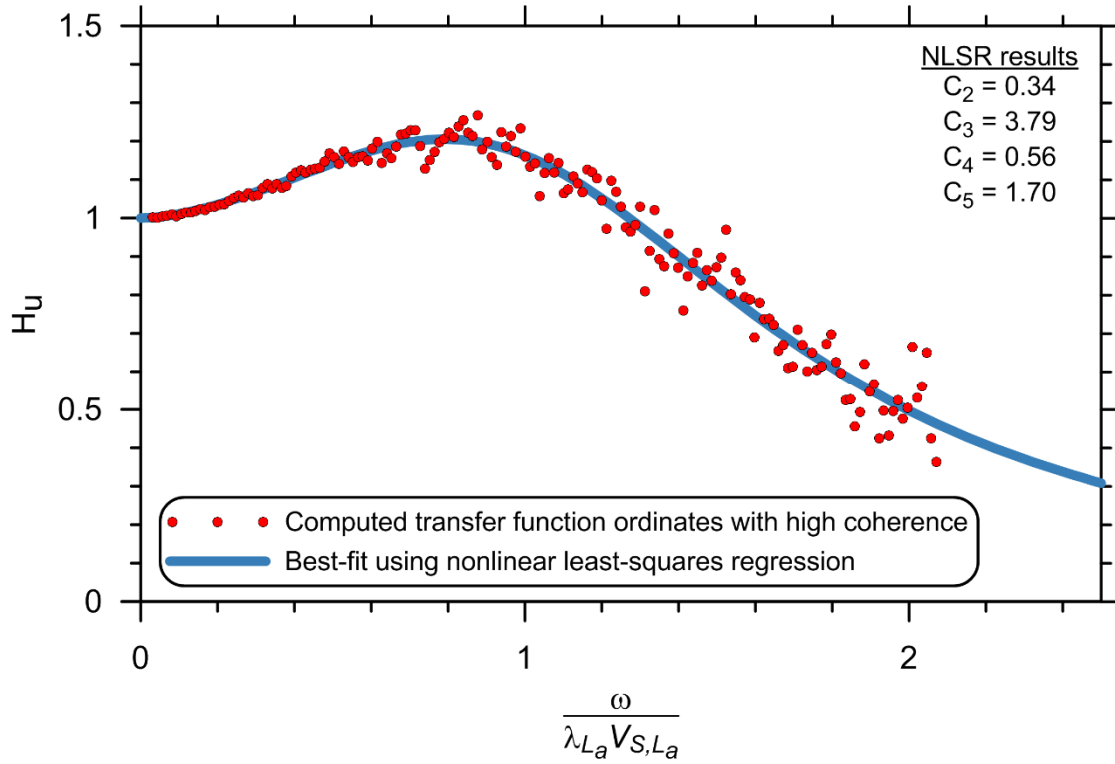


Figure 10-20: Example of nonlinear least-squares regression to determine coefficients for free-head pile functional form [Equation (10.7)] using computed data for $B = 2$ m, $L = 60$ m pile embedded in Site 4 and subjected to 1999 Hector Mine earthquake (NGA record sequence number 1786).

10.4.3 Models for Predicting Fixed-Head Transfer Function Coefficients

Models for predicting the coefficients to be used in Equation (10.6) are given in Equations (10.9) and (10.10). Metrics for assessing the statistical significance of the models are presented in Table 10-1 and Figure 10-21.

$$\log(C_0) = 0.47 \log \left[\left(\frac{f_m}{\lambda_{La} V_{S,La}} \right) \left(\frac{PGV}{V_{S,La}} \right) \right] - 1.37 \left(\frac{V_{S,La}}{V_{S,L}} \right) + 0.046 \left(\frac{PSA_{T=0.5s}}{PSA_{T=0.05s}} \right) + 2.60 \quad (10.9)$$

$$\log(C_1) = -0.065 \log \left[\left(\frac{f_m}{\lambda_{La} V_{S,La}} \right) \left(\frac{PGV}{V_{S,La}} \right) \right] + 0.38 \left(\frac{V_{S,La}}{V_{S,L}} \right) + 0.022 \left(\frac{PSA_{T=0.5s}}{PSA_{T=0.05s}} \right) - 0.14 \quad (10.10)$$

The physical interpretation and motivation for using each of the predictor variables that appear in (10.9) and (10.10) are summarized as follows:

- $\left(\frac{f_m}{\lambda_{L_a} V_{S,L_a}} \right)$ is essentially a dimensionless frequency term, inspired by the dependence of kinematic interaction on $\omega/(\lambda V_S)$. The difference is that the term used here corresponds to a single value of frequency f_m , which is the inverse of the mean period T_m defined by Rathje et al. (2004):

$$T_m = \frac{\sum_i FAS_i^2 (1/f_i)}{\sum_i FAS_i^2} \quad \text{for } 0.25 \text{ Hz} \leq f_i \leq 20 \text{ Hz, with } \Delta f \leq 0.05 \text{ Hz} \quad (10.11)$$

where FAS_i are the Fourier amplitude coefficients from the Fourier Amplitude Spectrum of the free-field ground surface motion, f_i are the frequencies corresponding to each FAS_i , and Δf is the frequency interval used in the FFT computation. This term will be referred to as “mean frequency” of the surface motion, although Rathje et al. do not use this terminology because they refer to it only in terms of period. Use of mean frequency as a predictor term is a convenient way to represent the frequency content of the ground surface motion with a single value. (Note— in order to be consistent with this model, f_m must be computed from the ground surface motion, not the input motion used for 1-D ground response analysis). Using mean frequency in a dimensionless frequency term effectively compares the pile characteristic length to the wavelength of free-field excitation corresponding to the predominant energy in the ground

motion. Finally, the λ_{La} term allows the coefficient to have a dependence on pile-to-soil stiffness contrast, which has been demonstrated to influence the results due to its effect on nonlinearity beyond what is captured by the dimensionless frequency term in the basic fixed-head functional form.

- $\left(\frac{PGV}{V_{S,L_a}} \right)$ is a proxy for shear strain in the free-field due to ground response,

and also serves as a general proxy for ground motion intensity. The former is based on the fundamental relationship of ground velocity normalized by shear wave velocity in the transverse direction being equal to shear strain (e.g., see Newmark 1967). Again, PGV is the peak ground velocity of the free-field ground surface motion, not the base input motion used for ground response analysis. In addition to producing a dimensionless ratio when normalized by shear wave velocity, PGV was found to be a strong predictor because it is mostly dependent on mid-range frequency content of the ground motion, which is where kinematic pile-soil interaction becomes significant.

- The preceding two terms are multiplied in order to allow the ground motion intensity to interact with the pile-to-soil stiffness term, which is an attempt to capture the increase in pile-soil interaction nonlinearity that is caused by increasing ground motion intensity.

- $\left(\frac{V_{S,L_a}}{V_{S,L}} \right)$ is the ratio of shear wave velocity over the uppermost pile active length (hence, near the ground surface) to the shear wave velocity over the

full length of the pile. This quantifies the increase, or lack thereof, in soil stiffness over the length of the pile.

- $\left(\frac{PSA_{T=0.5s}}{PSA_{T=0.05s}} \right)$ is the ratio of free-field ground surface acceleration response spectrum ordinates at 0.5 and 0.05 seconds, which serves as another descriptor of free-field ground motion frequency content. The periods 0.5 and 0.05 seconds ($f = 2$ to 20 Hz) were chosen because the transfer function corner frequencies and bandwidth over which significant deamplification occurs usually falls within this range (e.g., see Figure 10-16). The term may also capture, at least in part, the influence of free-field motion variable frequency-content on nonlinearity as discussed in §10.3.

Table 10-1: Fixed-head transfer function coefficient prediction model metrics.

Coefficient:	Adjusted R²	F-Statistic	P-Value
C_0	0.44	139	2.2E-16
C_1	0.19	43	2.2E-16

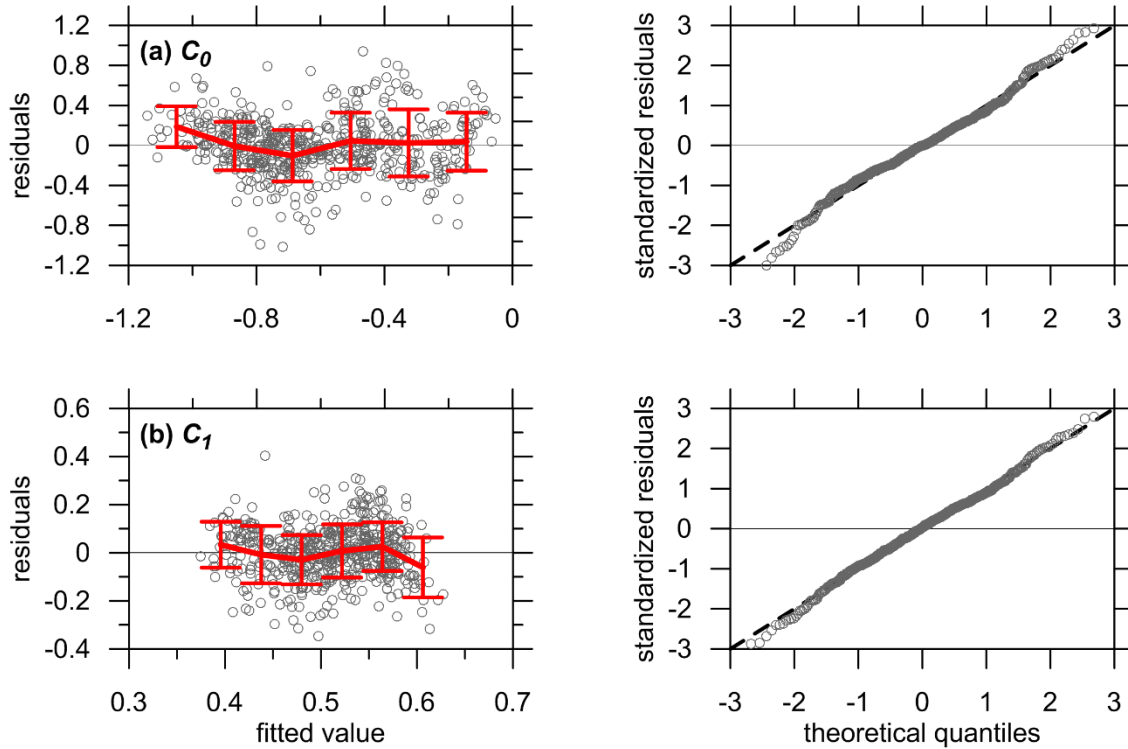


Figure 10-21: Residuals versus predicted values plots (left) and normal Q-Q plots (right) for fixed-head transfer function coefficient prediction models. Lines on residuals plots show trend and \pm one standard deviation.

As shown in Figure 10-19(a), there is a variability between the normalized transfer functions computed for the two diameters of piles considered in this study. This is shown again in terms of all computed transfer function ordinates with high coherence in Figure 10-22. This variability provides an opportunity to test the predictive capabilities of the coefficient models (10.9) and (10.10) by comparing the mean model predictions to the study results for each diameter independently. Figure 10-23 and Figure 10-24 show that the models match the overall trends exhibited by the two sizes of piles well. Note that although this variability is discussed here in terms of diameter, the actual behavior is better characterized by its dependence on $E_p I_p$, and diameter only appears in the functional form and coefficient prediction models through its inclusion in the $E_p I_p$ term.

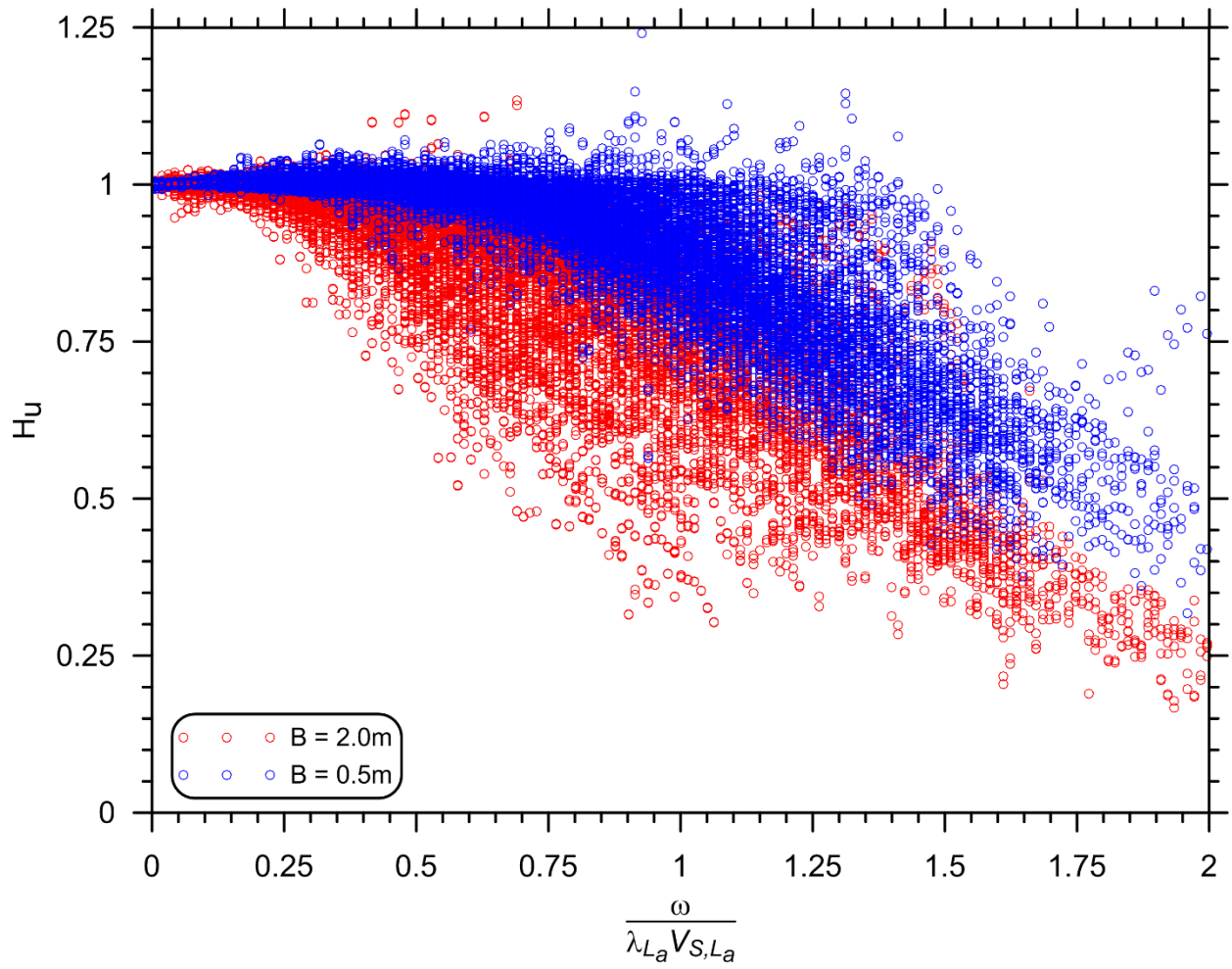


Figure 10-22: Variability in fixed-head transfer function results for the two pile diameters considered in this study.

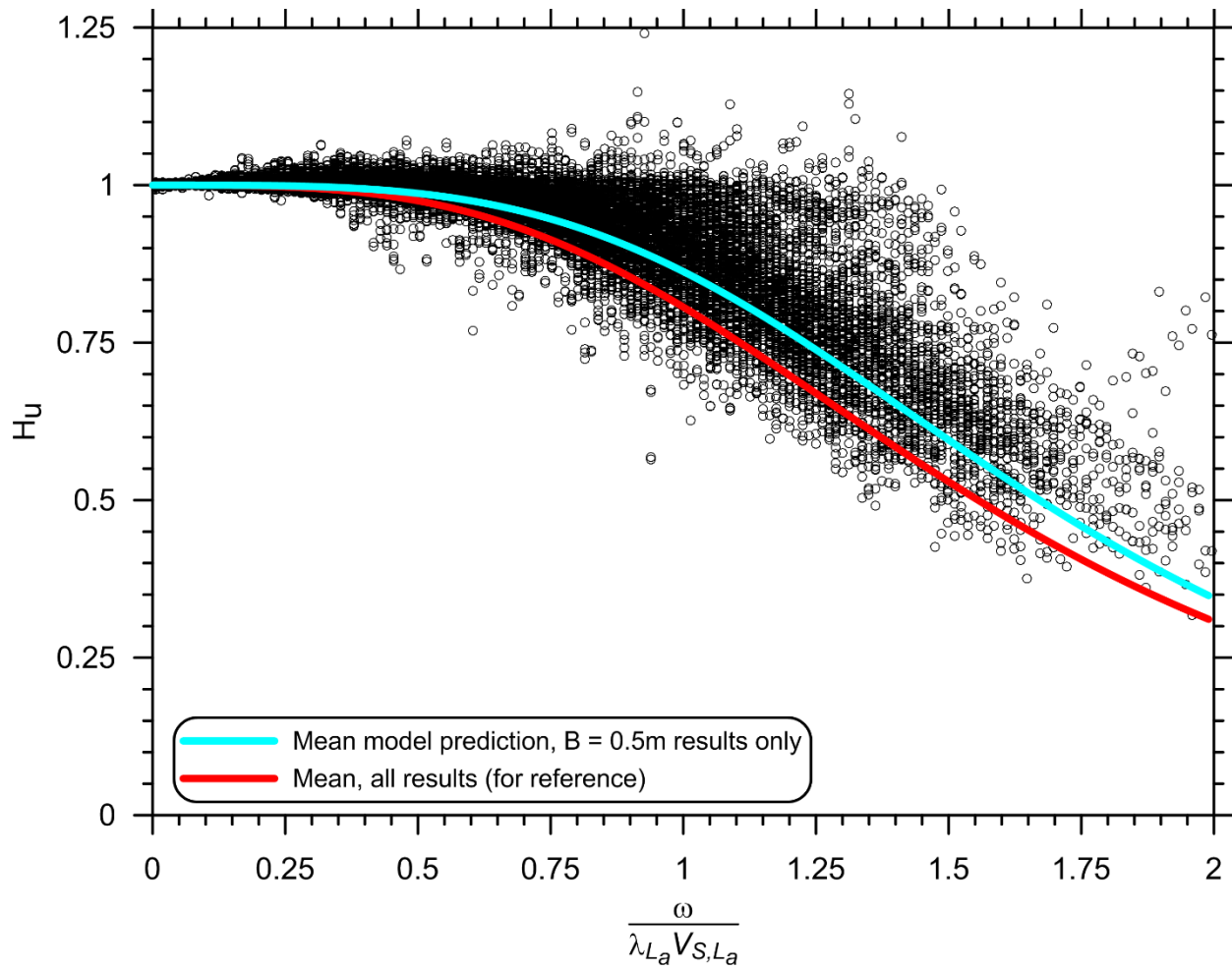


Figure 10-23: Mean fixed-head transfer function model prediction for $B = 0.5$ m compared to computed results.

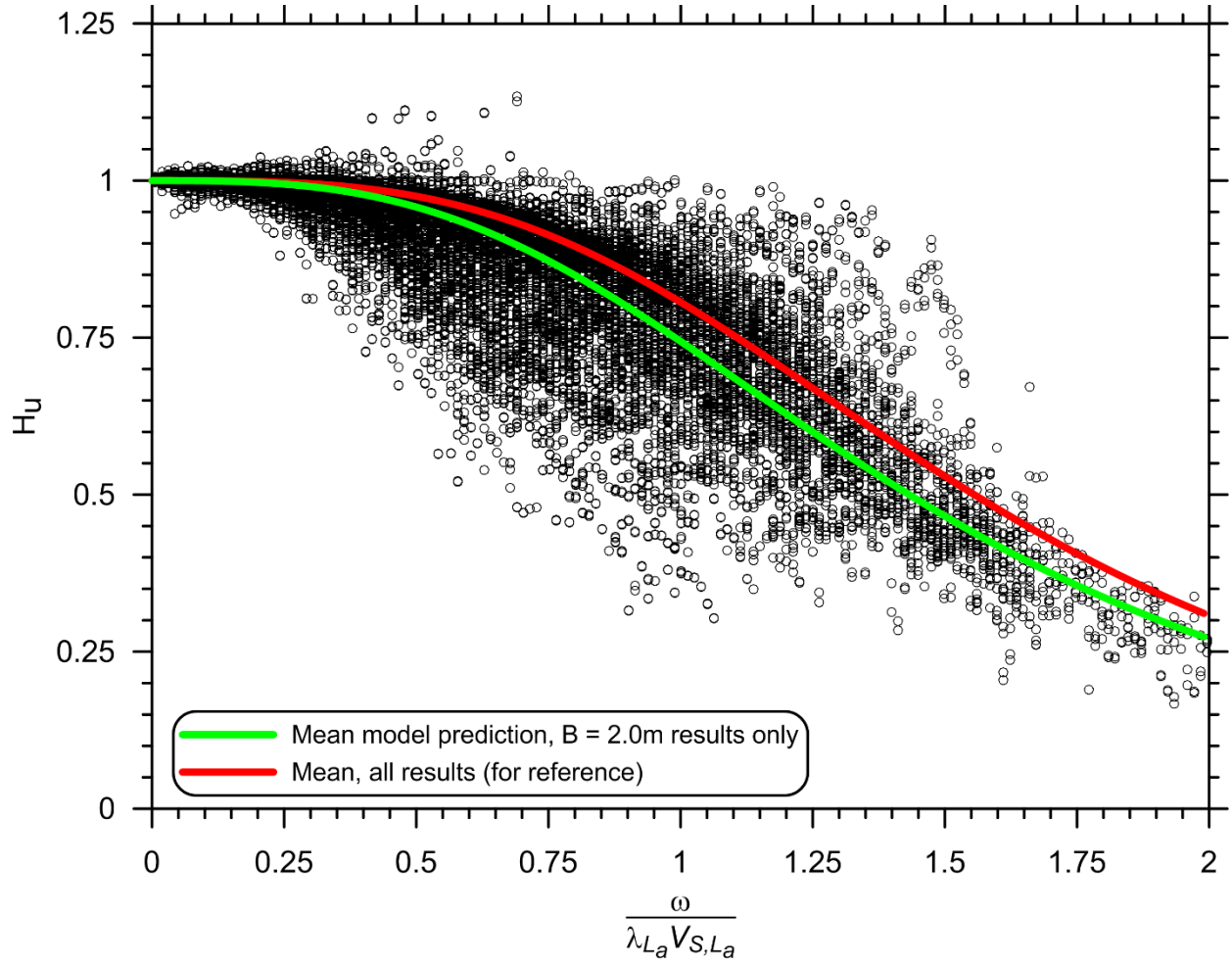


Figure 10-24: Mean fixed-head transfer function model prediction for $B = 2.0$ m compared to computed results.

10.4.4 Models for Predicting Free-Head Displacement Transfer Function Coefficients

Models for predicting the coefficients to be used in Equation (10.7) are given in Equations (10.12) through (10.15). Metrics for assessing the statistical significance of the models are presented in Table 10-2 and Figure 10-25. The same predictive parameters used for the fixed-head pile coefficient prediction models were used here for the free-head case, and the physical meaning and motivation for each parameter that was described above applies here as well.

$$\log(C_2) = 1.18 \log \left[\left(\frac{f_m}{\lambda_{La} V_{S,La}} \right) \left(\frac{PGV}{V_{S,La}} \right) \right] - 0.26 \left(\frac{V_{S,La}}{V_{S,L}} \right) + 0.11 \left(\frac{PSA_{T=0.5s}}{PSA_{T=0.05s}} \right) + 5.01 \quad (10.12)$$

$$(C_3)^{-0.79} = 0.10 \log \left[\left(\frac{f_m}{\lambda_{L_a} V_{S,L_a}} \right) \left(\frac{PGV}{V_{S,L_a}} \right) \right] - 0.074 \left(\frac{V_{S,L_a}}{V_{S,L}} \right) - 0.0015 \left(\frac{PSA_{T=0.5s}}{PSA_{T=0.05s}} \right) + 0.86 \quad (10.13)$$

$$(C_4)^{-0.31} = -0.63 \log \left[\left(\frac{f_m}{\lambda_{L_a} V_{S,L_a}} \right) \left(\frac{PGV}{V_{S,L_a}} \right) \right] + 0.20 \left(\frac{V_{S,L_a}}{V_{S,L}} \right) - 0.056 \left(\frac{PSA_{T=0.5s}}{PSA_{T=0.05s}} \right) - 1.73 \quad (10.14)$$

$$\log(C_5) = -0.049 \log \left[\left(\frac{f_m}{\lambda_{L_a} V_{S,L_a}} \right) \left(\frac{PGV}{V_{S,L_a}} \right) \right] + 0.18 \left(\frac{V_{S,L_a}}{V_{S,L}} \right) + 0.026 \left(\frac{PSA_{T=0.5s}}{PSA_{T=0.05s}} \right) - 0.20 \quad (10.15)$$

Table 10-2: Metrics for free-head displacement transfer function coefficient prediction models.

Coefficient:	Adjusted R²	F-Statistic	P-Value
C_2	0.51	72	2.2E-16
C_3	0.22	21	8.0E-12
C_4	0.47	62	2.2E-16
C_5	0.06	5	1.5E-3

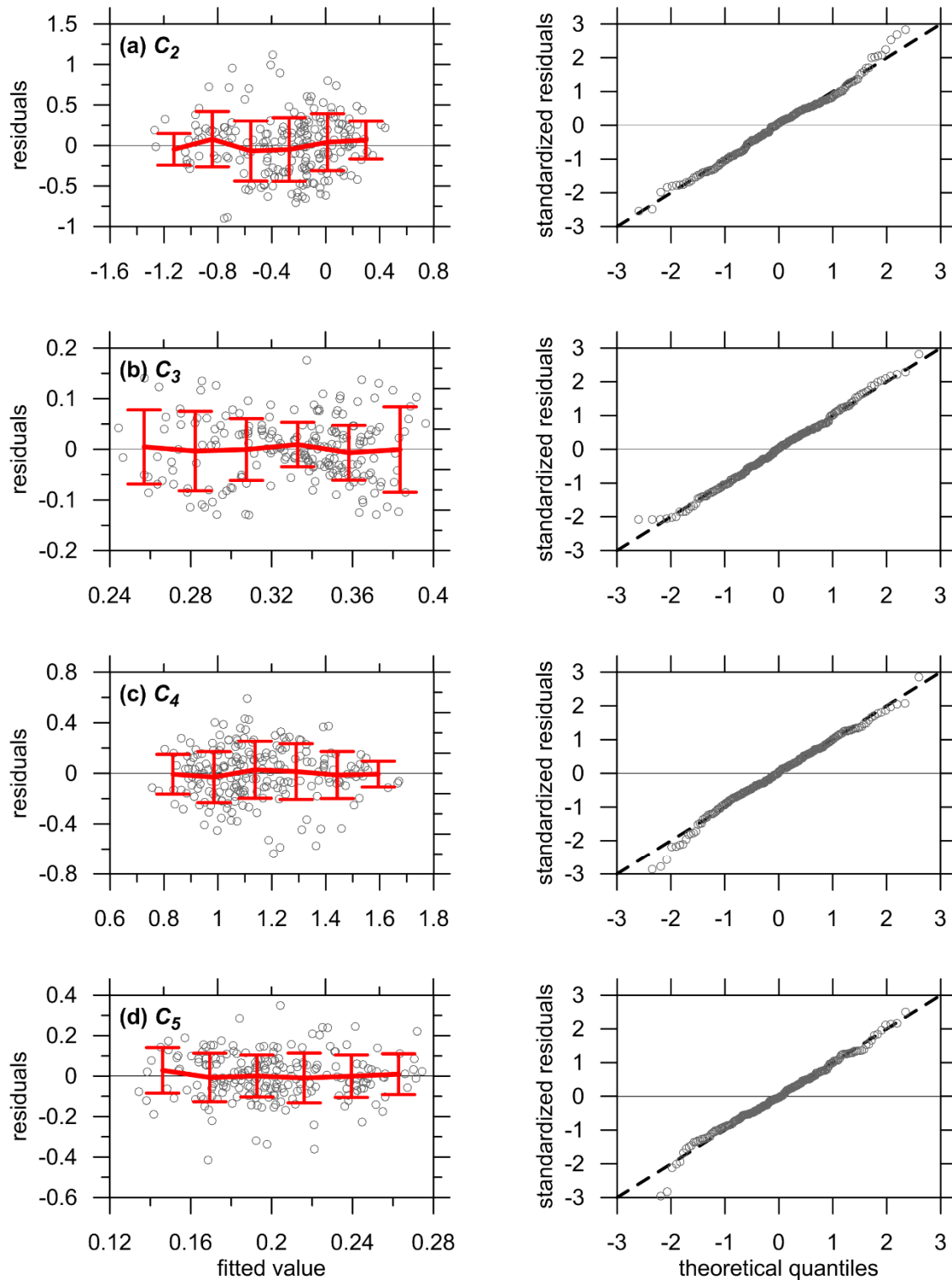


Figure 10-25: Residuals versus predicted values plots (left) and normal Q-Q plots (right) for free-head displacement transfer function coefficient prediction models. Lines on residuals plots show trend and \pm one standard deviation.

As for the fixed-head pile transfer functions, the free-head transfer functions exhibit variability between the two diameters considered in the study. Figure 10-26 and Figure 10-27 demonstrate that the coefficient prediction models are capable of capturing these trends well.

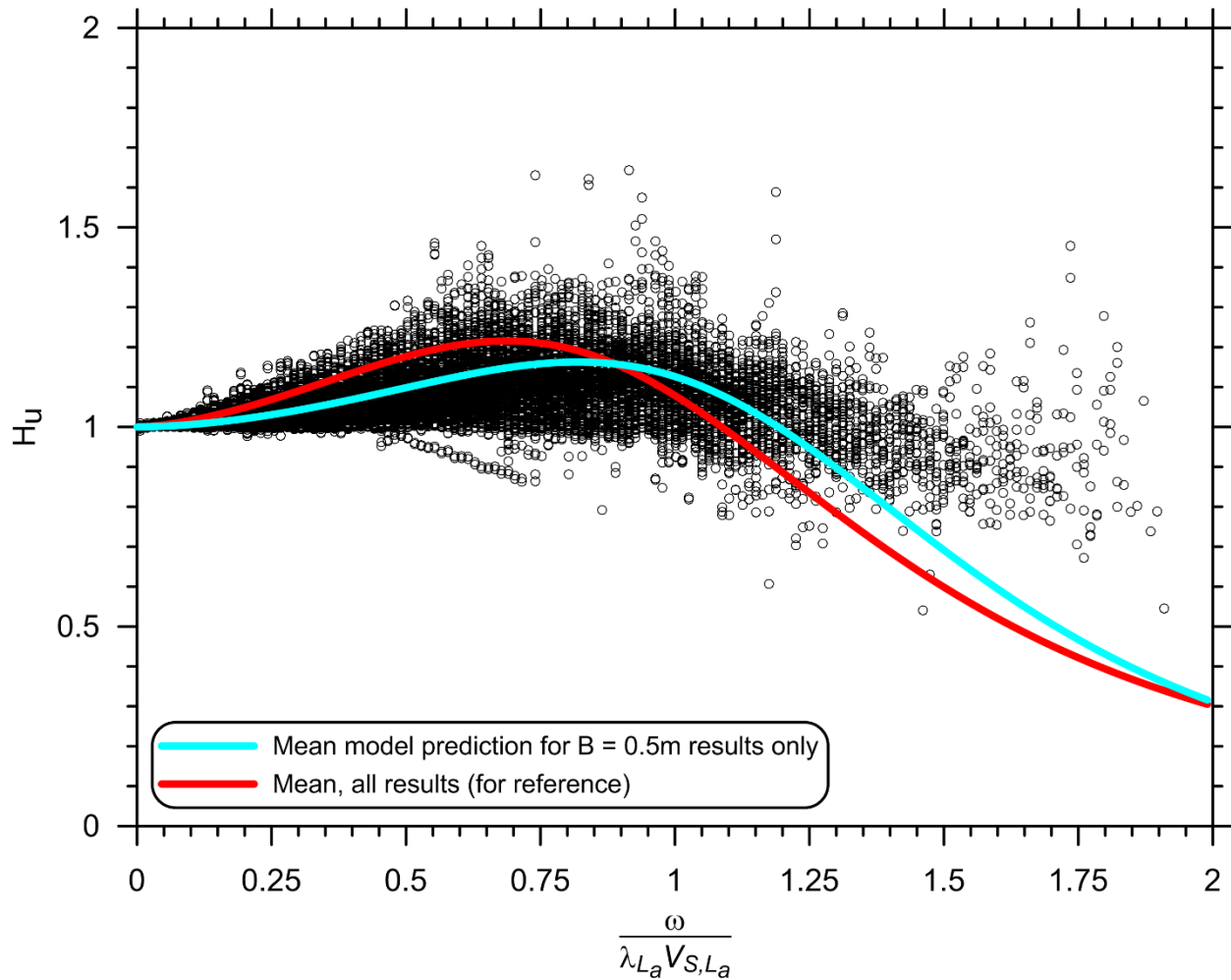


Figure 10-26: Mean free-head displacement transfer function model prediction for $B = 0.5$ m compared to computed results.

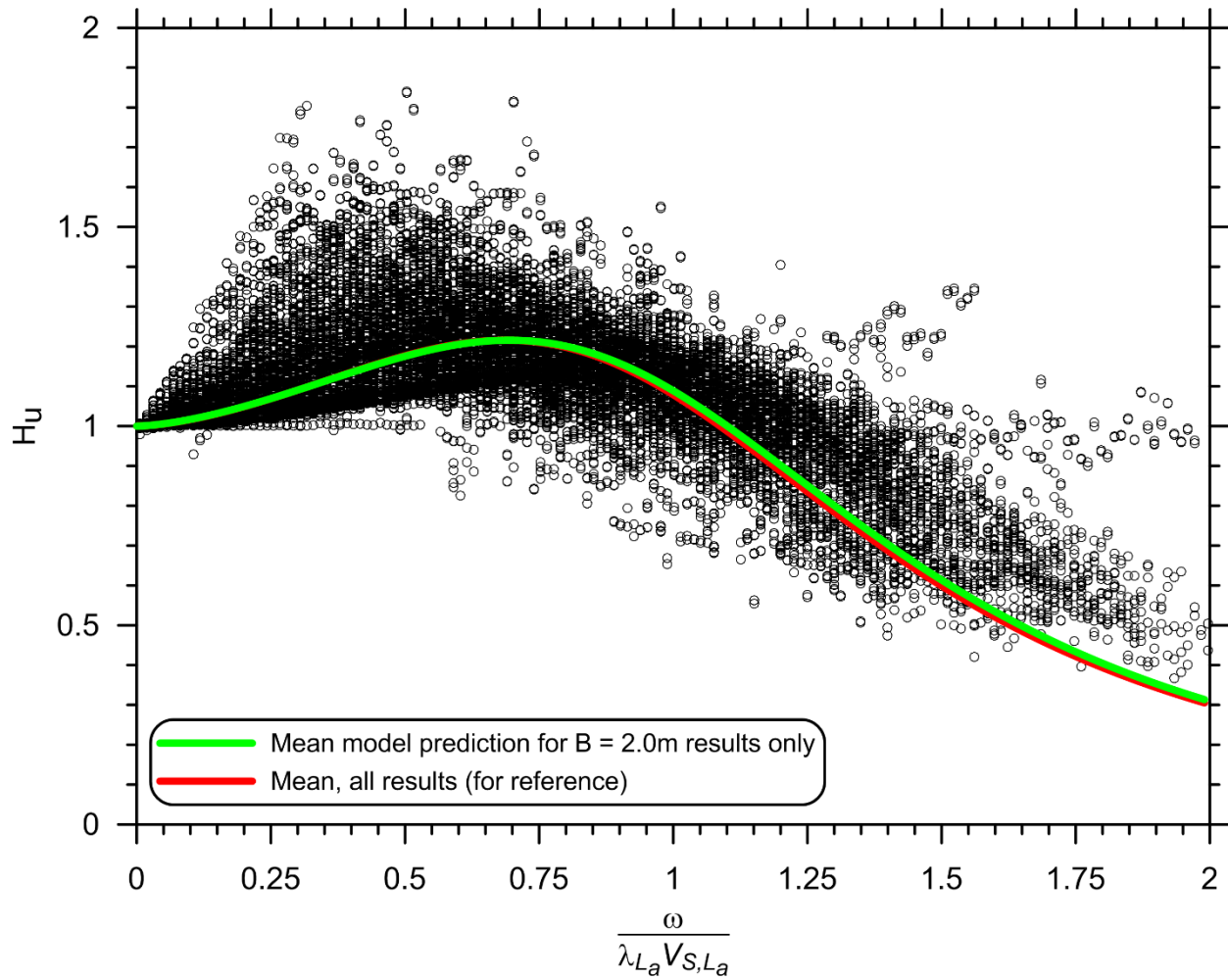


Figure 10-27: Mean free-head displacement transfer function model prediction for $B = 2.0$ m compared to computed results.

10.4.5 Models for Predicting Free-Head Rotation Transfer Function Coefficients

Models for predicting the coefficients to be used in Equation (10.8) are given in Equations (10.16) through (10.19). Metrics for assessing the statistical significance of the models are presented in Table 10-3 and Figure 10-28, and the ability to capture diameter-variability in the results (see Figure 10-29) is shown in Figure 10-30 and Figure 10-31.

$$(C_6)^{-0.69} = -0.44 \log \left[\left(\frac{f_m}{\lambda_{L_a} V_{S,L_a}} \right) \left(\frac{PGV}{V_{S,L_a}} \right) \right] + 0.31 \left(\frac{V_{S,L_a}}{V_{S,L}} \right) - 0.0066 \left(\frac{PSA_{T=0.5s}}{PSA_{T=0.05s}} \right) - 1.48 \quad (10.16)$$

$$(C_7)^{1.45} = -1.13 \log \left[\left(\frac{f_m}{\lambda_{L_a} V_{S,L_a}} \right) \left(\frac{PGV}{V_{S,L_a}} \right) \right] - 0.089 \left(\frac{V_{S,L_a}}{V_{S,L}} \right) - 0.16 \left(\frac{PSA_{T=0.5s}}{PSA_{T=0.05s}} \right) - 2.19 \quad (10.17)$$

$$\log(C_8) = 0.92 \log \left[\left(\frac{f_m}{\lambda_{L_a} V_{S,L_a}} \right) \left(\frac{PGV}{V_{S,L_a}} \right) \right] - 0.44 \left(\frac{V_{S,L_a}}{V_{S,L}} \right) + 0.12 \left(\frac{PSA_{T=0.5s}}{PSA_{T=0.05s}} \right) + 4.07 \quad (10.18)$$

$$(C_9)^{-1.31} = 0.10 \log \left[\left(\frac{f_m}{\lambda_{L_a} V_{S,L_a}} \right) \left(\frac{PGV}{V_{S,L_a}} \right) \right] + 0.057 \left(\frac{V_{S,L_a}}{V_{S,L}} \right) - 0.012 \left(\frac{PSA_{T=0.5s}}{PSA_{T=0.05s}} \right) + 0.63 \quad (10.19)$$

Table 10-3: Metrics for free-head rotation transfer function coefficient prediction models.

Coefficient:	Adjusted R²	F-Statistic	P-Value
C_6	0.52	40	2.2E-16
C_7	0.31	17	4.1E-09
C_8	0.44	29	1.3E-13
C_9	0.18	9	2.3E-05

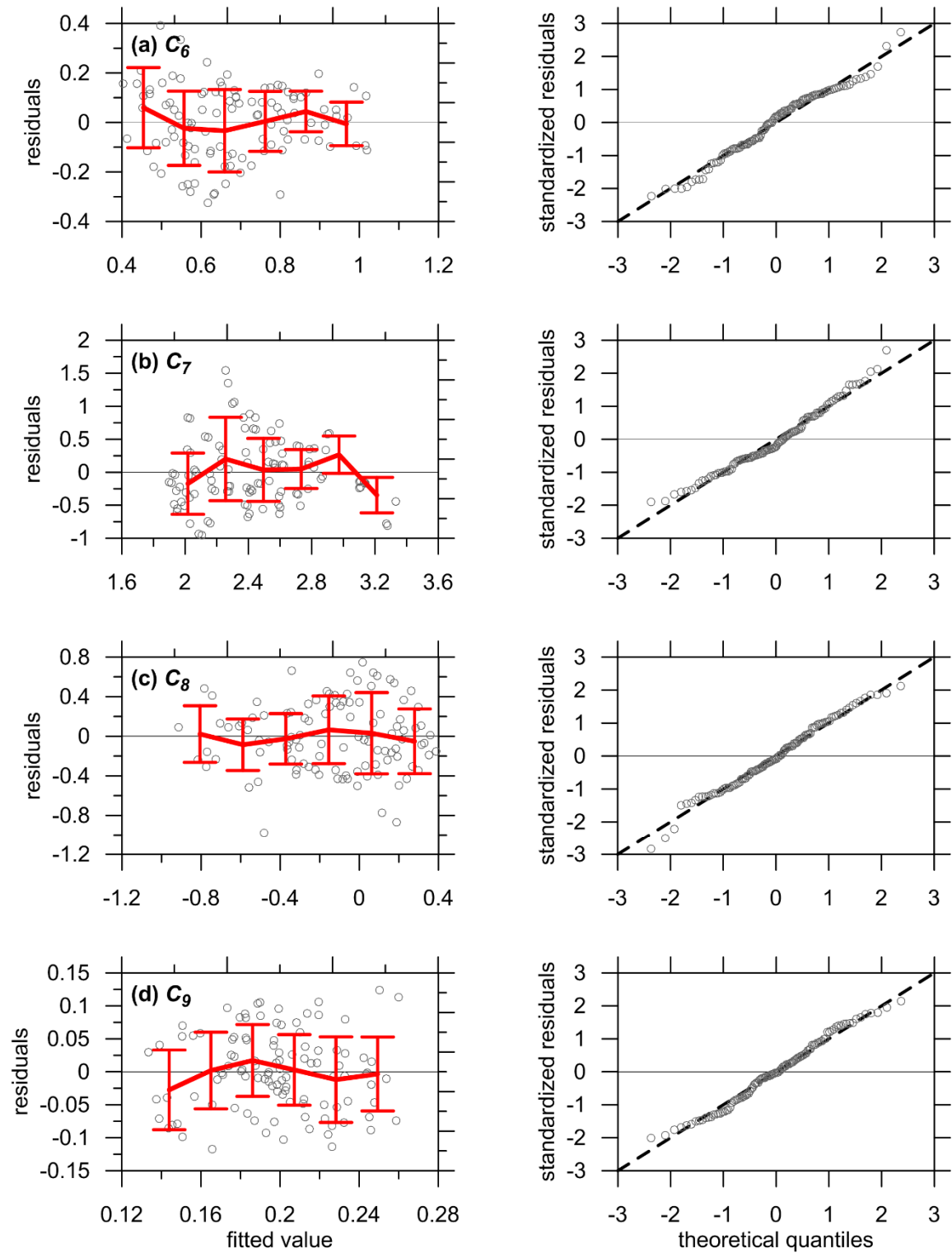


Figure 10-28: Residuals versus predicted values plots (left) and normal Q-Q plots (right) for free-head rotation transfer function coefficient prediction models. Lines on residuals plots show trend and \pm one standard deviation.

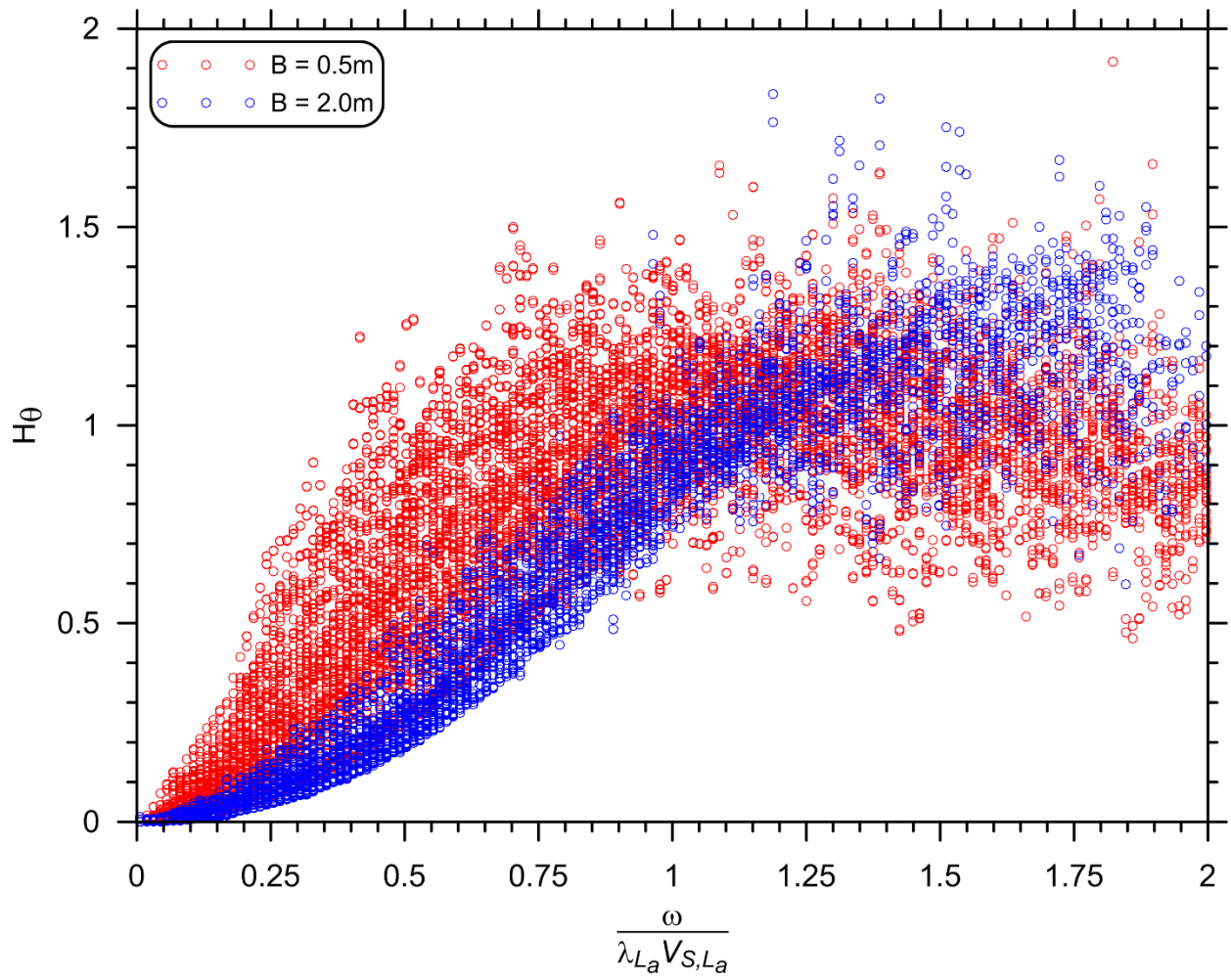


Figure 10-29: Variability in free-head rotation transfer function results for the two pile diameters considered in this study.

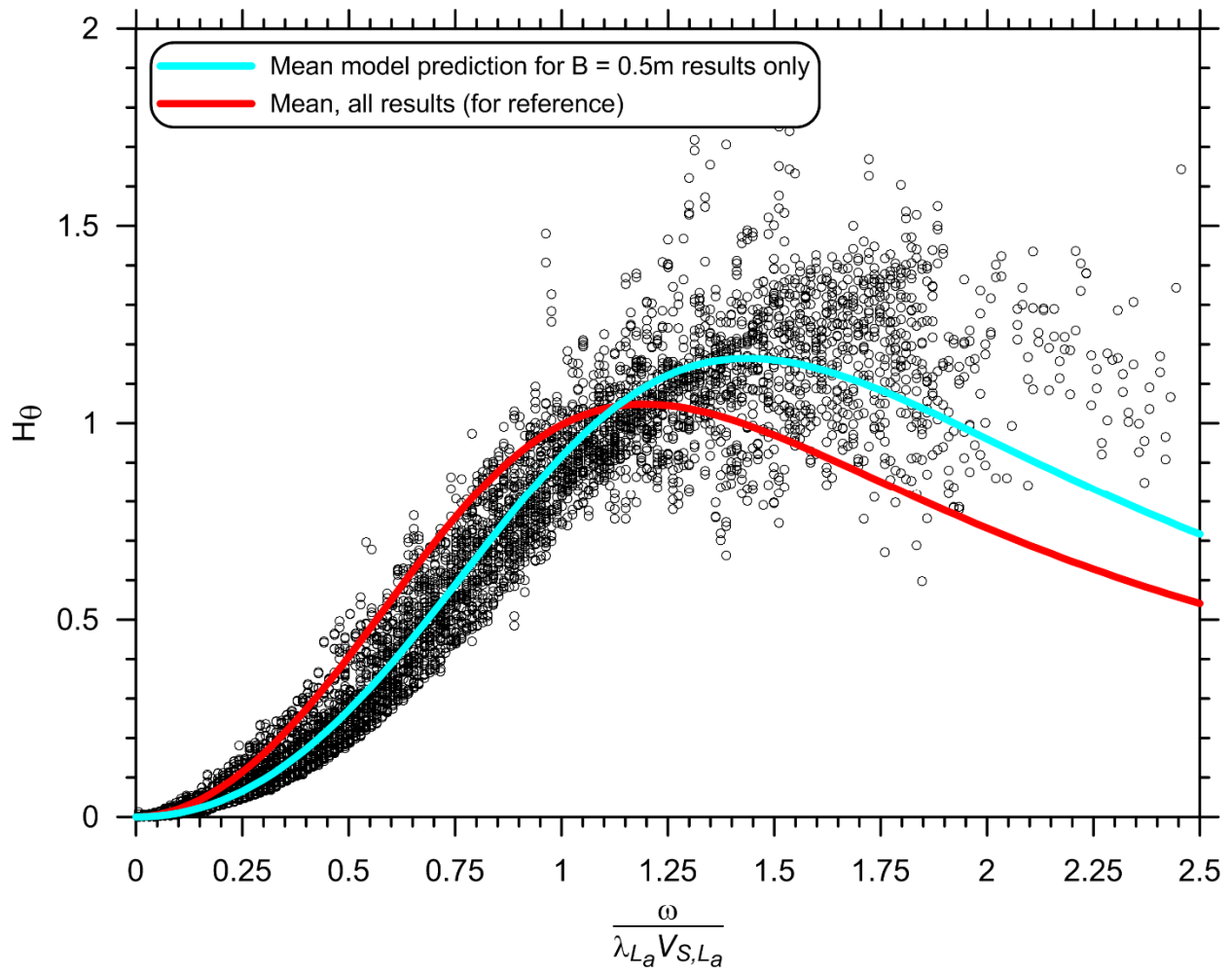


Figure 10-30: Mean free-head rotation transfer function model prediction for $B = 0.5$ m results.

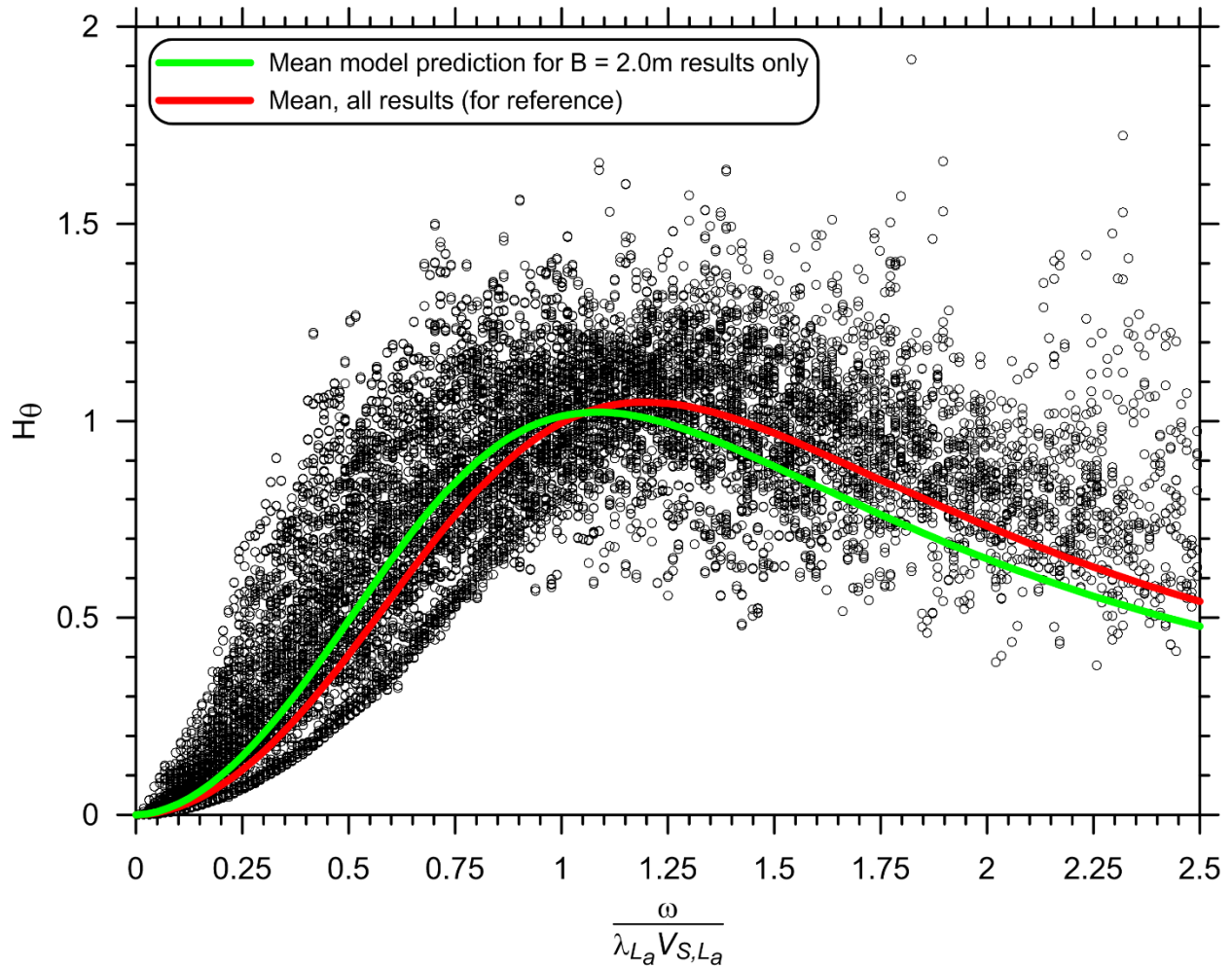


Figure 10-31: Mean free-head rotation transfer function model prediction for $B = 2.0$ m results.

10.5 GENERALIZED MODELS FOR PREDICTING SPECTRAL RATIOS

The same approach described above for development of transfer function prediction models was used to develop models for predicting spectral ratios that include variability due to the controlling parameters identified in §10.3. Spectral ratios primarily depend on the same physical mechanisms that influence transfer functions, except that short-period (high-frequency) spectral ordinates are controlled by the largest amplitude peak in the signals rather than the high-frequency energy. Response spectra used to compute spectral ratios were computed from the free-field ground surface and pile-head motions for 5-percent damping.

10.5.1 Functional Form

Spectral ratios for kinematic pile-soil interaction exhibit a characteristic form in which the ordinates generally decrease with decreasing period, down to some limiting value corresponding to the period T_{min} (see Figure 10-32). The minimum value defines a transition point in the pile-soil system behavior. At periods below T_{min} (i.e., frequencies above $1/T_{min}$), spectral acceleration of both the pile head and free-field ground surface motion are controlled by the largest amplitude peak in the respective motions. This behavior is maximized at $T=0$ s (i.e., PGA), when the spectral acceleration is simply equal to the maximum of the acceleration time series. The largest amplitude peak of design-level earthquake motions usually occurs within mid-range frequencies of 2 to 5 Hz (e.g., periods around 0.2 to 0.5 s), which corresponds to the range over which kinematic pile-soil interaction may be significant for stiff piles in soft soil, but relatively insignificant for smaller piles in stiffer soil (see Figure 10-16). Hence the spectral ratio ordinate at zero period depends on the level of kinematic pile-soil interaction that occurs at frequencies corresponding to the peak amplitude of the free-field ground surface motion, and for fixed-head piles will approach unity as the level of pile-soil interaction decreases.

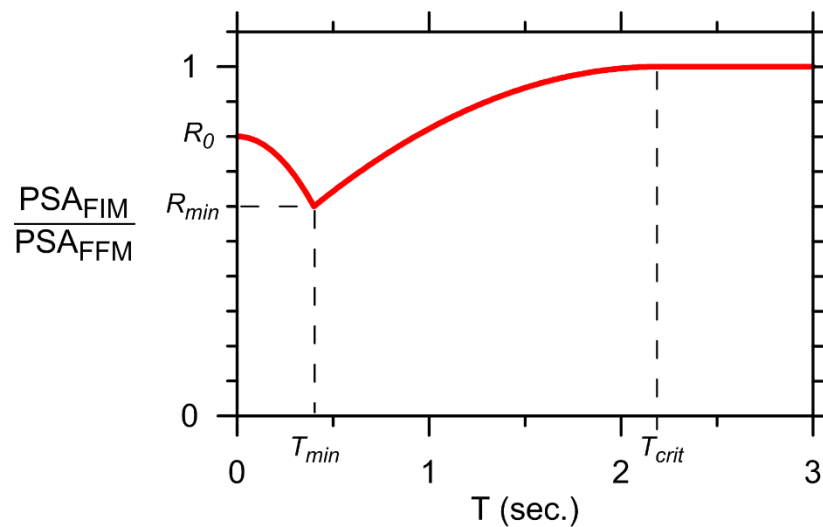


Figure 10-32: Fixed-head pile spectral ratio functional form after Di Laora and Sanctis (2013).

The only published work that the author is aware of in which kinematic pile-soil interaction spectral ratios are computed and discussed in terms of an underlying functional form is the elastic study by Di Laora and Sanctis (2013). The functional form used here for fixed-head piles is adopted from their study:

$$\frac{PSA_{FIM}}{PSA_{FFM}} = \begin{cases} R_0 - (R_0 - R_{min}) \left(\frac{T}{T_{min}} \right)^2; & T \leq T_{min} \\ 1 - (1 - R_{min}) \left(\frac{T_{crit} - T}{T_{crit} - T_{min}} \right)^2; & T_{min} \leq T \leq T_{crit} \\ 1 & T \geq T_{crit} \end{cases} \quad (10.20)$$

Equation (10.20) is a piecewise combination of two parabolas and a straight line, where R_0 and R_{min} are coefficients defining the spectral ratio at a period of zero and the minimum spectral ratio, and T_{min} , and T_{crit} are the period corresponding to the minimum spectral ratio and the period beyond which no significant reduction occurs, respectively. These parameters and the basic functional form are illustrated in Figure 10-32.

Di Laora and Sanctis only considered fixed-head piles; for free-head pile spectral ratios, the author is not aware of any published functional forms. The trend exhibited by free-head pile spectral ratios computed for this study is matched well by the following:

$$\frac{PSA_{FIM}}{PSA_{FFM}} = \begin{cases} R_0 - (R_0 - R_{\min}) \left(\frac{T}{T_{\min}} \right)^2; & T \leq T_{\min} \\ R_{\max} + \frac{(R_{\min} - R_{\max})(T - T_{\max})^2}{(T_{\max} - T_{\min})^2}; & T_{\min} \leq T \leq T_{\max} \\ 1 + \frac{(R_{\max} - 1)(T - T_{crit})^2}{(T_{\max} - T_{crit})^2}; & T_{\max} \leq T \leq T_{crit} \\ 1 & T \geq T_{crit} \end{cases} \quad (10.21)$$

Equation (10.21) is a modified version of the fixed-head form which captures the effect of kinematic amplification on the computed spectral ratios by adding a third parabolic leg to the piecewise formulation. The peak spectral ratio is defined by (R_{\max}, T_{\max}) as shown in Figure 10-33.

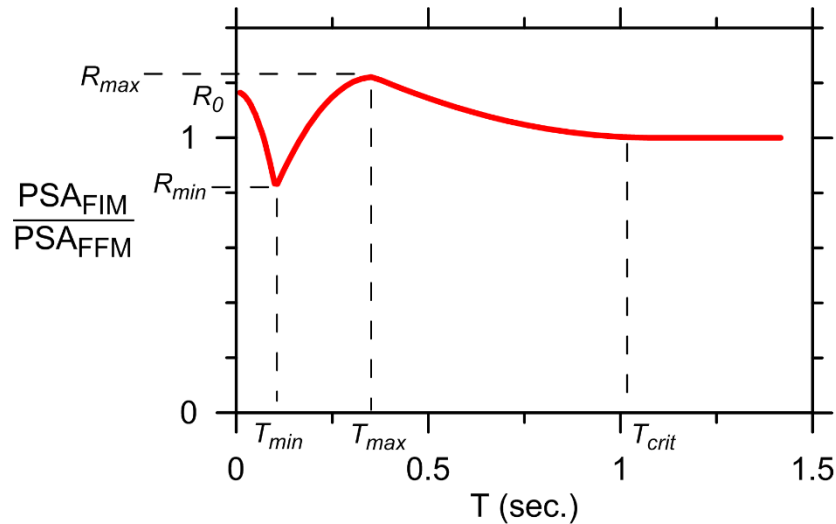


Figure 10-33: Free-head pile spectral ratio functional form.

10.5.2 Models for Predicting Fixed-Head Spectral Ratio Coefficients

Models for predicting the coefficients to be used in Equation (10.20) are given in Equations (10.22) through (10.25). Metrics for assessing the statistical significance of the models are presented in Table 10-4 and Figure 10-34.

$$R_{0,FXH} = -0.086 \log \left(\frac{f_0}{\lambda_{L_a} V_{S,L_a}} \right) + 0.047 \left(\frac{V_{S,L_a}}{V_{S,L}} \right) - 0.046 \log \left(\frac{PSA_{\max}}{g} \right) + 0.81 \quad (10.22)$$

$$R_{\min,FXH} = -0.38 \log \left(\frac{f_0}{\lambda_{L_a} V_{S,L_a}} \right) - 0.12 \left(\frac{V_{S,L_a}}{V_{S,L}} \right) - 0.026 \log \left(\frac{PSA_{\max}}{g} \right) + 0.16 \quad (10.23)$$

$$(T_{\min,FXH})^{-0.58} = -1.39 \log \left(\frac{f_0}{\lambda_{L_a} V_{S,L_a}} \right) + 4.53 \left(\frac{V_{S,L_a}}{V_{S,L}} \right) + 1.99 \log \left(\frac{PSA_{\max}}{g} \right) - 0.26 \quad (10.24)$$

$$\log(T_{\text{crit},FXH}) = 0.79 \log \left(\frac{f_0}{\lambda_{L_a} V_{S,L_a}} \right) - 0.53 \left(\frac{V_{S,L_a}}{V_{S,L}} \right) - 0.27 \log \left(\frac{PSA_{\max}}{g} \right) + 1.01 \quad (10.25)$$

Note that T_{\min} and T_{crit} in Equations (10.24) and (10.25) are in seconds.

The physical interpretation and motivation for using each of the predictor variables that appear in (10.22) through (10.25) are summarized as follows:

- Similar to the transfer function models, the $\left(\frac{f_0}{\lambda_{L_a} V_{S,L_a}} \right)$ term is a dimensionless frequency computed at a single frequency value. In this case f_0 is used, which is the inverse of the “smoothed spectral predominant period” period T_0 defined by Rathje et al. (2004):

$$T_0 = \frac{\sum_i T_i \cdot \ln \left(\frac{PSA(T_i)}{PGA} \right)}{\sum_i \ln \left(\frac{PSA(T_i)}{PGA} \right)} \quad \text{for } T_i \text{ with } \frac{PSA}{PGA} \geq 1.2, \Delta \log T_i \leq 0.02 \quad (10.26)$$

where T_i are the discrete periods in the acceleration response spectrum equally spaced on a log axis and $PSA(T_i)$ are the spectral accelerations at

periods T_i . If the spacing criterion is not satisfied, the spectral values must be interpolated over a closer log interval. Equation (10.26) essentially extracts the spectral ordinates that are greater than 1.2 times PGA, thus exhibiting significant amplification, and returns the period corresponding to the peak of a smoothed curve of these ordinates. The way in which T_0 is defined makes it mostly dependent on the moderate to high frequency content of a ground motion, which is the important range for kinematic pile-soil interaction. As demonstrated by Rathje et al, T_0 is also a better overall descriptor of the mean frequency content of the motion than the peak of the unsmoothed spectrum because it represents a weighted average of the entire period bandwidth over which amplification occurs, and thus is not controlled by a single peak that may have narrow bandwidth. Furthermore, f_0 was chosen because it is defined from the free-field ground surface motion response spectrum. For design applications in which spectral ratios for kinematic pile-soil interaction are desired, it would be impractical to have to compute a parameter like f_m which is defined by a ground motion time series instead of a response spectrum. The empirical relationships developed by Rathje et al. could also be used to predict f_0 for use in (10.22) —(10.25) at the planning stages of a project, or for cases when a site-specific seismic hazard analysis to define response spectra is not performed.

- $\left(\frac{V_{S,L_a}}{V_{S,L}} \right)$ quantifies changes in soil stiffness over the length of the pile.

- $\left(\frac{PSA_{\max}}{g}\right)$ is simply the maximum spectral acceleration normalized by gravity such that the term is dimensionless. This measure of ground motion intensity serves as a proxy for nonlinearity and was found to be a more effective predictor than spectral acceleration at any one specified period. As discussed above, the maximum spectral acceleration also plays an important role in defining the zero-period ordinate and thus is a powerful predictor of R_0 .

Table 10-4: Fixed-head spectral ratio coefficient prediction model metrics.

Coefficient:	Adjusted R²	F-Statistic	P-Value
R_0	0.19	74	2.2E-16
R_{min}	0.54	381	2.2E-16
T_{min}	0.33	157	2.2E-16
T_{crit}	0.70	734	2.2E-16

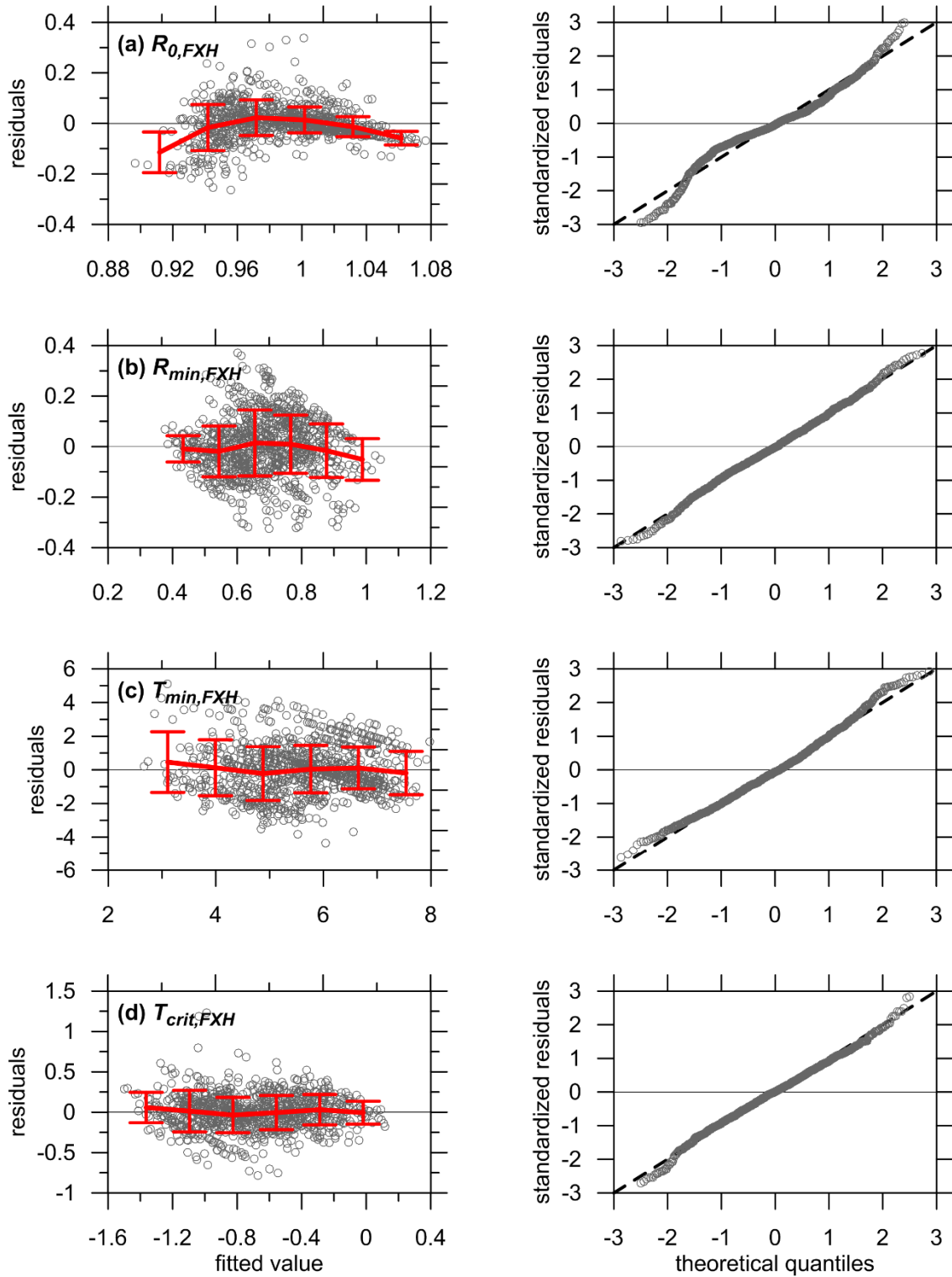


Figure 10-34: Residuals versus predicted values plots (left) and normal Q-Q plots (right) for fixed-head spectral ratio coefficient prediction models. Lines on residuals plots show trend and \pm one standard deviation.

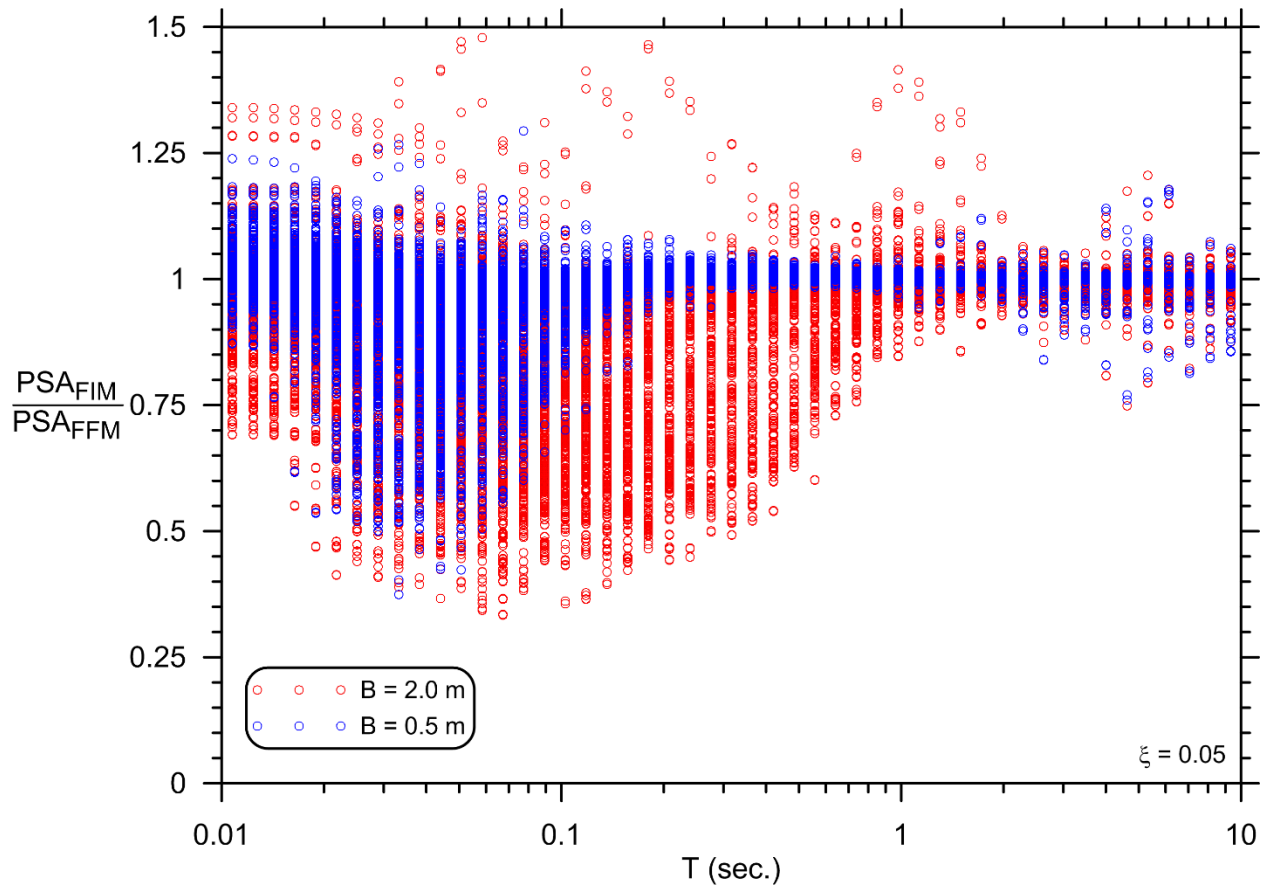


Figure 10-35: Fixed-head spectral ratio results.

As for the transfer functions, variability exists in the computed spectral ratios between the two diameters considered for this study (Figure 10-35). Since no normalization scheme is applied to the results—that is, the computed spectral ratios are presented versus period rather than a dimensionless combination of period and other variables—there is variability in the spectral ratio results that has effectively been removed (or at least reduced) from the corresponding normalized transfer function results by using a dimensionless frequency that captures the underlying physics (e.g., Figure 10-13 and Figure 10-14). While it would be possible to first normalize the spectral ratio results using a “dimensionless period” akin to the dimensionless frequency used for transfer functions, this would obscure the meaning of a spectral ratio at a given period. Moreover,

promoting the false notion that spectral ratios are simply the mirror image of transfer functions since period is the inverse of frequency is undesirable, so “dimensionless period” is avoided herein.

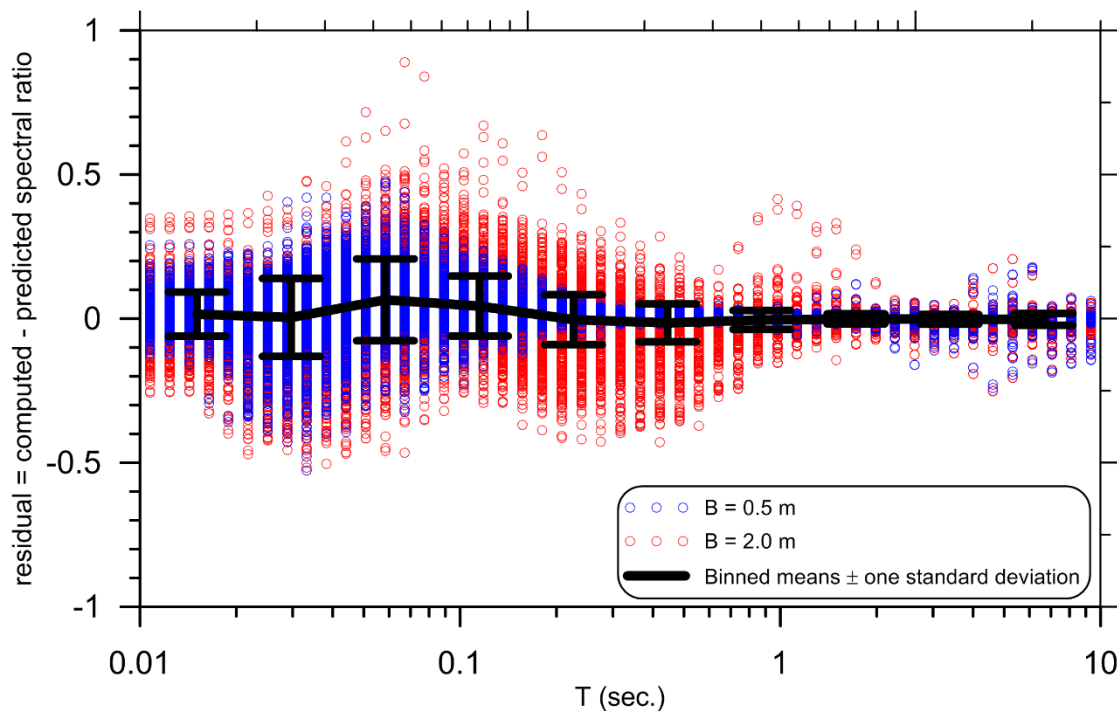


Figure 10-36: Fixed-head pile spectral ratio predictive model residuals.

Residuals between the predictive model and the computed spectral ratio results are shown in Figure 10-36. To compute these residuals, the coefficient prediction models [Equations (10.22) —(10.25)] were applied for a given combination of pile, site, and ground motion properties to predict spectral ratio values at each period. These predicted values were then subtracted from the spectral ratios computed in the parametric analyses for the same combination of pile, site, and ground motion properties. The mean trend exhibited by the residuals is close to zero, indicating that the predictive model is generally unbiased. Furthermore, the \pm one standard deviation error bars shown that the majority of the residuals fall close to zero. The \pm one standard deviation error bars are the best means of visually assessing these trends because the large number of points (over

60,000) shown on the plot make it visually difficult to assess where the greatest concentration of points lie.

The largest bias occurs around a period of 0.05 to 0.1 seconds, which is where the minimum spectral ratio occurs. The mean bias at this period is approximately 0.1, meaning that, on average, predicted spectral ratios are about 10-percent below those computed for this study. This bias is attributable to the difficulty in predicting the period and corresponding ordinate at which the local minimum in the spectral ratio will occur (T_{min} and R_{min} , respectively). In future studies it may be possible to reduce this bias, and/or to further reduce the total variability exhibited the residuals, thus improving the reliability of the model.

10.5.3 Models for Predicting Free-Head Spectral Ratio Coefficients

Models for predicting the coefficients to be used in Equation (10.21) are given in Equations (10.27) through (10.32). Metrics for assessing the statistical significance of the models are presented in Table 10-5 and Figure 10-37. The same predictor variables used in the fixed-head models are used here.

$$\left(R_{0,FRH}\right)^{-4.49} = -0.60 \log\left(\frac{f_0}{\lambda_{L_a} V_{S,L_a}}\right) - 0.032 \left(\frac{V_{S,L_a}}{V_{S,L}}\right) + 0.15 \log\left(\frac{PSA_{max}}{g}\right) - 0.26 \quad (10.27)$$

$$\left(R_{min,FRH}\right)^{1.67} = -0.24 \log\left(\frac{f_0}{\lambda_{L_a} V_{S,L_a}}\right) - 0.36 \left(\frac{V_{S,L_a}}{V_{S,L}}\right) - 0.093 \log\left(\frac{PSA_{max}}{g}\right) + 0.60 \quad (10.28)$$

$$\left(T_{min,FRH}\right)^{-0.73} = -3.86 \log\left(\frac{f_0}{\lambda_{L_a} V_{S,L_a}}\right) + 6.97 \left(\frac{V_{S,L_a}}{V_{S,L}}\right) + 4.38 \log\left(\frac{PSA_{max}}{g}\right) - 1.53 \quad (10.29)$$

$$\left(R_{\max,FRH}\right)^{-3.38} = -0.39 \log\left(\frac{f_0}{\lambda_{L_a} V_{S,L_a}}\right) + 0.076 \left(\frac{V_{S,L_a}}{V_{S,L}}\right) + 0.10 \log\left(\frac{PSA_{\max}}{g}\right) - 0.11 \quad (10.30)$$

$$\left(T_{\max,FRH}\right)^{-0.59} = -2.24 \log\left(\frac{f_0}{\lambda_{L_a} V_{S,L_a}}\right) + 2.34 \left(\frac{V_{S,L_a}}{V_{S,L}}\right) + 1.24 \log\left(\frac{PSA_{\max}}{g}\right) - 1.59 \quad (10.31)$$

$$\log\left(T_{crit,FRH}\right) = 0.73 \log\left(\frac{f_0}{\lambda_{L_a} V_{S,L_a}}\right) - 0.47 \left(\frac{V_{S,L_a}}{V_{S,L}}\right) - 0.24 \log\left(\frac{PSA_{\max}}{g}\right) + 1.09 \quad (10.32)$$

Note that T_{min} , T_{max} , and T_{crit} in Equations (10.29), (10.31), and (10.32) are in seconds.

Table 10-5: Metrics for free-head spectral ratio coefficient prediction models.

Coefficient:	Adjusted R²	F-Statistic	P-Value
R_0	0.47	203	2.2E-16
R_{min}	0.13	35	2.2E-16
T_{min}	0.41	163	2.2E-16
R_{max}	0.47	203	2.2E-16
T_{max}	0.58	313	2.2E-16
T_{crit}	0.60	350	2.2E-16

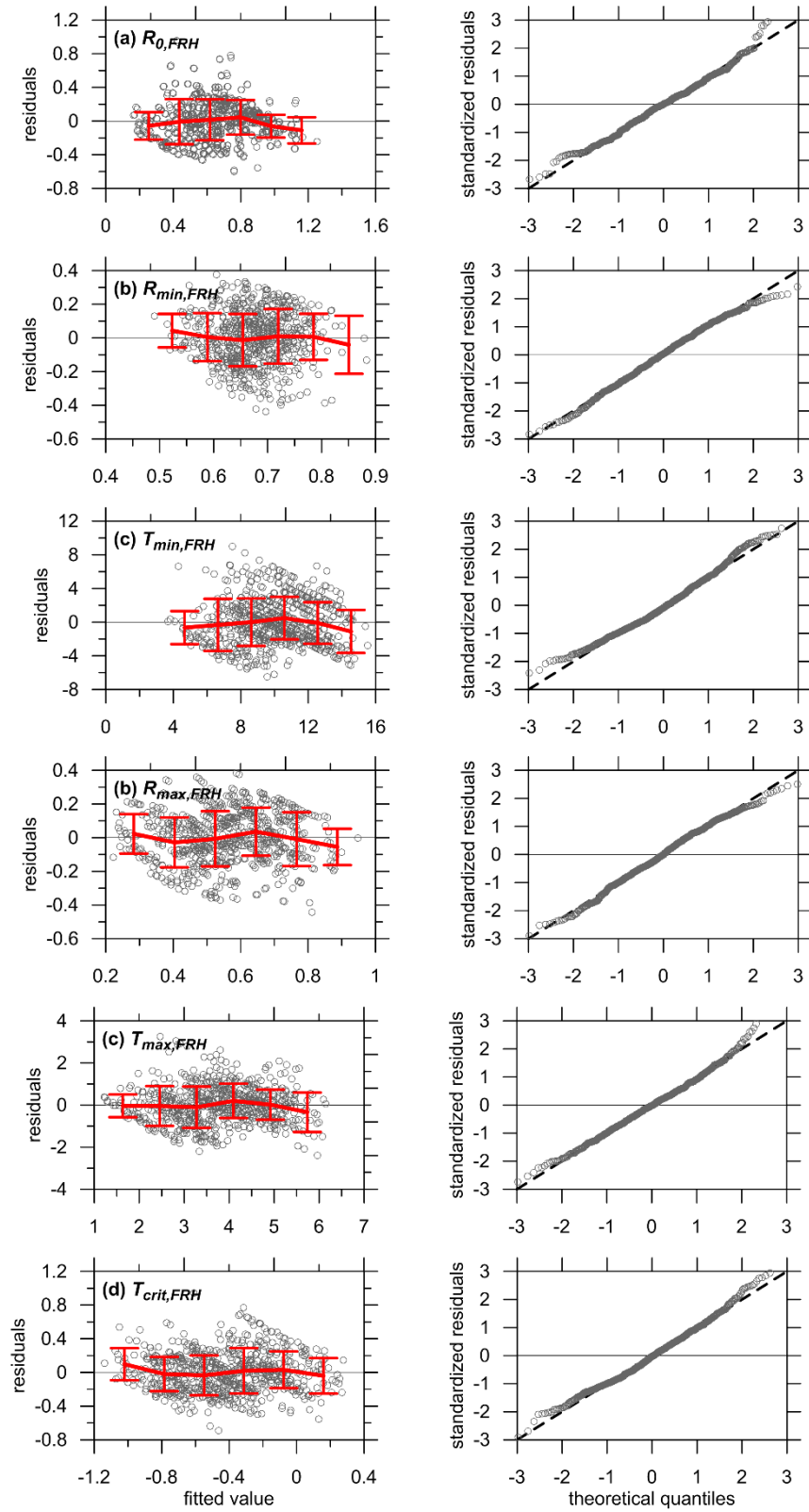


Figure 10-37: Residuals versus predicted values plots (left) and normal Q-Q plots (right) for free-head spectral ratio coefficient prediction models.

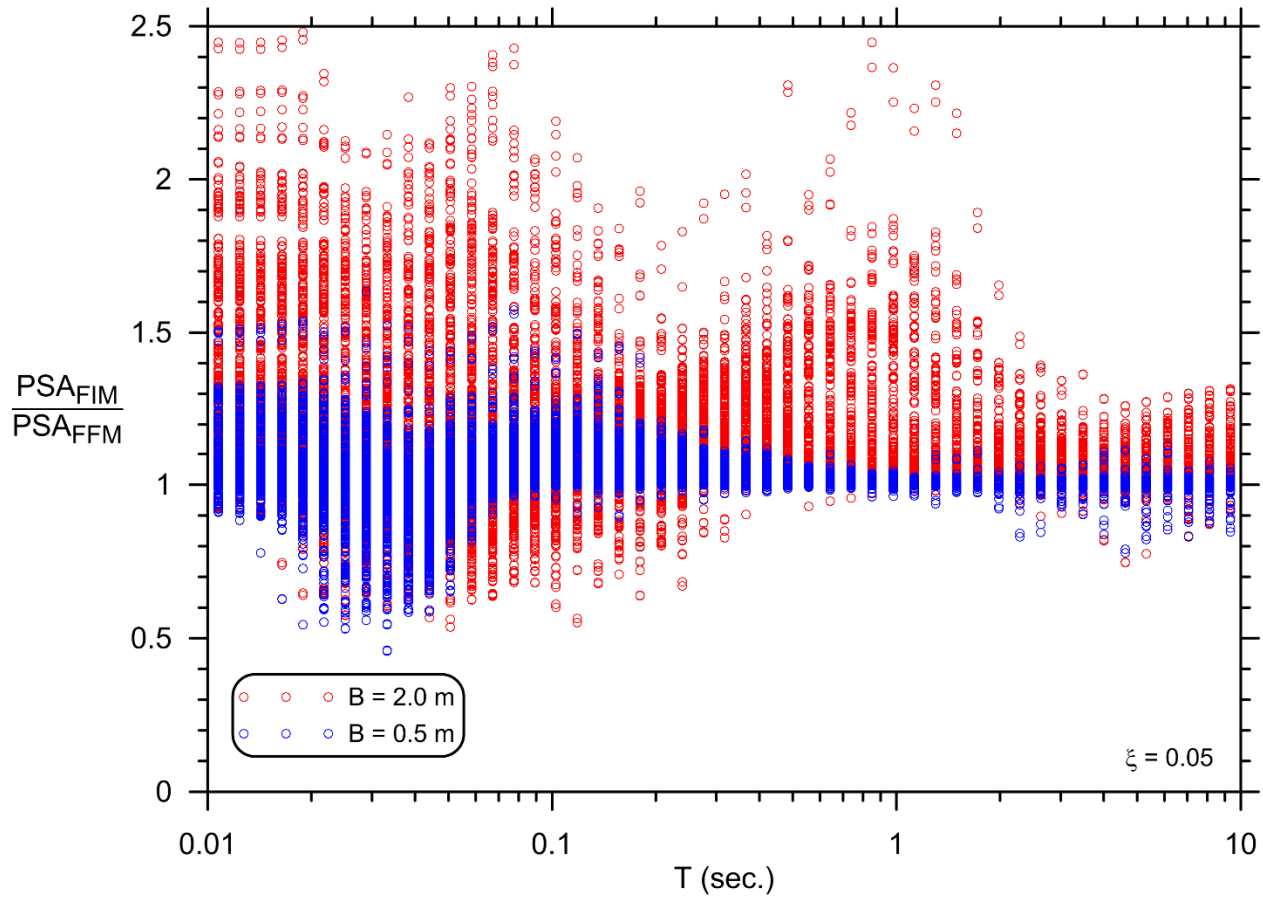


Figure 10-38: Free-head pile spectral ratio results.

Free-head pile spectral ratios show amplification (ordinates > 1.0) at short periods because kinematic amplification usually occurs during the largest-amplitude pulse in the ground motion, which is the component of the motion that controls PGA and short-period spectral ordinates. What appears to be a large number of points showing significant amplification at short periods in Figure 10-38 is somewhat exaggerated, however, because the points are approximately log-normally distributed, which is not visually apparent in Figure 10-38.

The ability of the predictive models to capture the effect of kinematic amplification at short periods is demonstrated in the plot of residuals shown in Figure 10-39. The average residual value is near zero at periods greater than about 0.1 seconds, and is around 0.05 to 0.1 at shorter periods.

This indicates that the predictive model underestimates the computed spectral ratio by, on average, about 5 to 10 percent. Future studies may be able to reduce this bias by adjusting the coefficient prediction models.

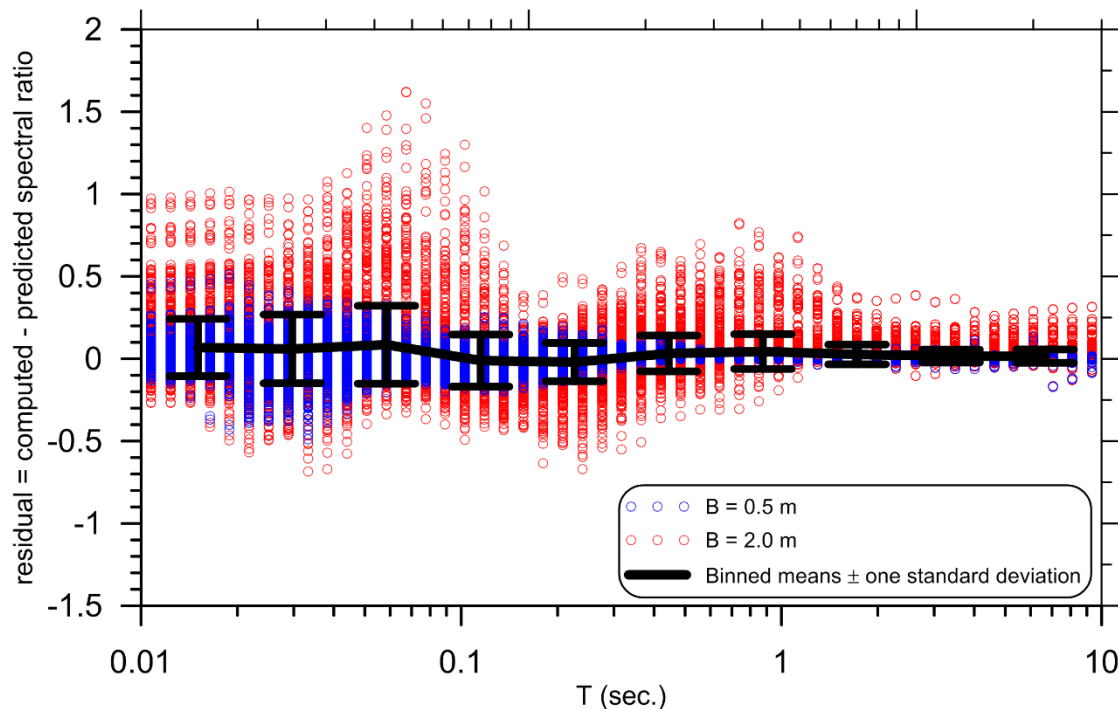


Figure 10-39: Free-head pile spectral ratio predictive model residuals.

10.6 PILE GROUP RESULTS

Simulations of pile groups subjected to incoherent ground motions generally showed that group effects were minimal for the parametric bounds considered here, which is consistent with previous findings based on elastic solutions. For stiff-pile/soft-site combinations for which single piles exhibit significant reduction of the free-field motion at low frequencies, the average trends exhibited by pile-group transfer functions typically ranged between 0 to 10 percent below the corresponding single-pile transfer functions computed for the same ground motion. For pile/site combinations with less of a pile-to-soil stiffness contrast, pile groups amplified narrow-bandwidth frequency components of some ground motions up to about 10-20 percent relative to the single

pile transfer functions, but the average trends of the group transfer functions still generally plotted slightly below the single pile results.

For design applications, a reasonable first-order approximation of pile group behavior could be estimated by reducing transfer functions predicted using the models presented in this chapter by an additional 5 percent at frequencies beyond the corner frequency. Because of the idiosyncratic nature of the group results, for critical projects, modeling of the type used for this study would be more appropriate than this rough approximation. Alternatively, group effects could be ignored due to their relatively insignificant contribution to kinematic pile-soil interaction. Pile-supported buildings which use a stiff mat foundation (i.e., piled-raft) or grade beams to connect piles over a large footprint could potentially experience a larger reduction due to the group averaging. This should be examined in future studies.

Examples results are shown in Figure 10-40 through Figure 10-42. Comparison of Figure 10-40 to Figure 10-41 (same pile/site combination, different motion) shows that the group transfer function varies based on the ground motion amplitude and frequency content in much the same manner as the single pile results. Comparison of Figure 10-41 to Figure 10-42 (same pile/motion, different site) shows that for stiffer sites, the pile groups may amplify or de-amplify certain frequency components, but the smoothed trend exhibits approximately the same difference between single pile and group pile results for both sites.

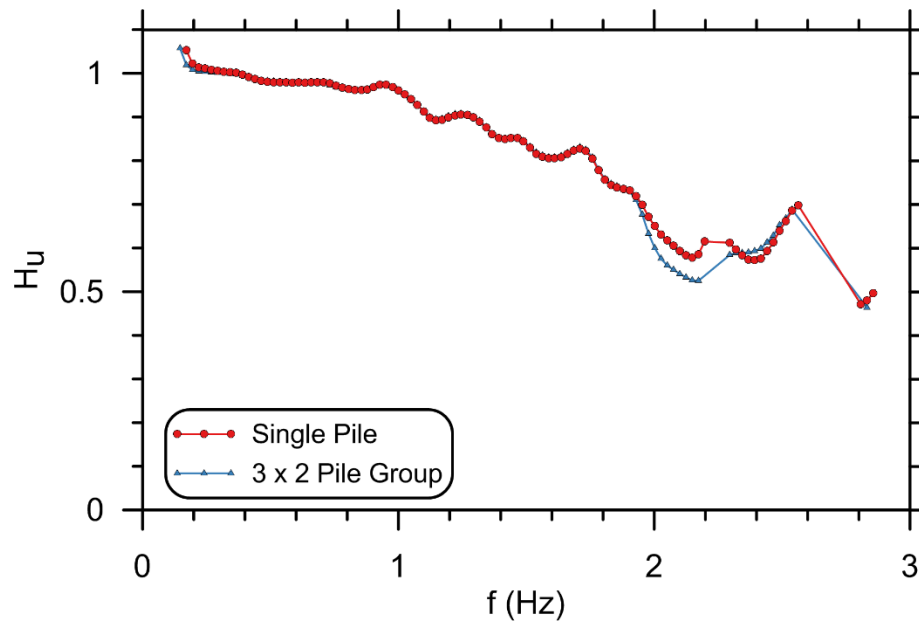


Figure 10-40: Group versus single-pile results for $B = 2.0$ m, $L = 30$ m pile, Site 1, subjected to 1994 Northridge earthquake (NGA record sequence number 957).

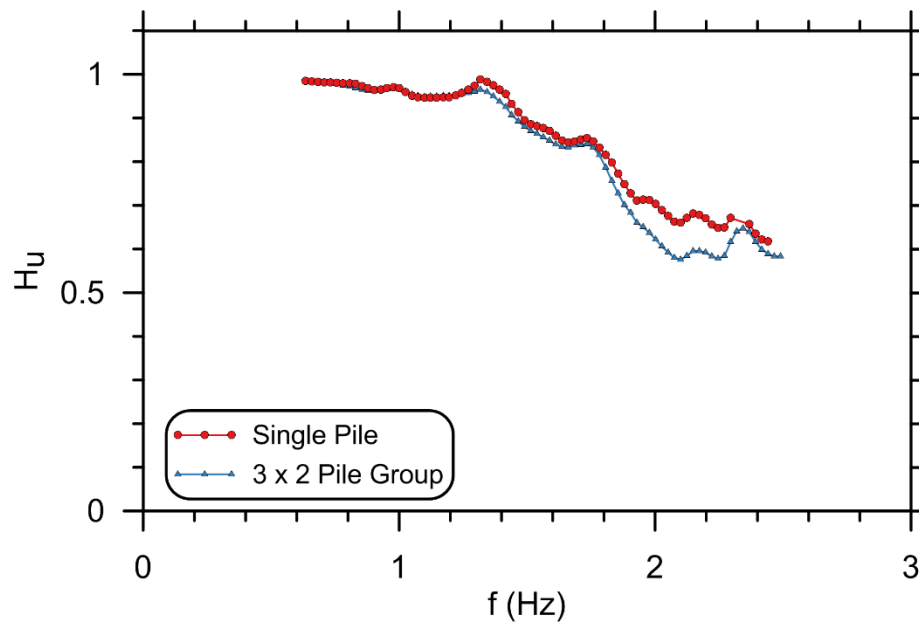


Figure 10-41: Group versus single-pile results for $B = 2.0$ m, $L = 30$ m pile, Site 1, subjected to 1971 San Fernando earthquake (NGA record sequence number 72).

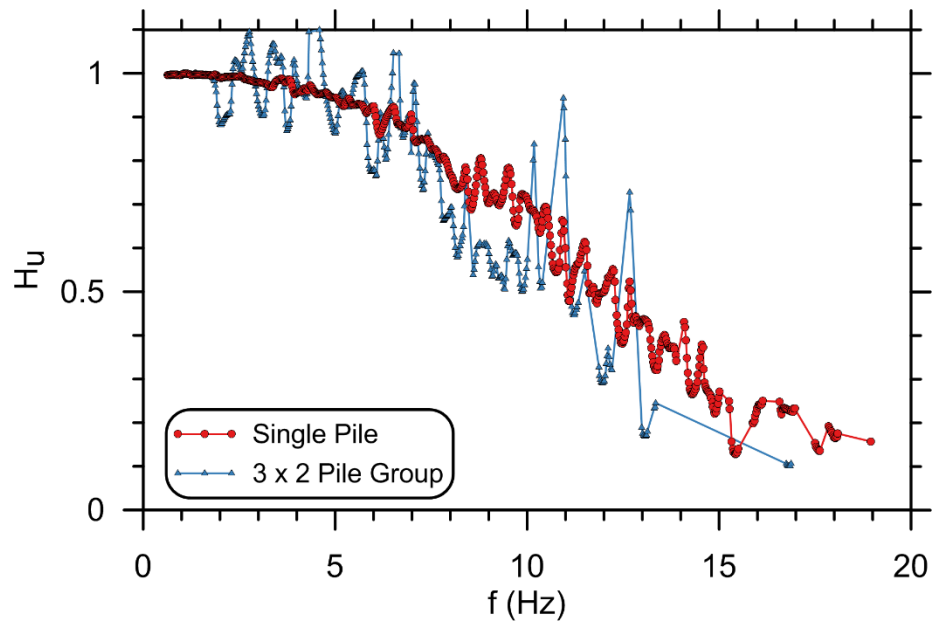


Figure 10-42: Group versus single-pile results for $B = 2.0$ m, $L = 30$ m pile, Site 4, subjected to 1971 San Fernando earthquake (NGA record sequence number 72).

11 Combination of Inertial and Kinematic Pile-Soil Interaction

11.1 COMBINING INERTIAL AND KINEMATIC SSI

For comparison of predictive models to empirical transfer functions (TF), and in a broader sense, for consideration of a structure's earthquake response considering soil-structure interaction (SSI), it is necessary to consider the combination of kinematic and inertial effects. Analytically decoupling these effects for use with the substructure method of design is convenient, but must be kept in check by considering important factors related to their combined effects. This chapter will discuss this topic prior to presentation of the example applications in the next chapter.

Three distinct motions will be considered in the context of combined inertial and kinematic SSI: the free-field motion (FFM), foundation-input motion (FIM), and foundation motion (FM). The FFM and FIM are consistent with the definitions given in previous chapters, and represent the modification of the free-field ground response due to kinematic pile-soil interaction. In the absence of inertia from the superstructure, the FM is the same as the FIM. When superstructure inertia is present, however, the FM will differ from the FIM because inertial force effects from the superstructure will induce additional foundation displacements and rotations, which is the concept of inertial SSI. In other words, the FM is influenced by both inertial and kinematic SSI.

When considering empirical TF's computed between recordings of instrumented structures and the adjacent free-field, it is important to keep in mind that the empirical TF represents the ratio of FM/FFM—as opposed to FIM/FMM—since inertial effects are present in the structure foundation-level recording. To make a meaningful comparison between an empirical TF and a purely kinematic TF model such as the ones developed in this study, it is necessary to simulate the response of the structure subjected to the FIM; the FM is an outcome of this analysis. An alternative method is to approximately remove inertial effects by ignoring the portion of an empirical TF that is near the first-mode frequency of the system, based on the assumption that this is where inertial effects are most pronounced (e.g., Mikami et al. 2008). However, this is often where the greatest reductions between FM and FFM are observed, so ignoring this frequency range can leave important questions unanswered.

For many applications, the structure response can be idealized as a single-degree-of-freedom oscillator (SDOFO), and the FM can be computed using the substructure analysis method. This process is illustrated in Figure 11-1 and can be summarized as follows:

1. Compute kinematic transfer function using site and pile parameters [Figure 11-1(a) and (b)]. This could be achieved using the generalized models presented in Equations (10.6) – (10.8) (depending on head-fixity) or by directly simulating the dynamic pile response to free-field motions at discrete depth intervals computed from a ground response analysis.
2. Convolve the transfer function from step 1 with the FFM to generate a FIM.
3. Impose this FIM on the free end of a spring representing foundation impedance for the appropriate degree of freedom. For example, K_{xx} represents the pile translational impedance in Figure 11-1(c). Additional impedance springs can be used to model pile rotation and/or vertical translation depending on the pile boundary conditions. The stiffness

of impedance springs can be computed for specific site conditions, or approximated using a simplified equivalent-linear approach [e.g., see NIST (2012)].

4. Compute dynamic response of system subjected to FIM through impedance spring(s), from which FM can be determined. The transfer function computed between the FM and FFM [Figure 11-1(d)] can be compared to empirical TF's for the system being modeled.

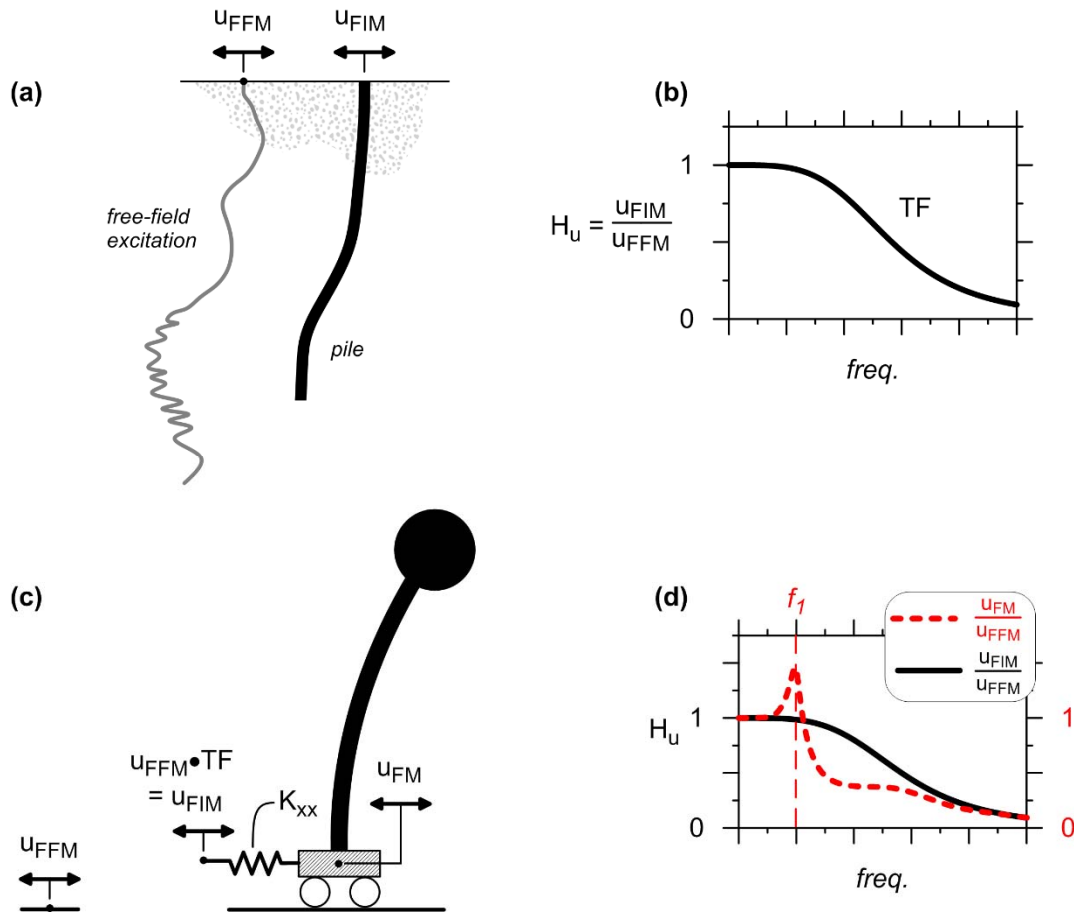


Figure 11-1: (a) Schematic of pile-soil kinematic interaction, which produces foundation-input motion (FIM) to free-field motion (FFM) transfer function (b), and (c) application of kinematic transfer function using substructure approach to represent a structure supported by a fixed-head pile. (d) The foundation motion (FM) transfer function differs from the FIM transfer function because of additional foundation displacements resulting from superstructure inertial forces.

11.1.1 Linear-Elastic SDOFO-Pile-Soil System

A series of dynamic simulations of the idealized linear-elastic system depicted in Figure 11-2 were conducted to illustrate the effects of combining inertial and kinematic SSI.

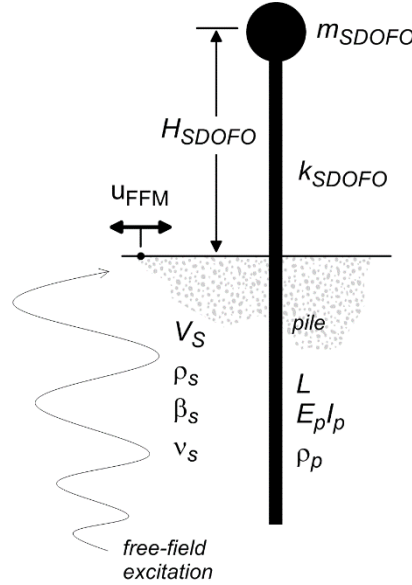


Figure 11-2: Idealized system used for direct analysis method.

A structure represented by a SDOFO is supported on a single pile, embedded in a homogeneous soil medium excited by vertically-propagating shear waves. The SDOFO is defined by a lumped mass (m_{SDOFO}) and a massless column of height H_{SDOFO} and swaying stiffness k_{SDOFO} . The swaying stiffness of a fixed-base SDOFO is related to the column flexural rigidity EI_{SDOFO} by:

$$k_{SDOFO} = \frac{3EI_{SDOFO}}{(H_{SDOFO})^3} \quad (11.1)$$

The first-mode fundamental frequency of the fixed-base SDOFO $f_{1,SDOFO}$ can be computed from its mass and stiffness using the following basic relationship:

$$\omega_{SDOFO} = \sqrt{\frac{k_{SDOFO}}{m_{SDOFO}}} = 2\pi f_{1,SDOFO} \quad (11.2)$$

Figure 11-3 compares a kinematic pile-soil interaction TF (i.e., FIM/FFM) to FM/FFM TF's computed with superstructure inertia included. The following system properties were used for the analyses:

- Soil: $V_S = 100$ m/s, $\rho_s = 17$ Mg/m³, $\beta_s = 0.05$, $\nu_s = 0.35$
- Pile: $L = 10$ m, elastic stiffness $E_p I_p = 84$ MN·m², $\rho_p = 24.5$ Mg/m³, and a fixed-head boundary condition
- Soil-Pile Interaction: interaction modulus $k = 37$ MPa, which represents a modulus reduction of about 20 percent from the initial elastic condition to approximate nonlinearity due to site response and pile-soil interaction, and 5-percent damping modeled as equivalent viscous damping through distributed dashpots.
- SDOFO: $H_{SDOFO} = 5$ m, $m_{SDOFO} = 10$ Mg, and $f_{1,SDOFO} = 7$ Hz, which corresponds to $EI_{SDOFO} = 81$ MN·m². Flexible-base (i.e., including foundation flexibility) first- and second-mode natural frequencies of $\tilde{f}_{1,SDOFO} = 6.1$ and $\tilde{f}_{2,SDOFO} = 33$ Hz were computed using the *eigen* command in *OpenSees*.
- Rayleigh damping was imposed on the structural elements corresponding to 5-percent damping at $\tilde{f}_{1,SDOFO}$ and $\tilde{f}_{2,SDOFO}$.
- Ground motion: sine-sweep motion of constant 0.1-m amplitude over a frequency range of 0.1 to 25 Hz, specified at the ground surface and computed at each depth increment of the pile using Equation (8.3).

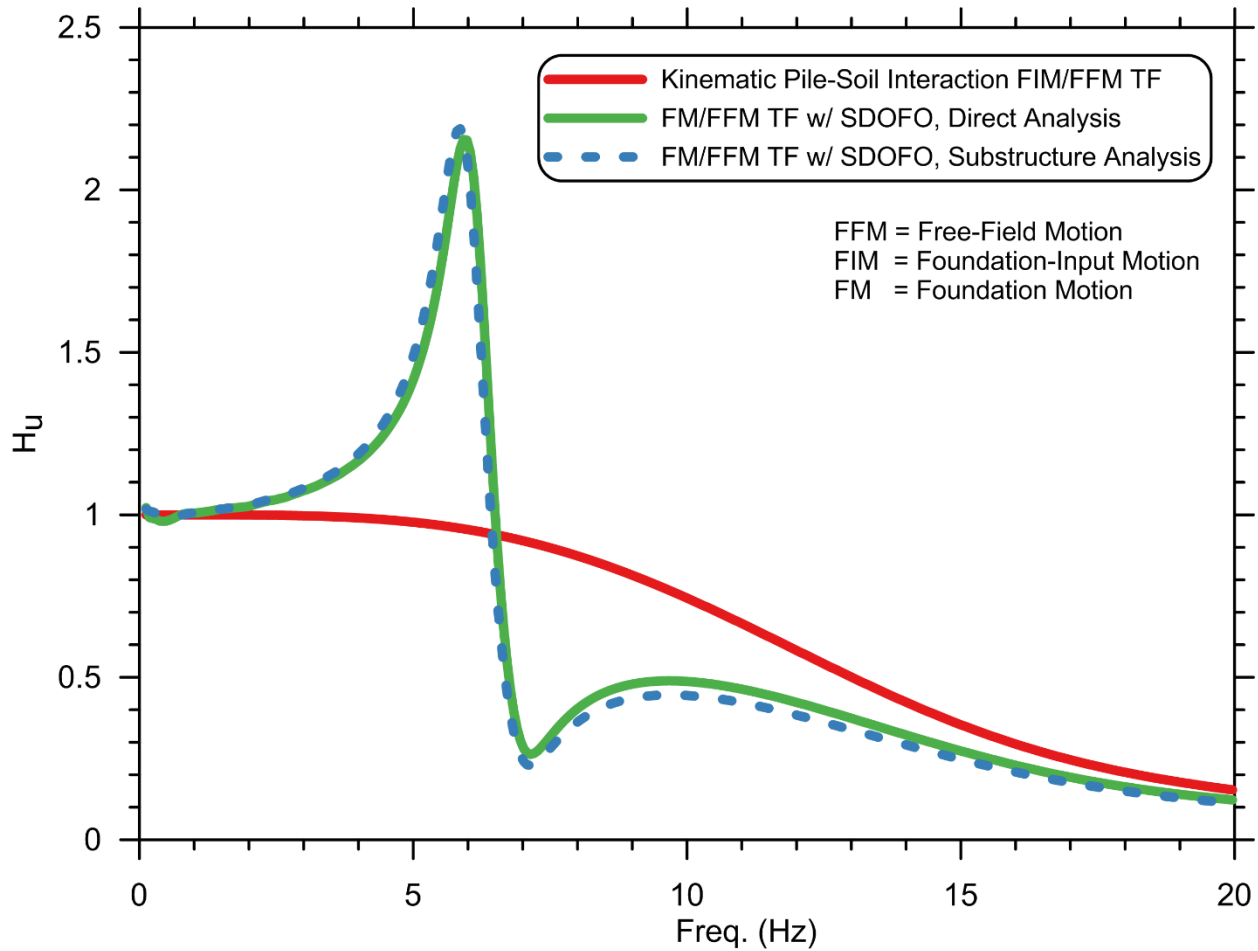


Figure 11-3: Comparison of transfer functions computed for pile-soil system and combined single-degree-of-freedom-oscillator and pile-soil systems using direct and substructure analysis methods.

The direct analysis TF in Figure 11-3 was computed from analyzing the complete system depicted in Figure 11-2, while the substructure analysis TF was computed from analyzing the system depicted in Figure 11-1(c). For the substructure analysis, the FIM was computed by convolving the free-field sine-sweep motion at the ground surface with the kinematic pile-soil interaction transfer function. The pile was replaced with an equivalent macroelement representing the foundation translational impedance. To determine the foundation impedance, a “pushover” analysis of the pile was performed by imposing a lateral force on a model of the pile-soil domain

(no SDOFO) and recording the lateral displacement. This produced a pile-head lateral force-versus-displacement stiffness $K_{xx} = 54.7 \text{ MN/m}$. To capture foundation damping, a dashpot with a coefficient of $142 \text{ kN}\cdot\text{s/m}$ was modeled in parallel with the spring. This dashpot coefficient corresponds to 5-percent damping at $\tilde{f}_{1,SDOFO}$ based on the following relationship relating damping ratio β to equivalent viscous damping (NIST 2012):

$$c_j = \frac{2\beta_j k_j}{\omega_j} \quad (11.3)$$

In (11.3), k is stiffness (in this case K_{xx}), ω is the frequency of interest, and the subscript j stands for the mode of interest, in this case first-mode.

The TF's computed from the direct and substructure analysis methods are in close agreement for this example. The slight misfit between them occurs because of the different modal properties of the two systems and the manner in which damping was implemented. While the substructure model with lumped mass and a single degree of freedom has only one defined mode, the direct-analysis model has multiple higher modes associated with deflection of the pile's distributed mass. Hence the modal-mass participation and mode-shapes of the two models are not identical. In addition, $\tilde{f}_{1,SDOFO}$ of the substructure model is slightly less than for the direct-analysis model (6.01 versus 6.12 Hz) because of the different distribution of mass and stiffness that occurs when the pile is replaced by a single macroelement. Nonetheless, the good agreement between the two approaches verifies that the substructure method can provide a reasonably accurate response for linear-elastic systems. Note that at a single frequency of interest, the substructure method can provide an exact match to the direct analysis method, but a perfect match cannot be achieved over a wide frequency bandwidth for a time-domain solution when Rayleigh damping and equivalent viscous damping are combined in the manner of this example.

Two deviations between the complete SDOFO-pile-soil system TF and the purely kinematic pile-soil TF are of interest. First, significant amplification occurs in the complete-system TF near $\tilde{f}_{l,SDOFO}$ as a result of resonance. At frequencies near $\tilde{f}_{l,SDOFO}$, the SDOFO mass undergoes displacements in excess of the ground displacement, which generates inertial base shear and moment acting on the foundation. Noting in Figure 11-3 that, for this example, the purely-kinematic pile-soil TF predicts a negligible difference between the FIM and FFM near $\tilde{f}_{l,SDOFO}$, it can be said that the FM is controlled by the structure response near $\tilde{f}_{l,SDOFO}$, and that kinematic pile-soil interaction has a negligible influence. This can be verified by repeating the substructure analysis with the FFM in place of the FIM—effectively bypassing kinematic pile-soil interaction. Figure 11-4 shows that this results in a nearly identical TF for frequencies up to the kinematic pile-soil interaction TF corner frequency (about 7 Hz). Only at frequencies above 7 Hz does the reduction of FIM due to kinematic pile-soil interaction result in a significant difference between the two TF's computed for the complete system.

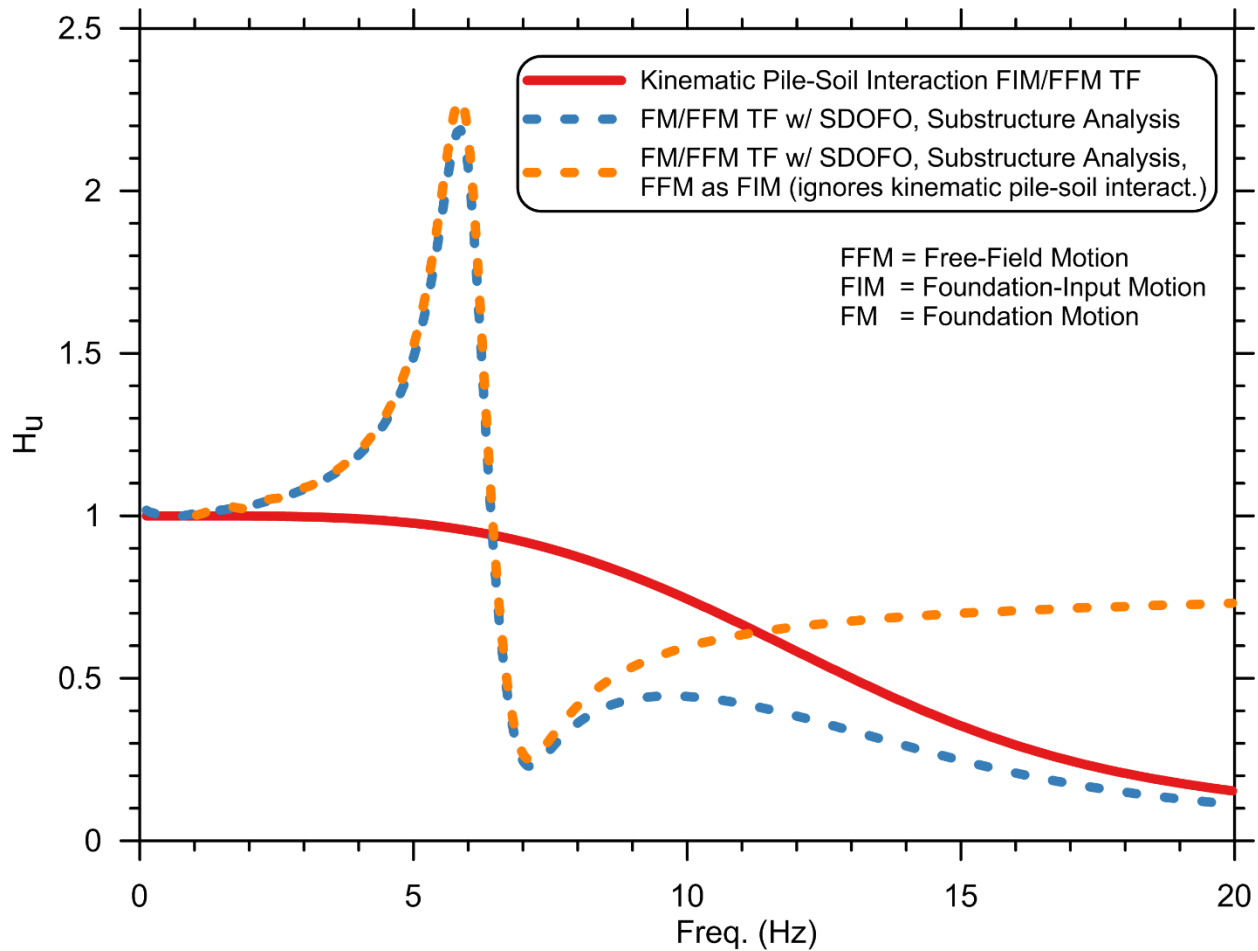


Figure 11-4: Comparison of transfer functions computed with and without consideration of kinematic pile-soil interaction.

The second difference of interest between the complete-system TF (i.e., including the SDOFO inertia) and pile-only kinematic TF is that the complete-system TF is significantly reduced relative to the pile-only kinematic TF at frequencies greater than the range where resonance occurs. For example, referring back to Figure 11-3, the complete-system TF is less than the pile-only kinematic TF at all frequencies shown in the plot above about 6.5 Hz. This is significant because it indicates that kinematic pile-soil interaction is not entirely responsible for reductions between FM and FIM that are observed in empirical TF's, even away from $\tilde{f}_{I,SDOFO}$. Even for the case where

the FFM was used in place of the FIM with the substructure method, shown as the dashed-orange TF in Figure 11-4, the TF plots below 1.0 at all frequencies shown above about 6.5 Hz.

This reduction occurs as a result of phase lag between the oscillator response and the ground surface motion, which is depicted for the system from the above example by the phase angle frequency-response curve in Figure 11-5(a). In this context, phase lag is defined as the time difference between the peak ground response and the subsequent peak SDOFO response. As described by Chopra (2007), phase lag of a single-degree-of-freedom system varies over three distinct frequency ranges based on the ratio of excitation frequency to the system first-mode fundamental frequency. Chopra's explanation is expanded here to include the SDOFO foundation-level response, including foundation flexibility, and the influence of pile-soil kinematic interaction—two factors not present for a truly single-degree-of-freedom system. When these additional system components are considered, four distinct regions of phase-lag behavior are observed as depicted in Figure 11-5 and Figure 11-6:

1. At low frequencies ($f \ll \tilde{f}_{1,SDOFO}$), the direction of base excitation changes slowly, hence inertial forces are low and damping is insignificant, so the stiffness of the system controls the response. Because insignificant inertial forces develop at the SDOFO mass-level, the SDOFO response is in-phase with the ground surface response at both the mass- and foundation-level. This is evident as near-zero phase-lag in the low frequency range of Figure 11-5(a).
2. As the excitation frequency approaches the system fundamental frequency ($f \approx \tilde{f}_{1,SDOFO}$), inertia increases, along with the corresponding displacement, velocity, and damping of the SDOFO. The magnitude of the peak SDOFO response at the mass-level, which occurs at $f / \tilde{f}_{1,SDOFO} = 1$, is dependent primarily on the system damping. The large base-shear and

moment resulting from inertia dominates the SDOFO foundation-level response, hence the response at mass-level and foundation-level are nearly in phase with each other. However, as illustrated in Figure 11-5(c) and Figure 11-6(e) and (f), the SDOFO response is approximately 90 degrees out-of-phase with the ground surface response near $f/\tilde{f}_{I,SDOFO} = 1$, meaning that the peak SDOFO response occurs when the ground surface displacement passes through zero. This is a fundamental property of resonance of a SDOF system.

3. At high frequencies ($f \gg \tilde{f}_{I,SDOFO}$), the direction of base excitation changes rapidly. The inertia of the SDOFO mass now opposes the rapidly-changing direction of ground displacement, hence the mass-level response approaches a phase lag of 180 degrees (perfectly out-of-phase). As shown in Figure 11-6(j)-(l), this means that when the ground surface displaces to the right, the SDOFO mass displaces to the left, and vice versa. As the SDOFO mass increases, the mass-level response approaches zero at high frequencies, hence the SDOFO response is controlled by its mass in this frequency range. The pile displaced shape is controlled by the profile of ground displacement rather than the SDOFO response, hence the pile-head motion (i.e., SDOFO foundation-level response) is in phase with the ground-surface response, so the phase lag returns to zero at high frequencies. The magnitude of the SDOFO foundation-level response is reduced from the ground-surface response by two mechanisms: (i) the tendency of the SDOFO mass to remain still due to its inertia, and (ii) kinematic pile-soil interaction, which would reduce the foundation-level response relative to the ground-surface response even in the absence of inertial forces.
4. A transition between (2) and (3) occurs when the foundation-level response shifts from being dominated by inertia to being controlled primarily by the ground displacement. This transition is marked by the peak in the foundation-level response phase-lag plot [red line

in Figure 11-5(a)] and the response history plot and graphics in Figure 11-5(d) and Figure 11-6(g)-(i). The local minimum of the complete-system TF occurring around 7 Hz in Figure 11-3 occurs approximately when the foundation-level response transitions from being out-of-phase with the ground surface response (phase lag > 90 degrees) to in-phase (phase lag < 90 degrees). The transfer function ordinate H_u may then increase slightly until kinematic pile-soil interaction becomes significant. This occurs between about 7 and 10 Hz in Figure 11-3.

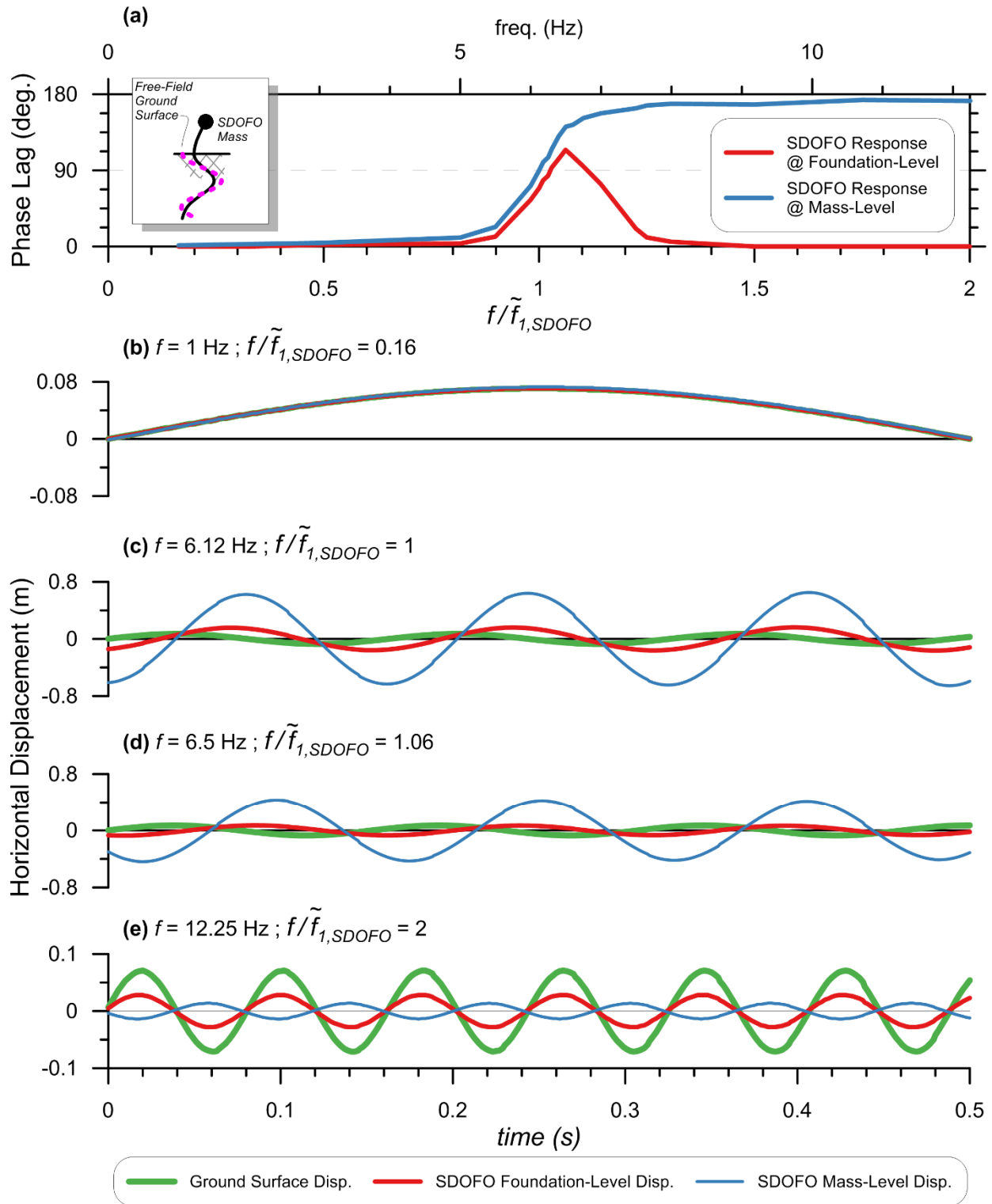


Figure 11-5: (a) Phase angle frequency-response curves for SDOFO-pile-soil system (inset) and (b)-(e) response history of system components at different frequencies of harmonic free-field excitation.

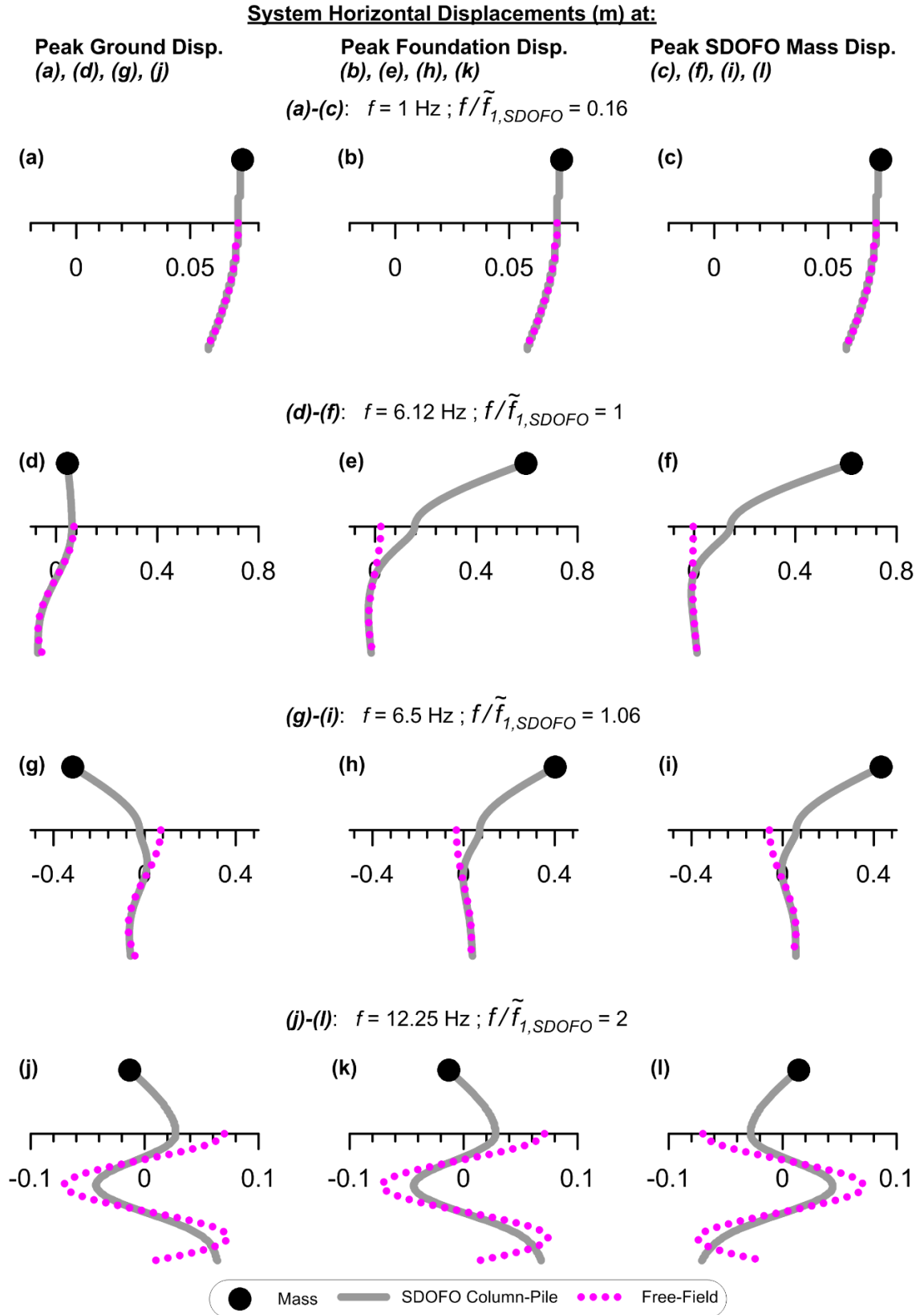


Figure 11-6: Response of SDOFO-pile-soil system to harmonic free-field excitation.

Several other issues can be investigated with the modeling framework presented above. A select few will be discussed in the following sections, although this is not meant to be an exhaustive treatment of the combination of kinematic and inertia SSI.

11.1.2 Effects of SDOFO Properties

In the familiar context of a response spectrum, a single-degree-of-freedom oscillator is defined solely by its fundamental frequency (or period). When representing an actual structure as a SDOFO, however, the height, mass, and stiffness of the system—not just the fundamental frequency—all affect its seismic response. This is because a change to any of these properties will affect the inertial base shear and moment imposed on the foundation, in-turn altering the overall seismic response. To illustrate these effects, the complete system with the “baseline” properties given in §11.1.1 was re-analyzed with the following modifications:

- m_{SDOFO} varied by a factor of three from the original 10 Mg to 3.33 and 30 Mg
- H_{SDOFO} varied by a factor of three from the original 5 m to 1.67 and 15 m.
- Free-head pile boundary condition considered in addition to fixed-head.

The fixed-base fundamental frequency of the SDOFO $f_{1,SDOFO}$ was held constant at 7 Hz by changing EI_{SDOFO} . TF computed from the results of these simulations are plotted in Figure 11-7, demonstrating that:

- The flexible-base fundamental frequency of the system $\tilde{f}_{1,SDOFO}$ is decreased when the mass or height are increased, and is always less than the fixed-base $f_{1,SDOFO}$.

- The amount of amplification near $\tilde{f}_{1,SDOFO}$ and deamplification at $f > \tilde{f}_{1,SDOFO}$ is also altered when the mass and height are changed,
- The trends of increasing versus decreasing the amount of amplification near $\tilde{f}_{1,SDOFO}$ relative to the baseline properties as a result of changes in mass are opposite for the free- and fixed-head-pile systems, and
- The effect of changes in height is negligible for the fixed-head pile system over the range of properties considered for this example.

The different behavior of the free- versus fixed-head-pile systems occurs because the inertial base shear and moment result in greater rotations and displacements of the free-head pile than for the fixed-head pile.

The effect of SDOFO properties on the combined inertial-kinematic TF is highlighted here simply for the purpose of demonstrating that accurate mass, height, and stiffness must be specified for a meaningful comparison to be made between an empirical TF and a simplified model. Unfortunately, adequate information to model an instrumented structure as a SDOFO is not always available even when recording of the structure and ground motions are available. Likewise for forward-design scenarios, it is important to accurately specify more than just the fundamental frequency of the structure for consideration of combined kinematic-inertial SSI effects.

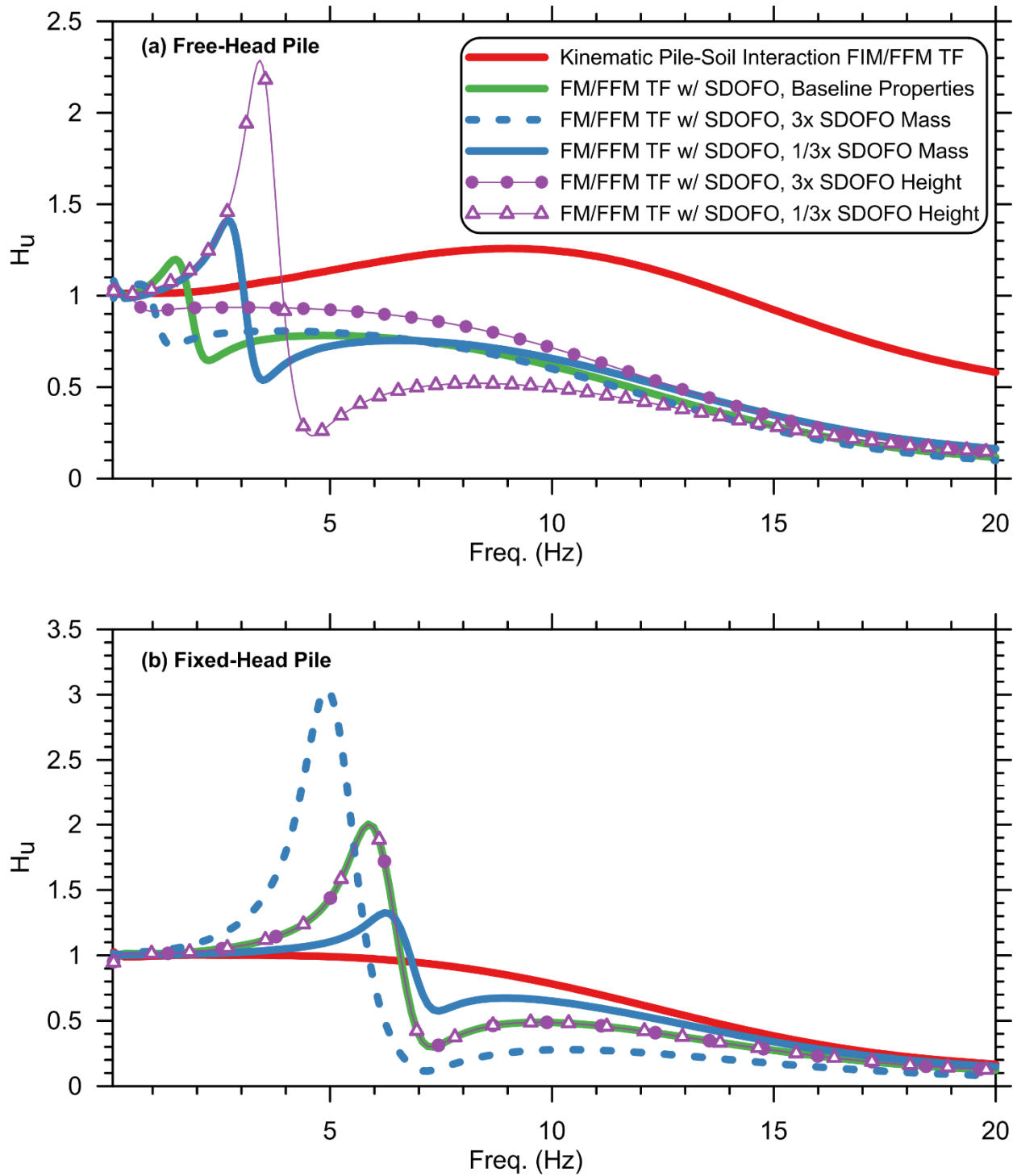


Figure 11-7: Transfer functions computed for variable single-degree-of-freedom oscillator properties. Note fixed-base fundamental frequency $f_{1,SDOFO} = 7$ Hz for all cases.

11.1.3 Effect of Pile-Soil Kinematic Interaction Corner Frequency versus SDOFO Fundamental Frequency

In the preceding examples, the corner frequency f_c of the purely kinematic pile-soil interaction TF's have always been greater than $\tilde{f}_{1,SDOFO}$ of the SDOFO-pile-soil system. (Recall that the corner frequency of the kinematic pile-soil interaction TF is the frequency beyond which significant deamplification of the FFM occurs, e.g. approximately 7 Hz in Figure 11-3). This means that over the range where amplification occurs for the complete-system TF due to inertial resonance (e.g., approximately 4-7 Hz in Figure 11-3), kinematic SSI is negligible. In this section the result of having f_c be approximately equal-to or less-than $\tilde{f}_{1,SDOFO}$ are briefly investigated, since this is a possibility for flexible structures supported on stiff piles in soft soil.

A series of dynamic simulations similar to those described in §11.1.1 were performed, except that $f_{1,SDOFO}$ was varied from 4 to 19 Hz while f_c remained constant at about 7 Hz. $H_{SDOFO} = 5$ m and $m_{SDOFO} = 10$ Mg were held constant, and EI_{SDOFO} was adjusted according to Equation (11.1) to yield the desired $f_{1,SDOFO}$. In other words, the only system component that is changed in order to vary $f_{1,SDOFO}$ is the column stiffness. Rayleigh damping coefficients were adjusted to achieve 5-percent damping at $\tilde{f}_{1,SDOFO}$ and $\tilde{f}_{2,SDOFO}$.

The results shown in Figure 11-8 show that the shape of the TF stays approximately the same as $f_{1,SDOFO}$ is varied relative to f_c ; only the magnitude of the amplification near $\tilde{f}_{1,SDOFO}$ and deamplification at $f > \tilde{f}_{1,SDOFO}$ change. For the example systems shown in the figure, the magnitude of these two mechanisms both increase as $f_{1,SDOFO}$ increases, but this is not solely a function of $f_{1,SDOFO}$ relative to f_c —inertial SSI increases as $f_{1,SDOFO}$ increases because the higher acceleration of the excitation results in greater inertial force, in turn resulting in greater peak amplification at resonance. (Recall that for the constant-amplitude input displacement used for the analysis, as frequency is increased, velocity and acceleration increase.)

The influence of kinematic SSI on the results is primarily on the amount of deamplification at $f > \tilde{f}_{l,SDOFO}$. For systems that have $\tilde{f}_{l,SDOFO} < f_c$, kinematic SSI is the primary mechanism controlling the TF at $f > f_c$. For example, the deamplification at frequencies greater than about 7 Hz for the $\tilde{f}_{l,SDOFO} = 4$ Hz TF is due almost entirely to kinematic SSI, whereas for the higher $\tilde{f}_{l,SDOFO}$ TF's, inertial SSI still plays a significant role at $f > f_c$. Hence, the following statement can be made: if $\tilde{f}_{l,SDOFO} < f_c$, kinematic pile-soil interaction is the dominant mechanism causing reduction (or lack thereof) of the FM relative to the FFM at frequencies greater than $\tilde{f}_{l,SDOFO}$; if $\tilde{f}_{l,SDOFO} > f_c$, both inertial and kinematic SSI influence the complete-system TF at frequencies greater than $\tilde{f}_{l,SDOFO}$.

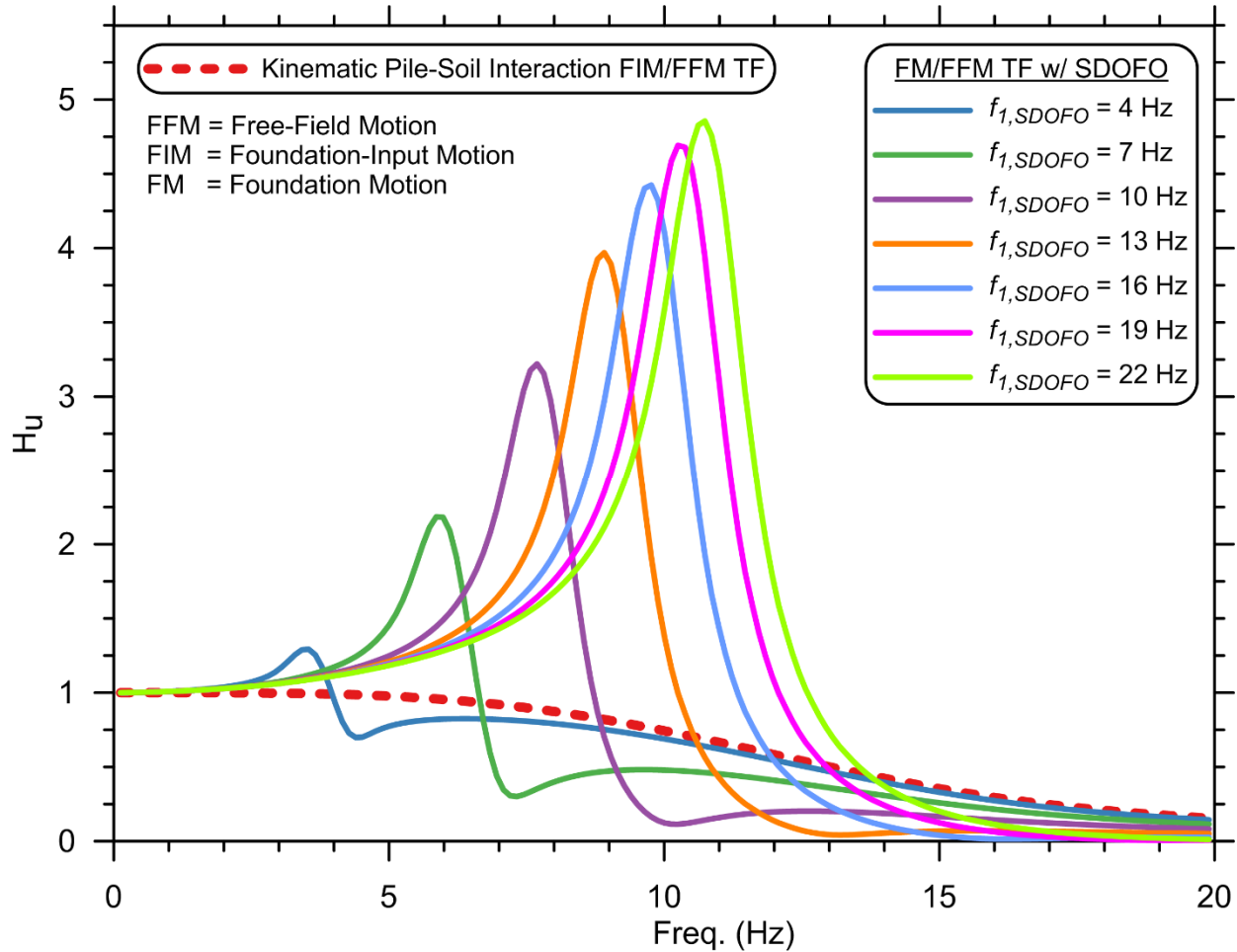


Figure 11-8: Effect of varying fixed-base fundamental frequency of SDOFO-pile-soil system relative to kinematic pile-soil interaction transfer function corner frequency

11.1.4 Effect of Pile-Soil Interaction Nonlinearity

The results presented in the previous chapter show that kinematic pile-soil interaction is strongly dependent on soil nonlinearity. This issue is significant because the principal of superposition produces an exact result only for linear-elastic systems, and the substructure methods relies on superposition to combine inertial and kinematic effects. In this section the error introduced to the substructure method as a result of neglecting nonlinear pile-soil interaction is examined. While not shown here, it should also be recognized that nonlinearity in other system components, such as free-field site response and nonlinear structural behavior, further violate the principal of superposition.

The SDOFO-pile-soil system with the properties given in §11.1.1 was again analyzed, except that the linear elastic soil springs and dashpots were replaced with nonlinear p - y springs for the direct analysis. For the substructure analysis, the pile was replaced by a single macro-element representing foundation impedance with either a nonlinear or equivalent-linear impedance spring. For the analyses previously presented in §11.1.1 through §11.1.3, the p - y modulus K_e was computed assuming a 20-percent modulus reduction to approximately account for nonlinearity. For the analyses in this section computed using nonlinear p - y springs, the initial elastic behavior was defined based on the full elastic stiffness (i.e., $K_e = 46$ MPa corresponding to $V_S = 100$ m/s), not a reduced value, since the *PySimple3* material inherently captures the nonlinear behavior at larger displacement.

Figure 11-9 presents results generated using the same sine-sweep motion of constant 0.1-m amplitude over a frequency range of 0.1 to 25 Hz. For this case, the substructure analysis performed with a nonlinear foundation impedance spring closely matches the direct analysis

results, with only a slight over-prediction of the peak response at resonance due to a minor mismatch in damping between the two systems.

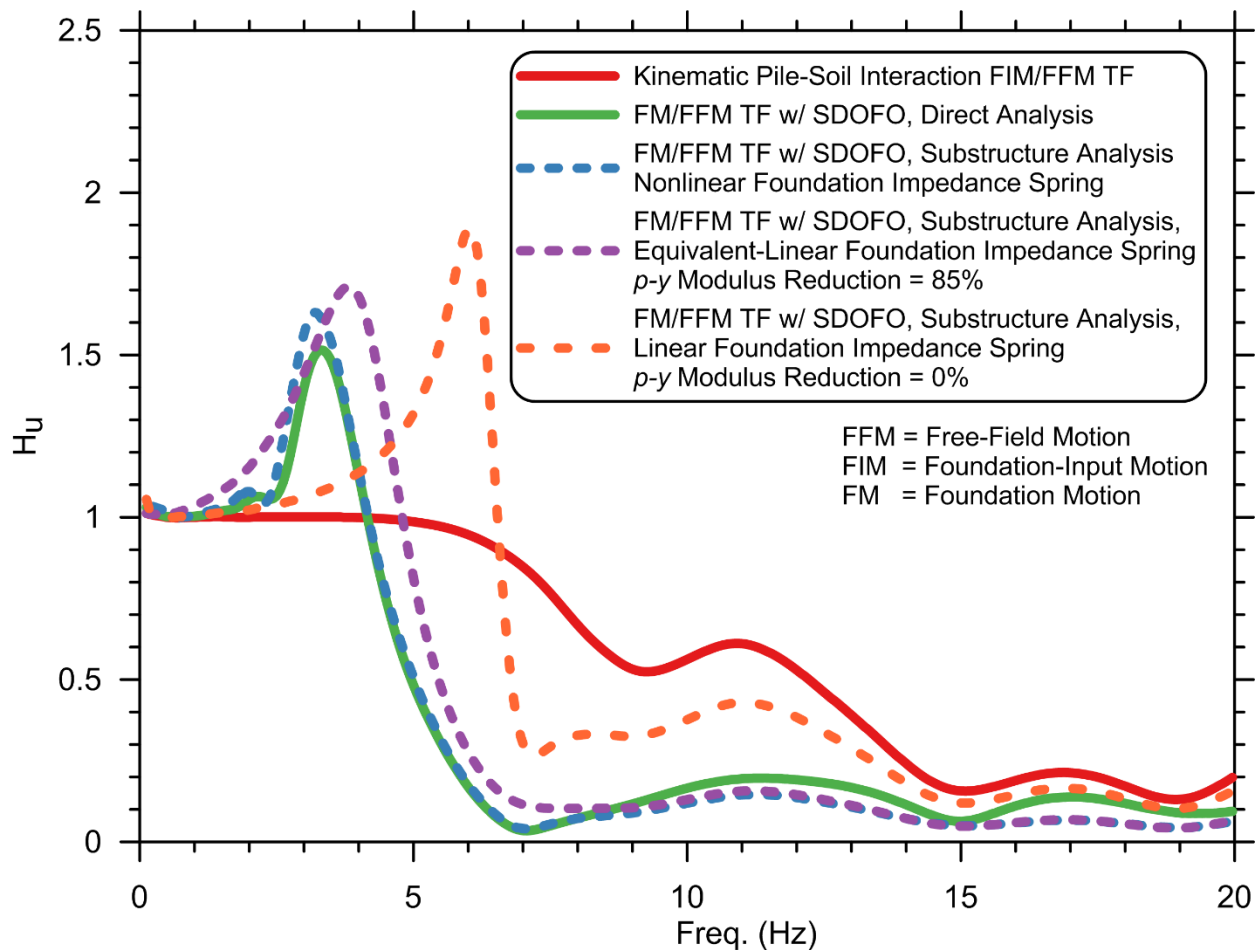


Figure 11-9: Effect of nonlinear pile-soil interaction on SDOFO-pile-soil system transfer functions for homogeneous soil subjected to sine-sweep free-field excitation.

Formulation of the nonlinear impedance spring is depicted in Figure 11-10. To begin, a pushover analysis of a model of the pile and soil was performed. Because nonlinear p - y springs were used, the pile-head versus lateral deformation relationship is nonlinear. A single *PySimple3* element was then formulated to approximately match the pushover curve as shown in the figure. A close match can easily be achieved given the flexible user control over the *PySimple3* shape. Besides faithfully capturing the nonlinear pushover behavior of the pile-soil system, using a

nonlinear impedance spring has an added benefit— the material and radiation damping that occur due to kinematic interaction are inherently captured by the pushover response (as long as the pushover analysis is performed at a velocity similar to the excitation velocity near the system $\tilde{f}_{l,SDOFO}$). Hence by closely fitting the pushover curve with the nonlinear impedance spring, the effects of these damping mechanisms are included in the complete system response during the substructure analysis.

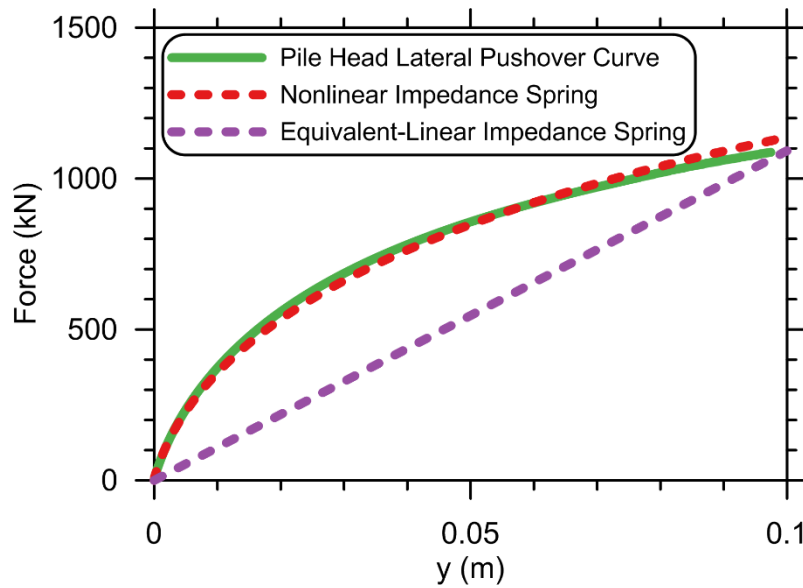


Figure 11-10: Formulation of nonlinear and equivalent-linear impedance spring macro-elements to replace pile in substructure method of analysis.

Also shown in Figure 11-10 is an equivalent-linear impedance spring with secant stiffness defined by passing through the origin and the peak displacement of approximately 0.1 m. The magnitude of the pushover displacement to which the impedance springs were matched was chosen based on the outcome of the direct analysis, which showed that the peak pile-head relative displacement was about 0.1 m. Since the nonlinear impedance spring matches the pushover curve over both small and large deformation regions, the largest displacement to which it is defined is not a critical factor, as long as it lies within the range of the subsequent analyses. On the contrary,

the modulus of the equivalent-linear impedance spring is directly dependent on the displacement at which it is defined, complicating the fitting process.

Furthermore, foundation damping must be modeled separately when using an equivalent-linear impedance spring. To some degree, foundation damping is inherently captured by fitting the equivalent-linear spring to the nonlinear pushover curve, since the nonlinear soil response implies non-zero hysteretic damping under cyclic loading, but it is difficult to quantify the extent to which this is the case. For these analyses it was found that use of a dashpot in parallel to the impedance spring resulted in spurious behavior at frequencies other than the frequency for which the dashpot coefficient was defined. Instead, foundation damping was imposed as Rayleigh damping corresponding to $\beta = 0.05$ at 25 Hz and $\beta = 0.22$ at $3.9 \text{ Hz} \approx \tilde{f}_{I,SDOFO}$. Foundation damping at $\tilde{f}_{I,SDOFO}$ was computed using the following equations from NIST (2012):

$$\beta = \frac{1}{4} \beta_p + \frac{3}{4} \beta_s + \frac{3}{4} \beta_r \quad (11.4)$$

$$\beta_r = \frac{3}{2\alpha(1+\nu_s)\delta} (a_0^p)^{\frac{3}{4}} \quad (11.5)$$

$$\alpha = 1 - \frac{3\pi}{32\delta} \left(\frac{\rho_p / \rho_s}{1 + \nu_s} \right) (a_0^p)^2 \quad (11.6)$$

In Equations (11.4) through (11.6), the damping subscripts p , s , and r stand for pile and soil material damping and radiation damping, respectively; α is the static stiffness modifier for pile lateral translation, δ is the Winkler coefficient taken as 1.0 for fixed-head piles, and a_0^p is dimensionless frequency defined at $\tilde{f}_{I,SDOFO}$ using the classical definition $\omega B/V_s$. Soil and pile material damping were approximated as 0.05.

When the equivalent-linear impedance spring is used with the substructure method, the computed system response is in reasonable agreement with the nonlinear impedance spring and direct analysis results for this example as shown in Figure 11-9. Given that the current state-of-practice for deep foundation lateral loading design is to use nonlinear p - y curves, the tools necessary for creating a nonlinear force vs. displacement head pushover curve to which an equivalent-linear stiffness can be matched are already available, and should be used. The equivalent-linear impedance spring result appears to have overestimated $\tilde{f}_{l,SDOFO}$ by about 10 percent and underestimated damping, causing an over-prediction of the peak FM/FFM ordinate by about 15 percent. Also shown for reference is the result computed using linear properties corresponding to the initial elastic soil properties, i.e. with no modulus reduction. This approach clearly produces an erroneous result, highlighting the importance—and difficulty—of selecting appropriate equivalent-linear properties. The equivalent-linear properties could be further refined to provide a closer match to the nonlinear system behavior in a design setting.

To assess the impact of pile-soil interaction nonlinearity for more realistic conditions, the analyses were repeated for the same SDOFO-pile system embedded in the soft soil Site 1 and subjected to the 1971 San Fernando Earthquake Lake Hughes #4 recording (known as ground motion 1 for this study; refer to §9.6 and §9.7 for site and motion descriptions). The mass of the SDOFO was varied from 10 Mg to 25 Mg to produce different amounts of period lengthening while the remaining system properties were held constant. Foundation impedance springs were formulated in the same manner depicted in Figure 11-10. The results are shown in Figure 11-11.

For both the $m_{SDOFO} = 10$ Mg and 25 Mg cases, the substructure analysis using a nonlinear foundation impedance spring gives a close match to the direct analysis result in terms of matching the correct $\tilde{f}_{l,SDOFO}$ and peak transfer function ordinates. However, the accuracy of the results does

appear to decrease slightly with increasing period lengthening. The results using the equivalent-linear impedance spring formulated from the nonlinear pushover curve also provide a reasonably close match to the direct analysis results. However, formulating these equivalent-linear springs and capturing the foundation damping required knowing the nonlinear behavior of the system in advance, which would not be known *a priori* if the equivalent-linear method was used as a standalone approach.

Also shown in Figure 11-11 are substructure analysis results computed with equivalent-linear impedance springs based on the modulus reduction values recommended in NIST (2012) Table 2-1 for SSI analysis. Based on a short-period spectral acceleration $S_{DS} \approx 0.2$ g for the ground motions that was used, the modulus reduction factor (G/G_{max}) for Site Class E ($V_{S,30} < 180$ m/s) is given as 0.60. Since p - y modulus is linearly related to soil shear modulus for the formulation used herein, these factors can be applied directly to K_e to approximately capture nonlinearity due to ground response for equivalent-linear pile-soil interaction modeling.

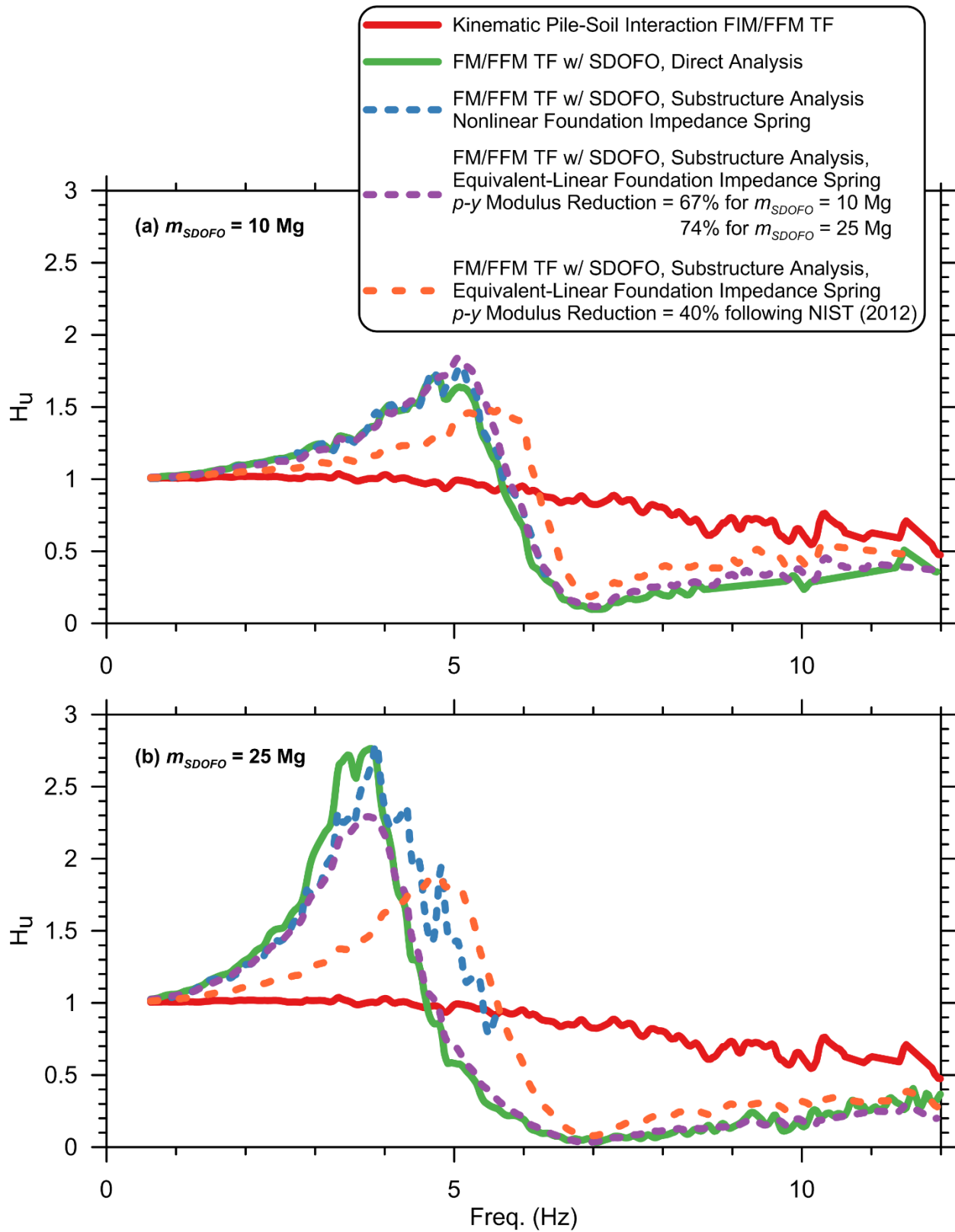


Figure 11-11: Effect of nonlinear pile-soil interaction on SDOFO-pile-soil system transfer functions for Site 1 subjected to 1971 San Fernando earthquake Lake Hughes #4 recording.

The results show that as the amount of period lengthening increases, the accuracy of the transfer functions computed with the NIST reduction factors decreases. For the $m_{SDOFO} = 10$ Mg system ($\tilde{f}_{1,SDOFO}/f_{1,SDOFO} \approx 0.75$), the peak transfer function ordinate is under-predicted by about 10 percent, and for the $m_{SDOFO} = 25$ Mg system ($\tilde{f}_{1,SDOFO}/f_{1,SDOFO} \approx 0.55$), the peak transfer function ordinate is under-predicted by about 20 percent and period lengthening is significantly underestimated. One of the reasons for this trend is that the NIST factors for estimating modulus reduction only depend on the magnitude of free-field excitation without consideration of the system properties such as mass, stiffness, and foundation flexibility, because they are only intended to capture modulus reduction due to site response, not SSI. Since the amount of pile-soil interaction nonlinearity depends on all of these properties, a proxy for quantifying nonlinearity based only on ground motion intensity is unlikely to provide a realistic estimate over a wide range of project conditions.

The period-lengthening ratio (or equivalently, the frequency-shortening ratio ($\tilde{f}_{1,SDOFO}/f_{1,SDOFO}$)) could therefore be a more useful metric for quantifying whether or not the error introduced to the substructure method of analysis by neglecting pile-soil interaction nonlinearity is significant. The results presented above indicate that $\tilde{f}_{1,SDOFO}/f_{1,SDOFO}$ below about 0.75 results could introduce significant errors to the substructure method, but a more comprehensive parametric study would be useful for refining this criterion. To make an accurate estimate of $\tilde{f}_{1,SDOFO}/f_{1,SDOFO}$, pile-soil interaction nonlinearity should be considered. Even for superstructure dynamic analysis using equivalent-linear foundation impedance springs, nonlinear pile-soil interaction analyses should be conducted to define the equivalent linear impedance properties.

12 Example Applications of Transfer Function and Spectral Ratio Prediction Models

In this chapter, the generalized kinematic pile-soil interaction transfer function (TF) and spectral ratio models developed in Chapter 10 will be compared to previously recorded empirical TF's and implemented for a bridge design scenario. This requires consideration of the effects of combined kinematic and inertia soil-structure interaction (SSI) discussed in Chapter 11.

12.1 EMPIRICAL CASE STUDIES

The empirical transfer functions for pile-supported buildings reported by Kim and Stewart (2003) and Givens et al. (2012) provide an opportunity to apply the predictive models developed for this study and investigate issues of combined kinematic and inertial SSI for real systems. The empirical transfer functions and attempts to replicate them in previous studies were originally discussed in §7.3.6.1. These case studies will be revisited in the following sections.

12.1.1 Sendai, Japan Site after Givens et al. (2012)

This site consists of an instrumented four-story reinforced-concrete building and adjacent free-field accelerographs located on the Tohoku Institute of Technology campus in Sendai, Japan. Multiple strong earthquakes have been recorded at the site. Transfer functions computed from

these earthquakes show a significant reduction of the foundation motion (FM) relative to the free-field motion (FFM) over a frequency bandwidth of approximately 2.5 to 8 Hz. As reported by Givens et al., the reductions were observed to be approximately equal ($H_u \approx 0.5$) for the **M** 7.1 2003 Off-Miyagi and **M** 9.0 2011 Tohoku earthquakes, despite significantly different recorded peak ground accelerations (PGA) of 0.23 g and 0.81 g for the two earthquakes, respectively. This behavior is inconsistent with the notion that kinematic pile-soil interaction should result in lower values of H_u for stronger shaking due to greater modulus reduction of the soil. The original researchers hypothesized that the misfit between existing kinematic transfer function models and the empirical data could be due to ground motion incoherence, and that perhaps nonlinear effects are not significant for kinematic interaction.

Further details regarding the site are presented in Figure 12-1 and Figure 12-2 based on information presented by Mikami et al. (2006), Givens et al. (2012), and from discussions with Professor Atsushi Mikami (personal communication, 2015). The building's lateral-force resisting system consists of shear walls in the transverse (narrow) direction and concrete moment frames in the longitudinal direction. A total of 24 reinforced-concrete $B = 0.75$ -m, $L = 8$ -m piles interconnected by stiff grade beams support the building. The piles pass through 6 m of soft to medium-stiff surficial soil ($V_s \approx 130$ to 200 m/s) and are socketed 2 m into soft mudstone ($V_s \approx 320$ m/s). Assuming good construction practices were followed, the piles likely exhibit significant base resistance given the diameter and stiffness of material at the base elevation.

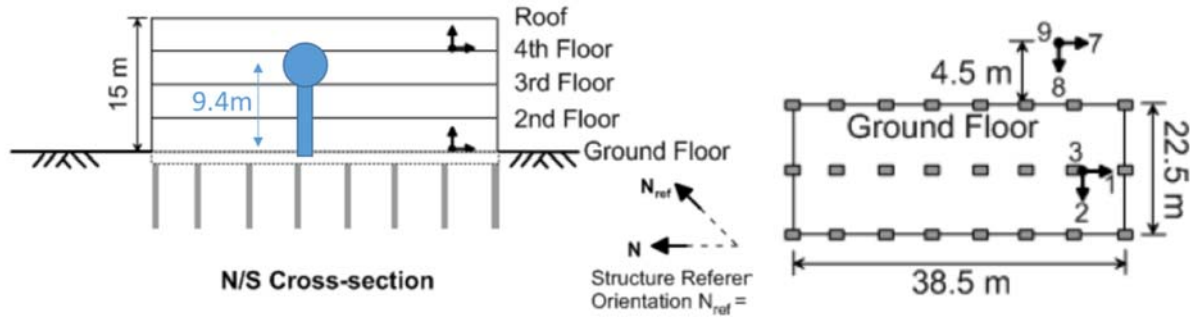


Figure 12-1: Tohoku Institute of Technology building layout after Givens et al. (2012) and idealized single-degree-of-freedom oscillator representation.

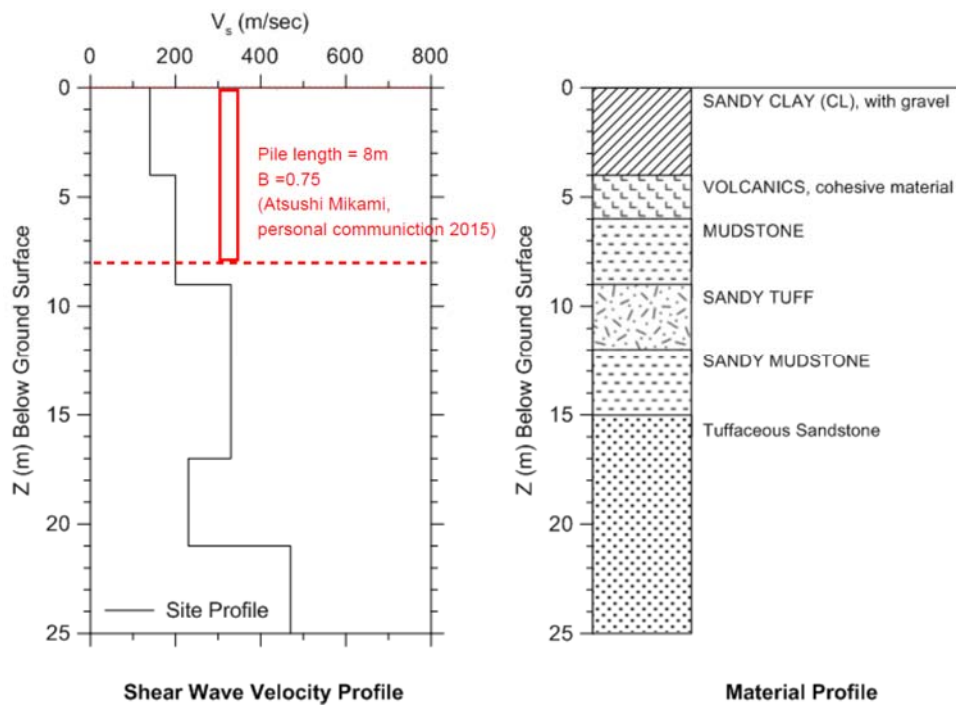


Figure 12-2: Subsurface information for Sendai site after Givens et al. (2012). Subsurface data originally reported by OYO Corporation (2007).

The substructure modeling approach presented in the previous chapter has been applied to this case study for the 2011 Tohoku earthquake recording originally reported by Givens et al. The modeling steps are summarized as follows:

- The generalized transfer function model for fixed-head piles presented in §10.4.3 was used to predict a kinematic pile-soil interaction TF relating

foundation-input motion (FIM) to FFM in the absence of superstructure inertia (i.e., FIM/FFM TF). This kinematic model considers only pile effects and not base slab averaging.

- The recorded FFM was convolved with the predicted kinematic FIM/FFM TF to produce a FIM for subsequent dynamic analysis.
- A beam-on-dynamic-nonlinear-Winkler-foundation (BDNWF) model of the pile embedded in the subsurface profile shown in Figure 12-2 was constructed in *OpenSees*. Nonlinear pile-soil interaction was modeled using *p-y* curves defined by the *PySimple3* material. A “pushover test” of this pile was simulated to produce a nonlinear pushover curve (e.g., see Figure 11-10) relating lateral force imposed at the pile head to lateral displacement.
- The structure was idealized as a pile-supported single-degree-of-freedom oscillator (SDOFO) with height 9.4 m and mass 75 Mg. The mass is based on four 38.5 m x 28.5 m above-grade floors supporting an assumed uniform dead load of 5 kPa, evenly distributed to the 24 piles. The height corresponds to the centroid of the above-grade floors as shown in Figure 12-1. The SDOFO-pile model represents a single pile and its tributary mass, but the response of this system is assumed to approximately represent the entire structure.
- The flexible-based period of the building is reported by Mikami et al. (2006) as 0.43 s ($\tilde{f}_{l,SDOFO} = 2.35$ Hz) based on system identification techniques. The SDOFO with mass = 75 Mg and height = 9.4 m described above was

added to the *OpenSees* pile-soil model. After specifying an initial trial value for fixed-base period $f_{l,SDOFO}$, from which SDOFO column stiffness was computed using Equations (11.1) and (11.2), the *eigen* command was used to compute $\tilde{f}_{l,SDOFO}$ of the combined SDOFO-pile-soil system. Using 2.35 Hz as the target $\tilde{f}_{l,SDOFO}$, the fixed-base frequency was adjusted until a good match was achieved using $f_{l,SDOFO} = 2.45$ Hz (0.41 s). This finding suggests that period lengthening was relatively insignificant, which is reasonable given the relatively flexible structure and stiff subsurface. Note that this calibration step would not have been possible if only the building period were known without information about its mass and stiffness.

- The pile and *p-y* springs in the *OpenSees* model were replaced with a single macroelement impedance spring calibrated to fit the nonlinear pushover curve. This nonlinear spring was modelled using the *PySimple3* material. Rayleigh damping was specified as 10 and 5 percent at frequencies of 2.35 and 25 Hz, respectively.
- A dynamic analysis was performed by imposing the FIM on the free end of the impedance spring macroelement to excite the SDOFO-macroelement system [e.g., see Figure 11-1(c)].
- The foundation motion (FM) recorded at the base of the SDOFO column during this analysis was then used to compute a FM/FFM transfer function for comparison to the empirical transfer function as shown in Figure 12-3.

The kinematic pile-soil interaction FIM/FFM TF (purple line in Figure 12-3) predicts negligible reduction of the FFM over the frequency range where the empirical $H_u \approx 0.5$. On the

other hand, the combined SDOFO-pile prediction computed using the substructure method (orange triangles) matches the empirical transfer function very well over this frequency range, including prediction of the sharp drop-off occurring just beyond $\tilde{f}_{I,SDOFO}$. It can be concluded from these results that the large reduction in the foundation-level motion relative to the free-field motion between 2.5 and 8 Hz is due primarily to the influence of inertial interaction, not the inability of the kinematic pile-soil interaction model to adequately capture the underlying mechanisms.

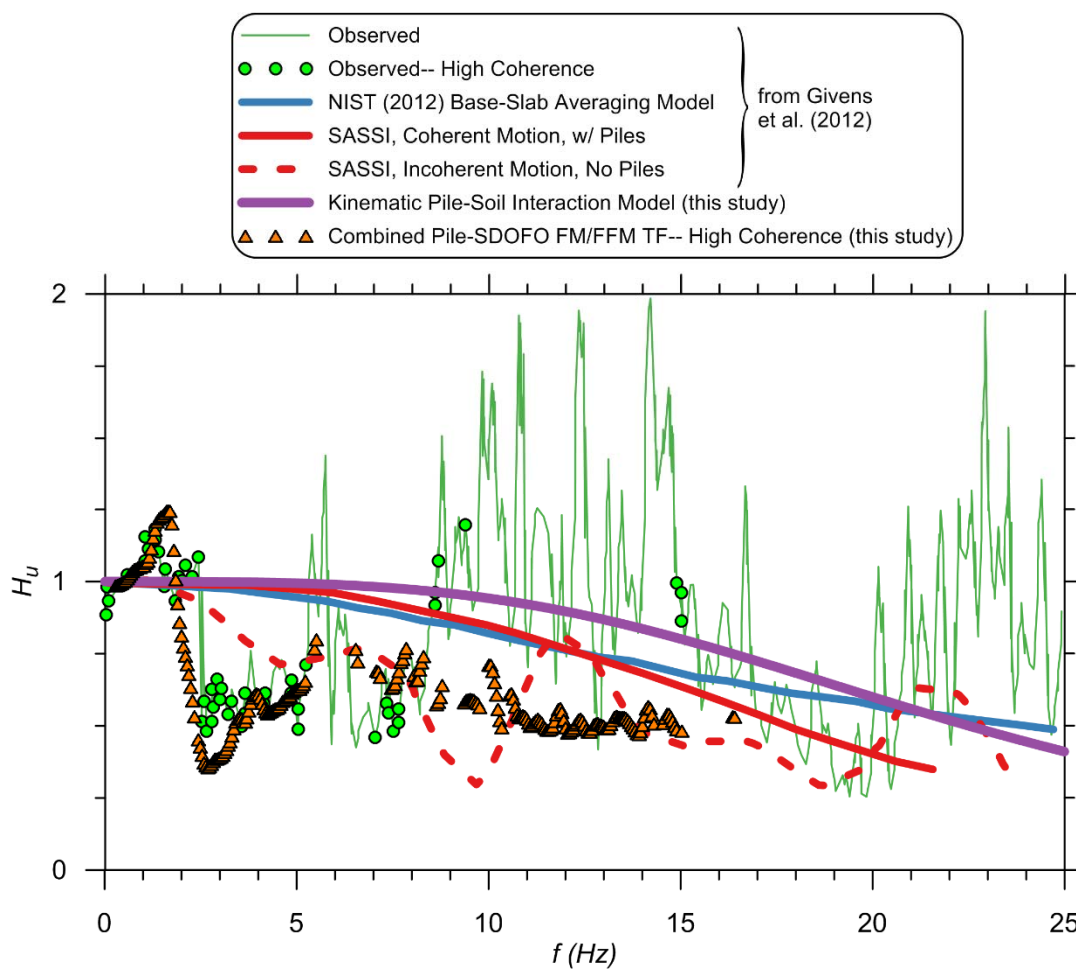


Figure 12-3: Model predictions versus empirical data for Tohoku Institute of Technology building during 2011 Tohoku earthquake after Givens et al. (2012).

12.1.2 Lancaster, California Site after Kim and Stewart (2003).

This site consists of a five-story pile-supported hospital building in Lancaster, California. During the 1994 **M** 6.7 Northridge earthquake, a free-field sensor located 360 ft (110 m) away from the building recorded a PGA of 0.071 g. The Lancaster site is included in a database of 57 structure and adjacent free-field recordings compiled by Stewart and Stewart (1997) for empirical evaluation of SSI. Kim and Stewart (2003) reanalyzed 16 of the buildings that were pile-supported and found that the Fan et al. (1991) elastic model generally under-predicted reductions in foundation-level motions (FM) relative to FFM. In many of these cases, including the Lancaster site, a base-slab averaging model by Veletsos et al. (1997) modified with an empirically-adjusted factor to approximate ground motion incoherence, foundation flexibility, and wave inclination effects was found to provide a better fit to the measured transfer functions. The authors concluded that interaction between shallowly-embedded or surface foundation elements dominated the foundation motion, and that piles played an insignificant role. Given the relatively stiff soil (estimated $V_S \approx 210$ to 370 m/s) and flexible $B = 20$ -inch (51 cm) piles at the Lancaster site, this hypothesis is consistent with the findings of the present study.

Re-evaluation of the Lancaster site therefore has two goals: (i) compare the kinematic model from this study to the measured TF, for which a poor match is expected, and (ii) determine if including inertial SSI effects provides a better match to the measured TF as was the case for the Sendai site.

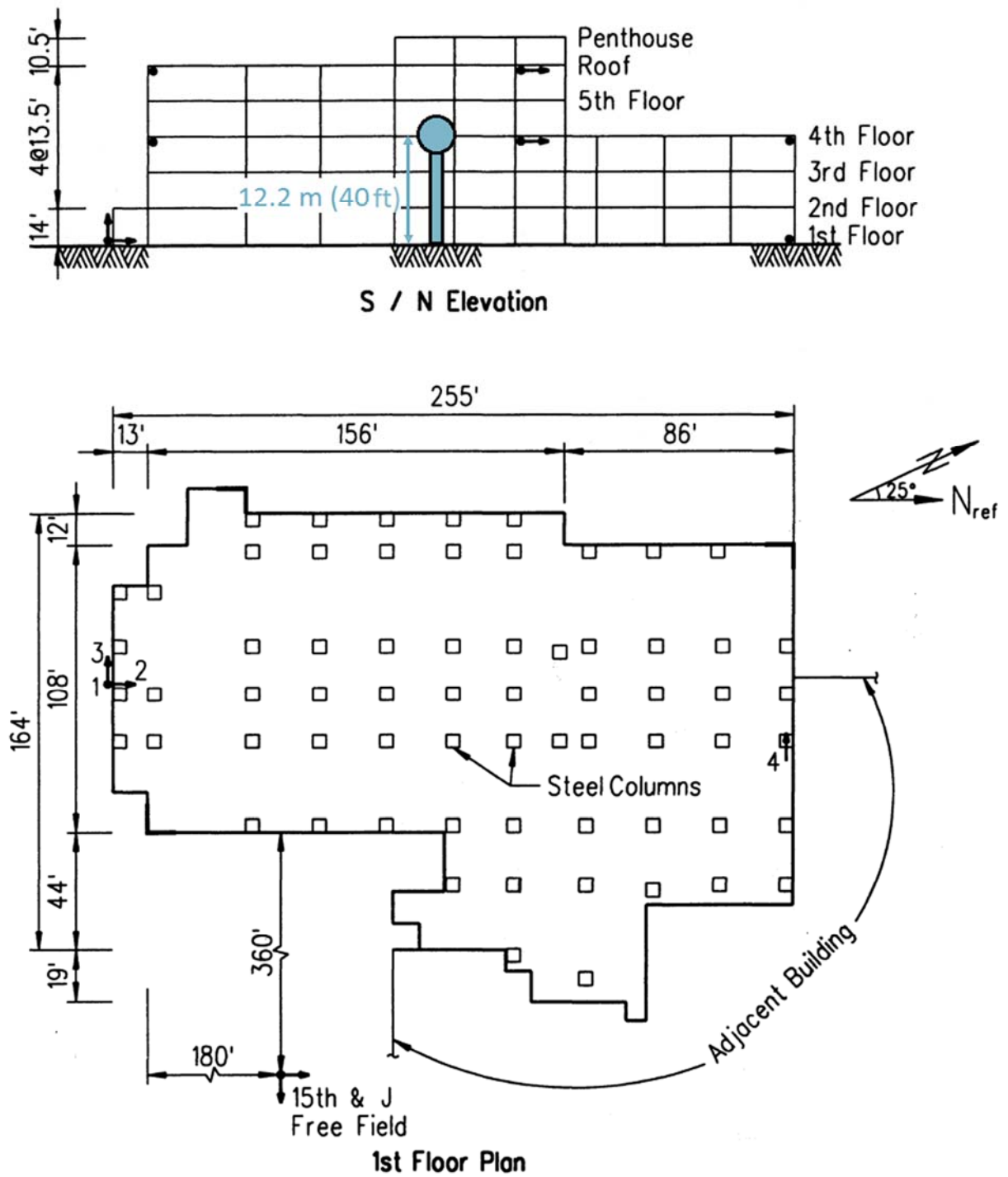


Figure 12-4: Lancaster, California hospital building layout and idealized single-degree-of-freedom oscillator representation after Stewart and Stewart (1997).

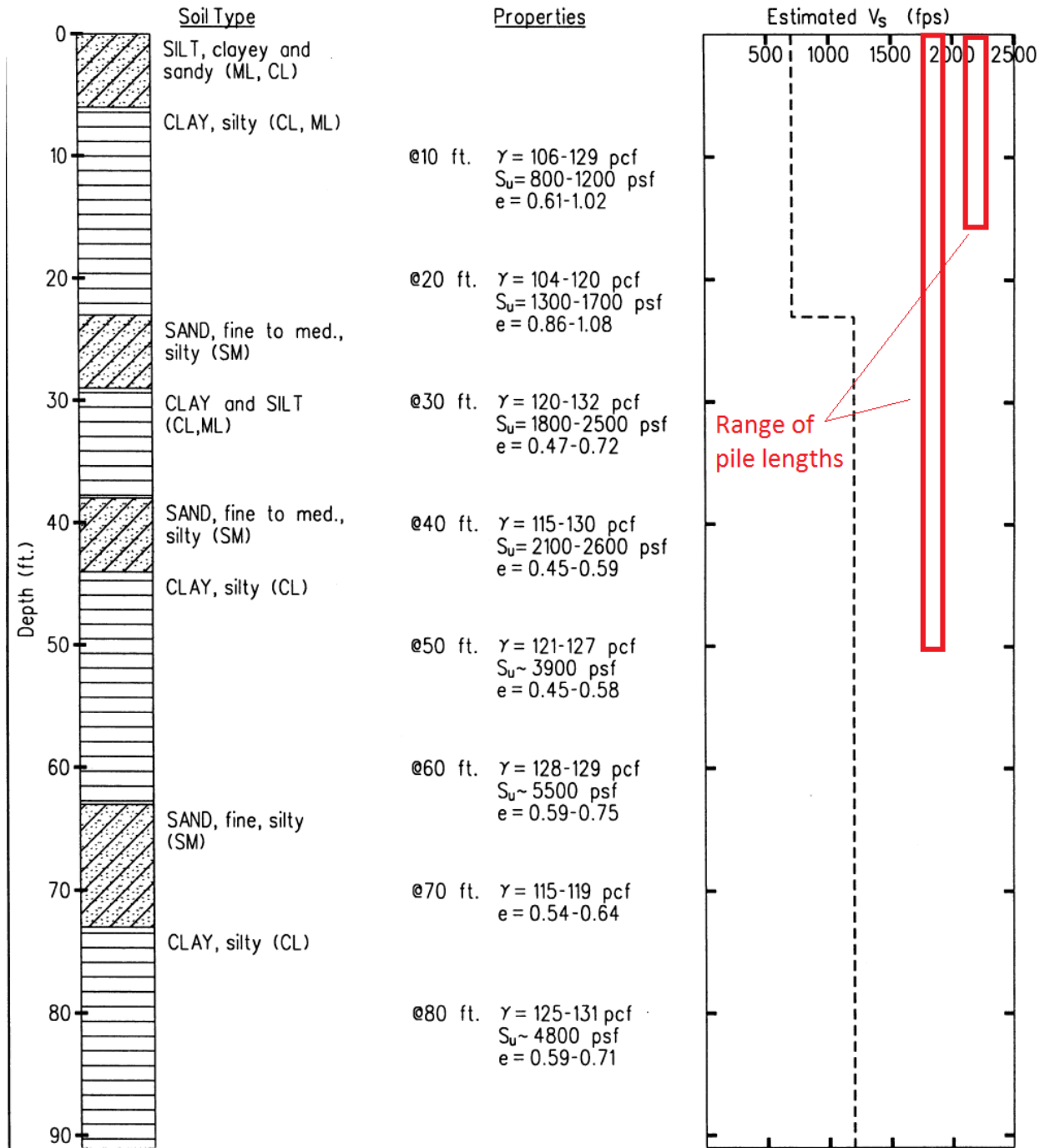


Figure 12-5: Subsurface conditions at Lancaster site after Stewart and Stewart (1997).

Further details of the building and site are presented in Figure 12-4 and Figure 12-5 based on original documentation presented in Stewart (1996) and Stewart and Stewart (1997), with additional information from Stewart et al. (1999b), Kim (2001), and Kim and Stewart (2003). The

building was designed circa 1986 with steel moment frames serving as the lateral force resisting system in both building directions. Steel columns are supported by $B = 20$ -inch (51 cm) drilled shafts ranging in length between 15 and 50 feet (4.6 – 15.2 m). Although not stated explicitly in the original documentation, based on the building layout shown in Figure 12-4 and typical design practices it assumed for the purpose of this analysis that each column is supported directly by an individual pile. The 1st floor of the building is not embedded below the ground surface. Fixed-base and flexible-base first-mode periods are reported by Stewart et al (1999b) as 0.69 and 0.73 s, respectively, corresponding to a relatively small period-lengthening value of 1.06. These values and the transfer functions computed below correspond to the building transverse direction, which is roughly east-west (see Figure 12-4). Subsurface conditions consist of interbedded medium dense to dense silty sand and medium stiff to very stiff silty clay. The unit weights and estimated shear wave velocity profile shown in Figure 12-5 were used to define the subsurface profile for the transfer functions computed for the present study.

The procedures for computing the purely kinematic FIM/FFM TF and combined SDOFO-pile FM/FFM TF are the same as for the Sendai site and so will not be repeated here. The exception is that the system identification work done by Stewart (1996) provides some parameters for the Lancaster site that had to be estimated for evaluating the Sendai case. These are the equivalent-SDOFO height (40 ft) and fixed-base period (0.69 s). As for the Sendai site, the building is modelled as a SDOFO supported by a single pile, where the mass of the SDOFO represents the estimated tributary mass supported by a single pile in the real structure. Using the same assumed uniform dead load of 5 kPa distributed over the floor plans shown in Figure 12-4, this resulted in an equivalent SDOFO mass of 145 Mg. The 50 foot pile length is used for the model. The measured TF ordinates with high coherence do not indicate that strong kinematic amplification occurred,

which would be indicative of a free-head pile condition, so the pile heads are assumed to be fixed. Although not shown on the building drawings or described in the original documentation, it is assumed that grade beams interconnect the piles and provide some resistance against rotation. The impedance spring macro-element used for the substructure analysis is defined to a stiffness of 0.01 m, which is in the range of the maximum differential displacement between the recorded FM and FFM.

The kinematic FIM/FFM TF predicted using the models presented in §10.4.3 is shown in Figure 12-6. Note that significant reduction of the FIM relative to the FFM is predicted only at frequencies above about 30 Hz, which is well beyond the range of interest for this case and for most buildings in general. The FIM/FFM TF is also shown versus dimensionless frequency with a comparison to the range of results computed for the parametric analysis done for this study (e.g., see Figure 10-13). This comparison shows that the predicted TF falls within the range of the study results.

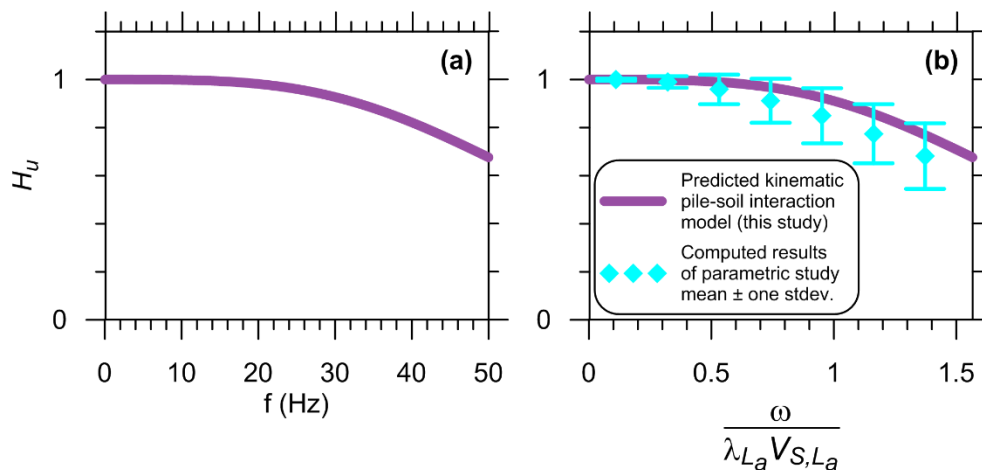


Figure 12-6: Predicted kinematic pile-soil interaction transfer function for Lancaster site plotted versus (a) plain frequency and (b) dimensionless frequency.

Comparison between the combined SDOFO-pile FM/FFM TF and recorded FM/FFM TF is shown in Figure 12-7. Note that a log-frequency scale is used to emphasize low frequencies near the building fundamental frequency. The computed TF (orange triangles) provides a good match to the recorded TF (green dots) up to the peak occurring around approximately 1.2 – 1.3 Hz, which occurs because of inertial resonance near the building’s flexible first-mode period. Immediately beyond this frequency, the computed TF predicts a significant drop-off down to $H_u \approx 0.5$, while the recorded TF only decreases to around $H_u \approx 0.75$.

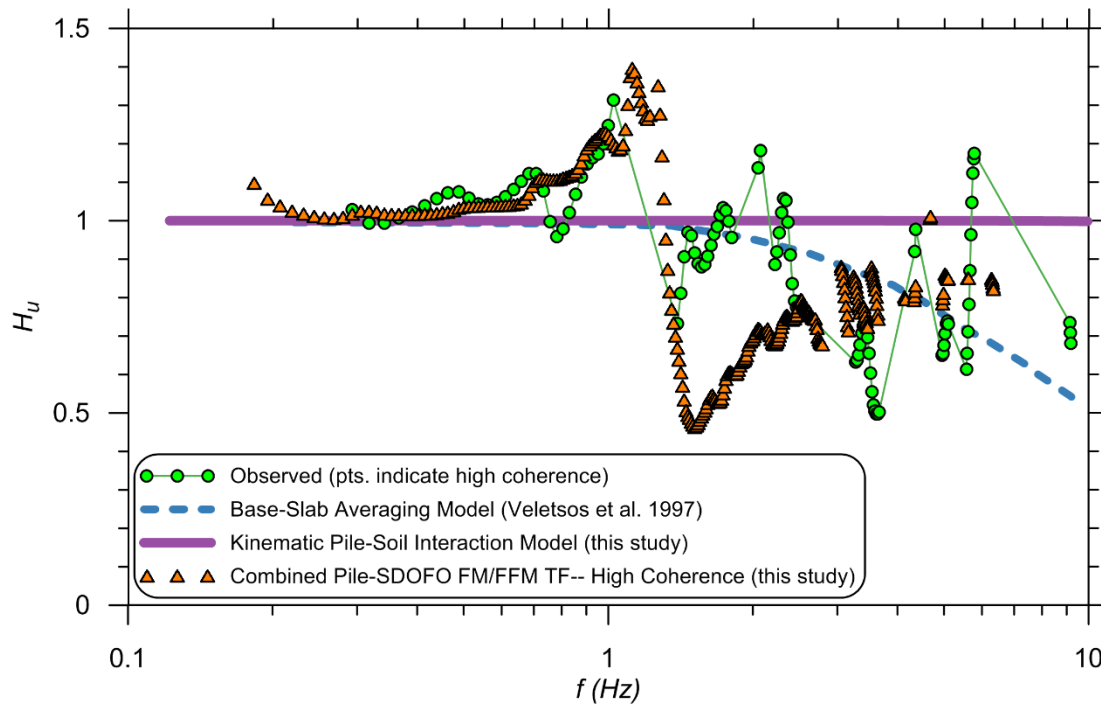


Figure 12-7: Model predictions versus empirical data for Lancaster building during 1994 Northridge earthquake after Kim and Stewart (2003).

Recalling Figure 11-5 and Figure 11-6, the local minimum in this region of the TF marks the transition between the foundation-level response being dominated by inertia to being controlled primarily by the ground displacement at higher frequencies. For the Lancaster case, over-prediction of the drop-off after $\tilde{f}_{l,SDOFO}$ is likely a result of not including the surface-foundation elements in the SDOFO-pile substructure model. Interaction of surface foundation elements

through base friction and rocking would decrease foundation-level motions in addition to the lateral resistance provided by piles, which in turn would decrease the effect of the foundation motion being dominated by inertia of the structure mass. Because the pile-to-soil stiffness contrast was relatively low at this site, and the piles are relatively small, base-slab averaging likely provides a better explanation for the observed behavior than the pile kinematic model, as concluded by the original researchers. Nonetheless, these results again highlight the fact that recorded FM/FFM transfer functions inherently contain inertial SSI effects, especially near the fundamental mode frequency, and comparison of empirical results to kinematic SSI models is more meaningful if the combined inertial-kinematic effects are explicitly considered.

12.2 EXAMPLE APPLICATION OF SPECTRAL RATIO PREDICTION MODEL FOR PILE-SUPPORTED BRIDGE

The California Department of Transportation (Caltrans) is currently in the process of replacing a bridge at the Highway 101—Linden Avenue overcrossing in Carpinteria, California. Construction plans for the replacement bridge, which are available online (Caltrans 2016)⁷, show that 78-inch diameter cast-in-steel-shell (CISS) piles will be used to support the single bent structure, shown in Figure 12-8 and Figure 12-9. CISS piles consist of a driven steel pile shell that is subsequently filled with concrete and reinforcing steel, resulting in a stiff foundation element. The first-mode natural frequency of the bridge in the longitudinal direction is 0.45 s (Caltrans, personal communication 2015). Based on the design response spectrum for free-field conditions shown in the plans (see Figure 12-10), the spectral acceleration at this period is approximately 1.34 g.

⁷ http://www.dot.ca.gov/hq/esc/oe/project_ads_addenda/05/05-4482U4/plans/

Using the proposed bridge foundations as an example, the spectral ratio prediction model for free-head piles presented in §10.5.3 will be used to modify the free-field acceleration response spectrum to account for kinematic pile-soil interaction.

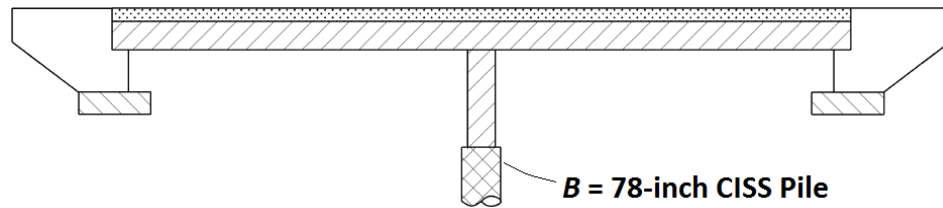


Figure 12-8: Longitudinal elevation view of proposed Linden Street overcrossing replacement (after Caltrans 2016).

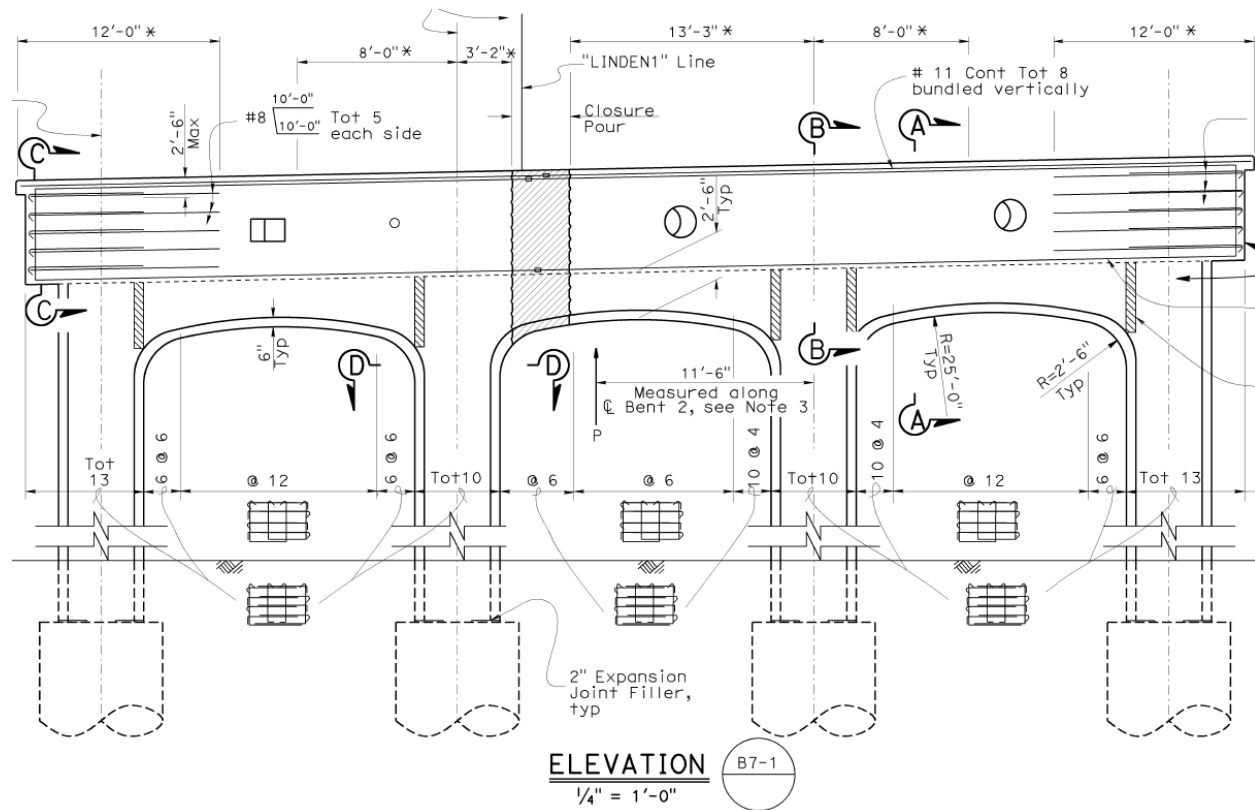


Figure 12-9: Transverse elevation view of interior bent for proposed Linden Street overcrossing replacement (after Caltrans 2016).

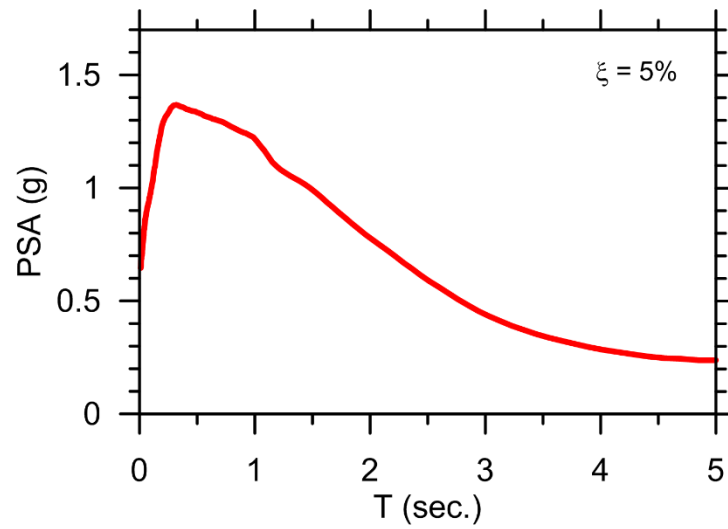


Figure 12-10: Acceleration response spectrum used for proposed Linden Street overcrossing replacement (after Caltrans 2016)

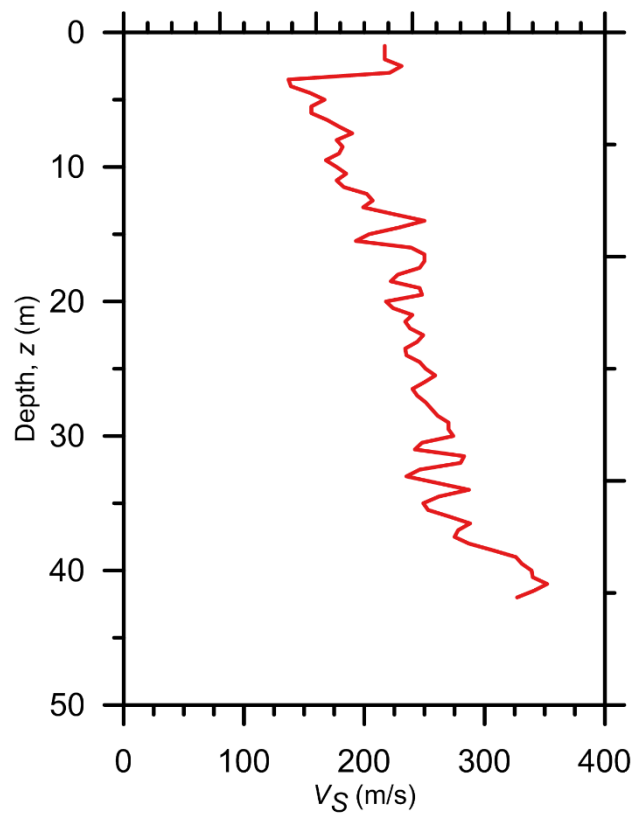


Figure 12-11: Shear-wave velocity profile measured using P-S suspension logging (after Caltrans 2016).

Subsurface conditions at the bent location generally consist of loose to medium dense silty sand and sandy silt interbedded with soft to medium-stiff lean clay. The CISS piles will extend from elevation +18 ft. to -58 ft., a total length of 75 ft. A shear wave velocity profile measured using P-S suspension logging is shown in Figure 12-11. Considering the V_s profile and based on a review of the borings and cone penetration test (CPT) soundings done at the site, the stratigraphy is idealized as consisting of a surface layer extending from the ground surface to a depth of 15 m with unit weight 108 pcf (17 kN/m³) overlying a denser layer with unit weight 120 pcf (19 kN/m³). Both layers are assumed to behave as predominately granular soils.

The following list summarizes how the parameters needed as inputs for the coefficient prediction models were defined based on information obtained from the construction plans and other references:

- The effective flexural rigidity (i.e., considering the reduced moment of inertia due to concrete cracking) was estimated from the following expression from AASHTO (2009) for concrete-filled steel structural members:

$$EI_{eff} = E_s I_s + 0.4 \left(\frac{E_c A_c}{A_s} \right) I_s \quad (12.1)$$

in which E , I , and A are the Young's modulus, moment of inertia, and cross-sectional area, respectively, and the subscripts c and s denote concrete and steel. The steel shell has a wall thickness of 1 inch (25.4 mm) and an assumed Young's modulus of 29,000 ksi (200 GPa). The concrete has a design strength of 3.6 ksi and assumed modulus of 3,420 ksi (23.6 GPa).

EI_{eff} computed using these parameters and the appropriate values of I and A

in the above equation is 28,100 MN·m². This value was also checked with a moment-curvature analysis, which showed good agreement.

- Active length L_a was computed as 50 ft. (15.4 m; about 8 times the pile diameter) using the iteration process described in §7.3.3. Based on this length, λ_{La} and $V_{S,La}$ were computed as 0.079 ft⁻¹ (0.26 m⁻¹) and 606 ft/s (185 m/s), respectively. The λ_{La} calculation was based on EI_{eff} and K_e computed from the shear wave velocities and unit weights given above, an assumed Poisson's ratio of 0.35, and $\delta = 3.0$ (for free-head piles) as described in §8.3.
- The frequency f_0 as defined by Rathje et al. (2004) computed from the design acceleration response spectrum is 2.05 Hz. This parameter describes the frequency corresponding to the predominant energy of the spectrum as discussed in §10.5.2. In order to meet the period spacing criterion established by Rathje et al, the spectrum was resampled on a log-evenly spaced period axis.

- From the preceding terms, $\left(\frac{f_0}{\lambda_{La} V_{S,La}} \right) = 0.043$.

- Time-averaged shear wave velocity over the full pile length is 656 ft./s (200 m/s), thus $\left(\frac{V_{S,La}}{V_{S,L}} \right) = 0.93$.

- The maximum spectral ordinate is $\left(\frac{PSA_{max}}{g} \right) = 1.37$.

The last three parameters in the above list are the inputs to the spectral ratio coefficient prediction models for free-head piles presented in §10.5.3. Using the coefficients predicted by Equations (10.27) through (10.32), the resulting spectral ratio curve defined by the Equation (10.21) functional form is presented in Figure 12-12.

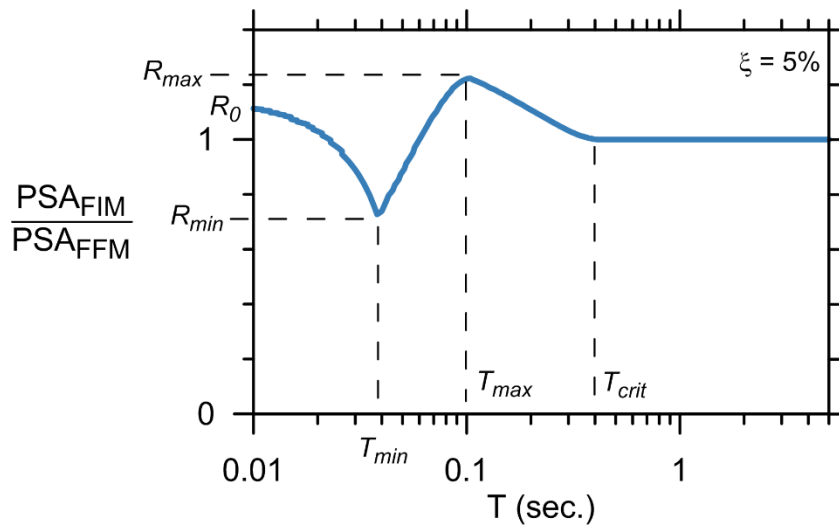


Figure 12-12: Predicted spectral ratios for Linden Street Overcrossing.

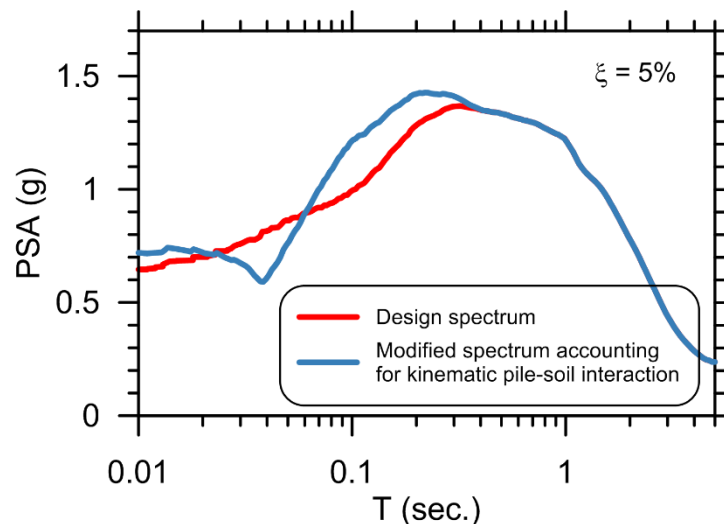


Figure 12-13: Kinematic pile-soil interaction effect on acceleration response spectrum.

The predicted spectral ratios in Figure 12-12 were multiplied by the design response spectrum to produce the modified spectrum shown in Figure 12-13. The modified spectral

acceleration at the first mode period of the Linden Avenue Overcrossing (0.45 s) is 1.34 g, which is unchanged from the free-field spectrum value. For this example, the first-mode period of the bridge lies just beyond the range where kinematic pile-soil interaction is predicted to cause a significant modification to the free-field spectrum.

13 Conclusions and Recommendations for Engineering Practice

A comprehensive parametric study of the influence of kinematic pile-soil interaction on foundation-input motions (FIM) by means of nonlinear numerical analysis has been presented. The analysis approach consisted of performing one-dimensional ground response analysis to define free-field motions, which were subsequently imposed on a beam-on-nonlinear-dynamic-Winkler-foundation model of a pile or pile group. The free-field ground surface motion (FFM) and top-of-pile “foundation-input motion” (FIM) computed from these results were then used to compute transfer functions and spectral ratios for use with the substructure method of seismic analysis. A total of 1,920 parametric combinations of different pile sizes, soil profiles, and ground motions were analyzed.

Results of the study show that significant reductions of the FFM due to kinematic pile-soil interaction occur for stiff, large-diameter piles in soft soil, which could result in a favorable reduction in design demands for short-period structures. Simulations of a 3 x 2 pile group subjected to incoherent ground motions showed that group effects further reduce the FIM relative to the FFM in comparison to an equivalent single pile, but typically by less than 10 percent, and only over a limited frequency range. Still, the simulations performed for this study confirm this trend, and it

is likely that consideration of ground motion incoherence over a larger spatial extent, such as the footprint of a building supported on a piled-raft foundation, could be more significant. The tools for generating incoherent motions based on the work of Ancheta and Stewart (2015) described in §9.7.3 could be used for this purpose for future studies.

The key parameters controlling kinematic pile-soil interaction are:

- Pile head-fixity condition,
- Pile-to-soil stiffness contrast,
- Variations in soil stiffness over the pile length,
- Nonlinear soil behavior due to pile-soil-interaction, which depends on relative pile-to-soil stiffness contrast, and due to free-field ground response,
- Radiation damping, and
- Variable frequency content of the free-field excitation, as opposed to harmonic excitation at a single frequency.

The first three items in the above list have long been recognized from the results of elastic studies (e.g., Flores-Berrones and Whitman 1982, Fan et al. 1991, Anoyatis et al. 2013). The key differences between simplified elastic solutions and the nonlinear results computed for the more realistic conditions considered in this study are caused by the latter three factors, including time-varying coupling and interference of these factors that is not captured when linear superposition is assumed.

The primary motivation for performing this study was to overcome the limitations of idealistic assumptions that have been employed in previous studies, such as linear-elastic material

behavior, drastically simplified stratigraphy, and harmonic oscillations in lieu of real ground motions. In order to capture the important influence of more realistic conditions such as material nonlinearity, subsurface heterogeneity, and variable frequency-content ground motions, a set of models for predicting transfer functions and spectral ratios has been developed through statistical regression of the results from this parametric study.

The results presented in Chapter 10 demonstrate that elastic solutions are approximately coincident with the average results of this study, but fail to capture the variability that is possible when more realistic subsurface conditions and ground motions are used along with explicit consideration of nonlinearity. While this suggests that elastic solutions provide a reasonable first-order approximation of behavior, it also means that they would *over*-predict the reduction in free-field ground motion due to kinematic pile-soil interaction roughly half of the time. A method that produces an erroneous prediction in the unsafe direction (i.e., an “un-conservative” estimate) half the time is generally unacceptable for engineering practice. A robust design approach should include measures for predicting the amount of variability that is anticipated due to realistic conditions.

Although a comparison to elastic analytical solutions provides a good means for checking that the results of this study fall within reasonable bounds (which has been confirmed), the importance of this comparison should not be weighted too heavily. Significant effort has been made to model realistic conditions for this study, which often represent a significant departure from the assumptions used in elastic analytical solutions, hence it is expected that the results will differ. The large amount of variability exhibited by the results of this study should not be viewed as a negative outcome, but rather a reflection of the amount of variability that should be anticipated for real system behavior.

The results of the numerical analyses performed for this study are likely skewed slightly in the direction of under-predicting kinematic pile-soil interaction, which is to say that the computed transfer function ordinates are slightly above what may be anticipated for real behavior. Reductions in free-field motions computed in this study thus error slightly on the safe side in a design sense. This judgment is based on the effects of assumptions made when defining two of the modeling parameters as discussed subsequently: (i) radiation damping and (ii) using a value of $\delta = 3.0$ for free-head piles.

Radiation damping manifests as an increase in stiffness for dynamic p - y curves (see §9.4.4). Increases in soil stiffness, which correspond to a decrease in pile-to-soil stiffness contrast, result in less kinematic interaction. For example, Figure 10-18 showed that radiation damping effectively outweighed the effect of p - y softening due to soil nonlinearity. The models used to define dashpot coefficients for radiation damping in this study are from elasticity-based solutions which assume perfect radiation of stress waves to infinity through homogeneous elastic media. For more realistic heterogeneous subsurface conditions, radiation damping may be a less efficient mechanism of energy dissipation than assumed by these models. Some portion of the energy due to stress waves generated at the pile-soil interface could be reflected back by other piles, adjacent structures, or geomaterial impedance contrasts. Hence, it is likely that the influence of radiation damping is being over-predicted in this study, but because this results in a decrease in kinematic pile-soil interaction, it is considered acceptable. Experimental measurements of these effects could provide justification for reducing the magnitude of radiation damping employed in future studies.

It is worth noting that conventional deep foundation design based on static or pseudo-static methods does not take damping into consideration. Ignoring damping is usually a reasonable assumption for typical design applications in which soil is relied upon to provide resistance to

loads generated in the superstructure and transmitted to the ground through foundations. For example, because ignoring the contribution of radiation damping to dynamic p - y stiffness effectively results in a softer curve, estimates of lateral pile displacements due to superstructure lateral loads would be expected to exceed the real behavior. Thus a safe design can be developed by assuring that the predicted displacements are within tolerable limits.

For free-head piles, the assumption of zero rotational restraint at the pile head is an oversimplification. For a system that can be represented by a single-degree-of-freedom oscillator, such as a sign pole supported on a single pile, complete lack of rotational restraint may be a reasonable approximation. But for the case of piles supporting a bridge bent, the tendency for the pile head to rotate due to free-field kinematic demands would be resisted by other bridge components via the connection between the top of the bent and the superstructure. For example, consider rotations in the longitudinal direction of the bent foundations shown in Figure 12-8, which would be resisted by the bent-to-deck connection and the abutment stiffness. This connection was found to play an important role in resisting lateral spreading demands in Part I of the dissertation, and likewise could play an important role in influencing pile behavior during transient kinematic loading, thus affecting the transfer of the foundation input motion to the superstructure. The most significant impact of this restraint would be to limit rotations of the pile near the ground surface, which should result in a smaller value of Winkler coefficient δ . Recall that $\delta = 3.0$ was used for free-head piles to account for the increases shear resistance mobilized in the soil due to pile rotation, while $\delta = 1$ was used for the fixed-head piles which undergo less rotation and thus exert predominantly compressive stresses in the direction of loading. Hence, the value of $\delta = 3.0$ used in this study for free-head piles may results in an overestimate of p - y stiffness and corresponding

underestimate of kinematic interaction for cases where significant restraint against rotation is provided by the superstructure, even if restraint is not provided at the ground surface elevation.

13.1 PREDICTIVE MODELS AND LIMITATIONS

Models for predicting transfer functions and spectral ratios were presented in §10.4 and §10.5. These models represent a means for predicting kinematic pile-soil interaction with consideration of nonlinear behavior, realistic subsurface condition, and real ground motion characteristics without the need to perform dynamic analysis of a pile-soil system. Input parameters for the predictive models are computed from the type of information typically known for real projects, and are consistent with the type of seismic design that will be performed. For example, the spectral ratio prediction equations use terms defined from the free-field response spectrum, while the transfer function prediction equations use terms defined from a free-field acceleration time series.

For design applications, a reasonable first-order approximation of pile group behavior could be estimated by reducing transfer functions predicted using the single-pile prediction models by an additional 5 percent at frequencies beyond the corner frequency. Because of the idiosyncratic nature of the group results, for critical projects, modeling of the type used for this study would be more appropriate than this rough approximation. Alternatively, group effects could be ignored due to their relatively insignificant contribution to kinematic pile-soil interaction.

Caution should be exercised when applying the transfer function and spectral ratio prediction models to conditions falling outside the bounds considered in this study. In particular, the kinematic pile-soil interaction behavior predicted by the models may differ significantly from actual behavior for:

- Sites with a strong ground response effect caused by, for example, an abrupt impedance contrast occurring over the length of the pile, or a stiff layer overlaying a significantly soft layer,
- Sites with time-averaged shear-wave velocity over the length of the pile ($V_{s,L}$) significantly below 100 m/s, which could result in soil nonlinearity during site response and due to pile-soil interaction that is beyond the amount of nonlinearity captured in this study,
- Cases of ground failure such as liquefaction, significant cyclic softening of cohesive soils, or permanent ground displacements.

For these cases, the nonlinear modeling approach used to generate the results for this study would be more appropriate than applying the generalized transfer function or spectral ratio predictions models.

13.2 REINTERPRETATION OF EMPIRICAL CASE STUDIES

Empirical transfer functions computed from pile-supported structures instrumented at the foundation level and adjacent free-field recordings are reported by Kim and Stewart (2003), Mikami et al. (2006), and Givens et al. (2012). In these studies it was found that elastic kinematic pile-soil interaction transfer function models (e.g., Fan et al. 1991) did not provide a good match to empirical observations, while in some cases base-slab averaging models considering ground motion incoherence provided a better match (e.g., see Kim and Stewart 2003). Based on these findings, the researchers posed questions as to whether consideration of ground motion incoherence in combination with an improved kinematic interaction model would provide a better match to the empirical observations.

As shown in §12.1, the trends exhibited by the empirical transfer functions turn out to be dominated by inertial interaction. Simulations using the substructure modeling approach that included a single-degree-of-freedom oscillator to represent the structure provided a close match to the observed behavior near the first-mode period of the system. The improved kinematic transfer function model developed herein produced a predicted kinematic transfer function that was not significantly different from previous kinematic models, suggesting that the ability or lack thereof to accurately capture kinematic interaction was not critical for interpreting these cases; it was more important to consider the combination of inertial and kinematic effects. The original researchers recognized that inertial effects are present in the recorded foundation-level motions, and thus focused their efforts on interpreting kinematic effects at frequencies away from the fundamental frequency of the structures. Combined kinematic-inertial analysis methods or closed-form analytical methods give the opportunity to study both effects simultaneously, which can be particularly useful when evaluating case studies.

Further issues related to the combined effects of inertial and kinematic interaction were explored in Chapter 11. These findings, along with the lessons learned from revisiting the case studies, highlight the fact that when superstructure inertia is present, the foundation motion (FM) differs from the FIM corresponding to a pile that does not support a structure. To compute a FM/FFM transfer function for comparison to empirical transfer functions requires performing a dynamic analysis of a structural model (e.g., a SDOF oscillator) subjected to the FIM, for example using the substructure method. Beyond just knowing the structure's period, this requires knowing enough information to form a reasonably accurate structural model.

13.3 FUTURE RESEARCH NEEDS

In addition to the transfer function and spectral ratio models presented herein, the analytical framework that is used to generate the results can be used to investigate further complexities. Likewise, future improvements to numerical modeling methods such as improved p - y curves can be incorporated.

The work performed for this study made it apparent that the following are important research needs in the field of pile dynamics:

- P - y - θ springs that explicitly consider pile rotation (applies to conventional static loading as well).
- Better quantification of δ through theoretical and rigorous numerical modeling approaches as well as experimental measurements.
- Better quantification of p - y curve ultimate resistance for sand based on rigorous theory and validated with experiments and rigorous three-dimensional numerical studies.
- Group analyses considering spatially-variable (incoherent) ground motions over the footprint of a typical building. Whereas group effects were relatively minor for the pile group layout considered here, which represents a typical bridge bent substructure, the larger footprint of a building could result in a greater group-averaging effect and further kinematic reduction of free-field motions.
- The analyses performed here decoupled free-field ground response from pile soil interaction for computational efficiency. In a real system, soil nonlinear behavior due to these two effects occurs simultaneously, and thus it is difficult to predict their combined effects *a priori* without a coupled simulation. A limited number of couple numerical

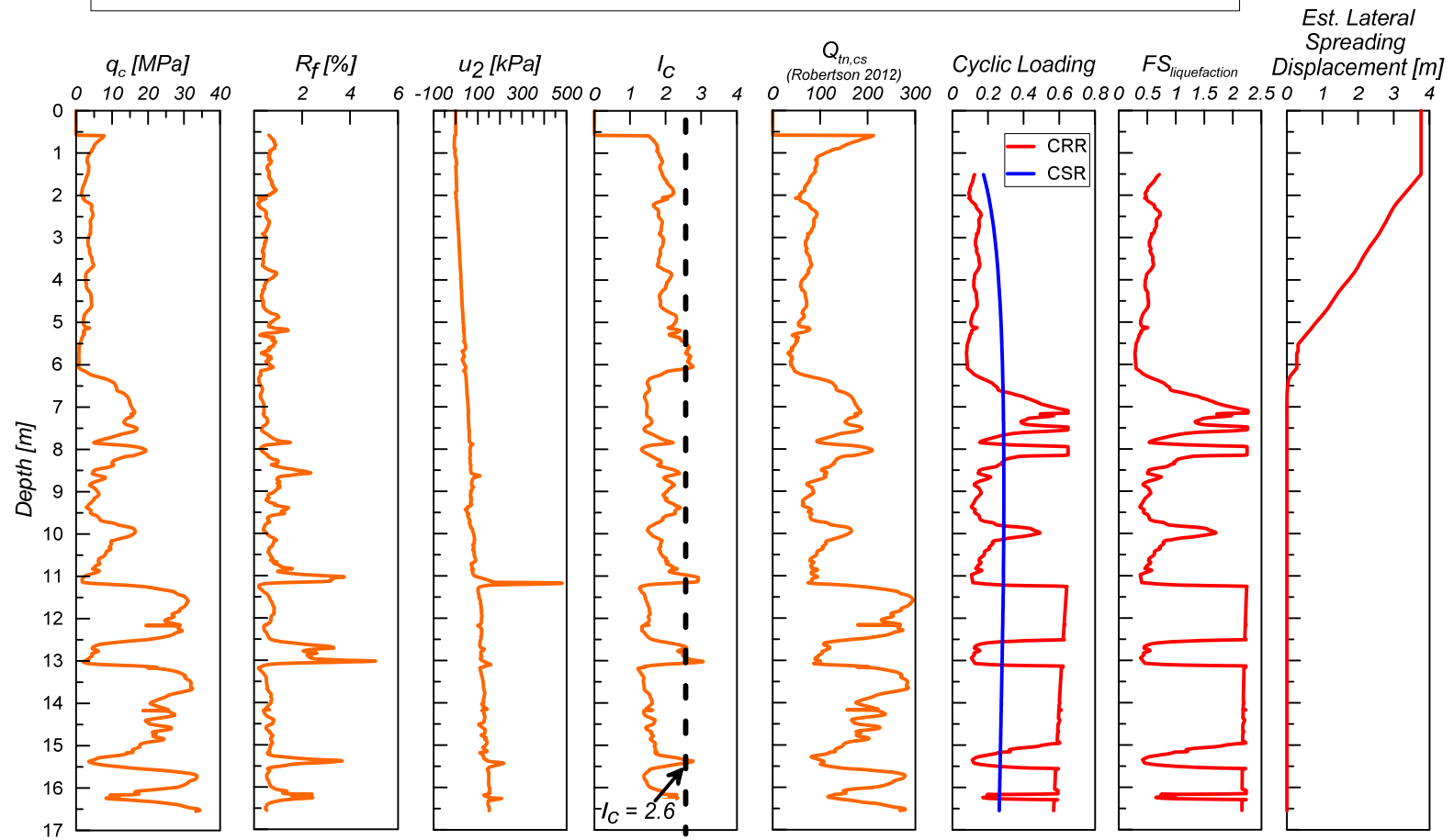
analyses and/or experimental data specifically targeted at studying the combined effects of nonlinearity due to ground response and kinematic pile-soil interaction would be helpful for validating the results of this study.

- Experimental measurements of kinematic pile-soil interaction; especially measurements of radiation damping.
- Thorough recommendations on the combination of inertial and kinematic soil-structure interaction effects, especially as affected by system nonlinearity.

Appendix A: Subsurface Investigations for Mexico Bridges Site

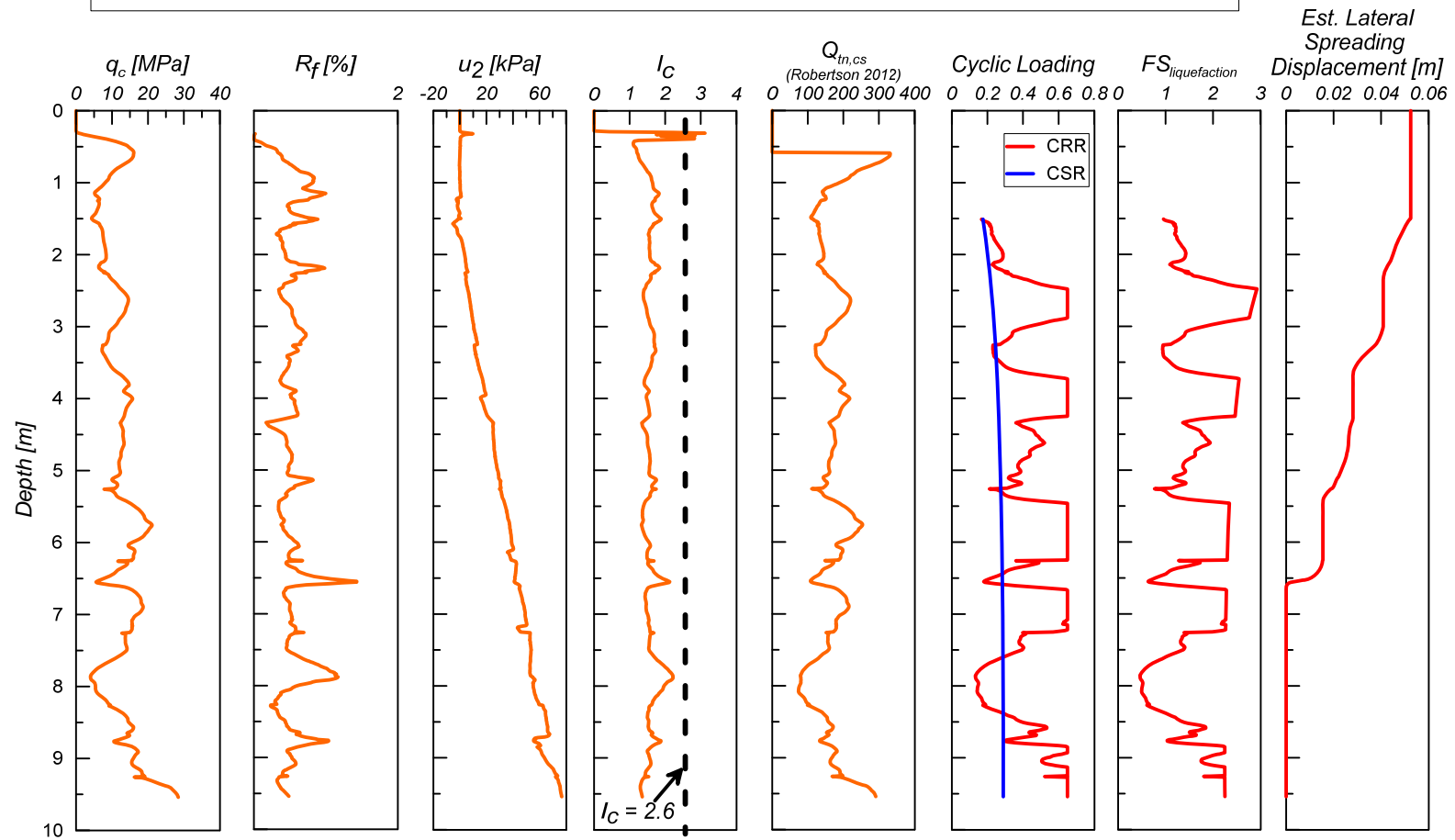
CPT-1 Data and Liquefaction Calculations

Project:	UCLA Earthquake Investigation	P.I.:	S. Brandenburg
Site:	San Felipe Bridge	Operator:	C. Krage
Start Date:	10/24/13	Helper(s):	B. Turner
End Date:	10/25/13	Rig:	Hogentogler 20 ton
Location:	Guadalupe Victoria, MX	Cone:	15 cm ² sCPTu (u ₂)
	32° 14.644' N 115° 03.180' W	Notes:	



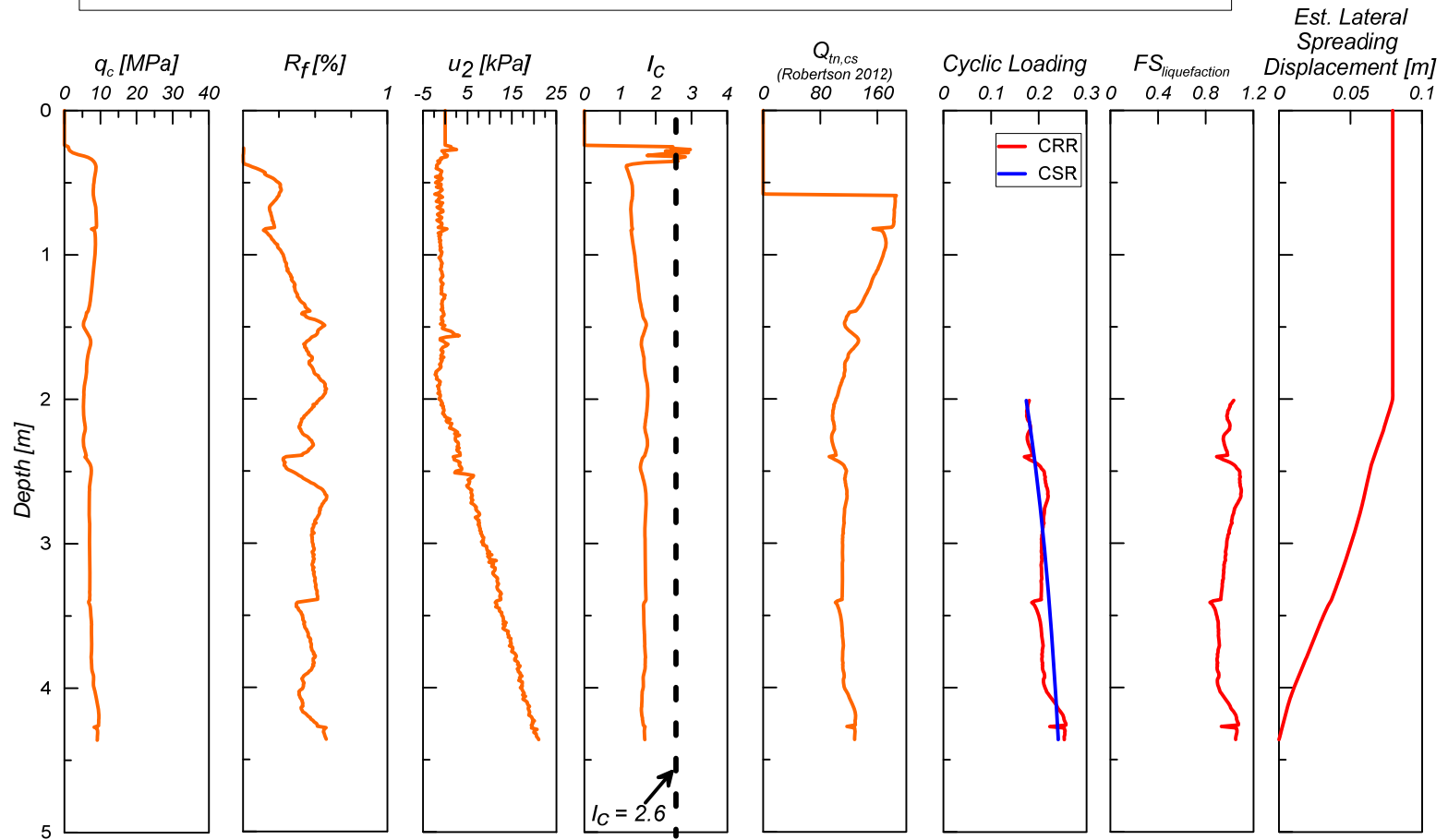
CPT-3 Data and Liquefaction Calculations

Project:	UCLA Earthquake Investigation	P.I.:	S. Brandenburg
Site:	San Felipe Bridge	Operator:	C. Krage
Start Date:	10/24/13	Helper(s):	B. Turner
End Date:	10/25/13	Rig:	Hogentogler 20 ton
Location:	Guadalupe Victoria, MX	Cone:	15 cm ² sCPTu (u_2)
	32° 14.644' N 115° 03.180' W	Notes:	



CPT-4 Data and Liquefaction Calculations

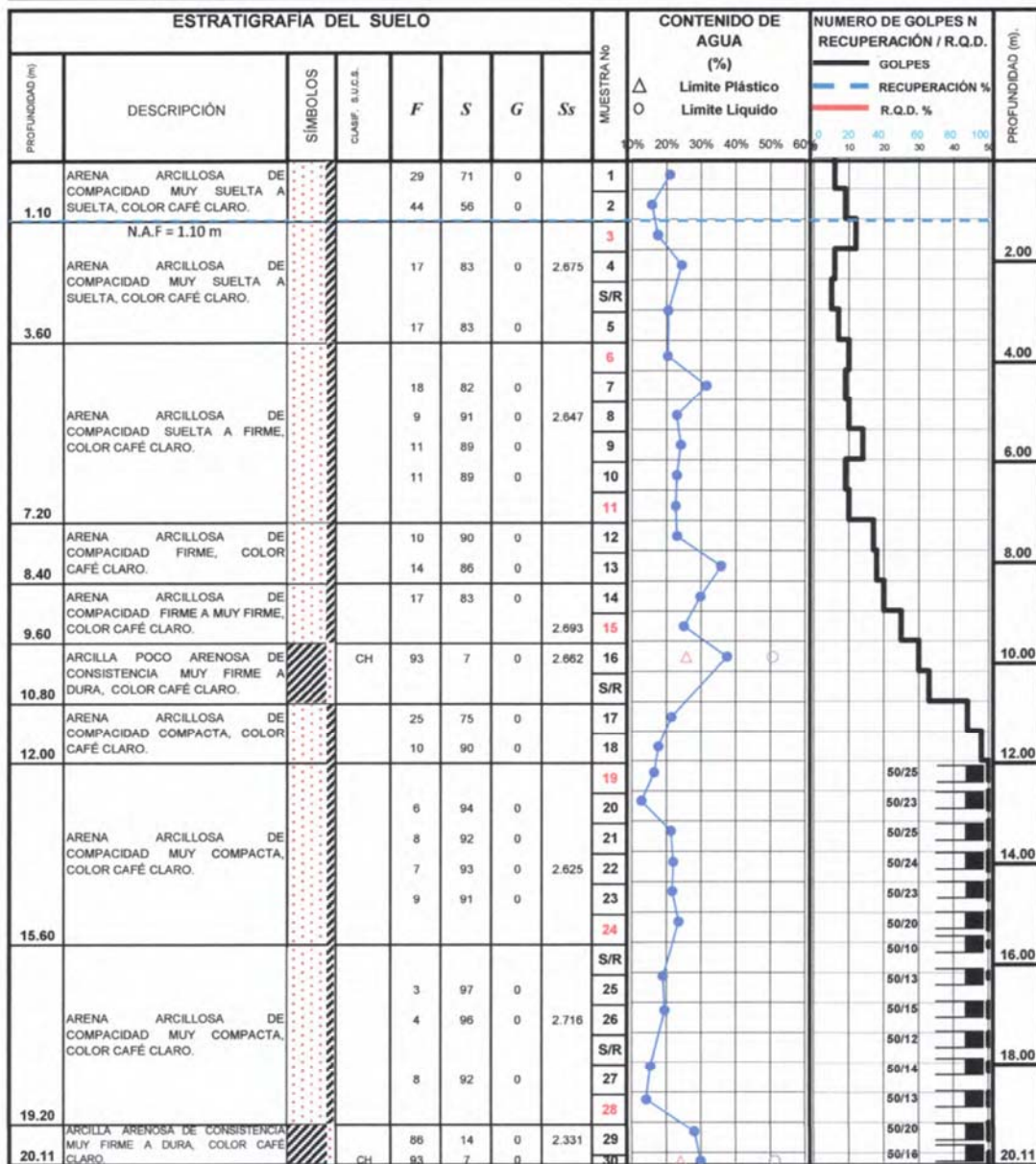
Project:	UCLA Earthquake Investigation	P.I.:	S. Brandenburg
Site:	San Felipe Bridge	Operator:	C. Krage
Start Date:	10/24/13	Helper(s):	B. Turner
End Date:	10/25/13	Rig:	Hogentogler 20 ton
Location:	Guadalupe Victoria, MX	Cone:	15 cm ² sCPTu (u ₂)
	32° 14.644' N 115° 03.180' W	Notes:	





Log of boring performed for Ferromex near Bent 5 of railroad bridge. Exact location unknown. Provided by SCT (personal communication, 2013).

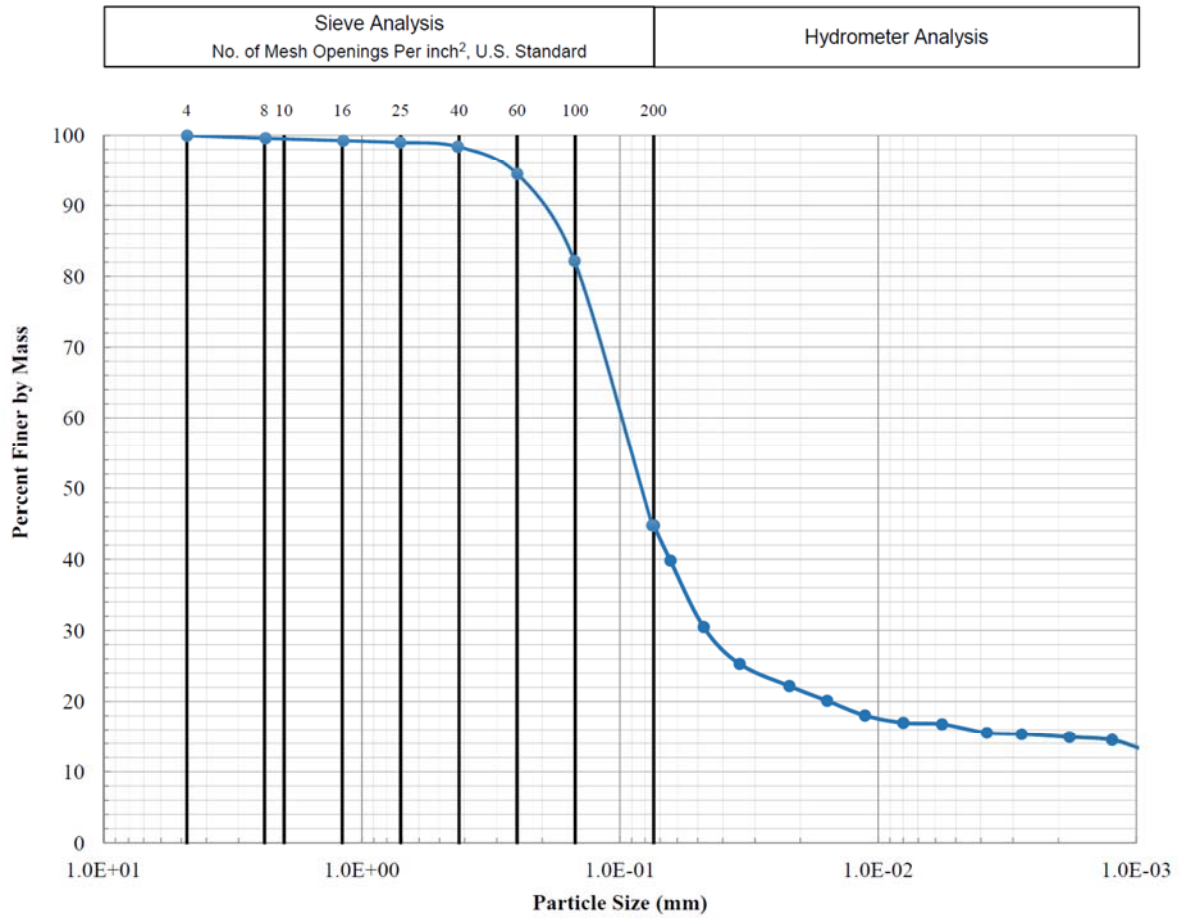
PROYECTO:	Puente Km. 49+95, Línea U, Tramo: División Hermosillo
LOCALIZACIÓN:	Mexicali
REALIZO:	Ing. Fredy García Cruz
REVISO:	Ing. Gonzalo García Rocha
SONDEO:	SPT-1
PROFUNDIDAD:	20.11 m



SIMBOLOGÍA				PROYECTO: Puente Km. 49+95, Línea U, Tramo: División Hermosillo	
	RELLENO		ARENA		Mas de 50 golpes
	ARCILLA		GRAVA	F=	Porcentaje de finos
	LIMO		ROCA	S=	Porcentaje de arena
				G=	Porcentaje de grava
				TS =	
				BD =	
				S/R =	SIN RECUPERACIÓN
PERFIL ESTRATIGRAFICO				SONDEO: SPT-1	
JUNIO-2012				FIGURA No. 5	

Appendix B: Laboratory Test Results for Mexico Bridges Project

Grain Size Distribution



Sample Designation	Depth (m)	U.S.C.S. Symbol	Sample Description	Fines %	Natural W.C. %	PI %	e _{min}	e _{max}
S-1	0 - 1	SM	Light-yellowish brown poorly-graded silty fine SAND; fines are nonplastic	45	8	0	0.58	1.04

Test Performed by: YTT

San Felipe Bridges
Geotechnical Site Investigation

Index Test Results

Date of Investigation: Oct. 2013

Fig. B-1

Appendix C: Sample Calculations for Lateral Spreading Equivalent-Static Analysis Procedure

This appendix presents a portion of the calculations that were performed in order to quantify the input parameters used for the finite element analyses described in Part I of the dissertation. Not all calculations are shown. The reader is encouraged to refer to the references cited in the report rather than simply change the numbers in these sample calculations to fit their project.

Section numbers refer to the section number in Part I of the dissertation in which the calculations being shown here are discussed. Note, trigonometric functions shown herein accept angles in radians as the argument.

Section 4.1 Soil Properties

Soil properties presented in Chapter 4 are primarily based on correlations to CPT measurements. Correlations were performed at each depth corresponding to the sampling interval of the CPT (every 1 cm), and then the correlated values were averaged over the depth interval of each layer of interest. Examples are provided below of the correlations for a single discrete depth interval.

Using data from CPT-1, at a depth of 3 m below ground surface: $d := 3$ (depth = 3m)

Stress:

$$\sigma_v := 1.5 \cdot 17 + 1.5 \cdot (18) = 52.5 \quad \text{Vertical total stress in kPa-- see Table 3.1 for unit wt.}$$

$$\sigma_{vp} := 1.5 \cdot 17 + 1.5 \cdot (18 - 9.81) = 37.8 \quad \text{Vertical effective stress in kPa}$$

$$p_a := 101.325 \quad \text{Atmospheric pressure in kPa}$$

Penetration resistance: *multiple methods will be used so that correlations to soil properties (e.g. relative density) can use the appropriate corrected penetration resistance as input*

$$q_t := 3468 \quad \text{Measured cone tip resistance in kPa}$$

Robertson (2012):

$$I_c := 1.928 \quad \text{Soil behavior type index, stress exponent, and overburden normalized cone tip resistance, respectively, using Robertson (2012) approach-- note requires iteration to determine stress exponent and soil behavior type index.}$$

$$n := 0.6$$

$$Q_{tn} := 61.1$$

$$K_c := 5.58 I_c^3 - 0.403 I_c^4 - 21.63 I_c^2 + 33.75 I_c - 17.88 = 1.22 \quad \text{Clean sand factor for } I_c > 1.64 \text{ [Robertson 2012 eqn. 22]}$$

$$Q_{tncs} := K_c \cdot Q_{tn} = 74.3 \quad \text{Equivalent clean sand overburden normalized cone tip resistance (Robertson 2012 eqn. 20)}$$

$$N_{60} := \frac{\left(\frac{q_t}{p_a} \right)}{10^{(1.1268 - 0.2817 I_c)}} = 9 \quad \text{Equivalent SPT N-value at 60% energy [Robertson 2012 eqn. 2]}$$

$$qc1n_{IB} := C_{NIB} \frac{q_t}{p_a} = 58$$

$$C_N := 1.6 \quad \text{because} \quad \frac{p_a}{\sigma_{vp}} = 2.68 \quad \text{is} > 1.6 \quad \text{SPT overburden correction factor [Cetin 2004]}$$

$$N1_{60} := C_N \cdot N_{60} = 14 \quad \text{Overburden and energy corrected equivalent SPT blowcount.}$$

Robertson and Wride [1998] method with Zhang [2002] update:

$$C_q := \left(\frac{p_a}{\sigma_{vp}} \right)^n = 1.81 < 2 \quad \text{Overburden correction factor.}$$

$$qc1N_{RWZ} := C_q \cdot \left(\frac{q_t}{p_a} \right) = 62 \quad \text{Overburden corrected normalized cone penetration resistance (RWZ subscript indicated Robertson & Wride (1998) method with Zhang (2002) updates)}$$

Idriss and Boulanger (2006, 2008) method-- requires iteration:

Initial guess for m_{ex} , stress exponent: $m_{ex} := 0.5$

$$\left(\frac{p_a}{\sigma_{vp}} \right)^{m_{ex}} = 1.64 < 1.7 \quad \text{therefore} \quad C_{NIB} := \left(\frac{p_a}{\sigma_{vp}} \right)^{m_{ex}} = 1.64 \quad \text{C(NIB) is the Idriss and Boulanger overburden correction factor.}$$

Evaluate $q(c1n)_{IB}$ using this correction factor:

$$qc1n_{IB} := C_{NIB} \frac{q_t}{p_a} = 56 < 254$$

Now re-compute the stress exponent, m using this normalized cone penetration resistance:

$$m_{ex} := 1.338 - 0.249 qc1n_{IB}^{0.264} = 0.62$$

Re-compute the overburden correction factor:

$$\left(\frac{p_a}{\sigma_{vp}} \right)^{m_{ex}} = 1.84 > 1.7 \quad \text{therefore} \quad C_{NIB} := 1.7$$

Re-compute normalized penetration resistance:

$$qc1n_{IB} := C_{NIB} \frac{q_t}{p_a} = 58 < 254$$

Re-compute m and $C(NIB)$:

$$m_{ex} := 1.338 - 0.249 qc1n_{IB}^{0.264} = 0.61 \quad \left(\frac{p_a}{\sigma_{vp}} \right)^{m_{ex}} = 1.83 > 1.7$$

$$C_{NIB} := 1.7$$

Re-compute normalized penetration resistance: $qc1n_{IB} := C_{NIB} \frac{q_t}{p_a} = 58 < 254$

After three iterations, the values of m , $C(NIB)$, and the overburden corrected normalized cone penetration resistance have stabilized.

$FC := 2.8 I_c^{2.6} = 15$ Estimated fines content. Is reasonable based on SCT boring logs.

$\Delta qc1n_{IB} := \left(5.4 + \frac{qc1n_{IB}}{16} \right) \cdot \exp \left[1.63 + \left(\frac{9.7}{FC + .01} \right) - \left(\frac{15.7}{FC + .01} \right)^2 \right] = 31$ Clean sand correction factor

$qc1n_{cs_{IB}} := qc1n_{IB} + \Delta qc1n_{IB} = 89$ Equivalent clean sand overburden corrected normalized cone penetration resistance [IB subscript indicated Idriss and Boulanger [2006, 2008] method].

Correlated parameters:

Friction angle:

$\phi_{cv} := 32$ Constant volume (critical state) friction angle depending on mineralogy, taken as 32 deg. for quartz sand.

$\phi := \phi_{cv} + 15.84 \left(\log(Q_{tncs}) \right) - 26.88 = 35$ Peak friction angle [Robertson 2012 eqn. 25]

Relative density-- use multiple correlations then take a weighted average:

Idriss and Boulanger (2008) methods:

$$Dr_{IBspt} := \sqrt{\frac{N1_{60}}{46}} = 0.56$$

Relative density based on correlations to SPT and CPT penetration resistances, respectively.

$$Dr_{IBcpt} := 0.478 (qc1n_{IB})^{0.264} - 1.063 = 0.33$$

Zhang et al. (2004) method:

$$Dr_{Zhang} := \frac{-85 + 76 \cdot \log(qc1N_{RWZ})}{100} = 0.51 \quad \text{for } qc1n < 200$$

Kulhawy and Mayne [1990] method:

$$Dr_{KM} := \sqrt{\frac{qc1N_{RWZ}}{325}} = 0.44$$

Weighted average of computed relative densities:

$$D_r := 0.3D_{r_{IBspt}} + 0.3D_{r_{Zhang}} + 0.1D_{r_{IBcpt}} + 0.3D_{r_{KM}} = 0.48$$

The Idriss & Boulanger [2008] method using CPT as the input consistently predicted lower D_r values than the other three methods, so it was assigned a lower weighting factor. Judgment should always be applied when considering which correlations provide the most reliable estimates for a given project.

Liquefaction susceptibility and triggering analysis:

Note-- use the appropriate normalized penetration resistance for each calculation. For example, do not use the Robertson [2012] Q_{tncs} values for the Idriss and Boulanger [2008] liquefaction triggering analysis, use the Idriss and Boulanger [2008] qc_{1n} .

Idriss and Boulanger (2006, 2008) method:

Susceptibility:

$$I_c = 1.93 < 2.6$$

...therefore susceptible. In addition, our index testing determined that the fines portion of the bulk sample we collected near the surface is nonplastic. The sample is considered to be reasonably similar to the soil at 3 m depth being considered herein.

Conclusion: the soil at this depth is susceptible to liquefaction

Triggering:

$$M := 7.2$$

Earthquake magnitude being considered (in this case magnitude of 2010 EMC earthquake)

$$PGA := 0.27$$

Peak ground acceleration estimated for SFB site.

$$qc_{1ncs_{IB}} = 89$$

Normalized cone penetration resistance to be used for computations

Nonlinear stress reduction factor, $r(d)$:

$$\alpha_z := -1.012 - 1.126 \sin\left(\frac{d}{11.73} + 5.133\right) = -0.134$$

$$\beta_z := 0.106 + 0.118 \sin\left(\frac{d}{11.28} + 5.142\right) = 0.015$$

$$r_d := \exp(\alpha_z + \beta_z \cdot M) = 0.977$$

$r_d = 0.98$ (check-- should be close to 1.0 near the ground surface)

$$CSR := 0.65 \cdot PGA \cdot \frac{\sigma_v}{\sigma_{vp}} r_d = 0.238$$

Cyclic stress ratio (CSR)-- estimate of demand

Overburden correction factor:

$$C_{\sigma} := \frac{1}{\left(37.3 - 8.27 \cdot qc1ncs_{IB}^{0.264}\right)} = 0.097 < 0.3 \quad K_{\sigma} := 1 - C_{\sigma} \cdot \ln\left(\frac{\sigma_{vp}}{p_a}\right) = 1.096 < 1.0 \quad (I\&B \ 2006)$$

therefore $K_{\sigma} := 1.0$

Assume ground is approx. level such that static shear stress correction factor is 1.0: $K_{\alpha} := 1.0$

Compute cyclic resistance ratio (CRR) for M 7.5, 1 atm. of effective overburden pressure, and level ground:

$$CRR_{M7.5\sigma1} := \exp\left[\frac{qc1ncs_{IB}}{540} + \left(\frac{qc1ncs_{IB}}{67}\right)^2 - \left(\frac{qc1ncs_{IB}}{80}\right)^3 + \left(\frac{qc1ncs_{IB}}{114}\right)^4 - 3\right] = 0.125$$

Compute magnitude scaling factor:

$$MSF := 6.9 \cdot \exp\left(\frac{-M}{4}\right) - .058 = 1.083$$

Correct CRR for appropriate value of earthquake magnitude and effective overburden stress:

$$CRR := CRR_{M7.5\sigma1} \cdot MSF \cdot K_{\sigma} = 0.136$$

Compute factor of safety against liquefaction:

$$FS_{liq} := \frac{CRR}{CSR} = 0.569 < 1 \quad \text{Solution: soil is predicted to liquefy during the M 7.2 EMC earthquake with a PGA of 0.27g.}$$

Post-liquefaction behavior

Estimate shear strain resulting from liquefaction [Idriss and Boulanger 2008]:

$$\gamma_{lim} := 1.859 \left(2.163 - 0.478 \cdot qc1ncs_{IB}^{0.264}\right)^3 = 0.4 < 0.5 \quad \text{Limiting shear strain (\%)}$$

$$F_{\alpha} := -11.74 + 8.34 \cdot qc1ncs_{IB}^{0.264} - 1.371 \cdot qc1ncs_{IB}^{0.528} = 0.87 \quad \text{Parameter F(alpha)}$$

$$FS_{liq} < F_{\alpha} = 1$$

Since factor of safety against liquefaction is less than parameter F(alpha), the estimated shear strain is taken as the limiting shear strain.

$$\gamma_{max} := \gamma_{lim} = 0.4$$

Post-liquefaction residual undrained shear strength:

$$s_{ur} := \sigma_{vp} \cdot \frac{0.02199 - 0.0003124Q_{tncs}}{1 - 0.02676Q_{tncs} + 0.0001783Q_{tncs}^2} = 11.7 \quad \text{Robertson [2010]}$$

$$0.03 < s_{ur} < \sigma_{vp} \cdot \tan\left(\frac{\pi}{180} \cdot \phi\right) = 1 \quad (\text{true}) \quad \text{Check that estimated value is greater than 0.03 and less than the shear strength under static conditions using the estimated friction angle.}$$

Excess porewater pressure ratio:

Since soil at depth = 3m is predicted to liquefy, assume $r(u) = 100\%$. For layers with estimated $FS(liq) > 1.0$, $r(u)$ was estimated using a hyperbolic decay function fit to the Marcuson et al. [1990] plot of $FS(liq)$ versus $r(u)$ and the Cetin and Bilge [2012] relationship between shear strain and $r(u)$ for comparison. The methods were found to provide similar results for $FS(liq)$ substantially greater than 1.0. The Marcuson et al. equation is presented below for an example $FS(liq) = 1.7$.

$$FS_{liqEx} := 1.7 \quad r_u := \frac{1}{1 + 14(FS_{liqEx} - 1)} = 0.09$$

P-multiplier for fully liquefied condition [$r(u) = 100\%$] using equation from Figure 3.7 in Caltrans lateral spreading guidelines [2013a]:

First compute equivalent clean sand ($N1$)₆₀ value using the Idriss and Boulanger [2008] formula:

$$N1_{60} = 14 \quad \Delta N1_{60} := \exp\left[1.63 + \left(\frac{9.7}{FC + 0.01}\right) - \left(\frac{15.7}{FC + .01}\right)^2\right] = 3$$

$$N1_{60cs} := N1_{60} + \Delta N1_{60} = 18$$

$$m_p := 0.0031N1_{60cs} + 0.00034N1_{60cs}^2 = 0.16$$

For layers with predicted factor of safety against liquefaction greater than 1.0, there is still excess porewater pressure buildup, which reduces effective stress and acts to soften load transfer. To account for this, a p-multiplier is determined based a linear interpolation between the estimated $r(u)$ and an $r(u)$ of 100% and the corresponding fully-liquefied p-multiplier (previous calculation). For example:

$$FS_{liqEx} = 1.7 \quad r_u := \frac{1}{1 + 14(FS_{liqEx} - 1)} = 0.09$$

$$N1_{60cs} := 33 \quad m_p := 0.0031N1_{60cs} + 0.00034N1_{60cs}^2 = 0.47 \quad (\text{fully-liquefied p-mult.})$$

$$m_{pNonLiq} := 1 - r_u \cdot (1 - m_p) = 0.95 \quad \text{interpolated p-multiplier to account for decreased effective stress.}$$

Computations for non-liquefied crust p-y springs following Caltrans lateral spreading guidelines [2013a]. For a graphical explanation of the dimensions, refer to Figure 3.2 in the Caltrans guidelines.

Highway Bridge:

$N_c := 4$	Number of extended-shaft columns
$B := 1.2$	Shaft diameter (meters)
$D := 0$	Crust thickness above top of transverse diaphragm (meters). Assume no flow between the short length of the shafts between the top of the transverse diaphragm and the ground surface such that the transverse diaphragm essentially extends to the surface.
$T := 1.5$	Transverse diaphragm height (meters)
$Z_c := 1.5$	Non-liquefied crust thickness (meters)
$Z_{bb} := 0$	Distance between bottom of transverse diaphragm and bottom of crust (meters).
$Z_t := Z_c - D = 1.5$	Distance between top of transverse diaphragm and bottom of crust (meters)
$W_t := 10.2$	Width of transverse diaphragm in the bridge transverse direction (meters)
$W_L := 1.2$	Width of transverse diaphragm in the bridge longitudinal direction (meters)
$W_{trib} := \frac{W_t}{N_c} = 2.55$	Tributary width of the transverse diaphragm assigned to the single shaft being analyzed (meters)

Soil properties in non-liquefied crust:

$\phi := 35$	Peak friction angle
$\sigma_{vp} := 0.5 \cdot Z_c \cdot 17 = 13$	Effective stress at mid-height of the crust layer (kPa); soil unit wt. is 17kN/m ³ .

Lateral earth pressure coefficients:

$$K_p := \tan^2 \left[\frac{\pi}{180} \left(45 + \frac{\phi}{2} \right) \right] = 3.69$$

Rankine passive L.E.P. coefficient

$$K_a := \tan \left[\frac{\pi}{180} \left(45 - \frac{\phi}{2} \right) \right]^2 = 0.27$$

Rankine active L.E.P. coefficient

$$k_w := 1 + (K_p - K_a)^{\frac{2}{3}} \cdot \left[1.1 \cdot \left(1 - \frac{T}{D + T} \right)^4 + \frac{1.6}{1 + 5 \frac{W_t}{T}} + \frac{0.4 (K_p - K_a) \left(1 - \frac{T}{D + T} \right)^3}{1 + \frac{0.05 W_t}{T}} \right] = 1.1$$

Adjustment factor for 3-d wedge-shaped failure surface

Compute forces from crust acting against bent:

$$F_{\text{passiveCap}} := \sigma_{vp} \cdot K_p \cdot T \cdot W_t \cdot k_w = 795$$

Passive force acting against "front" face of composite block formed by extended-shaft columns and transverse diaphragm (kN)

$$F_{\text{sidesCap}} := 2 \cdot \left(\sigma_{vp} \cdot \tan \left(\frac{\pi}{180} \cdot \frac{\phi}{3} \right) \right) \cdot W_L \cdot Z_t = 9$$

Force acting on sides of outside extended-shaft columns through the crust (kN)

The non-liquefied crust does not extend below the base of the transverse diaphragm, therefore the foundations do not contribute to the resistance within the crust --> $F(\text{piles}) = 0$

$$F_{\text{ultGroup}} := F_{\text{passiveCap}} + F_{\text{sidesCap}} = 804$$

Total force is sum of the passive and side forces (kN)

$$F_{\text{ultIndividual}} := \frac{F_{\text{ultGroup}}}{N_c} = 201$$

Total force acting on a single extended-shaft column's tributary width within the crust.

Determine displacement required to fully mobilize the non-liquefied crust passive pressure. Considers softened load-transfer relationship for a crust overlying liquefied layer [Brandenberg 2007].

Factors relating thickness of crust relative to width and thickness of pile cap:

$$f_{\text{depth}} := \exp \left[-3 \cdot \left(\frac{Z_c - D}{T} - 1 \right) \right] = 1$$

$$f_{\text{width}} := \frac{1}{\left(\frac{\frac{10}{W_t}}{T} + 4 \right)^4 + 1} = 0.58$$

$$\Delta_{\text{max}} := T \cdot (0.05 + 0.45 f_{\text{depth}} \cdot f_{\text{width}}) = 0.46$$

Estimated displacement (meters) required to mobilize full passive pressure

As shown in the Caltrans lateral spreading guidelines [2013a] in Figure 3.1, the load transfer curve for the crust is represented with a trilinear curve defined by three points: (1) the origin, (2) half of the ultimate force and 1/4 of the displacement required for full passive mobilization, and (3) the ultimate force and the full displacement. The curve then continues at zero slope for further displacement. It should be noted that displacement in this case refers to the relative displacement between the soil and the structure, not the absolute displacement of the laterally spreading ground.

$$\text{disp}_{\text{rel}} := \begin{pmatrix} 0 \\ \frac{\Delta_{\text{max}}}{4} \\ \Delta_{\text{max}} \\ 5 \cdot \Delta_{\text{max}} \end{pmatrix} = \begin{pmatrix} 0 \\ 0.12 \\ 0.46 \\ 2.32 \end{pmatrix} \quad \text{Force} := \begin{pmatrix} 0 \\ \frac{F_{\text{ultIndividual}}}{2} \\ F_{\text{ultIndividual}} \\ F_{\text{ultIndividual}} \end{pmatrix} = \begin{pmatrix} 0 \\ 101 \\ 201 \\ 201 \end{pmatrix}$$

When lateral load-transfer is represented through p-y curves, it is customary to express the load as force per unit length of the foundation.

$$p_{\text{HWB}} := \frac{\text{Force}}{Z_{\text{c}} - D} \quad y_{\text{HWB}} := \text{disp}_{\text{rel}} \quad \text{see p-y curve below}$$

Railroad Bridge (same procedure):

$D := 0$	Crust thickness above top of pile cap (meters). Since oblong pier-wall-type column is nearly as wide as the pile cap, assume a uniform block of soil will exert passive pressure from the base of the pile cap to the ground surface.
$T := 1.5$	Effective pile cap height (meters)
$Z_{\text{c}} := 1.5$	Non-liquefied crust thickness (meters)
$Z_{\text{bb}} := 0$	Distance between bottom of pile cap and bottom of crust (meters).
$Z_{\text{t}} := Z_{\text{c}} - D = 1.5$	Distance between top of pile cap and bottom of crust (meters)
$W_{\text{t}} := 6.5$	Width of pile cap in the bridge transverse direction (meters)
$W_{\text{L}} := 4.6$	Width of pile cap in the bridge longitudinal direction (meters)

Soil properties in non-liquefied crust same as for HWB.

Lateral earth pressure coefficients:

$$K_p = 3.69 \quad K_a = 0.27 \quad \text{Rankine passive and active L.E.P. coefficients}$$

$$k_w := 1 + (K_p - K_a) \cdot \frac{2}{3} \cdot \left[1.1 \cdot \left(1 - \frac{T}{D+T} \right)^4 + \frac{1.6}{1 + 5 \frac{W_t}{T}} + \frac{0.4(K_p - K_a) \left(1 - \frac{T}{D+T} \right)^3}{1 + \frac{0.05W_t}{T}} \right] = 1.16$$

Adjustment factor for 3-d wedge-shaped failure surface

Compute forces from crust acting against bent:

$$F_{\text{passiveCap}} := \sigma_{vp} \cdot K_p \cdot T \cdot W_t \cdot k_w = 532$$

Passive force acting against "front" face of composite block formed by pile cap and oblong column(kN)

$$F_{\text{sidesCap}} := 2 \cdot \left(\sigma_{vp} \cdot \tan \left(\frac{\pi}{180} \cdot \frac{\phi}{3} \right) \right) \cdot W_L \cdot Z_t = 36$$

Force acting on sides of pile cap (kN)

The non-liquefied crust does not extend below the base of the pile cap, therefore the foundations do not contribute to the resistance within the crust --> F(piles) = 0

$$F_{\text{ultGroup}} := F_{\text{passiveCap}} + F_{\text{sidesCap}} = 569$$

Total force is sum of the passive and side forces (kN)

Determine displacement required to fully mobilize the non-liquefied crust passive pressure.

Factors relating thickness of crust relative to width and thickness of pile cap:

$$f_{\text{depth}} := \exp \left[-3 \cdot \left(\frac{Z_c - D}{T} - 1 \right) \right] = 1$$

$$f_{\text{width}} := \frac{1}{\left(\frac{\frac{10}{\frac{W_t}{T} + 4}}{1} \right)^4 + 1} = 0.33$$

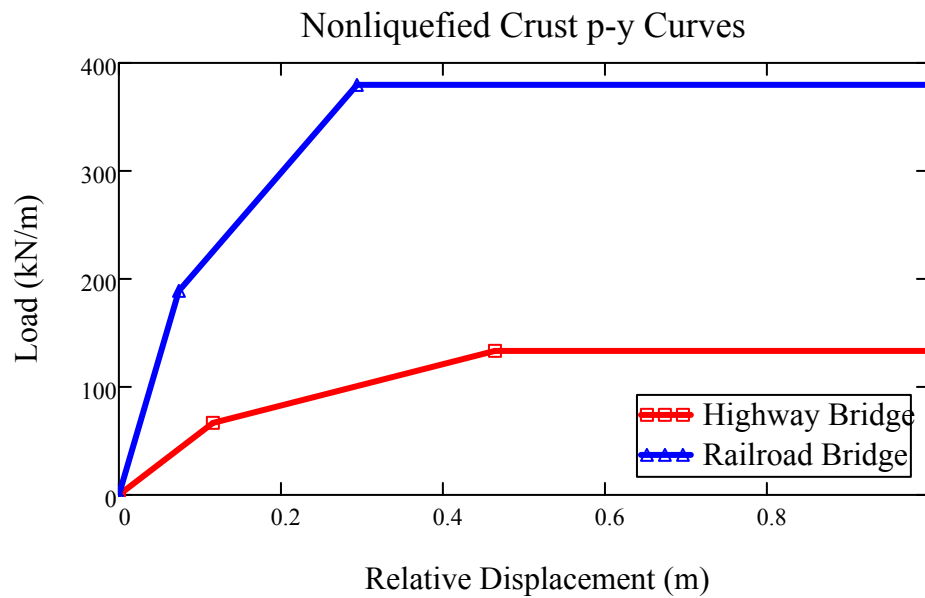
$$\Delta_{\text{max}} := T \cdot (0.05 + 0.45 \cdot f_{\text{depth}} \cdot f_{\text{width}}) = 0.29$$

Estimated displacement (meters) required to mobilize full passive pressure

$$\text{disp}_{\text{rel}} := \begin{pmatrix} 0 \\ \frac{\Delta_{\text{max}}}{4} \\ \Delta_{\text{max}} \\ 5 \cdot \Delta_{\text{max}} \end{pmatrix} = \begin{pmatrix} 0 \\ 0.07 \\ 0.29 \\ 1.47 \end{pmatrix} \quad \text{Force} := \begin{pmatrix} 0 \\ \frac{F_{\text{ultGroup}}}{2} \\ F_{\text{ultGroup}} \\ F_{\text{ultGroup}} \end{pmatrix} = \begin{pmatrix} 0 \\ 284 \\ 569 \\ 569 \end{pmatrix}$$

Express the load as force per unit length (in vertical direction) of the structure:

$$p_{\text{RRB}} := \frac{\text{Force}}{Z_c - D} \quad y_{\text{RRB}} := \text{disp}_{\text{rel}}$$



Section 4.2

Magnitude of Lateral Spreading Displacement

Lateral spreading index using the Zhang [2004] method as presented in Idriss and Boulanger [2008]:

$$t_{\text{layer}} := 0.01$$

Thickness of each layer for calculations is 1 cm (i.e., the CPT sampling interval.)

$$\Delta \text{LDI}_i := \gamma_{\text{max}} t_{\text{layer}} = 0.00401$$

This is the predicted lateral spreading index (LDI) for the 1-cm-thick layer at a depth of 3 m. This computation is repeated at each CPT sampling interval from the "bottom up" to generate a profile of cumulative LDI versus depth. LDI is then converted to an estimated lateral spreading displacement via a multiplicative factor that depends on the ground slope and the free face conditions. Refer to the main report and Zhang (2004) for more details.

Lateral spreading index using the modified Faris et al. [2006] method as presented in Caltrans lateral spreading guidelines [2013a]:

Lateral spreading is assumed to occur up to a depth of two times the free face height, about 7 m, meaning only the upper liquefied layer should be considered. For the upper liquefied layer (depth 1.5 to 6.5 m below ground surface), the average (N1)₆₀ value (using the methods presented above) is 12. Using an estimated fines content range of 15 to 20%, the fines correction factor is:

$$\text{FC}_{\text{lower}} := 15 \quad \Delta \text{N1}_{60\text{low}} := \exp \left[1.63 + \frac{9.7}{\text{FC}_{\text{lower}} + .01} - \left(\frac{15.7}{\text{FC}_{\text{lower}} + 0.01} \right)^2 \right] = 3.3$$

$$\text{FC}_{\text{upper}} := 20 \quad \Delta \text{N1}_{60\text{up}} := \exp \left[1.63 + \frac{9.7}{\text{FC}_{\text{upper}} + .01} - \left(\frac{15.7}{\text{FC}_{\text{upper}} + 0.01} \right)^2 \right] = 4.5$$

An approximate average of 4 will be used: $\Delta \text{N1}_{60\text{avg}} := 4$

$$\text{N1}_{60\text{cs}} := 12 + \Delta \text{N1}_{60\text{avg}} = 16$$

An additional correction based on fines content is recommended by Faris et al. [2004] to generate a corrected blowcount for use in estimating shear strain potential:

$$0.882 \text{N1}_{60\text{cs}} + 5 = 19 \quad \text{since this is greater than the average estimated fines content, the correction is zero}$$

$$\Delta \text{N}_{\text{FC}} := 0 \quad \rightarrow \quad \text{N1}_{60\text{cs}} := \text{N1}_{60\text{cs}} + \Delta \text{N}_{\text{FC}} = 16$$

Magnitude-corrected CSR:

$$CSR = 0.238 \quad CSR_{mc} := \frac{CSR}{MSF} = 0.22$$

Using these values of (N1)_{60cs} and magnitude-corrected CSR with Figure 3.12 from the Caltrans lateral spreading guidelines [2013a], the estimated strain potential index is about 10 - 11%. Using the equations in Appendix A of the Caltrans guidelines to get a more refined estimate:

$$\Delta n := N1_{60cs} \cdot \left[\frac{1}{\left(\frac{CSR_{mc} - 0.04}{0.56} \right)^{\frac{1}{3}}} - 1 \right] = 7.4$$

$$I_1 := 0.04 + 0.00207 N1_{60cs} = 0.073$$

$$I_2 := 0.04 + 0.0047 N1_{60cs} = 0.115$$

$$CSR_{mc} > I_2 = 1 \quad (\text{true}), \text{ therefore use: } \gamma_{maxCT} := 1.859 \left(1.1 - \sqrt{\frac{N1_{60cs} + \Delta n}{46}} \right)^3 = 0.108$$

Compute displacement potential index (DPI):

$$DPI := \gamma_{maxCT} (6.5 - 1.5) = 0.54$$

Estimate maximum displacement from DPI:

$$H_{max} := DPI^{1.07} = 0.52$$

Bent 5 is located near the river bank free face ($L/H < 4$), so the estimated displacement is amplified by a factor of 2:

$$F_{amp} := 2.0 \quad H_{max} := F_{amp} \cdot H_{max} = 1.04$$

The estimated displacement at the ground surface is about 1 m using the Caltrans [2013a] approach based on Faris et al. [2004; 2006], significantly less than the Idriss and Boulanger [2008] approach based on Zhang et al. [2004] of about 3.7 m. The difference is due primarily to the difference in shear strain predicted by the two methods. The equivalent clean sand corrected blow counts used for the Caltrans approach predict an average shear strain of about 10% for the upper liquefied layer, while the latter approach predicts an average shear strain of 37% in the layer. The equivalent SPT blowcounts used herein are based on the correlation to CPT resistance shown previously, but it should be noted the values compare relatively well to the Ferromex boring log for this layer. Ultimately the large difference between the two predictions illustrates the uncertainty in relating penetration resistance to shear strain potential and the further uncertainty in the empirical factors used to transform the computed displacement index values (DPI or LDI) to actual horizontal displacements.

Section 4.3.2 Elastomeric Bearings

Determine rotational and shear stiffness of elastomeric bearings for highway bridge.

AASHTO Approach per AASHTO LRFD Bridge Specs 6th Edition Chapter 14

$$L_b := 0.2\text{m} \quad W_b := 0.3\text{m} \quad t_{\text{bearing}} := 0.041\text{m} \quad \text{Length, width, and thickness of bearing}$$

$$A_b := L_b \cdot W_b = 0.06\text{m}^2 \quad I_{\text{bearing}} := \frac{1}{12} \cdot 0.3\text{m} \cdot (0.2\text{m})^3 = 0.0002\text{m}^4 \quad \text{Area and MOI}$$

$$G := 900000\text{Pa} \quad K_{\text{bulk}} := (2000000000)\text{Pa} \quad \text{Shear and bulk moduli}$$

$$h_{ri} := t_{\text{bearing}} = 0.041\text{m}$$

$$S_i := \frac{L_b \cdot W_b}{2 \cdot h_{ri} (L_b + W_b)} = 1.463 \quad \text{eqn. 14.7.5.1-1}$$

$$\lambda := S_i \cdot \sqrt{\frac{3G}{K_{\text{bulk}}}} = 0.054$$

$$B_a := (2.31 - 1.86\lambda) + (-0.9 + 0.96\lambda) \cdot \left[1 - \left(\min\left(\frac{W_b}{L_b}, \frac{L_b}{W_b} \right) \right) \right]^2 = 2.116 \quad \text{eqn. C14.7.5.3.3-7}$$

$$E_{\text{cAASHTO}} := 3 \cdot B_a \cdot G \cdot S_i^2 = 12233696\text{ Pa} \quad E_{\text{elastomer}} := E_{\text{cAASHTO}} = 12233696\text{ Pa}$$

$$K_r := \frac{E_{\text{elastomer}} \cdot I_{\text{bearing}}}{t_{\text{bearing}}} = 59677\text{ J} \quad (\text{per radian})$$

$$K_{\text{shear}} := \frac{A_b \cdot G}{t_{\text{bearing}}} = 1317073 \frac{\text{kg}}{\text{s}^2} \quad 1317 \frac{\text{kN}}{\text{m}} = 1317000 \frac{\text{kg}}{\text{s}^2}$$

Each bearing has a translational (shear) stiffness of 1317 kN/m. There are 7 bearings at each of the two abutments. The total translational stiffness provided by the abutment bearings is:

$$1317(2 \cdot 7) = 18438 \quad \text{----> } 18.4\text{ MN/m}$$

Each bent of the highway bridge has four extended-shaft columns, so the "tributary restraint" of a single column is:

$$\frac{18.44}{4} = 4.61 \quad \text{-----> } 4.6\text{ MN/m}$$

Section 4.3.2

Rotational restraint derived from rotation of top of column, railroad bridge. Refer to Fig. 20 in the report for schematic derivation of equations.

$w := 1325$ weight of one deck span

$\mu := 0.2$ coefficient of friction for sliding between top of elastomeric bearing and girders

$\text{width}_{BC} := 1.7$ width of bent cap in bridge long. direction (meters)

$\theta := 1$ derive rotational stiffness for a unit rotation (one radian)

$$M_{c1} := \cos(\theta) \cdot \frac{w \cdot \text{width}_{BC}}{4} = 304 \quad \text{Rotational stiffness for mechanism one [kN*m/rad.]}$$

$$M_{c2} := \sin(\theta) \cdot \frac{\mu \cdot w \cdot \text{width}_{BC}}{4} = 95 \quad \text{Rotational stiffness for mechanism two}$$

$$M_{c\text{Total}} := M_{c1} + M_{c2} = 399 \quad \text{Total rotational restraint}$$

Appendix D: Site Profiles for Kinematic Pile-Soil Interaction Analysis

D.1 INTRODUCTION

Stratigraphy and soil properties for the six sites used for baseline pile kinematic soil-structure interaction analyses are presented in this appendix. Each of the six sites is based on cone penetration test (CPT) data, including seismic shear wave velocity measurements, obtained from the United States Geological Survey CPT database website⁸. Note that several of the $V_{s,30}$ values presented on the USGS website are incorrect based on the data that is provided, the correct values are given in the site descriptions below. Soil properties presented in Appendix D were interpreted from the CPT data in a manner consistent with routine practice following the methods of Mayne et al. (2009) and Robertson (2012), unless otherwise noted.

The stratigraphy has been slightly modified from the conditions encountered during CPT as explained below in order to avoid significant impedance contrasts that would result in a strong site response effect. Analysis were also performed with these impedance contrast left in the profiles to evaluate their influence on the pile kinematic response. Below the maximum depth of the CPT explorations, the profiles were extended such that they exceeded the maximum pile depth considered for the analyses ($L = 60$ m) and reached a shear wave velocity of 760 m/s to be consistent with the input motions. The soil properties of these additional layers were computed based on stiffness versus depth scaling relationships as described in the main text.

The following sections briefly summarize the geologic setting and stratigraphy of each site.

⁸ <http://earthquake.usgs.gov/research/cpt/>

D.2 SITE 1

Site 1 is based on USGS CPT-ALC014, located on Alameda Island near the Alameda entrance to the Posey Tube tunnel that connects Alameda to Oakland. The original profile has been modified by removing the stiff layer at a depth of 22-23 m so that there is a relatively smooth increase in stiffness with depth. Layer properties of the idealized soil profile are presented the table below. Groundwater was estimated at a depth of 1.2 m below the surface during the CPT but is considered to be at the ground surface for the idealized profile used for analyses. $V_{S,30}$ of the idealized profile presented below is 111 m/s. $V_{S,30}$ computed using the actual data is 123 m/s.

Site 1 properties for *DEEPSOIL* analysis

Layer	Material Type	Depth Top	Thickness	Unit Weight	V_s	ϕ'	OCR	K_0	Shear Strength	PI
-	-	m	m	kN/m ³	m/s	degrees	-	-	kPa	-
1	clay	0	2	16.5	90	N/A	1.5	0.54	12	15
2	clay	2	2	16.5	90	N/A	1.4	0.53	12	15
3	clay	4	2	16.5	95	N/A	1.3	0.52	15	15
4	clay	6	2	16.5	95	N/A	1.2	0.50	18	15
5	clay	8	2	16.5	100	N/A	1.1	0.49	20	15
6	clay	10	2	16.5	100	N/A	1.0	0.47	22	15
7	clay	12	2	16.5	105	N/A	1.0	0.47	25	15
8	clay	14	2	17	110	N/A	1.0	0.47	28	15
9	clay	16	2	17	115	N/A	1.0	0.47	32	15
10	clay	18	2	17	120	N/A	1.0	0.47	35	15
11	clay	20	2	17	125	N/A	1.0	0.47	39	15
12	clay	22	2	17.5	130	N/A	1.0	0.47	42	15
13	clay	24	2	17.5	140	N/A	1.0	0.47	46	15
14	clay	26	2	17.5	145	N/A	1.0	0.47	50	15
15	clay	28	2	17.5	160	N/A	1.0	0.47	53	15
16	clay	30	2	18	200	N/A	1.0	0.47	57	15
17	sand	32	2	19	220	38	1.0	0.38	201	0
18	sand	34	2	19	224	38	1.0	0.38	215	0
19	sand	36	2	19	228	38	1.0	0.38	230	0
20	sand	38	2	19	231	38	1.0	0.38	244	0
21	sand	40	2	19	234	38	1.0	0.38	258	0

Layer	Material Type	Depth Top	Thickness	Unit Weight	V_s	ϕ'	OCR	K_0	Shear Strength	PI
22	sand	42	2	19	237	38	1.0	0.38	273	0
23	sand	44	2	19	241	38	1.0	0.38	287	0
24	sand	46	2	19	244	38	1.0	0.38	302	0
25	sand	48	2	19	246	38	1.0	0.38	316	0
26	sand	50	2	19	249	38	1.0	0.38	330	0
27	sand	52	2	19	252	38	1.0	0.38	345	0
28	sand	54	2	19	254	38	1.0	0.38	359	0
29	sand	56	2	19	257	38	1.0	0.38	373	0
30	sand	58	2	19	259	38	1.0	0.38	388	0
31	sand	60	2	19	262	38	1.0	0.38	402	0
32	sand	62	2	19	264	38	1.0	0.38	416	0
33	sand	64	2	19	266	38	1.0	0.38	431	0
34	sand	66	1	19	300	38	1.0	0.38	434	0
35	sand	67	1	19	350	38	1.0	0.38	441	0
36	sand	68	1	19	400	38	1.0	0.38	448	0
37	sand	69	1	19	450	38	1.0	0.38	456	0
38	sand	70	1	19	500	38	1.0	0.38	463	0
39	sand	71	1	19	550	38	1.0	0.38	470	0
40	sand	72	1	19	600	38	1.0	0.38	477	0
41	sand	73	1	19	650	38	1.0	0.38	484	0
42	sand	74	1	19	700	38	1.0	0.38	492	0
43	sand	75	1	19	760	38	1.0	0.38	499	0

D.3 SITE 2

Site 2 is based on USGS CPT-SCC069, which is located on the southern margin of the San Francisco Bay near San Jose. The surficial materials are classified as fine-grained Holocene alluvial fan and overbank flood deposits. Deeper layers may be marine sediments. Groundwater is at a depth of 2 m. $V_{s,30}$ of the idealized profile presented below is 192 m/s. $V_{s,30}$ computed using the actual data is 172 m/s. The difference is a results of modifications made to the upper 14 m of the idealized profile to remove stiff layers overlying soft layers. The “stiff over soft” condition is

considered in Site “2a” as described in the main text, which is closer to the conditions measured in the field.

Site 2 properties for *DEEPSOIL* analysis

Layer	Material Type	Depth Top	Thickness	Unit Weight	Vs	Friction Angle	OCR	K ₀	Shear Strength	PI
-	-	m	m	kN/m ³	m/s	degrees	-	-	kPa	-
1	clay	0	2	17	120	N/A	7.4	0.73	37	15
2	clay	2	1.5	17	130	N/A	5.3	0.60	44	15
3	clay	3.5	5.5	17	145	N/A	3.1	0.44	61	30
4	clay	9	3.5	17	165	N/A	3.4	0.45	73	15
5	clay	12.5	1.5	17	190	N/A	4.0	0.49	86	15
6	clay	14	2	18	206	N/A	3.9	0.48	96	15
7	clay	16	1.5	18	222	N/A	3.6	0.46	96	10
8	sand	17.5	1.5	18	251	37	3.4	0.40	127	0
9	clay	19	2.5	18	273	N/A	2.8	0.40	96	20
10	clay	21.5	2.5	18	276	N/A	2.6	0.38	101	15
11	clay	24	2	18	285	N/A	2.7	0.39	110	15
12	clay	26	2	18	302	N/A	3.4	0.43	143	15
13	clay	28	2	18	306	N/A	4.4	0.48	188	15
14	clay	30	2	18	315	N/A	4.3	0.47	197	15
15	clay	32	2	18	318	N/A	4.1	0.46	201	15
16	clay	34	2	18	321	N/A	4.0	0.45	205	15
17	clay	36	2	18	324	N/A	3.8	0.44	210	15
18	clay	38	2	18	328	N/A	3.7	0.43	214	15
19	clay	40	2	18	331	N/A	3.6	0.42	218	15
20	clay	42	2	18	334	N/A	3.4	0.42	223	15
21	clay	44	2	18	337	N/A	3.3	0.41	227	15
22	clay	46	2	18	340	N/A	3.3	0.40	231	15
23	clay	48	2	18	343	N/A	3.2	0.40	235	15
24	clay	50	2	18	346	N/A	3.1	0.39	239	15
25	clay	52	2	18	349	N/A	3.0	0.38	243	15
26	clay	54	2	19	343	N/A	2.9	0.38	248	15
27	clay	56	2	19	346	N/A	2.9	0.37	252	15
28	clay	58	2	19	349	N/A	2.8	0.37	257	15
29	clay	60	2	19	352	N/A	2.7	0.36	261	15
30	clay	62	2	19	355	N/A	2.7	0.36	266	15
31	sand	64	2	19	400	38	2.6	0.38	444	0
32	sand	66	2	19	450	38	2.6	0.38	458	0

Layer	Material Type	Depth Top	Thickness	Unit Weight	Vs	Friction Angle	OCR	K ₀	Shear Strength	PI
33	sand	68	2	19	500	38	2.5	0.38	472	0
34	sand	70	2	19	550	38	2.5	0.38	487	0
35	sand	72	2	19	600	38	2.4	0.38	501	0
36	sand	74	2	19	650	38	2.4	0.38	516	0
37	sand	76	2	19	700	38	2.4	0.38	530	0
38	sand	78	2	19	760	38	2.3	0.38	544	0

D.4 SITE 3

Site 3 is based off USGS CPT-MSC019, performed in point bar deposits in the Mississippi River Valley. Groundwater is at a depth of 4 m. $V_{s,30}$ of the idealized profile presented below is 208 m/s.

$V_{s,30}$ computed using the actual data is 217 m/s.

Site 3 properties for *DEEPSOIL* analysis

Layer	Material Type	Depth Top	Thickness	Unit Weight	Vs	Friction Angle	OCR	K ₀	Shear Strength	PI
-	-	m	m	kN/m ³	m/s	degrees	-	-	kPa	-
1	sand	0	3	17	150	34	N/A	0.44	34	0
2	sand	3	3	17	160	34	N/A	0.44	65	0
3	sand	6	2	17	170	34	N/A	0.44	72	0
4	sand	8	3	17	185	36	N/A	0.41	98	0
5	sand	11	2	17	205	40	N/A	0.36	118	0
6	sand	13	1	17	220	39	N/A	0.37	118	0
7	sand	14	2	18	235	40	N/A	0.35	141	0
8	sand	16	2	18	225	42	N/A	0.33	164	0
9	sand	18	2	18	233	42	N/A	0.32	182	0
10	sand	20	2	18	240	42	N/A	0.32	197	0
11	sand	22	2	18	280	42	N/A	0.33	209	0
12	sand	24	2	18	265	42	N/A	0.33	222	0
13	sand	26	2	18	285	42	N/A	0.34	235	0
14	sand	28	2	18	290	42	N/A	0.33	251	0
15	sand	30	2	19	295	42	N/A	0.33	269	0
16	sand	32	2	19	299	42	N/A	0.33	286	0

Layer	Material Type	Depth Top	Thickness	Unit Weight	Vs	Friction Angle	OCR	K ₀	Shear Strength	PI
17	sand	34	2	19	303	42	N/A	0.33	302	0
18	sand	36	2	19	307	42	N/A	0.33	319	0
19	sand	38	2	19	311	42	N/A	0.33	336	0
20	sand	40	2	19	315	42	N/A	0.33	352	0
21	sand	42	2	19	319	42	N/A	0.33	369	0
22	sand	44	2	19	322	42	N/A	0.33	385	0
23	sand	46	2	19	326	42	N/A	0.33	402	0
24	sand	48	2	19	329	42	N/A	0.33	418	0
25	sand	50	2	19	332	42	N/A	0.33	435	0
26	sand	52	2	19	335	42	N/A	0.33	451	0
27	sand	54	2	19	338	42	N/A	0.33	468	0
28	sand	56	2	19	341	42	N/A	0.33	484	0
29	sand	58	2	19	344	42	N/A	0.33	501	0
30	sand	60	2	19	347	42	N/A	0.33	518	0
31	sand	62	2	19	350	42	N/A	0.33	534	0
32	sand	64	2	19	352	42	N/A	0.33	551	0
33	sand	66	2	19	400	42	N/A	0.33	567	0
34	sand	68	2	19	450	42	N/A	0.33	584	0
35	sand	70	2	19	500	42	N/A	0.33	600	0
36	sand	72	2	19	550	42	N/A	0.33	617	0
37	sand	74	2	19	600	42	N/A	0.33	633	0
38	sand	76	2	19	650	42	N/A	0.33	650	0
39	sand	78	2	19	700	42	N/A	0.33	667	0
40	sand	80	2	19	760	42	N/A	0.33	683	0

D.5 SITE 4

Site 4 is based off USGS CPT-CHN007, performed in Pleistocene barrier-beach ridge deposits near Charleston, South Carolina. Groundwater is estimated to be at a depth of 2.5 m. $V_{S,30}$ of the idealized profile presented below is 253 m/s. $V_{S,30}$ computed using the actual data is 261 m/s.

Site 4 properties for *DEEPSOIL* analysis

Layer	Material Type	Depth Top	Thickness	Unit Weight	Vs	Friction Angle	OCR	K ₀	Shear Strength	PI
-	-	m	m	kN/m ³	m/s	degrees	-	-	kPa	-
1	sand	0	2	17	170	35	1.0	0.43	24	0
2	sand	2	3	18	200	35	1.0	0.43	55	0
3	clay	5	1.5	17	170	N/A	3.1	0.45	44	15
4	sand	6.5	3.5	18	210	32	1.0	0.47	75	0
5	clay	10	1	18	215	N/A	3.4	0.46	68	15
6	sand	11	3	18	255	35	1.0	0.43	105	0
7	clay	14	1	18	210	N/A	2.7	0.40	73	15
8	sand	15	5	18	260	35	1.0	0.43	146	0
9	sand	20	2	18	335	32	1.0	0.47	131	0
10	sand	22	2	19	365	32	1.0	0.47	142	0
11	sand	24	2	19	380	33	1.0	0.46	158	0
12	sand	26	2	19	420	33	1.0	0.46	172	0
13	sand	28	2	19	440	34	1.0	0.44	190	0
14	sand	30	2	19	447	36	1.0	0.41	220	0
15	sand	32	2	19	453	36	1.0	0.41	233	0
16	sand	34	2	19	460	36	1.0	0.41	247	0
17	sand	36	2	19	466	36	1.0	0.41	260	0
18	sand	38	2	19	472	36	1.0	0.41	273	0
19	sand	40	2	19	477	36	1.0	0.41	287	0
20	sand	42	2	19	483	36	1.0	0.41	300	0
21	sand	44	2	19	488	36	1.0	0.41	314	0
22	sand	46	2	19	493	38	1.0	0.38	352	0
23	sand	48	2	19	498	38	1.0	0.38	366	0
24	sand	50	2	19	503	38	1.0	0.38	380	0
25	sand	52	2	19	508	38	1.0	0.38	395	0
26	sand	54	2	19	512	38	1.0	0.38	409	0
27	sand	56	2	19	517	38	1.0	0.38	423	0
28	sand	58	2	19	521	38	1.0	0.38	438	0
29	sand	60	2	19	525	38	1.0	0.38	452	0
30	sand	62	2	19	529	38	1.0	0.38	466	0
31	sand	64	2	19	533	38	1.0	0.38	481	0
32	sand	66	2	19	550	38	1.0	0.38	495	0
33	sand	68	2	19	600	38	1.0	0.38	510	0
34	sand	70	2	19	650	38	1.0	0.38	524	0
35	sand	72	2	19	700	38	1.0	0.38	538	0
36	sand	74	2	19	760	38	1.0	0.38	553	0

D.6 SITE 5

Site 5 is based on USGS CPT-ALC046, which is located in the East San Francisco Bay in Albany, about 1 km from the Bay margin. The surficial materials are classified as Holocene alluvial fan and natural levee deposits. Groundwater is at a depth of 2.1 m. The profile generally consists of 18 m of soft to medium-stiff clay overlying stiff clay. $V_{s,30}$ of the idealized profile presented below is 301 m/s. $V_{s,30}$ computed using the actual data is 305 m/s.

Site 5 properties for *DEEPSOIL* analysis

Layer	Material Type	Depth Top	Thickness	Unit Weight	Vs	Friction Angle	OCR	K ₀	Shear Strength	PI
-	-	m	m	kN/m ³	m/s	degrees	-	-	kPa	-
1	clay	0	2	17	205	N/A	48.2	1.81	166	15
2	clay	2	1	17	220	N/A	17.2	1.06	101	15
3	clay	3	2	17	250	N/A	24.4	1.22	188	15
4	clay	5	1	17	240	N/A	18.7	1.07	157	15
5	clay	6	2	18	245	N/A	54.5	1.76	485	15
6	clay	8	1.5	18	280	N/A	14.3	0.91	185	15
7	clay	9.5	2.5	18	300	N/A	17.9	1.00	277	15
8	clay	12	2.5	18	310	N/A	20.7	1.05	362	15
9	clay	14.5	3.5	18	320	N/A	6.6	0.60	178	15
10	clay	18	2	19	340	N/A	23.7	1.10	526	15
11	clay	20	3	19	360	N/A	23.1	1.07	604	15
12	clay	23	4	19	380	N/A	21.9	1.03	686	15
13	clay	27	3	19	400	N/A	22.4	1.03	759	15
14	clay	30	2	19	403	N/A	21.4	1.00	767	15
15	clay	32	2	19	406	N/A	20.2	0.97	778	15
16	clay	34	2	19	409	N/A	19.2	0.94	788	15
17	clay	36	2	19	411	N/A	18.2	0.92	799	15
18	clay	38	2	19	414	N/A	17.4	0.89	809	15
19	clay	40	2	19	416	N/A	16.6	0.87	818	15
20	clay	42	2	19	419	N/A	15.9	0.85	828	15
21	clay	44	2	19	421	N/A	15.3	0.83	837	15

Layer	Material Type	Depth Top	Thickness	Unit Weight	Vs	Friction Angle	OCR	K ₀	Shear Strength	PI
22	clay	46	2	19	423	N/A	14.7	0.81	846	15
23	clay	48	2	19	425	N/A	14.2	0.79	854	15
24	clay	50	2	19	427	N/A	13.7	0.77	863	15
25	clay	52	2	19	429	N/A	13.2	0.76	871	15
26	clay	54	2	19	432	N/A	12.8	0.74	880	15
27	clay	56	2	19	433	N/A	12.4	0.73	888	15
28	clay	58	2	19	435	N/A	12.0	0.72	896	15
29	clay	60	2	19	437	N/A	11.6	0.71	903	15
30	clay	62	2	19	439	N/A	11.3	0.69	911	15
31	clay	64	2	19	486	N/A	14.1	0.77	1117	15
32	clay	66	2	19	488	N/A	13.7	0.76	1125	15
33	clay	68	2	19	512	N/A	14.9	0.79	1238	15
34	clay	70	2	19	534	N/A	16.0	0.81	1349	15
35	clay	72	2	19	556	N/A	17.0	0.83	1458	15
36	clay	74	2	19	576	N/A	18.0	0.86	1568	15
37	clay	76	2	19	645	N/A	23	1	1963	15
38	clay	78	2	19	704	N/A	28	1.1	2344	15

D.7 SITE 6

Site 6 is based on USGS CPT-SBC109, performed in stiff granular alluvial fan deposits on the north side of the San Gabriel Mountains near Adelanto, California. Groundwater depth is assumed to be 4 m for analyses. $V_{s,30}$ of the idealized profile presented below is 446 m/s. $V_{s,30}$ computed using the actual data to a depth of 18 m and then extrapolating to 30 m is 409 m/s. The increase between the idealized and measured $V_{s,30}$ values is a result of replacing the soft layers encountered during the CPT in the upper 4 m of the profile with stiffer layers to prevent a strong impedance contrast. Site “6a” includes these softer layers as described in the main text such that their influence on the pile kinematic response can be considered.

Site 6 properties for *DEEPSOIL* analysis

Layer	Material Type	Depth Top	Thickness	Unit Weight	Vs	Friction Angle	OCR	K ₀	Shear Strength	PI
-	-	m	m	kN/m ³	m/s	degrees	-	-	kPa	-
1	sand	0	2	18	320	43	N/A	0.32	17	0
2	sand	2	2	18	340	42	N/A	0.33	48	0
3	sand	4	3	18	360	41	N/A	0.34	74	0
4	sand	7	2	18	380	41	N/A	0.34	92	0
5	sand	9	1	18	480	43	N/A	0.32	107	0
6	sand	10	2	18	490	42	N/A	0.33	118	0
7	sand	12	3	19	500	41	N/A	0.34	133	0
8	sand	15	2	19	510	43	N/A	0.32	160	0
9	sand	17	3	19	510	43	N/A	0.32	185	0
10	sand	20	10	19	510	43	N/A	0.31	242	0
11	sand	30	2	19	535	41	N/A	0.34	271	0
12	sand	32	2	19	543	41	N/A	0.34	287	0
13	sand	34	2	19	551	41	N/A	0.34	303	0
14	sand	36	2	19	558	41	N/A	0.34	319	0
15	sand	38	2	19	565	41	N/A	0.34	335	0
16	sand	40	2	19	571	41	N/A	0.34	351	0
17	sand	42	2	19	577	41	N/A	0.34	367	0
18	sand	44	2	19	584	41	N/A	0.34	383	0
19	sand	46	2	19	590	41	N/A	0.34	399	0
20	sand	48	2	19	596	41	N/A	0.34	415	0
21	sand	50	2	19	601	41	N/A	0.34	431	0
22	sand	52	2	19	606	41	N/A	0.34	447	0
23	sand	54	2	19	612	41	N/A	0.34	463	0
24	sand	56	2	19	617	41	N/A	0.34	479	0
25	sand	58	2	19	622	41	N/A	0.34	495	0
26	sand	60	2	19	627	41	N/A	0.34	511	0
27	sand	62	2	19	632	41	N/A	0.34	527	0
28	sand	64	2	19	637	41	N/A	0.34	543	0
29	sand	66	2	19	650	41	N/A	0.34	559	0
30	sand	68	2	19	700	41	N/A	0.34	575	0
31	sand	70	2	19	760	41	N/A	0.34	591	0

Appendix E: A Framework for Full-Scale Experimental Measurements of Kinematic Pile-Soil Interaction

Experimental data for validating kinematic pile-soil transfer function models is scarce, and often includes superstructure inertia, making it difficult to isolate the kinematic effects. The author is not aware of any full-scale tests in which kinematic pile-soil transfer functions have been measured experimentally and without a superstructure supported on the pile(s).

In this appendix a pilot experimental field test is briefly described. Although the results of the pilot test program do not necessarily provide a reliable means for validating the models developed in Chapter 10, the approach is documented here in hopes that similar tests will be conducted in the future on a scale that does provide a means for validation.

The basic field test setup is depicted in Figure E-1. The goal is to replicate the modeling approach used for the numerical study described in the previous chapters in which a pile is subjected to free-field excitation and the pile head and free-field ground surface responses are recorded; experimental transfer functions can then be computed from these recordings. Since most piles are built to support structures, executing an experiment like this requires either gaining access to a construction site during the brief window between completion of the piles but prior to the beginning of superstructure construction, or the costly alternative of building a sacrificial test pile solely for the purpose of the experiment.

Ideally, the vibration source should excite the free-field to a level consistent with design earthquakes, but this would be difficult from a practical point of view. A more feasible approach is to measure small-strain soil behavior by exciting the ground with a shaker such as the type commonly used for geophysical testing methods like SASW (spectral analysis of surface waves). Ambient noise from traffic or other consistent sources could also provide enough energy to mobilize a small-strain response.

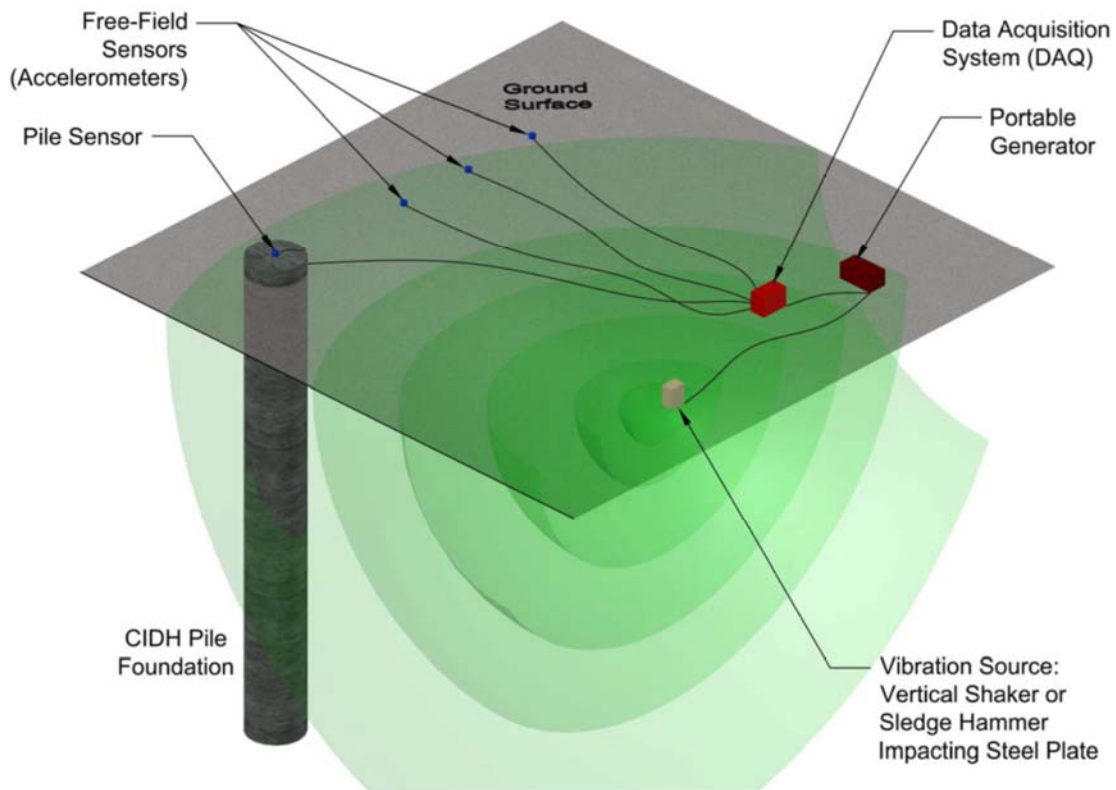


Figure E-1: Instrumentation for full-scale field measurements of kinematic pile-soil interaction.

E.1 PILOT STUDY

The pilot field study program was conducted at a Caltrans culvert construction project site in Goleta, California. A row of 16-inch diameter, $L = 60$ ft. open pipe piles with 0.625-inch wall thickness had been driven to support the culvert wall as shown in Figure E-2, and a brief window of time was available to perform the experiment prior to beginning of the wall construction.



Figure E-2: Goleta pilot study field test site.

The pile to be tested and adjacent free-field were instrumented with triaxial MEMS accelerometers⁹ housed in PVC tubing. The pile accelerometer was epoxied to the pile head, and the instrumentation end of the free-field accelerometer was buried in surficial gravel to improve coupling with the ground surface as shown in Figure E-3. The accelerometers were connected to a portable data acquisition system that interfaced with a laptop computer.

⁹ Model 4630 accelerometer manufactured by Measurement Specialties <http://meas-spec.com/>

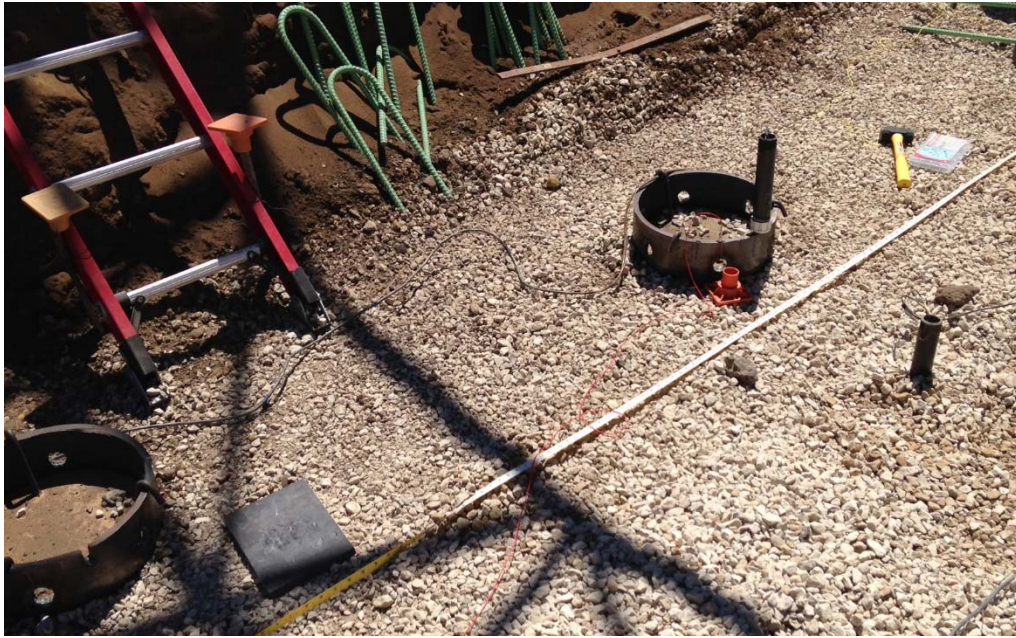


Figure E-3: Instrumentation setup.

A number of vibration sources were used in combination with various spacings between the pile and free-field sensors as well as different spacings between the pile and the vibration source. The attempted vibration sources included striking a steel plate vertically with a sledge hammer, striking adjacent piles vertically and in multiple horizontal directions relative to the orientation of a line between the test pile and the pile being struck (Figure E-4), dropping a 75-lb bag of aggregate from a ladder, and recording ambient noise from traffic and other sources. For each attempted source, a series of at least ten recordings were made, which were later stacked to improve the quality of the signals. This was necessary in part because of the relatively low quality of the MEMS accelerometers that were used.

Spacing between the pile and free-field sensors corresponded to either two pile diameters or 6 pile diameters. For the sledge-hammer-on-steel-plate and aggregate sack sources, the spacing between the vibration source and the test pile either corresponded to a “near-field” spacing of

approximately 3 pile diameters (steel plate visible in Figure E-3), or a “far-field” spacing of approximately 10 pile diameters.



Figure E-4: Striking adjacent pile to excite instrumented test pile.

E.2 RESULTS

Recorded time signals of the pile-head and free-field response were stacked and used to compute transfer functions. A lower-bound coherence cutoff of 0.8 was applied, consistent with the procedures implemented in the numerical study and by Mikami et al. (2008). The vibration sources that generated the strongest signals, and thus the most consistent trends in terms of their transfer functions, were striking the steel plate vertically and dropping the aggregate sack. Transfer functions for these sources are shown in Figure E-5. The figure also shows free-head pile elastic analytical transfer functions for vertically-propagating shear waves (derived in Chapter 8) and Rayleigh waves (after Makris 1994). The vertical S-wave analytical model significantly over-predicts the measured transfer functions, while the Rayleigh wave model appears to capture the

underlying trends. This is likely due to the fact that the vibration sources primarily produced surface waves rather than vertically-propagating shear waves.

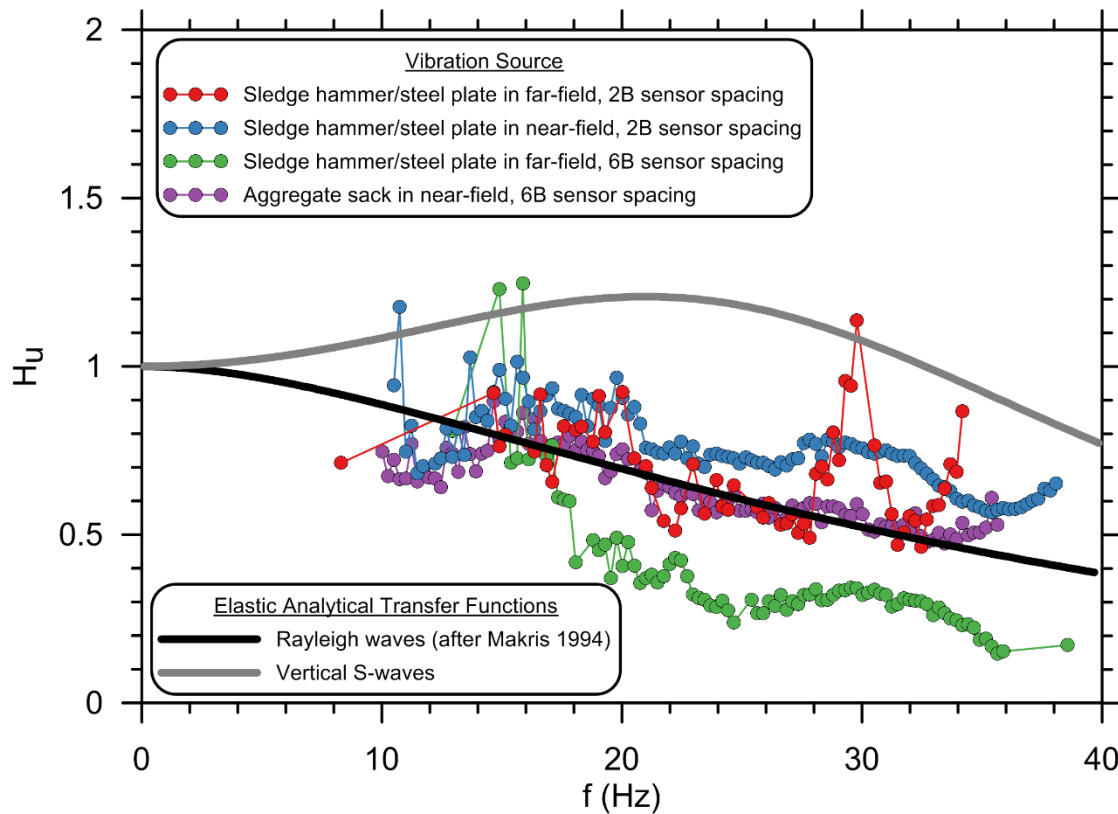


Figure E-5: Goleta pilot study experimental transfer functions.

The measured transfer functions show significant fluctuations, and only have high coherence over a relatively high- frequency range; they do not constrain the underlying trend over the lower frequency range of zero to 10 Hz that is of greater foundation engineering interest. Hence, they are not very useful for validating the models developed for this study. An experimental program in which transfer functions are measured using high-quality instrumentation that exhibit significant deamplification of the free-field motion over this lower frequency range would be extremely valuable for validation purposes.

REFERENCES FOR PART I

- AASHTO (2009). *Guide Specifications for LRFD Seismic Bridge Design*, 2nd ed., American Association of State Highway Transportation Officials, Washington D.C.
- AASHTO (2012). *LRFD Bridge Design Specifications*, 6th ed., American Association of State Highway Transportation Officials, Washington D.C.
- API (1993). *Recommended Practice for Planning, Design, and Constructing Fixed Offshore Platforms, API RP 2A-WSD*, 20th ed., American Petroleum Institute, API Publishing Services, Washington D.C.
- Ashford S.A., Boulanger R.W., Brandenberg S.J. (2011). Recommended design practice for pile foundations in laterally spreading ground, *PEER Report 2011/04*, Pacific Earthquake Engineering Research Center, University of California, Berkeley, CA, 43 pgs.
- Bolton M.D. (1986). The strength and dilatancy of sands, *Géotechnique*, 36(1): 65–78.
- Boore D.M., Stewart J.P., Seyhan E., Atkinson G.M. (2014). NGA-West 2 equations for predicting PGA, PGV, and 5%-damped PSA for shallow crustal earthquakes, *Earthquake Spectra*, 30(3), 1057-1085.
- Boulanger R.W., Brandenberg S.J. (2004). Neutral plane solution for liquefaction-induced down-drag on vertical piles. *Proceedings, Geotechnical Engineering for Transportation Projects, Geotechnical Special Publication No. 126*, M.K. Yegian and E. Kavazanjian, eds., ASCE, pp. 403–410.
- Boulanger R.W., Chang D., Brandenberg S.J., Armstrong R.J., Kutter B.L. (2007). Seismic design of pile foundations for liquefaction effects, *Proceedings, 4th Int. Conf. on Earthquake Geotechnical Engineering—Invited Lectures*, K.D. Pitilakis, ed., Springer, Netherlands, pp. 277–302.
- Bowles, JE (1996). *Foundation analysis and design*—5th edition. McGraw-Hill Book Co., New York. 1241 p.
- Brandenberg S.J. (2005). *Behavior of Pile Foundations in Liquefied and Laterally Spreading Ground*, Ph.D. thesis, Department of Civil and Environmental Engineering, University of California, Davis, CA.
- Brandenberg S.J., Bellana N., Shantz, T. (2010). Shear wave velocity as function of standard penetration test resistance and vertical effective stress at California bridge sites, *Soil Dyn. Earthq. Eng.*, 30 (10): 1026–1035.

- Brandenberg S.J., Boulanger R.W., Kutter B.L., Chang D. (2007). Liquefaction-induced softening of load transfer between pile groups and laterally spreading crusts, *J. Geotech. Geoenviron. Eng.*, ASCE, 133(1): 91–103.
- Bray, J.D., and Travasarou, T. (2007). Simplified procedure for estimating earthquake-induced deviatoric slope displacements. *J. of Geotech. and Geoenviron. Eng.*, ASCE, 130(12): 1314–1340.
- Brothers D.S., Driscoll N.W., Kent G.M., Harding A.J., Babcock J.M., Baskin R.L. (2009). Tectonic evolution of the Salton Sea inferred from seismic reflection data. *Nat. Geosci.*, 2(8): 581–584. doi:10.1038/ngeo590.
- Brown D., Turner J.P., Castelli R. (2010) Drilled shafts: construction procedures and LRFD design methods, *FHWA/NHI Publication 10-016*, Reference Manual and Participants Guide for National Highway Inst. Course 132014, 972 pgs.
- Caltrans (2013a). *Guidelines on Foundation Loading and Deformation due to Liquefaction Induced Lateral Spreading*, California Department of Transportation, Sacramento, CA, available: http://www.dot.ca.gov/research/structures/peer_lifeline_program/. Originally published 2011; revised 2013.
- Caltrans (2013b). *Seismic Design Criteria*, California Department of Transportation, Sacramento, CA, available: <http://www.dot.ca.gov/hq/esc/techpubs/manual/othermanual/other-engin-manual/seismic-design-criteria/sdc.html>.
- Cetin K.O., Seed, R.B., Der Kiureghian, A., Tokimatsu, K., Harder, L.F., Kayen, R.E., Moss, R.E. (2004). SPT-based probabilistic and deterministic assessment of seismic soil liquefaction potential. *J. Geotech. Geoenviron. Eng.*, 130(12): 1314–1340.
- Cetin K.O., Bilge H.T. (2012). Cyclic large strain and induced pore pressure models for saturated clean sands, *J. Geotech. Geoenviron. Eng.*, 138(3): 309–323.
- Chu D., Stewart J.P., Youd T.L., Chu B. (2006). Liquefaction-induced lateral spreading in near-fault regions during the 1999 Chi-Chi, Taiwan earthquake, *J. Geotech. Geoenviron. Eng.*, ASCE, 132(12): 1549–1565.
- Colin J.G. (2002). *Timber Pile Design and Construction Manual*, Timber Piling Council of the American Wood Preservers Institute, Fairfax, VA, 145 pgs.
- Davenport C., Fonseca I., Cruz P., de La Pena A. (1981). *Cerro Prieto Geothermal Field, CFE's Geophysical Studies* (Internet White Paper). Retrieved from <http://terraplus.ca/ch/recon/dave5.aspx>.

- DeJong J.T., Fritzges M.B., Nusslein K. (2006). Microbially induced cementation to control sand response to undrained shear, *J. Geotech. Geoenviron. Eng.*, ASCE, 132(11): 1381–1392.
- Dibblee T.W. (1984). Stratigraphy and tectonics of the San Felipe Hills, Borrego Badlands, Superstition Hills, and vicinity, in *The Imperial Basin; Tectonics, Sedimentation, and Thermal Aspects*, Rigsby, A.C. (ed.), Society of Economic Paleontologists and Mineralogists, Pacific Section, Los Angeles, CA, 40: 45–70.
- Dobry R., Taboada V., Liu L. (1995). Centrifuge modeling of liquefaction effects during earthquakes, *Proceedings, 1st International Conference on Earthquake Geotechnical Engineering*, K. Ishihara, ed., A.A. Balkema, Rotterdam, 3: 1291–1324.
- Dorsey R.J. (2010). Sedimentation and crustal recycling along an active oblique-rift margin: Salton Trough and northern Gulf of California, *Geology*, 38(5): 443–446, doi:10.1130/G30698.1.
- EERI (2010). The El Mayor Cucapah, Baja California earthquake, April 4, 2010, Earthquake Engineering Research Institute, J. Meneses, ed., *EERI Reconnaissance Report 2010-02*, available: <http://www.eeri.org>.
- Faris A.T. (2004). *Probabilistic Models for Engineering Assessment of Liquefaction-Induced Lateral Spreading Displacements*, Ph.D. thesis, Department of Civil and Environmental Engineering, University of California, Berkeley, CA, 436 pgs.
- Faris A.T., Seed R.B., Kayen R.E., Wu J. (2006). A semi-empirical model for the estimation of maximum horizontal displacement due to liquefaction-induced lateral spreading, *Proceedings, 8th National Conference on Earthquake Engineering*, Earthquake Engineering Research Institute, San Francisco, CA.
- Fellenius B.H. (1972). Downdrag on long piles in clay due to negative skin friction, *Can. Geotech. J.*, 9(4): 323–337.
- GEER (2010). Preliminary report on seismological and geotechnical engineering aspects of the April 4 2010 Mw 7.2 El Mayor-Cucapah (Mexico) earthquake, Geotechnical Extreme Event Reconnaissance, J.P. Stewart and S.J. Brandenberg, eds., *Report No. GEER-023*, available: [http://www.geerassociation.org/GEER_Post%20EQ%](http://www.geerassociation.org/GEER_Post%20EQ%20Report%2004%202010)
- Hauksson E., Stock J., Hutton K., Yang W., Vidal-Villegas J., Kanamori H. (2011). The 2010 M 7.2 El Mayor-Cucapah earthquake sequence, Baja California, Mexico and Southernmost California, USA: active seismotectonics along the Mexican Pacific Margin, *Pure Appl. Geophys.*, 168(8/9), 1255–1277, doi:10.1007/s00024-010-0209-7.
- Hogenstad E., Hanson N.W., McHenry D. (1955). Concrete stress distribution in ultimate strength design, *J. Am. Concr. Inst.*, 25(4): 455–479.

- Hough S.E.; Elliot A. (2004). Revisiting the 23 February 1892 Laguna Salada earthquake, *Bull. Seismol. Soc. Am.*, 94(4): 1571–1578.
- Idriss I.M., Boulanger R.W. (2006). Semi-empirical procedures for evaluating liquefaction potential during earthquakes, *J. Soil Dyn. Earthq. Eng.*, 26(2–4): 115–130.
- Idriss I.M., Boulanger R.W. (2008). *Soil Liquefaction during Earthquakes*, Monograph MNO-12, Earthquake Engineering Research Institute, Oakland, CA.
- Ishihara K., Yoshimine M. (1992). Evaluation of settlements in sand deposits following liquefaction during earthquakes, *Soils Found.*, 32(1): 173–188.
- Jaky J. (1948). Pressure in silos, *Proceedings, 2nd International Conference on Soil Mechanics and Foundation Engineering*, Balkema, Rotterdam, 1: 103–107.
- Kato, K., Gonzales, D., Ledezma, C., and Ashford, S. (2014). Analysis of pile foundations affected by liquefaction and lateral spreading with pinning effect during the 2010 Maule Chile Earthquake. Proc. 10th National Conference on Earthquake Engineering, Earthquake Engineering Research Institute, Anchorage, AK.
- Kramer S. (2013). *Personal communication*.
- Kwak D.Y., Stewart J.P., Brandenburg S.J., and Mikami A. (2016). Characterization of seismic levee fragility using field performance data. *Earthquake Spectra*, 32(1), 193–215.
- Kulhawy F.H., Mayne P.W. (1990). *Manual on Estimating Soil Properties, Report EL-6800*, Electric Power Research Institute, Palo Alto, CA.
- Lysmer J. (1970). Lumped mass method for Rayleigh waves, *Bull. Seismol. Soc. Am.*, 60(1): 89–104.
- Marcuson W.F., Hynes M.E., Franklin A.G. (1990). Evaluation and use of residual strength in seismic safety analysis of embankments, *Earthq. Spectra*, 6(3): 529–572.
- Martin G.R., Marsh L.M., Anderson D.G., Mayes R.L., Power M.S. (2002). Recommended design approach for liquefaction induced lateral spreads, *Proceedings, 3rd National Seismic Conference and Workshop on Bridges and Highways*, Portland, OR.
- McCrink T.P., Pridmore C.L., Tinsley J.C., Sickler R.R., Brandenburg, S.J., Stewart J.P. (2011). Liquefaction and other ground failures in Imperial County, California, from the April 4, 2010, El Mayor–Cucapah earthquake, *U.S. Geological Survey Open-File Report 2011–1071 and California Geological Survey Special Report 220*, 94 pgs. pamphlet, 1 pl., scale 1:51,440, available: <http://pubs.usgs.gov/of/2011/1071/>.
- MCEER/ATC-49 (2003). “Recommended LRFD guidelines for the seismic design of highway bridges.” Multidisciplinary Center for Earthquake Engineering Research, Report No. MCEER-03-SP03.

- McGann, C. and Arduino, P. (2014). Numerical assessment of three-dimensional foundation pinning effects during lateral spreading at the Mataquito River Bridge. *J. Geotech. Geoenviron. Eng.*, ASCE, 140(8), 10 p.
- McKenna F.T. (1997). *Object-Oriented Finite Element Programming: Frameworks for Analysis, Algorithms and Parallel Computing*, Ph.D. thesis, Department of Civil and Environment Engineering, University of California, Berkeley, CA.
- McKenna F.T., Scott, M.H., and Fenves, G.L. (2010). Nonlinear finite-element analysis software architecture using object composition. *J. of Computing in Civil Eng.*, ASCE, 24(1): 95-107.
- Merriam R., Bandy O.L. (1965). Source of upper Cenozoic sediments in Colorado Delta region, *J. Sediment. Res.*, 35(4): 911–916. doi:10.1306/74D713A2-2B21-11D7-8648000102C1865D.
- Mosher R.L. (1984). *Load Transfer Criteria for Numerical Analysis of Axial Loaded Piles in Sand*, U.S. Army Engineering and Waterways Experimental Station, Automatic Data Processing Center, Vicksburg, Miss.
- Olson, S. and Johnson, C. (2008). Analyzing liquefaction-induced lateral spreads using strength ratios. *J. Geotech. Geoenviron. Eng.*, ASCE, 134(8): 1035–1049.
- Ovesen N.K. (1964). Anchor slabs, calculation methods and model tests, *Bulletin No. 16*, The Danish Geotechnical Institute, Copenhagen, Denmark.
- Pacheco M., Martín-Barajas A., Elders W., Espinosa-Cardena J.M., Helenes J., Segura, A. (2006). Estratigrafía y estructura de la cuenca de Altar del NW de Sonora: implicaciones para la historia del delta del Río Colorado y de la cuenca Salton, *Revista mexicana de ciencias geológicas*, 23(1): 1–22.
- PEER (2013). *NGA-West2 database flatfile*, Pacific Earthquake Engineering Research Center, available: <http://peer.berkeley.edu/ngawest2/databases/>. Last accessed 20 November 2013.
- Reese L.C., Wang S.T., Isenhower W.M., Arrelaga J.A., Hendrix J.A. (2005). *LPILE plus version 5.0*. Ensoft, Inc., Austin, TX.
- Robertson P.K., Wride C.E. (1998). Evaluating cyclic liquefaction potential using the cone penetration test, *Can. Geotech. J.*, 35(3): 442–459.
- Robinson P.K., Bradley B.A., Cubrinovski M. (2012). Analysis of liquefaction-induced lateral spreading data from the 2010 Darfield and 2011 Christchurch earthquakes, *Proceedings, NZSEE Annual Technical Conference & AGM*, Christchurch, New Zealand.

- Robertson P.K. (2010). Evaluation of flow liquefaction and liquefied strength using the cone penetration test, *J. Geotech. Geoenviron. Eng.*, ASCE, 136(6): 842–853.
- Robertson P.K. (2012). Interpretation of in-situ tests—some insights, *Proceedings, 4th International Conference on Geotechnical and Geophysical Site Characterization (ISC-4)*, R.Q. Coutinho and P.W. Mayne, eds., Pernambuco, Brazil, 22 pgs.
- Rocscience, 2013. Phase2. Version 8.016, Rocscience Inc., Toronto, Can.
- Rodriguez-Marek A., Montalva G.A., Cotton F., Bonilla F. (2011). Analysis of single-station standard deviation using the KiK-net data, *Bull. Seismol. Soc. Am.*, 101: 1242–1258.
- Salgado R. (2006). *The Engineering of Foundations*, McGraw-Hill, New York. 882 pgs.
- SCT (2013). *Personal communication*, Secretaría de Comunicaciones y Transportes.
- TRC Software (2011). *XTRACT cross section analysis program for structural engineers*, Rancho Cordova, California. <http://www.imbsen.com/software-XTRACT.html>.
- Turner, B, Brandenburg, SJ, and Stewart, JP, 2014. Evaluation of collapse and non-collapse of parallel bridges affected by liquefaction and lateral spreading. PEER report 2014/10, Pacific Earthquake Engineering Research Center, University of California, Berkeley. 94 p.
- Turner, BJ, and Brandenburg, SJ (2015). Pile pinning and interaction of adjacent foundations during lateral spreading. *DFI Journal – The Journal of the Deep Foundation Institute*, 9(2), 92-102.
- Turner, B., Brandenburg, S., and Stewart, J. (2016). Case study of parallel bridges affected by liquefaction and lateral spreading. *J. Geotech. Geoenviron. Eng.*, DOI: [http://dx.doi.org/10.1061/\(ASCE\)GT.1943-5606.0001480](http://dx.doi.org/10.1061/(ASCE)GT.1943-5606.0001480).
- USGS (2010). *Magnitude 7.2 Baja California, Mexico, earthquake information*, U.S. Geological Survey, available: <http://earthquake.usgs.gov/earthquakes/eqinthenews/2010/ci14607652/> Last accessed 20 November 2013.
- USGS (2014). *ShakeMap Background*, U.S. Geological Survey available: <http://earthquake.usgs.gov/research/shakemap/> Last accessed March 10, 2014.
- Vijayvergiya V.N. (1977). Load-movement characteristics of piles, *Proceedings, Ports '77: 4th Annual Symposium of the Waterway, Port, Coastal, and Ocean Division*, Long Beach, CA, pp. 269–284.

- Wang R., Brandenburg S.J. (2013). "Beam on nonlinear Winkler foundation and modified neutral plane solution for calculating downdrag settlement." *J. Geotech. Geoenviron. Eng.*, 139(9), 1433-1442.
- Wei S., Fielding E., Leprince S., Sladen A., Avouac J.P., Helmberger D., Briggs R. (2011). Superficial simplicity of the 2010 El Mayor-Cucapah earthquake of Baja California in Mexico, *Nat. Geosci.*, 4(9): 615–618. doi:10.1038/ngeo1213.
- Yang Z. and Jeremić B. (2002). Numerical analysis of pile behavior under lateral loads in layered elastic–plastic soils, *Int. J. Numer. Anal. Geomech.*, 2: 1–31.
- Youd T.L., Hansen C.M., Bartlett S.F. (2002). Revised multi-linear regression equations for prediction of lateral spread displacement, *J. Geotech. Geoenviron. Eng.*, ASCE, 128(12): 1007–1017.
- Zhang G., Robertson P.K., Brachman R.W.I. (2002). Estimating liquefaction induced ground settlements from CPT for level ground. *Can. Geotech. J.*, 39: 1168–1180.
- Zhang G., Robertson, P.K., Brachman R.W.I. (2004). Estimating liquefaction-induced lateral displacements using the standard penetration test or cone penetration test, *J. Geotech. Geoenviron. Eng.*, ASCE, 130(8): 861–871.

REFERENCES FOR PART II

- AASHTO (2009). *Guide Specifications for LRFD Seismic Bridge Design*, 2nd ed., American Association of State Highway Transportation Officials, Washington D.C.
- Abrahamson, NA and Youngs, RR (1992). A stable algorithm for regression analyses using the random effects model. *Bulletin of the Seismological Society of America*, 82: 505–510.
- Ambardar, Ashok (1999). *Analog and digital signal processing*, 2nd ed. Brooks/Cole Publishing, Pacific Grove, CA. 807 p.
- American Petroleum Institute (API) (1993). *Recommended practice for planning, design, and constructing fixed offshore platforms*, API RP 2A-WSD, 20th Ed., API Publishing Services, Washington DC.
- Ancheta, TD (2010). *Engineering characterization of spatially variable earthquake ground motions*. PhD thesis, Department of Civil and Environmental Engineering, University of California at Los Angeles.
- Ancheta, TD, and Stewart, JP (2015). Conditional simulation of spatially variable motions on 2D grid. *Proc. 12th International Conference on Applications of Statistics and Probability in Civil Engineering ICASP12*, Vancouver, Canada, July 12-15, 2015.
- Angelides, DC, and Roesset, JM (1981). Nonlinear lateral dynamic stiffness of piles. *Journal of the Geotechnical Engineering Division, ASCE*, 107(11), 1443-1460.
- Anoyatis, G., Di Laora, R., Mandolini, A., and Mylonakis, G. (2013). Kinematic response of single piles for different boundary conditions: analytical solutions and normalization schemes. *Soil Dynamics & Earthquake Engineering*, 44, 183-195.
- ASCE. (2013). *Minimum design loads for buildings and other structures*. ASCE 7-10, Reston, VA.
- Ashford, SA, and Juirnarongrit, T. (2003). Evaluation of pile diameter effect on initial modulus of subgrade reaction. *Journal of Geotechnical and Geoenvironmental Engineering*, 129(3), 234-242.
- Ashlock, JC, and Pak, RYS (2009). Experimental response of piles in sand under compound motion. *Journal of Geotechnical and Geoenvironmental Engineering*, 135(6), 799-808.
- Badoni, D., and Makris, N. (1996). Nonlinear response of single piles under lateral inertial and seismic loads. *Soil Dynamics and Earthquake Engineering*, 15, 29–43.

- Banerjee, S, Stanton, JF, and Hawkins, NM (1987). Seismic performance of precast prestressed concrete piles. *Journal of Structural Engineering*, 113(2), 381-396.
- Baker, JW, Lin, T., Shahi, SK, and Jayaram, N. (2011). *New ground motion selection procedures and selected motions for the PEER Transportation Research Program*. PEER Technical Report 2011/03. 106p.
- Bentley, KJ, and El Naggar, MH (2000). Dynamic analysis for laterally loaded piles and dynamic p-y curves. *Canadian Geotechnical Journal*, 37, 1166–1183.
- Berger, E., Mahin, SA, and Pyke, R. (1977). Simplified method for evaluating soil-pile structure interaction effects. *Proceedings of the 9th Offshore Technology Conference*, OTC Paper 2954, Houston, Tex., pp. 589-598.
- Blaney, GW, Kausel, E., and Roesset, JM (1976). Dynamic stiffness of piles. *Proceedings, Numerical Methods in Geomechanics, Vol. II*, Ed. CS Desai, pp. 1001-1012.
- Blaney, GW, and O'Neill, MW (1986). Measured lateral response of mass on single pile in clay. *Journal of Geotechnical Engineering*, 112(4), 443-457.
- Bolton, MD (1986). The strength and dilatancy of sands. *Geotechnique*, 36(1), 65-78.
- Boore, DM, and Atkinson, G. (2008). Ground-motion prediction equations for the average horizontal component of PGA, PGV, and 5%-damped PSA at spectral periods between 0.01 s and 10.0 s. *Earthquake Spectra*, 24, 99-138.
- Boulanger, RW, Curras, CJ, Kutter, BL, Wilson, DW, and Abghari, A. (1999). Seismic soil-pile structure interaction experiments and analyses. *J. Geotechnical and Geoenvironmental Engineering*, 125(9), 750-759.
- Boulanger, RW, Kutter, BL, Brandenburg, SJ, Singh, P., and Chang, D. (2003). *Pile foundations in liquefied and laterally spreading ground during earthquakes: Centrifuge experiments and analyses*. Report No. Univ. of California Davis (UCD)/Center for Geotechnical Modeling (CGM)-03/01, Dept. of Civil Engineering, Univ. of California, Davis, CA.
- Bowles, JE (1997). *Foundation Analysis and Design, Fifth Edition*. McGraw-Hill, New York.
- Box, GEP, and Cox, DR (1964). An analysis of transformations. *Journal of the Royal Statistical Society, Series B*(26), 211-252.
- Bray, JD, Espinoza, RD, Soga, K., and Taylor, RL (1995). *GeoFEAP—Geotechnical finite element analysis program*. Dept. of Civ. and Envir. Engrg., University of California, Berkeley, Calif.

- Brown, D., Turner, JP, and Castelli, R. (2010) Drilled shafts: construction procedures and LRFD design methods, *FHWA/NHI Publication 10-016*, Reference Manual and Participants Guide for National Highway Inst. Course 132014, 972 p.
- Burr, JP, Pender, MJ, and Larkin, TJ (1997). Dynamic response of laterally excited pile groups. *Journal of Geotechnical and Geoenvironmental Engineering*, 123(1), 1–8.
- Caltrans—California Department of Transportation (2016). Construction plans for Linden Street Overcrossing (Replacement). Plans approval date 12-7-15. Last accessed 9 March 2016. Available: http://www.dot.ca.gov/hq/esc/oe/project_ads_addenda/05/05-4482U4/plans/
- Carter, DP (1984). *A non-linear soil model for predicting lateral pile response*. Report No. 359, Civil Engineering Dept., Univ. of Auckland, New Zealand.
- Chau, KT, and Yang, X (2005). Nonlinear interaction of soil-pile in horizontal vibration. *Journal of Engineering Mechanics*, 131(8), 847-858.
- Choi, JI, Kim, MM, and Brandenburg, SJ (2015). Cyclic p - y plasticity model applied to pile foundations in sand. *Journal of Geotechnical and Geoenvironmental Engineering*, 141(5), 04015013.
- Chopra, AK (2007). *Dynamics of structures, theory and applications to earthquake engineering*, third edition, Prentice Hall, Upper Saddle River, NJ.
- Dafalias, YF (1986). Bounding surface plasticity. I: Mathematical foundation and hypoplasticity, *Journal of Engineering Mechanics*, 112(9), 966-987.
- Darendeli, M. (2001). *Development of a new family of normalized modulus reduction and material damping curves*, Ph.D. thesis, Univ. of Texas, Austin, TX.
- Di Laora, R., and Sanctis, L. (2013). Piles-induced filtering effect on the foundation input motion. *Soil Dynamics and Earthquake Engineering*, 46, 52-63.
- Di Laora, R., and Rovithis, E. (2014). Kinematic bending of fixed-head piles in nonhomogeneous soil. *Journal of Geotechnical and Geoenvironmental Engineering*, 141(4), 04014126-1-10.
- Dobry, RM, O'Rourke, MJ, and Roesset, JM (1982). Horizontal stiffness and damping of single piles. *Journal of the Geotechnical Division, ASCE*, 108(GT3), pp. 439-459.
- Durante, MG, Di Sarno, L, Mylonakis, G., Taylor, CA, and Simonelli, AL (2015). Soil-pile-structure interaction: experimental outcomes from shaking table tests. *Earthquake Engineering and Structural Dynamics*, in-press, doi: 10.1002/eqe.2694.
- El-Marsafawi, H., Han, YC, and Novak, M. (1992). Dynamic experiments on two pile groups. *Journal of Geotechnical Engineering*, 118(4), 576–592.

- Elsabee, F., and Morray, JP (1977). *Dynamic behavior of embedded foundation*. Massachusetts Institute of Technology Research Publication No. R77-33, 55 pp.
- Fan, K., Gazetas, G., Kaynia, A., and Kausal, E., (1991). Kinematic seismic response of single piles and pile groups. *Journal of Geotechnical Engineering*, Vol. 117, No. 12, pp. 1860-1879.
- Flores-Berrones, R. (1974). *Response of pile foundations to earthquake loading*. Ph.D. thesis, National University of Mexico, 1974.
- Flores-Berrones, R., and Whitman, RV (1982) Seismic response of end-bearing piles. *Journal of the Geotechnical Engineering Division*, Vol. 108, No. 4, pp. 554-569.
- Gaul, RD (1958). Model study of a dynamically laterally loaded pile. *Journal of Soil Mechanics and Foundations Division, ASCE*, 84(SM-1), 1-32.
- Gazetas, G. (1983). Analysis of machine foundation vibrations: state of the art. *Soil Dynamics and Earthquake Engineering*, 2(1), 2-42.
- Gazetas, G. (1984). Seismic response of end-bearing single piles. *Soil Dynamics and Earthquake Engineering*, 3(2), 82-93.
- Gazetas, G. (1991). Foundation vibrations, in *Foundation Engineering Handbook*, H. Y. Fang, ed., Van Nostrand Reinholds, 553-593.
- Gazetas, G., and Dobry, R. (1984a). Horizontal response of piles in layered soils. *Journal of Geotechnical Engineering*, 110(1), 20-40.
- Gazetas, G., and Dobry, R. (1984b). Simple radiation damping model for piles and footings. *Journal of Engineering Mechanics*, 110(6), 937-956.
- Giannakou, A., Gerolymos, N., Gazetas, G., Tazoh, T., and Anastasopoulos, I. (2010). Seismic behavior of batter piles: elastic response. *Journal of Geotechnical and Geoenvironmental Engineering*, 136(9), 1187-1189.
- Givens, MJ, Atsushi, M., Toshihide, K, and Stewart, JP (2012). Kinematic soil-structure interaction effects from building and free-field seismic arrays in Japan. *Proc. 9th International Conference on Urban Earthquake Engineering/4th Asia Conference on Earthquake Engineering*, Center for Urban Earthquake Engineering, Tokyo Inst. Of Technology, Tokyo, Japan. 11 p.
- Han, Y., and Novak, M. (1988). Dynamic behavior of single piles under strong harmonic excitation. *Canadian Geotechnical Journal*, 25, 523-534.

- Hardin, BO, and Drnevich, VP (1972). Shear modulus and damping in soils: Measurements and parameter effects. *Journal of Soil Mechanics, ASCE Foundation Division*, 98(SM6), 603-624.
- Hashash, YMA, Musgrove, MI, Harmon, JA, Groholski, DR, Phillips, CA, and Park, D. (2015) *DEEPSOIL 6.1, User Manual*. Urbana, IL, Board of Trustees of University of Illinois at Urbana-Champaign.
- Hetenyi, M. (1946). *Beams on elastic foundation*. University of Michigan Press, Ann Arbor Michigan.
- Hussein, MN, Karray, M., Tobita, T. and Iai, S (2014). Effects of non-linear soil-structure interaction on dynamic characteristics of structures supported on piles. *Proc. GeoRegina 2014*, 67th Canadian Geotechnical Conference, Saskatchewan, Canada.
- Jaky, J., (1948). Pressure in silos, *Proc. 2nd Int. Conf. on Soil Mechanics and Foundation Eng.*, Rotterdam, Vol. 1, 103-107.
- Kachadoorian, R. (1968). *Effects of the earthquake of March 27, 1964, on the Alaska highway system*. United States Geological Survey Professional Paper 545-C, United States Department of the Interior, Washington, D.C., 74 pp.
- Kagawa, T., and Kraft, LM (1980). Seismic *p-y* response of flexible piles. *Journal of the Soil Mechanics and Foundation Division*, 98(SM6), 603-624.
- Kagawa, T, and Kraft, LM (1981). Lateral pile response during earthquakes. *Journal of the Geotechnical Engineering Division, ASCE*, 107(GT12), 1713-1731.
- Kampitsis, AE, Sapountzakis, EJ, Giannakos, SK, and Geolymos, NA (2013). Seismic soil-pile-structure kinematic and inertial interaction—A new beam approach. *Soil Dynamics and Earthquake Engineering*, 55, 211-224.
- Kausel, E. (2010). Early history of soil-structure interaction. *Soil Dynamics and Earthquake Engineering*, 30(9), 822-832.
- Kavvadas, M., and Gazetas, G. (1993). Kinematic seismic response and bending of free-head piles in layered soil. *Géotechnique*, 43(2), 207-222.
- Kaynia, AM, and Kausel, E. (1982). Dynamic behavior of pile groups. *Proceedings, Second International Conference on Numerical Methods in Offshore Piling*, Austin, TX, 1-25.
- Kaynia, AM, and Kausel, E. (1991). Dynamics of piles and pile groups in layered soil media. *Soil Dynamics and Earthquake Engineering*, 10(8), 386-401.
- Kaynia, AM, and Mahzooni, S. (1996). Forces in pile foundations under seismic loading. *Journal of Engineering Mechanics*, 122(1), 46-53.

- Kaynia, AM, and Novak, M., (1992). Response of pile foundations to Rayleigh waves and to obliquely incident body waves. *Earthquake Engineering and Structural Dynamics*, 21(4), 303-318.
- Khalili-Tehrani, P., Ahlberg, E., Rha, C., Lemnitzer, A., Stewart, J., Taciroglu, E., and Wallace, J. (2014). *Nonlinear load-deflection behavior of reinforced concrete drilled piles in stiff clay*. *Journal of Geotechnical and Geoenvironmental Engineering*, 140(3), 04013022.
- Kim, S. (2001). *Calibration of simple models for seismic soil-structure interaction from field performance data*. Ph.D. dissertation, Department of Civil and Environmental Engineering, University of California Los Angeles, 252 p.
- Kim, S., and Stewart, JP, (2003) Kinematic soil-structure interaction from strong motion recordings. *Journal Geotechnical and Geoenvironmental Engineering*, Vol. 129, No. 4, pp. 323-335.
- Klar, A., and Frydman, S. (2002). Three-dimensional analysis of lateral pile response using two-dimensional explicit numerical scheme. *Journal of Geotechnical and Geoenvironmental Engineering*, 128(9), 775-784.
- Kolozvari, K., Orakcal, K., and Wallace JW (2015a). Modeling of cyclic shear-flexure interaction in reinforced concrete structural walls. I: Theory. *ASCE Journal of Structural Engineering*, 141(5), 04014135.
- Kolozvari, K., Tran, T., Orakcal, K., and Wallace, JW (2015b). Modeling of cyclic shear-flexure interaction in reinforced concrete structural walls. II: Experimental validation. *ASCE Journal of Structural Engineering*, 141(5), 04014136.
- Kuhlemeyer, RL (1979). Static and dynamic laterally loaded floating piles. *Journal of the Geotechnical Engineering Division, ASCE*, 105(2), 289–304.
- Lam, IPO (2009). Diameter effects on p-y curves. *Proc. Deep Marine Foundations—A Perspective on the Design and Construction of Deep Marine Foundations*, Deep Foundations Institute, Hawthorne, NJ, 15 pp.
- Lysmer, J., and Kuhlemeyer, RL (1969). Finite dynamic model for infinite media. *Journal of Engineering Mechanics Division, ASCE*, 95(EM4), 859-877.
- Lysmer, J., Udaka, T, Tsai, C., and Seed, HB (1975). *FLUSH—a computer program for approximate #D analysis of soil-structure interaction problems*. Report No. EERC 75-30, Earthquake Engineering Research Center, University of California, Berkeley, Calif.
- Maheshwari, BK, Truman, KZ, El Naggar, MH, and Gould, PL (2004). Three-dimensional nonlinear analysis for seismic soil-pile-structure interaction. *Soil Dynamics and Earthquake Engineering*, 24, 343-356.

- Maiorano, RMS, de Sanctis, L, Aversa, S., and Mandolini, A. (2009). Kinematic response analysis of pile foundations under seismic loading. *Canadian Geotechnical Journal*, 46, 571-584.
- Makris, N. (1994). Soil-pile interaction during the passage of Rayleigh waves: An analytical solution. *Earthquake Engineering and Structural Dynamics*, 23, 153-167.
- Makris, N., and Gazetas, G. (1992). Dynamic pile-soil-pile interaction. Part II: lateral and seismic response. *Earthquake Engineering and Structural Dynamics*, 21, 145-162.
- Makris, N., Gazetas, G., and Delis, E. (1996). Dynamic soil-pile-foundation-structure interaction: Records and predictions. *Géotechnique*, 46(1), 33-50.
- Mamoon, SM, and Banerjee, PK (1992). Time-domain analysis of dynamically loaded single piles. *Journal of Engineering Mechanics*, 118(1), 140-160.
- Manna, B., and Baidya, DK (2010). Nonlinear dynamic response of piles under horizontal excitation. *Journal of Geotechnical and Geoenvironmental Engineering*, 136(12), 1600-1609.
- Massone, LM, and Lemnitzer, A. (2012). The influence of RC nonlinearity on p-y curves for CIDH bridge piers. *DFI Journal: The Journal of the Deep Foundations Institute*, 6(1), 33-40.
- Massone, LM and Wallace, JW (2004). Load – deformation responses of slender reinforced concrete walls. *ACI Structural Journal*, 101(1), 103-113.
- Matlock, H. (1970). Correlations for design of laterally loaded piles in soft clay. *Proc. 2nd Annual Offshore Technology Conference*, Houston, TX, 577-594.
- Marshall, PW, Gates, WE, and Anagnostopoulos, S. (1977). Inelastic dynamic analysis of tubular offshore structures. *Proc. 1977 Offshore Technology Conference*, Paper No. OTC 2908, Houston, TX.
- Matasovic, N. (1993). *Seismic response of composite horizontally-layered soil deposits*. Ph.D. Thesis, University of California, Los Angeles.
- Matlock, H., Foo, SHC, and Bryant, LM (1978). Simulation of lateral pile behavior under earthquake motion. *Proc. ASCE Geotechnical Engineering Division Specialty Conference on Earthquake Engineering and Soil Dynamics, Vol. II*, Pasadena, CA, 600-619.
- Mayne, PW, Coop, MR, Springman, SM, Huang, AB, and Zornberg, JG (2009). Geomaterial behavior and testing. *Proc. 17th Int. Conf. on Soil Mechanics and Geotechnical Engineering*, M. Hamza et al., Eds., 2777-2872.

- McClelland, B., and Focht, JA (1958). Soil modulus for laterally loaded piles. *American Society of Civil Engineers Transactions*, Paper No. 2954, 1049-1086.
- McKenna, FT (1997). *Object-oriented finite element programming: frameworks for analysis, algorithms and parallel computing*, Ph.D. thesis, Dept. of Civil Engineering, Univ. of California, Berkeley, CA.
- McKenna F.T., Scott, M.H., and Fenves, G.L. (2010). Nonlinear finite-element analysis software architecture using object composition. *J. of Computing in Civil Eng.*, ASCE, 24(1): 95-107.
- McManus, KJ, and Alabaster, D. (2004). Constant force shaking of a group of four drilled shafts. *Journal of Geotechnical and Geoenvironmental Engineering*, 130(20), 123-128.
- Menq, F.Y. (2003). *Dynamic properties of sandy and gravelly soils*. Ph.D. Dissertation, Dept. of Civil Eng., Univ. of Texas, Austin.
- Mikami, A., Stewart, JP, Ostadan, F., and Crouse, CB (2006). Representation of ground motion incoherence for the analysis of kinematic soil-structure interaction. *Proc. 8th U.S. National Conference on Earthquake Engineering*, Paper No. 1071, Earthquake Engineering Research Institute, Oakland, CA.
- Mikami, A., Stewart, JP, and Kamiyama, M. (2008). Effects of time series analysis protocols on transfer functions calculated from earthquake accelerograms. *Soil Dynamics and Earthquake Engineering*, 28, 695-706.
- Mizuno, H. (1987). Pile damage during earthquake in Japan (1923-1983). *Proceedings, Dynamic Response of Pile Foundations—Experiment, Analysis and Observation*, ASCE Geotechnical Special Publication No. 11, pp. 53-78.
- Mosher, RL (1984). *Load transfer criteria for numerical analysis of axial loaded piles in sand*. U.S. Army Engineering and Waterways Experimental Station, Automatic Data Processing Center, Vicksburg, Miss.
- Mylonakis, G. (2001). Simplified model for seismic pile bending at soil layer interfaces, *Soils and Foundations*, 41(4), 47-58.
- Mylonakis, G., and Gazetas, G. (1999). Lateral vibration and internal forces of grouped piles in layered soil. *Journal of Geotechnical and Geoenvironmental Engineering*, 125(1), 16-25.
- Mylonakis, G., and Gazetas, G. (2002). Kinematic pile response to vertical p-wave seismic excitation. *Journal of Geotechnical and Geoenvironmental Engineering*, 128(10), 860-867.
- Kutner, MH, Nachtsheim, CJ, and Neter, J. (2004). *Applied Linear Statistical Models*, 5th Edition. McGraw-Hill/Irwin, 1396 p.

- Newmark, NM (1967). Problems in wave propagation in soil and rocks. *Proc. International Symposium on Wave Propagation and Dynamic Properties of Earth Materials*, University of New Mexico Press, Albuquerque, pp 7-26.
- Nikolaou, S., Mylonakis, G., Gazetas, G., and Tazoh, T. (2001). Kinematic pile bending during earthquakes: analysis and field measurements. *Géotechnique*, 51(5), 425-440.
- Nishizawa, T., Tajiri, S., and Kawamura, S. (1984). Excavation and response analysis of damaged RC piles by liquefaction. *Proceedings, Eighth World Conference on Earthquake Engineering*, San Francisco, Vol. III, July.
- NIST (2012). *Soil-structure interaction for building structures*. Report No. NIST GCR 12-917-21, National Institute of Standards and Technology, U.S. Department of Commerce, Washington D.C. Project Technical Committee: Stewart, JP (Chair), CB Crouse, T Hutchinson, B Lizundia, F Naeim, and F Ostadan. 292 p.
- Nogami, T., and Konagai, K. (1988). Time domain flexural response of dynamically loaded single piles. *Journal of Engineering Mechanics*, 114(9), 1512-1525.
- Nogami, T., Otani, J., Konagai, K., and Chen, HL (1992). Nonlinear soil-pile interaction model for dynamic lateral motion. *Journal of Geotechnical Engineering*, 118(1), 89-106.
- Novak, M. (1974). Dynamic stiffness and damping of piles. *Canadian Geotechnical Journal*, 11, 574-598.
- Novak, M., and Grigg, RF (1976). Dynamic experiments with small pile foundations. *Canadian Geotechnical Journal*, 13, 372-385.
- Novak, M., Nogami, T., and Aboul-Ella, F. (1978). Dynamic soil reactions for plane strain case. *Journal of the Engineering Mechanics Division*, ASCE, 104(EM4), 953-959.
- Novak, M., Sheta, M., El-Sharnouby, B., and El-Hignawy, L. (1983). *DYNA2, a computer program for calculation of response of rigid foundation to dynamic loads*. Systems Analysis Control and Design Activity, Faculty of Engineering Science, University of Western Ontario, London, Ont.
- Novak, M., and El Sharnouby, B. (1984). Evaluation of dynamic experiments on pile group. *Journal of Geotechnical Engineering*, 110(6), 738-756.
- Novak, M., Sheta, M., El-Hifnawy, L., El-Marsafawi, H., and Ramadan, O. (1990). *DYNA3:A computer program for calculation of foundation response to dynamic loads*. Geotechnical Research Centre, the University of Western Ontario, London.

- O'Neill, MW, and Murchison, JM (1983). *An evaluation of p-y relationships in sand*. American Petroleum Institute Report PRAC 82-41-1, University of Houston, Department of Civil Engineering Research Report No. GT-DF02-83.
- Ostadan, F, 2005. Soil-structure interaction analysis including ground motion incoherency effects. *Proc. 18th International Conference on Structural Mechanics in Reactor Technology (SMiRT 18)*, Beijing, China.
- OYO Corporation (2007). *PS logging at Tokoku Institute of Technology campus in 2007*. Unpublished report, September 2007 (in Japanese¹⁰).
- Pacific Earthquake Engineering Research (PEER) Center (2013). *NGA-West2 database flatfile*. Available: <http://peer.berkeley.edu/ngawest2/databases/>. Last accessed 20 November 2013.
- Pak, RYS, and Jennings, PC (1987). Elastodynamic response of pile under transverse excitations. *Journal of Engineering Mechanics*, 113(7), 1101–1116.
- Pandit, SM (1991). *Modal and spectrum analysis*. Wiley, New York.
- Pecker, A. (2014). Kinematic soil structure interaction for bridge piled foundations. *International Journal of Bridge Engineering*, 2(3), 15-28.
- Pender, MJ (2004). Discussion of “Evaluation of pile diameter effect on initial modulus of subgrade reaction” by Scott A. Ashford and Terrawut Juirnarongrit. *Journal of Geotechnical and Geoenvironmental Engineering*, 130(9), 981-982.
- Penzien, J. (1970). Soil-pile foundation interaction. In *Earthquake Engineering* (ed. R. L. Wiegel), Ch. 14. New York: Prentice Hall.
- Penzien, J., Scheffey, C., and Parmelee, R. (1964). Seismic analysis of bridges on long piles. *Journal of Engineering Mechanics Division, ASCE*, 90(EM3), 223-254.
- Prevost, JH, Romano, JD, Abdel-Ghaffar, AM, and Rowland, R. (1981). Dynamic response of laterally-loaded piles in centrifuge. *Proceedings, Second Specialty Conference on Dynamic Response of Structures: Experimentation, Observation, Prediction and Control*, ASCE, ed. G. Hart, Atlanta, pp. 386-400.
- Rathje, EM, Faraj, F, Russell, S, and Bray, JB (2004). Empirical relationships for frequency content parameters of earthquake ground motions. *Earthquake Spectra*, 20(1), 119-144.
- R Core Team (2015). *R: A language and environment for statistical computing*. R Foundation for Statistical Computing, Vienna, Austria. Available: <https://www.R-project.org/>.

¹⁰ Data reported in Givens et al. (2012).

- Reese, LC, Cox, WR, and Koop, FD (1974). Analysis of laterally loaded piles in sand. *Proceedings, 6th Annual Offshore Technology Conference*, Vol. 2, Paper No. OTC 2080, Houston, Texas.
- Reese, LC, Cox, WR, and Koop, FD (1975). Field testing and analysis of laterally loaded piles in stiff clay. *Proceedings, 7th Offshore Technology Conf.*, Paper No. OTC 2321, Houston, Texas, 671-690.
- Reese, LC, Isenhower, WM, and Wang, ST (2006). *Analysis and Design of Shallow and Deep Foundations*. John Wiley & Sons, Hoboken, NJ, 626 pp.
- Reese, LC, and Sullivan, WR (1980). *Documentation of computer program COM624: Parts I and II, analysis of stresses and deflections for laterally-loaded piles including generation of p-y curves*. Geotechnical Engineering Software GS80-1, Geotechnical Engineering Center, Bureau of Engineering Research, University of Texas at Austin, TX.
- Reese, LC, Wang, ST, Isenhower, WM, Arrelaga, JA, and Hendrix, JA (2005). *LPILE plus version 5.0*. Ensoft, Inc., Austin, TX.
- Reese, LC, and Welch, RC (1975). Lateral loading of deep foundation in stiff clay. *Journal of the Geotechnical Engineering Division, ASCE*, 101(7), 633-649.
- Ridders, C. (1979). A new algorithm for computing a single root of a real continuous function. *IEEE Transactions on Circuits and Systems*, 26, 979-980.
- Robertson, PK (2012). Interpretation of in-situ tests—some insights, *Proc. of 4th International Conf. on Geotechnical and Geophysical Site Characterization (ISC-4)*, Pernambuco, Brazil, September 18-21, R.Q. Coutinho and P.W. Mayne, eds. 22 p.
- Rocscience, 2013. Phase2. Version 8.016, Rocscience Inc., Toronto, Can.
- Roesset, J. M., (1980a). Stiffness and damping coefficients of foundations. *Special Technical Publication on Dynamic Response of Pile Foundations: Analytical Aspects*, ASCE, O'Neill and Dobry, eds.
- Roesset, JM (1980b). The use of simple models in soil-structure interaction, *Proc. ASCE Specialty Conference on Civil Engineering and Nuclear Power*, Knoxville, TN, Vol. 2, 25 p.
- Roesset, JM (1994). Foreword in *Foundation vibration analysis using simple physical models* by Wolf, JP. PTR Prentice Hall, Upper Saddle River, NJ.
- Roesset, JM, Whitman, RV, and Dobry, R. (1973). Modal analysis for structures with foundation interaction. *Journal of the ASCE Structural Division*, 99(3), 399-416.

- Rovithis, EN, Pitilakis, KD, and Mylonakis, GE (2009). Seismic analysis of couple soil-pile-structure systems leading to the definition of a *pseudo*-natural SSI frequency. *Soil Dynamics and Earthquake Engineering*, 29, 1005-1015.
- Saitoh, M. Fixed-head pile bending by kinematic interaction and criteria for its minimization at optimal pile radius. *Journal of Geotechnical and Geoenvironmental Engineering*, 131(10), 1243-1251.
- Schnabel, PB, Lysmer, J., and Seed, HB (1972). *SHAKE: A computer program for earthquake response analysis of horizontally layered site*. Report no. UCB/EERC-72/12, Earthquake Engineering Research Center, Univ. of Calif., Berkeley, California, 102 pp.
- Scott, M. and Fenves, G. (2010). Krylov subspace accelerated Newton algorithm: Application to dynamic progressive collapse simulation of frames. *Journal of Structural Engineering*, 136(5), 473-480.
- Seed, HB, and Idriss, IM (1969). Influence of soil conditions on ground motion during earthquakes. *Journal of the Soil Mechanics and Foundations Division, ASCE*, 95, 99-137.
- Sen, R, Davies, TG, and Banerjee, PK (1985). Dynamic analysis of piles and pile groups embedded in homogeneous soils. *Earthquake Engineering and Structural Dynamic*, 13(1), 53-65.
- Sica, S., Mylonakis, G., and Simonelli, AL. (2013). Strain effects on kinematic pile bending in layered soil. *Soil Dynamics and Earthquake Engineering*, Vol. 49, pp. 231-242.
- Simo, JC, and Hughes, TJR (1998). *Computational inelasticity*, Springer, New York.
- Skempton, AW (1951). The bearing capacity of clays, *Proceedings of the Building Research Congress*, Division 1, Part 3, London, pp. 180-189.
- Stewart, JP (1996). *An empirical evaluation of soil-structure interaction effects on the seismic response of structures*. Ph.D. Dissertation, Univ. of California, Berkeley.
- Stewart, JP, and Stewart, AF (1997). *Analysis of soil-structure interaction effects on building response from earthquake strong motion recordings at 58 sites*. Rpt. No. UCB/EERC 97/01, Earthquake Engineering Research Center, Univ. of California, Berkeley, Calif., 742 p.
- Stewart, JP, Fenves, GL, and Seed, RB (1999). Seismic soil-structure interaction in buildings. I: Analytical methods. *Journal of Geotechnical and Geoenvironmental Engineering*, 125(1), 26-37.
- Stewart, JP, Seed, RB, and Fenves, GL (1999). Seismic soil-structure interaction in buildings. II: Empirical findings. *Journal of Geotechnical and Geoenvironmental Engineering*, 125(1), 38-48.

- Stewart, JP, Fenves, GL, and Seed, RB (2000). Closure to discussion by MD Trifunac on seismic soil-structure interaction in buildings, I: Analytical methods, and II: Empirical findings. *Journal of Geotechnical and Geoenvironmental Engineering*, 126(7), 671-672.
- Syngros, C. (2004). Seismic response of piles and pile-supported bridge piers evaluated through case histories, Ph.D. thesis, Civil Engineering Dept., City University of New York, NY.
- Tajimi, H. (1969). Dynamic analysis of structure embedded in elastic stratum. *Proceedings, 4th World Conference on Earthquake Engineering*, Santiago, Vol. III, pp. A-6 53-69.
- Tazoh, T., Shimizu, K. & Wakahara, T. (1987). Seismic observations and analysis of grouped piles. *Proceedings, Dynamic Response of Pile Foundations—Experiment, Analysis and Observation*, ASCE Geotechnical Special Publication No. 11, pp. 1-21.
- Terzaghi, K, and Peck, RB (1948). *Soil mechanics in engineering practice*, John Wiley & Sons, Inc., New York, N.Y.
- Timoshenko, S. (1948). *Strength of materials, part II, advanced theory and problems*, second edition. Van Nostrand, New York.
- Tokimatsu, K., Suzuki, H., and Sato, M. (2005). Effects of inertial and kinematic interaction on seismic behavior of pile with embedded foundation. *Soil Dynamics and Earthquake Engineering*, 25, 753-762.
- Trochanis, AM, Bielak, J., and Christiano, P. (1991). Three-dimensional nonlinear study of piles. *Journal of Geotechnical Engineering*, 117(3), 429-447.
- Vaziri, H. and Han, Y. (1992). Dynamic response of pile groups under lateral loading. *Soil Dynamic and Earthquake Engineering*, 11, 87-99.
- Veletsos, AS, and Prasad, AM (1988). *Seismic interaction of structures and soils: Stochastic approach*. Technical Report NCEER-88-021, State University of New York, Buffalo, N.Y.
- Veletsos, AS, Prasad, AM, and Wu, WH (1997). Transfer functions for rigid rectangular foundations. *Earthquake Engineering and Structural Dynamics*, 26(1), 87-102.
- Vesic, AS (1961). Bending of beams resting on isotropic elastic solids. *Journal of Engineering Mechanics Division, ASCE*. 87(2), 35-53.
- Vesic, AS (1977). *Design of pile foundations*. National Cooperative Highway Research Program Synthesis of Highway Practice NCHRP 42, Transportation Research Board, Washing, D.C.

- Vijayvergiya, VN (1977). Load-movement characteristics of piles, *Proceedings, Ports '77: 4th Annual Symposium of the Waterway, Port, Coastal, and Ocean Division*, Long Beach, CA, pp. 269-284.
- Vucetic, M. and Dobry, R., (1991). Effect of soil plasticity on cyclic response. *Journal of Geotechnical Engineering*, 117(1), 89-107.
- Wang, S, Kutter, BL, Wilson, DW, Boulanger, RW, and Abbas, A. (1998). Nonlinear seismic soil-pile structure interaction. *Earthquake Spectra*, 14(2), 377-396.
- White, LB, and Boashash, B. (1990). Cross spectral analysis of nonstationary processes. *IEEE Transaction on Information Theory*, 36(4), 830-835.
- Whitman, R. V. (1970). Soil-structure interaction. Chapter in *Seismic Design for Nuclear Power Plants*, Edited by Robert J. Hanson, The M.I.T. Press, Cambridge, Mass.
- Winkler, E. (1867). *Die Lehre von der Elastizitat und Festigkeit*. Dominicus, Prague (in German).
- Wolf, JP (1985). *Dynamic soil-structure interaction*. Prentice-Hall, Inc., Englewood Cliffs, N.J.
- Wu, G., and Finn, L (1997a). Dynamic elastic analysis of pile foundations using finite element method in the frequency domain. *Canadian Geotechnical Journal*, 34, 34-43.
- Wu, G., and Finn, L (1997b). Dynamic nonlinear analysis of pile foundations using finite element method in the time domain. *Canadian Geotechnical Journal*, 34, 44-52.
- Yee, E., Stewart, JP, and Tokimatsu, K. (2013). Elastic and large-strain nonlinear seismic site response from analysis of vertical array recordings. *Journal of Geotechnical and Geoenvironmental Engineering*, 139 (10), 1789-1801.